ISSN 2188-5001

MATERIALS DESIGN AND
CHARACTERIZATION LABORATORY
SUPERCOMPUTER CENTER

ACTIVITY REPORT
2021

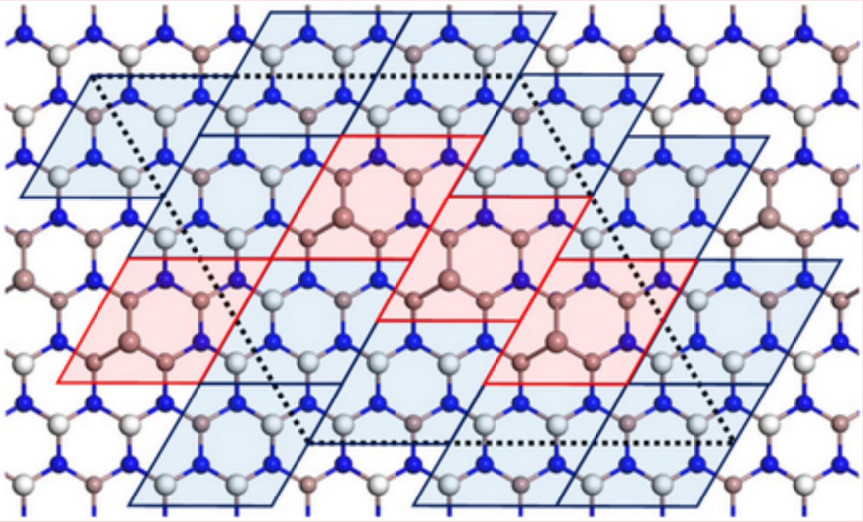

THE UNIVERSITY OF TOKYO

Materials Design and Characterization Laboratory (MDCL)

The MDCL was established as the third research facility of the Institute for Solid State Physics (ISSP) when the latter was reorganized in May 1996. Its aim is to promote material science with an emphasis on the “DSC cycle”, where DSC stands for design, synthesis and characterization, three processes for developing new materials.

The MDCL consists of two sections, Materials Design (MD) section and Materials Synthesis and Characterization (MSC) section. The Supercomputer Center of the ISSP (SCC-ISSP) is placed in the MD section, while in the MSC section there are seven laboratories for joint use; Materials Synthesis Laboratory, Chemical Analysis Laboratory, X-ray Diffraction Laboratory, Electron Microscope Laboratory, Electromagnetic Measurement Laboratory, Spectroscopy Laboratory, and High-Pressure Synthesis Laboratory.

Almost all the facilities of the MDCL are open to scientists in Japan through the User Programs conducted by two steering committees of the MDCL. One is the steering committee of the SCC-ISSP, under which the Supercomputer Project Advisory Committee is placed for reviewing proposals. The other is the steering committee of the MSC facilities. More than half of the members of these committees are from the outside of ISSP.

COVER FIGURE

Stable 6x6 surface structure obtained by Bayesian optimization. Brown, blue and white atoms correspond to Ga, N and H, respectively.
See Page 42–44, A. Oshiyama, ”Clarification of Microscopic Mechanisms of Semiconductor Epitaxial Growth and Device-Interface Formation by Large-Scale Quantum-Theory-Based Computations”.

PREFACE

The Supercomputer Center (SCC) is a part of the Materials Design and Characterization Laboratory (MDCL) of ISSP. Its mission is to serve the whole community of computational condensed-matter physics of Japan providing it with high performance computing environment. In particular, the SCC selectively promotes and supports large-scale computations. For this purpose, the SCC invites proposals for supercomputer-aided research projects and hosts the Steering Committee, as mentioned below, that evaluates the proposals.

The ISSP supercomputer system consists of two subsystems: System B, which was last replaced in Oct. 2020, is intended for larger total computational power and has more nodes with relatively loose connections whereas System C is intended for higher communication speed among nodes. System B (ohtaka) consists of 1680 CPU nodes of AMD EPYC 7702 (64 cores) and 8 FAT nodes of Intel Xeon Platinum 8280 (28 cores) with total theoretical performance of 6.881 PFlops. System C (enaga) consists of 252 nodes of HPE SGI 8600 with 0.77 PFLOPS, which stopped operation in Dec. 2021 for replacement. The new machine (kugui), which consists of 128 nodes of AMD EPYC 7763 (128 cores) and 8 nodes of AMD EPYC 7763 (64 cores) with total theoretical performance of 0.973 PFLOPS, will start operation in June 2022.

In addition to the hardware administration, the SCC puts increasing effort on the software support. Since 2015, the SCC has been conducting “Project for advancement of software usability in materials science (PASUMS).” In this project, for enhancing the usability of the ISSP supercomputer system, we conduct several software-advancement activities: developing new application software that runs efficiently on the ISSP supercomputer system, adding new functions to existing codes, help releasing private codes for public use, creating/improving manuals for public codes, etc. Three target programs were selected in fiscal year 2021 and developed or enhanced the ustablity of software were released as (1) ESM-RISM (proposal made by M. Otani (AIST)), and (2) 2DMAT (proposal made by T. Hoshi (Tottori Univ.)). In 2021, we also started the data repository service for storing results of numerical calculation and enhancing their reusability.

All staff members of university faculties or public research institutes in Japan are invited to propose research projects (called User Program). The proposals are evaluated by the Steering Committee of SCC. Pre-reviewing is done by the Supercomputer Project Advisory Committee. In fiscal year 2021, totally 321 projects were approved including the ones under the framework of Supercomputing Consortium for Computational Materials Science (SCCMS), which specially supports FUGAKU and other major projects in computational materials science.

The research projects are roughly classified into the following three (the number of projects approved):

First-Principles Calculation of Materials Properties (142)
Strongly Correlated Quantum Systems (29)
Cooperative Phenomena in Complex, Macroscopic Systems (128)

In all the three categories, most proposals involve both methodology and applications. The results of the projects are reported in 'Activity Report 2021' of the SCC. Every year 3-4 projects are selected for “invited papers” and published at the beginning of the Activity Report. In the Activity Report 2021, the following three invited papers are included:

"Theory, practice, and application of the van der Waals density functional",
Ikutaro HAMADA (Osaka Univ.)

"Development of permanent magnet materials—from the view point of first-principles calculation”,
Hisazumi AKAI (ISSP) and Shinji TSUNEYUKI (Univ. Tokyo)

"Development of Bayesian optimization tool and its applications in materials science",
Ryo TAMURA (NIMS), Yuichi MOTOYAMA (ISSP), and Kazuyoshi YOSHIMI (ISSP)

June 2, 2022

Naoki Kawashima
(Chairman of the steering committee, SCC, ISSP)

CONTENTS

PREFACE

1 OUTLINE

1.1 Supercomputer System

In School year 2021 (SY 2021), the ISSP supercomputer center provided users with System B - Dell PowerEdge C6525/R940 system named "ohtaka" and System C - HPE SGI 8600 system named "enaga". System B is a massively-parallel supercomputer with two types of compute nodes: 8 "Fat" nodes and 1680 "CPU" nodes. "Fat" nodes are each comprised of four Intel Xeon Platinum 8280 CPUs (28 cores/CPU) and 3 TB of memory per node. "CPU" nodes have two AMD EPYC 7702 CPUs (64 cores/CPU) and 256 GB of memory per node. System B achieves about 6.881 PFLOPS in theoretical peak performance with high power efficiency. The subsystem comprised of only CPU nodes ranks 87st in the Nov. 2020 Top 500 List, which is a ranking based on total performance measured by the HPL benchmark. The compute nodes communicate to each other through HDR100 Infiniband and are connected in fat tree topology. SY 2021 was the second year of the operation of the current System B. System C is a massively-parallel supercomputer with 252 "CPU" nodes, which have two Intel Xeon Gold 6148 CPUs (20 cores/CPU) and 192 GB of memory. System C achieves 774 TFLOPS in theoretical peak performance. SY 2021 was the last year of the operation of the current System C. For further details, please contact ISSP Supercomputer Center (SCC-ISSP).

[Correspondence: center@issp.u-tokyo.ac.jp]

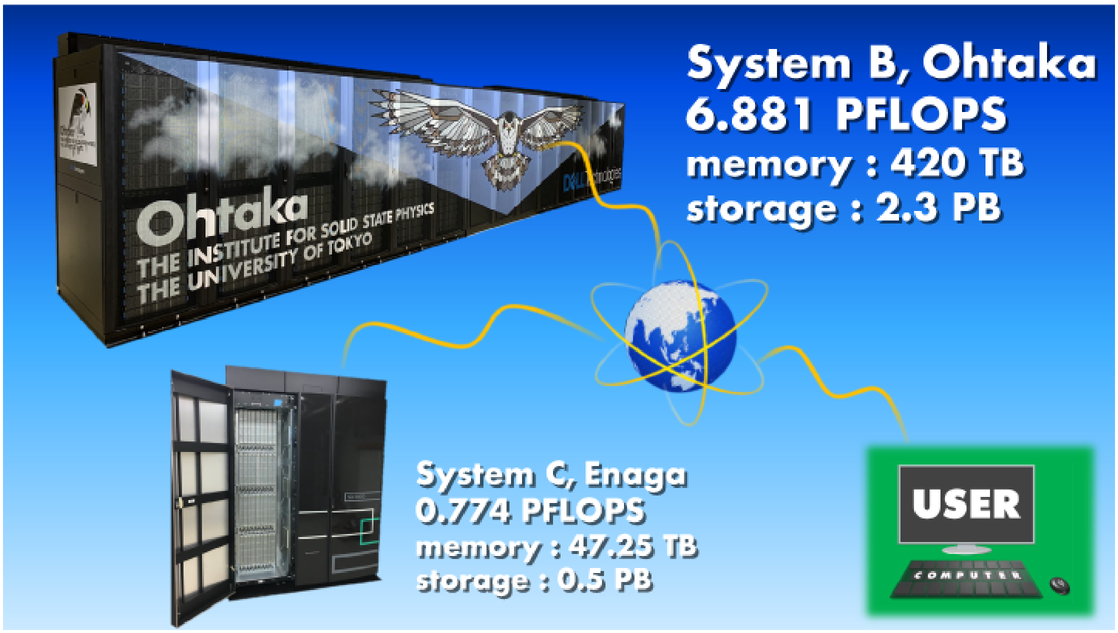

Figure 1: Supercomputer System at the SCC-ISSP

1.2 Project Proposals

The ISSP supercomputer system provides computation resources for scientists working on condensed matter sciences in Japan. All scientific staff members (including post-docs) at universities or public research institutes in Japan can submit proposals for projects related to research activities on materials and condensed matter sciences. These proposals are peer-reviewed by the Advisory Committee members (see Sec. 1.3), and then the computation resources are allocated based on the review reports. The leader of an approved project can set up user accounts for collaborators. Other types of scientists, including graduate students, may also be added. Proposal submissions, peer-review processes, and user registration are all managed via a web system.

The computation resources are distributed in a unit called “point”, determined as a function of available CPU utilization time and consumed disk resources. There were calls for six classes of research projects in SY 2021. The number of projects and the total number of points that were applied for and approved in this school year are listed in Table 1.

- Class A is for trial use by new users; proposals for Class A projects are accepted throughout the year.
- Proposals for projects in Classes B (small), C (mid-size), E (large-scale), and S (exceptional) can be submitted twice a year. Approved projects in Classes A, B, C, and E continue to the end of the school year.
- In Class D, projects can be proposed on rapidly-developing studies that need to perform urgent and relatively large calculations. An approved project continues for 6 months from its approval.
- Class S is for projects that are considered extremely important for the field of condensed matter physics and requires extremely large-scale computation. The project may be carried out either by one research group or cooperatively by several investigators at different institutions. A project of this class should be applied with at least 10,000 points; there is no maximum. We require group leaders applying for Class S to give a presentation on the proposal to the Steering Committee of the SCC-ISSP. Class S projects are carried out within one year from its approval.
- Project leaders can apply for points so that the points for each system do not exceed the maximum point shown in this table.

In addition, from SY 2016, ISSP Supercomputer has been providing 20% of its computational resources for Supercomputing Consortium for Computational Materials Science (SCCMS), which aims at advancing parallel computations in condensed matter, molecular, and materials sciences on the 10-PFlops K Computer and the exascale post-K project. From SY 2020, about 10% of the computational resources have been provided for SCCMS. Computational resources have also been allotted to Computational Materials Design (CMD) workshops, as well as CCMS hands-on workshops.

Table 1: Classes of research projects in SY 2021. Total points listed in this table are rounded. In Class D, we collect information about the projects ended in each semester. Note that the maximum points of Classes A and D in the first semester had been changed to those listed in the second semester since May 2021.

First semester (Apr.-Sep.)

Class	Maximum Points		Application	# of Proj.	Total points			
					Applied		Approved	
	Sys–B	Sys–C			Sys–B	Sys–C	Sys–B	Sys–C
A	100	50	any time	12	1.2k	0.5k	1.2k	0.5k
B	800	100	twice a year	58	40.9k	4.5k	23.2k	3.4k
C	8k	1k	twice a year	116	725.7k	71.1k	372.6k	50.8k
D	10k	1k	any time	0	0	0	0	0
E	24k	3k	twice a year	8	187.0k	24.0k	110.0k	17.3k
S	–	–	twice a year	0	0	0	0	0
SCCMS				11	26.1k	5.0k	26.1k	5.0k
Total				205	980.9k	105.1k	533.1k	77.0k

Second semester (Oct.-Mar.)

Class	Maximum Points		Application	# of Proj.	Total points			
					Applied		Approved	
	Sys–B	Sys–C			Sys–B	Sys–C	Sys–B	Sys–C
A	100	40	any time	5	0.5k	0.2k	0.5k	0.2k
B	800	40	twice a year	38	27.2k	0.8k	14.7k	0.7k
C	8k	400	twice a year	53	327.6k	8.5k	159.8k	6.6k
D	10k	400	any time	3	16.0k	0	13.5k	0
E	24k	1.2k	twice a year	6	136.0k	7.2k	83.0k	5.5k
S	–	–	twice a year	0	0	0	0	0
SCCMS				11	28.0k	2.4k	28.0k	2.4k
Total				116	535.2k	19.1k	299.5k	15.3k

1.3 Committees

In order to fairly manage the projects and to smoothly determine the system operation policies, the Materials Design and Characterization Laboratory (MDCL) of the ISSP has organized the Steering Committee of the MDCL and the Steering Committee of the SCC-ISSP, under which the Supercomputer Project Advisory Committee (SPAC) is formed to review proposals. The members of the committees in SY 2021 were as follows:

Steering Committee of the MDCL

KAWASHIMA, Naoki	ISSP (Chair person)
HIROI, Zenji	ISSP
OZAKI, Taisuke	ISSP
NOGUCHI, Hiroshi	ISSP
UWATOKO, Yoshiya	ISSP
SUGINO, Osamu	ISSP
KUBO, Momoji	Tohoku Univ.
ONO, Tomoya	Kobe Univ.
YAMAURA, Jun-ichi	Tokyo Tech.
TAKAHASHI, Hiroki	Nihon Univ.
MOTOME, Yukitoshi	Univ. of Tokyo
HOSHI, Takeo	Tottori Univ.
ISHIWATA, Shintaro	Osaka Univ.
HASEGAWA, Masashi	Nagoya Univ.
NAKATSUJI, Satoru	ISSP

Steering Committee of the SCC-ISSP

KAWASHIMA, Naoki	ISSP (Chair person)
NOGUCHI, Hiroshi	ISSP
OZAKI, Taisuke	ISSP
SUGINO, Osamu	ISSP
TSUNETSUGU, Hirokazu	ISSP
KATO, Takeo	ISSP
YAMASHITA, Minoru	ISSP
MORITA, Satoshi	ISSP
HIGUCHI, Yuji	ISSP
FUKUDA, Masahiro	ISSP
IDO, Kota	ISSP
KAWAMURA, Mitsuaki	ISSP
NAKAJIMA, Kengo	Univ. of Tokyo
HATANO, Naomichi	Univ. of Tokyo
MOTOME, Yukitoshi	Univ. of Tokyo
ONO, Tomoya	Kobe Univ.

TODO, Synge	Univ. of Tokyo
KUBO, Momoji	Tohoku Univ.
OBA, Fumiyasu	Tokyo Tech.
WATANABE, Hiroshi	Keio Univ.
YOSHINO, Hajime	Osaka Univ.
OKUMURA, Hisashi	NINS-RSCS
HOSHI, Takeo	Tottori Univ.
YOSHIMI, Kazuyoshi	ISSP
YATA, Hiroyuki	ISSP
FUKUDA, Takaki	ISSP

Supercomputer Project Advisory Committee

KAWASHIMA, Naoki	ISSP (Chair person)
OZAKI, Taisuke	ISSP
NOGUCHI, Hiroshi	ISSP
SUGINO, Osamu	ISSP
TSUNETSUGU, Hirokazu	ISSP
YAMASHITA, Minoru	ISSP
KATO, Takeo	ISSP
MORITA, Satoshi	ISSP
HIGUCHI, Yuji	ISSP
FUKUDA, Masahiro	ISSP
IDO, Kota	ISSP
KAWAMURA, Mitsuaki	ISSP
NAKAJIMA, Kengo	Univ. of Tokyo
HATANO, Naomichi	Univ. of Tokyo
MOTOME, Yukitoshi	Univ. of Tokyo
ONO, Tomoya	Univ. of Tsukuba
TODO, Synge	Univ. of Tokyo
KUBO, Momoji	Tohoku Univ.
OBA, Fumiyasu	Tokyo Tech.
WATANABE, Hiroshi	Keio Univ.
YOSHINO, Hajime	Osaka Univ.
OKUMURA, Hisashi	NINS-RSCS
HOSHI, Takeo	Tottori Univ.
TSUNEYUKI, Shinji	Univ. of Tokyo
SUZUKI, Takafumi	Univ. of Hyogo
YOSHIMOTO, Yoshihide	Univ. of Tokyo
TOHYAMA, Takami	Tokyo Univ. of Sci.
KITAO, Akio	Tokyo Tech.
ARITA, Ryotaro	Univ. of Tokyo
IKUHARA, Yuichi	Univ. of Tokyo
SHIBATA, Naokazu	Tohoku Univ.
AKAGI, Kazuto	Tohoku Univ.

YANASE, Yoichi	Kyoto Univ.
HATSUGAI, Yasuhiro	Univ. of Tsukuba
OKADA, Susumu	Univ. of Tsukuba
KOBAYASHI, Nobuhiko	Univ. of Tsukuba
NAKAYAMA, Takashi	Chiba Univ.
HOTTA, Takashi	Tokyo Metropolitan Univ.
MATSUKAWA, Hiroshi	Aoyama Gakuin Univ.
YAMAUCHI, Jun	Keio Univ.
HAGITA, Katsumi	National Defense Academy
KONTANI, Hiroshi	Nagoya Univ.
SAITO, Mineo	Kanazawa Univ.
KAWAKAMI, Norio	Kyoto Univ.
YUKAWA, Satoshi	Osaka Univ.
SUGA, Seiichiro	Univ. of Hyogo
TATENO, Masaru	Univ. of Hyogo
YASUDA, Chitoshi	Univ. of the Ryukyus
OGATA, Masao	Univ. of Tokyo
WATANABE, Satoshi	Univ. of Tokyo
HUKUSHIMA, Koji	Univ. of Tokyo
NEMOTO, Koji	Hokkaido Univ.
YABANA, Kazuhiro	Univ. of Tsukuba
FURUKAWA, Nobuo	Aoyama Gakuin Univ.
KUROKI, Kazuhiko	Osaka Univ.
YASUOKA, Kenji	Keio Univ.
TANAKA, Yukio	Nagoya Univ.
MASUBUCHI, Yuichi	Nagoya Univ.
KUSAKABE, Koichi	Osaka Univ.
SHIRAI, Koun	Osaka Univ.
SAKAI, Toru	Univ. of Hyogo
ISHIBASHI, Shoji	AIST
OTANI, Minoru	AIST
TOMITA, Yusuke	Shibaura Inst. Tech.
SHIRAISHI, Kenji	Nagoya Univ.
OGUCHI, Tamio	Osaka Univ.
KAWAKATSU, Toshihiro	Tohoku Univ.
KOBAYASHI, Kazuaki	NIMS
TATEYAMA, Yoshitaka	NIMS
KIM, Kang	Osaka Univ.
OTSUKI, Tomi	Sophia Univ.
MORIKAWA, Yoshitada	Osaka Univ.
ODA, Tatsuki	Kanazawa Univ.
OTSUKI, Junya	Okayama Univ.
KOGA, Akihisa	Tokyo Tech.
SHIMOJO, Fuyuki	Kumamoto Univ.
TAKETSUGU, Tetsuya	Hokkaido Univ.

TSURUTA, Kenji	Okayama Univ.
HAMAGUCHI, Satoshi	Osaka Univ.
NISHIDATE, Kazume	Iwate Univ.
KAGESHIMA, Hiroyuki	Shimane Univ.
ISHII, Fumiyuki	Kanazawa Univ.
TATETSU, Yasutomi	Meio Univ.
YANAGISAWA, Susumu	Univ. of the Ryukyus
SHUDO, Ken-ichi	Yokohama Natl. Univ.
OHMURA, Satoshi	Hiroshima Inst. Tech.
NOGUCHI, Yoshifumi	Shizuoka Univ.
NAKAMURA, Kazuma	Kyushu Inst. Tech.
GOHDA, Yoshihiro	Tokyo Tech.
HAMADA, Ikutaro	Osaka Univ.
RAEBIGER, Hannes	Yokohama Natl. Univ.
KAWARABAYASHI, Tohru	Toho Univ.
KATO, Yusuke	Univ. of Tokyo
NASU, Joji	Tohoku Univ.
HOTTA, Chisa	Univ. of Tokyo
ISOBE, Masaharu	Nagoya Inst. Tech.
HARADA, Ryuhei	Univ. of Tsukuba
TAMURA, Ryo	NIMS
TANAKA, Shu	Keio Univ.
TADA, Tomofumi	Kyushu Univ.

1.4 Staff

The following staff members of the SCC-ISSP usually administrate the ISSP Supercomputer.

KAWASHIMA, Naoki	Professor (Chair person)
NOGUCHI, Hiroshi	Associate Professor
OZAKI, Taisuke	Professor
SUGINO, Osamu	Professor
IDO, Kota	Research Associate
FUKUDA, Masahiro	Research Associate
HIGUCHI, Yuji	Research Associate
KAWAMURA, Mitsuaki	Research Associate
MORITA, Satoshi	Research Associate
YOSHIMI, Kazuyoshi	Project Researcher
MOTOYAMA, Yuichi	Project Researcher
YATA, Hiroyuki	Technical Specialist
FUKUDA, Takaki	Technical Specialist
ARAKI, Shigeyuki	Project Academic Specialist

2 STATISTICS (SCHOOL YEAR 2021)

2.1 System and User Statistics

In the following, we present statistics for operation time taken in the period from April 2021 to March 2022 (SY 2021). In Table 2, we show general statistics of the supercomputer system in SY 2021. The total numbers of compute nodes in System B "ohtaka" and System C "enaga" are 1688 and 252, respectively. Consumed disk points amount to about a few percent of the total consumed points in both System B and System C.

Table 2: Overall statistics of SY 2021

	System B ohtaka	System C enaga
total service time ($\times 10^3$ node·hours)	14396	1601
number of executed jobs	456984	46166
total consumed points ($\times 10^3$ point)	498	30
CPU points ($\times 10^3$ point)	480	29
disk points ($\times 10^3$ point)	18	2
total exec. time ($\times 10^3$ node·hours)	12980	1367
availability	97.34%	96.23%
utilization rate	90.14%	85.47%

In Fig. 2, availabilities, utilization rates, and consumed points in Systems B and C are plotted for each month. Throughout the school year, the availability and the utilization rates were very high : the availability and the utilization rates exceed about 90% and 80% throughout most of the year, respectively.

The user statistics are shown in Fig. 3. The horizontal axis shows the rank of the user/group arranged in the descending order of the execution time (hour × nodes). The execution time of the user/group of the first rank is the longest. The vertical axis shows the sum of the execution time up to the rank. From the saturation points of the graphs, the numbers of "active" users of Systems B and C are around 400 and 100, respectively. The maximum ranks in the graphs correspond to the number of the users/groups that submitted at least one job.

2.2 Queue and Job Statistics

Queue structures of Systems B and C in SY2021 are shown in Tables 3 and 4, respectively. In System B "ohtaka", users can choose from two types of compute nodes; jobs submitted to queues with "cpu" and "fat" at the end of their queue names are submitted to CPU and Fat nodes, respectively, while only CPU nodes are available in System C "enaga". See Sec. 1.1 for a description of each type of compute node. The user then has to choose the queue according to the number

Table 3: Queue structures of System B in SY 2021

System B, ohtaka

queue name	Elapsed time limit (hr)	# of nodes /job	# of nodes /queue	Memory limit (GB)	job points /(node·day)
F1cpu	24	1	600	230/node	1
L1cpu	120	1	300	230/node	1
F4cpu	24	2–4	216	230/node	1
L4cpu	120	2–4	108	230/node	1
F16cpu	24	5–16	288	230/node	1
L16cpu	120	5–16	144	230/node	1
F36cpu	24	17–36	72	230/node	1
L36cpu	120	17–36	36	230/node	1
F72cpu	24	72	576	230/node	1
L72cpu	120	72	288	230/node	1
F144cpu	24	144	432	230/node	1
L144cpu	120	144	144	230/node	1
i8cpu	0.5	1–8	72	230/node	1
F2fat	24	1–2	7	2900/node	4
L2fat	120	1–2	3	2900/node	4
i1fat	0.5	1	1	2900/node	4

of nodes to use and the duration of their calculation jobs. Queue names starting with “F” are for jobs taking 24 hours or less, while those starting with “L” can run much longer up to 120 hours. More nodes are allotted to “F” queues in order to maximize the turnaround time of user jobs. The queue names starting with “i” are used for interactive debugging of user programs and the elapsed time limit is 30 minutes. The number following “F”, “L”, or “i” correspond to the number of nodes that can be used by one user job. Although we do not mention here in detail, to promote utilization of the massively parallel supercomputer, background queues (queue name starting with “B”) for Systems B and C which charge no points for the jobs have also been open.

To prevent overuse of the storage, points are charged also for usage of disk quota in the three systems, as shown in Table 5. Disk points are revised often for optimal usage of the resources by examining usage tendencies each year.

The number of jobs, average waiting time, and total execution time in each queue are shown in Tables 6 and 7. In System B, a large portion of jobs have been executed in “F” queues. The largest amount of the execution time has been consumed in the large-scale “F72cpu” queues for ohtaka, respectively. However, substantial number of jobs were run in every queue, suggesting that a wide variety of user needs are met by this queuing scheme. In most of these queues, the queue settings meet the user’s tendencies in that the waiting times are on the order of the elapsed-time limit.

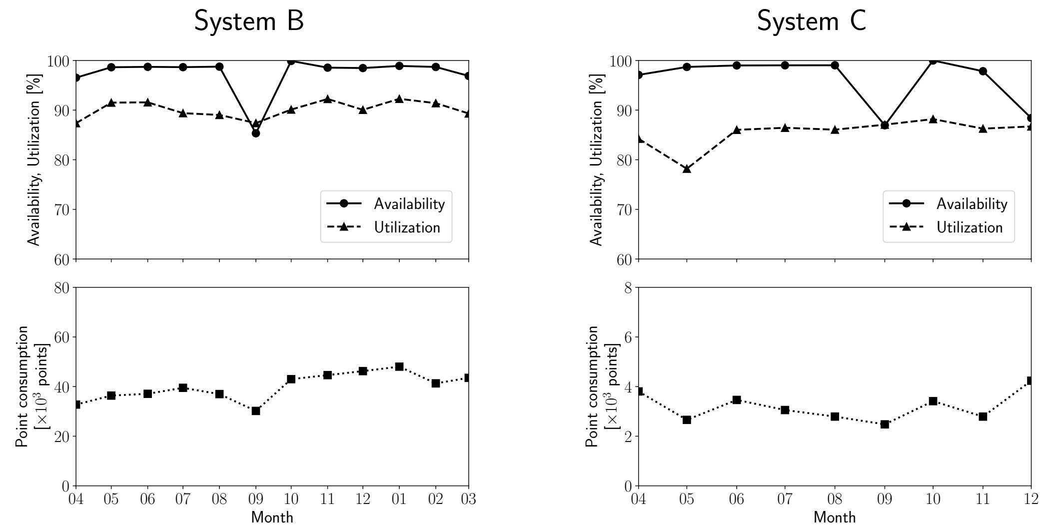

Figure 2: Availabilities, utilization rates and point consumptions of each month during SY 2021.

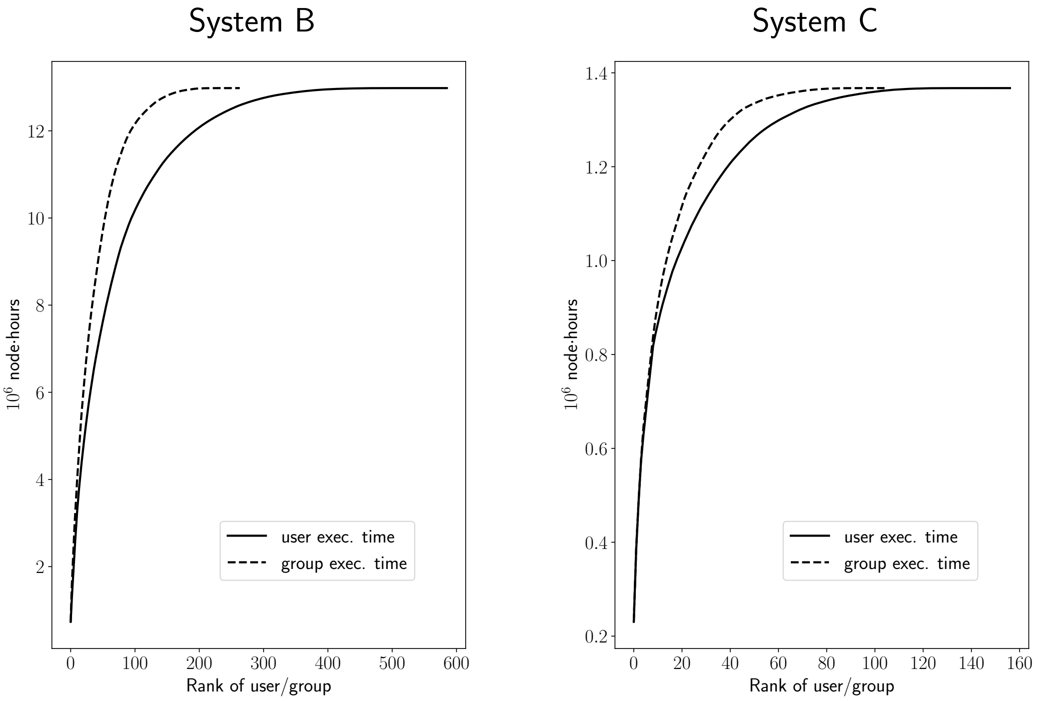

Figure 3: User statistics. The horizontal axis shows the rank of the user/group arranged in the descending order of the execution time (hour×nodes). The vertical axis shows the sum of the execution time up to the rank.

Table 4: Queue structures of System C in SY 2021

System C, enaga

queue name	Elapsed time limit (hr)	# of nodes /job	# of nodes /queue	Memory limit (GB)	job points /(node·day)
F4cpu	24	1–4	54	170/node	1
L4cpu	120	1–4	18	170/node	1
i4cpu	0.5	1–4	18	170/node	1
F9cpu	24	5–9	36	170/node	1
L9cpu	120	5–9	18	170/node	1
F36cpu	24	10–36	144	170/node	18(36)/(# of nodes)*
L36cpu	120	10–36	36	170/node	18(36)/(# of nodes)*

* For F/L36cpu queue, the number of occupied node increases in increments of 18 nodes.

Table 5: Disk points of Systems B and C

		point/day
System B ohtaka	`/home`	$0.001 \times \theta(q - 600)$
	`/work`	$0.0001 \times \theta(q - 6000)$
System C enaga	`/home`	$0.001 \times \theta(q - 150)$
	`/work`	$0.0001 \times \theta(q - 1500)$

* q is denoted in unit of GB.
* $\theta(x)$ is equal to the Heaviside step function $H(x)$ multiplied by x, i.e., $xH(x)$.

2.3 Project for Advancement of Software Usability in Materials Science

From School Year 2015, the supercomputer center (SCC) has started "Project for advancement of software usability in materials science". In this project, for enhancing the usability of the supercomputer system in ISSP, we perform some software-advancement activity such as implementing a new function to an existing code, releasing a private code on Web, writing manuals. Target programs are publicly offered in December and selected in the review by the Steering Committee of SCC. The projects are carried out by the software development team composed of three members in ISSP. In SY 2021, three projects were selected as listed in Table 8.

Table 6: Number of jobs, average waiting time, total execution time, and average number of used nodes per job in each queue of System B.

System B, ohtaka

queue	# of Jobs	Waiting Time (hour)	Exec. Time ($\times 10^3$ node·hour)	# of nodes
F1cpu	211125	16.62	320.55	1.00
L1cpu	10781	60.45	289.72	1.00
F4cpu	73536	11.69	1175.58	2.87
L4cpu	5619	17.66	400.57	2.53
F16cpu	21718	15.21	1505.98	10.18
L16cpu	1621	79.48	663.18	9.93
F36cpu	1633	67.66	315.88	27.74
L36cpu	87	51.37	93.18	21.63
F72cpu	7773	33.00	3494.10	72.00
L72cpu	133	68.15	373.04	72.00
F144cpu	3023	17.02	2062.21	144.00
L144cpu	134	141.08	677.79	144.00
i8cpu	91096	0.09	42.54	3.23
F2fat	3673	28.21	24.77	1.10
L2fat	282	39.31	15.96	1.23
i1fat	522	0.50	0.06	1.00

Table 7: Number of jobs, average waiting time, total execution time, and average number of used nodes per job in each queue of System C.

System C, enaga

queue	# of Jobs	Waiting Time (hour)	Exec. Time ($\times 10^3$ node·hour)	# of nodes
F4cpu	23663	5.24	185.74	1.78
L4cpu	727	50.21	80.59	1.59
i4cpu	7775	0.05	2.64	2.33
F9cpu	1434	6.11	68.23	7.22
L9cpu	77	11.94	22.05	6.68
F36cpu	1551	8.13	301.11	29.58
L36cpu	62	10.02	28.94	20.32

Table 8: List of Project for advancement of software usability in materials science for SY 2021.

Project Proposer	Project Name
Minoru Otani AIST CD-FMat	Improvement of Quantum ESPRESSO implementing the ESM RISM method
Takeo Hoshi Tottori University	Unified platform of experiment-data analysis for 2D material structure

2.4 ISSP Data Repository

From School Year 2021, the supercomputer center (SCC) has started to operate ISSP Data Repository (ISSP-DR) for accumulating and utilizing research data in materials science. GitLab is used as the data management system, and a portal site is provided as a data registration and search system for the registered data. By using ISSP-DR, it is possible to store and publish research data used in papers and datasets useful in the field of condensed matter science. Users of ISSP Supercomputer are welcome to apply for and use ISSP-DR.

Acknowledgments

The staffs would like to thank Prof. Takafumi Suzuki (now at University of Hyogo) for developing WWW-based system (SCM: SuperComputer Management System) for management of project proposals, peer-review reports by the SPAC committee, and user accounts. We also thank Ms. Reiko Iwafune for creating and maintaining a new WWW page of the ISSP Supercomputer Center.

3 RESEARCH REPORTS

3.1 Invited Articles

Theory, practice, and application of the van der Waals density functional

Ikutaro HAMADA
Department of Precision Engineering, Graduate School of Engineering, Osaka University
2-1 Yamadaoka, Suita, Osaka 565-0871, Japan

Abstract

The van der Waals density functional is a class of the density functional, which enables the description of the dispersion forces within the framework of density functional theory. In this article, theory and practice of the van der Waals density functional are reviewed, and applicability of a high-accuracy van der Waals density functional to various systems is demonstrated.

1 Introduction

Density functional theory (DFT) [1, 2] within the local density (LDA) and semilocal (GGA) approximations has been proven to be accurate in describing covalent, ionic, and metallic bondings, but has also been known to be unable to describe the dispersion forces (or often referred to as the van der Waals forces) [3] properly. This is because the dispersion forces originate from the instantaneous dipole-induced dipole interaction due to the electron fluctuation or the dynamic and nonlocal electron correlation, which are inherently missing in LDA and GGA. Wave function based theory and many body perturbation theory are shown to describe the dispersion interaction very accurately, but the computational cost is prohibitively large, hindering their application to complex systems, such as surfaces and interfaces.

There have been several proposals to correct the missing dispersion forces by adding the term proportional to $1/r^6$ (and higher-order terms) to the total energy within semilocal DFT, where r is the interatomic or interfragment distance. This type of approach was initiated in the field of the quantum chemistry (QC) [4], and has been established [5] and improved over the years by introducing accurate dispersion coefficients [6] and damping functions [7], as well as the environmental effects on the dispersion coefficients through the local electron density [8, 9] or coordination numbers [6]. Furthermore, accuracy of such pair-wise correction methods have been improved by introducing the three-body term[6] or the many-body dispersion[10]. See Refs. [11, 12, 13] for recent reviews.

The van der Waals density functional (vdW-DF) [14, 15, 16, 17, 18] is a versatile method that allows one to describe different interactions including the dispersion forces within the DFT framework. It is grounded on the electron gas tradition and the many-body perturbation theory as other constraint-based exchange-correlation (XC) functionals, and formally has no empirical or fitting parameters to reproduce the results of experiments or accurate theoretical calculations. The physical foundation of vdW-DF has been established [19], and theoretical and algorithmic improvements make it a method of choice in theoretical studies of materials and molecules.

In this article, I give a brief overview of the theory of vdW-DF and discuss a technical issue related to the use of pseudopotentials with applications. The Hartree atomic unit is used throughout unless otherwise specified.

2 Method

2.1 Theory

The XC energy, which is responsible for the quantum-mechanical electron-electron interaction, can be expressed exactly by using the adiabatic connection fluctuation dissipation theorem (ACFDT) [20, 21] as

$$E_{\mathrm{xc}} = -\int_0^1 \frac{d\lambda}{\lambda} \int_0^\infty \frac{du}{2\pi} \mathrm{tr}\left[\chi^\lambda(iu)V^\lambda\right] - E_{\mathrm{self}}, \tag{1}$$

where λ is the adiabatic parameter, which scales the electron-electron Coulomb interaction as $V^\lambda(\mathbf{r},\mathbf{r}') = \lambda/|\mathbf{r}-\mathbf{r}'|$, $\chi^\lambda(iu)$ is the reducible density-density response function at the adiabatic parameter λ and imaginary frequency $u = -i\omega$, and E_{self} is the electron-electorn self-energy defined by $E_{\mathrm{self}} = \mathrm{tr}\,[nV]$ with $V = V^{\lambda=1}$. Here, the trace is defined as $\mathrm{tr}[AB] = \iint d\mathbf{r}d\mathbf{r}' A(\mathbf{r},\mathbf{r}')B(\mathbf{r}',\mathbf{r})$ for arbitrary operators $\hat{A}$ and $\hat{B}$. $\chi^\lambda(\omega)$ is defined by $\delta n(\omega) = \chi^\lambda(\omega)\delta v_{\mathrm{ext}}(\omega)$, where $\delta n(\omega)$ and $\delta v_{\mathrm{ext}}(\omega)$ are the induced electron density and the external potential at the frequency ω, respectively.

The vdW-DF is constructed based on ACFDT as follows: E_{xc} may be split as

$$E_{\mathrm{xc}} = E^0_{\mathrm{xc}} + E^{\mathrm{nl}}_{\mathrm{c}}, \tag{2}$$

where E^0_{xc} and $E^{\mathrm{nl}}_{\mathrm{c}}$ are the semilocal exchange-correlation and the nonlocal correlation energy functionals, respectively, and in vdW-DF, a tractable form of $E^{\mathrm{nl}}_{\mathrm{c}}$ has been developed based on several physical constraints.

We first introduce $\tilde{\chi}^\lambda$, which is defined by $\delta n(\omega) = \tilde{\chi}^\lambda(\omega)\delta V^\lambda_{\mathrm{scr}}(\omega)$ with $\delta V^\lambda_{\mathrm{scr}}(\omega)$ being the screened potential. $\chi^\lambda(\omega)$ and $\tilde{\chi}^\lambda(\omega)$ are related via the Dyson-like equation $\chi^\lambda = \tilde{\chi}^\lambda + \tilde{\chi}^\lambda V^\lambda \chi^\lambda$. Then, the full-potential approximation (FPA) is introduced, which sets $\tilde{\chi}^\lambda = \tilde{\chi}^{\lambda=1}$ and is exact at the van der Waals asymptote ($|\mathbf{r}-\mathbf{r}'| \to \infty$). This enables the analytic integration over λ and leads to E_{xc} in FPA as

$$E_{\mathrm{xc}} = \int_0^\infty \frac{du}{2\pi} \mathrm{tr}\left\{\ln\left[1 - \tilde{\chi}^{\lambda=1}(iu)V\right]\right\} - E_{\mathrm{self}}. \tag{3}$$

This expression has a formal similarity with that obtained within the random phase approximation (RPA):

$$E_{\mathrm{xc}} = \int_0^\infty \frac{du}{2\pi} \mathrm{tr}\left\{\ln\left[1 - \chi^0(iu)V\right]\right\} - E_{\mathrm{self}}, \tag{4}$$

where χ^0 is the irreducible density-density response function, which is connected to χ^λ via a Dyson equation $\chi^\lambda = \chi^0 + \chi^0 V^\lambda \chi^\lambda$ within RPA. E_{xc} within FPA can also be expressed as

$$E_{\mathrm{xc}} = \int_0^\infty \frac{du}{2\pi} \mathrm{tr}\left\{\ln\left[\nabla \cdot \varepsilon(iu)\nabla G\right]\right\} - E_{\mathrm{self}}, \tag{5}$$

where ε is the dielectric function and G is the Coulomb Green's function, i.e., $G = -4\pi V$.

To extract $E^{\mathrm{nl}}_{\mathrm{c}}$, E^0_{xc} is approximated with that of homogeneous electron gas within FPA, which is also called the internal XC energy, as

$$E^{\mathrm{in}}_{\mathrm{xc}} = \int_0^\infty \frac{du}{2\pi} \mathrm{tr}\left\{\ln\left[\varepsilon(iu)\right]\right\} - E_{\mathrm{self}}, \tag{6}$$

to obtain

$$E^{\mathrm{nl}}_{\mathrm{c}} = \int_0^\infty \frac{du}{2\pi} \mathrm{tr}\left\{\ln\left[\nabla \cdot \varepsilon(iu)\nabla G\right] - \ln\left[\varepsilon(iu)\right]\right\}. \tag{7}$$

It is apparent that by construction, $E^{\mathrm{nl}}_{\mathrm{c}}$ vanishes in the uniform electron-gas limit.

The thus obtained $E^{\mathrm{nl}}_{\mathrm{c}}$ is expanded in terms of a response function $S = \ln\varepsilon \approx 1 - \varepsilon^{-1}$ up to the second order as

$$E^{\mathrm{nl}}_{\mathrm{c}} = \int_0^\infty \frac{du}{4\pi} \mathrm{tr}\left\{S^2(iu) - \left[\nabla S(iu) \cdot \nabla G\right]^2\right\} \tag{8}$$

and in the plane-wave representation as

$$E^{\mathrm{nl}}_{\mathrm{c}} = \int_0^\infty \frac{du}{2\pi} \int \frac{d\mathbf{q}}{(2\pi)^3} \int \frac{d\mathbf{q}'}{(2\pi)^3} \left[1 - \left(\hat{q}\cdot\hat{q}'\right)^2\right] \times S_{\mathbf{q},\mathbf{q}'}(iu) S_{\mathbf{q}',\mathbf{q}}(iu), \tag{9}$$

where $\hat{q} = \mathbf{q}/|\mathbf{q}|$ and

$$\begin{aligned} S(\omega) &= S(\mathbf{r},\mathbf{r}',\omega) \\ &= \int \frac{d\mathbf{q}}{(2\pi)^3} \int \frac{d\mathbf{q}'}{(2\pi)^3} e^{-i\mathbf{q}\cdot\mathbf{r}} S_{\mathbf{q},\mathbf{q}'}(\omega) e^{i\mathbf{q}'\cdot\mathbf{r}'} \end{aligned} \tag{10}$$

This $E^{\mathrm{nl}}_{\mathrm{c}}$ is made tractable by applying the plasmon-pole approximation to $S_{\mathbf{q},\mathbf{q}'}(\omega)$, which is expressed as

$S_{\mathbf{q},\mathbf{q}'}(\omega) = \frac{1}{2}\left[\tilde{S}_{\mathbf{q},\mathbf{q}'}(\omega) + \tilde{S}_{-\mathbf{q},-\mathbf{q}'}(\omega)\right]$ and

$$\tilde{S}_{\mathbf{q},\mathbf{q}'}(\omega) = \int d\mathbf{r} e^{-i(\mathbf{q}-\mathbf{q}')\cdot\mathbf{r}} \times \frac{\omega_{\mathrm{p}}(\mathbf{r})}{[\omega + \omega_{\mathbf{q}}(\mathbf{r})]\left[-\omega + \omega_{\mathbf{q}'}(\mathbf{r})\right]}. \tag{11}$$

Here, $\omega_{\mathrm{p}}(\mathbf{r}) = 4\pi n(\mathbf{r})$ is the plasma frequency, where $n(\mathbf{r})$ is the electron density, and $\omega_{\mathbf{q}}(\mathbf{r})$ is the plasmon dispersion. The specific form of the response function S has been determined to satisfy the following constraints: (i) the time-reversal symmetry, (ii) the f-sum rule, (iii) cancellation of the self-energy, and (iv) charge conservation.

By writing the internal XC energy as

$$E_{\mathrm{xc}}^{\mathrm{in}} = \int d\mathbf{r}\epsilon_{\mathrm{xc}}^{\mathrm{in}}(\mathbf{r})n(\mathbf{r}), \tag{12}$$

the internal XC energy per electron $\epsilon_{\mathrm{xc}}^{\mathrm{in}}$ reads

$$\epsilon_{\mathrm{xc}}^{\mathrm{in}}(\mathbf{r}) = \pi \int \frac{d\mathbf{q}}{(2\pi)^3}\left[\frac{1}{\omega_{\mathbf{q}}(\mathbf{r})} - \frac{2}{q^2}\right], \tag{13}$$

where $q = |\mathbf{q}|$ and the second term in the right-hand side is obtained by evaluating the self-energy term explicitly. The local plasmon dispersion is modeled by

$$\omega_{\mathbf{q}}(\mathbf{r}) = \frac{q^2}{2h[q/q_0(\mathbf{r})]} \tag{14}$$

with h being the switching function which controls the behavior of the plasmon depending on the wave vector and $q_0(\mathbf{r})$, an inverse length scale which depends on the electron density and its gradient $|\nabla n(\mathbf{r})|$. The functional form of h is determined in such a way that $\omega_{\mathbf{q}}(\mathbf{r})$ satisfies the small- and large-q cases (see below). By imposing

$$\int_0^\infty dy\,[h(y) - 1] = \frac{3}{4}, \tag{15}$$

q_0 is related to $\epsilon_{\mathrm{xc}}^{\mathrm{in}}$ as

$$\epsilon_{\mathrm{xc}}^{\mathrm{in}}(\mathbf{r}) = -\frac{3}{4\pi}q_0(\mathbf{r}). \tag{16}$$

In vdW-DF, $\epsilon_{\mathrm{xc}}^{\mathrm{in}}$ is made to be the GGA exchange plus LDA correlation functionals as

$$\epsilon_{\mathrm{xc}}^{\mathrm{in}}(\mathbf{r}) = F_{\mathrm{x}}^{\mathrm{in}}(s)\epsilon_{\mathrm{x}}^{\mathrm{LDA}}(\mathbf{r}) + \epsilon_{\mathrm{c}}^{\mathrm{LDA}}, \tag{17}$$

with the GGA exchange enhancement factor for the internal XC functional given by

$$F_{\mathrm{x}}^{\mathrm{in}}(s) = 1 - \frac{Z_{ab}}{9}s^2, \tag{18}$$

where $\epsilon_{\mathrm{x}}^{\mathrm{LDA}} = -3/4\pi k_{\mathrm{F}}$ with $k_{\mathrm{F}} = (3\pi^2 n)^{1/3}$ and $s = |\nabla n|/k_{\mathrm{F}}n$. By this choice, q_0 can be interpreted as k_{F} modulated by the energy ratio $\epsilon_{\mathrm{xc}}^{\mathrm{in}}/\epsilon_{\mathrm{x}}^{\mathrm{LDA}}$. In the first version of vdW-DF (vdW-DF1), $Z_{ab} = -0.8491$ based on the second-order gradient expansion for the slowly varying electron gas [22, 23], while in the second version of vdW-DF (vdW-DF2), $Z_{ab} = -1.887$ based on the second-order large-N expansion for the neutral atom [17].

The switching function h for the plasmon dispersion is determined to satisfy Eq. (15) and the following constraints. (i) $h(y) \approx \gamma y^2 + \cdots$ in the small-y limit, where γ is an arbitrary constant to ensure $h(0) = 0$, which corresponds to the charge conservation of the spherical XC hole model of the internal XC energy. (ii) $h(y) \to 1$ in the large-y limit, which corresponds to $\omega_{\mathbf{q}} \to q^2/2$ in the large q-limit. This constraint ensures the cancellation of the divergent term of E_{self} in the $q \to 0$ limit in $\epsilon_{\mathrm{xc}}^{\mathrm{in}}$. In Refs. [15, 17], the following form for h was used

$$h(y) = 1 - \exp(-\gamma y^2) \tag{19}$$

with $\gamma = 4\pi/9$, implying that the Gaussian form of the XC hole is used in $\epsilon_{\mathrm{xc}}^{\mathrm{in}}$ [19]. There is a freedom in the functional form of h and it is not limited to Eq. (19). Indeed, Berland *et al.* [24] proposed a functional form, which can improve the asymptotic behavior (and the so-called C_6 coefficient) of vdW-DF . To improve the accuracy of $E_{\mathrm{c}}^{\mathrm{nl}}$ as a part of the development of the third version of vdW-DF (vdW-DF3), Chakraborty *et al.* [25] proposed the following functional form

$$h(y) = 1 - \frac{1}{1 + \gamma y^2 + \gamma^2 y^4 + \alpha y^8}. \tag{20}$$

See Table 1 in Ref. [25] for the parameters γ and α. Note however, in the development of vdW-DF3, parameters in the functionals were optimized to the reference high-accuracy QC results of a large molecular data set. These parameters may vary when a plane-wave pseudopotential program is used in the optimization, depending on the pseudopotentials used.

After tedious but straightfoward calculations, one arrives at the following form of the nonlocal correlation functional

$$E_{\mathrm{c}}^{\mathrm{nl}} = \frac{1}{2}\iint d\mathrm{r}d\mathrm{r}' n(\mathbf{r})\phi(d,d')n(\mathbf{r}'), \tag{21}$$

where $d = q_0(\mathbf{r})|\mathbf{r}-\mathbf{r}'|$ and $d' = q_0(\mathbf{r}')|\mathbf{r}-\mathbf{r}'|$. The kernel function is given by

$$\begin{aligned}\phi(d,d') =& \frac{2}{\pi^2}\int_0^\infty daa^2\int_0^\infty dbb^2W(a,b)\\ &\times T[\nu(a),\nu(b),\nu'(a),\nu'(b)],\end{aligned} \tag{22}$$

where

$$\begin{aligned}W(a,b) =& 2\left[(3-a^2)b\sin a\cos b\right.\\ &+(3-b^2)a\cos a\sin b\\ &+(a^2+b^2-3)\sin a\sin b\\ &\left.-3ab\cos a\cos b\right]\end{aligned} \tag{23}$$

and

$$\begin{aligned}T(w,x,y,z) =& \frac{1}{2}\left[\frac{1}{w+x}+\frac{1}{y+z}\right]\\ &\times\left[\frac{1}{(w+y)(x+z)}\right.\\ &\left.+\frac{1}{(w+z)(y+x)}\right],\end{aligned} \tag{24}$$

with $\nu(y) = y^2/2h(y/d)$ and $\nu'(y) = y^2/2h(y/d')$ (d and d' are defined above). Calculating the ϕ on the fly is impractical, as the time-consuming double integral over the variables a and b is included. In practice, ϕ is calculated and tabulated in advance as a function of $D = (d+d')/2$ and $\delta = (d-d')/(d+d')$ ($0 \le D < \infty$ and $0 \le |\delta| < 1$) and the ϕ value is calculated on demand by interpolation. This approach works quite well, thank to the fact that ϕ is a smooth function of D and δ (See Fig. 1). Note that ϕ should be recalculated when different switching function h is employed, although the shapes of the h functions look similar, but $y^2/h(y)$, which is relevant to the plasmon dispersion, differs significantly [24, 25].

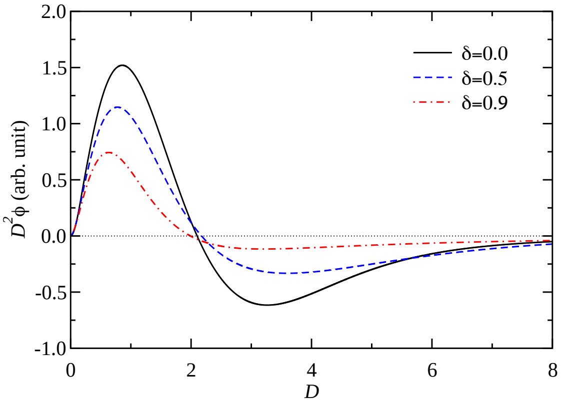

Figure 1: The kernel ϕ times D^2 as a function of D at various δ's obtained using an in-house kernel generation code [26].

Remaining task in the development of vdW-DF is to determine the semilocal XC functional. Using $E_{\mathrm{xc}}^{\mathrm{in}}$ as E_{xc}^{0} is the most consistent approach within the framework of vdW-DF, but in practice, it results in less accurate results. By allowing crossover in the exchange functional and letting

$$E_{\mathrm{xc}}^{0} = E_{\mathrm{xc}}^{\mathrm{in}} + \Delta E_{\mathrm{x}} = E_{\mathrm{xc}}^{\mathrm{GGA}} + E_{\mathrm{c}}^{\mathrm{LDA}}, \tag{25}$$

the local correlation energy can be consistent with that of $E_{\mathrm{xc}}^{\mathrm{in}}$, and the semilocal exchange energy has been investigated.

In vdW-DF for layered materials [14] and general geometry vdW-DF (vdW-DF1) [15], the revised Perdew-Burke-Ernzherof (PBE) [27] exchange (revPBE) of Zhang and Yang [28] was employed because it does not show spurious binding of rare gas dimers from exchange only. However, it turns out that the revPBE exchange tends to overestimate the Pauli repulsion, leading to a too large separation between the fragments. In searching for more accurate exchange energy functional, Klimeš *et al.* [29] proposed a set of exchange functionals, leading to optPBE-vdW and optB88-vdW, based on the optimization to the reference QC results. Cooper [30] proposed an exchange functional (C09) which satisfies the following constraint: (i) The gradient expansion approximation (GEA) form in the slowly varying electron density (small-s) limit, i.e., $F_{\mathrm{x}}(s) = 1 + \mu s^2$ with $\mu = 0.0864$ [31], which is mainly responsible for the covalent interaction. (ii) The revPBE behavior in the homogeneous electron density (large-s) limit which is relevant to the vdW bonding. Although the μ value is not exactly the same as that of GEA for the slowly varying electron gas ($\mu_{\mathrm{GEA}} = 10/81$ [32]), this work demonstrated the importance of GEA in predicting accurate interaction energies and atomic geometries. Murray *et al.* [33] showed that the exchange enhancement factor should be proportional to $s^{2/5}$ in the large-s limit. They developed the revised PW86 [31] functional (PW86R), which obeys GEA in the small-s limit and has the $s^{2/5}$ behavior in the large-s limit for the exchange enhancement factor, and paired with a new $E_{\mathrm{c}}^{\mathrm{nl}}$, to propose vdW-DF2 [17]. Klimeš *et al.*[34] developed the optB86b exchange functional (and optB86b-vdW) in which the exchange enhancement factor obeys the gradient expansion approximation (GEA) in the slowly varying density (small-s) limit with μ_{GEA} and has the $s^{2/5}$ behavior in the large s-limit. Berland and Hyldgaard [35] proposed an exchange functional (LV-PW86R), which is exactly the same as that of the internal exchange-correlation functional in the small-s region, while it reproduces the PW86R behavior in the large-s region. This semilocal exchange functional is the most consistent with that of the internal XC functional (consistent exchange), and thus the resulting vdW-DF functional is named vdW-DF-cx. Hamada [37] proposed an alternative one (B86R) based on the B86b [36] exchange functional, whose enhancement factor obeys GEA in the small-s limit and reproduces the original B86b behavior (proportional to $s^{2/5}$) in the large-s region. The B86R exchange is paired with $E_{\mathrm{c}}^{\mathrm{nl}}$ of vdW-DF2 and dubbed rev-vdW-DF2. In the latest development of vdW-DF (vdW-DF3) [25], B88 [38] and B86b [36] forms of the exchange enhancement factors are used. They are both designed to obey GEA in the small-s limit, and the remaining parameters are optimized to the reference QC results. The proposed GGA enhancement factors for vdW-DF are shown in Fig. 2, along with those for Perdew-Burke-Ernzerhof (PBE) [27] and PBEsol [39], the latter of which also obeys GEA in the slowly-varying density limit.

Although the precise performance of the vdW-DF functional depends on the combination of exchange and nonlocal correlation functionals, newly proposed functionals are shown to be more accurate than the original one, and are versatile tools for accurate prediction of structures and energetics of materials, molecules, and interfaces. See Refs. [24, 25, 40, 41, 42, 43] for assessments of the different vdW-DF functionals on various materials and molecules.

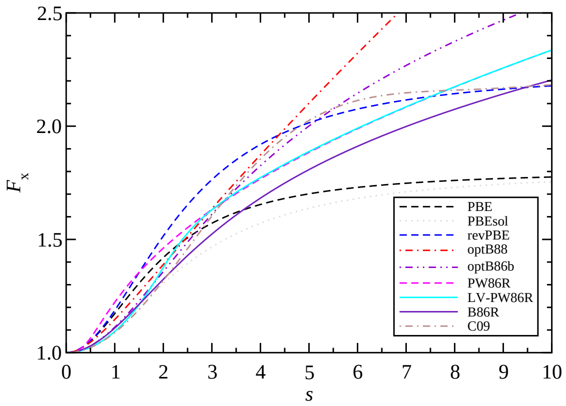

Figure 2: GGA enhancement factors (F_{x}) proposed for various exchange-correlation functionals as a function of reduced density gradient (s).

2.2 Pseudopotentials

In electronic structure calculations, the pseudopotential and projector augmented wave (PAW) [44] methods are often used, in which (pseudo)potentials generated using certain XC functionals are used. As a rule of thumb, the XC functional used to generate pseudopotentials should be consistent with that for the calculations of materials and molecules, but this issue has not been discussed in vdW-DF calculations. This is presumably because the appropriate XC functionals for atomic systems have not known nor been discussed for the vdW-DF calculations. However, it should not be overlooked, given that the vdW-DF employs different exchange and nonlocal correlation functionals and is not a simple dispersion correction to a semilocal XC functional. Callsen and Hamada [45] proved that $E_{\mathrm{c}}^{\mathrm{nl}}$ vanishes in an isotropic system and showed that the XC functional to be used to generate (pseudo)potentials for specific vdW-DF functional is uniquely determined. For instance, the B86R exchange plus LDA correlation functional should be used to generate potentials

Table 1: vdW-DF functional and corresponding exchange and correlation functionals to be used in the atomic calculation and pseudo- and PAW-potential generation.

vdW-DF functional	exchange	correlation
vdW-DF1	revPBE	LDA
vdW-DF2	PW86R	LDA
optB88-vdW	optB88	LDA
optB86b-vdW	optB86b	LDA
vdW-DF$^{\mathrm{C09_x}}$	C09	LDA
vdW-DF-cx	LV-PW86R	LDA
rev-vdW-DF2	B86R	LDA

for the rev-vdW-DF2 calculations of molecular/extended systems. See Table 1 for the exchange and correlation functionals to be used in the pseudo- and PAW-potential generation for vdW-DF calculations.

3 Application

In the following, applications of rev-vdW-DF2 to selected systems are presented. Emphasis is put onto the comparison of the results obtained using (psuedo)potentials generated with different XC functionals, i.e., the PBE and the B86R exchange plus LDA correlation (B86Rx+LDAc), the latter of which is compatible with rev-vdW-DF2. All the calculations were based on the PAW method and self-consistent vdW-DF as implemented [23, 46] in the Quantum-ESPRESSO [47] code. The proper extension of vdW-DF to the spin polarized system [48, 49] was adopted when necessary. The PAW potentials were generated using the input files supplied in the PSLIBRARY [50].

I first calculated the interaction energies for the S22 dataset [51], a set of 22 noncovalently bonded molecular duplexes. The calculations were performed at the S22 geometries [51] without any further optimization. Figure 3 depicts the deviations of the binding energies obtained using PBE and B86Rx+LDA potentials, with respect to the reference results obtained by the coupled cluster calculations with singlet, doublet, and perturbative triplet excitations [CCSD(T)] [52], along with the difference between the deviations obtained using different potentials. The binding energies obtained with PBE and B86Rx+LDA potentials are virtually the same (within the difference of 2 meV), and the mean absolute deviations are 20.5 and 20.8 meV for the former and the latter, respectively, validating the use of the PBE potentials in the vdW-DF calculations.

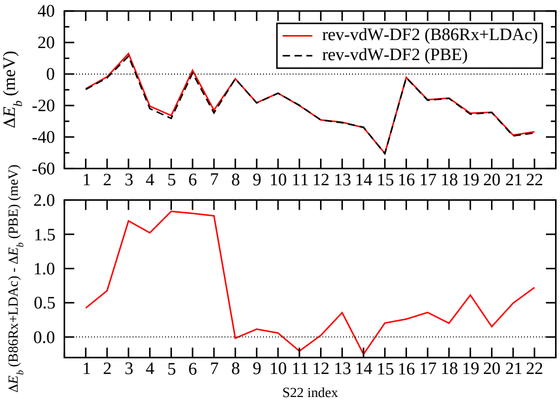

Figure 3: Deviations of the binding energies obtained using rev-vdW-DF2 with different PAW potentials with respect to the reference CCSD(T) results (ΔE_b, upper panel) and difference between the ΔE_b's obtained with different potentials (lower panel).

I then calculated the interlayer binding energy of graphite as a function of interlayer distance, as shown in Fig. 4. The equilibrium in-plane lattice constant is 2.46 Å, and interlayer distance and binding energy are 3.33 Å and 59.4 meV/atom, respectively, using both potentials. The interlayer binding energy is slightly overestimated as compared with quantum Monte-Carlo (56±5 meV/atom [53]), ACFDT-RPA (48 meV/atom [54]), and experiment (52±5 meV/atom [55]) but is in reasonable agreement with them.

I also performed the calculations of a benzene crystal. Figure 5 shows the binding energy of the benzene crystal in the *Pbca* symmetry as a function of the unit cell volume. The calculated equilibrium volume is 460 Å^3 with both potentials, and the binding energies are 532 and 531 meV/molecule with B86Rx+LDAc and PBE potentials, respectively, which are in reasonable agreement with the most recent experimental estimate of 573±23 meV/molecule [56]. Optimized cell parameters are a = 7.273 Å, b = 9.418 Å,

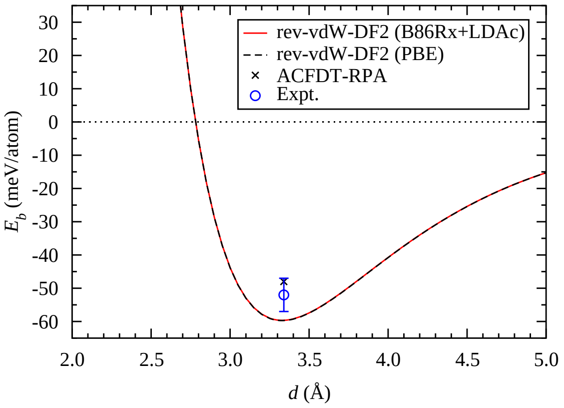

Figure 4: Binding energy of graphite (E_b) as a function of interlayer distance (d) using rev-vdW-DF2 with different potentials, along with the equilibrium energy and distance from ACFDT-RPA (Ref. [54]) and experiment (Ref. [55])

and c = 6.723 Å, which are also in reasonable agreement with the experimental values of $a = 7.36$ Å, $b = 9.37$ Å, and $c = 6.70$ Å [57].

These results suggest that the effect of using the potentials generated using the PBE functional is minor in vdW-DF calculations, at least with rev-vdW-DF2, although benchmark calculations on a larger set of materials and molecules need to be done.

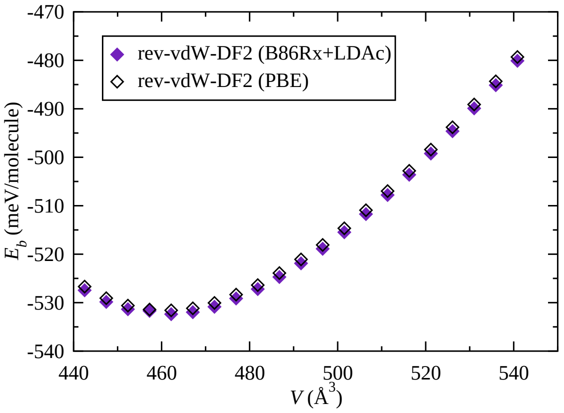

Figure 5: Binding energy of benzene crystal in the *Pbca* symmetry (E_b) as a function of unit cell volume (V) obtained using rev-vdW-DF2 and different potentials.

Finally, as a critical assessment of rev-vdW-DF2, I chose to calculate graphene adsorbed on Ni(111) in the atop-fcc configuration. In this calculation, B86Rx+LDAc potentials were used but the result obtained using PBE potentials was found to be virtually identical. I also confirmed that present result is consistent with the one reported in Ref. [37] but with a different code. Figure. 6 shows the binding energy as a function of graphene-Ni surface distance by using PBE and rev-vdW-DF2 functionals (PBE potentials were used for the PBE calculations). It was found that the rev-vdW-DF2 slightly overestimates the binding energies, but is able to reproduce the binding energy curve with two local minima obtained using the ACFDT-RPA [58, 59], which is suggested to be a result of competing chemical and physical interactions. This demonstrates the accuracy of rev-vdW-DF2 in describing the adsorption system.

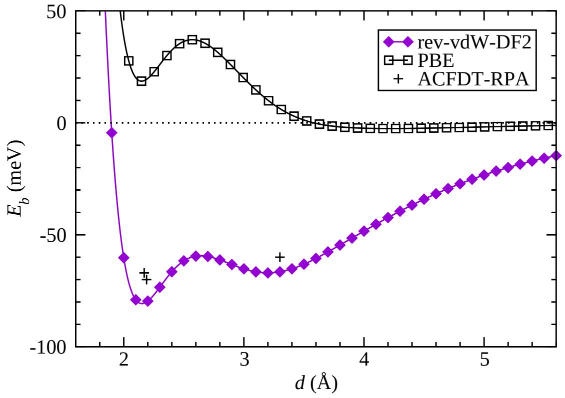

Figure 6: Binding energy of graphene on Ni(111) (E_b) as a function of distance from the surface (d) using rev-vdW-DF2 and PBE, along with the ACFDT-RPA results from Refs. [58, 59].

4 Summary

I give a brief review of the theory of vdW-DF, present recent theoretical advancements and some applications based on a variant of vdW-DF, rev-vdW-DF2. I discuss the proper choice of the XC functional to be used in the pseudo- and PAW-potential generation for vdW-DF calculations. It was found that the use of PBE potentials in rev-vdW-DF2 calculations has a minor impact on the calculated results, which may assure vdW-DF calculations in the literature. The accuracy of rev-vdW-DF2 in describing the adsorption system is also demonstrated, and it is anticipated that its applicability is further broadened by introducing a fraction of the unscreened/screened Fock exchange, i.e., nonempirical hybrid vdW-DF [60, 61, 62].

Acknowledgements

The present work has been supported partly by Grants in Aid for Scientific Research on Innovative Areas "Hydrogenomics" (No. JP18H05519). Numerical calculations were in part performed using the super computers in Institute for Solid State Physics (ISSP), the University of Tokyo.

References

[1] P. Hohenberg and W. Kohn, Phys. Rev. **136**, B864 (1964).

[2] W. Kohn and L. J. Sham, Phys. Rev. **140**, A1133 (1965).

[3] F. London, Z. Physik **63**, 245 (1930).

[4] J. Hepburn, G. Scoles, and R. Penco, Chem. Phys. Lett. **36**, 451 (1975).

[5] S. Grimme, J. Comput. Chem. **27**, 1787 (2006).

[6] S. Grimme, J. Antony, S. Ehrlich, and H. Krieg, J. Chem. Phys. **132**, 154104 (2010).

[7] A. D. Becke and E. R. Johnson, J. Chem. Phys. **123**, 154101 (2005).

[8] A. Tkatchenko and M. Scheffler, Phys. Rev. Lett. **102**, 073005 (2009).

[9] T. Sato and H. Nakai, J. Chem. Phys. **131**, 224104 (2009).

[10] A. Tkatchenko, R. A. DiStasio, R. Car, and M. Scheffler, Phys. Rev. Lett. **108**, 236402 (2012).

[11] S. Grimme, A. Hansen, J. G. Brandenburg, and C. Bannwarth, Chem. Rev. **116**, 5105 (2016).

[12] J. Hermann, R. A. DiStasio, and A. Tkatchenko, Chem. Rev. **117**, 4714 (2017).

[13] E. Caldeweyher and J. G. Brandenburg, J. Phys. Condens. Matter **30**, 213001 (2018).

[14] H. Rydberg, *et al.*, Phys. Rev. Lett. **91**, 126402 (2003).

[15] M. Dion, *et al.*, Phys. Rev. Lett. **92**, 246401 (2004).

[16] M. Dion, *et al.*, Phys. Rev. Lett. **95**, 109902 (2005)

[17] K. Lee, *et al.*, Phys. Rev. B **82**, 081101 (2010).

[18] K. Berland, *et al.*, Rep. Prog. Phys. **78**, 066501 (2015).

[19] P. Hyldgaard, K. Berland and E. Schröder, Phys. Rev. B **90**, 075148 (2014).

[20] O. Gunnarsson and B. I. Lundqvist, Phys. Rev. B **13**, 4274 (1976).

[21] D. C. Langreth and J. P. Perdew, Phys. Rev. B **15**, 2884 (1977).

[22] D. C. Langreth and S. Vosko, Adv. Quantum Chem. **21**, 175 (1990).

[23] T. Thonhauser, *et al.*, Phys. Rev. B **76**, 125112 (2007).

[24] K. Berland, D. Chakraborty, and T. Thonhauser, Phys. Rev. B **99**, 195418 (2019).

[25] D. Chakraborty, K. Berland, and T. Thonhauser, J. Chem. Theory Comput. **16**, 5893 (2020).

[26] I. Hamada, vdwphi_drsll: A code to calculate the kernel function of the van der waals density functional, https://github.com/ikuhamada/vdwphi_drsll.

[27] J. P. Perdew, K. Burke, and M. Ernzerhof, Phys. Rev. Lett. **77**, 3865 (1996).

[28] Y. Zhang and W. Yang, Phys. Rev. Lett. **80**, 890 (1998).

[29] J. Klimeš, D. R. Bowler, and A. Michaelides, J. Phys. Condens. Matter **22**, 022201 (2009).

[30] V. R. Cooper, Phys. Rev. B **81**, 161104 (2010).

[31] J. P. Perdew and W. Yue, Phys. Rev. B **33**, 8800 (1986).

[32] P. R. Antoniewicz and L. Kleinman, Phys. Rev. B **31**, 6779 (1985).

[33] É. D. Murray, K. Lee, and D. C. Langreth, J. Chem. Theory Comput. **5**, 2754 (2009).

[34] J. Klimeš, D. R. Bowler, and A. Michaelides, Phys. Rev. B **83**, 195131 (2011).

[35] K. Berland and P. Hyldgaard, Phys. Rev. B **89**, 035412 (2014).

[36] A. D. Becke, J. Chem. Phys. **85**, 7184 (1986).

[37] I. Hamada, Phys. Rev. B **89**, 121103 (2014).

[38] A. D. Becke, Phys. Rev. A **38**, 3098 (1988).

[39] J. P. Perdew, *et al.*, Phys. Rev. Lett. **100**, 136406 (2008).

[40] T. Björkman, J. Chem. Phys. **141**, 074708 (2014).

[41] T. Rangel, *et al.*, Phys. Rev. B **93**, 115206 (2016).

[42] F. Tran, *et al.*, Phys. Rev. Materials **3**, 063602 (2019).

[43] S. Yanagisawa and I. Hamada in *Theoretical Chemistry for Advanced Nanomaterials: Functional Analysis by Computation and Experiment*, edited by T. Onishi (Springer Singapore, Singapore, 2020).

[44] P. E. Blöchl, Phys. Rev. B **50**, 17953 (1994).

[45] M. Callsen and I. Hamada, Phys. Rev. B **91**, 195103 (2015).

[46] R. Sabatini *et al.* J. Phys. Condens. Matter **24**, 424209 (2012).

[47] P. Giannozzi, *et al.* J. Phys. Condens. Matter **21**, 395502 (2009).

[48] T. Thonhauser, *et al.*, Phys. Rev. Lett. **115**, 136402 (2015).

[49] C. M. Frostenson, *et al.*, Electron. Struct. **4**, 014001 (2022).

[50] A. Dal Corso, Comput. Mater. Sci. **95**, 337 (2014).

[51] P. Jurečka, J. Sponer, J. Cěrný, and P. Hobza, Phys. Chem. Chem. Phys. **8**, 1985 (2006).

[52] T. Takatani, *et al.*, J. Chem. Phys. **132**, 144104 (2010).

[53] L. Spanu, S. Sorella, and G. Galli, Phys. Rev. Lett. **103**, 196401 (2009).

[54] S. Lebégue, *et al.*, Phys. Rev. Lett. **105**, 196401 (2010).

[55] R. Zacharia, H. Ulbricht, and T. Hertel, Phys. Rev. B **69**, 155406 (2004).

[56] J. Yang, *et al.*, Science **345**, 640 (2014).

[57] W. David, R. Ibberson, G. Jeffrey, and J. Ruble, Physica B **180-181**, 597 (1992).

[58] F. Mittendorfer, *et al.*, Phys. Rev. B **84**, 201401 (2011).

[59] T. Olsen and K. S. Thygesen, Phys. Rev. B **87**, 075111 (2013).

[60] Y. Jiao, E. Schröder, and P. Hyldgaard, J. Chem. Phys. **148**, 194115 (2018).

[61] V. Shukla, Y. Jiao, C. M. Frostenson, P. Hyldgaard, J. Phys. Condens. Matter **34**, 025902 (2022).

[62] V. Shukla *et al.*, arXiv:2203.06682.

Development of permanent magnet materials—from the view point of first-principles calculation

Hisazumi AKAI[1] and Shinji TSUNEYUKI[2]
[1]*The Institute for Solid State Physics, The University of Tokyo*
Kashiwa-no-ha, Kashiwa, Chiba 277-8581, Japan
[2] *Graduate School of Science, The University of Tokyo*
Hongo, Bunkyo-ku, Tokyo 113-0033, Japan

Abstract

Theoretical approaches investigating the intrinsic properties of permanent magnet materials are reviewed. Three topics, namely, possible maximum performance of magnetic materials, high-throughput calculation surveying candidates for the high-performance magnetic materials, and the finite temperature magnetic properties, are discussed. Emphasis is put on the importance of large scale first-principles as well as high-throughput calculations.

1 Introduction

The properties featuring high-performance permanent magnets such as $Nd_2Fe_{14}B$ originate from subtle combination of micro, macro and metallographic structures. This means that intrinsic properties of permanent magnet materials are not directly reflected to the properties of permanent magnets. On the other hand, it is also true that the performance of a permanent magnet as a whole is severely limited by the intrinsic properties of constituent materials. For example, the upper bound of coercivity is the magnetocrystalline anisotropy—reality is that it is usually only 20~30% of the latter. Among those intrinsic properties, important ones are, in addition to the magnetocrystalline anisotropy, the magnetic moment and Curie temperature. The higher the values, the better the performance expected. The importance of first-principle calculation arises here: although predicting the properties of permanent magnets is very difficult task, it would be still possible to predict better materials for permanent magnets on the basis of first-principles calculation. Also, the approach is powerful to analyze the mechanism inherent to certain specific electronic and magnetic properties.

In the past decade, many works based on first-principles calculation have been done from the above point of view [1]. There are two aspects existing in those works: the first one is the accumulation of results of first-principles calculations and their analyses. The second is the development of methodology that enables us to perform such attempts. In this paper, we will present some of our results as examples of the former, putting emphasis upon the importance of the latter.

We first will discuss the possible maximum performance of permanent magnet on the basis of the first principles calculation [2]. In spite of the intensive efforts, no essentially novel magnet showing better performance than $Nd_2Fe_{14}B$ magnet has been so far invented. Then, one might question if there exists any permanent magnet materials at all superior to the already known ones. Or, might it be better to proceed to other directions such as pursuing magnets less expensive but with reasonable performance, and hence, replacing ferrite magnets? In answering this, we will show that there exists a possible maximum performance that we can expect for permanent magnets. Fortunately, this maximum has not be reached by currently used permanent magnet materials and it is worthwhile seeking further possibilities.

One of ways to seek such possibilities may be performing first-principles calculation over a wide range of composition space of magnetic materials. Since most of those materials contain more than several elements, in many cases as solid solutions, the procedure inevitably becomes a high-dimensional search requiring high-throughput calculations. A machinery based on the Korringa–Kohn–Rostoker Green's function method combined with the coherent potential approximation (KKR-CPA) is quite efficient for this purpose [3] .

For the high throughput calculations, it is desirable to perform calculations for many systems with different compositions in parallel. We have devised such a system, called HOFMAN, which realizes this procedure for KKR-CPA efficiently and have been applied to various systems. Some examples will be given in a later section.

The problem arising in first-principles calculations of rare-earth permanent magnets is a treatment of f-states playing a main role in provoking the magnetocrystalline anisotropy. In the local density approximation (LDA), or the generalized gradient approximation (GGA), the strongly localized f-states cannot be treated properly. So far, no real solution for this problem exists. As a compromise, one may use the exact-exchange [4] instead of the LDA/GGA exchange. Since the f-states in rare-earth elements are sufficiently localized, the exchange energy for f-states may be replaced with that of local f-orbitals. This can be simply done by subtracting self-interaction from the Hartree energy—self-interaction correction (SIC) [5]—because the exchange in the present case is mostly the self-exchange.

The permanent magnets in electric vehicles and wind turbines are used mostly at temperatures 100∼ 200° higher than the room temperature. Therefore, the importance is on the performance at rather high temperatures. Although finite temperature magnetic properties of materials is out of the scope of Kohn–Sham scheme, we can still access this problem through perturbative ways. Namely, we can estimate the effects of low lying excitation by constructing a low energy effective Hamiltonian through DFT as a problem of the ground state of constrained systems [6]. The results of such calculations give rise to a set of parameters for the effective Hamiltonian, from which we can obtain the finite temperature electronic and magnetic properties.

There are several kinds of excitations that have to be taken into account when discussing finite temperature magnetic properties of magnetic materials. Among them are phonons and magnons [7, 8, 9]. Usually, single electron excitations at the Fermi surfaces do not contribute significantly to the magnetic properties at the temperature range below the Curie temperature. In the following we neglect such excitations. The treatment of phonons is the following: We apply a static approximation for phonons and treat them as external field acting on electrons. This problem can be treated in the framework of DFT. The statistical average can be taken, in principle, by performing a functional integral with suitable probability weights. However, this being practically impossible, we further introduce an approximation to make it tractable. We employ a single-site approximation, where the functional integral is reduced to a configuration average using CPA. In this scheme, the effects of phonons are nothing but those of random displacements of atoms around their equilibrium positions. The average displacements are estimated from either the Debye model or first-principles phonon calculations: no noticeable difference between them was found.

The treatment of magnons is somewhat subtle because the motion of the magnetic moments has to be separated from the electron degrees of freedom. We rely on the fact that the time scale of local spin fluctuations is much slower than that of remaining dynamics. Then we can expand the magnetic energy into the local spin fluctuations as

$$E_{\mathrm{mag}}[\boldsymbol{S}(\boldsymbol{r})] = -\frac{1}{2}\iint d\boldsymbol{r}d\boldsymbol{r}' \\ \boldsymbol{S}(\boldsymbol{r})\,\chi(\boldsymbol{r})^{-1}\chi(\boldsymbol{r},\boldsymbol{r}')\chi(\boldsymbol{r}')^{-1}\,\boldsymbol{S}(\boldsymbol{r}'), \quad (1)$$

where $\boldsymbol{S}(\boldsymbol{r})$ is the spin density, $\chi(\boldsymbol{r})$ and $\chi(\boldsymbol{r},\boldsymbol{r}')$

are the local and non-local susceptibilities, respectively. Such an expansion can be performed in the framework of constrained DFT as long as the above separation of degrees of freedom and the static approximation are employed. This provides us with a low energy effective Hamiltonian of the system, as is already mentioned. If the longitudinal fluctuations neglected, it is nothing but the Heisenberg Hamiltonian. Now, we can take the same approach as used for phonons: instead of random displacement of atoms, random flipping of the local magnetic moments with probability determined self-consistently at each temperature is considered within KKR-CPA.

We have studied the effects of phonons and magnons on finite temperature magnetism, targeting at permanent magnet materials.

We discuss the possible maximum performance of permanent magnets in Sec. 2. Several examples of high-throughput calculation are presented in Sec. 3. Section 4 is devoted for the finite temperature properties of magnetic materials under the existences of phonons and magnons. We summarize in Sec. 5.

2 Maximum performance of permanent magnet materials

We assume that $3d$ magnetic ions are the main origin of magnetic polarization (magnetization). On the other hand, $4f$ ions are of main concern for the magnetic anisotropy energy (MAE) although $3d$–$5d$ transition metal ions partly contribute to it, in particular, at high temperature. For this reason, we will discuss MAE in a somewhat different way than we do for the magnetic polarization J_S and Curie temperature T_C. The discussions are based on all-electron first-principles electronic structure calculations performed within the framework of the local density approximation (LDA/GGA) of density functional theory (DFT). We used a KKR-CPA package (AkaiKKR) [3], and for the calculation of T_C, Liechtenstein's method [10] was exploited.

Figure 1 shows the overall behavior of magnetic moment $M(a, Z)$ per atom of $3d$ elements plotted against the lattice constant a and atomic number Z. The crystal structure is fixed to bcc. Here, the fractional atomic number of a fictitious atom is used: Z = 25, 26, and 27 corresponds to Mn, Fe, and Co atoms, respectively. Whereas M is a decreasing function of Z for a large lattice constant ($a \sim 3.2$ Å), it shows a usual Slater-Pauling type behavior [11] for a lattice constant of bcc Fe (2.867 Å at room temperature): it takes the maximum value of 2.35 μ_B/atom at $Z = 26.2$ and decreases to both sides. The peak position shifts towards larger Z with decreasing lattice constant. Meanwhile, the peak height decreases rapidly. These behaviors are the results of the facts: (1) the position where the transition from strong to weak ferromagnetism takes place is shifted, and (2) the position where the instability of ferromagnetism against volume collapse takes place is shifted, both occurring when atomic number decreases.

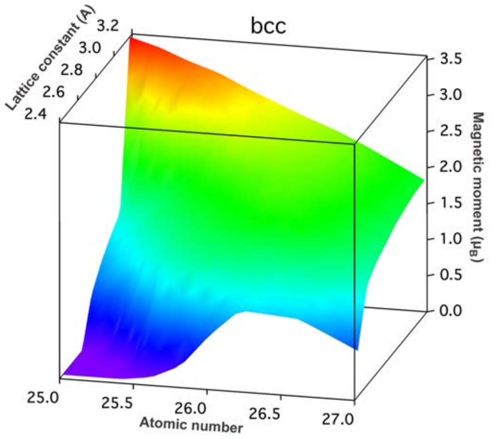

Figure 1: Magnetic moment per atom M against the lattice constant a(Å) and the atomic number Z of a fictitious atom

The behavior of saturation magnetic polarization J_S shown in Fig. 2 does not obey that of the magnetic moment. The most prominent feature is that it has a dome-like structure appearing around a = 2.65 Å and z=26.4, where J_S takes the maximum value of 2.66 T. Such a feature is not seen in M. We point out, not going into details, that this is related to the fact that in the bcc structure, the interatomic distance between nearest neighbor pairs is rather small, forming a considerable bonding–

antibonding splitting and the associated pseudo gap. Unfortunately, the lattice constant $a = 2.65$ Å is 7 % too small compared with the equilibrium lattice constant of bcc Fe. It should be noticed that, contrary to the behavior of the magnetic moment, the magnetic polarization increases with decreasing a up to the point where the magnetic state starts to rapidly collapse.

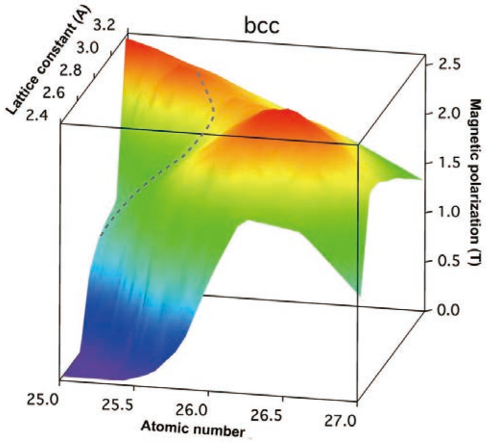

Figure 2: Saturation magnetic polarization J_S of the system against the lattice constant a (Å) and the atomic number Z of a fictitious atom. The ferromagnetic state is unstable in the region to the left of the dashed line.

Magnetic polarization takes on a large value at one of the corner points in the Z-a plane, $Z = 25$ and $a = 3.2$ Å, but this is not real. The truth is that in a broad region of the Z-a plane—the region to the left of the dashed line in Fig. 2—the ferromagnetic state is unstable as will be seen below. If we combine this fact with the information given by Fig. 2, we may conclude that a large J_S is expected only in the vicinity of the dome-like structure seen in Fig. 2, and the upper limit of J_S would not exceed ~ 2.7 T.

Figure 3 shows the overall behavior of magnetic transition temperature T_C. Here, we again see a dome-like structure near $Z = 26.5$ and $a = 2.9$ Å. This position approximately coincides with the position of the similar dome-like structure in J_S. This indicates that if $Z = 26.5$ and $a = 2.9$ Å is forced by some means (crystal structure, chemical composition, pressure, temperature, etc.), $J_\mathrm{S} \sim 2.7$ T is achieved. T_C drops rapidly toward the corner in the Z-a plane, $Z = 25$ and $a = 3.2$ Å, where T_C becomes negative, meaning that the antiferromagnetic state should be the ground state. Although the region of stable ferromagnetism does not appear to be extensive, there is hope in the fact that, in most of the region where the ferromagnetism is stable, T_C is well above 1000 K, which is much higher than the usual working temperature range. Now, we may say that the upper limit of T_C is ~ 2000 K (if fcc structure were assumed, the upper limit would be ~ 1500 K).

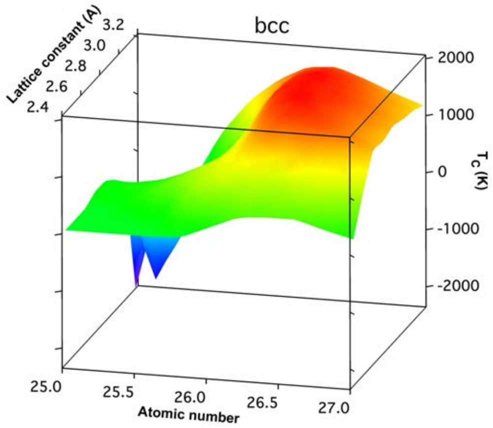

Figure 3: Magnetic transition temperature T_C against the lattice constant a (Å) and atomic number Z of a fictitious atom. The negative value of T_C means that the antiferromagnetic state is more stable than the ferromagnetic state.

There are two origins of MAE: one is spin orbit coupling and the other is magnetic shape anisotropy. The magnetic shape anisotropy is caused by the dipole interactions between two magnetic moments. In the case of rare earths, the former is the main origin of MAE and is well described within each LS multiplet by the effective Hamiltonian given by $H_\mathrm{so} = \lambda \boldsymbol{L} \cdot \boldsymbol{S}$, where $\lambda = \pm\zeta/n$ is the spin-orbit coupling constant for the ground state LS multiplet. The plus sign is for the less-than-half-filled f shell and vice versa; ζ is the single electron spin-orbit coupling constant, n the number of unpaired electrons. For the 3d–5d cases, we use the single electron spin-orbit interactions given by $H_\mathrm{so} = \sum_i \zeta_i \boldsymbol{\ell}_i \cdot \boldsymbol{s}_i$, where the sum is over

	ζ (eV)			
	s	p	d	f
Fe	8.18	0.231	0.068	0.001
Sm	10.0	1.36	0.218	0.163
Pt	44.2	2.72	0.762	0.001

Table 1: Absolute values of the single electron spin-orbit coupling ζ (eV) of element materials Fe, Sm, and Pt. ζ at the Fermi energy are given.

all electrons. Table 1 shows the values of the spin-orbit coupling constant ζ for some representative elements.

Assuming that the orbitals are firmly bound to the lattice, the upper limit of the magnetic anisotropy constant K_1 for Sm (Sm^{3+} in Sm-type Sm element) estimated from the value of ζ, together with the values of $\langle L \rangle$, is as large as $\sim$ 1000 MJm^{-3}. The upper limit of K_1 for other lanthanides, if scaled by the value of L, also would be similar to the Sm case. This value obtained under the assumption that the $4f$ orbitals are firmly bound to the lattice, however, seems too large: one order of magnitude smaller, i.e., ~100 MJm^{-3} would be realistic.

3 High-throughput calculation

The purpose of high-throughput calculation in the present context is to generate data of intrinsic properties of magnetic materials spreading over multi-dimensional composition space. This enable us to construct permanent magnet materials databases that might be used to find new candidates of high-performance permanent magnet materials. Given a structure and a set of components, e.g., $\mathrm{Sm(Fe_{1-x}Co_x)_{12}(N_{1-y}S_y)}$, we typically need calculations for 100~1000 different systems. Since these systems are compositionally disordered, usual band structure calculation is not sensible. An efficient way to manage this problem is to use the KKR-CPA method [3] , which can take a configurational average of disordered systems rather accurately. Unfortunately, the full-potential scheme is not implemented in the present version of KKR-CPA—full-potential KKR-CPA codes (FP-KKR) exist but they do not suit the high-throughput calculation because of the heavy computational demands. On the other hand, the pseudo-potential codes can calculate the ordered system quite efficiently although their accuracy has to be checked from time to time through comparisons with the results obtained by other reliable method such as FPKKR and FLAPW. Considering the above, one of the practical ways to do is to combine KKR-CPA and pseudo-potential codes: use pseudo-potential codes for the end points, i.e., ordered alloys, of composition space and use KKR-CPA to interpolate whole the region of composition space. A computational system HOFMAN constructed under such a strategy is now running.

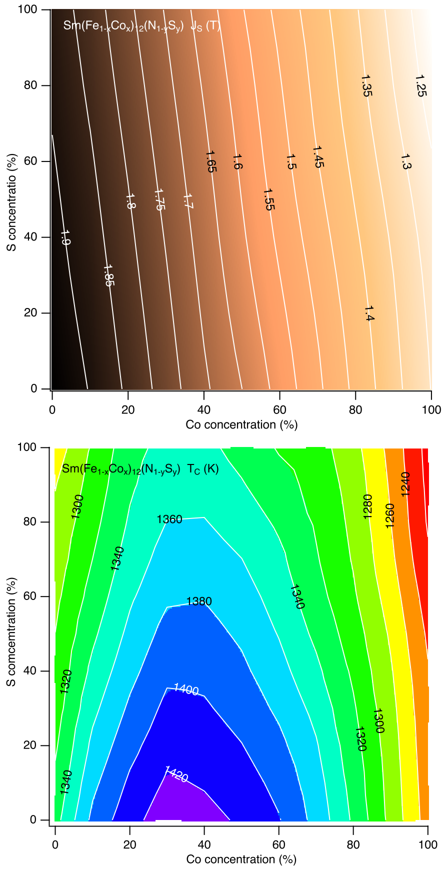

Figure 4: Magnetic polarization (T) (top) and T_C (K) (bottom) of $\mathrm{Sm(Fe_{1-x}Co_x)_{12}(N_{1-y}S_y)}$.

An example of the usage of HOFMAN system is seen in Fig. 4, where a new alloy system

$Sm(Fe_{1-x}Co_x)_{12}(N_{1-y}S_y)$ is examined. The results show that the Curie temperature rises by replacing Fe with Co by ~40% whereas it decreases the magnetic polarization. On the other hand, replacing N with S turned out not to be promising as for the magnetic properties.

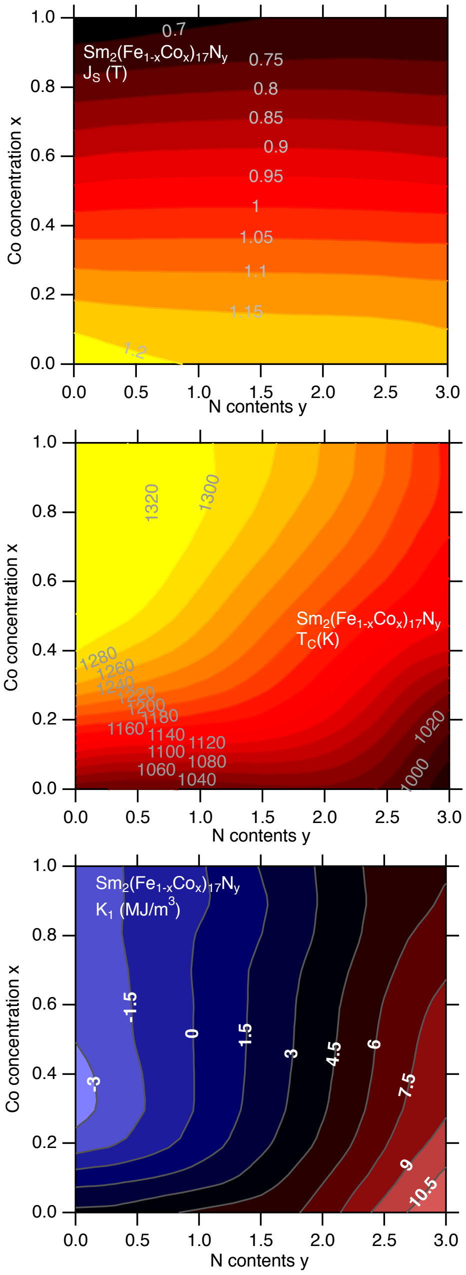

Figure 5: Magnetic polarization (T) (top) and T_C (K) (middle), and K_1 (MJ/m^3) (bottom) of $Sm(Fe_{1-x}Co_x)_{12}N_y$.

Another example is for $Sm_2(Fe_{1-x}Co_x)_{17}N_y$, where the content of N y takes $0 \leq y \leq 3$ (Fig. 5). Here the magnetic anisotropy constant K_1 was also calculated. In this case, T_C monotonically increases as the concentration of Co increases. Although the addition of N lowers T_C, it enhances the uniaxial magnetic anisotropy K_1. This fact was already known for $Sm_2Fe_{17}N_y$ but addition of Co further enhances this tendency is a new finding.

4 Finite temperature properties of permanent magnet materials

There are many cases that there exist experimental data of magnetic polarization J_S at several different temperatures around the room temperature. What we would like to do is to estimate the temperature dependence of J_S in whole the range of temperature below T_C from these rather restricted data. One of the ways to do this is the following: First, the Curie temperatures, which are not necessarily known experimentally, are estimated by fitting the temperature dependence of magnetic moment by Kuz'min's empirical formula [12]. Meanwhile, the theoretical Curie temperature and 0K magnetic moment are obtained by first-principles calculation using KKR-CPA. Then theoretical temperature dependence of magnetization is obtained again using Kuz'min's formula. Finally, the temperatures are scaled using experimentally estimated Curie temperatures. Examples of such estimation of temperature dependence of J_S are depicted in Fig. 6 for $SmFe_{12}$ family with several different compositions. The theoretical estimations reasonably fit the experimental data and also provide the extrapolation to the whole range of temperature.

Before entering the discussion of the temperature dependence of magnetic properties including the effects of phonons and magnons, it might be useful to see the effects of magnon excitations to the Curie temperature. Such effects comes in through the parameters $\iint drdr'\boldsymbol{S}(\boldsymbol{r})\,\chi(\boldsymbol{r})^{-1}\chi(\boldsymbol{r},\boldsymbol{r}')\chi(\boldsymbol{r}')^{-1}\,\boldsymbol{S}(\boldsymbol{r}') = J_{ij}$ in eq. (1). Here the integral are performed within each atomic cell surrounding i-th or j-th atom. There are two limiting cases in the calculations of

J_{ij}: one is the calculation at the ground state and another is the calculation above T_C where the directions of local moments align randomly without any short-range order. Which is more realistic depends on the characteristic of the spin-fluctuations. The former is realistic for the system where the local fluctuation of the magnetic moments does not play a role. The latter is suitable for the opposite cases.

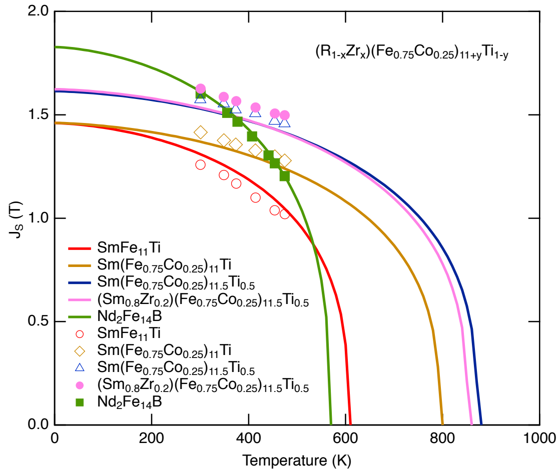

Figure 6: Temperature dependence of magnetization of various systems of $SmFe_{12}$ family.

Figures 7 and 8 show the results of calculation of T_C of $R_2(Fe,Co)_{14}B$ (R = La, Ce,..., Lu, Y). The results under the above two options are compared with the experiments. For the Fe based cases, the calculation assuming that the local fluctuation is dominant (red) gives good agreement with the experiments (blue) whereas the assumption that the long range fluctuation determined T_C (green) seems very reasonable for Co cases.

The above discussion is only for T_C with magnons excitations. For the finite temperature properties below T_C and also with not only magnons but also phonons need more elaobrate treatment as mentioned in Sec. 1.

Table 2: Calculated T_C of $Nd_2Fe_{14}B$

	phonons only	plus magnons
0K	1062K	561K
500K	1198K	548K

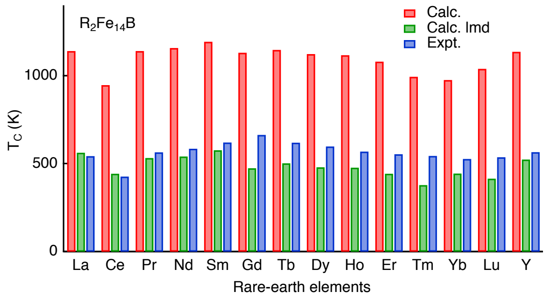

th]

Figure 7: Calculated T_C of $R_2Fe_{14}B$ compared with experiments.

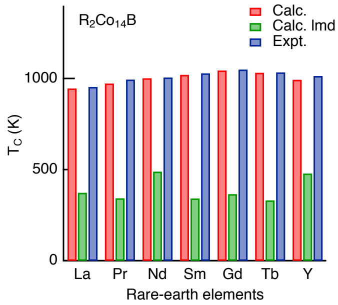

th]

Figure 8: Calculated T_C of $R_2Co_{14}B$ compared with experiments.

It was fond that, in the case of bcc Fe, there is a significant effect of electron–phonon scattering on the Curie temperature T_C, while that of magnons is not prominent (not shown). On the other hand, the effect of magnons, becomes remarkable in the case of $Nd_2Fe_{14}B$ permanent magnet materials. Some examples of calculated T_C of $Nd_2Fe_{14}B$ are given in Table 2. The first column indicates the temperature in which the average displacement due to phonons is calculated. The experimental value of T_C is 585K.

Figure 9 shows the calculated magnetic polarization of $Nd_2Fe_{14}B$. Both the effects of phonons and magnons are included. The theoretical curve shows a weak first-order transition at the magnetic transition temperature, which occurs as a result of electron–phonon coupling. The temperature is scaled so that T_C reproduces the experimental value of 585K although the scaling factor is close to 1. The calculated results are fairly consistent with experiments, is concluded.

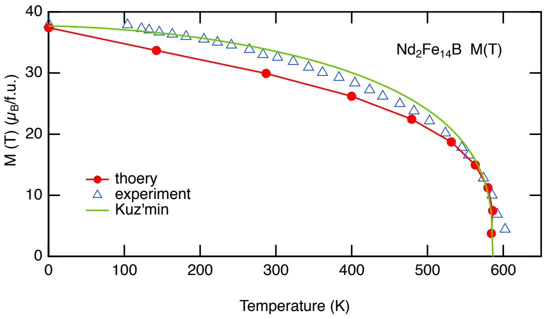

Figure 9: Calculated and experimental magnetic polarization vs. temperature of $Nd_2Fe_{14}B$

5 Summary

We discuss the theoretical approached to investigate the intrinsic properties of permanent magnet materials, focusing on three subjects: possible maximum performance of magnetic materials, high-throughput calculation to survey the candidate of the high-performance magnetic materials in multi-dimensional composition space, and the finite temperature magnetic properties. Admittedly, we have not yet succeeded in inventing any new permanent magnet materials that realize the performance exceeding that of $Nd_2Fe_{14}B$, the best permanent magnet materials so far known. However, we put emphasis on the fact that the remaining composition space not yet searched is immensely large and we still have much chance to get a leap. For this, large scale first-principle calculation such as reviewed here is one of most powerful approaches. In addition, it is clear that schemes fully equipped with machine learning technique provide us with a complementary approach for the development of new permanent magnet materials

References

[1] See, e.g., T. Miyake, Y. Harashima, T. Fukazawaa, and H. Akai, Sci. Tech. Adv. Mater.Sci. Tech. Adv. Mater. **22**, 543 (2021)

[2] H. Akai, Scr. Mater. **154**, 300 (2018).

[3] H. Akai, AkaiKKR, `http://kkr.issp.u-tokyo.ac.jp/` (2002).

[4] T. Kotani, Phys. Rev. B **50**, 14816 (1994).

[5] A. Filippetti, C.D. Pemmaraju, S. Sanvito, P. Delugas, D. Puggioni, and V. Fiorentini, Phys. Rev. B **84**, 195127 (2011) and references therein.

[6] P.H. Dederichs, S. Blügel, R. Zeller, and H. Akai, Phys. Rev. Lett. **53**, 2512 (1984).

[7] N. H. Long, M. Ogura, and H. Akai, Phys. Rev. B **85**, 224437 (2012).

[8] S. Kou and H. Akai, Solid State Commun. **296**, 1 (2018).

[9] H. Shinya, S. Kou, T. Fukushima, A. Masago, K. Sato, H. Katayama-Yoshida, and H. Akai, Appl. Phys. Lett. **117**, 042402 (2020).

[10] A. I. Liechtenstein, M. Katsnelson, V. Antropov, V. Gubanov, J. Magn. Magn. Mater. **67**, 65 (1987).

[11] P.H. Dederichs, R. Zeller, H. Akai, and H. Ebert J. Magn. Magn. Mater. **100**, 241 (1991).

[12] M. D. Kuz'min, Phys. Rev. Lett. **94**, 107204 (2005).

Development of Bayesian optimization tool and its applications in materials science

Ryo Tamura[a,b], Yuichi Motoyama[c], and Kazuyoshi Yoshimi[c]
[a] *International Center for Materials Nanoarchitectonics (WPI-MANA)*
National Institute for Materials Science
1-1 Namiki, Tsukuba, Ibaraki 305-0044, Japan
[b] *Graduate School of Frontier Sciences, The University of Tokyo*
5-1-5 Kashiwanoha, Kashiwa, Chiba 277-8561, Japan
[c] *Institute for Solid State Physics, University of Tokyo, Chiba 277-8581, Japan*

1 Introduction

Recently, materials informatics has established an important position in materials science [1, 2, 3, 4, 5, 6, 7, 8, 9, 10, 11]. As a feature of materials science, it is not always easy to obtain materials data whether by experiments or simulations. In contrast, when general machine learning and artificial intelligence techniques are applied to materials data, it is necessary to use a large amount of data to gather meaningful results. Therefore, to achieve success in materials informatics research, it is necessary to use some ingenuities in treating small-data problems. One strategy to overcome small-data problems is to start with a small amount of data and gradually increase the amount of data with the help of machine learning. This is called black-box optimization. One of the typical techniques is Bayesian optimization.

In this paper, we introduce a Bayesian optimization method that can effectively select the next candidate for an experiment or simulation with the help of machine learning. We also give examples of its application in materials informatics. In Bayesian optimization, Gaussian processes are used as a machine-learning surrogate model, which is constructed to predict the target material properties using already obtained materials data. Based on the predictions, the next candidate for the experiment or simulation is selected to improve the materials properties. By repeating these processes, *training* and *selection* using machine learning, materials with better properties can be found using the fewest number of experiments or simulations. Recently, many successful examples of Bayesian optimization have been reported in materials science [12, 13, 14, 15, 16].

2 Algorithm of Bayesian optimization

2.1 Problem setting

Let us explain an algorithm for Bayesian optimization. In materials research, the variables that describe materials are called descriptors, and include compositions, structures, processes, and simulation parameters. A descriptor vector with dimension d is denoted by $\mathbf{x} \in \mathrm{Re}^d$. Additionally, the materials property is expressed as y which is obtained through experiments or simulations when $\mathbf{x}$ is given. Evidently, the relationship between $\mathbf{x}$ and y cannot be explicitly expressed as a simple function in materials science. Thus, in materials informatics, we replace this relationship with a machine learning surrogate model. That is, the machine-learning surrogate model $f_{\mathrm{ML}}(\mathbf{x})$

is introduced, and y for any $\mathbf{x}$ is approximately obtained as follows:

$$y \simeq f_{\mathrm{ML}}(\mathbf{x}). \tag{1}$$

Using such a machine learning surrogate model, Bayesian optimization can find $\mathbf{x}$ with the better material properties y among the many candidates of $\mathbf{x}$. For example, a problem may be set up for Bayesian optimization as follows:

- There are N candidate materials expressed by $\{\mathbf{x}_i\}_{i=1,\ldots,N}$.
- Among $\{\mathbf{x}_i\}_{i=1,\ldots,N}$, we search for materials with a better material property value y. In addition, the number of experiments or simulations to obtain y is minimized as much as possible.
- Experiments or simulations for M candidate materials have been completed, and M material properties have been obtained. Currently, we have dataset $D = \{\mathbf{x}_k, y_k\}_{k=1,\ldots,M}$.
- We select the next candidate material expressed by $\mathbf{x}_{M+1}$ using $f_{\mathrm{ML}}(\mathbf{x})$. That is, the surrogate model is trained using the training data D, and the potential of a material is evaluated by using the trained model. To evaluate the potential, the acquisition function is introduced. Here, the Bayesian optimization uses a Gaussian process as a surrogate model.
- After evaluating the value of y_{M+1} on the selected material $\mathbf{x}_{M+1}$ by experiments or simulations, the $M+1$-th pair $(\mathbf{x}_{M+1}, y_{M+1})$ is added to D. Then, the next candidate material is selected by using the updated surrogate model.

The Bayesian optimization cycle is shown in Fig. 1.

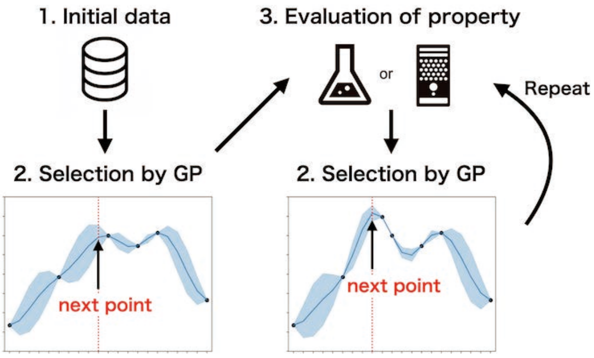

Figure 1: Flow of Bayesian optimization. In step 2, the Gaussian process (GP) regression is trained by the already obtained data and the next point is selected based on the acquisition functions. In step 3, the materials property of the selected material is evaluated by experiments or simulations. By repeating of steps 2 and 3, we select better materials.

2.2 Gaussian process

In the Gaussian process which is used as the surrogate model in Bayesian optimization, when the training data D are given, the conditional probability distribution for y at $\mathbf{x}$ is given by

$$P(y|D) = N(\mu(\mathbf{x}), \sigma(\mathbf{x})). \tag{2}$$

Here, $\mu(\mathbf{x})$ is the mean of the predicted value by the Gaussian process regression when $\mathbf{x}$ is the input, and the variance $\sigma(\mathbf{x})$ is the uncertainty, when $D = \{\mathbf{x}_k, y_k\}_{k=1,\ldots,M}$. These are defined as follows:

$$\mu(\mathbf{x}) = \mathbf{k}^\top (K + \lambda I)^{-1}\mathbf{y}, \tag{3}$$

$$\sigma(\mathbf{x}) = k(\mathbf{x},\mathbf{x}) + \lambda - \mathbf{k}^\top (K + \lambda I)^{-1}\mathbf{k}, \tag{4}$$

where λ is the hyperparameter, I is the identity matrix, and $\mathbf{y} = (y_1 \cdots y_M)^\top$. In addition,

$\mathbf{k}$ and K are defined as follows:

$$\mathbf{k} = \begin{pmatrix} k(\mathbf{x}_1, \mathbf{x}) & \cdots & k(\mathbf{x}_M, \mathbf{x}) \end{pmatrix}^\top , \quad (5)$$

$$K = \begin{pmatrix} k(\mathbf{x}_1, \mathbf{x}_1) & \cdots & k(\mathbf{x}_1, \mathbf{x}_M) \\ \vdots & \ddots & \vdots \\ k(\mathbf{x}_M, \mathbf{x}_1) & \cdots & k(\mathbf{x}_M, \mathbf{x}_M) \end{pmatrix}, \quad (6)$$

where $k(\mathbf{x}_i, \mathbf{x}_j)$ is a Gaussian kernel function,

$$k(\mathbf{x}_i, \mathbf{x}_j) = \exp\left[-\frac{1}{2\gamma^2}\|\mathbf{x}_i - \mathbf{x}_j\|^2\right]. \quad (7)$$

Here, γ is a hyperparameter.

2.3 Acquisition functions

To evaluate the potential of the material, acquisition functions are introduced. There are many types of acquisition functions, such as the probability of improvement (PI) [17], the expected improvement (EI) [18], and the Thompson sampling [19]. Firstly, the PI represents the probability of exceeding the current maximum value of the already obtained y: $y_{\max} = \max_k y_k$. This score is defined as follows:

$$\begin{aligned} \mathrm{PI}(\mathbf{x}) &= \mathbb{P}\left[y(\mathbf{x}) > y_{\max}\right] \\ &= F\left(t(\mathbf{x})\right), \end{aligned} \quad (8)$$

where $F(\cdot)$ is the cumulative distribution function of $\mathcal{N}(0,1)$ and $t(\mathbf{x}) = (\mu(\mathbf{x}) - y_{\max})/\sigma(\mathbf{x})$. Here, $\mu(\mathbf{x})$ and $\sigma(\mathbf{x})$ are obtained using the Gaussian process.

Next, the EI is the expected value of how much $y_{\max}$ updates when $\mathbf{x}$ is observed. This is defined as

$$\begin{aligned} \mathrm{EI}(\mathbf{x}) &= \mathbb{E}\left[\max(y(\mathbf{x}) - y_{\max}, 0)\right] \\ &= \sigma(\mathbf{x})\left[t(\mathbf{x})F(t(\mathbf{x})) + f(t(\mathbf{x}))\right], \end{aligned} \quad (9)$$

where $f(\cdot)$ denotes the probability density of $\mathcal{N}(0,1)$.

Finally, we consider Thompson sampling, and the acquisition function using Thompson sampling is as follows:

$$\mathrm{TS}(\mathbf{x}) = \mathbf{w}^{*\top}\phi(\mathbf{x}). \quad (10)$$

Here, a coefficient vector $\mathbf{w}^*$ was sampled according to the posterior distribution in the Gaussian process. $\phi(\mathbf{x})$ is a random feature map and $\phi(\mathbf{x})^\top\phi(\mathbf{x})$ expresses the Gaussian kernel, approximately.

In Bayesian optimization, the material expressed by $\mathbf{x}$ with the largest value of the acquisition function is selected as the next candidate for the experiment or simulation. By using these acquisition functions, we can incorporate into the selection process not only the predicted value $\mu(\mathbf{x})$ but also information on the uncertainty of the prediction $\sigma(\mathbf{x})$. This makes the selection more effective than if the next candidate is randomly selected.

3 PHYSBO package

To realize fast and scalable Bayesian optimization, we developed PHYSBO (optimization tools for PHYSics based on Bayesian Optimization) [20, 21] which is a Python library developed under the support of the "Project for advancement of software usability in materials science" by the Institute for Solid State Physics, University of Tokyo. In PHYSBO, a random feature map, Cholesky decomposition, and Thompson sampling are used to accelerate the calculations required for Bayesian optimization. Note that PHYSBO is an updated version of COMBO [22] and includes some new functions.

The following are the features of PHYSBO.

- PHYSBO can be used to find better solutions for both single and multi-objective optimization problems.
- At each cycle in Bayesian optimization, a single proposal or multiple proposals can be selected.
- Parallel calculation can be performed. The results of parallelization performance are shown in Fig. 2.
- Detailed manual is provided.

PHYSBO is available from `https://github.com/issp-center-dev/PHYSBO`.

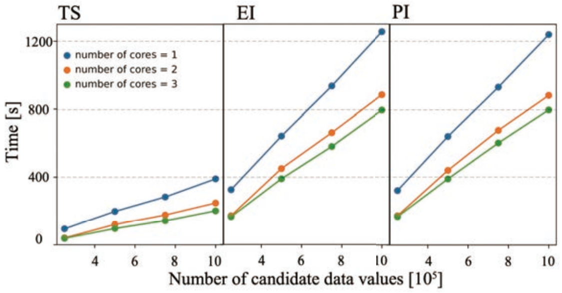

Figure 2: Selection time as a function of the number of candidate data values for different scores depending on the number of cores. As the number of cores increases, the selection times steadily decrease. Computing time is measured using CPU: 2.3 GHz Quad Core i7. Panels reproduced with permission from Ref. [20].

4 Examples in materials science

In this section, some results obtained by performing Bayesian optimization in materials science are introduced. In Secs. 4.1-4.3, single-objective problems are the focus for discussion. Sections 4.1 and 4.2 consider the cases where Bayesian optimization is combined with experiments, and in Sec. 4.3, the results where simulation data is used are introduced. In addition, the multi-objective optimization results are presented in Sec. 4.4.

4.1 Composition optimization for Li ion conductivity

Li-ion conductive oxides are attractive electrolytes for Li-ion secondary batteries owing to their stability and low toxicity. To increase the Li-ion conductivity of a material, doping of additives or mixing heterogeneous materials have been considered. However, it is difficult to determine the optimal chemical compositions using experimental methods. This is because it is practically impossible to cover all compositions because of the large number of possibilities in the search space. Thus, to reduce the number of experiments, Bayesian optimization is a useful tool.

To investigate the efficiency of Bayesian optimization, we attempted to optimize the composition of the ternary oxide solid electrolyte Li_3PO_4-Li_3BO_3-Li_2SO_4 [23, 24]. The mixed material was stable under atmospheric conditions and could be combined by sintering with both positive and negative electrode materials. As the initial traial, we prepared 15 samples with a composition ratio interval of 25%. Using these 15 data points, a ternary component heat map of Li-ion conductivity was drawn by the Gaussian process regression, which is shown in Fig. 3 (a). We can see that in samples 7 and 8, the Li-ion conductivity increased. Bayesian optimization was performed using this as the initial state, and 10 samples were further synthesized. Using all data, the ternary component heat map is shown in Fig. 3 (b). We obtained an optimum polycrystalline material with a composition of 25:14:61 (mol %) for Li_3PO_4-Li_3BO_3-Li_2SO_4, which is three times the Li-ion conductivity (4.9×10^{-4} S/cm at 300 °C) compared with the highest case in binary compounds.

4.2 Process optimization for gas atomization

The use of metal 3D printing is rapidly advancing in aerospace engines, and low-cost production and a ready supply of superalloy powders have become essential in the industry. In particular, for high-pressure turbine disks, which are important components of engines, it is necessary to produce high-quality superalloy powders with a high sphericity, uniform structure, high yield, and low cost. Most of these powders are produced by gas atomization, and the desired powder is produced using the industrial equipment used in the manufacturing process.

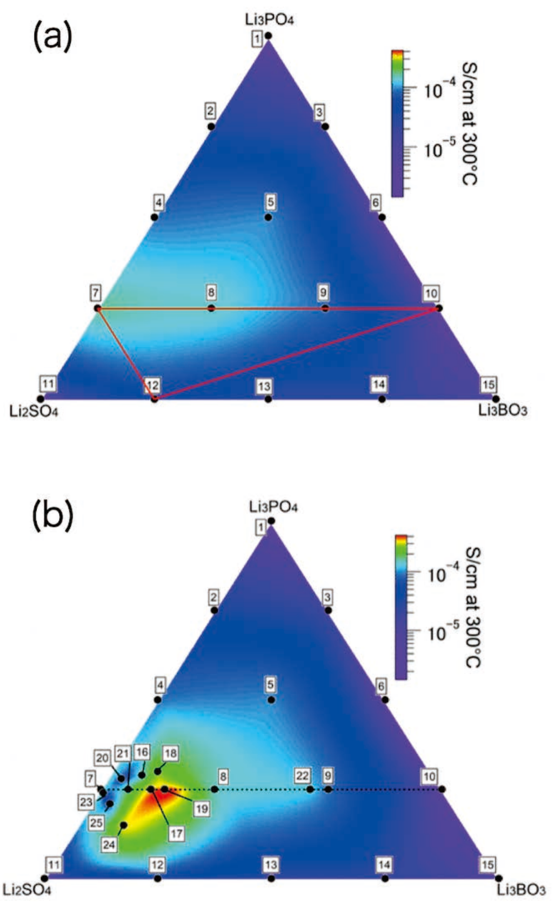

Figure 3: Heat maps of the Li-ion conductivity interpolated by the Gaussian process for (a) initial 15 data and (b) 25 data after Bayesian optimization. Panels reproduced with permission from Ref. [23].

To do this it is necessary to optimize multiple process conditions such as the melting temperature of the metal and gas pressure. Even with the expertise of specialists, this optimization task requires enormous cost, time, and human resources.

In this study, Bayesian optimization was used to optimize the gas atomization process without the use of expert knowledge or historical data (Fig. 4 (a)) [25]. A Ni-Co based superalloy for high-pressure turbine disks with excellent heat resistance was chosen for investigation. The target powder specifications are a size of 53 μm or less, which is suitable for turbine disk fabrication. The process of maximizing the yield of these powers was explored. Melting temperature of the metal and gas pressure were chosen from the various gas atomization processes as a focus for the optimization.

First, as initial data, superalloy powders were produced by three different processes, and the yield under 53 μm was evaluated by sieve classification. Using these data as the training data, a Gaussian process was trained to predict the yields of the candidate processes and estimate the errors. Here, in the candidates processes, the melting temperature is $T = 50 \times i + 1400$ [°C] $(i = 1, ..., 5)$ and the gas pressure is $P = i + 4$ [MPa] $(i = 1, ..., 5)$. Based on the results of the prediction, we selected the process with the highest acquisition function and conducted powder production using the selected process. By repeating this optimization loop thrice, we succeeded in determining the process conditions to obtain the target powder finer than 53 μm in approximately 78% yield, when it is typically a 10-30% yield. The yields obtained from these six trials and unit costs of the raw materials are shown in Fig. 4 (b). By performing Bayesian optimization, the yield was improved, and the unit cost of the raw material was cheaper. The superalloy powder produced by the process found by Bayesian optimization succeeded in reducing the cost by approximately 72% compared with commercially available powder (values estimated from the unit cost of raw materials).

4.3 Model parameter estimation

In condensed matter physics, knowing the effective model of a material is one method used to understand the target material [27, 28]. Bayesian statistics are useful for solving inverse problems [29], in which an effective model is derived that explains the given simulation results or experimental results. Based on Bayesian statistics, plausible model parameters in the effective model that explain the given physical quantity are determined by

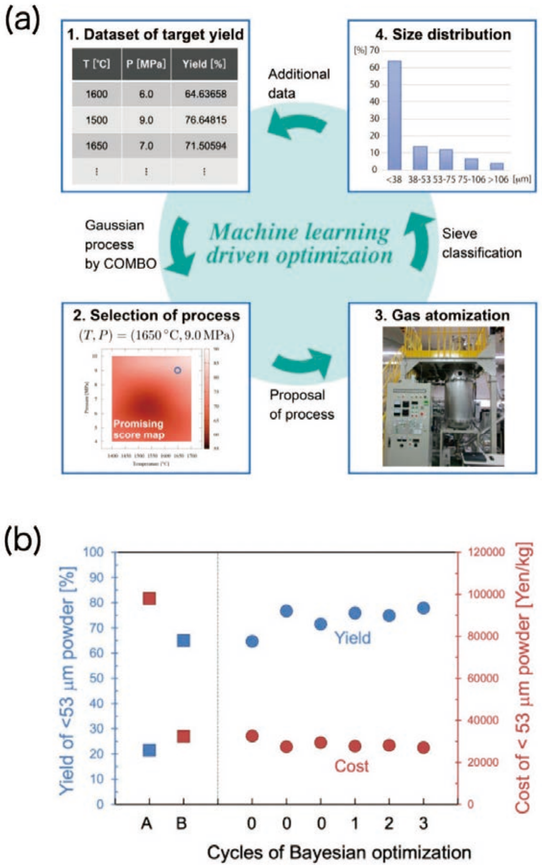

Figure 4: (a) Cycle of Bayesian optimization in process optimization of gas atomization. (b) Yields and the unit cost depending on the cycles. Values obtained for commercial gas atomized powders prepared by Company A and Company B [26] are also plotted. Panels reproduced with permission from Ref. [25].

maximizing the posterior distribution, which is defined as

$$P(\mathbf{x}|y^{\mathrm{target}}) \propto \exp[-E(\mathbf{x})], \tag{11}$$

where the energy function $E(\mathbf{x})$ as a function of model parameters $\mathbf{x}$ is given by

$$\begin{aligned} E(\mathbf{x}) &= 1/(2\sigma^2)(y^{\mathrm{target}} - y^{\mathrm{cal}}(\mathbf{x}))^2 \\ &\quad - \log[P(\mathbf{x})], \end{aligned} \tag{12}$$

where y^{target} and $y^{\mathrm{cal}}(\mathbf{x})$ are the sets of physical quantities given as targets and those calculated from the effective model characterized by $\mathbf{x}$, respectively. In addition, $P(\mathbf{x})$ is the prior distribution that expresses prior knowledge of the model parameters $\mathbf{x}$. To estimate an effective model, the maximizer of the posterior distribution should be determined. This problem can be solved using Bayesian optimization, where the value of y is generated from the posterior distribution.

As a sample problem, the estimation of magnetic interactions of the spin-1/2 Heisenberg chain model at 12 sites from a magnetization curve was set as a challenge. Here, three types of magnetic interactions that need to be estimated are considered: nearest neighbor J_1, next-nearest neighbor J_2, and 3rd-nearest neighbor J_3. Thus, the Hamiltonian can be written as

$$\begin{aligned} \mathcal{H} &= \sum_{i=1}^{12} J_1 \mathbf{S}_i \cdot \mathbf{S}_{i+1} \\ &\quad + J_2 \mathbf{S}_i \cdot \mathbf{S}_{i+2} + J_3 \mathbf{S}_i \cdot \mathbf{S}_{i+3}, \end{aligned} \tag{13}$$

where $\mathbf{S}_i$ denotes the vector of the spin operator at i-th site. In addition, a periodic boundary condition is imposed as follows: $\mathbf{S}_i = \mathbf{S}_{i+12}$.

In the model parameter estimation, firstly, the target magnetization curve $\{m^{\mathrm{target}}(h_j)\}_{j=1,\ldots,N_h}$ is given. Here, h_j is the magnetic field and N_h is the number of magnetizations with different h_j. Instead of the value of posterior distribution itself, we used the difference between the target and calculated magnetization curves as y in Bayesian optimization, which is given as

$$y = -\sum_{j=1}^{N_h} [m^{\mathrm{target}}(h_j) - m(h_j; J_1, J_2, J_3)]^2, \tag{14}$$

where $\{m(h_j; J_1, J_2, J_3)\}_{j=1,\ldots,N_h}$ is the calculated magnetization curve when the interaction values (J_1, J_2, J_3) are given. By searching for (J_1, J_2, J_3) such that y is maximized, the difference between the target and calculated magnetization curves is minimized, and we can estimate the model parameters that describe the target magnetization curve.

We prepared the target magnetization curve using the Hamiltonian with $(J_1, J_2, J_3) = (1.0, 0.5, 0.3)$; that is, these values are the solution to the model estimation problem. We used $\mathcal{H}\Phi$ package [30] to calculate the magnetization curve, which is a quantum lattice solver that uses the exact diagonalization method. In Bayesian optimization, the search space is set as a grid in which each magnetic interaction is discretized between 0 and 2 in increments of 0.1 for J_1, J_2, and J_3. Thus, the total number of input candidates is $21^3 = 9261$. The best difference as a function of the number of cycles in Bayesian optimization is shown in Fig. 5. Using Bayesian optimization, we demonstrated that better parameters for an effective model can be found.

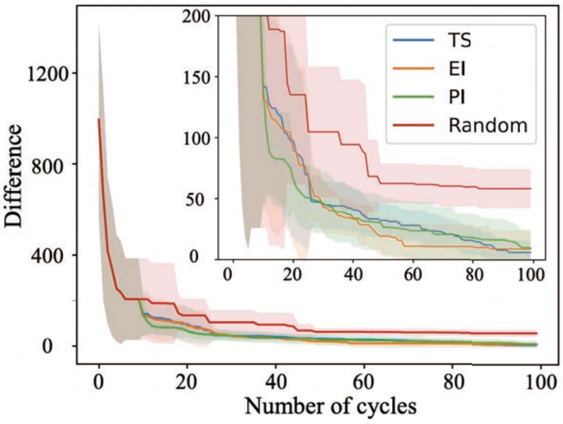

Figure 5: Best difference ($= -y$) during the optimization as a function of the number of cycles. The results are compared with the results of random sampling. The inset is an enlarged view. Panels reproduced with permission from Ref. [20].

4.4 Materials screening for multi-objective optimization

Finally, the results of multi-objective optimization problems using Bayesian optimization are introduced. The purpose of multi-objective optimization is to find as many Pareto solutions as possible. Here, the Pareto solution is defined as the optimal solution obtained by varying the balance of the objective functions. A metric for determining whether better Pareto solutions are found is the dominated region, which is the area dominated by Pareto solutions in the objective function space. The target problem is materials screening, where we search for materials with a large bandgap and a large electronic dielectric constant. In general, these properties exhibit a trade-off tendency, in other words, as the bandgap increases, the electronic dielectric constant decreases. In order to address this problem, we used the semiconductor database from Ref. [31], and found the number of materials is 1277. First principles simulation results are presented in this database. We use the compositional descriptors generated by Magpie [32] as $\mathbf{x}$.

The number of Pareto solutions obtained by performing Bayesian optimization with multiple objectives as a function of the number of cycles is plotted in Fig. 6 (a). For Bayesian optimization, three types of scores were used for multi-objective optimization, called TS, EHVI, and HVPI. The results show that Bayesian optimization was able to find many more Pareto solutions than random sampling. The area of the dominated region was calculated for the results after 200 cycles. A large value of this area indicates that better Pareto solutions are found. Figure 6 (b) shows a violin plot for this area using 10 independent runs. Bayesian optimization produced a significantly larger dominated area than random sampling.

5 Summary

We introduced a Bayesian optimization technique and demonstrated its application in materials science. Bayesian optimization is a machine learning method that can effectively select the next experiments or simulations. The efficiency of Bayesian optimization is recognized in materials science, and thus, many

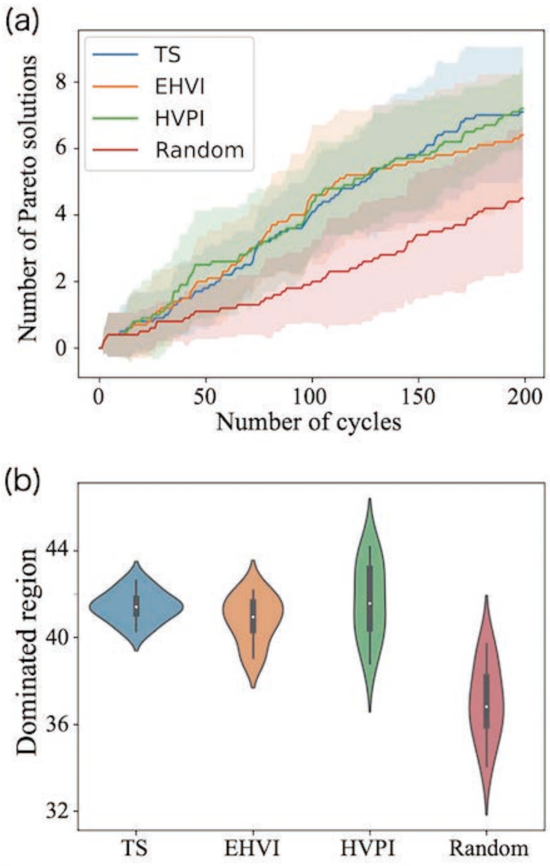

Figure 6: (a) Number of Pareto solutions found as a function of the number of cycles by PHYSBO for a multi-objective optimization problem. (b) Dominated region depending on the method when the number of cycles is 200. Panels reproduced with permission from Ref. [20].

problems can be solved using this technique in the future. In particular, using the PHYSBO package, massive parallel calculations can be performed using supercomputers, and we expect that more complicated problems can be solved.

Acknowledgements

We wish to thank Koji Tsuda, Kei Terayama, Masato Sumita, Tsuyoshi Ueno, Koji Hukushima, and Naoki Kawashima for their helpful discussions. PHYSBO was developed with the support of the “Project for advancement of software usability in materials science” in fiscal year 2020 by the Institute for Solid State Physics, University of Tokyo.

References

[1] A. Seko, A. Togo, H. Hayashi, K. Tsuda, L. Chaput, and I. Tanaka, Phys. Rev. Lett. **115** (2015) 205901.

[2] S. Ju, T. Shiga, L. Feng, Z. Hou, K. Tsuda, and J. Shiomi, Phys. Rev. X **7** (2017) 021024.

[3] V. Stanev, C. Oses, A.G. Kusne, E. Rodriguez, J. Paglione, S. Curtarolo, and I. Takeuchi, npj Comput. Mater. **4** (2018) 1.

[4] K. Terayama, R. Tamura, Y. Nose, H. Hiramatsu, H. Hosono, Y. Okuno, and K. Tsuda, Phys. Rev. Mater. **3** (2019) 033802.

[5] T. Fukazawa, Y. Harashima, Z. Hou, and T. Miyake, Phys. Rev. Mater. **3** (2019) 053807.

[6] K. Kitai, J. Guo, S. Ju, S. Tanaka, K. Tsuda, J. Shiomi, and R. Tamura, Phys. Rev. Res. **2** (2020) 013319.

[7] R. Katsube, K. Terayama, R. Tamura, and Y. Nose, ACS Mater. Lett. **2** (2020) 571.

[8] R. Tamura, M. Watanabe, H. Mamiya, K. Washio, M. Yano, K. Danno, A. Kato, and T. Shoji, Sci. Technol. Adv. Mater. **21** (2020) 540.

[9] K. Terayama, M. Sumita, R. Tamura, and K. Tsuda, Acc. Chem. Res. **54** (2021) 1334.

[10] I. Ohkubo, Z. Hou, J. N. Lee, T. Aizawa, M. Lippmaa, T. Chikyow, K. Tsuda, and T. Mori, Mater. Today Phys. **16** (2021) 100296.

[11] R. Tamura, Y. Takei, S. Imai, M. Nakahara, S. Shibata, T. Nakanishi, and M. Demura, Sci. Technol. Adv. Mater. Methods **1** (2021) 152.

[12] M. M. Noack, K. G. Yager, M. Fukuto, and G. S. Doerk, R. Li, and J. A. Sethian, Sci. Rep. **9** (2019) 1.

[13] R. Vargas-Hernández, Y. Guan, D. Zhang, and R. Krems, New J. Phys. **21** (2019) 022001.

[14] T. Yamashita, N. Sato, H. Kino, T. Miyake, K. Tsuda, and T. Oguchi, Phys. Rev. Mater. **2** (2018) 013803.

[15] F. Häse, L. M. Roch, C. Kreisbeck, and A. Aspuru-Guzik, ACS Cent. Sci. **4** (2018) 1134.

[16] K. Terayama, K. Tsuda, and R. Tamura, Jpn. J. Appl. Phys. **58** (2019) 098001.

[17] H. J. Kushner, J. Basic Eng. **86** (1964) 97.

[18] J. Mockus, V. Tiesis, and A. Zilinskas, Towards Global Optimization **2** (1978) 2.

[19] S. Q. Yahyaa and B. Manderick, The 23rd European Symposium on Artificial Neural Networks, Computational Intelligence and Machine Learning (2015).

[20] Y. Motoyama, R. Tamura, K. Yoshimi, K. Terayama, T. Ueno, and K. Tsuda, arXiv: 2110.07900 (2021).

[21] https://www.pasums.issp.u-tokyo.ac.jp/physbo

[22] T. Ueno, T. D. Rhone, Z. Hou, T. Mizoguchi, and K. Tsuda, Mater. Discov. **4** (2016) 18.

[23] K. Homma, Y. Liu, M. Sumita, R. Tamura, N. Fushimi, J. Iwata, K. Tsuda, and C. Kaneta, J. Phys. Chem. C **124** (2020) 12865.

[24] M. Sumita, R. Tamura, K. Homma, C. Kaneta, and K. Tsuda, Bull. Chem. Soc. Jpn. **92** (2019) 1100.

[25] R. Tamura, T. Osada, K. Minagawa, T. Kohata, M. Hirosawa, K. Tsuda, and K. Kawagishi, Mater. Des. **198** (2021) 109290.

[26] C. Lehnert, B. Sitzmann, F. Pfahls, H. Franz, and M. Hohmann, The Special Steel **65** (2016) 10.

[27] R. Tamura and K. Hukushima, Phys. Rev. B **95** (2017) 064407.

[28] R. Tamura, K. Hukushima, A. Matsuo, K. Kindo, and M. Hase, Phys. Rev. B **101** (2020) 224435.

[29] R. Tamura and K. Hukushima, PLOS ONE **13** (2018) e0193785.

[30] M. Kawamura, K. Yoshimi, T. Misawa, Y. Yamaji, S. Todo, and N. Kawashima, Comput. Phys. Commun. **217** (2017) 180.

[31] A. Takahashi, Y. Kumagai, J. Miyamoto, Y. Mochizuki, and F. Oba, Phys. Rev. Materials **4** (2020) 103801.

[32] L. Ward, A. Agrawal, A. Choudhary, and C. Wolverton, npj Comput. Mater. **2** (2016) 16028.

3.2 First-Principles Calculation of Material Properties

Clarification of Microscopic Mechanisms of Semiconductor Epitaxial Growth and Device-Interface Formation by Large-Scale Quantum-Theory-Based Computations

Atsushi Oshiyama
Institute of Materials and Systems for Sustainability, Nagoya University
Furo-cho, Chikusa-ku, Nagoya 464-8601

In the fiscal year of 2021, on the basis of the total-energy electronic-structure calculations and molecular dynamics simulations within the density-functional theory (DFT), we have studied the epitaxial growth of wide-gap power semiconductors, atomic and electronic structures of semiconductor-insulator interfaces. The main computational tools are our RSDFT (Real Space DFT) code and RS-CPMD (Car-Parrinello Molecular Dynamics) code as well as VASP code. Specifically, we have studied 1) the atom-scale mechanism of GaN epitaxial growth [1], 2) the mechanism of the adatom diffusion on SiC stepped surface [2], 3) the formation of dangling-bond free interface of GaN and a gate insulator [3], and 4) the structural identification of the nano-meter-scale GaN growth surface using Bayesian optimization [4]. We have also developed 5) an order-N orbital-free DFT (OF-DFT) scheme by inventing kinetic-energy functional using the neural-network [5]. The below is the explanation of the issues 4) and 5) above.

Structural identification of GaN (0001) by Bayesian optimization

GaN, a premier material in optoelectronics is now emerging in power electronics due to its superior physical properties. However, to guarantee the expected high performance of the devices, it is necessary to forge high-quality epitaxial films of GaN. Despite many experimental efforts in this decade, the current quality of GaN crystalline films is unsatisfactory for replacing Si power devices in the market. To unveil the growth phenomena, atom-scale identification of the surfaces on which atomic reactions take place is an essential prerequisite.

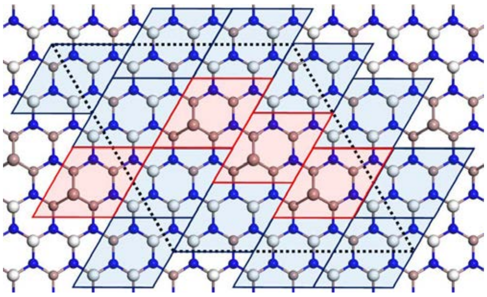

Fig.1: Top view of the stable 6x6 surface structure discovered by the present Bayesian optimization (structure name #130 in Fig. 2). The black dashed line indicates a 6x6 area. Brown, blue and white atoms correspond to Ga, N and H, respectively.

We have identified the stable structure of nanometer-scale GaN (0001) surfaces with Ga- and H-adsorbates, which are the fundamental basis for crystal growth modeling, by large-scale density-functional calculations combined with machine learning Bayesian optimization technique. We have been able to reach a single stable structure (Fig. 1) with satisfactorily low mixing enthalpy by 130 trials based on Bayesian optimization among ${}_{23}C_{15}$=490,314 candidate structures (Fig. 2). We have found that the obtained structure lacks any postulated high symmetry previously introduced by human intuition, satisfies electron counting rule locally, and shows a complex adsorbate-rearrangement, leading to lower mixing enthalpy. The present scheme of Bayesian optimization combined with first-principle calculations paves a way toward identifying surface structures with a larger scale and more complex adsorbate-arrangements, and then determination of surface phase diagrams for design of further preferred growth conditions.

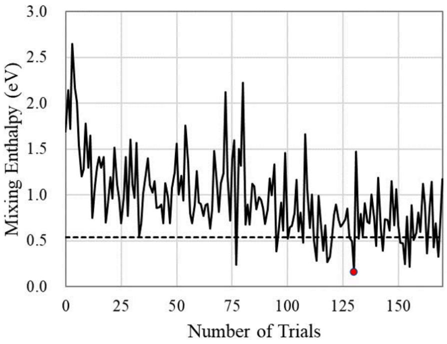

Fig. 2: History of the exploration of the surface structure by Bayesian optimization. The objective is to minimize the mixing enthalpy. The black dashed line corresponds to the minimum value of the baseline models, and the red marker corresponds to the most stable structure #130 in the present exploration.

Order-N OFDFT scheme with machine learning

A scheme in DFT in which the kinetic energy functional is expressed by the sum of single-particle orbitals squared is introduced by Kohn and Sham (KSDFT) and has been applied to a numerous number of applications with unprecedented success.

However, solving the Kohn-Sham equations for all the occupied orbitals in the system is a computational burden scaling with the system size N as $O(N^3)$. The scheme with lower-order scaling is highly demanded in materials science and also in advancing DFT. One of the solutions in a legitimate way is the orbital-free density-functional theory (OFDFT) in which the kinetic energy functional is expressed as a functional of the electron density $\rho(r)$ itself and an single Euler equation rather than Kohn-Sham equations is solved, being expected to be $O(N)$ scheme.

We express the kinetic energy functional as

$$T[\rho] = \int \tau^{TF}(r) F(s^2, q; \mathbf{W}) dr \ ,$$

where τ^{TF} is the Thomas-Fermi kinetic energy density, the enhancement factor F is expressed as a gradient expansion with $s = |\nabla\rho| / [2(3\pi^2)^{1/3}\rho^{4/3}]$ and $q = \nabla^2\rho / [4(3\pi^2)^{2/3}\rho^{5/3}]$. The enhancement factor is determined by the deep learning using the neural network where the set of weight parameters $\mathbf{W}$ is determined so as to minimize the cost function L expressed in terms of the kinetic energy functional derivative $\delta T/\delta\rho$:

$$L = \frac{1}{N_t}\sum_{n=1}^{N_t}\frac{1}{2}\left[\frac{\delta T}{\delta\rho}(r_n) - \frac{\delta T^{KS}}{\delta\rho}(r_n)\right]^2 ,$$

where the kinetic-energy functional derivative is computed at each real-space mesh points and compared with the corresponding values by the Kohn-Sham scheme. As a training data, we use the functional derivative in diamond-structured (ds) carbon at some mesh points.

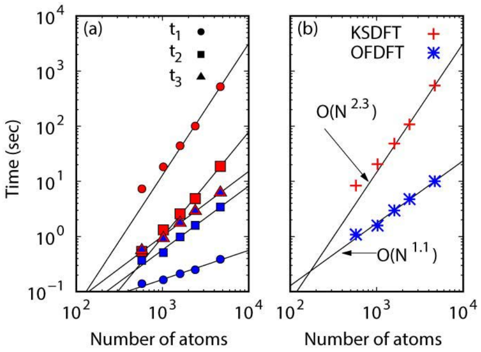

Fig. 3: Computational time of KSDFT and OFDFT. Comparison of (a) t1 (subspace diagonalization), t2 (conjugate gradient minimization and gram-schmidt diagonalization), and t3 (SCF mixing), and (b) total time for the SCF iteration. The test system is 4H-SiC supercell with the number of atoms of 576 -4704. In both (a) and (b), data points obtained by KSDFT and OFDFT are plotted in red and blue colors, respectively.

The transferability of the kinetic-energy functional obtained by the deep learning with the training data of only diamond has been examined by the application to 23 test systems which include semiconductors, metals, ionic insulators and some of their polytypes: diamond, graphene, ds-Si, face-centered-cubic(fcc)-Si, beta-tin Si, zinc-blende (3C)-SiC, body-centered-cubic(bcc)-Li, fcc-Al, fcc-Cu, bcc-Na, and NaCl. The structural properties, i.e., lattice constants and bulk moduli of all those materials obtained by the present functional shows better agreement with the corresponding values by the Kohn Sham scheme.

The order *N* behavior of the computation time in the present OFDFT scheme is clearly shown in Fig. 3.

The group id codes for the achievements above are k0042 and m0037.

Related publications

[1] K. M. Bui, K. Shiraishi and A. Oshiyama, Appl. Surf. Sci. **557**, 149542 (2021).

[2] K. Seino and A. Oshiyama, Appl. Surf. Sci. **561**, 149927 (2021).

[3] K. Chokawa, K. Shiraishi and A. Oshiyama, Appl. Phys. Lett. **119**, 011602 (2021).

[4] A. Kusaba, Y. Kangawa, T. Kuboyama and A. Oshiyama, Appl. Phys. Lett. **120**, 021602 (2022).

[5] F. Imoto, M. Imada adn A. Oshiyama, Phys. Rev. Research **3**, 033198 (2021).

First-principles prediction of stability and functionality of complex materials

Osamu SUGINO
Institute for Solid State Physics,
The University of Tokyo, Kashiwa-no-ha, Kashiwa, Chiba 277-8581

In recent years, considerable progress has been made in predicting material properties using the density functional theory (DFT) simulations and the DFT-based model simulations. In our group, we have developed a scheme to construct the exchange-correlation (xc) functional of the Kohn-Sham DFT by machine-learning the many-body wave function of small molecules [1,2]. In our prior study [1], small molecular systems were simply used as the learning set, but the success was limited to molecular systems only; problems remain in crystalline systems. To overcome this problem, physical conditions applicable to general materials were introduced into the learning process, and the resulting xc functional within the meta-GGA format was found to significantly improve the applicability [2]. The improved xc functional was implemented to an electronic structure calculation package VASP and is ready to distribute to supercomputer users. For further progress, we focused on techniques for the DFT for classical systems (classical DFT) and, in this case, low-density approximation of the n-particle density was found to be effective [3]. We consider that applying this method to electronic systems will also be effective not only for electronic systems but also the hybrid solvation models that we have long been studying.

In view of ability of meta-GGA in describing the Mott insulators, this functional was used for our study on exotic materials such as the solid oxygens in the high-pressure phases and the Hg-cuprate ($HgBa_2Ca_{n-1}Cu_nO_{2n+2+x}$) [4]. We found that the lattice parameters and the bandgaps become consistent with experiments with this functional, indicating that we are now at the start line of quantitative research.

One of the open problems of DFT-based simulation is to incorporate the nuclear quantum effect. Although the path integral molecular dynamics (PIMD) simulation is an established first-principles scheme, it becomes difficult to reduce the statistical fluctuation as the temperature is reduced and thus different scheme is needed. To overcome this problem for the hydrogen diffusion on metal surfaces, we have reformulated the quantum transition state theory that is based on a semi-classical approximation using an apparently full-quantum formulation. The fluctuation effect was found to be significantly reduced with the new method

[5].

We have also investigated the effect of nuclear quantum motion on the bandgap of insulators. This was done using the Allen-Heine-Cardona (AHC) theory and its extensions [6]. Herein the Debye-Waller terms of AHC was reformulated using the momentum operator, by which some of the electron-phonon coupling terms can be added to infinite order.

The description of electrochemical interfaces is a challenging problem of first-principles simulations, on which our group has long been studying. The difficulty of the simulation is due to existence the electric dipole layer (EDL) that can extend macroscopically. The thickness of EDL, however, is reduced to several nm when the ions are densely distributed as in strong acidic/alkaline solutions, but methods for the simulation has been developed only for the solution side. Therefore, EDL existing in the solid side of the interface remains to be a challenge; this is the case when semiconducting electrode is used. To simulate the ZrO_xN_{2-x} electrode, which is a candidate for Pt-free electrode of the next-generation fuel-cells, we have applied the first-principles Monte Carlo simulation with abICS [7] and then sped it up with the help of a machine-learned model potential. By the simulation, we could successfully obtain the distribution of oxygen vacancies and the nitrogen impurity atoms, and the result was used to describe the EDL. We further investigated efficiency of the oxygen reduction reaction occurring thereon and considered the effect of liquid water as well. These results were shared with experimentalists and helped them in planning the electrode development.

References

[1] R. Nagai et al.: Phys. Rev. Res. **4** (2022) 013106.

[2] R. Nagai et al.: npj Compt. Mater. **6** (2020) 1.

[3] T. Yokota et al.: Phys. Rev. **E 104** (2021) 014124.

[4] A. Tatan et al.: arXiv cond-mat 2204.05719 (2022).

[5] Y. Kataoka et al: unpublished.

[6] K. Ishii et al.: Phys. Rev. **B 104** (2021) 245144.

[7] S. Kasamatsu: https://github.com/issp-center-dev/abICS

Analyses related to atomic structures and atom dynamics at complex structures such as surfaces, interfaces and defects

Satoshi WATANABE
Department of Materials Engineering, the University of Tokyo
7-3-1 Hongo, Bunkyo-ku, Tokyo, 113-8656

1 Introduction

Keeping in mind the importance and difficulty of atomistic simulations on structures and dynamics at surfaces, interfaces and defects toward development of novel information and energy devices, we have been investigating atomic structures and atom dynamics in various systems by first-principles calculations, in some cases combining them with multi-scale or machine-learning approaches. In the following, two of our recent results are described.

2 Band alignment of $LiTi_2O_4$ and $SrTiO_3$

Recently, it was found in thin-film solid-state Li batteries using $LiTi_2O_4$ thin films as positive electrodes, the spontaneous Li-ion migration between the solid electrolyte (Li_3PO_4) and $LiTi_2O_4$ occurs in the case of the conducting substrate, Nb-doped $SrTiO_3$(001) [1]. That is, the $LiTi_2O_4$ turned to the $Li_2Ti_2O_4$ phase spontaneously.

To understand the above, we have investigated the band alignment of the $LiTi_2O_4/SrTiO_3$ superlattice model using the density functional theory (DFT) calculations. Here, we adopted the $SrTiO_3$ without Nd doping to examine the band alignment before the charge transfer. The calculated projected density of states (pDOS) reveals that the bottom of the conduction band is located above the Fermi level E_F in the central region of the $SrTiO_3$ layer. Since E_F of the Nb-doped $SrTiO_3$ is considered to be located near the bottom of the conduction band, this result suggests the electron transfer from the Nb-doped $SrTiO_3$ to $LiTi_2O_4$. From this result and the absence of a potential gradient in the metallic $LiTi_2O_4$ layer, we can say that the transferred electrons charge on the surface of $LiTi_2O_4$, which leads to a decrease in the electrochemical potential of Li ions at the $LiTi_2O_4$ surface. Consequently, the spontaneous migration of the Li ions occurs.

The present result suggests the possibility to control the spontaneous Li-ion migration between the solid electrolyte and $LiTi_2O_4$ by tuning the electrochemical potential difference via the substrate selection.

3 Neural network potential for multiple charge states of defects

In semiconductors and insulators, defects and impurities sometimes take various charge states depending on E_F. To examine the point defect behavior in such multiple charge states, we have proposed a new scheme of neural network potential (NNP) [2]. In our scheme, only minimal modifications to the conventional scheme [3] is needed: One system charge (Q_sys) node is added in the input layer. Here, Q_sys

is defined as a constant value times a charge state of the considered supercell divided by its volume.

We have applied this scheme to wurzite-GaN with a nitrogen vacancy [2]. For the charge states of the vacancy, 0, 1+, 2+, and 3+ have been considered. By performing molecular dynamics simulations using the Stillinger-Weber potential, we have generated 4,550 pristine GaN structures and 4,550 structures with a N vacancy in total. Then the DFTdata have been obtained for these sturctures. Total number of the DFT data is 22,750, because calculations have been performed for 0, 1+, 2+ and 3+ charge states in the cases of the structures with a N vacancy.

The NNP constructed using our scheme and the aforementioned data predict the total energies and atomic forces accurately for all the charge states: The root-mean-square-errors of the total energies and atomic forces were, respectively, 1.45 meV/atom and 63.8 meV/Å for the training dataset and 1.44 meV/atom and 64.6 meV/Å for the test dataset. Moreover, it has reproduced the phonon band structures and themodynamic properties of the defective systems fairly well.

References

[1] K. Nishio, S. Ichinokura, A. Nakanishi, K. Shimizu, Y. Kobayashi, N. Nakamura, D. Imazeki, R. Shimizu, T. Hirahara, S. Watanabe, and T. Hitosugi: Nano Lett. **21** (2021) 10086.

[2] K. Shimizu, Y. Dou, E. F. Arguelles, T. Moriya, E. Minamitani, and S. Watanabe: arXiv:2203.16789.

[3] J. Behler and M. Parrinello: Phys. Rev. Lett. **98** (2007) 146401.

Quantum Simulations on Dynamical Heterogeneous Catalysts

Y. J. WONG, J. I. ENRIQUEZ, H. H. HALIM, S. E. M. PUTRA, T. N. PHAM,
Y. HAMAMOTO, K. INAGAKI, I. HAMADA, and Y. MORIKAWA
Department of Precision Engineering, Graduate School of Engineering,
Osaka University, 2-1 Yamadaoka Suita, Osaka 565-0871

In 2021-2022, we carried out theoretical investigation of chemical processes at surfaces and interfaces, adsorption and reaction of polymeric formic acid on Cu(111), NO adsorption and dissociation on Cu(100), oxygen vacancy migration in $SrFeO_{3-\delta}$ and $Sr_3Fe_2O_{7-\delta}$, dry reforming of methane on Co catalysts, and adsorption of CO_2 on terrace, stepped and defect sites on Pt surfaces.

In this report, we report the dry reforming of methane on Co catalysts,[1]. The emissions of greenhouse gases (CH_4 and CO_2) are rising exponentially due to human activities and increased energy demand, contributing to global warming and climate changes. To make use of CH_4 and CO_2 into renewable energy, catalytic dry reforming of methane (DRM) is an efficient pathway to convert them into syngas (CO and H_2). Currently, active transition metals known to be capable of catalyzing DRM are mainly group VIII elements such as Ru, Rh, Ni, Co and Pt. Among them, supported Ni could be the most studied catalyst due to its relatively high activity and low cost. However, the efficiency of Ni is widely known to be easily suppressed by carbon deposition.

On the other hand, Co is particularly interesting due to its excellent catalytic activity and considerably low carbon deposition. Experimentally, Co is more carbon resistant than Ni. Co could enhance the adsorption of CO_2, which helps to inhibit the deposition of carbon and enhance carbon removal.

To gain insight into the occurrence of carbon deposition vs removal during DRM, we calculated the CO* formation reaction through the surface reaction of C* and O*, and the CC* formation reaction through the C-C coupling. The present direct quantitative comparison between the activation energies of the involved reactions would clarify the competition between carbon deposition vs removal over different Co surfaces. In addition, we further compared our results with those of Ni to reveal the cause of the lower carbon deposition on Co than on Ni. The quantitative comparison of CO_2 activation, C-C coupling, and CO* formation over Co and Ni could reveal the theoretical underlying mechanism of lower carbon deposition on Co than Ni.

The overall energy diagram illustrating the minimum energy pathway for reactions between CO_2 and C* on all the investigated Co surfaces, which includes CO_2 activation (green region), O* and C* diffusion (blue region), and the competition between CO* formation and C-C coupling (red region), is summarized in Figure 1. We consider the reaction of CO_2 with two predeposited C*. As observed in Figure 1, the rate-determining step for the reaction between CO_2 and C* on all the investigated Co surfaces is located in the red region, indicated by the energy needed for CO* or CC* dimer formation. Two conclusions can be drawn from evaluating the competition between CO* and CC* dimer formation on each surface. First, carbon graphitization is dominant on (111) and possibly on (110) because the CC* dimer final state is of lower or equal energy r elative to its respective initial state, indicating that the CC* dimer is stable and does not dissociate into atomic C*. In addition, CC* dimer formation on these surfaces has a lower activation energy than CO* formation. Even though the CO* final state is more stable than the CC* dimer, the stability of the CC* dimer compared to its initial state might give rise to nonreversible carbon graphitization, which could eventually cover the active surfaces. Thus, on (111) and (110), CC* dimer formation has a higher degree of preference than CO* formation. By combining this result with the fact that (111) is the most exposed surface of a Co nanoparticle, as indicated by the Wulff constructions, we hereby deduce that the origin of carbon deposition that leads to catalyst poisoning during DRM is caused by the high degree of preference for C-C coupling than CO* formation, especially on (111). Second, on (100), (211), and (221), CC* dimer formation is not favorable because the CC* dimer final state has a higher energy level than its respective initial state, indicating that the CC* dimer is easily dissociated into two atomic C*s. In addition, the CO* final state is more stable than the CC* dimer. The combination of the above mentioned points implies a higher degree of preference for CO* formation on (100), (211) and (221), even though the energy needed for CC* formation might be lower than that of CO* formation. On the other hand, other surface reactions, such as CO_2 activation and surface diffusion of O* and C* have lower activation energies than those of CO* and CC* dimer formation on each respective surface (Figure 1). The low energy needed for CO_2 activation implies that surface O*s are sufficiently supplied for CO* formation. In addition, the kinetic rate constants for CO* formation, CC* formation, and CC* dissociation over all the investigated surfaces were calculated and discussed in Section 12, S.I.. The result corresponds well with the findings where C-C coupling has the highest degree of preference on (111), followed by (110), however, is not favorable on (100), (211), and (221).

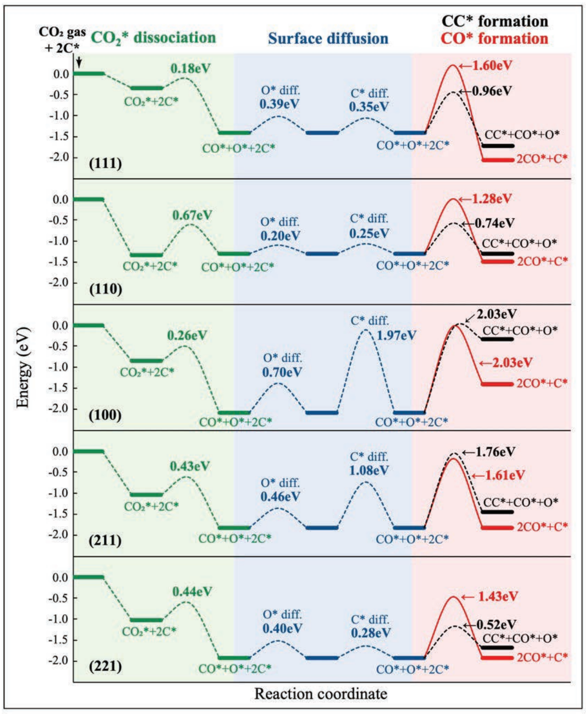

Figure 1: Energy diagram showing the minimum energy pathways of reactions between CO_2 and two C* on FCC Co (111), (110), (100), (211), and (221).

The present study provides a comprehensive clarification on the mechanism of DRM, specifically on the surface reaction of CO_2 and C* on the major flat and step FCC Co surfaces, namely, (111), (110), (100), (211), and (221). and/or promoted Co nanoparticles for DRM to restrict C-C coupling.

References

[1] Y.-J. Wong, H. H. Halim; N. F. Khairudin, T. N. Pham, S. E. M. Putra, Y. Hamamoto, K. Inagaki, I. Hamada, A. R. Mohamed, and Y. Morikawa: J. Phys. Chem. C **125**, 21902-21913 (2021).

Understanding superionic conductivity in disordered systems using machine learning potential molecular dynamics and Monte Carlo sampling

Shusuke KASAMATSU

Academic Assembly (Faculty of Science),

Yamagata University, Kojirakawa, Yamagata-shi, Yamagata 990-8560

The competition between order and disorder in materials leads to a wide variety of materials functionalities such as electronic, ionic, and thermal conductivity/insulation and catalytic activity. However, because of the huge number of degrees of freedom in disordered systems, successes in theory-driven design of such functionalities have been rather limited. In this research project, we tackled this problem through a combination of first-principles calculation and machine learning.

For disordered crystalline systems, we employed our abICS (ab Initio Configuration Sampling) framework for deriving an on-lattice neural network model from first-principles calculations [1] and used that to perform replica-exchange Monte Carlo sampling. One system that we have been examining is heavily Sc-doped $BaZrO_3$, which is known as a promising perovskite proton conductor for solid oxide fuel cells [2]. The oxygen vacancy is known to be the active site for the hydration reaction, which is the key reaction to introduce protons into the system. However, it is yet unclear which of the three types of vacancy environments, Sc-V_O-Sc, Sc-V_O-Zr, or Zr-V_O-Zr, are responsible for the hydration behavior. Using abICS, we have clarified that the former two are active sites for hydration, while the Zr-V_O-Zr site seldom exists under normal thermodynamic conditions and contributes little to the hydration reaction [3].

In the case of amorphous systems, we considered the use of the neural network potential (NNP) approach originally proposed by Behler and Parinello [4]. Although the neural network potential methodology seems to be a well-established approach at this point, we have found that it is quite a challenge to apply to many-component glass systems. This is because the NNP requires that the training set sufficiently covers the thermodynamically relevant configuration space, which will be huge for many-component glasses. We observe regularly that NNP molecular dynamics (MD) calculations ‘fall apart’ and exhibit completely unphysical structures after it wonders into regions of previously unlearned configuration space. To tackle this issue, we have been trying an active learning cycle approach where we take structures from the NNP-MD trajectory, perform DFT calculations on those structures, add them to the training set, and run the NNP-MD again with the new NNP. As shown in Fig. 1 for the AgI-As_2Se_3 superionic mixed glass system, increasing the number of cycles leads to improvement in the NNP predictions, although we have not been able to fully converge the low energy structures yet.

We have also been examining the feasibility of training on DFT data using high-cost functionals such as the HSE06 hybrid. Since it is not feasible to obtain a long enough MD trajectory to use as the training set with HSE06, we first performed first-principles MD using the relatively low-cost GGA functional. Afterwards, we took a subset of the structures (~1500 structures) and recalculated them using HSE06, which were then used as the training set in NNP training. This approach was applied to amorphous GeO_2, and we were able to obtain structure factors in excellent agreement with experiment (Fig. 2). This shows that NNP technology is promising for realizing long-time and large-scale MD simulations with the accuracy of high precision (and high cost) electronic structure methods.

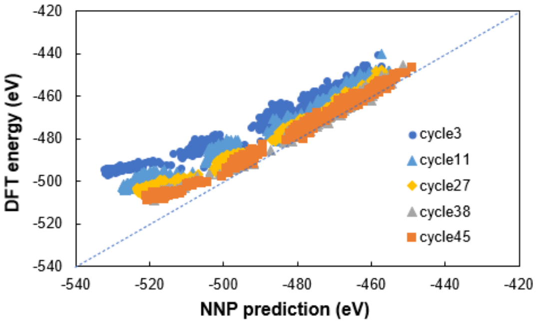

Fig. 1: Improvement of NNP accuracy with active learning iterations for AgI-As_2Se_3

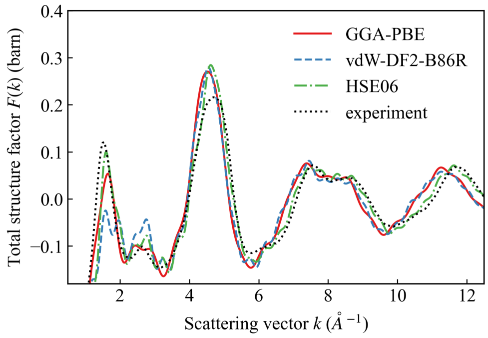

Fig. 2: Total structure factors from NNPs trained on various functionals and compared to experiment.

References

[1] S. Kasamatsu, ISSP Supercomputer Center Activity Report 2020, pp. 16-26.

[2] J. Hyodo et al.: Adv. Energy. Mater. J. Phys. Soc. Jpn. (2020) 2000213.

[3] K. Hoshino, S. Kasamatsu, et al., in preparation.

[4] J. Behler: Int. J. Quant. Chem. **115** (2015) 1032-1050.

Formation energy calcuation of defects in candidates of thermoelectric materials

KAZUHIKO KUROKI
Department of Physics, Osaka University
1-1 Machikaneyama, Toyonaka, Osaka, 560-0043, Japan

CAAL$_2$SI$_2$-TYPE ZINTL PHASE COMPOUNDS CAZN$_2$$X_2$ (X = AS,P)

Thermoelectric performance of many kinds of CaAl$_2$Si$_2$-type Zintl phase compounds has been theoretically estimated by first-principles band calculations[1]. This work suggests that CaZn$_2$X$_2$ (X = Sb, As, P) exhibits large ZT values in the electron-doped regime due to its high valley degeneracy of the electronic band structure. Indeed, this kind of 122 Zintl phase compounds have been synthesized and their electronic structure have also been investigated theoretically. However, these 122 Zintl phase compounds become p-type semiconductors because the cationsite vacancies are easily formed under usual synthesis conditions.

Given the above background, in 2021 fiscal year, we have explored the possibility of n-type (electron carrier) doping of CaZn$_2$X$_2$ (X = As, P) using first principles calcuation[2]. We have considered the possibility of n-type doping into CaZn$_2$X$_2$ for the following two situations: interstitial-site doping of the alkaline earth metals AE (= Mg, Ca, Sr, Ba) and group 3 elements $G3$ (= Sc, Y, La), and G3 substitutional doping for the Ca site. The former is analogous to Mg$_3$(Sb,Bi,Te)$_2$, in which excess Mg is introduced to the interstitial site of Mg3Sb2 so as to realize n-type doping[3]. On the other hand, the latter is another possible way to introduce electron carriers utilizing the difference in the valence number of the ion (Ca 2+ and G3 3+) , and the relevant compounds with full rare earth substitution including La, CaAl$_2$Si$_2$-type arsenides $RE_{2/3}$Zn$_2$As$_2$ (RE = La, Ce, Pr, Nd, Sm), do exist in reality.

In order to describe dopants and defects in a crystal under periodic boundary conditions, the supercell approach was adopted in our calculations. The atomic positions in the supercell were relaxed in the structural optimization after the lattice constants and atomic positions of the primitive cell are optimized. To consider the possibility of chemical doping, its defect formation energy of charged states was calculated using the supercells. To numerically evaluate the defect formation energy of chemical doping in CaZn$_2$X$_2$ (X = As, P), we have performed first-principles calculations within the generalized gradient approximation using VASP. We perform DFT calculations with the Perdew-Burke-Ernzerhof (PBE) exchange-correlation functional and the projector augmented wave method.

We find that the interstitial-site doping of AE = Ca, Mg or $G3$ = Sc, Y, and $G3$ = La, Y substitutional doping for the Ca site is favorable both for CaZn$_2$$X_2$ (X = As, P) in terms of energy stability. In particular, the formation energy of the La substitutional doping is the lowest among the considered cases both for CaZn$_2$X$_2$ (X = As, P) and is negative, so that La is expected to be substituted for the Ca site and provide electron carriers spontaneously (Fig.1). We also find that the formation energy for CaZn$_2$As$_2$ is smaller than that for CaZn$_2$P$_2$, so that n-type doping is considered to be relatively easier in CaZn$_2$As$_2$ than in CaZn$_2$P$_2$.

LAOXS$_2$ (X = SB, BI)

In LnOX Ch_2, electron carriers are usually introduced by fluorine substitutional doping for oxygen, or the valence fluctuation of cerium ions for Ln = Ce compounds. Since atoms in insulating layers work as a charge reservoir in both ways, the charge carrier can be introduced without a large change in the electronic state of the conducting layers, which is also advantageous for studying their transport properties. In fact, our previous theoretical study showed that the thermoelectric properties of LnOX Ch_2 can become very good, provided that electron doping by introducing defects makes the system metallic without largely changing the elec-

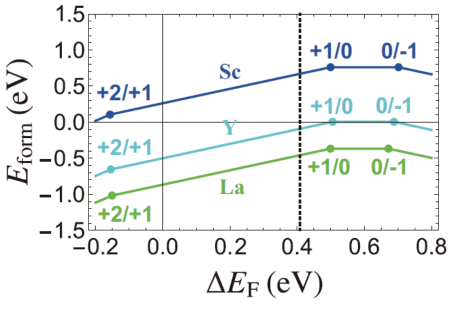

FIG. 1. The formation energy of the G3 substitution for the Ca site against the Fermi energy $\Delta E_F = E_F - E_V$ for CaZn$_2$As$_2$. The group 3 elements $G3$ (= Sc, Y, La) are chosen as dopant D. The dotted line denotes the position of the conduction band minimum[2].

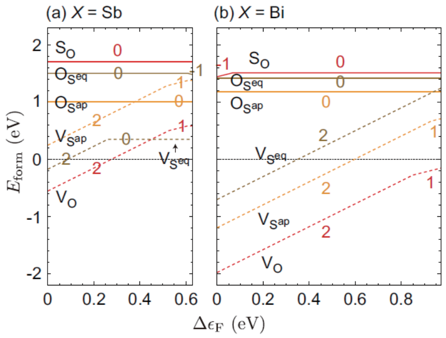

FIG. 2. Defect formation energies of anion point defects for (a) $LaOSbS_2$ (X = Sb) and (b) $LaOBiS_2$ (X = Bi). The horizontal line (the Fermi level) is restricted to the energy range between the band edges. The values of the charge q of the defects are shown beside the line[6].

tronic structure[4]. However, it has recently been found that it is experimentally difficult to enhance the electrical conductivity in X = Sb compounds against their robust insulating nature[5].

In 2021 fiscal year, in order to shed light on the puzzling transport properties of the doped layered pnictogen dichalcogenides, we have systematically investigated the defect formation energy of several point defects in $LaOXS_2$ (X = Sb, Bi) using first-principles calculation[6]. We used the PBE parametrization of the generalized gradient approximation and the projector augmented wave method as implemented in VASP.

We have found that anion replacements S_O (replacement of O by S) and O_S are not stable while V_O (O vacancy) and V_S can take place, where the formation energy of V_O is higher in X = Sb than in X = Bi (Fig.2). A characteristic feature is that $V_{S_{eq}}$ (S_{eq} is the in-plane S) becomes much more stable in X = Sb than in X = Bi, due to the formation of an Sb_2 dimer and the occupation of the impurity energy levels. The formation energies of cation defects, X_S, and S_X are found to be positive. We have also found that Fluorine likely replaces oxygen for both X = Sb and Bi. The defect formation energy of F_O is negative for both compounds, while that for X = Sb is much higher than X = Bi. Our study has clarified the stability of several point defects and suggested that the in-plane structural instability is enhanced in X = Sb. We expect that, although further study is necessary, the knowledge obtained in the study should be helpful for understanding/controlling the transport properties of $LaOXS_2$ and related compounds by impurity doping.

[1] H. Usui and K. Kuroki, J. Phys. Soc. Jpn. **89** (2020) 124707.
[2] K. Nishiguchi, M. Ochi, C.H.Lee, and K. Kuroki, to appear in J. Phys. Soc. Jpn.
[3] H. Tamaki, H.K. Sato, and T. Kanno, Advanced Materials **28** (2016) 10182.
[4] M. Ochi, H. Usui, and K. Kuroki, Phys. Rev. Appl. **8** (064020) (2017).
[5] Y. Goto *et al.*, J. Phys. Soj. Jpn. **289** (2019) 38.
[6] M. Ochi and K. Kuroki, Phys. Rev. B **105** (2022) 094110.

Studies on superconductivity in nickelates from a multiorbital viewpoint

KAZUHIKO KUROKI
Department of Physics, Osaka University
1-1 Machikaneyama, Toyonaka, Osaka, 560-0043, Japan

DESIGNING NICKELATE SUPERCONDUCTORS WITH $d^{8+\delta}$ ELECTRON CONFIGUATION

In 2020 fiscal year (the last fiscal year), we theoretically designed unconventional nickelate superconductors with d^8 electron configuration[1]. We considered d^8 nickelates with K_2NiF_4 structure, where the apical oxygens are replaced by halogens or hydrogens. One of the best candidates was electron-doped $Ca_2NiO_2Cl_2$. The key point was that the large crystal field splitting of the orbital energy levels, induced by replacing the apical oxygens by halogens or hydrogens, is approximately equivalent to large interlayer hopping in a bilayer system. Applying the fluctuation exchange approximation to the five orbital model of these materials, we showed that the maximum superconducting transition temperature of some of them may be even higher than that of the high-T_c cuprates.

A major drawback of our proposal was that $Ca_2NiO_2Cl_2$ has never been synthesized previously, and it may indeed be difficult to synthesize. On the other hand, a similar material $Sr_2NiO_2Cl_2$ has been synthesized experimentally[2], but its lattice constant is too large compared to $Ca_2NiO_2Cl_2$, resulting in a smaller crystal field splitting, and hence the predicted superconducting T_c, if any, is low. In fact, a high spin state is suggested in $Sr_2NiO_2Cl_2$, which is unfavorable for our mechanism to work, Given this background, in 2021 fiscal year, we studied the hydrostatic pressure effect on $Sr_2NiO_2Cl_2$ in an attempt to mimic the situation of $Ca_2NiO_2Cl_2$. The structural parameters under pressure has been determined using VASP. We have obtained five orbital models through Wannierization, and studied the model using the fluctuation exchange approximation. This is still an ongoing research, and we plan to publish the results as soon as possible.

EFFECT OF RESIDUAL HYDROGEN IN THE INFINITE LAYER NICKELATE SUPERCONDUCTORS

Our theory on desigining $d^{8+\delta}$ nickelate superconductors may also be related to another newly discovered superconductor (Nd,Sr)NiO_2[3]. In this superconductor, the nickel electron configuration is expected to be close to d^9, but this might be affected, e.g., by the reduction process during the synthesis of the material. Since the band structure of (Nd,Sr)NiO_2 itself, due to the absence of apical oxygens, resembles that of the proposed mixed anion-nickelates, (unintentional) reduction of the electron number in (Nd,Sr)NiO_2 may also result in a similar $s\pm$-wave superconductivity.

In 2021 fiscal year, we have studied the effect of residual hydrogen using the adopting the supercell approach, which contains multiple Ni atoms in a unit cell due to the presence of eccess hyrdogens added at the apical site periodically. The structural parameters were determined using VASP. We have so far constructed 10 and 20 orbital models of these systems through Wannierization. We plan to analyze the possibility of superconductivity in these multiorbital models.

---

[1] N. Kitamine, M. Ochi and K. Kuroki, Phys. Rev. Res. **2**, 042032(R).

[2] Y. Tsujimoto, C.I. Sathish, Y. Matsushita, K. Yamaura, and T. Uchikoshi, Chem. Commun. **50**, 5915 (2014).

[3] D. Li *et al.*, Nature (London) **572**, 624 (2019).

First principles studies of impurity-dislocation complexes in GaN

Kenji SHIRAISHI

Institute of Materials and Systems for Sustainability,

Nagoya University, Furo-cho, Chikusa-ku, Nagoya, Aichi 464-8601

Line defects and points defects have intensively studied so far [1, 2]. However, complexes composed of line defects and point defects have not been considered yet. In this project, we have studied dislocation-impurity-complexes in GaN by the first principles calculations.

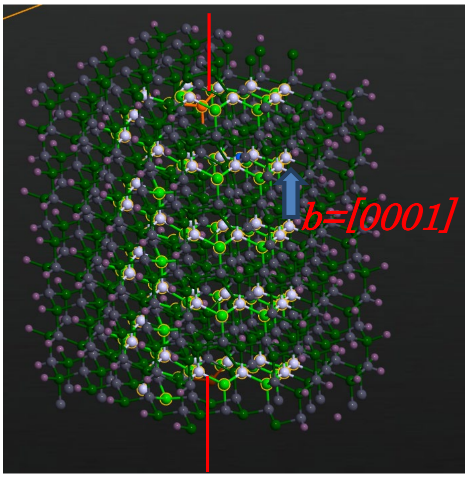

Fig.1: Atomistic Structures of a calculation model of the complex composed of GaN screw dislocation and Mg and H impurities.

Calculations were performed by VASP package. We prepared 800 atom unit cells which contain a screw dislocation and Mg and H impurities as shown in Fig.1.

It is well-known in bulk GaN that Mg and H impurities tend to form complexes of the Mg-N-H local structure. However, calculated results indicate that Mg-H complexes do not form near the screw dislocation, although screw dislocations attract both Mg and H atoms.

Figure 2 shows the atomistic structures of the complex composed of a GaN screw dislocation and Mg and H impurities. As shown in this figure, the local Mg-N-H structure which is observed in bulk GaN is broken by the effect of the screw dislocation. This indicate that properties of point defects are totally changed by the effect of line defects in the dislocation-impurity complexes.

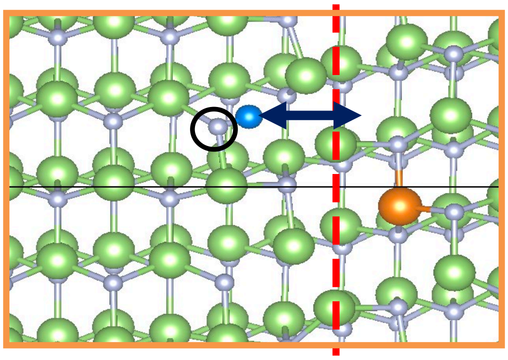

Fig.2: Atomistic structures of a complex composed of a GaN screw dislocation and Mg and H impurities.

References

[1] S. Berber et al. : Phys. Rev. B 77, (2008) 165405.

[2] K. Matsunaga: Acta Mater. , 195, (2020) 645.

First Pricnciples Study of N Vacancies in Si_3N_4 for Flash Memory Application

Kenji SHIRAISHI

Institute of Materials and Systems for Sustainability,

Nagoya University, Furo-cho, Chikusa-ku, Nagoya, Aichi 464-8601

Defects in Si3N4 are now used for the application of 3D NAND flash memories. Among Defects in Si_3N_4, N vacancies are considered as the physical origins of charge traps used in memory functions [1, 2]. Recently, the charge transfer between charge traps in Si_3N_4 has become serious problem in the miniaturized 3D NAND flash memories. However, the physical mechanisms of this charge transfer is not clarified. In this study, we investigated the charge transfer mechanism by the first principles calculations.

First, we calculated the formation energies of a N vacancy (V_N). The results are shown in Fig. 1. As shown in Fig. 1, stable charged states are -1, 0 and +1 in the Si_3N_4 Fermi energy. Next, we calculated the formation energies of a V_N-H complex as shown in Fig. 2. As shown in Fig. 2, stable charged states are -2, 0, and 2 in the Si_3N_4 Fermi energy. This indicate that H diffusion from one V_N to another V_N causes charge transfer when V_N traps electrons.

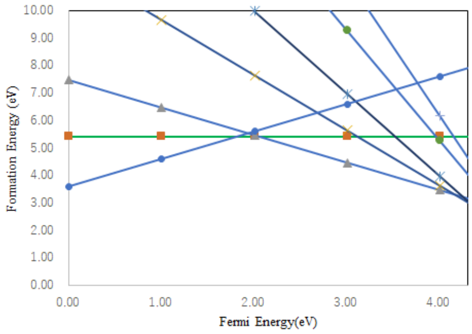

Fig.1: Formation energies of various charged state of the N vacancy as a function of system Fermi energy. -1, 0 and +1 charged states are stable.

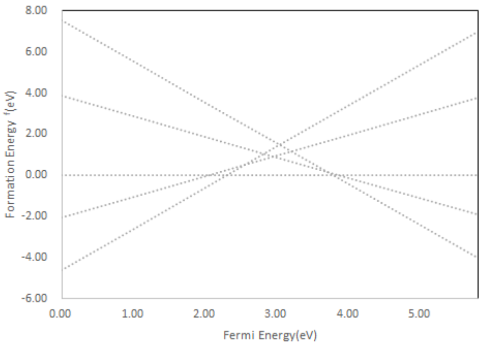

Fig. 2: Formation energies of various charged state of the N vacancy as a function of system Fermi energy. -2, 0 and +2 charged states are stable.

References

[1] K. Yamaguchi, A. Otake, K. Kobayashi, and K. Shiraishi, Tech. Digest of IEEE Int. Electron DevicesMeeting (IEDM), Baltimore, MD, USA, 2009, pp. 1–4.

[2] K. Yamaguchi, A. Otake, K. Kamiya, Y. Shigeta, and K. Shiraishi,Jpn. J. Appl. Phys.,50, (2011) 04DD05.

Development of quantum algorithm for imaginary-time evolution

Yu-ichiro MATSUSHITA
Tokyo Tech Academy for Convergence of Materials and Informatics (TAC-MI),
Tokyo Institute of Technology, Ookayama, Meguro-ku, Tokyo 152-8550

Recently, the development of materials computation methods using quantum computers has attracted a great deal of attention. In particular, we have paid attention to the imaginary-time evolution method, which has been known for a long time in materials computation, and have worked on the development of algorithms for its execution on a quantum computer. As a result, we have succeeded in developing an algorithm for quantum imaginary-time evolution methods [1].

On a quantum computer, only unitary transformations and observations must be used to achieve the desired computation. The imaginary-time evolution operator is a non-unitary transformation, and its realization on a quantum computer is non-trivial. One approach developed in this study is to realize the approximated imaginary-time evolution operator on a quantum computer by finding a unitary operator that best approximates the quantum state after the operation of the imaginary-time evolution operator. This method uses a classical computer in finding the unitary operator, and its unique feature is that it is a hybrid classical-quantum algorithm.

We have developed a so-called “nonlocal” approximation as a method for finding approximate unitary operators, and have developed the method to realize quantum imaginary-time evolution with a quantum circuit shallower than the conventional methods of imaginary-time evolution. We constructed an actual quantum circuit and applied it to the MAXCUT problem. For the calculations, we verified the effectiveness of the algorithm with a quantum circuit simulator. The results showed that the quantum imaginary-time algorithm does work, and at least 94% of accuracy is achieved for unweighted 3-regular MAXCUT problems with ten vertices. At the same time, we have found that there is an accuracy limit due to the introduction of an approximate unitary operator, and the algorithm does not completely match the exact solution.

References

[1] H. Nishi: npj Quantum Information **7** (2021) 85.

First-Principles Molecular-Dynamics Study of Structural and Electronic Properties of Covalent Liquids and Glasses under Pressure

Fuyuki SHIMOJO

Department of Physics, Kumamoto University, Kumamoto 860-8555

It is important for the investigation of the dynamic properties of covalent liquids and glasses under pressure to consider the stability of materials states under various conditions from the viewpoint of free energy. For this purpose, the thermodynamic integration (TI) method based on the first-principles molecular dynamics (FPMD) simulations is useful and effective. However, the system size and simulation time are limited due to the high calculation cost of FPMD. To solve this cost problem, we have used machine-learning interatomic potential based on artificial neural networks (ANN) trained from the results of FPMD simulations.

In this study, we have calculated the melting temperature of diamond, one of the typical covalently bonded materials, using the TI method with the ANN potential as a function of pressure. Figure 1 shows the pressure dependence of calculated melting temperature. The results of this study are indicated by the red diamond symbols. The triangle up and down symbols indicate the results of the previous theoretical study, which carried out the direct simulation of solid/liquid coexistence by using a so-called two-phase simulation method based on FPMD [1]. Both results are in reasonable agreement with each other.

We have also obtained the melting temperature of binary alkali Na_xRb_{1-x} mixture [2] as a function of concentration x, and found that the melting temperature minimum occurs at $x = 0.2$, being in agreement with the experimental observation. These two findings for diamond and alkali mixture demonstrate the validity and usefulness of the current method.

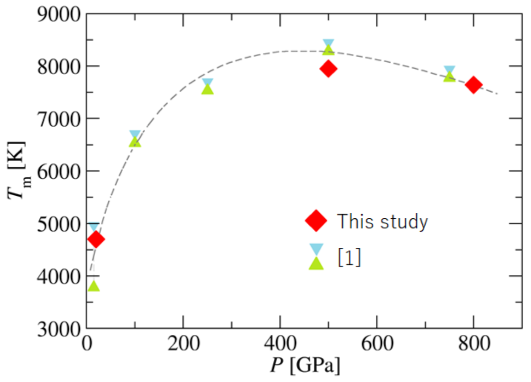

Fig. 1: Pressure dependence of melting temperature of diamond.

References

[1] A. A. Correa *et al*., PNAS **103**, 1204 (2006).

[2] A. Irie et al., J. Phys. Soc. Jpn. **91**, 045002 (2022).

Development of first-principles electronic-structure and transport calculation code RSPACE and simulations for device

Tomoya ONO
Graduate School of Engineering, Kobe University
Rokkodai-cho, Nada, Kobe 657-8501

Silicon carbide (SiC) attracts attention because it is one of the most promising wide-bandgap semiconductors for developing next-generation switching devices operating in high-power and high-frequency applications. However, the potential of 4H-SiC has not been fully utilized owing to the low carrier mobility of 4H-SiC-based metal-oxide-semiconductor field-effect transistors, which is caused by defects at the 4H-SiC/SiO_2 interface. To reduce the density of interface defects and increase the channel mobilities, post-oxidation annealing using N_2O, NO, or N_2 gas has been proposed. In this study, we propose the interface atomic structures in which N atoms are incorporated by replacing C atoms, and we investigate the total energies and electronic structures of the nitride layers by density functional theory (DFT) calculation. Universal atomic-scale models describing 4H-SiC with a high-N-atom-density layer in arbitrary crystal planes are proposed. To explore the most preferable crystal plane of 4H-SiC for N-atom incorporation, we study the stability and electronic states of the nitride layers on a 4H-SiC surface. We find that the nitride layers grow along the a face, which is consistent with the conclusion obtained using the bulk model[1]. Any defect states in the bandgap of 4H-SiC are not generated in our structure. The formation energy of the nitride layers at the topmost layer of the interface is smaller than that at the second layer, indicating that the N atoms accumulate at the interface.

In our model, the surface of the 4H-SiC substrate is terminated with OH groups to imitate the SiO_2 layer and the other side of the substrate is terminated with H atoms. The rectangular supercells of 10.1 Å × 10.7 Å × 26.3 Å for the a-face model, 10.1 Å × 12.3 Å × 27.3 Å for the m-face model, and 12.3 Å × 10.7 Å × 26.8 Å for the Si(C)-face model were employed. The z-axis is taken to be the direction perpendicular to the surface. The numbers of atoms for the a-face, m-face, and Si(C)-face models are 176, 208, and 208. We considered the modification incorporating four Si vacancies (V_{Si}s) and 16 N atoms at C sites (N_Cs). The cases in which V_{Si}s are arranged parallel to the surface were investigated to evaluate the anisotropy of the formation energy of the nitride layer. In our model, the areal N-atom density is on the order of 10^{14} cm^{-1}, which is consistent with the experimental results. Although there are two inequivalent lattice sites of 4H-SiC, i.e., h (hexagonal) and k (quasi-cubic) sites, our previous studies have shown that nitride layers tend to grow at the k site. Thus, we consider the cases in which V_{Si}s are arranged at the k site. The interfaces with the nitride layer at the second layer are also investigated for all the faces. For the first-principles calculation, we used the RSPACE code[2, 3], which is based on the real-space finite-difference approach within the frameworks of DFT and is developed in this project.

We employed the local density approximation of the DFT to describe the exchange and correlation effects. Electron–ion interactions are approximated by the projector-augmented wave method. We adopt $6 \times 6 \times 1$ Monkhorst-pack k-point meshes including a Γ-point in the Brillouin zone. The real-space grid spacing is chosen to be ~ 0.21 Å. The structural optimization is performed until the residual forces are smaller than 0.001 Hartree/Bohr radius.

We assumed the interaction of the SiC substrate and the arriving NO molecule at the interface as

$$\mathrm{SiC}^{(\mathrm{w/o\ mod})} + 24\mathrm{NO} \rightarrow \mathrm{SiC}^{(\mathrm{w/\ mod})} + 4\mathrm{SiO_2} + 16\mathrm{CO} + 4\mathrm{N_2},$$

with $\mathrm{SiC}^{(\mathrm{w/o\ mod})}$ ($\mathrm{SiC}^{(\mathrm{w/\ mod})}$) being the interface without (with) the modification incorporating four V_{Si}s and 16 N_{C}s. The formation energy of the above interaction for generating one V_{Si} is obtained as

$$E_{\mathrm{form}} = E_{\mathrm{total}}^{(\mathrm{w/\ mod})}/4 + E(\mathrm{SiO_2}) + 4\mu_{\mathrm{CO}} + 2\mu_{\mathrm{N}} - E_{\mathrm{total}}^{(\mathrm{w/o\ mod})}/4 - 6\mu_{\mathrm{NO}}, \quad (1)$$

where $E(\mathrm{SiO_2})$ is the total energy of a $\mathrm{SiO_2}$ unit in a bulk of quartz $\mathrm{SiO_2}$. $E_{\mathrm{total}}^{(\mathrm{w/o\ mod})}$ and $E_{\mathrm{total}}^{(\mathrm{w/\ mod})}$ represent the total energies of the interface without and with N-atom incorporation, respectively. In addition, μ_{NO}, μ_{CO}, and μ_{N} are the chemical potentials of a NO molecule, a CO molecule, and N atoms in a $\mathrm{N_2}$ molecule, respectively. We set the temperature at 1000 K and the partial pressure of NO gas (p_{NO}) at 1 atm. The partial pressures of CO (p_{CO}) and $\mathrm{N_2}$ ($p_{\mathrm{N_2}}$) gases are set at 10^{-5} atm and 0.25×10^{-5} atm.

The formation energies of the nitride layers are shown in Table 1. We find that all the reactions are exothermic and the nitride layers growing along the a face are the most stable among those along the a, m, C, and Si faces. The formation energy of the nitride layer at the topmost layer is smaller than that at the second layer, resulting in the localization of the N atoms at the interface. Note that the NO annealing generates the nitride layers immediately below the $\mathrm{SiO_2}$ layers without any transition layers. The difference in the formation energy between the nitride layers at the topmost and second layers is the largest for the a face. This result agrees well with the observation that the formation energy of the nitride layer along the a face is the smallest. The local densities of states of the interfaces reveal that there are no gap state at the interface. These results imply that NO annealing after the oxidation can contribute to the reduction in the density of interface defects by forming the nitride layer immediately below the $\mathrm{SiO_2}$ layer of the interface.

Table 1: Formation energy of nitride layers defined by Eq. (1).

face	layer	E_{form} (eV)
a	top	−7.43
a	2nd	−7.10
m	top	−7.13
m	2nd	−7.07
Si	top	−7.07
Si	2nd	−7.01
C	top	−7.14
C	2nd	−7.01

References

[1] M. Uemoto, N. Komatsu, Y. Egami, and T. Ono, J. Phys. Soc. Jpn. **90**, 124713 (2021).

[2] T. Ono and K. Hirose, Phys. Rev. Lett. **82**, 5016 (1999).

[3] K. Hirose, T. Ono, Y. Fujimoto, and S. Tsukamoto, *First Principles Calculations in Real-Space Formalism, Electronic Configurations and Transport Properties of Nanostructures* (Imperial College, London, 2005).

Analysis of Surface Reactions in Atomic Layer Etching Processes

Satoshi HAMAGUCHI
Center for Atomic and Molecular Technologies,
Osaka University, 2-1 Yamadaoka, Suita, Osaka 567-0871

Thermal atomic layer etching (ALE) can be used for precise and damageless etching. For example, it can be used to fabricate magnetic tunnel junction (MTJ) stacks of magnetoresistive random-access memory (MRAM) devices [1]. The aim of this study is to understand the mechanisms of thermal ALE of metal in general, whose cycle consists of an oxidation step and an exposure step to β–diketones, such as; hexafluoroacetylacetone (hfacH), trifluoroacetylacetone (tfacH), and acetylacetone (acacH) molecules. For instance, thermal ALE of Ni with hfacH starts with the deprotonation of hfacH molecules after the oxidation of the Ni surface. By increasing the surface temperature in the range of 300 ~ 400 °C, volatile nickel complex Ni(hfac)2 and water H2O molecules are formed on the surface and remove the NiO layer. In this process, once a new metallic Ni surface appears, no further etching occurs, which ensures the self-liming nature of the thermal ALE process [2-5].

First, we examined the interaction of β–diketones with a metallic Ni surface, using STATE [6,7]. STATE is a simulation code based on density functional theory (DFT) with pseudo-potentials and a plane wave basis set. It has been found that the cleavage of a C-F or C-H bond of a β–diketone is more likely to take place than the deprotonation on a metal surface. The surface roughness can also help to form C-Ni bonds, which were also observed in experiments. The reaction mechanisms that we observed in these simulations have revealed the self-limiting nature of thermal ALE for metals with β–diketone gases in general, which is consistent with earlier experimental observations [5,8].

Second, we examined the interaction of β–diketones with oxidized metal surfaces, using TURBOMOLE program [9]. It has been found that, as β–diketones approach an oxidized metal surface, they deprotonate. In this way, volatile metal complexes and H_2O molecules can be formed when β–diketone molecules interact with an oxidized metal surface. The reaction energies of such interactions have been evaluated from the simulations and we found that etch oxidized metal has its own desorption energy or temperature to volatilize its metal complex. Therefore, the applied temperature can be used as a self-limiting condition if the target contains different materials. In addition, hfacH is found to get more stably bonded than acacH or tfacH with an oxidized metal surface because the negatively charged F atoms in CF_3 are repelled by O atoms of the surface, which forces a deprotonated hfac to adsorb on the surface nearly vertically. This does not happen to acacH, whose CH_3 groups tend to interact directly with the metal oxide. As a result, hfacH is considered more suited for ALD processes than other β-diketones.

In addition, we also examined the interaction of Y_2O_3 with incident F_+ and CF_3^+ ions, using ion beam experiments with XPS and DFT simulations. It has been found that the penetration depth of F atoms in Y_2O_3 exposed to F^+ or CF_3^+ ion injection depends essentially on the incident energy and hardly depends on the ion dose once a sufficient amount of fluorine is provided to the surface and saturate. We also obtained the atomic concentration depth profiles by XPS measurement. The results indicate that carbon contained in the incident CF_3^+ ions remove oxygen of Y_2O_3 more efficiently. Furthermore, high-energy incident CF_3^+ ions promoted the formation of Y-F bonds near the surface region of Y_2O_3 films more efficiently than low-energy incident CF_3^+ ions. Our simulation results are found to be consistent with these experimental observations.

REFERENCES

[1] G. S. Oehrlein and S. Hamaguchi, Plasma Sources Sci. Technol. 27, 023001 (2018).

[2] A. H. Basher et al., JJAP 59, 090905 (2020).

[3] A. H. Basher et al., JVST A 38, 052602 (2020).

[4] A. H. Basher et al., JVST A 38, 022610 (2020).

[5] T. Ito, et al., AVS 65th (2018).

[6] I. Hamada, Physical Review B 89 (12), 121103, (2014).

[7] Y. Morikawa et al., Phys. Rev. B, 69, 041403 (2004).

[8] H. L. Nigg and R. I. Masel, JVST A 17, 3477, (1999).

[9] TURBOMOLE V7.5 2020, https://www.turbomole.org.

First-principles study on atomic and electronic structures of graphene/SiC interfaces

Yoshiyuki EGAMI
Division of Applied Physics, Faculty of Engineering, Hokkaido University
Kita 13, Nishi 8, Kita-ku, Sapporo, Hokkaido 060-8628

Graphene is in the limelight as a post-silicon material in next-generation devices due to its unique electronic and mechanical properties and conductivity. In recent years, the epitaxial growth in the silicon carbide (SiC) pyrolysis method has attracted attention as one of useful methods for producing large-scale and high-quality graphene. However, in the pyrolysis method, the bottom graphene layer is covalently bonded to the Si atom of the SiC substrate. To separate the bottom layer from the substrate, atomic intercalation technique is employed. As the result, the bottom layer becomes an ideal single-layer graphene, and the Dirac cone appears in the electronic band structure. On the other hand, atomic vacancies are formed in the graphene during the epitaxial growth process. Since the intercalants can be bonded to the dangling bonds, which are affected on the energy band structure and the position of the Dirac point of graphene.

In this study, fluorine atoms are adopted as intercalants, and the effect of the bond between a fluorine atom and a dangling bond on the electronic state of graphene is investigated using the first-principles calculation code: RSPACE[1, 2]. We investigate the difference in the effects of the number of fluorine atoms adsorbed on the single vacancy in the graphene on the electronic state. It is found that, in the model where two fluorine atoms are bonded to the defect, the dangling-bond state is hybridized with the conduction band bottom of SiC substrate. Moreover, the conjugated π state of graphene is extended over the energy range in which the bandgap of SiC substrate is located (Fig. 1). On the other hand, in the system produced by hydrogen intercalation, the dangling bond state is in the middle of the band gap of the SiC substrate and extends to the inside of the substrate, which can cause a large leakage current.

This work has been performed on System B of the Supercomputer Center, the Institute for Solid State Physics, the University of Tokyo.

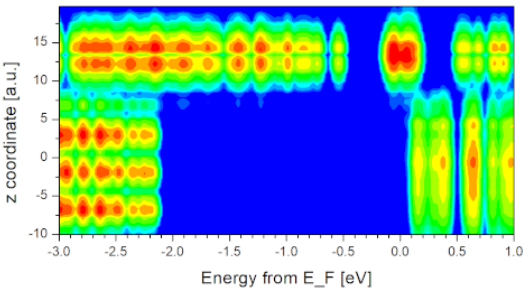

Figure 1: Local density of states of graphene with single vacancy on fluorine-intercalated SiC substrate. Two of dangling bonds are terminated by fluorine atoms.

References

[1] K. Hirose *et al.*: First-principles calculations in real-space formalism (Imperial College Press, 2005).

[2] Y. Egami, S. Tsukamoto and T. Ono: Phys. Rev. Res. **3**, 013038 (2021).

High-Throughput Polymer Electret Material Screening Based on Solid-State Quantum Chemical Calculation and Deep Learning

Yucheng ZHANG, Zetian MAO, and Yuji SUZUKI

Department of Mechanical Engineering

The University of Tokyo, Hongo, Bunkyo-ku, Tokyo 113-8656

Electret is a dielectric material with quasi-permanent charges and can trap charges stably for decades. Vibrational electret energy harvester (VEEH) can generate electricity efficiently from kinetic energy via the electrostatic induction. The VEEH with bipolar (both positively and negatively charged) electret leads to four times output power theoretically, thus specifying the importance of designing high-performance bipolar polymer electrets.

CYTOP (Cyclic Transparent Optical Polymer, AGC Chemicals) is one of the best polymer electret materials, with three commercialized types displayed in Fig. 1. Recently, we utilized quantum chemical analysis for evaluating the charge trap of CYTOP electrets [1]. It is found that although the repeat-unit-number of CTX-A is above 1000, the trapped charge is localized at the amide bond, which is formed by dehydration reaction between the carboxyl end group and the amine introduced. It is also shown that the computed electron affinities (EAs) and ionization potentials (IPs) by the density functional theory (DFT) with polarizable continuum model (PCM) correction agree well with the trends of the surface charge density and charge stability measured by the wet experiments.

Most recently, by employing the de novo molecule generation and the functional group enrichment analysis, we successfully proposed the electret CTX-A/APDEA with high bipolar charging performance via combining CTX-A with N-(3-aminopropyl) diethanolamine [2]. This result encouraged us to move further to search new amines in the open-source database PubChem, aimed at designing better bipolar polymer electret based on CYTOP CTX-A after the dehydration reaction.

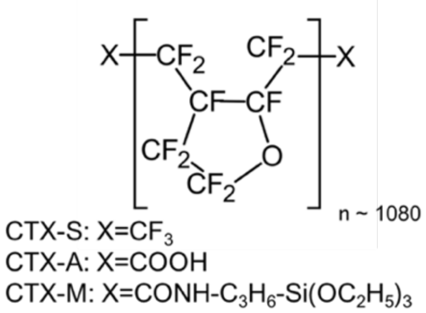

Fig. 1. Chemical structure of CYTOP series.

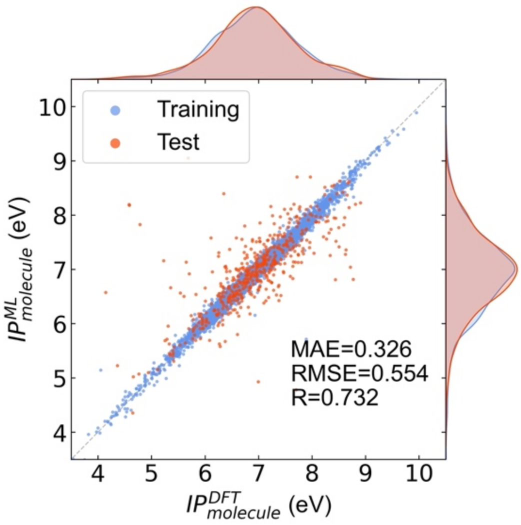

Fig. 2. Prediction of PCM-DFT IPs for training and test sets using MEGNet.

Although solid-state quantum chemical calculation based on PCM-DFT can give quantitative EA and IP values, the average computation time is 41.4 CPU hours per monomer molecule and even as high as 2500 CPU hours per hexamer molecule. To reduce such heavy computational cost, we employ deep learning models to approximate the EAs and IPs efficiently.

To prepare the labeled data, 5522 amines were initially sampled from the PubChem. Thereafter, the virtual dehydration reaction was conducted and PCM-DFT computation was automatically made. Subsequently, a dataset mapping the PCM-DFT IPs and molecular structures was establised and splited into training-validation-test sets with the ration of 80%, 10%, and 10%, where the training set was used to teach the deep learning models and the performance of the models were tested on the test set.

Fig. 2 illustrated the prediction results on the established dataset with one kind of deep learning models named MEGNet [3]. The mean absolute error (MAE) of IP is as small as 0.326 eV, with computational cost decreased significantly. Therefore, the present approach will be employed for screening bigger database for new high-performance bipolar polymer electrets.

The geometry of the molecule is relaxed under the open-shell condition and then the energy of both open-shell and closed-shell system are calculated and compared. All the quantum chemical calculations are made with the software GAUSSIAN [4] at the DFT level with the CAM-B3LYP functional and 6-31+G(d,p) basis set, while PCM is combined for solid-state analysis due to the solvation effect correction.

This work was partially supported by JST CREST Grant Number JPMJCR15Q3 and JPMJCR19Q1. The calculations are performed with SGI ICE XA ISSP system B and every calculation is done with 1 node (24 CPUs).

References

[1] Kim S., et al., J. Phys. Chem. B, Vol. 124, No. 46, pp. 10507-10513 (2020).

[2] Zhang, Y., et al., Appl. Phy. Lett., 118, 223904 (2021).

[3] Mao, Z., et al., IEEE Conf. Electr. Insul. Dielectr. Phenom., pp. 667-670 (2021).

[4] M. Frisch et al., “Gaussian 09, Rev. A. 1,” Gaussian, Inc. Wellingford, CT, (2009).

First-principles calculations on muon in solids

Mineo SAITO
Institute of Science and Technology, Kanazawa University
Kakuma, Kanazawa, 920-1192 Japan

Hydrogen plays an important role in semiconductor materials; Well known examples are hydrogen passivation and carrier injection. The muon spin resonance is an effective tool to determine the dynamics of hydrogen in semiconductors since muonium consisting of a positive muon and an electron bears similarities to hydrogen. Observed hyperfine structures provide useful information on the atomic site of muonium, and thus that of hydrogen. In a previous study, we clarified that negative Fermi contact terms are caused by the electron correlation and observing the negative value suggests the formation of resonance bond of hydrogen [1].

One of the scientifically important new targets is hydrogen impurity in barium silicide ($BaSi_2$), which is a candidate for solar cell materials. It is known that hydrogen passivates the defect level of Si vacancy. This crystal includes Si tetrahedrons and electrons transfer from barium to silicon. We first confirm that this crystal has an indirect gap and the gap value calculated based on the hybrid density functional theory is 1.36 eV, which is close to the experimental value. On the other hand, the value calculated based on the GGA is small (0.71 eV). The Si monovacancy is found to form a triangle of the C_{2v} symmetry and to induce a mid-gap level having large amplitudes at the equivalent two atomic sites.

We find that the monohydrogen-vacancy pair induces the gap level. On the other hand, we find that dihydrogen passivates the defect level. It is suggested from out calculation that trihydrogen-vacancy pair leads to n-type doping. We conclude that hydrogenation plays various roles in barium silicide, which depends on the concentration of hydrogen. The muon spin resonance measurement is expected to confirm the atomic geometry of the monohydrogen-vacancy pair.

[1] M. N. Manal, S. Minami, F. Ishii and M. Saito, Jpn. J. Appl. Phys., 58 (2019) 081008.

GW + BSE calculation of RIXS spectra by the all-electron mixed basis program, TOMBO

Kaoru OHNO

Graduate School of Engineering, Yokohama National University
79-5 Tokiwadai, Hodogaya-ku, Yokohama 240-8501

The initial state of X-ray emission spectroscopy (XES) and resonant inelastic X-ray emission spectroscopy (RIXS) is a highly excited eigenstate with a deep core hole after the X-ray photoelectron spectroscopy (XPS) and X-ray photoabsorption spectroscopy (XAS) processes, so that the XES and RIXS calculation offers a good example of extended quasiparticle theory (EQPT) [1] associated with many-body perturbation theory. Moreover, to overcome the basis set incompleteness problem, we adopt the all-electron mixed basis program, TOMBO, which uses both plane waves and numerical atomic orbitals as basis functions. We have successfully applied this approach in our previous XES [2] study. Here we applied the standard one-shot *GW* + Bethe--Salpeter equation (BSE) approach in MBPT to this problem on the basis of EQPT and analyze XES and RIXS energies for CH_4, NH_3, H_2O, and CH_3OH molecules.

Figure 1 shows the RIXS spectra of a CH_3OH molecule calculated by our method together with the experimental data [3]. Both results coincides very well without introducing any empirical fitting parameter.

Moreover, according to extended Kohn- Sham theory [4], we gave a justification and comment of applying the method relying on time-dependent density functional theory as well as the one-shot *GW* + BSE approach to this problem.

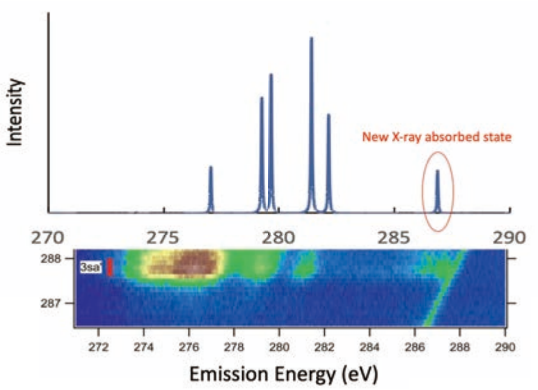

Fig. 1: Calculated (above) and experimental [3] (below) RIXS spectra of a CH_3OH molecule.

References

[1] K. Ohno, S. Ono, and H. Isobe: J. Chem. Phys. **146** (2017) 084108.

[2] T. Aoki and K. Ohno: Phys. Rev. B **100** (2019) 075149.

[3] A. Benkert, F. Meyer, D. Hauschild, M. Blum, W. Yang, R. G. Wilks, M. Bär, F. Reinert, C. Heske and L. Weinhardt,: J. Phys. Chem. A **120** (2016) 2260.

[4] T. Nakashima, H. Raebiger, and K. Ohno: Phys. Rev. B **104** (2021) L201116.

Theoretical study of electric double-layer structure of MXene electrode dependent on surface functional groups

Atsuo YAMADA

Department of Chemical System Engineering,

The University of Tokyo, Bunkyo-ku, Hongo, Tokyo 113-8656

Aqueous electric double-layer capacitor (EDLC) is promising candidate for large-scale stationary storage due to non-flammability, low materials cost, and non-toxicity of aqueous electrolyte. Transition metal carbides/nitrides (MXenes) are appealing electrode materials for aqueous EDLCs owing to their high specific capacitance (> 300 F/g) in conventional aqueous electrolyte. Herein, we investigated the dependence of EDL capacitances on the surface functional groups of the MXene electrodes [1].

The ESM-RISM method was adopted to evaluate the capacitance of the MXene electrodes. The simulation cells are composed of MXene $Ti_3C_2T_2$ with different surface functional groups (T = F, Cl, Br, and I) and the 1 M KOTf/H_2O electrolyte. Here, MXene electrodes were treated quantum-mechanically using the density functional theory method, while electrolytes were described using the RISM method. All the ESM-RISM calculations were conducted with Quantum Espresso code.

The calculated EDL capacitance increased with the increase in the atomic number of halogen atoms (F < Cl < Br < I) (Fig.1a). The increased EDL capacitance is due to the biased distribution of excess electrons in the electrode toward the electrolyte, thus reducing the EDL thickness (Fig. 1b). The induction of electrode electrons into the EDL region is facilitated by the smaller negative charges of surface halogen atoms with lower electronegativity. Therefore, lowering the valence numbers of the MXene surface atoms should enhance the capacitance.

References

[1] T. Shimada N. Takenaka, Y. Ando, M. Otani, M. Okubo, A. Yamada, *Chem. Mater.*, **34**, 2069 (2022).

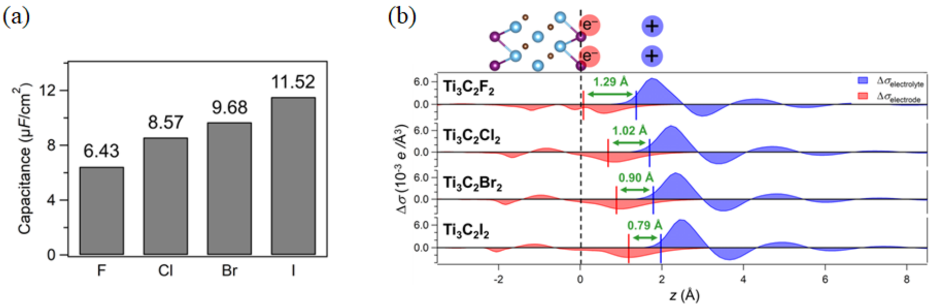

Figure 1 (a) Calculated capacitances per unit surface area of MXene. (b) Spacial distributions of excess electrons of the electrode (red) and counter positive charges of the electrolyte (blue) at the electrode/electrolyte interface.

Elucidation of mechanism and theoretical prediction of super-functional materials using high-density hydrogen

Shinji TSUNEYUKI
Department of Physics, School of Science,
The University of Tokyo, 7-3-1 Hongo, Bunkyo-Ku, Tokyo 113-0033
Institute for Solid State Physics,
The University of Tokyo, Kashiwa-no-ha, Kashiwa, Chiba 277-8581

Hydrogen, a ubiquitous element, is present as an impurity in various materials and is known to significantly change materials' electrical and mechanical properties by assuming different charge states depending on the atoms' environment. In recent years, record-breaking superconductors and superionic conductors have been discovered in which protons and hydrides are major components. One of the most common problems in studying these materials is the difficulty in experimentally quantifying and observing the position of hydrogen, which has no inner-shell electrons.

Electronic structure calculations based on density-functional theory and first-principles molecular dynamics methods allow quantitatively predicting materials' structure and physical properties without empirical parameters. By these methods, the energy of the system and the forces acting on the atoms can be calculated using atomic configurations as input data. In principle, it is possible to predict how much and where hydrogen atoms are stable in a crystal and what physical properties they will exhibit without experiments. In this project, we applied the methods to elucidate the mechanism of the photo-induced metallization of Yttrium oxyhydride recently discovered by a Tokyo Tech group experimentally [1].

In their experiment, light irradiation significantly reduced the electrical resistance of an insulator YO_xH_y epitaxial thin film, and the metallic state was maintained on a scale of several days. Conventional polycrystalline YO_xH_y on glass substrates exhibits a one-digit decrease in electrical resistance upon solar irradiation, while the epitaxial thin film has achieved a resistance reduction of more than three orders of magnitude. Furthermore, UV laser irradiation of the epitaxial thin film reduced the electrical resistance by more than seven orders of magnitude.

To explain these results, we constructed a structural model based on high-resolution measurements of the local structure and chemical composition, and calculated the electronic structure based on this model. As a result, we found that the hydrogen atoms change their position and the charge state, leading to the long-life metallization [1,2].

Another topic in this project is the study of ionic superconductor $LiCB_9H_{10}$. We first applied the data assimilation method for structure prediction [3] to find no significant difference between the high-T and low-T structures. From a first-principles molecular dynamics simulation, we found that the motion of Li ions strongly correlates with the rotation of the $CB_9H_{10}^-$ complex. Finally, by constructing neural-network interatomic potentials, we calculated the ion conductivity by a large-scale molecular dynamics simulation in good agreement with experiments. Through these simulations, we found that the ion conductivity of the high-T phase is enhanced one order of magnitude by the concerted motion of Li ions and another one order of magnitude by the rotation of the $CB_9H_{10}^-$ complex [4].

References

[1] Y. Komatsu et al.,, Chem. Mater. 34, 3616 (2022).

[2] R. Sato et al., to be submitted.

[3] N. Tsujimoto, D. Adachi, R. Akashi, S. Todo and S. Tsuneyuki, Phys. Rev. Materials 2, 053801 (2018).

[4] R. Sato et al., submitted.

Reduction of Rare Metals in Fuel Cell Catalysts and Hydrogen Permeable Membrane

Norihito Sakaguchi

Center for Advanced Research of Energy and Materials, Faculty of Engineering,

Hokkaido University, Sapporo, Hokkaido 060-8628

We investigated the catalyst adsorption and diffusion properties on light-element doped graphene supported on the magnetic substrates and hydrogen dissolution and diffusion properties in the amorphous ceramic materials, with the aid of the first-principles calculation based on the density functional theory (DFT) and machine learning potentials.

At first, we investigated the stabilities of Pt atoms on light-element doped graphene supported on the magnetic substrates. We considered Fe and Ni as the magnetic substrates. We performed the total energy and electronic structure calculations using The Vienna Ab initio simulation package (VASP). We revealed that the adsorption of Pt atoms on light-element doped graphene with flat structures becomes stronger through supporting on the magnetic substrates. However, in most cases of steric light-element doped graphene, the magnetic substrates weaken the Pt adsorption on the light-element doped graphene. We also found that the magnetic substrates reduce the diffusion barriers of Pt atoms. Therefore, the magnetic substrates enhance the catalyst diffusion and coarsening. In addition, we also revealed that the Cl^- ion adsorption enhances the anisotropic catalyst nanorod growth.[1]

We also investigated the hydrogen dissolution and diffusion properties in the amorphous ceramic materials. We considered the Al_2O_3 as the hydrogen permeation membrane. Since DFT calculations of amorphous materials require quite large computing costs, we constructed the machine learning potential to reproduce the interatomic potentials obtained with DFT calculations. We performed melt-quenching technique to obtain the amorphous structure. We performed 2000 DFT calculations with various hydrogen positions in amorphous Al_2O_3 to construct the database for machine learning. The obtained machine learning potentials reproduce the stable adsorption structures, however, cannot reproduce the diffusion barriers obtained with DFT calculations

References

[1] M. J. Saw, M. T. Nguyen, Y. Kunisada, T. Tokunaga, T. Yonezawa, ACS Omega 7 (2022) 7414.

Reduction of Rare Metals in Formic Acid Decomposition Catalysts and Oxygen Storage Materials

Yuji KUNISADA
Center for Advanced Research of Energy and Materials, Faculty of Engineering,
Hokkaido University, Sapporo, Hokkaido 060-8628

We investigated the catalyst adsorption and diffusion properties on light-element doped graphene supported on the magnetic substrates with the aid of the first-principles calculation based on the density functional theory (DFT). Besides, we performed electron energy loss spectroscopy (EELS) simulations of heteroatom-substituted brownmillerite-type oxides to characterize the EELS spectra obtained with transmission electron microscopy.

At first, we investigated the stabilities of Cu atoms on light-element doped graphene supported on the magnetic substrates. We considered Fe and Ni as the magnetic substrates. We performed the total energy and electronic structure calculations using The Vienna Ab initio simulation package (VASP). We installed a parallelized VASP with Intel® MPI Library and Intel® Math Kernel Library. We revealed that the adsorption of Cu atoms on light-element doped graphene becomes stronger with the magnetic substrates. However, in cases of some light-element dopants, the magnetic substrates weaken the Cu adsorption on the light-element doped graphene. This is because the active dangling bond forms strong chemical bonds with magnetic surfaces, hence, Cu atoms cannot form stable chemical bonds with the light-element doped graphene. We also investigated the diffusion properties of Cu atoms on light-element doped graphene supported on the magnetic substrates. We found that the magnetic substrates reduce the diffusion barriers of Cu atoms. In addition, we also revealed the effect of Cl^- ions on the catalyst nanorod growth.[1]

We performed EELS spectra of the partially substituted Ca_2AlMnO_5. We considered Sr dopants, which show promising oxygen absorption properties.[2] The obtained EELS spectra show good agreement with the experimental results.

References

[1] M. J. Saw, M. T. Nguyen, Y. Kunisada, T. Tokunaga, T. Yonezawa, ACSOmega 7 (2022) 7414.

[2] K. Tanahashi, Y. Omura, H. Naya, K. Miyazaki, G. Saito, Y. Kunisada, N. Sakaguchi, T. Nomura, ACS Sustain. Chem. Eng. 9 (2021) 9317.

First-principles calculation of energy materials

Fumiyuki ISHII, Naoya YAMAGUCHI, Rifky SYARIATI,
Hikaru SAWAHATA, Hana Pratiwi KADARISMAN, Kaiki SHIBATA,
Sefty YUNITASARI, Yaotang ZHANG, Vierta SARASWATI,
Takahiro TOMINAGA, Yedija Yusua Sibuea TEWENG, Juhri HENDRAWAN
Nanomaterials Research Institute, Kanazawa University
Kanazawa, 920-1192, Japan

1. *Topological thermoelectric materials*

Thermoelectric conversion based on the anomalous Nernst effect has received a lot of attention as ANE achieves more efficient heat recovery and heat recovery from more heat sources than those based on the Seebeck effect. For the anomalous Nernst effect, the topological nature of the wave functions, and the Berry curvature, a fictitious magnetic field, is essential. We have studied the anomalous Nernst effect of iron-based ferromagnetic materials such as Fe_3X(X=Al, Ga)[1] and FeCl_2[2] by first-principles density functional calculations. To evaluate the anomalous Nernst coefficient, a detailed Fermi energy dependence of the anomalous Hall conductivity is required. We have implemented a finite difference algorithm in OpenMX[3] to calculate the Berry curvature of *metallic* system given by the averaged *local Berry phase* of the momentum space[4]. This implementations open up the possibility of efficient thermoelectric material design based on high-throughput screening.

2. *Photovoltaics*

Material property data was extracted from about 1500 papers on organic thin film non-fullerene solar cell materials, and high-performance material conditions were derived based on data statistical methods[5]. One of the conditions obtained was the empirically known "open-circuit voltage (Voc) of 0.8-0.9 V is appropriate", and the database we created rediscovered this rule of thumb. In addition, it was suggested that the sulfur atom content is an important factor for high performance photovoltaics materials.

We have performed first-principles calculations of the topological phase transition in strained inorganic halide perovskite CsPbI_3. For the experimental lattice constant, the bandgap decreases from 0.15 eV to 0 eV when a strain of $c/a > 1$ is applied. Increasing the strain will gradually open the bandgap. We calculated the topological Z_2 invariants that characterize the topological insulating phase. From the results, the bulk crystal CsPbI_3 showed a strain-induced topological phase transition, changing from a trivial insulator to a topological insulator phase. This topological phase transition of the strained inorganic halide perovskite has the potential to be applied to new energy devices.

3. *Graphene and diamond*

Applying the supercell scheme to the study of alloys and various perturbed system including impurities and vacancies raises band folding problems. The unfolding method is expected to obtain the meaningful energy-momentum relationships by avoiding it. The method proposed by Chi-Cheng Lee et al proved[6] very useful for calculating the electronic structure of a vacancies system with OpenMX code. We have calculated and observe the graphene flake size dependence of Dirac cone in the unfolding band structures.

Negatively charged diamond nitrogen-vacancy centers are promising for many applications, such as high-resolution sensors for electric fields and quantum computer Qubits . Density functional calculations are often performed in supercell systems. However, as the number of supercells increases, the first Brillouin zone (FBZ) shrinks and the band becomes more complex. An unfolding band method calculation was performed to study the electronic properties of the nitrogen vacancy center diamond using the OpenMX code. Our results show that the unfolded band of the bulk diamond supercell and the nitrogen vacancy center of the diamond have fewer lines than those of the traditional folded band. The shape of the unfolded energy band matches the primitive cell band. The dedailed electronic band structure of diamond with nitrogen vacancy center are analyzed.

The Al_2O_3 /diamond(111) interface containing three types of impurities was calculated. We predicted three different Al_2O_3/diamond(111) interface structures and investigated their band edge changes. Band edges are evaluated by calculating the local electron density. Compared to diamond bulk, the band of Al_2O_3 bulk is generally shifted downward. The band offsets for dangling bonds, C-H bonds, the ideal O-terminal interface are estimated. Our research helps to assess the impact of interface structure on device performance and provide a reference for improving experimental methods.

4. *Crystal structure prediction for spintronics materials*

Bismuth tellurium iodide (BiTeI) has attracted great interest as a potential material for spintronics device. We have performed crystal structure prediction for BiTeI crystals by genetic algorithms and density functional calculations. We found 4 BiTeI crystal structures with high stability , including one structure that has been observed in experiments and 3 brand new structures, and then performed detailed first-principles analysis of the elctronic structures to predict their physical properties. We calculated the Z_2 topological invariant and spin-textures of the new structures. Among the 3 new structures, we found that two structures with centro symmetry were strong topological insulators, and one structure without centrosymmetry had wide band gap and strong Rashba splitting.

References

[1] A. Sakai, S. Minami, T. Koretsune, T. Chen, T. Higo, Y. Wang, T. Nomoto, M. Hirayama, S. Miwa, D. Nishio-Hamane, F. Ishii, R. Arita and S. Nakatsuji, Nature **581**, 53(2020).

[2] S. Rifky, S. Minami, H. Sawahata, and F. Ishii, APL Materials **8**, 041105 (2020).

[3] T. Ozaki *et al.*, http://www.openmx-square.org/

[4] H. Sawahata, N. Yamaguchi, S. Minami, and F. Ishii, arXiv:2204.05949.

[5] N. Yamaguchi, H. Sano, H. Sawahata, M. Nakano, T. Taima, F. Ishii, M. Karakawa, Jpn. J. Appl. Phys. **61** 030905 (2022), *selected for Spotlights 2022.*

[6] C-C. Lee, Y. Yamada-Takamura, and T. Ozaki, J. Phys.: Condens. Matter **25** 345501 (2013).

Development of crystal structure prediction methods using machine learning

Tomoki YAMASHITA
Top Runner Incubation Center for Academia-Industry Fusion,
Nagaoka University of Technology
1603-1 Kamitomioka-machi, Nagaoka, Niigata, 940-2188

We search for solid electrolyte materials that can be synthesized in the systems of Li-Mg-SiO_4 using crystal structure prediction (CSP) by CrySPY [1]. We investigate whether it is possible to synthesize structures with high ionic conductivity by changing the ratio of Li to Mg from Li_2MgSiO_4. We performed CSP simulations with random search. In the CSP simulations, first-principles calculations were carried out using the VASP code [2], and a generalized gradient approximation was employed for exchange-correlation functional. The compositions calculated in this study were Li_2MgSiO_4, $Li_{1.5}Mg_{1.25}SiO_4$, and $Li_{2.5}Mg_{0.75}SiO_4$. The number of searching trials for each composition was 200, which were conducted using the ISSP supercomputer. Our calculated formation energies showed that Li_2MgSiO_4 can be synthesized, however, $Li_{1.5}Mg_{1.25}SiO_4$ and $Li_{2.5}Mg_{0.75}SiO_4$ are unlikely to be synthesized, leading to phase separation. These results are consistent with our experiments. Therefore, it is difficult to synthesize solid electrolytes in the system of Li-Mg-SiO_4 except for Li_2MgSiO_4.

We have also studied on algorithm development for CSP. Look Ahead based on Quadratic Approximation (LAQA), which is one of the selection-type algorithms we previously developed [3], can control the optimization priority of the candidates. We have proposed an improved score of LAQA, where the stress term is added to overcome the drawbacks of the previous score. CSP simulations by this improved algorithm are performed to investigate the searching efficiency for typical materials such as Si (16 atoms), Al_2O_3 (10 atoms), NaCl (16 atoms), and $SrCO_3$ (20 atoms). We used the CrySPY code for the CSP simulations. For the system of $SrCO_3$, we employed the VASP code to evaluate the energy and to carry out the local structure optimization using the ISSP supercomputer. For the other systems, the QUANTUM ESPRESSO was also used. The total-energy calculations were performed using the density functional theory with the projector-augmented wave method. The generalized gradient approximation was used for exchange-correlation functional. Figure 1 illustrates the number of total optimization steps required to find the most stable structure, obtained by the CSP simulations using random search (RS), Greedy, and LAQA. The searching efficiencies of LAQA with the weight parameter of stress w_S of 10 (red bars in Fig. 1) are not always the best, however, it demonstrates high searching efficiency on various data sets. In other words, the introduction of the stress term makes LAQA more robust and versatile [4].

References

[1] T. Yamashita, S. Kanehira, N. Sato, H. Kino, H. Sawahata, T. Sato, F. Utsuno, K. Tsuda, T. Miyake, and T. Oguchi: Sci. Technol. Adv. Mater. Meth. **1** (2021) 87.

[2] G. Kresse and J. Furthmüller: Phys. Rev. B **54** (1996) 11169.

[3] K. Terayama, T. Yamashita, T. Oguchi, and K. Tsuda, npj Comut. Mater.: **4** (2018) 32.

[4] T. Yamashita and H. Sekine: Sci. Technol. Adv. Mater. Meth. **2** (2022) 84.

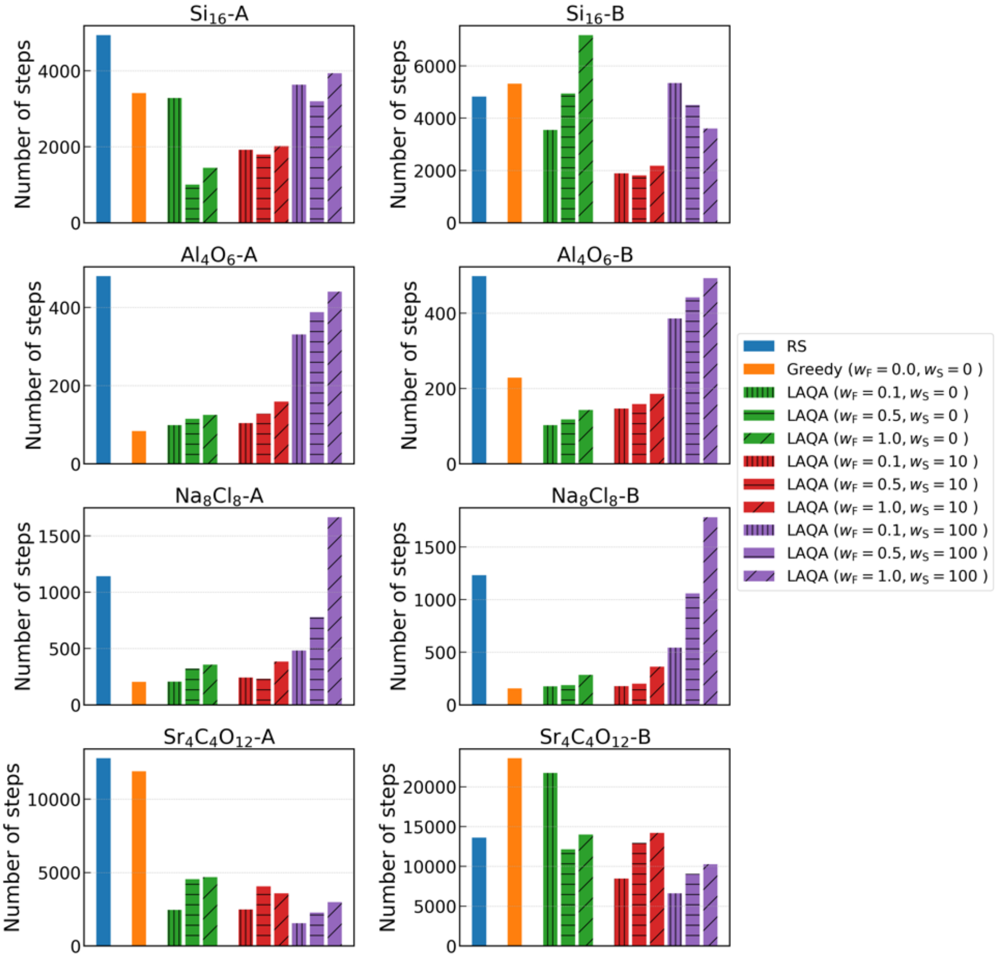

Fig. 1: Number of total optimization steps required to find the most stable structure.

Development of Exciton Maps for Identifying Active/Inactive Thermally Activated Delayed Fluorescence Molecules

Yoshifumi NOGUCHI
Department of Applied Chemistry and Biochemical Engineering, Graduate School of Engineering, Shizuoka University, Johoku 3-5-1, Hamamatsu, Shizuoka 432-8561, Japan

A high internal electroluminescence quantum efficiency in the third-generation organic light-emitting diodes is based on the mechanism of thermally activated delayed fluorescence (TADF), in which triplet spin excitons are converted to singlet spin excitons via reverse intersystem crossing (RISC). The existing energy barrier between a singlet spin exciton and a triplet spin exciton, commonly named as singlet-triplet splitting (Δ^{ST}), should be almost zero for TADF to occur. In recent experimental studies, however, certain carbazole benzonitrile (CzBN) derivatives, in which the carbazole moiety acts as an electron donor and the benzonitrile moiety acts as an electron acceptor, can be TADF active and inactive: nevertheless, their Δ^{ST} are typically about 0.2 eV. However, we must reconsider the mechanism of TADF to completely understand it. We have studied the mechanism of TADF using the first-principles GW+Bethe-Salpeter method and exciton analysis method with exciton wave functions [2]. Before discussing the optical properties of CzBN, we compared the simulated photoabsorption spectra with the available experimental spectra and confirmed that our method successfully reproduced the spectra. By sandwiching an arbitrary operator with the exciton wave functions, we estimated the expected values such as the exciton size, electron-hole separation distance, electron (or hole) delocalization, and exciton binding energy based on two-particle picture and proposed an exciton map [2]. We revealed that the TADF active/inactive molecules could be classified well in the exciton map by choosing the exciton binding energy as the vertical axis and the ratio of electron and hole delocalization as the horizontal axis. Indeed, we concluded that there are two kinds of TADF active molecules existed based on the following: first, the ratio of electron and hole delocalization was proportional to the exciton binding energy, and second, the hole state spatially localized more than the electron.

References

[1] T. Hosokai, H. Noda, H. Nakanotani, T. Nawata, Y. Nakayama, H. Matsuzaki, and C. Adachi, J. Photonics Energy, **8**, (2018) 032102.

[2] Yoshifumi Noguchi, J. Chem. Phys., **155**, (2021) 204302.

Maximization of interface magnetoelectric coupling with Bayesian optimization

Yoshihiro GOHDA
Department of Materials Science and Engineering, Tokyo Institute of Technology
J1-3, Nagatsuta-cho 4259, Midori-ku, Yokohama 226-8502, Japan

To reduce energy consumption in magnetic devices, the control of magnetism by the electric current through the magnetic field should be replaced with that by the electric field. Interface multiferroicity is promising, because the magnetoelectric (ME) coupling is much larger than that of single phase multiferroics [1]. In addition to choosing optimal materials for ferromagnetic and ferroelectric phases, the interface modification is also a choice to enhance the ME coupling.

In this project, we performed large-scale first-principles calculations of multiferroic interfaces [2, 3, 4]. We explored better insertion of transition-metal atomic layers into $Fe_3Si/BaTiO_3(001)$ interfaces using the Bayesian optimization. As is shown in Fig. 1(a), the Bayesian optimization improved the interface ME coupling by 55% that is obviously much better than the random search.

As a by-product of the Bayesian optimization, we successfully provided an explanation of the mechanism for the multiferroicity enhancement [2]. Figure 1(b) shows the dependence of the change in the interface magnetic moment on the exchange-correlation functional and the electron localization controlled by the Hubbard U parameter. The large ME coupling due to the change in the magnetic moment in V comes from the nearly half occupied $3d$ bands causing peaks in the density of states close to the Fermi level [2]. In contrast, the following three cases exhibit tiny ME coupling. Insufficient occupancy causes stronger ionicity reducing interaction with Ti. Excess occupancy makes the hybridized states too deep. In addition, $4d$ electrons are too itinerant to have sufficient hybridization with Ti.

In addition, the enhancement of the ME coupling due to the change in the magnetic anisotropy has also been studied. Changes in the magnetic anisotropy of a whole ferromagnet by the exchange coupling [5] are further enhanced by the strain effect at the interface [3].

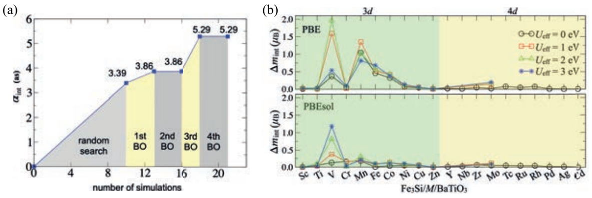

Figure 1: (a) The Bayesian optimization of $Fe_3Si/BaTiO_3$ interfaces with inserted atomic layers. (b) The change in the interface magnetic moments.

[1] T. Taniyama, J. Phys.: Condens. Matter **27**, 504001 (2015).

[2] R. Costa–Amaral and Y. Gohda, Phys. Rev. Appl. **15**, 064014 (2021).

[3] S. Fujii, Y. Gohda, *et al.*, NPG Asia Mater., in press.

[4] S. Tsuna, R. Costa–Amaral, and Y. Gohda, submitted.

[5] K. Fujita and Y. Gohda, Phys. Rev. Appl. **11**, 024006 (2019).

First-Principles Design of Spin-Polarized Bandstructure at $MoTe_2/Bi_2Se_3$ Interface

Kunihiko Yamauchi

Institute of Scientific and Industrial Research (ISIR-SANKEN), Osaka University, 8-1 Mihogaoka, Ibaraki, Osaka 567-0047

We are studying magnetism and topological properties in various materials by means of the first-principles density functional theory (DFT) calculations aiming at the spintronics application.

Since last year, we have investigated the magnetic stability in 2D magnetic material VI_3 making a comparison with CrI_3 using the VASP code at the ISSP *ohtaka* supercomputer. In VI_3, it turned out that under the trigonal crystal field with D_{3d} point group, the t_{2g} orbital state is split into a_{1g} and e_g' states. The a_{1g} orbital state plays an important role in inter-layer magnetic exchange interaction in a bilayer structure. By using Wannier90 code that is interfaced with the VASP code, we estimated the hopping integral and discussed the inter-layer magnetic exchange interaction based on the virtual-hopping mechanism. This finding may pave a way to the spintronics application with 2D materials [1].

Next, we explored a heterostructure that consists of transition-metal dichalcogenide and 3D topological-insulator to investigate the hybrid spin state in which the out-of-layer spin polarization and the helical spin polarization may merge. We show that $MoTe_2$ and Bi_2Se_3 lattices match well and in-plane strain provides a handle to manipulate the spin-polarized band alignment near the Fermi energy. This interface shows the various spin degree of freedom, and it may be useful as an advanced spin generator [2].

In this year, we also studied the cathode properties of sodium transition-metal oxides (such as Na_2NiTiO_4) by means of DFT calculations and the machine-learning approach to reduce reliance on Li-ion batteries and aim at the sustainable development goals. We found a strong relation between the cation ionic radii and the structural stability. This finding may lead to the future industrial application to the sodium-ion rechargeable battery [3].

References

[1] T. P. T. Nguyen, K. Yamauchi*, T. Oguchi, D. Amoroso, and S. Picozzi, Phys. Rev. B **104**, 014414 (2021).

[2] K. Yamauchi, R. Shimazu, and T. Oguchi, J. Phys. Soc. Jpn. **91**, 044705 (2022).

[3] K. Yamauchi, H. Momida, and T. Oguchi, J. Phys. Soc. Jpn. **91**, 034704 (2022) .

First-principles lattice-dynamics calculations for negative-thermal-expansion materials

Yasuhide Mochizuki,[1] Soungmin Bae,[2] and Hannes Raebiger[2]

[1] *Department of Materials Science and Engineering,*

Tokyo Institute of Technology, 2-12-1 O-okayama, Meguro-ku, Tokyo

[2] *Department of Physics,*

Yokohama National University, Yokohama 240-8501

Negative-thermal-expansion (NTE) materials have attracted considerable attention because they contribute to sustaining largely expanding materials and also because of their fascinating and counter-intuitive thermal properties. The well-known and representative NTE materials are Si [1], ReO_3 [2], ScF_3 [3] ZrW_2O_8 [4] and $KZr_2P_3O_{12}$ [5]. Since the reports of negative thermal expansion in various materials in the past few decades, it has been widely known that the mechanism for NTE is the transverse acoustic phonon modes, which have negative Grüneisen parameters. However, the detailed mechanisms for the NTE properties are uncovered ever since now. Here, we report our progress for elucidating the microscopic origin of NTE in Si, ReO_3, and $KZr_2P_3O_{12}$.

Our first-principles calculations were performed by using the projector augmented-wave method [6] as implemented in VASP [7]. The phonon band structures were derived from the calculated force constants using PHONOPY [8].

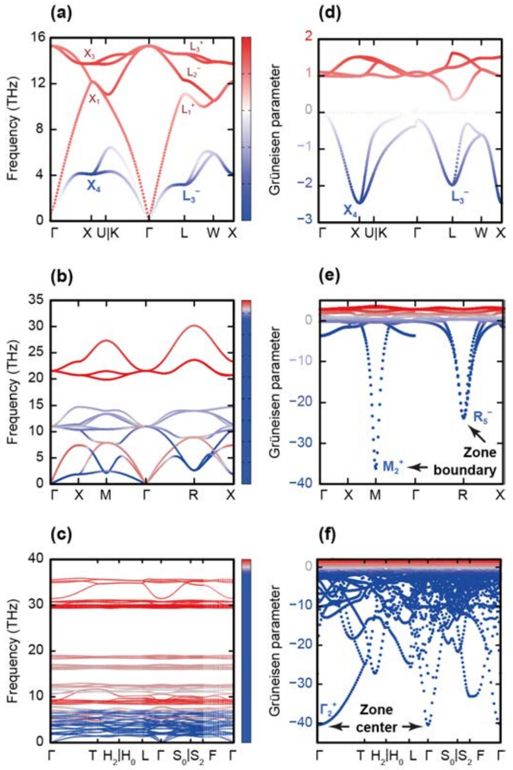

Fig 1. Calculated phonon bands for (a) Si, (b) ReO_3, and (c) $KZr_2P_3O_{12}$ and Grüneisen parameters for (d) Si, (e) ReO_3, and (f) $KZr_2P_3O_{12}$. The red and blue respectively indicate the degrees of positive and negative values of Grüneisen parameters.

As shown in Fig. 1, we present the calculation results of phonon band with Grüneisen parameters for Si, ReO_3, and

$KZr_2P_3O_{12}$. From Figs. 1(a, b, d, e), one can see that the zone-boundary phonon modes in Si and ReO_3 generate negative Grüneisen parameters, triggering the NTE. In Si, the most important phonons for realizing NTE are the atomic vibration eigenvectors which transform as irreducible representations X_4 and L_3^-. On the other hand, in ReO_3, the most important phonons for the NTE are the eigenvectors transforming as irreducible representations M_2^+ and R_5^-. The phonon modes of M_2^+ and R_5^- correspond to the ReO_6 octahedral rotations. Note that these zone-boundary phonon modes of Si and ReO_3 are low-energy transverse acoustic phonon modes. It is also noteworthy that transverse acoustic phonon modes do have crystal momentums, which clearly indicate that they must be Brillouin-zone-boundary phonon modes. Very intriguingly, however, as shown in Figs. 1(c, f), a Brillouin-zone-boundary mode transforming as irreducible representation Γ_2^+ in $KZr_2P_3O_{12}$ contributes to NTE the most. These results suggest that not all negative Grüneisen parameters are from transverse acoustic phonons.

Further, to confirm the validity of our calculation results for $KZr_2P_3O_{12}$, we also prepared the polycrystal of $KZr_2P_3O_{12}$ and examined the thermal expansion coefficient by conducting X-ray diffraction in relevant temperatures. As shown in Fig. 2, our calculations are qualitatively consistent with the experimental results.

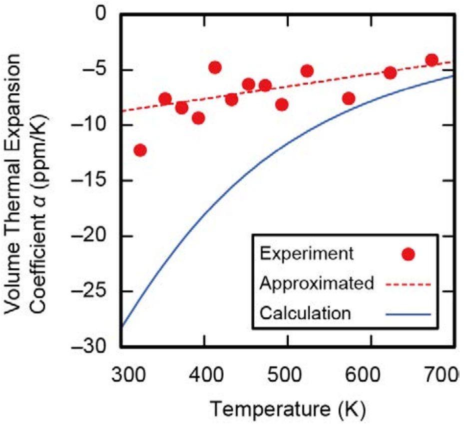

Fig 2. Theoretical and experimental thermal expansion coefficients for $KZr_2P_3O_{12}$. The blue and red colors respectively indicate the results from calculations and experiments. The red broken line is derived by least-square method.

References

[1] S. Biernacki and M. Scheffler, *Phys. Rev. Lett.* **63**, 290 (1989).

[2] T. Chatterji *et al.*, *Phys. Rev. B* **78**, 134105 (2008).

[3] B. K. Greve *et al.*, *J. Am. Chem. Soc.* **132**, 15496 (2010).

[4] C. Martinek and F. Hummel, *J. Am. Ceram. Soc.* **51**, 227 (1968); T. A. Mary *et al.*, *Science* **272**, 90 (1996).

[5] W. Miller *et al.*, *J. Mater. Sci.* **44**, 5441 (2009).

[6] P. E. Blöchl, *Phys. Rev. B* **50**, 17953 (1994).

[7] G. Kresse and J. Furthmüller, *Phys. Rev. B* **54**, 11169 (1996); G. Kresse and D. Joubert, *ibid* **59**, 1758 (1999).

[8] A. Togo and I. Tanaka, *Scr. Mater.* **108**, 1 (2015).

Analyses on electronic structure and magnetoelectric effect in high-performance spintronics and magnetic materials

Tatsuki ODA[1,2], Ko HYODO[2], Daiki YOSHIKAWA[2], Daichi TAKAGI[2], Masao OBATA[1,2]
[1]*Institute of Science and Engineering, Kanazawa University, Kanazawa, Ishikawa 920-1192*
[2]*Graduate School of Natural Science and Technology, Kanazawa University, Kanazawa, Ishikawa, 920-1192*

We have studied several systems in high-performance spintronics and magnetic materials on electronic structure and magnetoelectric effect. In these investigations, we took some attempts for improving physical accuracy or finding new candidates in the materials of spintronics application. Here, we report the developments of (A) investigation on magnetic anisotropy energy (MAE) in antiferromagnet (AFM) $L1_0$-MnX (X=Ir, Pt), (B) optimization in a computational code for quasi-particle self-consistent GW (QSGW) method, and (C) investigation on electronic structure in magnetic shape memory alloy (MSMA) Ni_2MnGa.

(A) MAE in AFM MnX (X=Ir, Pt)

We investigated the control of magnetic properties by structural strain using the first-principles calculations based on spin-density functional theory (SDFT) in $L1_0$-type Mn alloy; MnIr and MnPt. Contributions to the MAE were calculated from both the magnetocrystalline anisotropy energy (MCAE) arising from the spin-orbit coupling and the shape magnetic anisotropy energy (SMAE) arising from the magnetic dipole interaction energy. The MCAE was evaluated using the total energy (TE) and grand-canonical force theorem (GCFT) [1,2]. Our self-consistent calculations revealed that the intra-c-plane AFM configuration was stabilized as the ground state for both of the materials. The MCAE is obtained to be negative, indicating a favor of in-plane anisotropy. The absolute value of MCAE tends to decrease as the ratio of lattice constants *c/a* increases. The SMAE is always positive, reflecting the AFM configuration. In MnPt, we obtained an anisotropy transition in the investigated range of strain, namely, the whole MAE became positive (perpendicular to *c*-plane) at larger *c/a*, from the in-plane anisotropy. Through this investigation, the approach GCFT was confirmed to be an efficient approach to analysis of MAE.

(B) QSGW method

It is well known that the DFT suffers from many deficiencies such as small band gap, electron over binding property, etc.. To improve these deficiencies, extension methods of DFT such as DFT+*U* have been developed. However, they often have a semiempirical character, and are not universal and parameter-free. In the other

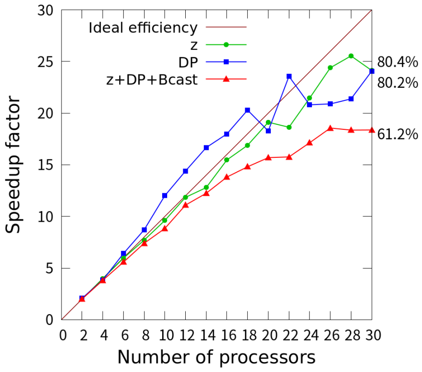

Fig. 1: Speedup factor in the new code.

hand, QSGW is a universal approach to the reliable prediction of electronic structure [3]. The idea of QSGW is an optimization of the one-body Hamiltonian by performing a self-consistent calculation in the many-body approach with GW approximation, where the self-consistency is constructed to minimize the perturbation. QSGW has already had success in the estimation of band gaps and other properties for a wide range of materials. The requirement to be paid is computational cost. QSGW needs roughly 100-1000 times more expensive in computational time than DFT. We parallelized the part of calculation for the polarization function (PF) in GW approach, which is one of the most expensive (time-consuming) parts in QSGW. As a result, the computational time of PF was reduced from 11 hours to 1 hour in the application to 4O structure (16 atoms in the unit cell) of Ni_2MnGa. The parallelization efficiency, as shown in Fig. 1, was almost ideal when the number of processor elements (PEs) was small, but decreased as the number of PEs increases; with an efficiency of 60% at 30 PEs. This decrease in parallelization efficiency was found to be due to the communication time among PEs.

(C) Electronic structure in Ni_2MnGa

Recent results on Ni_2MnGa show that the modulated martensite phase is more energetically stable than the non-modulated (NM) phase, supporting an importance of electron-correlation effect [4]. The GGA+U reveals that the stability of the austenite and martensite phases is dependent on U. We investigated the electronic structure of MSMA Ni_2MnGa using QSGW [4,5]. The Ni e_g orbitals in the cubic (austenite) phase, which lead to martensite phase transition by band Jahn-Teller effect, were found to locate on the Fermi level.

The NM and 4O structures of Ni_2MnGa were calculated with QSGW. The peak of density of states near the Fermi level for the minority-spin channel was located above the Fermi level in NM and below the Fermi level in 4O. This difference might be related to the presence of nanotwin double layer in modulated martensite phases.

References

[1] I. Pardede *et al.*, J. Magn. Magn. Mater., **500**, 166357 (2020).

[2] I. Pardede et al., Crystals **10**, 1118 (2020).

[3] T. Kotani, J. Phys. Soc. Jpn. **83**, 094711 (2014); ecalj: https://github.com/tkotani/ecalj/.

[4] M. Zelený et al., Materials&Design, **209**, 109917 (2021).

[5] M. Obata et al., submitted, (2022).

Prediction of new crystal structures based on the densest ternary sphere packings

Ryotaro Koshoji and Taisuke Ozaki
Institute for Solid State Physics,
The University of Tokyo, Kashiwa-no-ha, Kashiwa, Chiba 277-8581

Densest unary sphere packing was proven to be the FCC structure in the 2000s, but the densest binary and ternary sphere packings have not yet been identified analytically. To discover the unknown putative densest packings, we have created an algorithm to explore them, and we successfully found the 12 putative densest binary sphere packings (PDBSPs) with confirming the known PDBSPs with a small correction of the phase diagram [1].

On top of the success of the discovery, we planned to explore the putative densest ternary sphere packings (PDTSPs). If we only search the periodic packings of n different sizes of spheres, the packing fraction at a given composition ratio is maximized by filling the space with not more than n kinds of packing structures. Since no seminal study seems to construct the phase diagram, we made the ternary phase diagrams to identify the PDTSPs that are denser than any other combination of packing structures. The example of the ternary phase diagram is shown in Fig. 1.

As a result, we have discovered the 59 kinds of PDTSPs [2,3]. The newly found PDTSPs have unique structural properties, and some of them have high symmetry. The (4-3-1) has the P6/mmm symmetry, and if a line of small sphere in the (4-3-1) structure is replaced of one small sphere, we can get the crystal of $SmCo_5$. Note that we name a PDTSP consisting of l small, m medium, and n large spheres per unit cell as (l-m-n) structure, and the small, medium, and large spheres in figures are represented by pink, yellow, and purple balls, respectively. The (9-7-3), (10-6-3), and (13-3-1) structures can be derived from the Perovskite structure, and they have the $Pm\bar{3}m$ symmetry. Remarkably, an edge of unit cell of the (9-7-3) structure is constituted by a line of four medium spheres. The (13-2-1) has the $Fm\bar{3}m$ symmetry. Large spheres constitute the FCC structure without contact, and a tetrahedral site is occupied by one medium sphere. The medium and large spheres are surrounded small spheres constituting semi-

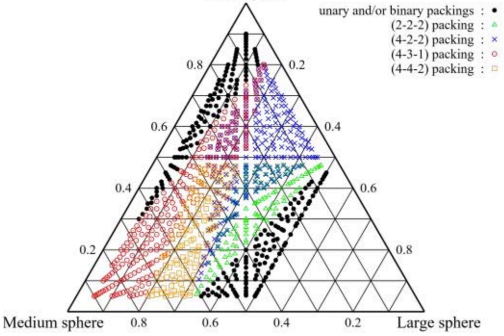

Fig.1: An example of ternary phase diagram

regular polyhedrons. This structure is predicted to become the PDTSP at the several radius ratios such as 0:44 : 0:64 : 1:00, at which small and medium spheres would be too large to be placed in the tetrahedral and octahedral sites if large spheres comprising the FCC structure with contacts. Finally, large spheres in the (16-2-2) structure are surrounded by the network structures of small and medium spheres.

The six exemplified PDTSPs might be used as the structural prototypes for crystals under pressure. For example, the (13-2-1) and (13-3-1) structures might be realized by metal hydrides with replacing small spheres of hydrogen atoms. We have been exploring the quartic metal hydrides that have the isotypic crystal structures to the (13-2-1) and (13-3-1) structures, but the calculations have not yet been finished.

The computational cost of the structural optimizations is low, so all the process can be finished in one processor, so the exploration of the structures was effectively parallelized.

References

[1] R. Koshoji, M. Kawamura, M. Fukuda and T. Ozaki: Phys. Rev. E 103 (2021) 023307.

[2] R. Koshoji and T. Ozaki: Phys. Rev. E 104 (2021) 024101.

[3] R. Koshoji and T. Ozaki: arXiv:2110.15505

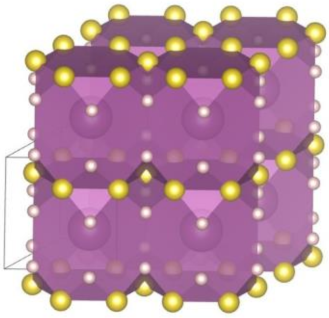

Fig. 2: (4-3-1)

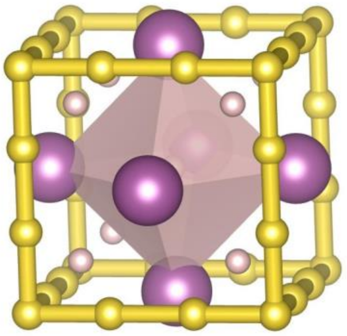

Fig.3: (9-7-3)

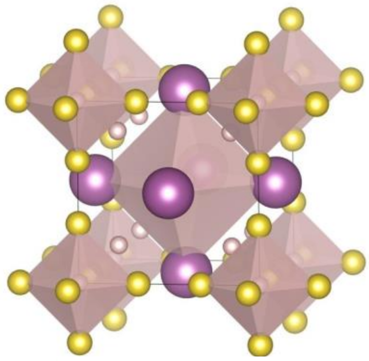

Fig.4: (10-6-3)

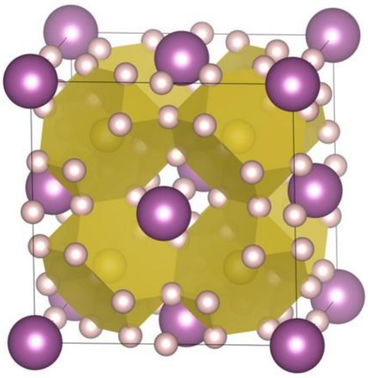

Fig.5: (13-2-1)

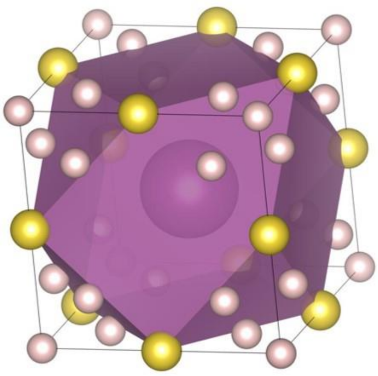

Fig.6: (13-3-1)

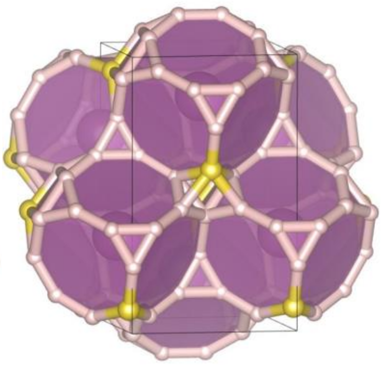

Fig.7: (16-2-2)

Low Thermal Conductance Generated by van Der Waals Interaction

Masato OHNISHI
Department of Mechanical Engineering,
The University of Tokyo, 7-3-1 Hongo, Bunkyo-ku, Tokyo 113-8656, Japan

Clathrate compounds are promising candidates for thermoelectric materials in terms of the “electron-crystal phonon-glass” concept. Clathrate compounds are composed of guest atoms encapsulated in cagelike structures. It is expected that electrons can transport in the framework with much less scattering rate than that for phonons because of guest atoms leading to significant phonon scattering. Particularly, in type-I clathrate compounds, guest atoms vibrate in a strong anharmonic potential because they are composed of a Weaire-Phelan structure, which divides a space with the maximum volume with the same cross-sectional area (Fig. 1(a)). In this study, we have studies type-I $Ba_8Ga_{16}X_{30}$ (BGX, X = Si, Ge, Sn) to gain insights of the effect of phonon anharmonicity on heat transport.

Phonon properties were calculated with the self-consistent phonon (SCP) theory [1] and unified theory [2]. The SCP theory is used to consider effects of forth-order anharmonic potential and to obtain temperature-dependent harmonic interatomic force constants (IFCs). Using the unified theory, one can consider the coherent contribution, that of interbranch tunneling, to heat transport as well as the population contribution, which is considered also in the context of Peierls Boltzmann transport theory. We have employed ALAMODE package [1] to perform the above approaches and VASP to calculate forces on atoms.

While phonon dispersion have imaginary (negative) frequencies when guest atoms have negative harmonic potential at low temperatures, negative frequencies became positive at finite temperatures, as shown in Fig. 1(b). For type-I BGSn, harmonic potential was positive above 100 K, and

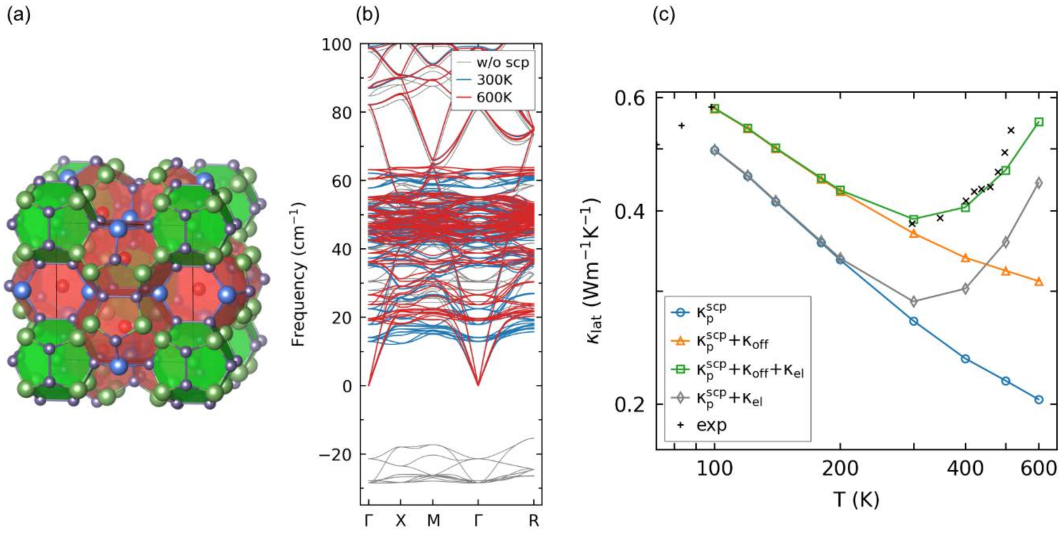

Fig. 1 Phonon properties of type-I clathrate compounds. (a) Crystal structures of type-I clathrate. (b) Phonon dispersion of $Ba_8Ga_{16}Sn_{30}$ (BGSn) without considering renormalization (grey), at 300 K (blue), and at 600 K (red). (c) Temperature-dependent thermal conductivities of BGSn. Population (blue), coherent (orange), and electron (green and red) contributions were considered.

thermal conductivities could be calculated at this temperature range. The calculated thermal conductivities including all the contributions (population, coherent, and electron contributions) were in good agreement with experimental data, as shown in Fig. 1(c). To gain insights into the effect of phonon anharmonicity, we have also analyzed mode dependent phonon properties at high temperatures in details (> 100 K). While a unique temperature-dependence of type-I clathrate at low temperatures (≈ 10 K) have been widely studies, we have revealed intriguing phonon properties at high temperatures in type-I clathrate [3].

References

[1] T. Tadano and S. Tsuneyuki, J. Phys. Soc. Jpn. 87, 041015 (2018).

[2] M. Simoncelli et al., Nat. Phys. 395, 1 (2019).

[3] M. Ohnishi et al., arXiv:2103.00413.

A Unified Understanding of Thermodynamic Properties in Icy Planets and Icy Moons

Yu KOMATSU[†‡], Terumasa TADANO [¶], Yasunori HORI[†‡]
[†]*Astrobiology Center, 2-21-1 Osawa, Mitaka, Tokyo 181-8588, Japan.*
[‡]*National Astronomical Observatory of Japan, 2-21-1 Osawa, Mitaka, Tokyo 181-8588, Japan.*
[¶]*Research Center for Magnetic and Spintronic Materials,*
National Institute for Materials Science, Tsukuba 305-0047, Japan.

The high-pressure properties of hydrogen sulfide have drawn considerable attention in terms of its superconductivity and metalization [1]. Astronomical observations have detected H_2S from the atmosphere of icy planets (ice giants) like Neptune and Uranus [2, 3], and also in plumes coming from the interior ocean of Enceladus, a Jupiter icy moon [4]. These findings provide insight for estimating the interior of icy bodies and their physical and chemical origins. Although H_2S would be one of the typical minor components of ice mantle in icy planets and satellites inside and outside our solar system [5], the phase diagrams and properties of H_2S and its mixture have not yet been revealed, especially at high P-T conditions.

Our project aims to elucidate possible mixing states and thermodynamic conditions in the icy bodies by *ab initio* calculations. We focus on the properties of H_2S as the first onset from the interest above and perform density functional molecular dynamics (DFT-MD) simulations for H_2S in the temperature range of 500 $\sim$ 10,000 K and the density range of 1 $\sim$ 5 g/cm^3 using the QUANTUM ESPRESSO package. More than 10 ps for MD simulations are allowed after thermal relaxation with a 2 × 2 × 2 supercell containing 32 H_2S molecules, and the ion temperature is controlled in the NVT ensemble with an energy cutoff of 80 Ry.

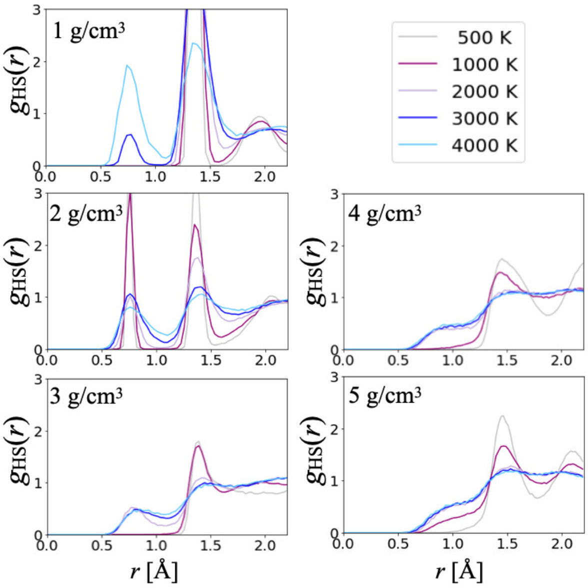

Figure 1: Radial distribution function g_{HS} for Pmc2_1 structure.

Pressures in our calculations were up to $\sim$ 250 GPa, corresponding to the values at the deep mantle of ice giants [6]. Figure 1 presents the radial distribution function between H and S atoms for Pmc2_1 phase of H_2S. The fluid phase emerged at higher temperatures (e.g., ∼3,000 K with 3 $\sim$ 5 g/cm^3), and at lower densities like 1 g/cm^3, the phase appeared at more higher temperatures. Moreover, diffusion coefficients in Figure 2 implicate the transition from the solid phase to the superionic and then to the fluid, like H_2O and NH_3 [6]. The difference in diffusion between hydrogen and sulfide becomes more prominent at higher

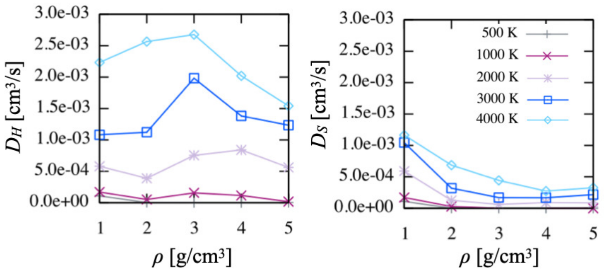

Figure 2: Diffusion coefficient of H and S for Pmc2_1 structure.

temperatures (all the conditions are not plotted in Figure 2). Thermodynamic quantities, e.g., free energy, are being evaluated, and an equation of state (EOS) including H_2S is being constructed, which are significant for understanding conditions realized in icy bodies.

The computation was partly carried out using the computer resource offered under the category of General Projects by the Research Institute for Information Technology, Kyushu University.

References

[1] Li, Y.; Hao, J.; Liu, H.; Li, Y.; Ma, Y. *The Journal of Chemical Physics* **2014**, *140*, 174712.

[2] Irwin, P. G. J.; Toledo, D.; Garland, R.; Teanby, N. A.; Fletcher, L. N.; Orton, G. A.; Bézard, B. *Nature Astronomy* **2018**, *2*, 420–427.

[3] Irwin, P. G. J.; Toledo, D.; Garland, R.; Teanby, N. A.; Fletcher, L. N.; Orton, G. S.; Bézard, B. *Icarus* **2019**, *321*, 550–563.

[4] Waite, J. H., Jr; et al. *Nature* **2009**, *460*, 487–490.

[5] Johnson, T. V.; Mousis, O.; Lunine, J. I.; Madhusudhan, N. *The Astrophysical Journal* **2012**, *757*, 192.

[6] Cavazzoni, C.; Chiarotti, G. L.; Scandolo, S.; Tosatti, E.; Bernasconi, M.; Parrinello, M. *Science* **1999**, *283*, 44–46.

First-principles transport calculations for single-molecular junctions

Tatsuhiko OHTO

Graduate School of Engineering Science,

Osaka University, 1-3 Machikaneyama, Toyonaka, Osaka 560-8531

Single-molecule devices attract attentions because of possible bottom-up construction, potential for device miniaturization, and utilization of unique electrical responses of organic materials. Since it is not possible to directly observe the bridging structure of the molecule between electrodes, the presence of the molecule should be confirmed through the conductance histogram. The conductance histogram is normally broad, ranging orders of conductance values, while conventional first-principles transport calculations are performed only for the most stable structure, which is assumed to be the peak top value of the conductance histogram. A combined molecular dynamics and transport calculation is required to reproduce the broad conductance histogram and discuss the structure-property relationship.

In this work, a reactive force field to simulate the break junction procedure has been developed. Three junction structures (on top, bridge, and hollow) were prepared and 200 break junctions for each structure were simulated using the molecular dynamics (MD) method. We further performed first-principles transport calculations using the SMEAGOL codes for the snapshots for the MD trajectory. We observed that the peak top value largely depends on the molecular junction structures.

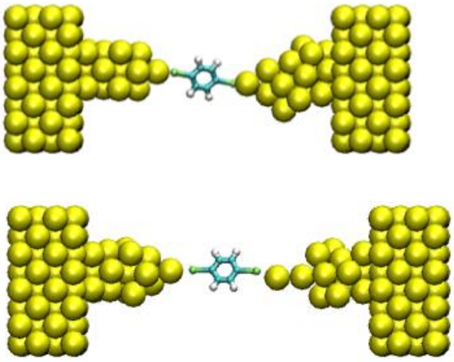

Fig. 1: Snapshots of the molecular dynamics trajectory.

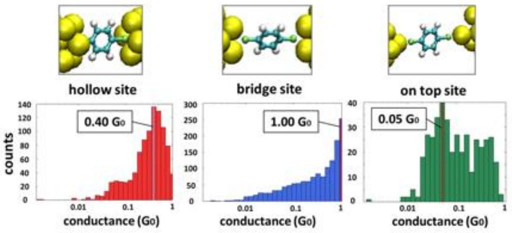

Fig. 2: Calculated conductance histograms for Au-BDT-Au molecular junctions.

References

[1] A. R Rocha et al. Phys. Rev. B **73**, 085414 (2008).

First-principles study of quantum transport in nanostructures

NOBUHIKO KOBAYASHI
Department of Applied Physics, University of Tsukuba
1-1-1 Tennodai Tsukuba Ibaraki 305-8573

An atomic-scale understanding of quantum transport properties in materials is an important issue in materials science and nanotechnology. The aim of this project is to reveal and predict quantum transport properties in materials from first-principles. We have developed the nonequilibrium Green's function (NEGF) method, and the O(N) time dependent wave-packet diffusion (TD-WPD) method on the basis of the density functional theory (DFT). By using these methods, we have investigated charge, head and spin transport properties of materials. [1]

We have developed a Simulation code for Atomistic Kohn-sham Equation (SAKE) for the ab-initio electron transport calculation based on the DFT and NEGF formalism. [2] We have applied the method to analyses of thermoelectricity of Heusler compounds. The electronic structures and thermoelectric properties are analyzed, and high performance systems are designed.

We developed the O(N) TD-WPD method for the quantum transport calculation of huge systems of up to 100 million atoms a decade ago. It is possible to calculate the conductivity and the mobility of the system with micron-order lengths at room temperature at the atomistic levels. We have recently expand the method to analyze thermoelectric properties, and demonstrated Seebeck coefficient and power factor calculations for a huge system of 100 million atoms.

Furthermore, we have analyzed the gate induced modulation effects of electronic states in monolayer organic field-effect transistor as shown in Fig. 1. [3] Organic field-effect transistors with ionic liquids have attracted much attention, since the ionic liquids induce an intense electric field at a semiconductor interface, resulting in a high concentration of charge carriers. We elucidated that strong electric fields and highly doped charges induce significant modulation effects on the electronic band structure and the mobility.

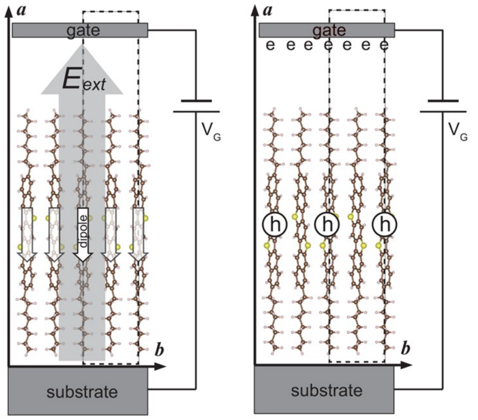

Figure 1: Schematic pictures of the C_8-DNBDT monolayer organic field-effect transistor.

References

[1] N. Kobayashi, H. Ishii, K. Hirose, in *3D Local Structure and Functionality Design of Materials* eds H. Daimon, Y. C. Sasaki (World Scientific, 2018) p133.

[2] H.Takaki, N.Kobayashi, K.Hirose, *J. Phys.: Condens. Matter.* 32 325901(2020)

[3] H. Ishii, N. Kasuya, N. Kobayashi, K. Hirose, S. Kumagai, S. Watanabe, and J. Takeya, *Appl. Phys. Lett.* 119 223301 (2021).

First-principles study on charging-induced structure phase transitions of thin film oxides

Takashi NAKAYAMA

Department of Physics, Chiba University
1-33 Yayoi, Inage, Chiba 263-8522

HfO_2 has various crystal structures depending on the growth conditions. Although the orthorhombic (Ortho) HfO_2 is thermodynamically unstable, it can be grown on metal electrode substrates such as TiN and Pt and has giant ferroelectricity, thus being expected as a promising material for future memory devices. However, it has not been clarified why such unstable Ortho phase is realized in experiments. In this work, we study the stabilization mechanism of Ortho HfO_2 phase using the first- principles calculations.

Since the ferroelectric phase of representative $BaTiO_3$ is normally realized by the substrate-induced strain, we first consider the effect of strain. Fig.1 shows formation energies of stable monoclinic (Mono) and unstable Ortho phases in bulk and thin-film forms as a function of the cross-section area, i.e., biaxial strain. The energy increase in thin films occurs due to the surface energy loss. As seen in both figures, by applying tensile or compressive strain, the Mono phase increases the energy compared to the Ortho phase. This is because the Mono phase is stabilized by lowing its crystal symmetry and the deformation from such stable structure promotes large energy loss. However, the Ortho phase always has larger energy than the Mono one. Thus, the strain is not a single origin of the Ortho-phase formation.

Next, we consider the effect of oxygen vacancy (Vo), which is a representative defect and is often generated in oxides. Vo produces an electron-occupied state below the conduction bands, thus stabilized by the positive ionization. Fig.2 shows the energy difference between Ortho and Mono phases as a function of Vo ionization charge. From this figure, we know that the Ortho phase becomes the most stable when the 4-5% Vo's exist and they are +2 charged. However, considering that the formation energy of Vo, is relatively large around 4-5eV, the assumed composition 4-5% is still large. Thus, the ionization of Vo is also not a single origin of the Ortho-phase formation.

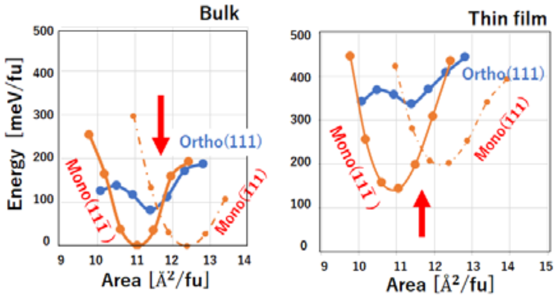

Fig.1. Calculated formation energies of Mono and Ortho HfO_2 in bulk (left) and thin-film (right) forms under (111) biaxial strain, relative to the most stable Monoclinic bulk phase, as a function of an area of formula unit.

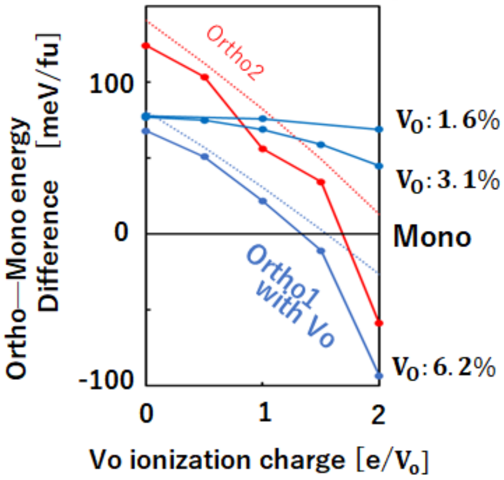

Fig.2. Calculated difference in energy between Ortho and Mono phases in bulk forms, as a function of the ionization charge of oxygen vacancy (Vo). The zero energy corresponds to the Mono phase.

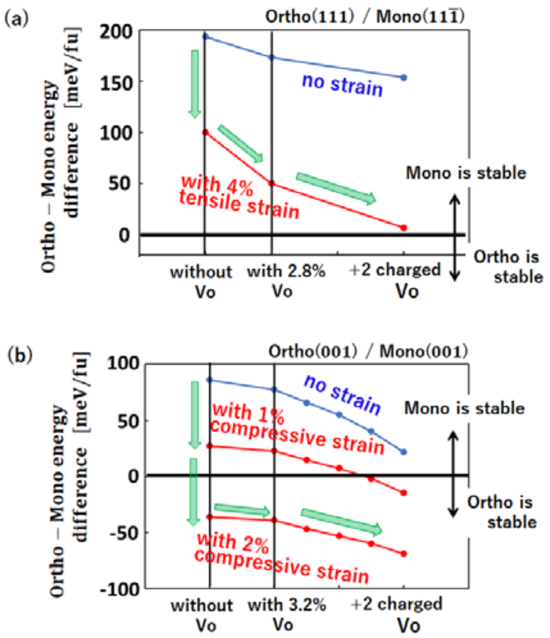

Fig.3. Calculated difference in energy between Ortho and Mono phases in thin-film forms, with/without 1-4% strain and 3% charged oxygen vacancy (Vo). The cases of (a) (111) tensile strain and (b) (001) compressive strain are shown.

Then, we consider the case when both the strain and the Vo ionization coexist in HfO_2. Fig.3 shows the energy difference between Ortho and Mono phases for the cases with/without strain and Vo charging. Figures 3(a) and 3(b) respectively correspond to the cases of (111) tensile strain and (001) compressive strain. It can be seen that both the strain and the Vo charging work cooperatively to stabilize the Ortho phase. In these ways, we can conclude that not only the substrate-induced strain but also the ionization of Vo are important factors to grow and stabilize the ferroelectric Ortho phase.

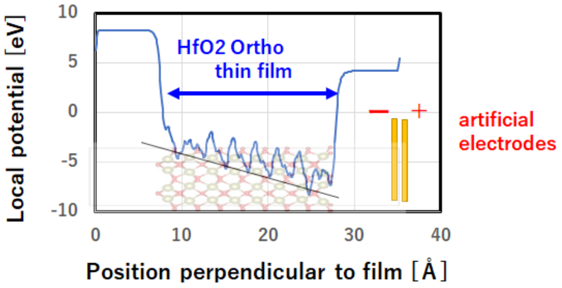

Fig.4. Calculated local-potential profile around Ortho HfO_2 (001) thin film. To correct the periodic boundary condition of the repeated slab geometry, the artificial electrodes are inserted in vacuum region so as to keep the horizontal potential.

Finally, we consider the ferroelectricity of Ortho HfO_2. It is well known that the polarization charge of ferroelectric material can be calculated by the Berry phase method using the bulk unit cell. The result by this method corresponds to the free standing ferroelectric film located isolate in the vacuum. However, in experiments, such material is grown on some substrates. In order to study the effect of the substrate on the ferroelectricity, the calculation method using the thin film geometry should be developed. Thus, we try to calculate the polarization charge using the conventional repeated-slab unit cell.

Due to the cancellation of electric fields caused by the front and back surfaces of the film, the potential should be flat outside the ferroelectric film. To realize such situation, we arrange the artificial electrodes (dipole) in the vacuum region in the unit cell, as shown in Fig.4. Then, we calculate the polarization charge using the Ortho HfO_2 (001) thin film. The calculated polarization charge is about 53μC/cm^2, which agrees with the values by the Berry phase method around 40-50μC/cm^2 and the observed values around 40μC/cm^2. In the future, we will use this method and study how the polarization changes with varying the substrate.

All these calculations were performed using the xTAPP, VASP, and our original pspwf codes. In order to realize the calculations for the present thin-film systems, because the system is made of a large number of atoms (1000-2000 atoms), the advanced computing facility having multi-task and higher-speed CPU (more than 1280 cores × 2.0G Hz), larger-size memory (around 256GB), and larger-size strange (more than 2 TB) is indispensable. These conditions are realized only by the present ISSP supercomputing systems.

Elucidation of surface structure and reactive property of (100) exposed CeO_2 nanocubes through first-principles calculation

Akira Yoko

Advanced Institute for Material Research,

Tohoku University, Katahira 2-1-1, Aoba-ku, Sendai, Miyagi 980-8577

CeO_2 nanocubes with (100) facet exposed have been synthesized by supercritical method, and it was found to have high oxygen storage capacity. In this study, the stabilization of the (100) facet by organic modification was studied by using first-principles calculations.

Another approach to improve oxygen storage capacity of CeO_2 is metal doping into the structure. In this study, Cr-doping into CeO_2 was also studied. The structural effects by doping were investigated.

In this study, first principles simulations based on density functional theory (DFT) was conducted. Plane wave basis DFT simulations were conducted using VASP code. Structures of CeO_2 at surface and bulk were calculated with generalized gradient approximation proposed by Perdew, Burke, and Ernzerhof (PBE) [1]. The valence configurations of the pseudopotentials were $5s^25p^64f^15d^16s^2$ for Ce, $3s^23p^63d^54s^1$ for Cr, and $2s^22p^6$ for O. The DFT+U method introduced by Dudarev et al. [2]was used to treat electron localization. The parameter U-J was set to 3.5 eV for Cr3d, 5.0 eV for Ce4f, and 5.5 eV for O2p states, respectively, based on previous studies of Cr_2O_3 and CeO_2 [3]. The Monkhorst-Pack k-point mesh of 4×4×4 was used for the unit cell of CeO2. The defect simulations were conducted with supercell of 2 × 2 × 2 extension (96 atoms).The slab model exposing (100) facet includes 60 atoms, and that for (111) facet includes 108 atoms. The Monkhorst -Pack k-point mesh for the slab model was 4×4×.

Figure 1a and 1b show CeO_2 (100) and (111) surface structure. The (111) facet of CeO_2 is nonpolar, contrary to the polar surface of (100). For the (100) facet model, half of the oxygen was moved to the other side to exclude polarity keeping the CeO_2 composition. The surface energy obtained from these calculations were 1.46 J/m^2 for (100) and 0.78 eV/m^2 for (111). The CeO_2 (111) is more stable than CeO_2 (100). The instability of (100) is the origin of high activity as catalysts. When CeO2 is synthesized with organic surfactant, it is known that (100) facet exposes. In Figure 1c, structure of carboxylic acid attachment on CeO2 (100) is shown. When calculating carboxylic attachment, dipolar correction implemented in VASP was used. After the deprotonation of the carboxylic acid one oxygen of COO locates between two

Ce atoms and the other oxygen locates on one Ce atom. The adsorption energy was found to be -26.6 kJ/mol. The apparent surface energy including the adsorption energy of the surfactant is lower in (100) than (111).

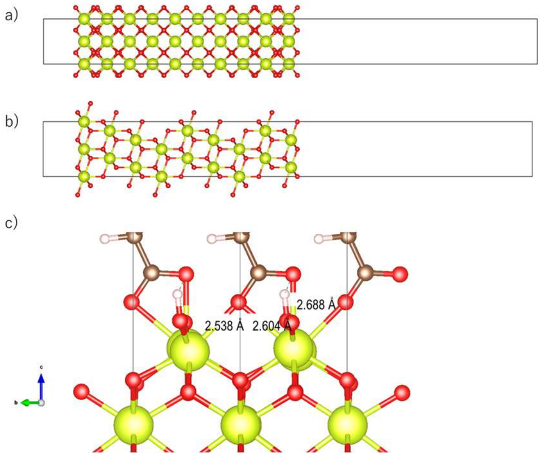

Fig. 1 Surface structures of CeO_2. a) CeO_2 (100), b) CeO_2 (111), c) Carboxylic acid adsorption on CeO_2(100).

The bulk calculation was conducted to obtain the oxygen vacancy formation energy in the Cr-doped system. The supercell consisting 96 atoms were used. Figure 2 shows the local structure around oxygen vacancies. The information about the structures is summarized in Table 1. Figure 2a shows the pure CeO_2, which includes an oxygen vacancy. Two Ce^{3+} ions exist in the next nearest neighbor (NNN) of the oxygen vacancy. The oxygen vacancy formation energy was 2.00 eV. Figure 2b shows the structure of Cr doped CeO2, which one of the Ce are substituted with Cr. The doping concentration is corresponding to 3 at%. In this case four oxygen atoms coordinates Cr, and Cr exists as 4+. Figure 2c shows the structure that one of the oxygen coordinating Cr (O-1 in Figure 2b) was removed. As a result of the vacancy introduction, local structure around Cr changed to six-coordination, and Cr became 3+ state, and the oxygen vacancy formation energy was 0.99 eV. The significant decrease in oxygen vacancy formation energy was observed. Also in this case, Ce3+ exits in the next nearest neighbor of oxygen vacancy. Further oxygen removal (O-2 in Figure 2c) occurred with lower oxygen vacancy formation energy as 0.65 eV. The local structure and the valence of Cr did not change, and two more Ce3+ are formed at the next nearest neighbor of the oxygen vacancy. At the vicinity of Cr dopant oxygen vacancy can be formed easily. Moreover, an oxygen atom, which is not at the next of Cr surrounded by four Ce^{4+} (O-3 in Figure 2d) was removed. As a result, the structure shown in Figure 2e was obtained. For the three oxygen vacancies, one Cr3+ and 5 Ce3; was formed. Five Ce3+ locates not at the nearest neighbor (NN) of oxygen vacancy but at the next nearest neighbor of the oxygen vacancies. The oxygen vacancy in this case was 1.20 eV, and significantly lower than pure CeO2 although the local structure was similar. This is not the oxygen vacancies around dopant. Doping affects whole the structure occurring distortion, which results in the lower oxygen vacancy formation energy at far position from the dopant.

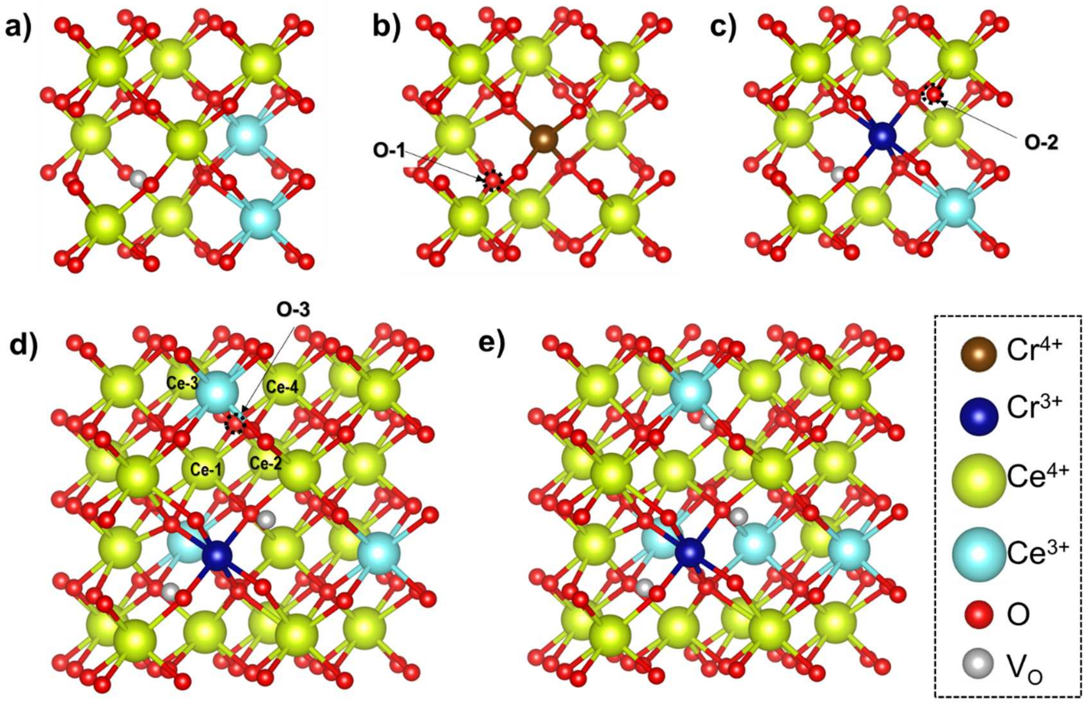

Figure 2 Structure of Cr 3% doped CeO_2 a)Non-doped CeO_2 with an oxygen vacancy, b) Cr4+ substituted CeO_2, c) ～ e) Cr doped CeO_2 with 1-3 oxygen vacancies

Table 1 Structural information about Cr 3% doped CeO_2

<table>
<tr><th rowspan="2">Structure</th><th colspan="5">Bader charge, |e|</th><th rowspan="2">V_O positions (distance from Cr)</th><th rowspan="2">E_{V_O} [eV]</th><th rowspan="2">Ce^{3+} positions relative to V_O</th></tr>
<tr><th>Ce^{3+}</th><th>Ce^{4+}</th><th>Cr^{3+}</th><th>Cr^{4+}</th><th>O</th></tr>
<tr><td>Non-doped CeO_2 with 1 V_O (Figure 6A)</td><td>+2.11</td><td>+2.44</td><td colspan="2">n/a</td><td>-1.28 to -1.20</td><td>n/a</td><td>2.00</td><td>NNN ($2Ce^{3+}$)</td></tr>
<tr><td>Cr^{4+} doped CeO_2 (Figure 6B)</td><td>n/a</td><td>+2.45</td><td>n/a</td><td>+2.00</td><td>-1.24 to -1.16</td><td>No V_O</td><td>n/a</td><td>n/a</td></tr>
<tr><td>Cr^{3+} doped CeO_2 with 1 V_O (Figure 6C)</td><td>+2.15</td><td>+2.44</td><td>+1.86</td><td>n/a</td><td>-1.26 to -1.17</td><td>O-1 in Figure 6B (2 Å)</td><td>0.99</td><td>NNN ($1Ce^{3+}$)</td></tr>
<tr><td rowspan="2">Cr^{3+} doped CeO_2 with 2 V_O (Figure 6D)</td><td rowspan="2">+2.15</td><td rowspan="2">+2.43</td><td rowspan="2">+1.85</td><td rowspan="2">n/a</td><td rowspan="2">-1.27 to -1.20</td><td>O-1 in Figure 6B (2 Å)</td><td></td><td rowspan="2">NNN ($3Ce^{3+}$)</td></tr>
<tr><td>O-2 in Figure 6C (2 Å)</td><td>0.65</td></tr>
<tr><td rowspan="3">Cr^{3+} doped CeO_2 with 3 V_O (Figure 6E)</td><td rowspan="3">+2.13</td><td rowspan="3">+2.42</td><td rowspan="3">+1.85</td><td rowspan="3">n/a</td><td rowspan="3">-1.37 to -1.20</td><td>O-1 in Figure 6B (2 Å)</td><td></td><td rowspan="3">NNN ($5Ce^{3+}$)</td></tr>
<tr><td>O-2 in Figure 6C (2 Å)</td><td></td></tr>
<tr><td>O-3 in Figure 6D (6 Å)</td><td>1.20</td></tr>
</table>

発表（投稿）論文等

1．Hao, X., **Yoko, A.**, Inoue, K., Xu, Y., Saito, M., Chen, C., Seong, G., Tomai, T., **Takami, S.**, Shluger, A.L., Xu, B., Adschiri, T., Ikuhara, Y.

“Atomistic Origin of High-Concentration Ce^{3+} in {100}-Faceted Cr-Doped CeO_2 Nanocrystals”

Acta Materialia, 203, 116473 (2021)

DOI: 10.1016/j.actamat.2020.11.015

References

[1] J.P. Perdew, K. Burke, M. Ernzerhof, Generalized gradient approximation made simple, Phys. Rev. Lett., 77 (1996), p. 38650.

[2] S. Dudarev, G. Botton, S. Savrasov, C. Humphreys, A. Sutton, Electron-energy-loss spectra and the structural stability of nickel oxide: An LSDA+ U study, Phys. Rev. B, 57 (1998), p. 1505

[3] P.R. Keating, D.O. Scanlon, B.J. Morgan, N.M. Galea, G.W. Watson, Analysis of intrinsic defects in CeO2 using a Koopmans-like GGA+ U approach, J. Phys. Chem. C, 116 (2012), pp. 2443-2452

Magnetocaloric Effect of Transition-Metal Alloys

Hung Ba TRAN[1] and Tamio OGUCHI[1,2]
[1]*SANKEN, Osaka University, Mihogaoka, Ibaraki, Osaka 567-0047, Japan*
[2]*CSRN, Osaka University, Machikaneyama, Toyonaka, Osaka 560-8531, Japan*

We study the magnetocaloric effect of transition-metal alloys by combining first-principles calculations and Monte-Carlo simulations. Several types of the magnetocaloric effect such as conventional (direct) magnetocaloric effect, giant magnetocaloric effect, anisotropic magnetocaloric effect, and inverse magnetocaloric effect can be considered by using our in-house program [1–6]. The peak in magnetization when applying an intermediate magnetic field along the hard axis of CrI_3, a well-known 2D material for the spintronic application, is successfully reproduced by using our program as shown in Fig. 1. The origin comes from the competition between magnetic anisotropy and external magnetic fields, where the temperature dependence of magnetic anisotropy energy plays the role. The finite magnetic anisotropy at slightly higher than Curie temperature is reproduced, where the magnetization anisotropy and anisotropic magnetic susceptibility is the crucial factor. The high accuracy in the estimation of anisotropic magnetic entropy change in CrI_3 paves the way to predict the magnetocaloric properties of new materials. In the next step, we have some ideas to enhance the accuracy and predict some novel properties of magnetic materials within the theoretical framework.

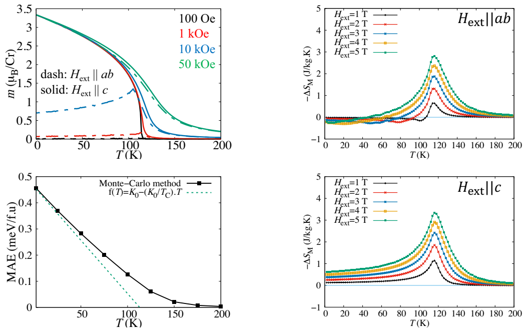

Figure 1: Magnetization, magnetic anisotropy energy, and anisotropic magnetocaloric effect of CrI_3 [6].

References

[1] H. B. Tran, T. Fukushima, K. Sato, Y. Makino, and T. Oguchi, J. Alloys Compd. **854**, 157063 (2021).

[2] H. B. Tran, T. Fukushima, Y. Makino, and T. Oguchi, Solid State Commun. **323**, 114077 (2021).

[3] H. B. Tran, T. Fukushima, H. Momida, K. Sato, Y. Makino, and T. Oguchi, Comput. Mater. Sci. **188**, 110227 (2021).

[4] H. B. Tran, T. Fukushima, H. Momida, K. Sato, Y. Makino, and T. Oguchi, Direct and Inverse Magnetocaloric Effects in FeRh Alloy: A Theoretical Study, http://dx.doi.org/10.2139/ssrn.3799705.

[5] H. B. Tran, H. Momida, Y. Matsushita, K. Sato, Y. Makino, K. Shirai, and T. Oguchi, Phys. Rev. B **105**, 134402 (2022).

[6] H. B. Tran, H. Momida, Y. Matsushita, K. Shirai, and T. Oguchi, Acta Mater. **231**, 117851 (2022).

Electrochemical reaction analysis using density functional calculation + implicit solvation model 3

Jun HARUYAMA

Institute for Solid State Physics,

The University of Tokyo, Kashiwa-no-ha, Kashiwa, Chiba 277-8581

We have studied electrochemical reaction systems using density functional combined with implicit solvation model, called ESM-RISM simulations [1–4]. This year, we focused on the adsorption structures of Pt(111)-H_2O (see Fig. 1a). The understanding of this metal/water interface system is important for basic electrochemical reactions such as oxygen/hydrogen reduction/evolution reactions.

Fig. 1a shows the most stable structure, Pt(111) √39×√39-H_2O including 5- and 7-membered rings, which is consistent with experiment. Fig. 1b shows the pair distribution functions of the obtained structure, which shows the Pt-O and O–O peaks of 2.3 Å and 2.5 Å. This small O–O distance could induce the redshift of OH vibrational frequencies. We also conducted the analysis of vibrational frequencies of the obtained structure. As a result, calculated vibrational frequencies were in good agreement with experiments. However, the adsorption energy of this structure is less than the activation energy of desorption from experiment, which indicates that the Pt-H_2O interaction should be improved by more sophisticated density functional.

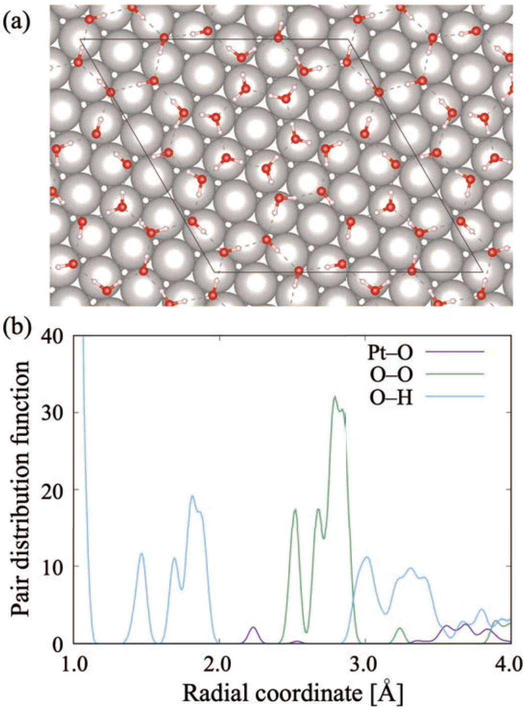

Fig. 1: (a) Adsorption structure of Pt(111)-H_2O. (b) Pair distribution function of Pt(111)-H_2O.

References

[1] M. Otani and O. Sugino: Phys. Rev. B **73** (2006) 115407.

[2] S. Nishihara and M. Otani: Phys. Rev. B **96** (2017) 115429.

[3] J. Haruyama, T. Ikeshoji, and M. Otani, Phys. Rev. Mater. **2** (2018) 095801.

[4] J. Haruyama, T. Ikeshoji, and M. Otani: J. Phys. Chem. C **122** (2018) 9804.

Study of Efficient Training Data Generation Method for Constructing Artificial Neural Network Force Field III

Kohei Shimamura

Department of Physics,

Kumamoto University, 2-39-1 Kurokami, Chuo-ku, Kumamoto 860-8555

Machine Learning Interatomic Potential (MLIP) not only achieves high accuracy by learning from first-principles molecular dynamics (MD) data, but also has low computational cost. Active Learning is the driving force behind the recent development of MLIPs. This approach primarily uses the uncertainty in the output of MLIPs to discover and generate unlearned data for efficiently constructing robust potentials. In this study, we continued to work on improving Active Learning. The MLIP using artificial neural network (called ANN potential) was used. In the previous studies, the use of standard deviation of atomic force is considered effective for finding unlearned data. We have also found that the method worked well.

On the other hand, we found that the MLIPs training method needs to be improved. The current standard training method does not guarantee the accuracy of pressure required for MD. We have demonstrated that the training of pressure is essential for ANN potentials to reproduce the solid-liquid phase transition [1]. Pressure training is also essential for thermal conductivity calculations using MLIPs. The heat flux in the Green-Kubo formula for ANN potentials is closely related to pressure. Thus, it has been found that without pressure training, obvious errors can occur in thermal conductivity [2].

Since the current MLIPs are trained not only with potential energy but also with atomic force and pressures, the cost function is composed of the corresponding terms. For efficiently training, adjustable coefficients are therefore introduced into these terms having different units and data size. Although previous studies did not emphasize the importance, we demonstrated that the coefficient adjustment was a significant effect on the accuracy of ANN potentials [3].

No matter how efficiently untrained data can be obtained, it becomes meaningless if the training is inadequate. As the application of MLIPs expands, the training of pressure and the coefficient adjustment would become essential.

References

[1] A. Irie, *et al.*: J. Phys. Soc. Japan **90**, 094603 (2021).

[2] K. Shimamura, *et al.*: Chem. Phys. Lett. **778**, 138748 (2021).

[3] A. Irie, *et al.*: J. Phys. Soc. Japan **91**, 045003 (2022).

Structure stability and electronic structures of point defects in wide-gap oxide materials

Hiroyoshi MOMIDA
Institute of Scientific and Industrial Research (SANKEN), Osaka University
8-1 Mihogaoka, Ibaraki, Osaka 567-0047

The wide-gap oxide materials such as Al_2O_3 and Ga_2O_3 have been attracted great interests in applications for power electronics devices. In this work, we have studied the structural and electronic properties of oxygen defects (vacancies or interstitials) in several amorphous oxides by the first-principles calculations.

The amorphous model structures of a-Al_2O_3 and a-Ga_2O_3 are generated by the first-principles molecular dynamics simulations and the melt-and-quench techniques. Figure 1 shows an example of the generated model structures using the 120-atom supercells. The mass densities are set to be 3.3 g/cm^3 for a-Al_2O_3 and 4.5 g/cm^3 for a-Ga_2O_3, which are in their respective experimental ranges and are lower than those of the α crystal phases (4.0 and 6.4 g/cm^3 for Al_2O_3 and Ga_2O_3, respectively). The O coordination numbers around Al are four (60.4%), five (29.2%), and six (10.4%) in a-Al_2O_3, and those around Ga are four (66.7%) and five (33.3%) in a-Ga_2O_3.

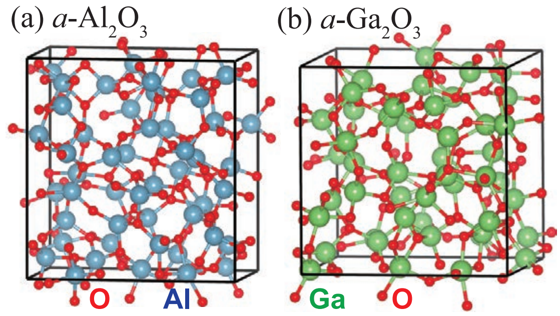

Figure 1: Amorphous structures of (a) a-Al_2O_3 and (b) a-Ga_2O_3 120-atom supercell models.

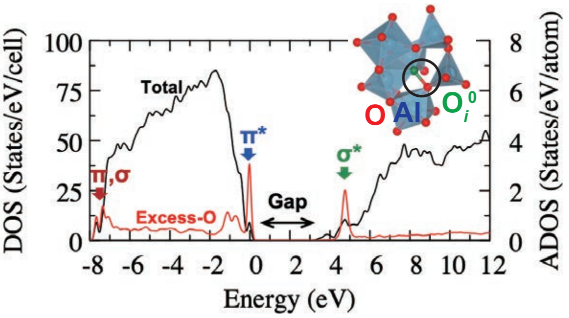

Figure 2: Density of states (DOS) of a-Al_2O_3 with the excess O (O_i^0). Total (black line with left scale) and O_i^0 (red line with right scale) DOSs are shown. The inset shows the local structure near O_i^0, forming the peroxy linkage.

The O defects are introduced by adding and removing O (interstitials O_i^q and vacancies V_O^q) in the pristine oxide models, considering the charged states q of defects. In the charge neutral state ($q = 0$), it is found that O_i^0 tends to form the O–O peroxy linkage, giving the π^*- and σ^*-type O_2-like states near the valence band top and the conduction band bottom regions, respectively (Fig. 2). It is also found that such the O_2-like states show interesting behavior by changing q, and similar properties of O_i^q are confirmed in a-Ga_2O_3 and in several oxide crystals. We also study electric properties due to V_O^q in oxides to discuss ReRAM [1].

References

[1] H. Momida and T. Ohno: Appl. Phys. Lett. **117** (2020) 103504.

Theoretical study for magnetic-nano-particles formation from first-principles calculations

Yasutomi TATETSU

Meio University, Biimata, Nago, Okinawa 905-8585

There is a growing interest in searching novel materials that are not only thermodynamically stable, but also thermodynamically unstable for applications. Chemical synthesize techniques, which control nano particles precisely, are being developed in order to find new functional materials for technologies. Recently, Teranishi's group at Kyoto University found a new behavior of crystal structure transformation for an ionic nanocrystal [1], and a new $Z3$-type Fe(Pd,In)$_3$ crystal structure, which was synthesized by introducing a third element of In into $L1_2$-FePd$_3$ [2].

In this report, we performed first-principles non-collinear calculations in order to explain the higher coercivity value in the $Z3$-Fe(Pd,In)$_3$ structure. We used the ab-initio code, OpenMX [3], for calculating the magnetic anisotropy energies of $L1_2$-(Fe,In)Pd$_3$ and $Z3$-Fe(Pd,In)$_3$ structures and compared these energies to find easy axes. In each calculation, the spin directions of each atom in these systems were set from [001] to [100] when $\varphi = 0$ and from [100] to [110] when $\theta = 0$. We found that the magnetic anisotropy energies show −1.38 μeV/atom for the $L1_2$-(Fe,In)Pd$_3$ structure and −0.213 meV/atom for the $Z3$-Fe(Pd,In)$_3$ structure. The easy axis for $Z3$-Fe$_8$(Pd$_{20}$,In$_4$) is the c axis, as shown in the figure. The tendency which the $Z3$-Fe(Pd,In)$_3$ structure has higher coercivity values than the $L1_2$-(Fe,In)Pd$_3$ structure is consistent with the experimental measurement. We assume that added In atoms might be one of the reasons to increase the magnetic anisotropy of the $Z3$-Fe(Pd,In)$_3$ structure. Further theoretical studies are needed to explain the mechanism of the coercivity increase in the $Z3$-Fe(Pd,In)$_3$ structure.

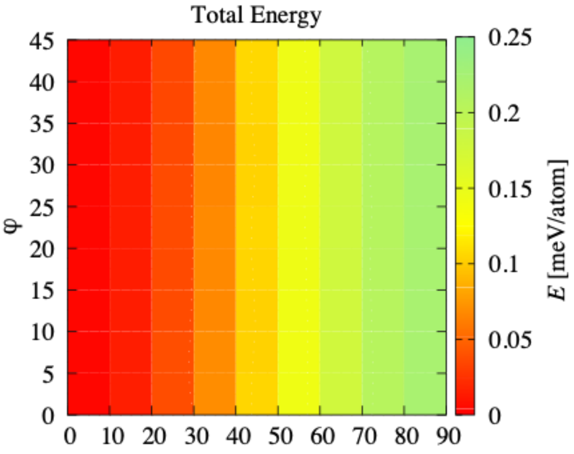

Figure: Total energy analysis for the Z3-Fe(Pd,In)3 structure depending on the spin directions.

References

[1] Z. Li, M. Saruyama, T. Asaka, Y. Tatetsu, and T. Teranishi, Science, **373**, 332 (2021).

[2] K. Matsumoto *et al.*, Nat. Commun., **13**, 1047 (2022).

[3] http://www.openmx-square.org

Evolutionary algorithm for simulation of fast chemical reaction process

Koichi KUSAKABE
Graduate School of Science, University of Hyogo
Kouto, Kamigori, Hyogo 5-8581

1 Introduction

One methodology in the quantum materials informatics, based on density functional theory to evaluate many-body correlation effects, has recently been used to determine the electronic phase diagram of oxides [1], to design high-temperature superconductors [2], and spin-electronic devices based on atomic layer material [3]. Materials design of measurement-based quantum computing devices [4, 5], and the elucidation of unknown photo-induced phase transitions based on measured data [6] were performed. We have also designed an activation method of catalytic properties and evolutionary operations for detonation processes.

2 Alkane dehydrogenation on nanographene catalyst

To support designed activated nanographene catalysts for dehydrogenation of alkane, several dehydrogenation reaction pathways were determined based on density functional theory calculations. The catalytic effect of vacancy created graphene surfaces is simulated using the alkane decomposition reaction as an example.

The effect of the atomic defects was investigated, and the effect of lowering the reaction energy barrier due to substitution by nitrogen and other group V elements was confirmed. Furthermore, the characteristics of the nanographene catalyst, in which multiple active sites are involved in the reaction, confirm that propylene generation from propane on our catalytic structure has the effect of significantly lowering the endothermic reaction heat.

At the same time, in-situ AI analysis of time-dependent small-scale data during the synthesis of catalytic materials was requested to elucidate the experimental procedures. Theoretical analysis of emission spectra during the material conditioning (activation process by high-energy particle irradiation) was performed. As a result, it became possible to develop a measurement method to support in-situ observation of molecular desorption by adopting machine-learned classification using ResNet.

3 Algorithms for elucidation of detonation reaction paths

We are also promoting the elucidation of the detonation reaction mechanism by combining evolutionary algorithms, which reveals oxidation and reduction reactions in the TNT-RDX composite that produces the detonation diamond. An evolutionary algorithm systematically generates intermediate states of chemical reaction processes.

Stable crystals initiate rapid chemical reactions triggered by mass transport. We introduced mass transport into the evolutionary algorithm. The basis for the continuation of the reaction was found by structural optimization calculations, first-principles molecular dynamics calculations, and the migration paths of radicals within the crystal.

Consider that radical species are supplied to adjacent material phases in the processes of redox reactions. To determine the initiation process of this chain reaction, we applied the accelerated chemical reaction simulation using the generational operation of the evolutionary process. We applied this method to oxidation of RDX and reduction of TNT, and confirmed that our acceleration method works

The initiation point of the detonation process is considered to be the formation of OH radicals by electron transfer excitation. The OH radicals pull out hydrogen atoms and rapidly destabilize RDX. RDX then decomposes to form NO$_2$. (Figure 1 (a), (b))

Hydrogen radicals are supplied to TNT from the destabilized RDX. When a certain amount of hydrogen radicals are added, the nitro groups of TNT are decomposed to generate water, resulting in nitroso groups. This nitroso group functions to join adjacent carbon skeletons. (Figure 1 (c)) From these carbon skeleton linkages, the formation of clusters with larger carbon skeletons may follow.

By confirming that the supply of hydrogen radicals to TNT and OH radicals to RDX initiate rapid reactions, and by successfully drawing the initial reaction cycle, we confirmed that our method has potential for providing insight into real-time evolution problems.

Acknowledgement

The author is grateful to Dr. T. Ishikawa, Mr. Y. Makino, and Prof. S. Sakamoto for their collaboration. This work is partly supported by collaborative joint research in 2021 on “Research of detonation soot as a non-oxidative dehydrogenation catalyst” and “Study of detonation reaction mechanisms combining molecular dynamics and evolutionary algorithms” with Daicel engineering science joint research in Osaka university.

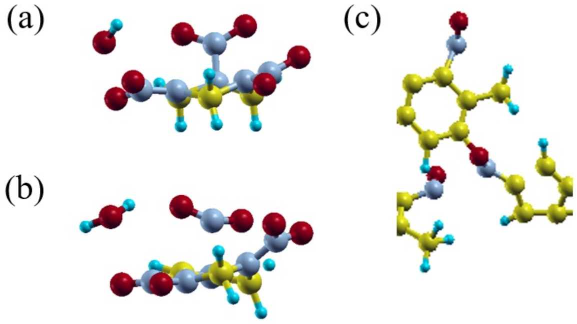

Figure 1: Molecular structures arising from operations of evolutionary algorithms. (a) RDX, which is destabilized by the addition of hydroxyl radical, generates (b) a water molecule and simultaneously releases of NO$_2$. (c) TNT destabilized by hydrogenation can generate carbon clusters bridged by NO groups.

References

[1] S. Teranishi, K. Nishiguchi, S. Yunoki, K. Kusakabe, J. Phys. Soc. Jpn., **90**, 094707 (2021).

[2] S. Teranishi, K. Nishiguchi, K. Kusakabe, J. Phys. Soc. Jpn., **90**, 054705 (2021).

[3] H. Harfah, Y. Wicaksono, G. K. Sunnardianto, M. A. Majidi, K. Kusakabe, Nanoscale Adv., **4**, 117 (2022).

[4] N. Morishita, Y. Oishi, T. Yamaguchi, K. Kusakabe, Appl. Phys. Express **14**, 121005 (2021).

[5] N. Morishita, K. Kusakabe, Phys. Lett. A, **408**, 127462 (2021).

[6] M. Nagai, Y. Higashitani, M. Ashida, K. Kusakabe, H. Niioka, A. Hattori, H. Tanaka, G. Isoyama, N. Ozaki, Research square, DOI:10.21203/rs.3.rs-130295/v1 (Preprint).

Study on Hydration Process of Cellobiose by First Principles Calculations

Tomomi Kondo[1,2], Daisuke Akazawa[1,2], Takehiko Sasaki[1], Motoyuki Shiga[2]

1 *Department of Complexity Science and Engineering, Graduate School of Frontier Sciences, The University of Tokyo, Kashiwa-no-ha, Kashiwa, Chiba 277-8561*

2 *Center for Computational Science and E-Systems, Japan Atomic Energy Agency 148-4 Kashiwanoha Campus, 178-4 Wakashiba, Kashiwa, Chiba, 277-0871*

Cyclization dehydration reaction of polyalcohol in hot water has been proven to be efficient method for utilization of biomass materials [1]. For this purpose we proposed a new method of refinement (improved metadynamics method: Refined MTD), and applied it to cyclization dehydration of 2,5-Hexanediol (HDO) [2]. Based on these results we studied cyclization dehydration process of d-sorbitol (SBT) yielding 1,4-Anhydro-d-sorbitol (1,4-AHSO), 2,5-Anhydro-d-sorbitol (2,5-AHSO) and 1,5-Anhydro-d-sorbitol (1,5-AHSO) as shown in Fig. 1.

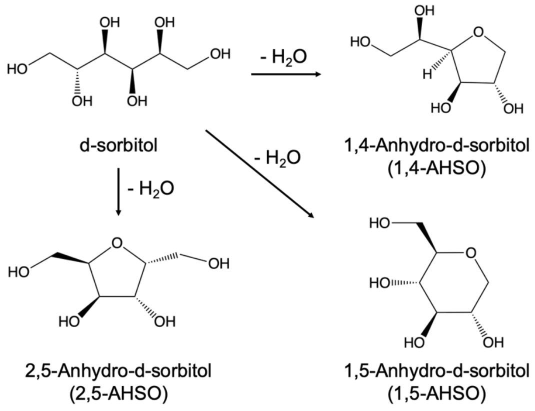

Fig. 1 Cyclization dehydration process of d-sorbitol.

Calculations were conducted using software PIMD [3] working with DFTB or VASP. The calculation system consists of 1 SBT molecule, 30 water molecules, and acidic molecules such as HCl added under the same thermodynamic conditions as in Experiment [1] (20 MPa, 523 K). CV is defined for each product as shown in Table 1. Fig. 2 shows the illustration for 1,4-AHSO3 as one example. The dihedral angle ϕ between the hydroxyl group and the main chain, the difference d in the O-C distances of leaving and bonding, and the proton coordination number n of the hydroxyl group were set according to the reaction path. Reaction processes in HCl(aq), H_2CO_3 (aq) and pure water were examined.

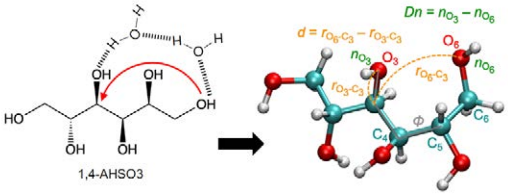

Fig. 2 Illustration for CV of 1,4-AHSO3

Table 1 Definitions of CVs

CVs	1,4-AHSO3	1,4-AHSO6	1,5-AHSO2	1,5-AHSO6	2,5-AHSO2	2,5-AHSO5
Difference of the bond length d	O_6, C_3, O_3	O_3, C_6, O_3	O_6, C_2, O_2	O_2, C_6, O_6	O_5, C_2, O_2	O_2, C_5, O_5
Dihedral ϕ	O_3-C_3-C_4-C_5	O_6-C_6-C_5-C_4	O_2-C_2-C_3-C_4	O_6-C_6-C_5-C_4	O_2-C_2-C_3-C_4	O_5-C_5-C_4-C_3
Difference of the Coordination number of H D_n	O_3, O_6	O_6, O_3	O_2, O_6	O_6, O_2	O_2, O_5	O_5, O_2

According to DFTB based calculations over 3 ns dehydration reaction was observed and the transition state was found on the free energy contour map at CV with $\phi=155°$, d=0.0 and n=2.1. Molecular dynamics calculations were conducted around this transition state so that the real time mechanism is visualized. After proton is bonded on the oxygen atom (Fig. 3 ①) the dehydration (Fig. 3 ②) and the formation of O-C bond (Fig. 3 ③) occur almost simultaneously, indicating that the five-membered ring is formed via S_N2 process.

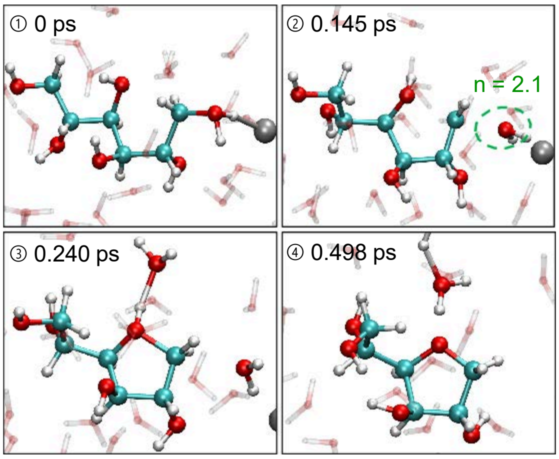

Fig. 3 Reaction process from SBT to 1,4-AHSO

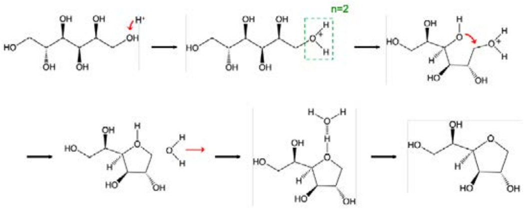

Fig. 4 Dehydration mechanism for SBT.

The mechanism is summarized in Fig. 4. The simulation results predict that the reaction is faster in HCl solution than in carbonic acid solution, due to the acid-catalyzed mechanism. In most of the calculated conditions, the reaction barriers for two of the pathways leading to the five-membered ring products, 1,4-AHSO and 2,5-AHSO were found to be lower than those leading ot the six membered ring product, 1,5-AHSO. This is in agreement with experiments where only the five-membered ring products were detected. The reaction pathway to the five-membered ring products goes through a metasbable state of SBT in the confined conformation. These results were published in [4].

We also calculated ab initio molecular dynamics (MD) simulations for cellobiose aqueous solution using PIMD and CP2K program and the subsequent C-K edge XAS spectra simulation using CP2K. Experimental XAS spectra can be interpreted by water molecules interacting with the cellobiose molecule [5].

References

[1] A. Yamaguchi *et al.*, *Green Chem.*, **13**, 873 (2011).

[2] T. Kondo *et al.*, *J. Comput. Chem.*, **42**, 156 (2021).

[3]http://ccse.jaea.go.jp/ja/download/pimd/index.jp.html.

[4] T. Kondo *et al.*, *J. Comput. Chem.*, **42**, 1783(2021).

[5] D. Akazawa *et al.*, *J. Chem. Phys.*, **156** 044202 (2022).

Ab initio calculation for structural stability of transition-metal-oxide superlattice

Kazuma NAKAMURA
Quantum Physics Section, Kyushu Institute of Technology
1-1 Sensui-cho, Tobata, Kitakyushu, Fukuoka, 804-8550

In this study, we investigate the structural stability of transition-metal-oxide superlattices using first-principles calculations. We consider superlattices built by polar and non-polar transition-metal oxides. The polar type is a transition-metal oxide in which the charge neutrality of the constituent parts is not maintained, but the entire charge neutrality is maintained. For example, in a perovskite $\mathrm{LaAlO_3}$, it is made as the stacking structure consisting of a LaO plane charged with +1 valence and an $\mathrm{AlO_2}$ plane charged with −1 valence. On the other hand, in the non-polar type, the charge neutrality is maintained including the partial system; for example, in $\mathrm{SrTiO_3}$, it consists of charge-neutral SrO and $\mathrm{TiO_2}$ planes. We consider 10 types of superlattices consisting of $\mathrm{SrTiO_3}$, $\mathrm{SrVO_3}$, $\mathrm{BaTiO_3}$, $\mathrm{LaAlO_3}$, $\mathrm{CaCuO_2}$. In the present report, we focus on $\mathrm{SrTiO_3/SrVO_3}$ (STO/SVO) and $\mathrm{CaCuO_2/SrTiO_3}$ (CCO/STO) superlattices. Also, we write the superlattice as $\mathrm{A}_n/\mathrm{B}_n$ where A and B specify materials, and n is their number. We used xTAPP [1]

To discuss the structural stability of the superlattice, we calculate the n dependence of the following standard enthalpy of formation $\Delta H(n)$ as

$$\Delta H(n) = \Delta H_I(n) + \Delta H_S(n), \tag{1}$$

where $\Delta H_I(n)$ and $\Delta H_S(n)$ are defined as

$$\Delta H_I(n) = \frac{E[\mathrm{A}_n/\mathrm{B}_n]}{n} - \left[E(\mathrm{A}, a_n^{\parallel}) + E(\mathrm{B}, a_n^{\parallel})\right], \tag{2}$$

and

$$\Delta H_S(n) = \left[E(\mathrm{A}, a_n^{\parallel}) - E(\mathrm{A})\right] + \left[E(\mathrm{B}, a_n^{\parallel}) - E(\mathrm{B})\right], \tag{3}$$

respectively. $\Delta H_I(n)$ is an interface energy due to the interface formation, and $\Delta H_S(n)$ is a strain-storage energy due to the lattice mismatch. Also, $a^{\parallel}$ is an in-plane lattice parameter of the superlattice.

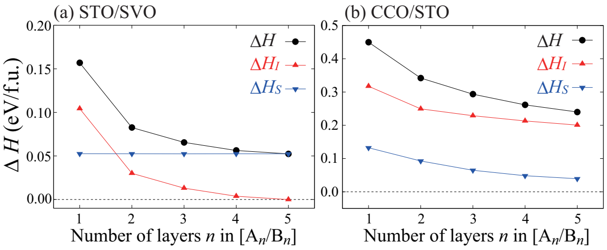

Figure 1: Calculated standard formation enthalpy $\Delta H(n)$ (black lines) for the (a) $(\mathrm{STO})_n/(\mathrm{SVO})_n$ and (b) $(\mathrm{CCO})_n/(\mathrm{STO})_n$ superlattices. Red and blue lines are an interfacial contribution $\Delta H_I(n)$ due to the interface formation, and a strain-storage one $\Delta H_S(n)$ due to the lattice mismatch.

Figure 1 shows our calculated standard formation enthalpy $\Delta H(n)$ (black lines), as well as its decomposition $\Delta H_I(n)$ (red lines) and $\Delta H_S(n)$ (blue lines). Panels (a) and (b) are the results for STO/SVO and CCO/STO superlattices, respectively. The case $\Delta H_I(n) > \Delta H_S(n)$ indicates that superlattice does not develop epitaxially; the STO/SVO superlattice is stable with the epitaxial growth, while the CCO/STO superlattice is unstable.

About the optimized structure of the superlattice, the following trends were observed:

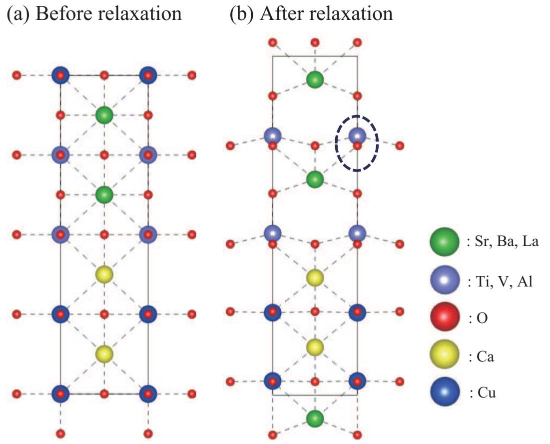

Figure 2: Ferroelectric displacement occurred in the CCO-based superlattice.

1. In the superlattices composed only of the perovskite-type oxides, an in-plane lattice constant $a_{\|}$ shows a tendency to converge to an averaged value of the two materials that make up the superlattice.
2. The average c length of of each block constituting the superlattice basically reflects the bulk parameters.
3. In the superlattice of polar and insulating non-polar transition-metal oxides, a significant ferroelectric displacement occurs in the non-polar side (Fig. 2).

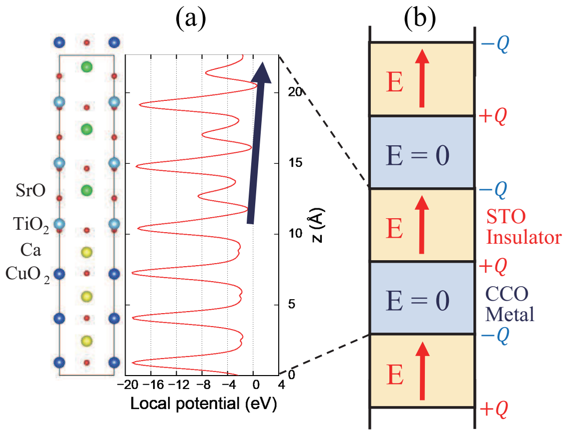

Figure 3: Left: Calculated effective potential for electrons in the superlattice, along the stacking direction z. Right: A schematic figure for the resulting electric field.

Table 1: Interfacial charge in the CCO-based superlattice. Unit of e.

	Interfacial charge			
n	2	3	4	5
CCO/STO	0.33	0.30	0.28	0.27
CCO/BTO	0.33	0.33	0.31	0.29
CCO/LAO	0.38	0.31	0.28	0.26
LAO/SVO	0.25	0.20	0.19	0.16

To understand the tendency of the standard formation enthalpy (Fig. 1) and the ferroelectric displacement in the CCO-based superlattice (Fig. 2), we calculated an effective potential for electrons in the superlattice along a stacking direction z. Figure 3 (a) displays results for the CCO/STO superlattice. From the figure, we see that a potential gradient is occurring in the STO side (blue arrow), leading to the electric field from TiO_2/Ca to CuO_2/SrO interfaces. From the behavior of this effective potential, the CCO/STO superlattice can be regarded as dielectric inserted into a capacitor [Fig. 3 (b)]. With this view, the interfacial charge can be estimated from the classical electromagnetism as

$$Q = \sqrt{\left(\frac{\epsilon}{\epsilon_0}\right)\epsilon_0\frac{dv(z)}{dz}\Delta S}. \tag{4}$$

Table 1 shows our estimated interfacial charges for the CCO-based superlattice, we show an n dependence. The resulting charge is near 0.3 e, which gives the electric field of 0.87 V$\AA^{-1}$.

References

[1] http://xtapp.cp.is.s.u-tokyo.ac.jp

Study on Removal Mechanism of Single-Crystalline Si Planarized by Catalyst-Referred Etching in Pure Water

Pho Van BUI, Taku HAGIWARA, Kiyoto KAYAO, Daisetsu TOH, Kouji INAGAKI, Yoshitada MORIKAWA
Graduate School of Engineering,
Osaka University, 2-1 Yamada-oka, Suita, Osaka 565-0871

There is a growing demand for ultra-precision optical components for scientific and industrial applications, especially in extreme ultraviolet (EUV) and X-ray regimes. Using short-wavelength light, scientific imaging of cutting-edge materials/biological samples and nanoscale lithography has become possible thanks to the ultra-precision optical components. Si is the material of choice for optical components, thanks to its attractive properties, such as higher cleanliness, machinability, and workability. A highly ordered surface with a root mean square roughness at the level of several tens of picometer is greatly desired for the highest reflectivity and the lowest unwanted scattering [1].

In this study, we apply catalyst-referred etching (CARE), an abrasive-free polishing method, to the planarization of a crystalline Si surface, using Pt as the catalyst and pure water as the etching solution [2]. An atomically smooth surface with sub-Angstrom root-mean-square roughness is achieved on the Si substrate.

Our recent studies indicated that the removal mechanism of SiC and SiO_2 etching via CARE is a hydrolysis reaction, in which the catalyst assists water dissociation and stabilization of the hypervalent state, increasing the rate of the reaction [3]. Thus, the purpose of the proposed research is to clarify the removal mechanism of Si etching via CARE using first-principles calculations. Additionally, in Si polishing, the effect of self-oxidation by oxygen and water is still not well understood due to the instability of Si under ambient conditions. Thus, the oxidation effects of oxygen and water are also taken into account.

The mechanistic removal pathway of CARE for Si(111) has been clarified and shown in Fig. 1. In the pathway with the Pt catalyst, at first, a water molecule is dissociatively adsorbed on Pt. In the next step, the adsorbed OH is transferred to the targeted Si, forming the five-fold coordinated state in the metastable state (MS). At this state, the Si-Si back-bond is elongated and weekend. Finally, the Si─Si back-bond is broken by a proton transfer at the final state (FS). The activation barrier is reduced from 1.0

eV (without the Pt) to 0.6 eV (with the Pt). Similar results are observed on a Si(100).

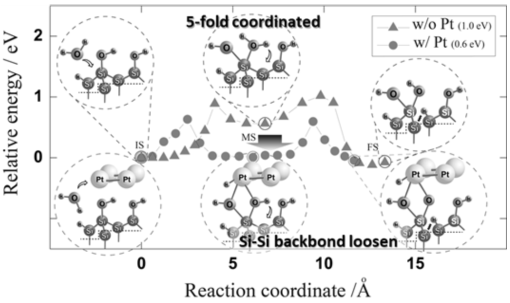

Fig. 1: Mechanistic reaction pathways of the Pt-catalyzed water etching of Si(111).

To investigate the effect of oxidation for an HF-treated Si(100) surface, Si(100) with an H-terminated surface was used. Si-H and Si-OH exchange reaction is investigated, as shown in Fig. 2. The activation barrier is 0.75 eV.

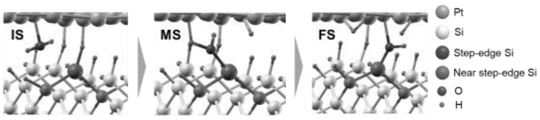

Fig. 2: Oxidation effect of Si(100) by water

To investigate the effect of oxidation by oxygen at the terrace and step-edge sites, Si(111) is employed, as illustrated in Fig. 3. The corresponding activation barriers are 0.46 and 0.15 eV, respectively (Fig. 4).

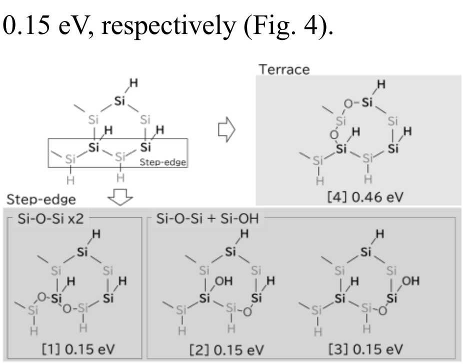

Fig. 2: Si(111) oxidation effects by oxygen at the terrace and step-edge sites (top-view).

The obtained results indicated that the oxidation occurs readily in the air at a step-edge site but not at a terrace site. The obtained results are consistent with the previous study [4]. The obtained results also explained why the wettability of the Si surface could last for several hours in the ambient conditions in the previous experimental study [5].

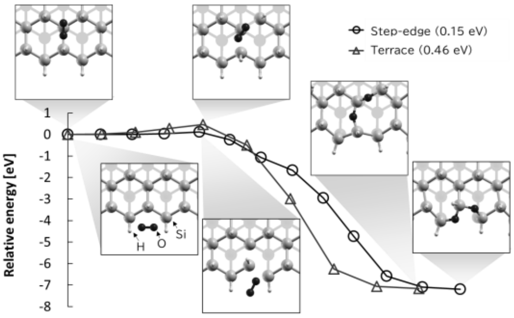

Fig. 4: Oxidation by an oxygen molecule at a step-edge and a terrace site.

The study has clarified the mechanistic removal pathway of CARE for Si in pure water and the oxidation effect of a Si surface by oxygen or water. Oxygen plays a main role in surface oxidation. Moreover, the combined oxidation effects of oxygen and water might be an important factor to be considered in future studies.

References

[1] R. J. Noll: Opt. Eng. **19** (1980) 249.

[2] H. Hara et al.: J. Electron Mater. **35** (2006) L11.

[3] P.V. Bui at al.: Jpn. J. Appl. Phys. **57** (2018) 055703.

[4] F. A. Soria, E. M. Patrito, and P. Paredes-Olivera: J. Phys. Chem. C **116** (2012) 24607.

[5] M. Niwano at al.: J. Appl. Phys. **76** (1994) 2157.

Ab initio molecular dynamics study on ion-conduction mechanisms of perovskite-type oxide

Satoshi OHMURA

Department of Environmental and Civil Engineering,

Hiroshima Institute of Technology, Miyake 2-1-1, Saeki-ku, Hiroshima 731-5193

We have investigated the mechanism of photoinduced oxygen dynamics in cobalt double-perovskite crystal using density functional theory (DFT) based quantum-molecular-dynamics (QMD) simulations.

We adopted the LR-TDDFT for calculating light-absorption spectra, which are calculated as folded oscillator strengths

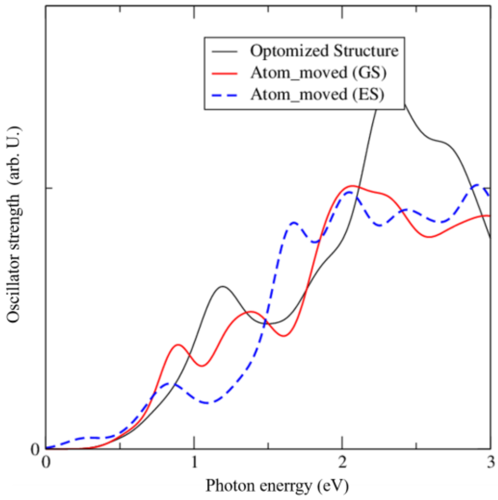

Fig. 1. Calculated oscillator strength of EuBaCo$_2$O$_{5.39}$ crystal

We found that the photoexcitation with an energy exceeding 3 eV provides the oxide ion with excess energy, arrowing it to pass through the barrier. The oxide ion may travel to the crosswise position from the potential valleys of the ground state via intersection of the potential energy curves in the excited and ground state at ~1 Å. Figure 2 shows the ionic configurations of the oxide ion (O1) as it moves from the diagonal to the crosswise position. The oxide ion is subjected to the repulsive and attractive forces from the other oxide and cobalt ions, respectively.

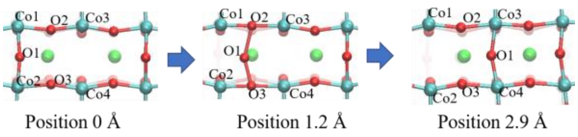

Fig. 2. Ionic configurations during the travel of the oxide ion

References

[1] M. Hada, S. Ohmura et al.: Carbon. **18** (2021) 612.

[2] M. Hada, S. Ohmura et al.: Appl. Mater. Today 24 (2022) 101167.

Atomic structure of metal-oxide interfaces and oxide grain boundaries

Kazutoshi INOUE[1], Mitsuhiro SAITO[2], and Yuichi IKUHARA[1,2,*]
[1] *Advanced Institute for Materials Research, Tohoku University, Sendai, Miyagi, 980-8577*
[2] *Institute of Engineering Innovation, The University of Tokyo, Yayoi, Tokyo, 113-8656*

The atomic structures of SiO_2/4H-SiC (0001) [Si face] and (000$\bar{1}$) [C face] interfaces were analyzed by first-principles molecular dynamics (MD) calculations combined with aberration-corrected scanning transmission electron microscopy (STEM). MD simulations were performed using the Vienna ab initio Simulation Package (VASP). The generalized gradient approximation (GGA) in the form of the Perdew–Burke–Ernzerhof (PBE) exchange-correlation functional was implemented. A kinetic energy cutoff of 450 eV was used for the expansion of the charge density, and all calculations were performed using a Brillouin zone sampling with $2 \times 2 \times 1$ k-mesh. The cell sizes are 1.070 nm ($\sim$ 4 unit cells of SiC) along the [1$\bar{1}$00] axis and 0.926 nm ($\sim$ 3 unit cells of 4H-SiC) along the [11$\bar{2}$0] axis where 6 Si-C bilayers along the [0001] axis were involved as the 4H-SiC substrates. SiO_2 structures were constructed by randomly distributed 30 Si and 60 O atoms on each faces as the initial models. The opposite side of the 4H-SiC {0001} slabs was passivated by hydrogen atoms to eliminate the effects of dangling bonds, and a vacuum slab with a thickness of 1.5 nm along the [0001] axis was embedded into the outer side of SiO_2 amorphous layer to avoid unwanted interactions. The supercell includes 246 atoms in total, including 102 silicon, 72 carbon, 60 oxygen and 12 hydrogen atoms. The initial model was heated at 3500 K for 15.0 ps, cooled at -355 K/ps, and then relaxed at 300 K for 9.0 ps. Finally, the atomic positions were fully relaxed until the maximal force on each atom decreased to below 0.05 eV/Åand the total energy converged to less than 1.0×10^{-4} eV/atom.

We observed the interfacial O atoms on the amorphous SiO_2 layer on the Si face show clear atomic ordering with a rigid O-Si bridge structure across the SiO_2/4H-SiC interface, which indicates a slow oxidation rate. The C face interface, on the other hand, was atomically rough and formed many dangling bonds with high oxidation rate. We concluded that the formation of a stable and flat oxidation front by O atom ordering and the suppression of interface defects or residual C will be useful for designing high-performance 4H-SiC MOSFET devices [1].

Polycrystalline ZnO is widely used and its properties are largely influenced by grain boundaries (GBs). We systematically investigated [0001]-symmetrical tilt GBs in polycrystalline wurtzite ZnO by first-principles calculations and atomic-resolution aberration-corrected STEM. The Zn sites form an octahedron capped by Zn tetrahedra, with O atoms located at the center, forming a Zn octahedron which can be regarded as a hexagon viewed along the $\mathbf{c}$ = [0001]-axis. The misorientation of ZnO [0001]-symmetrical tilt GBs is defined by the dihedral angle 2θ between the (11$\bar{2}$0) planes in adjacent grains, where θ is the dihedral angle between the (11$\bar{2}$0) and $(p\,q\,\overline{p+q}\,0)$-GB planes.

The stable structures of the $\Sigma 7\,(12\bar{3}0)$ at

21.79°, $\Sigma13$ $(25\bar{7}0)$ at 27.80° and $\Sigma13\,(13\bar{4}0)$ at 32.20° CSL GBs were independently simulated. The upper crystal was shifted toward the lower crystal by 0.01 nm along the x-, y-, and z-directions. Static lattice calculations were carried out with General Utility Lattice Program (GULP) using the Buckingham-form two-body interatomic potential for ZnO. The local minima were then optimized in the first-principles calculations with the plane-wave basis projector-augmented wave method included in VASP. The GGA was used for the exchange-correlation potentials in the PBE form and the cutoff energy was 400 eV for all plane-wave basis sets. All ionic positions as well as the supercell volume were relaxed such that all forces were $< 1.0\times10^{-5}$ eV/Å, and the residual force on each relaxed atom was < 0.05 eV/Å under the constant pressure of 0 Pa and constant temperature of 0 K. The Brillouin-zone integrations were performed over a $4 \times 2 \times 4$ k-point mesh generated by the Monkhorst-Pack scheme.

The GB and bulk structural units found in this study are similar to capped trigonal prisms (CTPs) and octahedra, corresponding to octagons and hexagons viewed along the **c**-axis, respectively. After relaxation, the stable atomic structures were obtained for the $\Sigma7\,(12\bar{3}0)$ GB at 21.79° concave octagons are aligned periodically and are filled in by two hexagons. On the other hand, the stable atomic structure for the $\Sigma13\,(13\bar{4}0)$ GB at 32.20° was alternative arrangement of a hexagon and a concave octagon in a period. The stable atomic structure calculated for the $\Sigma13$ $(25\bar{7}0)$ GB is composed of four hexagons alternately arranged with three octagons, which is reportedly a one-to-one combination of the $\Sigma7\,(12\bar{3}0)$ GB at 21.79° and the $\Sigma13\,(13\bar{4}0)$ GB at 32.20°. These hexagons and concave octagons are fundamental structural units to describe [0001]-symmetrical tilt GBs in wurtzite ZnO, and we found that the arrangement of structural units changes around the critical angle of 32.20°, where the $(13\bar{4}0)$ GB at 32.20° is considered a singular GB. The zigzag arrangements are achieved because of the octagons inclined at ±30° to the GB plane above 32.20°, exhibiting the same core structure as the $\Sigma7\,(12\bar{3}0)$ GB at 21.79° [2].

References

[1] M. Saito, H. Li, K. Inoue, H. Matsuhata, Y. Ikuhara: Acta Mater. **221**, 117360 (2021).

[2] K. Inoue, J.Y. Roh, K. Kawahara, M. Saito, M. Kotani, Y. Ikuhara: Acta Mater. **212**, 116864 (2021).

Structure and Property of Basalt Melt and Glass

Toshiaki IITAKA
RIKEN Center for Computational Science,
2-1 Hirosawa, Wako, Saitama, 351-0198 JAPAN

Knowledge of the macroscopic physical properties of silicate melt (magma) under high temperature and high pressure is extremely important for understanding the phenomena of terrestrial planets such as the formation of the early Earth, the transport of volatile elements, and volcanic eruptions.

We study the influence of the microscopic structures (structural factors, radial distribution function, coordination number, network topology, etc.) of basalt melts and basalt glasses, which are related to the history of earth formation, on their macroscopic physical properties (density, diffusivity, viscosity, thermal conductivity, etc.), paying particular attention to the medium-range structure, trace elements, and entropy effect (temperature effect).

Transport properties like diffusivity and viscosity of melts dictated the evolution of the Earth's early magma oceans. We reported the structure, density, diffusivity, electrical conductivity and viscosity of a model basaltic ($Ca_{11}Mg_7Al_8Si_{22}O_{74}$) melt from first-principles molecular dynamics calculations at temperatures of 2200 K (0 to 82 GPa) and 3000 K (40–70 GPa). A key finding is that, although the density and coordination numbers around Si and Al increase with pressure, the Si–O and Al–O bonds become more ionic and weaker. The temporal atomic interactions at high pressure are fluxional and fragile, making the atoms more mobile and reversing the trend in transport properties at pressures near 50 GPa. The reversed melt viscosity under lower mantle conditions allows new constraints on the timescales of the early Earth's magma oceans and also provides the first tantalizing explanation for the horizontal deflections of superplumes at ~1000 km below the Earth's surface [1, 2].

References

[1] A. Majumdar *et al.*, Nature Communications **11**, 4815 (2020). http://dx.doi.org/10.1038/s41467-020-18660-w

[2] S. Q. Feng *et al.*, Phys. Chem. Miner. **48**, 41 (2021). http://dx.doi.org/10.1007/s00269-021-01165-3

First principles calculations of two-dimensional ordering process at organic/inorganic materials interface

Tomoya Shiota,[1] Yuuichi Orimoto,[2] Yuriko Aoki[2]

[1]Department of Molecular and Material Sciences, Interdisciplinary Graduate School of Engineering Sciences, Kyushu University, Fukuoka 816-8580, Japan.

[2]Department of Material Sciences, Faculty of Engineering Sciences, Kyushu University, Fukuoka 816-8580, Japan

We have studied dynamic processes at the interface between the organic and inorganic semiconductor materials by means of the first-principles calculations and the kinetic Monte Carlo simulations. All the first-principles calculations were conducted within the density functional theory (DFT) via the Vienna ab initio simulation package (VASP), version 5.4.4 in the ISSP's massively parallel supercomputer system.

In this project, a system of 3,4,9,10 - perylene tetracarboxylic dianhydride (PTCDA) molecules adsorbed on a Ge(001) surface was employed as a prototype of the organic-inorganic semiconductor interface. Previously, we found that a solely adsorbed PTCDA molecule is not mobile at 500K but is mobile at 700K. Furthermore, it was found that the PTCDA molecules diffuse concertedly with the dynamics of Ge(001) surface, involving the flip-flop motion of the Ge buckled dimers. [1]

First, we explored the diffusion process of PTCDA molecules under the intermolecular interactions. As a result, it was found that the diffusion mechanism of PTCDA molecules under the intermolecular interactions is similar to that of the lone adsorbed molecule, and the PTCDA molecules were found to be mobile even under the intermolecular interactions at 500K. The kinetic Monte Carlo simulation at 500K using the energy barriers obtained by the DFT calculations generally reproduced the experimental observation.

Toward a more accurate simulation, we investigated the flip-flop motions of surface buckled dimers both for the clean Si and Ge(001) as elementary processes because their flip-flop motions are well known for their dynamic properties on both surfaces. It was found that the flip-flop motion is not a simple seesaw motion but a two-step motion. In addition, by considering the flip-flop motion, the diffusion barriers of a PTCDA molecule on Ge(001) were reduced by about 20%.

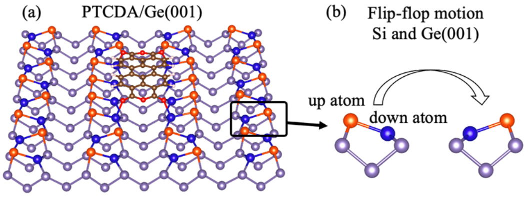

Fig. 1. (a) Adsorption of PTCDA on Ge(001) surface. (b) The flip-flop motion of the Si and Ge(001) surfaces.

References

[1] T. Shiota, W. Mizukami, H. Tochihara, K. Yagyu, T. Suzuki, and Y. Aoki, J. Phys. Chem. C **124**, 24704 (2020)

RSDFT calculation of atomic displacement captured by energy dissipation channel of noncontact atomic force microscope

Toyoko ARAI[1], Takahiro Kato[1], Jun-Ichi Iwata[2], Atsushi Oshiyama[3]

[1]*Graduate school of Natural Science and Technology, Kanazawa University, Kanazawa, Ishikawa, 920-1192*

[2] *Institute of Innovative Research, Tokyo Institute of Technology, Tokyo 152-8550*

[3]*IMaSS, Nagoya University, Nagoya, Aichi 464-8601*

In the last two decades the conservative and non-conservative (dissipative) force interactions between a tip and a sample in proximity have been intensively examined by non-contact atomic force microscopy (nc-AFM). In particular, the channel of nc-AFM to measure the energy dissipation through the non-conservative force interactions has been regarded to have great potential to explore nano-mechanical phenomena; the dissipation channel gives the change in the amount of mechanical energy to maintain the constant oscillation amplitude of an AFM cantilever. We had experimentally found that, when the nc-AFM image showed the high resolution for the individual adatoms on a Si(111)-(7×7) surface, the simultaneously obtained energy dissipation signal increased in close proximity over the hollow sites surrounded by a Si adatom and a Si rest atom with a dangling bond per each [1]. Based on the experimental results, the dynamic atomic processes responsible for the dissipation had been discussed in regard to breaking of the backbonds of the Si adatom and subsequent bond formation in an alternative atomic configuration of the Si surface atoms, including the Si atom at the apex of AFM tip as shown in Fig. 1. In this study, to explicate the mechanism of the phenomena, the forces between Si tip and Si(111)-(7×7) surface were calculated using real-space density functional theory (RSDFT) [2]. RSDFT is a first-principles program developed by Oshiyama and Iwata, which uses a real-space difference method and a pseudopotential method.

First, we optimized the structure of a Si(111)-(7×7) reconstructed surface consisting of 298 Si atoms, the back surface of which was terminated with 49 H atoms, and the structure of a [001]-oriented Si tip by RSDFT; the tip consisted of 30 Si atoms having a Si dimer at the tip apex, the back side of which was terminated with 18 H atoms, named “dimer tip” [3]. Next, we calculated the structure changes and the forces acting between the tip and the Si surface during tip approaching and retracting over the hollow

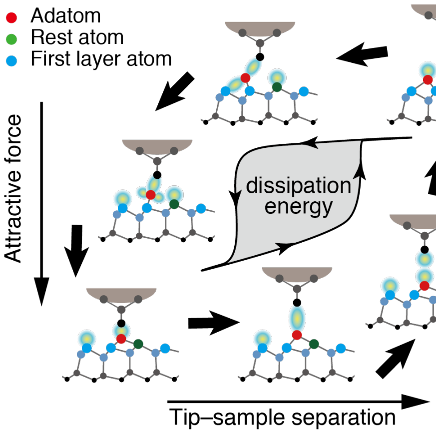

Fig. 1 Model of backbond breaking and formation during a tip approach and retraction cycle with a hysteresis loop in the force-distance curve, which is estimated from experimental results.

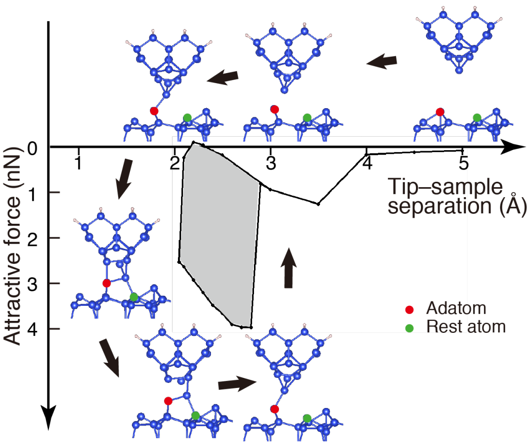

Fig. 2 Force–distance (separation) curve with the optimized structures of the Si tip and Si(111)-(7×7) surface, calculated by RSDFT.

site at the separations between the tip apex atom and the Si adatom on the surface from 5.0 to 2.0 Å, as shown in Fig. 2. On the approaching at 3.5 Å, one of the three backbonds of the adatom was broken, and the adatom was pulled toward the tip. At 2.2 Å, the force between the tip and the surface turned to repulsive. At 2.05 Å, the tip apex atom bonded with the rest atom under a strong attractive force. Starting from the structure of the tip and the Si surface, we calculate the optimized structure by retracting the tip by 0.1 Å step, which was the separation between the H-terminated Si planes of the tip and the Si surface. Up to the separation of 2.8 Å, the attractive force became stronger, and at 2.9 Å the structure and the force almost reverted to those at 2.9 Å on the approaching. When being further retracted, the structure and the force were the same as those on approaching. The force-distance curves with hysteresis loop were obtained by RSDFT calculations. The greyed area surrounded the curves in Fig. 2, corresponding to the nonconservative dissipation energy, was about 1.6 eV. This value was larger than the value of about 0.4 eV that was experimentally measured in ref. 1. This means that the initial structure of the tip should be reconsidered to clarify the mechanism for the dissipation energy of the tip–sample system.

References

[1] T. Arai, R. Inamura, D. Kura, and M. Tomitori, Phys. Rev. B **97**, 115428 (2018).

[2] J.-I. Iwata, D. Takahashi, A. Oshiyama, T. Boku, K. Shiraishi, S. Okada, and K. Yabana, J. Comput. Phys. **229**, 2339 (2010).

[3] P. Pou, S. A. Ghasemi, P. Jelinek, T. Lenosky, S. Goedecker and R. Perezet, Nanotechnology **20**, 264015 (2009).

Elucidation of Photocatalytic Reaction Mechanism by Ab Initio Calculations

Tatsuya JOUTSUKA
Institute of Quantum Beam Science, Graduate School of Science and Engineering, Ibaraki University, Hitachi, 316-8511 Ibaraki, Japan
Frontier Research Center for Applied Atomic Sciences, Ibaraki University, 162-1 Shirakata, Tokai, Ibaraki 319-1106, Japan.

We have studied the reaction mechanism of photocatalytic oxidation in TiO_2 [1] using cp2k program package (MPI parallelization with multiple threads). We focused on the energetics and dynamics during the polaron migration. This is a collaborative work with the Prof. Satoshi Yamauchi at Ibaraki University, who conducted the LPCVD experiment.

This experimental and theoretical study clarifies the facet dependence of the photocatalytic reaction at the anatase TiO_2 surface. The <112>-oriented anatase TiO_2 layer is deposited on the Ru(0001) substrate at 360°C by low-pressure chemical vapor deposition. The deposition rate is three times higher than that of the multi-orientation layer on the Pylex glass. The density functional theory (DFT) calculations using the constrained DFT method [2-3] and the hybrid functionals show that the (112) surface stabilizes the adsorbed water molecule most strongly.

We are extending this study to analyze the dynamical properties by the constrained DFT[1-3] and the dynamical reaction path analysis, [4] and compute the band structure in titania and the other photocatalysts.

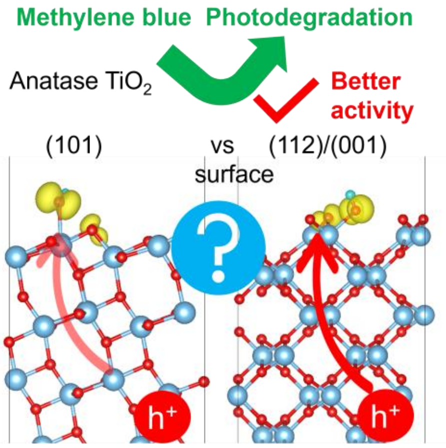

Fig. 1: Molecular mechanism of hole migration.

References

[1] T. Joutsuka, H. Yoshinari, and S. Yamauchi: Bull. Chem. Soc. Jpn., **94** (2021) 106–111. (Selected Paper, Inside Cover, Open Access).

[2] T. Joutsuka and K. Ando: J. Phys. Chem. B, **124** (2020) 8323–8330.

[3] T. Joutsuka and K. Ando: Chem. Lett., **50** (2021) 1325–1328.

[4] T. Joutsuka and K. Ando: J. Phys. Chem. A, **115** (2011) 678–684.

Theoretical Analysis of Metal Film Growth Mechanism in Chemical Vapor Deposition

Tatsuya JOUTSUKA
Institute of Quantum Beam Science, Graduate School of Science and Engineering, Ibaraki University, Hitachi, 316-8511 Ibaraki, Japan
Frontier Research Center for Applied Atomic Sciences, Ibaraki University, 162-1 Shirakata, Tokai, Ibaraki 319-1106, Japan.

We have studied low-pressure chemical vapor deposition of Cu on Ru substrate using CuI using cp2k and VASP program packages (MPI parallelization with multiple threads). In this year, we also studied the mechanism of Cu nanoparticles by reducing spinel type oxides. This is a collaborative work with the experimentalists [1-3] (Prof. Satoshi Yamauchi and Assistant Prof. Shohei Tada at Ibaraki University), who conducted the experiment.

In this study, we elucidated the molecular mechanism of Cu deposition using copper(I) iodide (CuI) on Ru substrate by low-pressure chemical vapor deposition through density functional theory (DFT) molecular dynamics (MD) simulations by cp2k. In addition, the charge and chemical environment around Cu atoms in spinel type oxide Cu-doped $MgAl_2O_4$. Figure 1 shows the proposed formation mechanism of Cu nanoparticles after reducing inverse spinel-type Cu-doped $MgAl_2O_4$.

Based on this study, we are developing the computational method to compute the surface acidity on solid oxides, [4-5] and improving the catalytic performance by chemically modifying the catalytic reaction field.

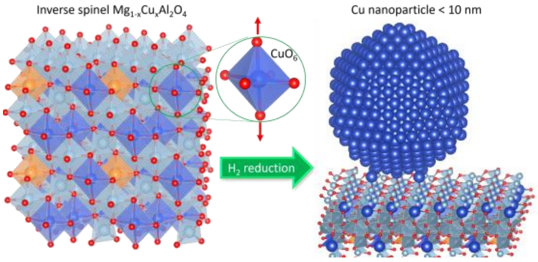

Fig. 1: Formation mechanism of Cu nanoparticles by H_2 reduction of inverse spinel type Cu-doped $MgAl_2O_4$.

References

[1] T. Joutsuka, S. Yamauchi: Chem. Phys. Lett. **741** (2020) 137108.

[2] T. Nishikawa, K. Horiuchi, T. Joutsuka and S. Yamauchi: J. Cryst. Growth, **549** (2020) 125849.

[3] T. Joutsuka, S. Tada, et al.: submitted.

[4] T. Joutsuka and K. Ando: Chem. Lett., **50** (2021) 1325–1328.

[5] T. Joutsuka: submitted (DOI: 10.26434/chemrxiv-2022-9t6vf).

Prediction of properties of organic ferroelectrics and piezoelectrics by first-principles calculation

Shoji ISHIBASHI
Research Center for Computational Design of Advanced Functional Materials (CD-FMat),
National Institute of Advanced Industrial Science and Technology (AIST)
Tsukuba, Ibaraki 305-8568

Among hydrogen-bonded systems consisting of small organic molecules, some shows ferroelectricity or antiferroelectricity [1]. They contain neither toxic nor rare elements and are expected as environmentally friendly materials. Spontaneous polarization, which is one of the most important properties for the ferroelectrics, can be predicted by electronic-structure calculations together with the Berry phase theory. We calculated polarization values for seven representative hydrogen-bonded ferroelectrics (croconic acid (CRCA), 2-phenylmalondialdehyde (PhMDA), 3-hydroxyphenalenone (HPLN), cyclobutene-1,2-dicarboxylic acid (CBDC), 2-methylbenzimidazole (MBI), 5,6-dichloro-2-methylbenzimidazole (DC-MBI), and 3-anilinoacrolein anil (ALAA)) and the obtained results are in excellent agreement with the experimental results [2]. These calculations were performed using experimentally obtained crystal structures with only hydrogen positions computationally optimized. It is well known that hydrogen positions are difficult to accurately determine by x-ray diffraction analysis. Accurate experimental structure data are not always available. In such cases, computational optimizations for all of the crystal structure parameters are necessary. Nonetheless, the van der Waals interaction, which is often crucial in organic solids, cannot be accurately described by the local density approximation (LDA) or the generalized gradient approximation (GGA). In the present study, we apply van der Waals density-functional theory (vdW-DFT) calculations to reproduce crystal structure parameters of the seven compounds mentioned above. For the vdW-DFT method, we used two forms: the van der Waals density-functional consistent-exchange (cx) method [3] and the revised Vydrov–van Voorhis (rVV10) method [4]. Calculations were performed using the QMAS code.

Figure 1 shows the deviations of the calculated structure parameters (lattice parameters a, b, and c, and hydrogen-bond length d, namely, the O···O or N···N distance) (a) from room-temperature experimental results and (b) from 0-K extrapolated values, as well as (c) their averages and bounds [5]. The calculated results obtained by the LDA and the PBE version of the GGA are also shown. The experimental structures are at room temperature, whereas the calculation results correspond to 0 K. Unfortunately, only a limited number of low-temperature structures have been reported and the 0-K values were extrapolated using them to prepare Fig. 1 (b). The vdW-DFT results show good agreement with experimental results, implying that an important step for the computational materials design of organic ferroelectrics has been achieved. Spontaneous polarization values obtained by the vdW-DFT calculations are again in good agreement with the experimental results. The success in reproducing the structure parame-

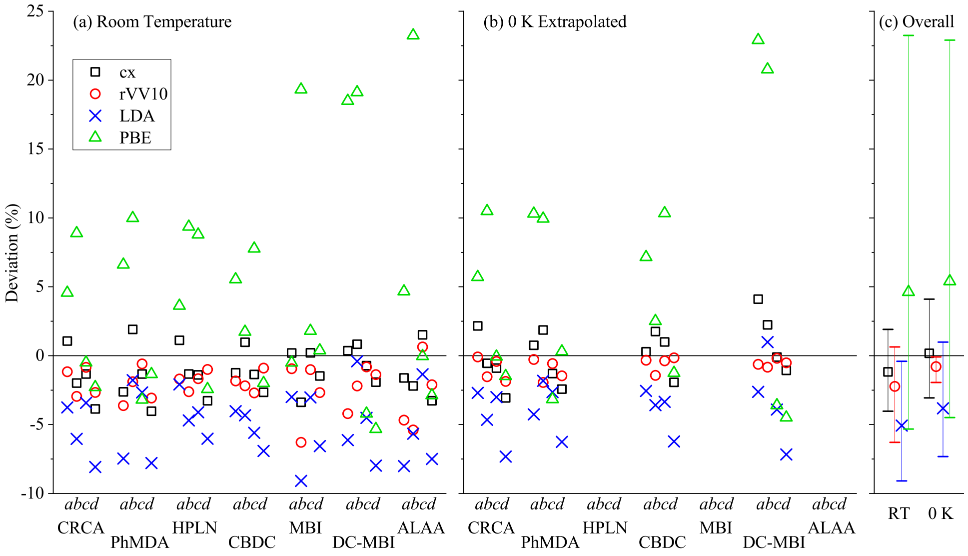

Figure 1: Deviations of calculated structure parameters (a) from room-temperature experimental results and (b) from 0-K extrapolated values, as well as (c) their averages and bounds (S. Ishibashi, S. Horiuchi, and R. Kumai, "Hydrogen-bonded single-component organic ferroelectrics revisited by van der Waals density-functional theory calculations", Phys. Rev. Mater. **5**, 094409 (2021), DOI: 10.1103/PhysRevMaterials.5.094409).

ters also enables the simulation of electromechanical responses. Direct and converse piezoelectric coefficients are evaluated for CRCA, PhMDA and DC-MBI and the resultant values show acceptable agreement with the experimental values if possible objective factors are considered [5].

Organic antiferroelectrics also are promising. For example, their applications as high-power electrical energy storage materials are expected utilizing electric-field-induced phase changes. Usually, they consist of two or more polar subunits. For squaric acid (SQA), we have demonstrated that the polarization of the electric-field-induced phase can be estimated by proper summation of the subunit polarization vectors [6]. By applying this procedure, we have successfully predicted polarization values for the electric-field-induce phases of several organic antiferroelectrics and the obtained results are in excellent agreement with experimental results [7].

References

[1] S. Horiuchi and S. Ishibashi, J. Phys. Soc. Jpn. **89**, 051009 (2020).

[2] S. Horiuchi, K. Kobayashi, R. Kumai, and S. Ishibashi, Nat. Commun. **8**, 14426 (2017).

[3] K. Berland and P. Hyldgaard, Phys. Rev. B **89**, 035412 (2014).

[4] O. A. Vydrov and T. Van Voorhis, J. Chem. Phys. **133**, 244103 (2010); R. Sabatini, T. Gorni, and S. de Gironcoli, Phys. Rev. B **87**, 041108(R) (2013).

[5] S. Ishibashi, S. Horiuchi, and R. Kumai, Phys. Rev. Mater. **5**, 094409 (2021).

[6] S. Horiuchi, R. Kumai, and S. Ishibashi, Chem. Sci. **9**, 425 (2018).

[7] S. Horiuchi and S. Ishibashi, Chem. Sci. **12**, 14198 (2021).

Global search for the stable structures of two-dimensional materials based on Gaussian process regression

Yuji HAMAMOTO

Department of Precision Engineering, Graduate School of Engineering,
Osaka University, Yamada-oka, Suita, Osaka 565-0871

Silicene, a silicon analog of graphene has drawn a great deal of attention not only as a promising candidate for topological insulators from a scientific point of view, but also as an atomically thin semiconductor material from an application point of view. On the Ag(111) surface, however, the sp^3-like buckling nature of its honeycomb lattice leads to the emergence of a varieties of phases characterized by different patterns of buckling structures as compared with the freestanding structure predicted theoretically [1], hindering the elucidation of the whole picture of the electronic and structural properties of silicene supported on solid surfaces.

First-principles calculation based on the density functional theory (DFT) is a powerful technique to predict stable structures of new materials, but its performance depends on the initial guesses, and the global search for stable structures is computationally demanding in most cases. To tackle the difficulty in the global structure search by the DFT calculation, we adopt an efficient machine-learning technique named global optimization with first-principles energy expression (GOFEE) [2], which is based on Gaussian process regression and evolutionary algorithms. As an example, we here apply GOFEE to the global search for the stable structures of silicene supported on the Ag(111) surface. Our results reveal that GOFEE not only reproduces successfully the stable structures identified so far, but also predicts the existence of a variety of metastable structures which are too subtle to determine experimentally.

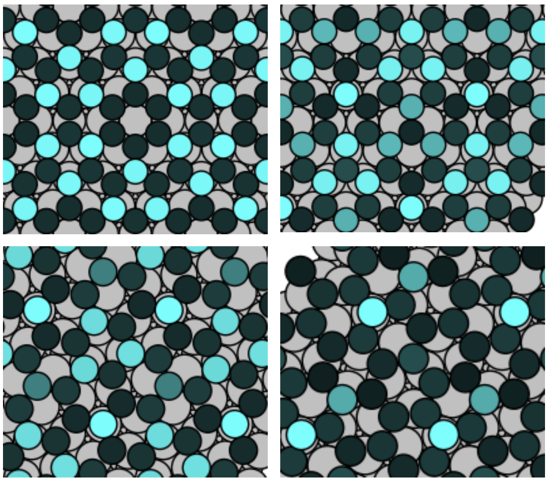

Figure: Obtained structures corresponding to the 4×4-α and β (top left and right) and the √13×√13-α and β (bottom left and right) phases of silicene on the Ag(111) surface.

References

[1] K. Takeda and K. Shiraishi, Phys. Rev. B **50**, 14916 (1994).

[2] M. K. Bisbo and B. Hammer, Phys. Rev. Lett. **124**, 086102 (2020).

First-principles study on the origin of phase stability of Mg–Zn–Y alloys with long-period stacking order

Takao TSUMURAYA
POIE, Kumamoto University, Kumamoto 860-8555, Japan
Magnesium Research Center, Kumamoto University, Kumamoto 860-8555, Japan

The design of alloys based on magnesium (Mg) has attracted much attention since Mg is the lightest substance element for structural metals. A dilute Mg alloy containing one at.% of Zn and two at.% of Y showed high-strength properties with a tensile yield strength of ∼600 MPa [1]. This strength is coupled with the appearance of a unique crystal structure called long-period stacking order (LPSO). In the LPSO-based Mg alloy, solute atoms of Zn and Y are enriched in a few layers of the (0001) plane of the hexagonal close-packed (HCP) Mg matrix [2]. Shockley partial dislocation (stacking faults) occurs in the solute atoms enriched layer, which orders periodically along the [001] direction of the hexagonal lattice. Furthermore, structural analysis using scanning transmission electron microscopy (STEM) revealed that $L1_2$-type clusters of solute elements (Zn and Y) are embedded in the Mg matrix near the stacking fault [3].

In this study, the electronic origin of the phase stability of Mg–Zn–Y based alloys with LPSO is studied based on first-principles density-functional theory (DFT) calculations. In particular, we aim to understand the role of the Zn atom in $18R$–$Mg_{58}Zn_7Y_8$ alloy, and the possible realization of Zn vacancy formation is studied using a convex hull energy diagram. The heat of formation as a function of the number of Zn vacancies is calculated, and we show how the electronic structure near the Fermi level affects structural stability. In the present DFT calculations used a pseudopotential technique with plane-wave basis sets adopting the projected augmented-wave method implemented in Quantum ESPRESSO. The exchange-correlation functional is the generalized gradient approximation proposed by Perdew, Burke, and Ernzerhof.

For calculating the heat of formation, the number of Zn atoms in $Mg_{58}Zn_7Y_8$ is deduced using the fixed number of Mg and Y atoms to understand whether the Mg-Zn-Y alloy includes Zn vacancies that can be formed from the elemental metals of Mg, Zn, and Y. The obtained scatter plot of the heat of formation as a function of the Zn composition ratio indicates that all phases, including Zn vacancies, are thermodynamically unstable and decomposed into $Mg_{58}Zn_7Y_8$ ($x = 0$) and elemental metals of 58Mg+8Y phases. Nevertheless, the hull distance decreases as vacancies (x) decrease. Therefore, we consider the state in which Zn_7Y_8 clusters with an $L1_2$ structure are already formed and plot the convex hull diagram. Zn vacancies with $x = 1$ and 3 are on the convex hull. These states should be observed below the decomposition temperature. Therefore, we conclude that the Zn atoms in the LPSO alloy are stable even if they are about half of the number of Y atoms.

In general, the density of states (DOS) for HCP metal is characterized by a deep valley or dip near the Fermi level (E_F), where E_F is at the lowest position of the valley. The depth of the valleys in the DOS represents the magnitude of splitting the prominent peaks of the

DOS between those in occupied and unoccupied states. The width of the valley or dip appears as a difference in the enthalpy of formation (or cohesive energy) between different metals [4, 5]. By focusing on the partial DOS of Zn and its neighboring Mg, we find that the formation of the bonding state between Zn and the surrounding Mg atoms has a crucial role in stabilizing the LPSO structure.

References

[1] Y. Kawamura, K. Hayashi, A. Inoue, and T. Masumoto, Mater. Trans. **42** 1172 (2001).

[2] E. Abe, Y. Kawamura, K. Hayashi, and A. Inoue, Acta Metall. **50** 3845 (2002).

[3] D. Egusa and E. Abe: Acta Mater. **60** 166 (2012).

[4] S. Inoue and J. Yamashita: J. Phys. Soc. Jpn **35** 677 (1973).

[5] T. Tsumuraya, I. Watanabe, and T. Sawaguchi: Phys. Rev. Research **3** 033215 (2021).

Metastability of 2D and 3D binary ordered alloys

Shota ONO
Department of Electrical, Electronic and Computer Engineering, Gifu University
Gifu 501-1193

It is well-known that the fcc (hcp) metals in the hcp (fcc) structure are dynamically stable, while the fcc (bcc) metals in the bcc (fcc) structure are unstable [1]. To understand the metastability relationship between different crystal structures, we calculated phonon dispersions for 2D and 3D systems using density-functional perturbation theory implemented in Quantum ESPRESSO [2]. The calculations were done using system B and C.

In our previous work, we showed that if the elementals metals in the 2D hexagonal structure is dynamically stable, then the fcc and hcp strcutures are also dynamically stable, showing that 2D structures serve as building blocks for constructing the 3D structures [3]. In the present work, we extend this investigation to binary ordered alloys of CuX with X being 46 metallic elements [4, 5]. We showed that if the CuX in the AB layer structure is dynamically stable, then that in the AB and ABC stacking structures is also dynamically stable (see Fig. 1 for the crystal structures). In addition, we calculated phonon dispersions for the CuX, AgX, and AuX in the AB layer structure, and found that 48 out of 135 ordered alloys are dynamically stable, predicting that those alloys in the AB and ABC stacking structures are also dynamically stable [5]. The present work has shed light on the 2D structures as a building block for computational material design.

We also predicted potential substrates that allow immiscible metals (Pb and Sn) to form the surface alloys by using density-functional theory [6]. The prediction of their surface geometry is left for future work.

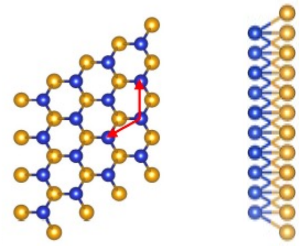

AB layer (buckled honeycomb)

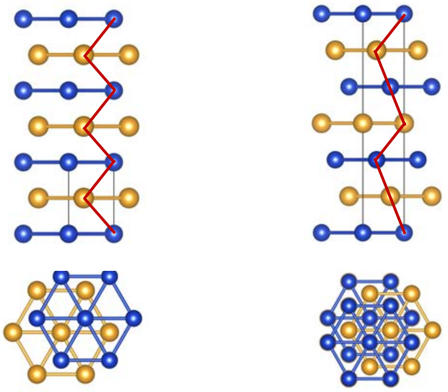

AB stacking (B_h) ABC stacking ($L1_1$)

Figure 1: Schematic illustration of 2D and 3D strcutures.

References

[1] G. Grimvall *et al.*, Rev. Mod. Phys. **84** (2012) 945.
[2] P. Giannozzi *et al.*, J. Phys.: Condens. Matter **29** (2017) 465901.
[3] S. Ono: Phys. Rev. B **102** (2020) 165424.
[4] S. Ono: Sci. Rep. **11** (2021) 14588.
[5] S. Ono: Phys. Rev. Materials **5** (2021) 104004.
[6] S. Ono, J. Yuhara, and J. Onoe: Chem. Phys. Lett. **776** (2021) 138696.

Ab Initio Molecular Dynamics Study on Static Structure of Glass Materials

Akihide KOURA

Technical division,

Kumamoto University, Kurokami, Chuo-ku, Kumamot,o 860-8555

We have studied a condensed matter system which are crystal, liquids, and amorphous. In this project, we focused on the static structure of amorphous V_2O_5 state. The *ab initio* molecular dynamics (AIMD) simulations were performed with our original QXMD code [1].

In order to investigate the static structure of amorphous V_2O_5, we employed the machine learning method using artificial neural network (ANN) to construct the interatomic potential [2]. The Aenet package [2] was used for training based on the AIMD simulations of liquid and amorphous V_2O_5. Figure 1 shows the root mean square errors (RMSE) and partial radial distribution functions $g_{\alpha\beta}(r)$ $(\alpha, \beta \in \mathrm{V}, \mathrm{O})$ of liquid V_2O_5. According to our previous study [3], considering not only energy but also atomic force and virial tensor improves ANN potential better. Based on the learning condition, our MD simulation using the ANN potential basically represent the FPMD simulations except for the unreasonable peak of $g_{\mathrm{OO}}(r)$ at approximately r = 0.4 Å. In the future work, we develop the training method by other technics, e.g., active learning from the result of MD simulations with ANN potential for liquid systems.

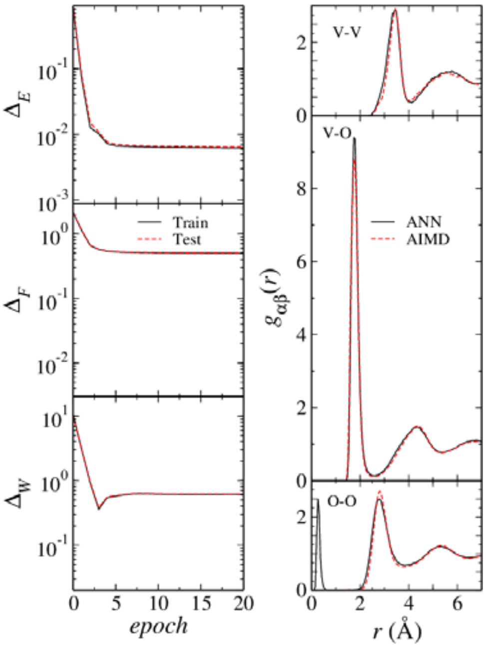

Fig. 1: (Left) Root mean square errors and (right) partial radial distribution functions.

References

[1] F. Shimojo, S. Fukushima, H. Kumazoe, M. Misawa, S. Ohmura, P. Rajak, K. Shimamura, L. Bassman, S. Tiwari, R. K. Kalia, A. Nakano, and P. Vashishta: SoftwareX **10** (2019).

[2] N. Artrith and A. Urban: Comput. Mater. Sci. **114** (2016) 135.

[3] A. irie, S. Fukushima, A. Koura, K. Shimamura, and F. Shimojo, J. Phys. Soc. Jpn. **90**, 094603 (2021).

Atomistic simulations for excited materials by strong laser

Yasushi Shinohara[1,2], Mizuki Tani[3]
[1]*Photon Science Center,*
The University of Tokyo, Hongo, Bunkyo-ku, Tokyo 113-8656.
[2]*NTT Basic Research Laboratories,*
NTT Corporation, 3-1 Morinosato Wakamiya, Atsugi, Kanagawa 243-0198.
[3]*Department of Nuclear Engineering and Management*
The University of Tokyo, Hongo, Bunkyo-ku, Tokyo 113-8656.

We have performed investigations that describe nonequilibrium electron-ion dynamics realized by strong laser fields irradiation. Complex pathways accompany these dynamics along different phases depending on time and positions. These multi-physical and nonequilibrium characteristics prohibit direct measurements for the intermediate processes of the dynamics. Our investigation is aimed to understand what processes could happen in the laser-excited materials, including insulators and metals, via theoretical simulations.

We have accumulated simulated electronic structure data just after ultrashort laser pulse by using SALMON code [1] based on time-dependent density-functional theory [2]. This data is the key quantity of the laser-excited dynamics' initial process, which triggers whole subsequent processes. We reported Rabi-type absorption oscillation in bulk Al with resonant excitation by increasing the intensity of the electric field [3]. By analyzing the occupation evolution as a function of the intensity, the electron occupation shows symptom of multiple Rabi-flopping to higher energy bands for bulk Al.

We have developed a semiclassical theoretical framework for electron-ion coupled dynamics under a strong laser field [3]. Free-electronic behavior of metal is accurately reproduced with more than 50-times lighter computational cost than TDDFT. The lightweight cost allows us to simulate spatially larger systems, including non-uniform structures, such as surfaces or impurity, and electron-ion coupled dynamics for the laser-excited material response.

References

[1] Erich Runge and E. K. U. Gross, Phys. Rev. Lett. **52** (1984) 997.

[2] M. Noda, et al., Comp. Phys. Comm. **235** (2018) 356.

[3] Mizuki Tani, Tomohito Otobe, Yasushi Shinohara, and Kenichi L. Ishikawa, Phys. Rev. B **104** (2021) 075157.

Study on structural elementary excitations at semiconductor surfaces and interfaces

Hiroyuki KAGESHIMA
Graduate School of Natural Science and Technology, Shimane University
1060 Nishi-Kawatsucho, Matsue, Shimane 690-8504

In this project, we have been focused on physical properties of structural elementary excitations of semiconductor surfaces and interfaces. In this year, we have focused on the physical properties of defects in SiO_2. The calculations were performed based on the first-principles calculation. Program package PHASE/0 was employed. [1]

Defects in SiO_2 have been widely studied because they are the source of device performance degradation for MOS field-effect transistors (MOSFETs), which is widely used for the integrated circuits. The gate insulator of MOSFET is made of silicon oxide SiO_2. Those studies revealed that O vacancies, one of typical defects, can trap charges, assist gate leak current, and also lead to the formation of eternal gate leakage paths. They also revealed the role of post oxidation annealing. However, recent progress of integrated circuit technology have forced the MOSFET device structure from planar to three dimensional. If we consider the vertical body-channel-MOSFET with silicon oxide gate insulator, the oxide can be strained because of the device formation process. The interface oxide might be compressed and the surface oxide be expanded due to the thermal oxidation of silicon for the gate formation process. The compressive and expanded strain are expected as much as 3% in the worst case. Such strain should affect on the physical properties of defects in silicon oxide gate insulator

Therefore, we first focused on the O vacancy and studied strain dependence of its formation energy and diffusion barrier. Based on these results, in this year, we have studied stability of various defects including the O vacancy, the charging effects on them, and their strain dependences. Some of the vacancies we have studies are fully terminated by H atom or OH group, and other are partially terminated. We modeled the host SiO_2 by alpha-quartz crystal with supercell containing 24 Si and 48 O atoms.

First, we have found a novel O vacancy defect which has only two -OSi bonds. This defect is unique because the widely known O vacancy defect has three -OSi bonds. This new O vacancy defect is stable because it accompanies a three-Si-member ring within the model, while ordinary alpha-quartz just contains only six-Si-member rings. Next, we have found that a dangling bond of Si can surely assist the gate leakage current because they show charging levels in the middle of band gap. Then, we have found that the compressive strain makes it easier to release the terminators H or OH, while it does not significally change the charging level positions. From these results, we have confirmed that strain in the gate insulator silicon oxide surely enhances the device performance degradation. Careful device formation process must be necessary.

References

[1] https://azuma.nims.go.jp

Ab-initio molecular-dynamics calculations for molecule-modified nanointerfaces

Kenji TSURUTA, Masaaki MISAWA, Narumi MACHIDA,

Kyosuke SATO, and Satoshi OHMURA[a]

Graduate School of Natural Science and Technology, Okayama University, Okayama 700-8530
[a] Department of Civil and Environmental Engineering, Hiroshima Institute of Technology, Hiroshima 731-5193

Surfaces and/or interfaces of oxide materials are often modified by other molecules in order not only to stabilize their structure against deterioration but also to control surface morphology. Calcium carbonate ($CaCO_3$), which is widely used as filler in resins, plastics, and rubber materials to improve their physical, mechanical, and thermal properties, is a typical example of such phenomena. To control particle morphology and to improve affinity with base materials, calcium carbonate is often surface-treated with organic compounds. This activated calcium carbonates (ACCs) not only exhibit excellent application properties, but also can be applied as eco-friendly inorganic-organic hybrid materials. It has been reported [1] that surface deposits with ~5 nm thickness exist on the (104) surface of calcite covered with stearic acid (SA). Since this thickness corresponds to about twice the length of a SA molecule, it is suggested that SA bilayers may be formed on the calcite (104) surface, but the detailed adsorption state has not been clarified to date.

In this study, we performed first-principles calculations based on density functional theory using the Vienna Ab initio Simulation Package (VASP). We created a simulation model for three types of SA-SA and two types of calcite-SA interfaces as shown schematically in Fig. 1 A-E. First-principles molecular dynamics (FPMD) simulations with canonical ensembles at room temperature were performed for these models, and the presence or absence of adsorption was verified by observing changes in the interface structure in each model. We also verified the stability of the interface structures by analyzing the energetic properties in the relaxed system.

According to the results of the FPMD simulations, we considered that the interface structure in the A, B, and E models are intrinsically unstable because the interatomic distance of the bonding part in each model gradually increased at room temperature . On the other hand, such behavior has not been observed in the C and D models. Comparing of the potential energy of the C model with that of two isolated SA molecule, it was found that the energy of the C model was 0.4 eV lower. This result indicates that the C model is energetically favorable and stable interface structure may be formed with an adsorption with C model. From these results, it is considered that despite the first SA layer is favorable with D model, some molecules on the first layer may be inverted (or "alternately aligned") in order to adsorb the second layer with C model in the SA bilayer on calcite (104) surface[2]. Further computation with larger system size is necessary to validate this hypothesis. Development of an effective interatomic potential based on a Deep-Learning (DL)-based molecular design methods [3] is in progress for simulations of the bilayer system.

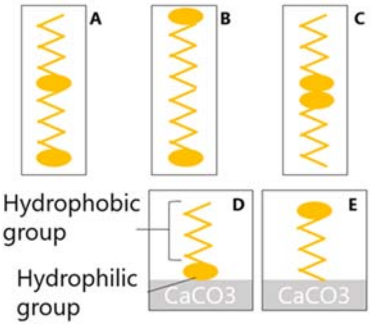

Fig. 1 Schematic illustration of the simulation models for SA-SA (A-C) and calcite-SA (D, E) interfaces.

References

[1] M. Ricci *et al.*, Langmuir **31**, 7563 (2015).
[2] N. Machida, M. Misawa, Y. Kezuka, and K. Tsuruta (to be published).
[3] K. Sato and K. Tsuruta, Mater. Sci. Forum **1016**, 1492 (2021).

First-principles Calculations of Magnetic Insulators Under Uniform Electric Fields

Naoya YAMAGUCHI
Nanomaterials Research Institute (NanoMaRi), Kanazawa University
Kakuma-machi, Kanazawa, Ishikawa 920-1192

This year, we tried to focus on electric field effects of magnetic insulators. We have developed a linear-combination-of-pseudo-atomic-orbital (LCPAO) scheme of a finite electric field method based on the modern theory of polarization [1] and implemented it to the OpenMX code [2], a first-principles calculation code based on the density functional theory (DFT). Through the scheme, one can consider electric field effects even for periodic systems such as bulk insulators. We improved our implemented code this year. The so-called egg box effect causes numerical errors due to the real space grid, especially in the LCPAO method, and it disturbs evaluation of the forces, dipole moment and stress tensor. It can be resolved by the grid cell sampling to repeat the evaluations for the shifted grid several times based on the frozen LCPAO density matrix, and we implemented the function in the previous year. We found that a solution was the "one-shot" grid cell sampling, that is, the forces under the fine grid were evaluated from the density matrix obtained from the rough grid without the grid shifts. We calculated electronic and static dielectric constants and Born effective charges of III-V and II-VI semiconductors and group IV insulating materials. The calculated values coincided with the reported computational values even in the GGA case that the density gradient is sensitive to the egg box effect, and they were an agreement with the experimental values. In addition, we also debugged the implemented code for the non-collinear spin density functionals applicable to materials that spin-orbit interaction (SOI) is important. We also found that the SOI has a non-negligible influence on the dielectric constants of cases including the heavy elements. For the magnetic insulator cases, we confirmed that the debugged code worked well for the antiferromagnetic NiO for different U parameters based on the DFT+U scheme through the comparison to the previous study. For some insulators with noncollinear spins, the self-consistent-field (SCF) calculations were difficult to get converges because the careful mixing during the SCF calculations were essential. Our implementation will become a powerful tool to expand subjects of researches on materials in investigating the electric field effects.

We also developed the new evaluation scheme for the anomalous Hall and Nernst conductivity without constructing the Wannier functions or explicit evaluation of the Kubo formula [3]. We reproduced the intrinsic contribution of the typical metals such as bcc iron. Our scheme has advantages of efficiency and stability: it is the non-iterative scheme unlike Wannierization and can avoid numerical instability such as the k-space Dirac monopole. The scheme is more appropriate for not only large scale cases but also high-throughput calculations than a Wannier function method.

References

[1] N. Yamaguchi and F. Ishii, https://doi.org/10.48550/arXiv.2203.10441.

[2] http://openmx-square.org.

[3] H. Sawahata, N. Yamaguchi, S. Minami and F. Ishii, https://doi.org/10.48550/arXiv.2204.05949.

Optical conductivity of $Ca_5Ir_3O_{12}$ by first-principles calculations

Shoya Kawano
Department of Electrical and Electronic Engineering, Kyushu Institute of Technology,
Kitakyushu, Fukuoka, 804-8550

We have studied the title compound $Ca_5Ir_3O_{12}$ which have attracted attention due to the its strong spin-orbital interaction (SOI) [1]. Such strong SOI is affected to the physical properties. This compound shows an antiferromagnetic ordering below 7.8 K, a second order phase transition at 105 K and non-linear conductivity along *c*-axis and so on. We performed synchrotron radiation-based infrared (SR-IR) spectroscopy to reveal the its electronic property for single crystal of $Ca_5Ir_3O_{12}$. From this measurement, we observed reflectivity and optical conductivity. Then, we investigated reflectivity and optical conductivity of $Ca_5Ir_3O_{12}$ by first-principles calculations to discuss about our experimental results.

We performed density functional calculations by using Quantum ESPRESSO code [2]. These results were used to calculate reflectivity and optical conductivity by using RESPACK code [3]. In Quantum ESPRESSO, we use the norm-conserving pseudo potentials generated by the code ONCVPSP (Optimized Norm Conserving Vanderbilt PSeudopotential), and are obtained them from the PseudoDojo [3]. The exchange-correlation function is used Perdew-Burke-Ernzerhof type. Γ-point-centered 5×5×13 and 10×10×25 k-points samplings is set to be compared.. We use the energy cutoff of 96 Ry for the wave function, a convergence criterion for the electronic self-consistency loop of 10^{-10} Ry, and the Gaussian smearing method with a smearing width of 0.002 Ry. We included the SOI effect. In RESPACK, the polarization function is calculated within random phase approximation. For this calculation, we set cutoff energy for polarization function of 6 Ry. Smearing value used in tetrahedron calculation is set to 0.01 eV. Lattice parameters of $Ca_5Ir_3O_{12}$ is referred to previous report [5].

Fig 1 shows band structure of $Ca_5Ir_3O_{12}$ from 5 × 5 × 13 and 10 × 10 × 25 k-point sampling. E = 0 is fermi level. Both results are consistent with previous report []. As shown previous report, this material is metal on this level of density functional calculation. This metallic trend is different from experimental observation which shows as semiconducting electrical properties. This is limitation of this level calculation. From this result, we use 5×5×13 k-point sampling for polarization function calculation because this calculation is time consuming.

Fig. 2 shows the calculated reflectivity of $Ca_5Ir_3O_{12}$ parallel to c-plane and c-axis. This shows reflectivity $R = 1.0$ at $\omega = 0$ because of metallic behavior in our results. The broad peak is shown around 5000 cm^{-1}.

Fig. 3 shows the calculated optical conductivity of $Ca_5Ir_3O_{12}$ parallel to c-plane and c-axis. These have two peaks at about 1000 cm^{-1} and about 5000 cm^{-1} for parallel to *c*-plane and *c*-axis. We considered that the peak of about 1000 cm-1 is shown due to the metallic behavior in the calculation. Experimental result has the peak at about 4000 cm^{-1}. This seems to be good agreement with our 5000 cm^{-1} peak. However, we note that the calculation and experiment have difference of metal or semiconductor.

We need to more discussion by using these results, and also improvement such as metallic behaviour in the calculation. Using ISSP Supercomputer, we achieved the first principles calculation of optical properties such as the compound $Ca_5Ir_3O_{12}$.

References

[1] K. Matsuhira et al. J. Phys. Soc. Jpn. **87**, (2018).

[2] https://www.quantum-espresso.org

[3] https://sites.google.com/view/kazuma7k6

[4] http://www.pseudo-dojo.org

[5] M. Charlebois et al. Phys. Rev. B **104**, 075153, (2021)

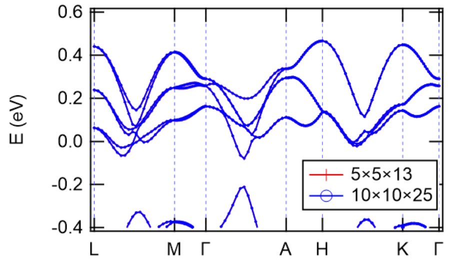

Fig. 1 Band structure of $Ca_5Ir_3O_{12}$ from different *k*-point sampling. $E = 0$ is fermi level.

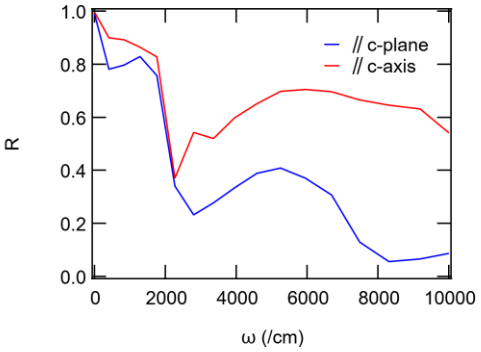

Fig. 2 Calculated reflectivity of $Ca_5Ir_3O_{12}$ parallel to *c*-plane and *c*-axis.

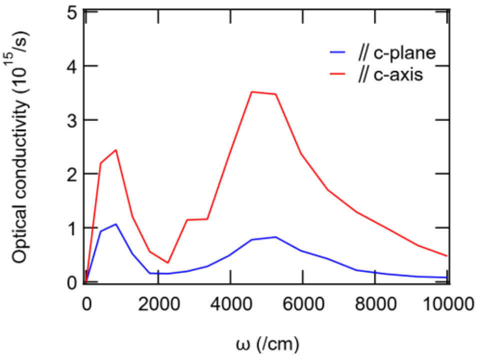

Fig. 3 Calculated optical conductivity of $Ca_5Ir_3O_{12}$ parallel to *c*-plane and *c*-axis.

Critical exponent of metal-insulator transition in doped semiconductors and spin ordering

Yosuke HARASHIMA
Center for Computational Sciences, University of Tsukuba
Tennodai, Tsukuba, Ibaraki 305-8577
Devision of Material Sciences, Nara Institute of Science and Technology
Takayama-cho, Ikoma, Nara 630-0192

Impurity doping have an important effect on the conduction properties of semiconductors. Evaluating electrical conductivity at a zero temperature, the material becomes an insulator at low impurity concentrations, a metal at high impurity concentrations, and a metal-insulator transition occurs at some concentration in between. This metal-insulator transition is known to occur in many materials regardless of semiconductor or impurity type and is a general and fundamental property of quantum transport.

Electrons in semiconductors are scattered by randomly aligned impurities and the phase shifts of wavefunctions are distributed randomly. When those waves overlap, they cancel each other out and a localized state appears. This is Anderson localization, and the metal-insulator transition mentioned above is considered to be the Anderson transition between the Anderson localized phase and the delocalized phase. Continuous transitions such as the Anderson transition can be classified according to the critical exponent. The critical exponent ν characterizes the divergence of the correlation length $\xi \propto |n - n_\mathrm{c}|^{-\nu}$ at the transition point (n and n_c are impurity concentrations and the critical concentration). It is universal and independent of the details of the system. The critical exponent represents the universality of the phase transition, therefore, deriving its exact value is an essential problem.

Two different values for this critical exponent have been reported from experiments, $\nu \approx 0.5$ and ≈ 1.0, but the origin of this discrepancy has not been clarified. This problem is called the exponent puzzle. To solve this exponent puzzle, the actual situation in the doped semiconductor needs to be simulated from first-principles.

In this study, we consider a system of randomly distributed P impurity donor ions in Si. For the analysis of its electronic structure, we used a program we implemented that self-consistently solves the Kohn-Sham equation based on density functional theory. Experiments suggest that the spin order changes near this metal-insulator transition point, and thus, the present calculations take into account the spin degrees of freedom.

We generated random impurity configurations. The impurity concentration is ranged from $\approx 0.8 \times 10^{18}\mathrm{cm}^{-3}$ to $\approx 2.1 \times 10^{18}\mathrm{cm}^{-3}$, and the system size is taken by 228.6, 285.8, 342.9, and 400.1 Å. The critical concentration has been predicted by convolutional neural network [1]. We sampled $\approx 180,000$ data in the vicinity of the predicted concentration, and solved the electronic state self-consistently.

References

[1] Y. Harashima, *et al.*: J. Phys. Soc. Jpn. **90** (2021) 094001.

Exploration of exotic surface sites for catalyst informatics

Yoyo HINUMA

National Institute of Advanced Industrial Science and Technology (AIST)

1-8-31, Midorigaoka, Ikeda, Osaka 563-8577

Surface point defects of metal oxides, for instance O vacancies, have a dominant effect on heterogeneous catalysis. The Mars-Van Krevelen mechanism is one of the most frequently encountered catalytic process. In one example, O vacancies on a metal oxide catalyst surface act as reaction sites. The energy minimum required to remove O from a surface, which is denoted as the surface O vacancy formation energy (E_{Ovac}), can be used to rationalize and predict catalytic performance in such a catalytic process. Calculation of E_{Ovac} requires a slab-and-vacuum model with sufficient spacing between O vacancies, hence some estimation of E_{Ovac} from less costly calculations, such as slab-and-vacuum model calculations with minimum cell size and even bulk calculations, will be effective in screening materials for a given purpose.

Computational exploration of previously unknown reactive sites is a powerful strategy for emergence of new catalytic reactions. Exotic surfaces can be theoretically investigated, but there are very few, if any, computational models of high index orientations that considers reconstruction of the surface. A workflow to efficiently obtain a set of accessible terminations by removing those that are metastable against macroscopic facet formation and by comparing cleaved surfaces and surfaces suggested by a genetic algorithm (GA) for promising orientations is proposed and demonstrated using 34 orientations of β-Ga2O3 and θ-Al_2O_3. Seven and six terminations considered experimentally accessible are found for β-Ga_2O_3 and θ- Al_2O_3, respectively, where the highest surface energy was roughly twice of the lowest. The lowest surface O vacancy formation energy (EOvac) in an accessible surface is 3.04 and 5.46 eV in the (101) and (20-1) terminations for β-Ga_2O_3 and θ-Al2O3, respectively, where the decrease in E_{Ovac} from the most stable surface is 1.32 and 1.11 eV, respectively. The E_{Ovac} in accessible surfaces showed a good correlation with descriptors of the local coordination environment, suggesting that exploiting surface O in an unfavorable environment in an accessible termination would enhance O vacancy-related catalyst performance even in materials that do not show reactivity on the most stable surface.

Analysis of the electronic structure of ferromagnetic shape memory alloy and ferrimagnetic spinel oxide

Masao OBATA[1,2]

[1]*Institute of Science and Engineering, Kanazawa University, Kanazawa, Ishikawa 920-1192*

[2]*Graduate School of Natural Science and Technology, Kanazawa University, Kanazawa, Ishikawa, 920-1192*

We have investigated the electronic and magnetic structure of the magnetic shape memory alloy of Ni_2MnGa and ferrimagnetic spinel oxide of $NiCo_2O_4$. In these materials, the LDA/GGA level investigation showed inconsistency with experimental facts, such as the period of martensite modulation due to Fermi surface nesting and the properties of electrical resistivity, respectively. Since these discrepancies may originate from electron correlation effects, we employed the quasi-particle self-consistent GW (QSGW) approach, which is one of the beyond LDA/GGA methods, to investigate the electronic structure of those materials. The first-principles calculation package ecalj [1] is used for this study.

(A) Ni_2MnGa

The Ni_2MnGa ferromagnetic shape memory alloys, which have magnetic and shape memory properties, have been attracted as magnetic actuator materials. We applied the QSGW to the high-symmetry (cubic) and low-symmetry (tetragonal) phases of Ni_2MnGa. We found that the Fermi surface of the cubic phase expands compared to GGA, resulting in the reduction of vector length in Fermi surface nesting. The obtained nesting vector from the generalized susceptibility is consistent with the experimentally observed crystal structure at low temperatures, such as 10M or 14M long-period modulated structures [2]. We also estimated the effect of Mn's on-site Coulomb interaction on the tetragonal phase [3].

(B) $NiCo_2O_4$

The $NiCo_2O_4$ spinel has drawn much attention for its material application due to its low cost, high electronic conductivity, redox reaction, and high electrochemical activity. However, its electronic structure is not well understood. We investigated the inverse spinel β structure by QSGW. We found that the e_g orbital of Co tetrahedral site appears on the Fermi-level and splits due to the uniaxial crystal symmetry, stabilizing $3z^2$ and destabilizing x^2-y^2 orbitals.

References

[1] https://github.com/tkotani/ecalj/

[2] M. Obata, T. Kotani, T. Oda, submitted.

[3] M. Zelený, P. Sedlák, O. Heczko, H. Seiner, P. Veřtát, M. Obata, T. Kotani, T. Oda, L. Straka, Mater. Des., **209**, 109917 (2021).

First-principles calculations of complex metallic alloy surfaces

Kazuki NOZAWA
Department of Physics and Astronomy, Kagoshima University
1-21-35, Korimoto, Kagoshima 890-0065

We studied the adsorption of pentacene on the 2-fold surface of an icosahedral Ag-In-Yb quasicrystal [1](QC). An STM experiment reported that pentacene molecules adsorbed in a quasiperiodic manner on this surface[2].

The QC surface has approximated by a disk-shaped atomic cluster with a radius of 2.2 nm (Fig. 1). Atomic positions of the QC surface has extracted from the structural data of an X-ray diffraction experiment for the isostructural $Cd_{5.7}Yb$ quasicrystal[3], where Ag and In atoms occupy the Cd sites in the Ag-In-Yb QC. In the calculations, the molecular axis of pentacene is constrained to be parallel to the surface, and all atomic positions, including the substrate atoms, are fixed. Calculations are carried out with the VASP code mainly on the system-B as bulk jobs using 72 nodes.

First, we carefully checked the cluster thickness dependence of the adsorption energy. And we confirmed that the thin film composed only of the top layer atoms well describes the interactions with pentacene. Thus, we describe the results below using the thin film as the substrate.

The adsorption energy of pentacene shows strong orientational dependence on the molecular axis of pentacene. Figures 2(a) and (b) show the adsorption energies of pentacene with its molecular axis aligned to two different 2-fold axes, 2f-90° and 2f-180°, which are parallel to the surface and perpendicular to each other. It is clearly shown that pentacene favors one of them (2f-90° direction shown in Fig. 2(a)). Comparably stable orientational configurations are found when the molecular axis is aligned to two 5-fold axes on the surface. Obtained orientational dependence of the adsorption energy well explains the result of statistical analysis from an STM experiment[2].

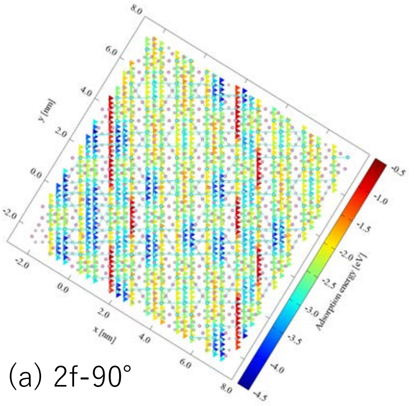

(a) 2f-90°

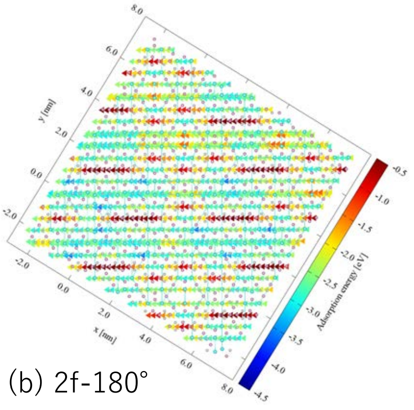

(b) 2f-180°

Figure 1: Adsorption energy of pentacene with the molecular axis parallel to the 2-fold (a) 90° and (b) 180° directions.

We also studied the adsorption of oxygen atoms on the (111) surface of the PdZn inter-metallic compound. We used the VASP code with a slab model consisting of six atomic layers. Using a 2x2 unit cell containing eight atoms in the top layer, we investigated the adsorption structures for various oxygen coverages between 0.125 - 1.0 monolayer (ML). Calculations were mainly carried out on the system-C as flat MPI jobs with 4-9 nodes. At high oxygen coverages, we found that Zn atoms form a Zn-O layer with a hexagonal ring reminiscent of the Wurtzite ZnO. PdZn is known as a candidate catalyst for the methanol steam reforming (MSR) because of its higher thermal stability than the traditional Cu-based catalyst. It has been reported that a ZnO patch is formed on the PdZn catalyst during the MSR reaction, and considered that the high CO_2 selectivity of PdZn in MSR is due to the formation of the ZnO patch[4]. However, there is still no report of the first-principles calculations about the formation of the Zn-O layer.

References

[1] M. Sato, Master Thesis (Kagoshima University, 2022).

[2] A. Alofi *et al.*, Mat. Trans. **62**, 312(2021).

[3] H. Takakura *et al.*, Nature Matter. **6**, 58(2007).

[4] M. Friedrich *et al.*, Angew. Chem. **52**, 4389 (2013).

Atom exchange of fcc metal surfaces

Tsuneo FUKUDA[†]

Department of Physical Electronics and Informatics, Graduate School of Engineering,
Osaka City University, 3-3-138 Sugimoto, Sumiyoshi-Ku, Osaka 558-8585

The migration of an adsorbed atom (adatom) impinged from gas phase to a surface is one of the fundamental processes for crystal growth. In some adatom-surface combinations, instead of migration of an adatom on the surface, an adatom may be embedded in the surface layer by displacing the surface atom, and the released atom migrates on the surface, which is often called "displacive adsorption". Such substitutions between adatoms and surface atoms are frequently reported by using field ion microscopy (FIM) [1].

We have investigated adatom migration and adatom-surface atom substitution from theoretical point of view. We chose the Ni(100) and Ni (110) surfaces as model systems and investigated the migration and the substitution of Ni and Cu atoms based on first-principles calculations. We employed a popular first-principles calculation code VASP, and the nudged elastic band (NEB) method was applied to the evaluation of adatom migration and exchange potentials [2].

Surface models are shown in Figs. 1. We employed 7-layer slab model with ~0.8 nm vacuum layer for both sides for both the Ni(110) and Ni(100) surfaces. After fully relaxed atomic structures of slabs for pristine surfaces, Ni or Cu adatom was located and adsorbed surfaces were again relaxed by keeping atomic positions of bottom 4 layers fixed. Electronic and ionic iteration parameters are listed in Table 1. The NEB method was performed for 5 images with both the initial and final structures being fixed (IMAGE=4). Near the potential maximum, the migration potential was further evaluated by dividing these images.

The obtained migration potential barriers are listed in Tables 2 and 3. For the Ni(110) surface, a simple surface diffusion of adatom along [110] direction, path A in Fig. 1(a), had a

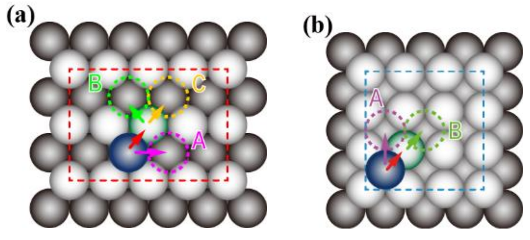

Fig. 1: Adatom migration pathways for (a) Ni(110) and Ni(100) surfaces. The unit cells used in the structural calculation are shown by the dotted lines. Initial adatom position is indicated by blue circle, and path A, B, and C on the Ni(110) surface and path A and B on the Ni(100) surface are indicated by purple, green, and yellow, respectively.

[†] Present address: Division of Electronics and Physics, Graduate School of Engineering, Osaka Metropolitan University, 3-3-138 Sugimoto, Sumiyoshi-Ku, Osaka 558-8585

Table 1 Parameters for present calculation

VASP Version	5.3.5
slab geometry	Ni(110): 4×2 unit 7 layer Ni(100): 3×3 unit 7 layer
k-points	Ni(110): 12×16 Ni(100): 12×12
potential	PBE [3]
cut off energy	384.08 eV
Fermi level smearing	Methfessel & Paxton $\sigma = 0.12$ eV
convergence condition	Electronic:10^{-6} eV Ionic: 0.01 eV/Ang.
SCF mixing parameters	AMIX = 0.02 BMIX = 0.0001 AMIX_MAG = 0.08 BMIX_MAG = 0.0001 (linear mixing)
Time period	POTIM = 1.0
Number of core	576 (192/image)

Table 2 Migration potentials of Ni adatom corresponding paths shown in Figs. 1

face	path	Potential energy [eV]
Ni(110)	Path A	0.321
	Path B	0.444
	Path C	0.443
Ni(100)	Path A	0.728
	Path B	1.105

Table 3 Migration potentials of Cu adatom corresponding paths shown in Figs. 1

face	path	Potential energy [eV]
Ni(110)	Path A	0.309
	Path B	0.426
	Path C	0.428
Ni(100)	Path A	0.523
	Path B	1.080

lowest energy. Atom exchange processes such as path B and C have higher energy than path A. Experimentally, only path C was seen by FIM study [1]. Although the present calculation of the energy barrier of path C gave 0.36 mV lower than that of path B, but we failed to reproduce the experimentally observed large difference in the exchange probability between path B and C [1]. This seems to indicate the thermal effect, i.e., collective motion of adatoms and surface atoms is crucial to the atom exchange process and molecular dynamic study should be required for understanding this discrepancy.

For the Ni(100) surface, adatom diffusion along the [110] direction, path A in Fig. 1(b), again had a lower energy than atom exchange process path B, in agreement with the previous report.[4]

In conclusion, the present calculation showed that in addition to the surface migration of adatom such as Ni and Cu, atom exchange may be possible on the Ni(110) surface, but slightly higher energy, i.e., higher temperature is needed for replace surface atom with adatom on the Ni(100) surface.

References

[1] G. Antezak and G. Ehrlich, Surf. Sci. Reports **62** (2007) 39.

[2] H. Jonsson, G. Mills and K. W. Jacobsen, *Condensed Phase Simulations*, ed. B. J. Berne, G. Ciccotti and D. F. Coker (World Scientific, 1998).

[3] J. P. Perdew, K. Burke, and M. Ernzerhof, Phys. Rev. Lett. **77** (1996) 3865.

[4] B. Müller, B. Fischer, L. Nedelmann, A. Fricke, and K. Kern, Phys. Rev. Lett. **76** (1996) 2358.

Development of the first-principles method for calculating T_c based on density functional theory for superconductors

Ryosuke AKASHI
Department of Physics, The University of Tokyo

The first-principles prediction of the superconducting transition temperature T_c of metals is a challenging goal in the condensed matter physics. For phonon-mediated superconductors, accurate calculation schemes is now available on the basis of the Eliashberg theory and density functional theory for superconductors (SCDFT) [1, 2]. In this year, we conducted a development of a first-principles method with the latter theory.

In the conventional superconductors, the phonon-mediated attraction is the dominant source of the electronic pairing interaction, where the electron-electron Coulomb repulsion has only a secondary role that it partially cancels the attraction. On the other hand, as the Coulomb interaction becomes stronger, there emerges a chance for it to affect the superconductivity in a different way. A prominent example is the plasmon-mediated pairing mechanism [3, 4]: the frequency dependence of the screened Coulomb interaction enhances the pairing. Another is the spin-fluctuation mechanism, where ferromagnetic fluctuation strongly suppress the singlet pairing [5, 6, 7, 8]. We have developed an SCDFT based method to calculate T_c with the plasmon and spin fluctuation effects included. In this project, we made further progress along this line. In the SCDFT, the superconducting T_c can be evaluated by solving the following gap equation

$$\Delta_{n\mathbf{k}} = -\mathcal{Z}_{n\mathbf{k}}\Delta_{n\mathbf{k}} -\frac{1}{2}\sum_{n'\mathbf{k}'}\mathcal{K}_{n\mathbf{k}n'\mathbf{k}'}\frac{\tanh[(\beta/2)E_{n'\mathbf{k}'}]}{E_{n'\mathbf{k}'}}\Delta_{n'\mathbf{k}'}.(1)$$

The kernels $\mathcal{K}$ and $\mathcal{Z}$ represent the effect of the electron-phonon and electron-electron Coulomb interactions. By developing new forms of $\mathcal{K}$ we can in principle incorporate novel interaction effects. β is the inverse temperature and $E_{n\mathbf{k}}$ is the Kohn-Sham energy eigenvalue.

First, we constructed a formalism of the exchange-correlation functional in the SCDFT based on the adiabatic connection formula [9]. We formally confirmed that this formalism reproduces the previous one.

Next, we extended this formalism and derived a formula for the exchange-correlation kernel beyond the local density approximation. As this is numerically too demanding, we are continuing exploration of efficient numerical implementation of the newly developed formula.

We also tested an implementation of the SCDFT-based T_c calculation in SUPERCONDUCTING TOOLKIT [10] to see if the previously published values [8], calculated with another in-house code, are well reproduced. The calculated values (Table 1), though fairly agreeing with the previously published ones, were generally larger. The overestimation is likely attributed to a subtle implementation details like how to numerically integrate the internal frequencies. These calculation were performed in System B (Ohtaka) with parallelization within a single node. The elapsed time for each T_c

was approximately less than 30 minutes.

Table 1: Superconducting transition temperature T_c (K) calculated with the SCDFT gap equation Eq. (1) using SUPERCONDUCTING TOOLKIT, with and without the spin fluctuation effects. In RPA and LDA, the exchange correlation kernels entering the $\mathcal{K}$ formula [7] are ignored and incorporated, respectively.

	RPA		LDA	
	w.o. SF	w. SF	w.o. SF	w. SF
V	20.5	2.8	18.1	2.5
Al	1.2	0.6	0.9	0.4

References

[1] M. Lüders, *et al.*, Phys. Rev. B **72** (2005) 024545.

[2] M. A. L. Marques, *et al.*, Phys. Rev. B **72** (2005) 024546.

[3] Y. Takada, J. Phys. Soc. Jpn. **45** (1978) 786.

[4] R. Akashi and R. Arita, Phys. Rev. Lett. **111** (2013) 057006.

[5] N. F. Berk and J. R. Schrieffer, Phys. Rev. Lett. **17** (1966) 433.

[6] F. Essenberger, A. Sanna, A. Linscheid, F. Tandetzky, G. Profeta, P. Cudazzo, and E. K. U. Gross, Phys. Rev. B **90** (2014) 214504.

[7] M. Kawamura, Y. Hizume, and T. Ozaki, Phys. Rev. B **101** (2020), 134511.

[8] K. Tsutsumi, Y. Hizume, M. Kawamura, R. Akashi and S. Tsuneyuki: Phys. Rev. B **102** (2020) 214515.

[9] D. C. Langreth and J. P. Perdew, Solid State Commun. **17** (1975) 1425.

[10] M. Kawamura, R. Akashi and S. Tsuneyuki, Phys. Rev. B **95** (2017) 054506 .

Calculation of photoelectron angle distribution in the photoexcitation process on the organic molecules adsorbed surface

Kaori Niki

Graduate school of science

Chiba University, Yayoi-cho, Inage-ku, Chiba 263-8522

In recent years, it has been reported electronic and physical properties of organic molecules which interact with the surface using Wave number space resolved Photoelectron Spectroscopy. We have investigated the copper (Ⅱ) phthalocyanine (CuPc) - monolayer substrate system. Monolayer $TiSe_2$ have two typically phases depending on the temperature. A (1 × 1) structure (normal phase) is shown at room temperature and a (2 × 2) superstructure (CDW phase) is realized under the 200 K. Each phase has band gap of 83 meV and 153 meV, respectively [1, 2]. We have adopted this interesting thin film as the substrate and reported the structural changes depending on the temperature in the previous year. In this year, we investigated the electronic state of a (1 × 1) monolayer $TiSe_2$. Based on these results, we optimized the structure of CuPc adsorbed on $TiSe_2$.

1. Band calculation of $TiSe_2$ monolayer

We performed density functional theory (DFT) calculations using the Vienna Ab Initio Software Package (VASP) version 5.4.4 [3,4]. The exchange correlation effects were described by the Generalized Gradient Approximation (GGA) within the Perdew-Burke-Ernzerhof (PBE) formalism. We used a unit cell with lattice constants a = b = 3.53 Å, c = 20.0 Å, $\alpha = \beta = 90°$ and $\gamma = 120°$, and plane-wave basis set with the projector augmented wave (PAW) approach with an energy cutoff of 380 eV. The Brillouin zone integration was performed on a Monkhorst-Pack of 18×18×1 grid of k-points. The energy convergence criterion was chosen for the self-consistency cycle was 1×10^{-7} eV. To account for Fermi surface broadening, temperature parameter σ for Methfessel-Paxton smearing was applied [5].

We investigated a local Coulomb repulsion of Ti 3d electrons and the effect of the electronic smearing parameter σ on the band gap. We calculated band gaps with different sets of Coulomb repulsion U and σ. Fig. 1(a) show a negative bandgap without considering U and σ. On the other hand, fig. 1(b) and (c) have positive bandgaps close to 0. It is found that both σ and U increase the gap between the top of Se 4p band (Γ, red point) and the bottom of Ti 3d band (M, blue point). However, the rise in σ push up the upper end of the Se4p band above the fermi surface, so Fig. (b) is also excluded. As a result, we find the parameter set

(U = 3.9 eV and σ = 0.01 eV) which reproduce experimental result [6]. We used these parameters for optimization of CuPc / $TiSe_2$ structure.

(a) σ =0.01 eV, U_{Ti}=0.0 eV

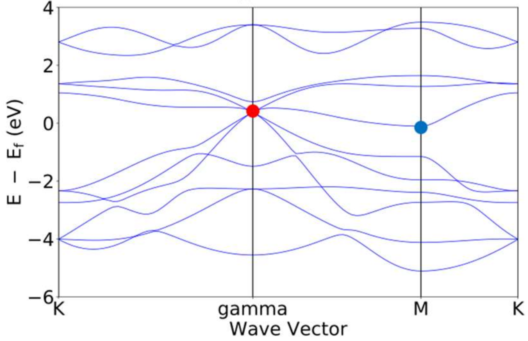

(b) σ =0.8 eV, U_{Ti}=0.0 eV

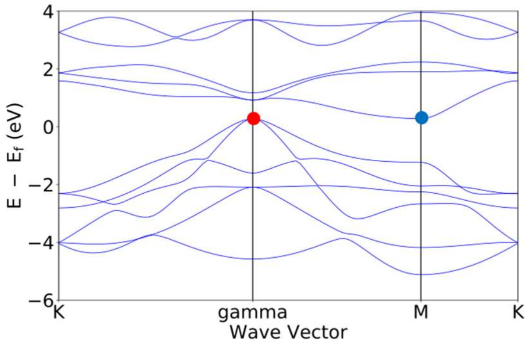

(c) σ =0.01 eV, U_{Ti}=5.0 eV

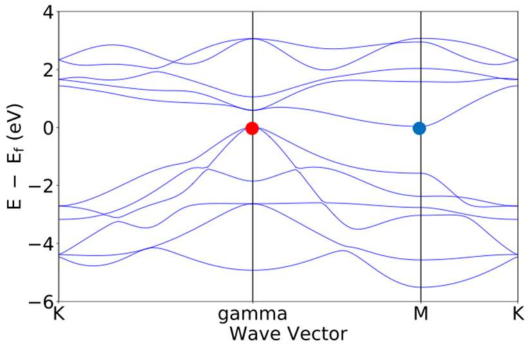

Figure 1 Band dispersion of the (1×1) monolayer $TiSe_2$ with different electronic smearing parameter σ and effective Hubbard parameter U for Ti**.**

2. Structural optimization of CuPc/$TiSe_2$

We expanded above model for an 8 × 8 structure of the monolayer $TiSe_2$ with lateral dimensions of 693 $Å^2$. For Cu atom of CuPc, U value was adjusted to 4.0 eV which could reproduce the qualitative orbital ordering of isolated CuPc. In addition, CuPc had an unpaired electron, thus we considered spin polarization. Ionic positions were optimized until the residual force on each ion was less than 1×10^{-2} eV/Å. When starting with a random wave function, it took about 12 hours to converge one electronic state using 5 nodes with total 144 cores. From this structure optimization calculation, it is found that the adsorption distance between molecule and substrate is 3.16 Å, resulting in a flat molecule structure.

We have reached the stage where it is possible to calculate the Wave number space resolved Photoelectron Spectroscopy. We are planning to perform this calculation next year.

References

[1] J.-P. Peng *et. al.*, Phys. Rev. B **91**, 121113 (2015).

[2] P. Chen *et. al.*, Nat. Commun **6**, 8943 (2015).

[3] G. Kresse and J. Furthmuller, Phys. Rev. B, **54**, 11169 (1996).

[4] G. Kresse and J. Hafner, Phys. Rev. B, 49 14251 (1994).

[5] M. Methfessel and A. T. Paxton, Phys. Rev. B **40**, 3616 (1989).

[6] R. Bianco *et.al.*, Phys. Rev. B **92**, 094107 (2015).

Physical properties of layered graphene

Yoshitaka FUJIMOTO
Depertment of Physics, Tokyo Institute of Technology
Oh-okayama, Meguro, Tokyo 152-8551

Graphene is one of the most promising materials for electronics devices including field effect transistors and molecular sensors. Bilayer of graphene would have rich properties because electronic structures of graphene change depending on how two layers interact with each other. Here, we study the stacking-pattern effects on the electronic transport and molecular adsoprtion of bilayer graphene using a first-principles density-functional calculation [1, 2, 3].

It has been reported that the bilayer graphenes with three different stacking patterns (AA, AA′, and AB) have been synthesized and observed experimentally. Table 1 lists the adsorption energies and the binding distances between the B atom and the adsorbed molecule for various molecules on the B-doped bilayer graphenes with three different stackings. For all stacking patterns, CO and CO_2 molecules are adsorbed not strongly but weakly, whereas NO and NO_2 molecules can bind strongly with the large adsorption energies and the short binding distances. O_2 and N_2 molecules weakly bind with small adsorption energies. Therefore, only NO and NO_2 molecules in air are adsorbed with chemical bonds on the B-doped bilayer graphene without depending on the stacking patterns.

We study electronic transport of the pristine bilayer graphene for the three different stackings. The conductance for the AB stacking has the linear dispersion near $E = 0$ eV as in the case of the monolayer. On the other hand, unlike monolayer, the slope of the conductance curve between 0 eV and $\sim \pm 0.25$ eV is different from that between $\sim \pm 0.5$ eV and ± 1.0 eV, respectively. Due to the difference of the slope of the conductance curve in different energy ranges, the transport properties induced by the adsorption of molecules would be different from that of the monolayer. The finite conductivity in the AB-stacked bilayer graphene was reported theoretically and observed experimentally. The conductance of the AA-stacked bilayer graphene seems to have constant value from the energies $E = -0.25$ eV to $+0.25$ eV, and it increases linearly below -0.25 eV and above $+0.25$ eV. Unlike the AA-stacked bilayer graphene, the conductance of the AA′ stacking shows asymmetric behaviors near the Fermi energy. Thus, it is interesting that the conductances of the bilayer graphenes with AA, AA′ and AB stackings are different from one another.

We study the molecular adsorption effects on the transport of the B-doped bilayer graphenes for three different stackings, and define $\Delta G(E) = (G_a - G_b)/G_b \times 100(\%)$, where G_a and G_b are the conductances of the B-doped bilayer graphene with and without molecules, respectively. When NO and NO_2 molecules are adsorbed on the AB-stacked bilayer graphene, the conductances at the energy $E = 0$ eV change with $\Delta G(0) = +8.2\%$ and $+3.0\%$, respectively. For the AA stacking, the adsorptions of NO and NO_2 molecules can induce $\Delta G(0) = +2.1\%$ and -17.4% in the conductances, respectively. In the case of the AA′ stacking, there are sizable conductance changes of -17.2% and -47.7% for the adsorptions of NO and NO_2 molecules, respectively.

In summary, the stacking-dependent behaviors of the transport and the adsorption properties of molecules of bilayer graphene have been investigated for various molecules including environmentally polluting or toxic molecules and common molecules (NO, NO_2, CO, CO_2, O_2, and N_2) using a first-principles density-functional study. Irrespective of stack-

Table 1: Adsorption energy E_a (eV) and distance d (Å) between molecule and B atom for each molecule adsorbed on B-doped bilayer graphenes with AA, AA′, and AB stackings.

Stacking		NO	NO_2	CO	CO_2	O_2	N_2
AA	E_a	−1.20	−1.12	−0.12	−0.04	−0.16	−0.28
	d	2.15	1.60	2.90	2.87	1.76	2.96
AA′	E_a	−1.22	−1.15	−0.12	−0.04	−0.19	−0.28
	d	2.15	1.60	2.90	2.87	1.75	2.96
AB	E_a	−1.19	−1.13	−0.12	−0.03	−0.20	−0.27
	d	2.14	1.60	2.89	2.84	1.75	2.93

Table 2: Percentage of changes in the conductance at the Fermi energy $E = 0$ [$\Delta G(0)$] for each molecules adsorbed on B-doped bilayer graphene with AA, AA′, and AB stackings. The changes in the conductance are calculated with respect to the B-doped bilayer graphene.

	AA	AA′	AB
NO	2.1	-17.2	8.2
NO_2	-17.4	-47.7	3.0

ing patterns, only NO and NO_2 molecules in air can bind strongly on B-doped bilayer graphene. It is found that the conductance curves of bilayer graphenes change depending on the stacking patterns and the presence of the NO/NO_2 molecule, and the variation of the conductances induced by molecular adsorptions could be used by gas sensing devices such as field-effect transistors under low bias voltages.

References

[1] Y. Fujimoto and S. Saito, Appl. Surf. Sci. Adv. **1**, 100028 (2020).

[2] Y. Fujimoto, Mod. Phys. Lett. B **35**, 2130001 (2021).

[3] Y. Fujimoto and S. Saito, J. Electrochem. Soc. **169**, 037512 (2022).

Computational materials design of Ag and Cu chalcogenide based thermoelectric materials

Ho Ngoc Nam[a)] and Kazunori Sato [a, b)]

[a)]*Graduate School of Engineering, Osaka Univ., Yamadaoka, Suita, Osaka 565-0871*

[b)]*CSRN, Graduate School of Engineering Science, Osaka Univ., Toyonaka, Osaka 560-8531*

The development of compact, wearable, and especially self-charging personal electronics has become more feasible in recent years. As a continuous power supply for an uninterrupted operation, it is desirable that these electronic devices can convert directly the waste heat of the human body or environment into electricity via flexible thermoelectric (TE) generators. A recent study discovered the extraordinary ductility of the inorganic semiconductor silver sulfide (Ag_2S) [1] paving the way for flexible TE developments. In this study, we use first-principles calculations combined with the Boltzmann transport theory to investigate the electronic and transport properties of Ag and Cu chalcogenide materials.

First of all, we have chosen the exchange - correlation functional SCAN+rVV10 in order to reproduce band gap energy and lattice constants of α-Ag_2S reasonably. According to the calculations of the formation energy of typical intrinsic defects, it is found that the intrinsic defects greatly affect the system’s conductivity where Ag vacancy and interstitial Ag act as p-type and n-type defects, respectively [2]. The effects of the doping of transition metal impurities were investigated and the results were consistent with the experimental observations [2]. We have also found that experimental transport properties were reasonably reproduced by using the electron-phonon coupling method, showing the suitability of this scattering model in estimating the relaxation time [3].

In addition to Ag chalcogenides, we have also applied our calculation procedures to Cu sulfide systems and found that the defect formation energy and transport properties can be simulated by using the acanthite-like structure for this material. Based on these knowledges, we will extend our computational materials design for $(Ag_{1-x}, Cu_x)(S_{1-y}, Se_y)_2$ chalcogenides to realize flexible TE materials.

References

[1] X. Shi et al., Nat. Mater. **17** (2018) 421.

[2] H. N. Nam et al., Phys. Chem. Chem. Phys. **23** (2021) 9773.

[3] H. N. Nam et al., Appl. Phys. Lett. Accepted.

[4] H. N. Nam et al., Phys. Rev. B105 (2022) 075205.

Thickness-Dependent Electronic Properties of Atomically Thin Boron Monosulfide

Masayuki TOYODA
Department of Physics, Tokyo Institute of Technology
Ookayama, Meguro, Tokyo 152-8551

Rhombohedral boron monosulfide (r-BS) is a meta-stable phase of binary boron-sulfer system obtained under high-temperature and high-pressure condition [1]. Recently, Kondo et al. have succeeded to exfoliate atomically thin layers of r-BS from its bulk.

We have studied the electronic structures of thin layers of r-BS using the first-principles density functional theory calculations. The calculations have been performed using the massively parallel computers in ISSP, University of Tokyo.

From the electron localization function (ELF) analysis, we have found that B and S atoms are covalently bonded in each S-B-B-S unit layer (Fig. 1). The valence-band maximum (VBM) states are consisted of hybridized B-p_z and S-p_z orbital states. By the stacking of layers, the VBM states exhibit splitting, resulting in the systematic narrowing of the band gap (Fig. 2). This band-gap narrowing has also been observed in the optical experiement [2] and is suggesting the potential application of r-BS as 2D semiconductos with tunable band gap.

References

[1] T. Sasaki, H. Takizawa, K. Ueda, and T. Endo, phys. stat. sol. (b) **223**, 29 (2001).

[2] H. Kusaka, R. Ishibiki, M. Toyoda, et al., J. Mater. Chem. A **9**, 24631 (2021).

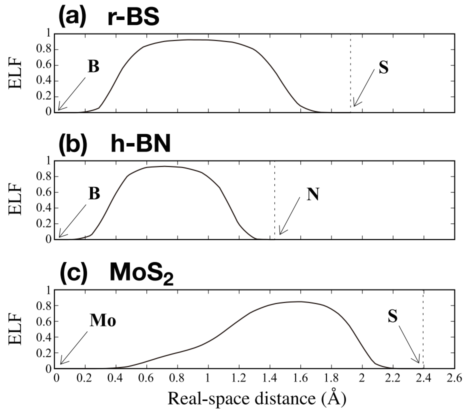

Figure 1: Electron localization function along the atomic bonds in (a) r-BS, (b) h-BN, and (c) MoS_2.

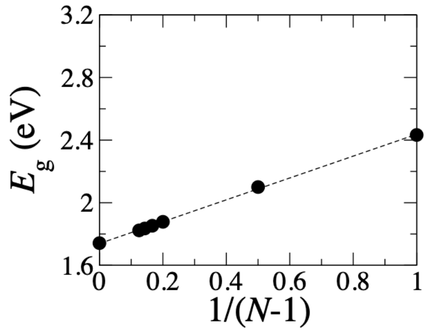

Figure 2: Calculated band gap values of thin-layer ($1 < N < \infty$) and bulk ($N = \infty$) r-BS.

Large-Scale Molecular Dynamics Simulations on Non-Equilibrium Phenomena Using First-Principles Calculation and Machine Leaning

Masaaki MISAWA

Faculty of Natural Science and Technology, Okayama University

Artificial neural network (ANN) potential, which is an interatomic potential constructed by machine-leaning, attracts attention as a promising method to achieve extra-large-scale molecular dynamics (MD) simulation with first-principles accuracy [1]. Application of this ANN-MD to far-from-equilibrium phenomena, such as fracture and pressure-induced transformation, is important to understand structural properties of materials under extreme conditions. For this purpose, we have tried to perform ANN-MD simulation of shock-induced structural transformation of silica.

To compute shock-compression behaviors within the framework of MD method, the multiscale-shock technique [2] was employed in our simulations. Potential energy of shock-compressed α-quartz obtained by first-principles MD (FPMD) method is used as a reference data for training of ANN-potential. As a result of ANN-MD simulation for elastic shock-wave region, elastic-deformation behaviors of α-quartz was successfully reproduced with high-accuracy [3]. On the other hand, for plastic shock-wave region, the ANN-potential has completely failed on prediction of both structure and energy, because of that irregular structure appears and rapid movement of atoms occurs during the elastic-to-plastic transition process.

In order to improve the predicting ability of ANN-potential, we introduce a more accurate training method that uses not only potential energy but also atomic force and pressure as reference data [4]. Using this improved ANN-potential, it was succeeded that reproducing the elastic-to-plastic transition behavior and plastic deformation of α-quartz with an accuracy close to FPMD simulation. Thus, the ANN-potential trained with energy, force, and pressure is a potentially powerful tool to investigate wide range of far-from-equilibrium phenomena and will also provide useful information for solid earth physics field in future.

References

[1] J. Behler and M. Parrinello, *Phys. Rev. Lett.* **98**, 146401 (2007); N. Artrith and A. Urban, *Comput. Mater. Sci.* **114**, 135 (2016).

[2] E. Reed *et al., Phys. Rev. Lett.* **90**, 235503 (2003).

[3] M. Misawa *et al., J. Phys. Chem. Lett.* **11**, 4536 (2020).

[4] K. Shimamura *et al.*, *J. Chem. Phys.* **153**, 234301 (2020).

Defect formation energy and band structure of Pb-based topological insulators

Yuki TOKUMOTO
Institute of Industrial Science,
The University of Tokyo, Komaba, Meguro-ku, Tokyo 153-8505

$PbBi_2Te_4$ topological insulator (TI) is considered as one of the promising candidates for future spintronics material with a large spin current density. However, experimental studies of its surface transport properties have not yet been reported, owing to a lack of bulk insulating crystals. So far, we achieved bulk insulating states in $Pb(Bi,Sb)_2Te_4$ topological insulators by tuning compositional ratio of Bi and Sb [1]. Although such control of compositional ratio leads to a change in the type and concentrations of intrinsic point defects, the Fermi level is not necessarily well tuned. For further success in achieving the bulk-insulating state, not only the reduction of absolute amount of charged defects but also the enhancement of the activation energy is required. Recently, it was reported that Sn doping for Bi_2Te_2Se TI is effective for lowering carrier concentrations and activated resistivities, with a localized impurity band that acts as a charge buffer occurring inside the bulk band gap.

We carried out band structure calculation of $PbBi_2Te_4$ based on density functional theory (DFT) using Vienna ab-initio simulation package (VASP) version 6.2.1. We adopted generalized gradient approximation (GGA) proposed by Perdew, Burke, and Ernzerhof (PBE) as the exchange correlation energy functional. For all calculations, we included spin-orbit coupling (SOC). We obtained band gap of 115 meV for $PbBi_2Te_4$, which is much lower than experimentally reported value ~230 meV. In order to estimate band gap more accurately, the Heyd-Scuseria-Ernzerhof (HSE06) and HSE03 hybrid functional was employed. As a result, band gap was further underestimated. We found that the HSE is not effective for accurate estimation of band gap of narrow-gap semiconductors.

In 2022, we plan to calculate defect formation energies using GGA-PBE including SOC.

References

[1] Y. Hattori, Y. Tokumoto, and K. Edagawa: Phys. Rev. Mater. **1** (2017) 074201.

Electronic structure of the interfaces between diamond and alkali metals

Toshihiro SHIMADA

Division of Applied Physics, Faculty of Engineering

Hokkaido University, Kita-13 Nishi-8, Kita-ku, Sappooro, Hokkaido 060-8628

The interaction between diamond surfaces and liquid alkali metals has been little investigated. We observed the etching process upon heating and the change in fluorescence of nitrogen impurities (NV^- centers). DFT calculations using the ISSP supercomputer were performed to investigate the electronic structure, and it was shown that the experimental results can be explained by the difference in band bending.

Experimental observation revealed that the etching of diamond occurred in heated lithium. K and Na did not show etching. The fluorescence of the NV- center was significantly reduced only in contact with molten K. This is understandable if we consider that the negatively charged NV^- that emits fluorescence is lost due to upward band bending. Although the extent of band bending depends on the doping state of the semiconductor, the amount and direction of band bending can be estimated by determining the positional relationship between the Fermi level of the undoped semiconductor (in this case diamond) and the metal using DFT calculations. We used VASP[2] with PBE functional. The initial structure for the optimization was created considering the bulk lattice constants of the Li, Na, and K. 3 × 3 × 4 unit cells of the diamond with 4 layers of alkali metal atoms on both sides were employed. We tried several starting structures do the alkali metals (lattice constant, orientation and shift), and the final structures were almost the same. The results are shown in Fig. 1. An upward shift in the density of states of interfacial carbon is observed, and it is stronger at the interface with (c) K.

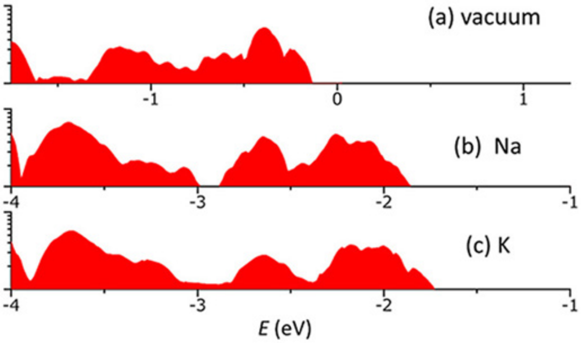

Fig.1 Density of states of carbon at diamond interfaces with various materials [1].

References

[1] H. Takehana et al. Carbon **182** (2021) 585.

[2] https://www.vasp.at

Automatic generation of first-principles effective models based on MLO

Hirofumi SAKAKIBARA
Advanced Mechanical and Electronic System Research Center (AMES),
Tottori University, Tottori, Tottori 680-8525

To the goal of material informatics, automatic generation of data is the central part of calculations. According to the density functional theory (DFT) and local density approximation (LDA), we can calculate electronic structure, which generally controls the most part of material properties, systematically without any empirical inputs. The DFT calculation itself is not so much demanding in computational resources as long as we consider tens of atoms per unit cell. Therefore, DFT calculations have been taken advantage of material informatics.

The band structure within few eV measured from Fermi energy is effective for material properties at low temperature. In other words, whole band structure contains excess information. Even the drastic development of computational power, the computational cost beyond the DFT calculations, for example many body calculations, are still sometimes demanding. Therefore, for mining new functional material such as magnets and/or superconductors driven by electronic many body effects, it is convenient that we can automatically construct a model which only contains the low-energy part of electronic structure. Historically, we already have the technique of Maximally Localized Wannier Function (MLWF) [1], however, MLWF contains several difficulties or automation especially for the system spanned by s- and p-orbitals like semi-conductors. Therefore, for calculating mixed system (superlattice and so on) containing not only the localized electrons such as d-electron but also (s- or p-) delocalized electrons, MLWF is not a perfect method.

For the goal of automation, we have already constructed a new method named Muffin-tin Like Orbital (MLO). MLO is given as a linear combination of atomic basis functions, which is used for the first-principles calculations based on LMTO algorithm. Thanks to the PMT method [2], we can take into account the effects of extended electron orbital such unoccupied states can be considered in the localized basis. Here, PMT is a mixed basis function for first-principles calculation between Plane-wave and Linear Muffin-Tin orbital. By a kind of weighted sum method, we can take into account the effect of unoccupied orbital to the low-energy models's energy eigen values numerically.

For the benchmark materials, we have

chosen four simple samples: Si(already shown Fig.1 of the 2020's report), SiO2(cubic), SrTiO3, and graphene. For all samples, the automation of model construction is succeeded. For SrTiO3, components described by plane-wave (namely, interference of unoccupied orbitals to the low-energy model) bases is few. This can be interpreted that LMTO is a sufficiently accurate basis function for SrTiO3. For graphene, we can obtain a two-orbital model which contains only C-pz' π -bond orbitals forming the Fermi surface (or, Dirac cone). Surprisingly, it is revealed that such π-bonds contains much plane-wave components. For SiO(cubic), we find that an empty sphere in a relatively large interstitial region is necessary to reproduce the extended orbital shaping like a free electron's Bloch orbital.

For the future work, we have to simplify and sophisticate MLO algorithm to save the computational times and to adopt for more larger system such as superlattice, hetero junctions, and surfaces.

References

[1] N. Marzari and D. Vanderbilt, Phys. Rev. B **56**, 12847 (1997).

[2] T. Kotani, H. Kino, and H. Akai, J. Phys. Soc. Jpn. **84**, 034720 (2015).

Theoretical Study on Electronic Properties in New Nanoscale Surfaces and Interfaces

Katsuyoshi KOBAYASHI
Department of Physics, Ochanomizu University
2-1-1 Otsuka, Bunkyo-ku, Tokyo 112-8610

We theoretically studied the electronic structures of VSe_2 monolayers. Recently monolayers of transition-metal dichalcogenides (TMD) are extensively studied. Much attention is paid to magnetic properties of TMD monolayers in recent years. Room temperature ferromagnetism was reported for VSe_2 monolayers in 2018 [1]. However, there is a controversy over its emergence. A recent experiment suggested that VSe_2 monolayers are on the verge of ferromagnetism [2]. We performed a density-functional calculation on this system.

We used the program package VASP for the density-functional calculation. Figure 1 shows the calculated result. Figure 1(a) and (b) show band structures of the VSe_2 monolayer in nonmagnetic (NM) and antiferromagnetic (AFM) states, respectively. The magnetic structure of the AFM state is shown in Fig. 1(c). We used a $\sqrt{3} \times \sqrt{3}$ supercell of the primitive cell in the calculation. Γ is the center in the two-dimensional Brillouin zone. M is the point at the half of a primitive reciprocal lattice vector. We found that the band structures of NM and AFM states are very similar.

In addition to the VSe_2 monolayers we performed calculations of electronic structures of V_5Se_8. We unfolded the calculated band structures in order to compare with experimental band structures obtained from angle-resolved photoelectron spectroscopy.

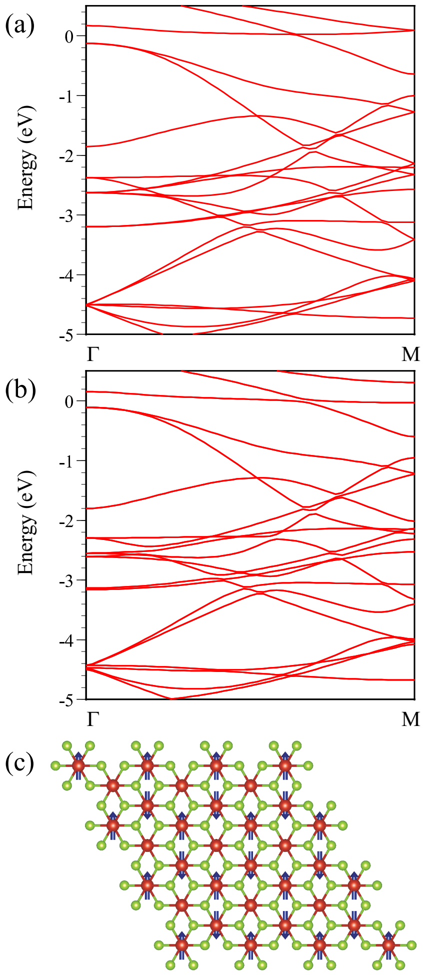

Figure 1: Band structures of a VSe_2 monolayer in nonmagnetic (a) and antifferomagnetic (AFM) (b) states. The magnetic structure of the AFM state is shown in (c). Red and green circles show V and Se atoms, respectively. Arrows express the spin structure.

References

[1] M. Bonilla *et al.*: Nat. Nonotech. **13** (2018) 289.

[2] K. Sumida *et al.*: Phys. Rev. Materials **6** (2022) 014006.

First-principles calculation of graphitization of diamond surface and its exfoliation process

Kouji Inagaki

Graduate School of Engineering, Division of Precision Engineering and Applied Physics

Osaka University, Yamada-oka 2-1, Suita, Osaka 565-0871

Diamond has a wide bandgap electronic property and high mechanical strength; application of diamond to semiconductor electronic devices or to mechanical cutting tools are expected [1]. In electronic device applications, polishing is required to produce a flat surface, but diamond is the hardest material and it is not easy. On the other hand, in tool applications, a serious wear property in cutting iron-based materials is reported. By utilizing this wear phenomenon, it may be possible to realize a novel diamond surface flattening method. Currently, two possible causes of wear are proposed: graphitization of diamond surface, and diffusion of C atoms into metal. This issue remains unclear, particularly in the mechanism how strong C-C bonds break.

In this study, we investigated weakening of C-C bond by the effect of Fe atom to confirm graphite layer peeling. Figure 1 (a) and (b) shows side views of the surface structures of diamond (221) with and without Fe atom, and (c) peeled structure with Fe atom. (Peeled in pristine structure is also perfomed but not shown.) A DFT-based STATE code is employed to obtain stable structures and energies. Peeled structures are obtained by pulling-up terminal atoms (shown in (a) and (b)). This is carried out by artificially adding a constant value of 0.002 Bohr to z axis of the terminal atoms in every quenched MD step with optimizing along x and y directions for the atom and other surface atoms. This procedure is repeated until saturated. The bond breaking energy 2.1eV is obtained by the energy difference between (b) and (c), while corresponding value of pristine surface is much larger energy of 3.2 eV. This indicates C-C bond is effectively weakened by a Fe atom.

It is concluded that a Fe atom can play a catalytic role in peeling graphite layer formed on diamond surfaces. Further investigations will be required to evaluate metal element, atomic environment effect, etc.

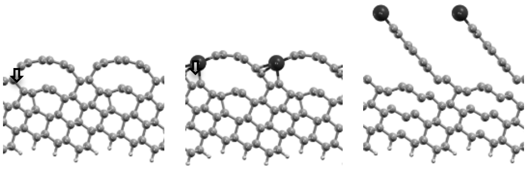

(a) Pristine (b) Fe inserted (c) Peeled

Fig. 1: Peeling of graphite layer formed on diamond (221). Bright, dark and small atoms indicate C, Fe and H atom. Atoms directed by arrow are pulled-up to obtain peeled structures.

Reference

[1] J.Wang, G.Zhang, N.Chen, M.Zhou, Y.Chen Int. J. Adv. Manufac. Technol. 113 (2021) 3027.

AB type 2D materials search by high-throughput DFT calculations

Masahiro FUKUDA

Institute for Solid State Physics,

The University of Tokyo, Kashiwa-no-ha, Kashiwa, Chiba 277-8581

Recent rapid research progress of two-dimensional (2D) materials have revealed that 2D materials are expected to be good candidates for future applications and devices. In our previous research, we construct a structure map [1] and a web-based database [2] of AB_2 type monolayers by high-throughput DFT calculations using OpenMX [3].

In this project, a structure map for AB type monolayers of 2016 compounds which are all the combinations of 63 elements selected from the periodic table (except for noble gases, lanthanoids and actinoids) is constructed by high-throughput calculations based on the DFT (GGA-PBE) with the symmetry-unconstrained geometry optimizations and variational cell optimizations starting from several structures such as ferromagnetic planar square lattice and planar honeycomb lattice structures as initial states. We classified the converged structures by planarity, the number of atoms in a unit cell, 2D Bravais lattice and space-group symmetry. The classification makes it clear that most of the AB type monoatomic layers are understood as basic planar structures and their derivation patterns such as the shape of the primitive cell, distortion, buckling and so on.

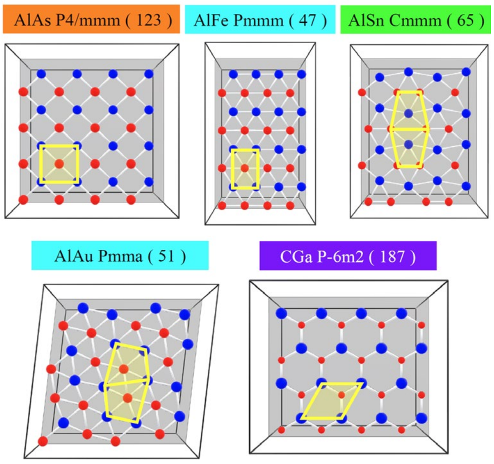

Fig.1: Examples of basic planar structures of AB type monolayers.

The genealogical classification helps us to understand phase transitions caused by lattice matching with a substrate, stacking layers, external bending, tensile and compressive stresses, and so on, when we invent new devices.

References

[1] M. Fukuda, J. Zhang, Y.-T. Lee, T. Ozaki, Mater. Adv., 2, 4392 (2021).

[2] Structure map and database of AB_2 type 2D materials (www.openmx-square.org/2d-ab2/).

[3] OpenMX, http://www.openmx-square.org

Charge storage mechanism of $Ti_3C_2\mathit{Ch}_2$ (Ch = O, S, Se, Te)

Kosuke Kawai, Masashi Okubo

Department of Electrical Engineering and Bioscience, School of Advanced Science and Engineering, Waseda University, 3-4-1 Okubo, Shinjuku-ku, Tokyo 169-8555

We have investigated the charge storage mechanisms of transition metal carbides (MXene) based on density functional theory (DFT) calculations. This year, we focused on the dependence on termination function group of a $Ti_3C_2T_x$ monolayer.

DFT calculations were performed with the Vienna ab initio simulation package (VASP). The projected augmented wave method and a plane basis set implemented in the VASP code were utilized with a cutoff energy of 520 eV and *k*-point sampling on a 4×4×2 grid.[1] The generalized gradient approximation of the Perdew–Burke–Ernzerhof exchange-correlation functional was used.[2] To prepare the slab model of $Ti_{27}C_{18}\mathit{Ch}_{18}$ (Ch = O, S, Se, Te), all Al atoms and a Ti_3C_2 monolayer were removed from $Ti_6Al_2C_4$, which was obtained from the Materials Project (ID: mp-3747), and expanded to a superstructure of 3×3×1 (**Fig. 1a**). Structure optimization calculations were carried out before and after adsorption of Zn atom on A–C sites (**Fig. 1b**). Bader charge analysis was performed using the script provided by Henkelman's group.[3]

Adsorption at A and B sites are preferred to that at C site (**Fig. 2a**) due to more coordination number with *Ch* atoms (3 for A and B site *vs*. 1 for C site). Averaged adsorption energy, which would be inversely proportional to

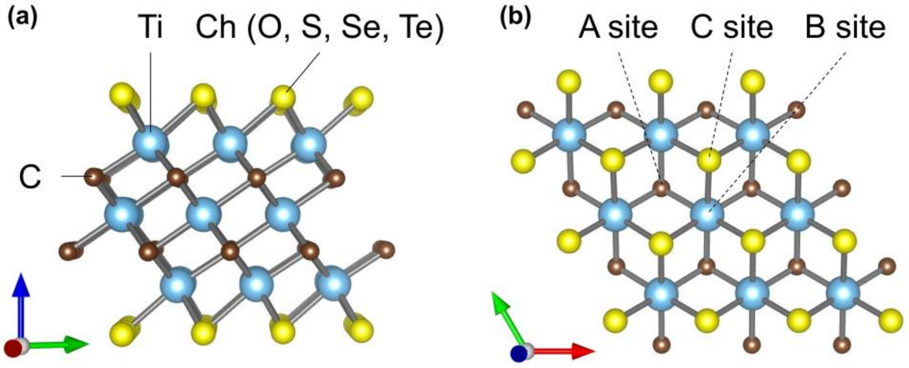

Fig. 1 (a) The model structure of $Ti_{27}C_{18}\mathit{Ch}_{18}$ (Ch = O, S, Se, Te) and (b) absorption sites on the $Ti_{27}C_{18}\mathit{Ch}_{18}$ monolayer. These structures were described using VESTA.[4]

charge/discharge rates, was in the order of Te < Se < O < S. Net charge transfer through Zn adsorption increased in the order of Te < Se < S < O (**Fig. 2b**), which likely arises from more electronic interaction with more electronegative atoms. These results imply that *Ch* = O is the most preferable to achieve both a large capacitance and fast charge/discharge rates simultaneously in electrochemical capacitors using Zn^{2+} ion as an adsorbed species.

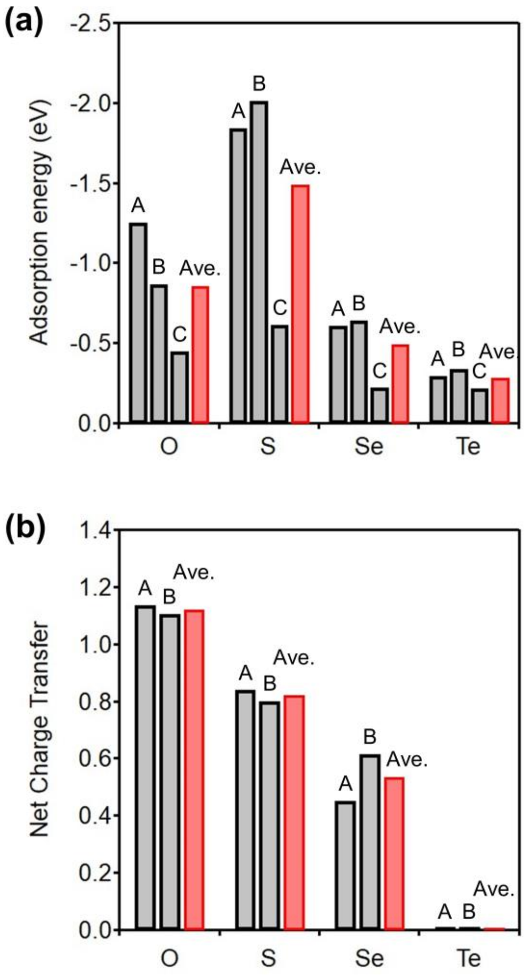

Fig. 2 (a) Adsorption energy and (b) net charge transfer for Zn atom on the $Ti_{27}C_{18}Ch_{18}$ (*Ch* = O, S, Se, Te) monolayer.

References

[1] G. Kresse, J. Furthmüller: Phys. Rev. B **54** (1996) 11169−11186.

[2] J. P. Perdew, K. Burke, M. Ernzerhof: Phys. Rev. Lett. **77** (1996) 3865−3868.

[3] W. Tang, E. Sanville, G. Henkelman: J. Phys.: Compute Mater. **21** (2009) 084204.

[4] K. Momma, F. Izumi: J. Appl. Crystallogr. **41** (2008) 653−658.

Diffusion behavior of hydrogen in tungsten-rhenium alloy

Kazuhito Ohsawa

Institute for Applied Mechanics, Kyushu University,

Kasuga-koen, Kasuga, Fukuoka 816-8580

Introduction

Tungsten (W) and its alloys are plausible candidates for plasma facing materials (PFMs) used in fusion reactors because of their excellent properties, e.g. high melting point, low hydrogen (H) solubility, and toughness for irradiation. However, a large amount of H and H isotopes are retained in vacancy (V) and vacancy type lattice defects in the W specimen nucleated under the irradiation circumstance. In particular, tritium (T) retention in the PFMs is a serious problem for safety operation of fusion reactors.

By the way, rhenium (Re) is created in the W specimen by nuclear transmutation in the neutron irradiation circumstance in fusion reactors. The effects of Re addition on the W specimen were investigated. Fortunately, the material properties are improved by the Re addition. For example, the H retention is decreased because vacancy nucleation is suppressed by the presence of Re. Besides, the plasticity is also improved. Therefore, the application of W-Re alloys are positively considered for the PFMs instead of pure W.

In the present work, properties of H in W-Re alloys is investigated. In particular, diffusion behavior of H in the W-Re alloys.

Simulation Method

The stable positions of H in the W-Re alloys and their energy levels are calculated in terms of first-principle calculations based on density functional theory. We use Vienna ab-initio simulation package (VASP). Large simulation cell composed of 5x5x5 bcc lattice (250 atoms) are used to avoid the effects of periodic boundary condition imposed on the simulation cell. The cut-off energy of plane wave is 350eV. Re density is assumed to be low (less than 0.8 atomic percent) in the W-Re alloys. Besides, energy profiles of H along the migration paths in the W-Re alloys are estimated by nudged elastic band (NEB) method.

We investigate energy profiles of H in two type of W-Re model alloys, including one and two Re atoms, as shown in FIG. 1 and 2, respectively.

Results

H atom in the pure W and W-Re alloy is suited at tetrahedral interstitial site (T-site). Migration energies are estimated as barrier heights for H to move to the neighboring T-sites. In pure W lattice, migration energy for H is estimated to be about 0.21eV.

In FIG. 1, T-sites (a-i) in the vicinity of a Re atom and migration path of H from T-site (a) to (i) are shown. T-site (a) and (b) situated nearest to the Re atom are geometrically equivalent. Energy profiles of H at the T-sites and along the migration path A are shown in FIG. 3. H located at T-site (a) and (b) are about 0.1 eV unstable, compared with that located far enough away from the Re. Therefore, T-sites close to Re are supposed to be unfavorable for H.

FIG. 2 shows likely migration path of H in the W-Re alloy including two Re atoms. The path is assumed to avoid T-sites close to the Re atoms. FIG. 4 shows energy profile of H along the migration path B from T-site (1) to (12). The migration path B keeps an appropriate distance from the two Re atoms. So, the migration energies of H to move the neighboring T-site are estimated to be 0.21-0.22 eV, which is almost same as that in pure W.

Summary and Discussion

According to H energy profile, H will keep away from Re in the W-Re alloys. Therefore, the higher Re density becomes, the lower H solubility becomes. If Re density is low, the migration energy of H in the W-Re alloy is estimated to be about 0.21eV, which is similar to that in pure W. However, the room available for H diffusion becomes smaller by the Re addition. So, H diffusivity in W-Re alloy would be lower, compared with that in pure W.

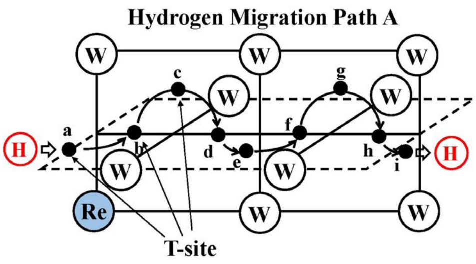

FIG. 1: Schematic view of W-Re alloy including one Re and H migration path A.

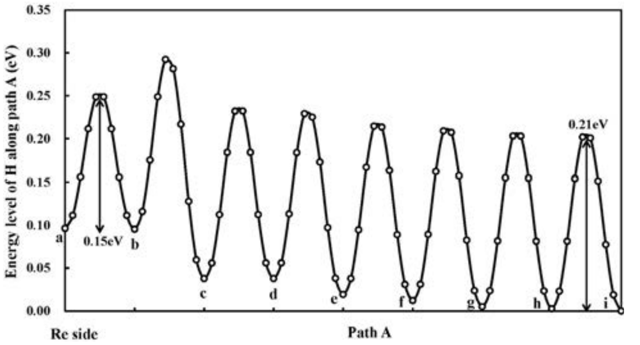

FIG. 3: Energy profile of H along the path A in FIG. 1.

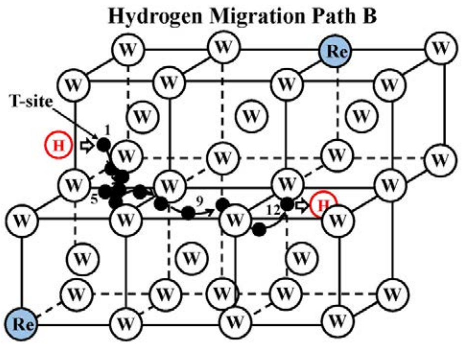

FIG. 2: Schematic view of W-Re alloy including two Re and H migration path B.

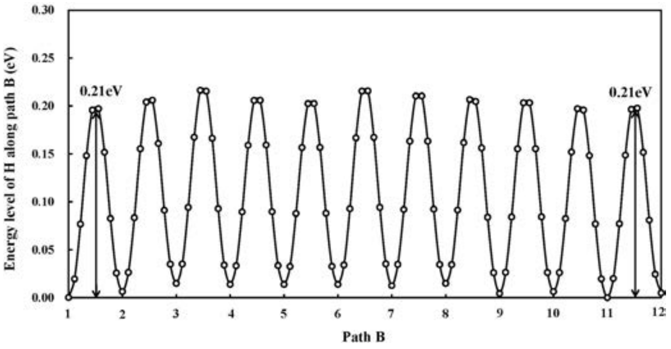

FIG. 4: Energy profile of H along the path B in FIG. 2.

Clarification of atomistic mechanism application of process design for adhesion interface between metal and plasma-treated fluoropolymers using first principles calculation

Yuji Ohkubo, Misa Nishino, and Kouji Inagaki
Graduate School of Engineering,
Osaka University, 2-1 Yamadaoka Suita, Osaka 565-0871

Recently, increasing frequency of the digital signals is necessary because the amount of information communication is increasing. However, the higher the frequency, the greater the transmission loss is. Therefore, polytetrafluoroethylene (PTFE) which has low relative dielectric constant and dielectric loss tangent is considered as suitable as dielectrics of high frequency printed wiring boards. However, PTFE has low adhesion property, so adhering PTFE to Cu is difficult. We have achieved generation of oxygen-containing functional groups and adhesion strength of 0.94 N/mm between PTFE and Cu when PTFE was He-plasma-treated at over 200℃ under atmospheric pressure[1]. However, the factor improving adhesion property, such as the chemical reaction at PTFE/Cu interface and the value of adsorption energy has not been investigated. Therefore, in this study, in order to explore functional groups contributing to improvement in adhesion property, the reaction between Cu(111) surface and fluorinated molecules was analyzed and the adsorption energy was calculated by means of first-principles calculations.

Our calculations were performed using the STATE (Simulation tool for atom technology) code with plane-wave basis and ultra-soft pseudopotential[2, 3]. The wave function and the charge density of cutoff energies were 36 and 400 Ry, respectively. Generalized gradient exchange-correlation functional based on Predew-Burke-Ernzerhof (PBE) was used for the exchange-correlation functional and DFT-D2 was used for the dispersion correction method[2, 3]. Cu surface was modeled Cu(111) 4×4 slab composed of 3 atomic layers. As the model of as-received PTFE, CF_3–CF_3 was calculated. In addition, CF_2=CF_2, CF_3–CF_2–$OO^{\cdot}$, CF_3–CF_2–OH, and CF_3–CF=O were calculated as the model of plasma-treated PTFE. These were the models of molecule containing oxygen-containing functional groups observed by C1s-XPS spectrum of the plasma-treated PTFE surface. Cu surface, fluorinated molecules, and adsorption systems were optimized then total energies were calculated. The adsorption energy was defined as the difference between the sum of total energy of Cu surface and fluorinated molecules and total energy of adsorption system.

Fig. 1 shows the optimized atomic geometries for $CF_3–CF_3$. $CF_3–CF_3$ was not bonded to Cu surface and the value of adsorption energy was 0.25 eV in case of both on top site and on bridge site. This is because C–F bonding energy of 5.02 eV[4] is large and C–F bond is stable. After optimization for $CF_3–CF_2–OO^{\cdot}$, O–O bond in $CF_3–CF_2–OO^{\cdot}$ was broken and $CF_3–CF_2–O^{\cdot}$ and O were bonded to Cu surface, respectively. In this case, the sum of adsorption energies of $CF_3–CF_2–O^{\cdot}$ and O was calculated as the adsorption energy of $CF_3–CF_2–OO^{\cdot}$. Therefore, the calculation of adsorption energy of $CF_3–CF_2–O^{\cdot}$ which is broken O–O bond at initial state was added. **Fig. 2** shows the optimized atomic geometries for $CF_3–CF_2–OO^{\cdot}$ and $CF_3–CF_2–O^{\cdot}$. The adsorption energy was 3.10 eV, and the highest adsorption energy was obtained. **Table 1** shows the value of adsorption energies by calculation. The value of adsorption energies of $CF_3–CF_3$, $CF_2=CF_2$, $CF_3–CF_2–OO^{\cdot}$, $CF_3–CF_2–O^{\cdot}$, and $CF_3–CF=O$ was 0.25 eV, 0.68 eV, 4.73 eV, 3.10 eV, 0.60 eV, and 0.74 eV, respectively. In case of molecules containing $COO^{\cdot}$, the adsorption energy was the highest and the molecule was stable.

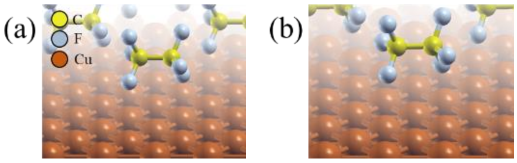

Fig. 1 Atomic geometries for $CF_3–CF_3$ model (a) on top site and (b) on bridge site.

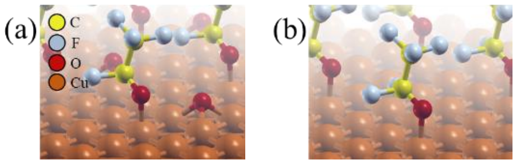

Fig. 2 Atomic geometries for (a) $CF_3–CF_2–OO^{\cdot}$ model and (b) $CF_3–CF_2–O^{\cdot}$ model.

Table 1 Value of adsorption energies on Cu(111).

Molecule	Adsorption energy [eV]
$CF_3–CF_3$	0.25
$CF_2=CF_2$	0.60
$CF_3–CF_2–OO^{\cdot}$	4.73
($CF_3–CF_2–O^{\cdot}$	3.10)
$CF_3–CF_2–OH$	0.60
$CF_3–CF=O$	0.39

In this study, the functional groups contributing to improvement in adhesion property were explored by calculating the adsorption energies by means of first-principles calculations. From the result of calculations, the adsorption energy of molecules containing $COO^{\cdot}$ was the highest. Therefore, generating the functional groups containing $COO^{\cdot}$ is possible to generate PTFE surface having high adhesion property. However, the calculations about Cu surface having different miller indices are needed because Cu surface has not only Cu(111), but also Cu(100) and Cu(110). In addition, the calculations copper oxide such as CuO and Cu_2O are also needed because Cu surface is likely to be oxidized.

References

[1] M. nishino et al., INTERFINISH2020 Abstract, C-SEP06-004 (2020) 210.

[2] K. Toyoda et al., *J. Chem. Phys.* **132** (2010) 134703.

[3] K. Toyoda et al., *J. Nanosci. Nanotechnol.* **11** (2011) 2836–2843.

[4] H. O. Pritchard et al., *Chem. Rev.* **55** (1955) 745–786.

First-principles electronic structure calculation of double-perovskite photocatalyst

Kazume NISHIDATE
Department of Systems Innovation Engineering, Graduate School of Science and Engineering, Iwate University, 4-3-5 Ueda, Morioka, Iwate, 020-8551

Double-perovskite oxides, $A_2B'^{\,\mathrm{III}}B''^{\,\mathrm{V}}O_6$, have been extensively studied due to their intriguing physical and chemical properties originating in their mixed valence nature[1]. Above all, $Ba_2B'^{\,\mathrm{III}}B''^{\,\mathrm{V}}O_6$ was found to show an efficient photo catalytic activity to dissolve water molecules into oxygen and hydrogen gases. While TiO_2 has been known to be an practical photo catalyst, it uses only the ultraviolet rays which is less than 3 % of the sunlight pouring on the earth surface. On the other hand, the catalytic function of $Ba_2B'^{\,\mathrm{III}}B''^{\,\mathrm{V}}O_6$ double perovskite is activated under visible light and hence has a great potential as a photo catalyst in daily use. In this work, we study the surface electronic properties of Ba_2PrBiO_6 double-perovskites. We used the DFT code of Quantum ESPRESSO throughout our study. PAW potentials were employed to represent the core region and the PBE functional was applied for exchange correlation. We also used the HSE06 hybrid functional to evaluate the band gap values. We constructed slab system with three units along the z-axis exposing (001) surface. The vacuum region was taken to be 20 Å height. Where two types of surfaces can be exposed as the (001), namely, the Ba-O polar-surface and the Pr-Bi polar-surface. We calculated the surface band structures and identified the band gaps as well as their work functions for these polar-surfaces.

As an example, we show the Ba-O surface band structure calculated within the PBE exchange-correlation functional (Figure 1). Top components of the valence band are comprised of oxygen orbitals, while the isolated bottom part of the conduction band is derived from the Bi orbitals. The surface band gap value was estimated to be 1.93 eV within the HSE hybrid functional level. The band gap value of the bulk system with the HSE is found to be 3.70 eV, therefore we think that the bulk band gap is significantly modified at the surface region. However, experimentally obtained optical band gap value is 1.07 eV and which is still half of the surface band gap obtained in this study. We think the origin of the discrepancy is the B-site disordering (Pr↔Bi). Now, we have been studying the effect of the B-site disordering by evaluating the band gap of the system.

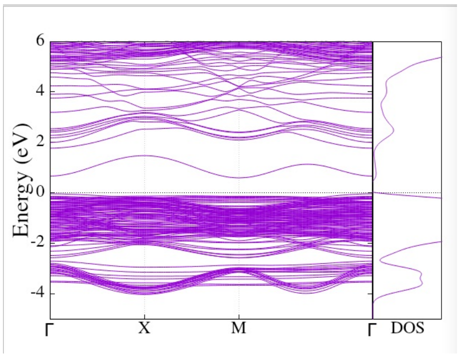

Figure 1: Ba-O surface band structure.

References

[1] S. Vasala and M. Karppinen: Prog. in Solid State Chem. **43** (2015) 1.

Electronic structure calculation for a transition-metal monoxide using a four-atom-configuration model

Takayuki MAKINO

Research Center for Development of Far-Infrared Region,

University of Fukui, Bunkyo, Fukui, 910-8507

We have studied an electronic property of a transition-metal monoxide. Recently, this monoxide was reported to have an indirect gap whose energy is *ca*. 0.2 eV [1]. It is well known that these compounds have been poorly described by the density functional theory (DFT) with using commonly used approximate functionals. It was very difficult for us to reproduce this insulating ground state of this monoxide, only with the simple DFT+*U* calculation. The word “simple” means an application of only the on-site Hubbard energy on the *d* electrons. In this work, we explain about several extensions [2] that we learned from literatures [2] and used to reproduce the insulating ground state. We used the `pwscf` codes included in the `Quantum ESPRESSO` (QE) package [3]. We performed the following jobs to obtain the theoretical electronic and vibronic properties.

Self-Consistent Field Calculation – No matter what physical quantity is calculated; one must first determine the electron density. We used a 50 Ry energy cutoff for the electronic wave functions and a small smearing width of 0.02 Ry which required a 6×6×6 *k*-point mesh. Adopted pseudopotentials are based on the projector augmented-wave method.

Introduction of Hubbard *U* – It should be noted that in addition to the Hubbard *U* on the *d* orbital (U_d) in the transition-metal element, we introduced that (U_p) on the *p* orbital of the oxygen atom. An additional introduction of U_p is believed to be useful to open the gap (i.e., leading to a correct insulating ground state) due to the existence of the exchange-induced splitting. The value of U_p (*ca*. 21 eV) has been determined by the self-consistent linear response approach. On the other hand, if we tried to decide the value of U_d self-consistently, we could not reproduce the insulating ground state theoretically. Therefore, as a compromise, we set U_d of *ca*. 4.4 eV. We did not adopt the magnetic exchange *J* parameter for this calculation.

Spin-polarized DFT+*U* – The primitive cell of the rock-salt structure is composed of two atoms (one is anion, while the other is cation). To implement the antiferromagnetic ordering, we adopted four-atom-configuration including two cations with up and down spins. By adopting this configuration, we can expect an effective lowering of the symmetry which may be useful to open the gap.

Structural optimization – We also optimized the structure by using the Broyden–Fletcher–Goldfarb–Shanno method. This turned out to be essential to make the Fermi energy lie in the splitting region of the *d* electrons. Otherwise, one cannot reproduce the insulating ground structure with the experimental lattice spacings. This resulted in the structure with the symmetry C_{2h} (2/m). It is known that the theoretical ground state depends on the starting eigenstates (occupation) during the spin-polarized DFT+*U* calculations. In some of transition-metal monoxides such as cubic FeO and CuO, this adjustment is essential to reproduce the insulating ground state [2]. This is also true in our case. The example of the output is shown in Fig. 1.

Band dispersion and electronic DOS calculations –It should be noted that all of the above-mentioned extensions such as non-zero U_p, the spin polarization, structure optimization, and occupational adjustments turned out to be essential to open an indirect gap (0.55 eV) in our case with a transition between L and Γ points. This is qualitatively consistent with the experimental observation [1]. The ground state obtained in the four-atom cell has slightly lower energy per the cation-anion pair compared to the nonmagnetic and metallic two-atom primitive cell, and thus the antiferromagnetic insulating ground state is energetically favored.

The result of the density-of-states calculation suggests that both the valence and conduction bands are mainly composed of the *d* electron, consistent with the narrow Mott-Hubbard gap [1].

```
atom    1   Tr[ns(na)] (up, down, total) =
2.48039  1.01275  3.49314
   spin  1
    eigenvalues:
  0.292  0.292  0.448  0.449  1.000
                         ⋮
   spin  2
    eigenvalues:
  0.151  0.151  0.192  0.259  0.259
                         ⋮
```

Fig. 1: An example of the orbital level output after the initial eigenvalue settings are reflected.

References

[1] K. Kaminaga *et al.*, Appl. Phys. Lett. **108**, 1 (2016).

[2] B. Himmetoglu *et al.*, Phys. Rev. B. **84**, 115108 (2011).

[3] P. Giannozzi *et al.*, J. Phys.: Condens. Matter **21,** 395502 (2009).

Interactions in transition-metal-phthalocyanine monolayer weakly bound to metal surfaces

Tetsuya ARUGA
Department of Chemistry, Graduate School of Science, Kyoto University
Kitashirakawa-Oiwakecho, Sakyo, Kyoto 606-8502

Phthalocyanine is a π-conjugated planar molecule with a size of $\sim 1.2 \times 1.2$ nm^2. Two H atoms at the center of the molecule can be substituted by a variety of transition metal ions (M^{2+}), yielding a transition metal phthalocyanine (MPc). The M^{2+} ions are coordinated by lone pairs of four N atoms arranged in a planar tetragonal geometry. The adsorption of MPc on transition metal surfaces [1, 2] has been widely studied experimentally.

We recently have studied experimentally the adsorption and ordering of metal phthalocyanine molecules on a bilayer indium film fabricated on Si(111) surface [3, 4, 5] , on which the interaction of MPc with the substrate is expected to be weaker than the transition-metals substrates. Our aim is to establish nearly-free-standing transition metal phthalocyanine monolayers effectively decoupled from the substrate.

The experimental studies of MPc adsorption on metal surfaces commonly show that the phthalocyanine molecules form monolayers with long range order, in which the symmetry axes of molecules are aligned at a particular azimuthal angle which is not parallel to the axes of the translational symmetry of the two-dimensional lattice the molecules form. This has sometimes been ascribed to the direct interaction of nitrogen atoms (imide N) of the molecule with the substrate metal atoms.

Our computational result suggests that the electronic interaction between phthalocyanine and In substrate is indeed week due to a large van der Waals gap between the molecular plane and the topmost In atomic layer of the substrate and further to the weak electronic interaction of the π orbitals of the molecules with the *sp* electrons of the In bilayer.

In order to highlight the intermolecular interaction, we studied the “free-standing” MPc monolayer by first-principles calculation by VASP. The molecules were assumed to be ordered in a nearly square translational symmetry which exactly is the one observed on In/Si(111). Note that the characteristics of the molecular arrangement is more or less similar on other metal surfaces studied. The total energy of the molecular film was calculated as a function of the azimuthal rotation angle of the molecule. It was found that the total energy is minimized at an azimuthal angle close to that observed experimentally for the molecule adsorbed on many metallic surfaces. This implies that the molecular configuration in the MPc monolayer is governed by the intermolecular interaction. We have examined several possibilities of the physical origin of the in-plane intermolecular interaction between MPc molecules and succeeded in identifying the interaction that stabilizes the free-standing MPc monolayer.

We also studied the d electronic structure of M^{2+} ions in the metal phthalocyanine adsorbed on In/Si(111) surface to probe the interaction with the substrate *sp* electrons. A good correspondence between the density of states measured by photoemission experiments with those obtained by the calculation yielded an insight into the interaction between central metal ions and metallic substrate in this system.

References

[1] H. Koshida, Y. Takahashi, H. Okuyama, S. Hatta, and T. Aruga, e-Journal of Surface Science and Nanotechnology, **20** (2022) 25.

[2] H. Koshida, H. Okuyama, S. Hatta, T. Aruga, Y. Hamamoto, I. Hamada, Y. Morikawa, J. Phys. Chem. C **124** (2020) 17696.

[3] S. Terakawa, S. Hatta, H. Okuyama, T. Aruga, Phys. Rev. B **105** (2022) 125402.

[4] S. Terakawa, S. Hatta, H. Okuyama, T. Aruga, Phys. Rev. B **100** (2019) 115428.

[5] J. W. Park and M. H. Kang, Phys. Rev. Lett. **109** (2012) 166102.

Electronic Structure and Fermiology of *d*-electron compounds

Isaki Kinjo, Juno Iraha, Yasutomi Tatetsu[1], and Takahiro Maehira[2]
Graduate school of Engineering and Science, Nishihara, Okinawa 903-0213
[1]*Center for Liberal Arts Education, Meio University, Nago, Okinawa 905-8585*
[2]*Faculty of Science, University of the Ryukyus, Nishihara, Okinawa 903-0213*

The monocarbides of transition elements from the group-IVB, -VB, and -VIB columns of the Periodic Table are well known for their great hardness and strength, high melting temperatures, metal-like thermal and electrical resistivities, nonstoichiometry, and superconducting properties [1, 2]. Most experimental and theoretical efforts to understand the fundamental properties of these technologically important materials have focused thus far on the group-IVB and -VB carbides, all of which crystallize with the cubic rocksalt structure. The compound WC has two phases: a low temperature phase is hexagonal WC and a high temperature phase above 2525°C is cubic WC. We studied simple hexagonal WC with a space group of P6m2 which contains one molecule in the unit cell. The lattice parameters a and c are 2.906 and 2.837 Å, respectively [1]. The calculation for the energy band structures was carried out by using the OpenMX code(`http://www.openmx-square.org/`). First, we discuss the calculated results for WC as shown in Figure 1, in which we depict the energy band structure along the symmetry axes in the Brillouin zone, which is shown in Figure 1, in the energy region from -20.0 to 20.0 eV. The Fermi level E_{F} is at 0.0 eV. for WC and indicated by dashed lines in Figure 1. With respect to the energy band structure near E_{F}, we emphasize that there is always hybridization between the W 5d and C 2p states in WC. The total number of holes is equal to that of electrons, which represents that WC is a compensated metal. We move to discuss the Fermi surface of WC. Three bands cross the E_{F}, therefore WC has three Fermi surfaces in Figure 2. The color on the Fermi surface illustrates the distribution of the Fermi velocity components. Fermi surfaces for WC centered at the A, K, and M points, respectively. The 5th band has one dog's bone-like hole sheet centered at the each Γ point. The Fermi surfaces were calculated with FermiSurfer [3].

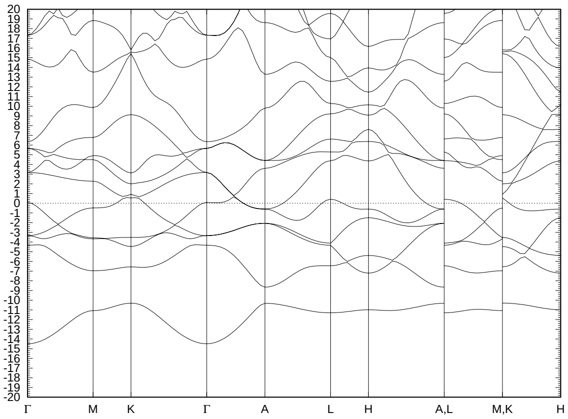

Figure 1: The energy band structure for WC, the symmetry points and axis for the simple hexagonal-type structure. E_{F} indicates the position of the Fermi level.

ReO$_3$-type structures can be described as ABX$_3$ perovskites in which the A-cation site is unoccupied. They therefore have the general composition BX$_3$, where B is normally a cation and X is a bridging anion. The chem-

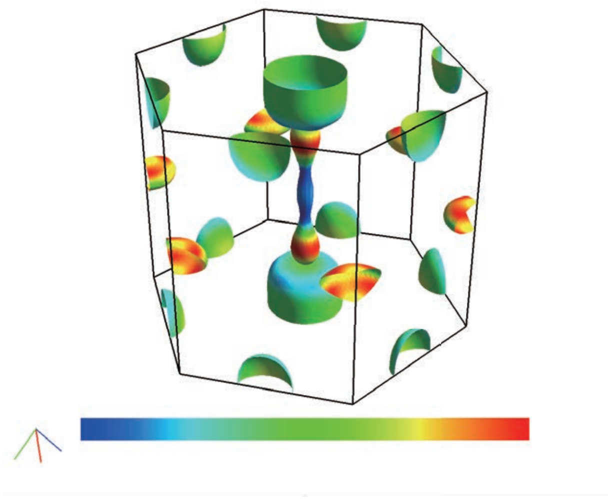

Figure 2: The Fermi surface for WC centered at Γ point. Colors indicate the Fermi velocity components on the Fermi surface.

ical diversity of such structures is very broad, ranging from simple oxides and fluorides, such as WO_3 and AlF_3, to more complex systems in which the bridging anion is polyatomic, as in the Prussian blue-related cyanides such as $Fe(CN)_3$ and $CoPt(CN)_6$. We found that the energy bands near the Fermi level are mainly because of the hybridization between the Re 5d and O 2p electrons in Figure 3. Since the lowest twelve bands are fully occupied, as shown in Figure 3, the next three bands are partially occupied, while higher bands are empty. This compound is compensated metal because of having two chemical units in the unit cell. The calculated total density of states (DOS) for ReO_3 is shown in Figure 4, in the energy region from -25.0 to 25.0 eV. The total density of states for ReO_3 is shown by the solid black line and the s, p, d and f states are shown by the solid color lines, respectively. This figure tells us that the DOS of the d states is higher than that of the f states at the Fermi level. The Fermi surface of ReO_3 is found to consists of two hole sheets and two electron sheets.

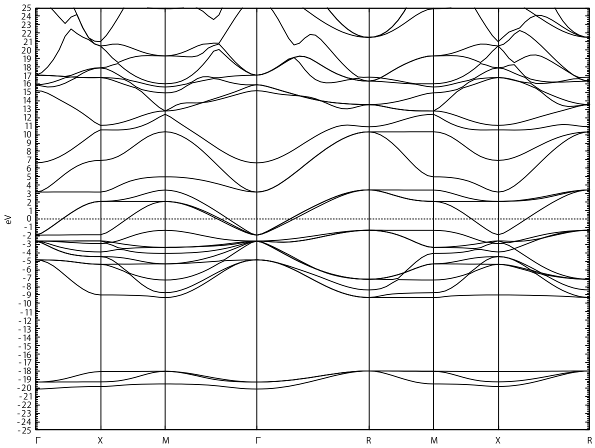

Figure 3: The energy band structure for ReO_3. E_F indicates the position of the Fermi level.

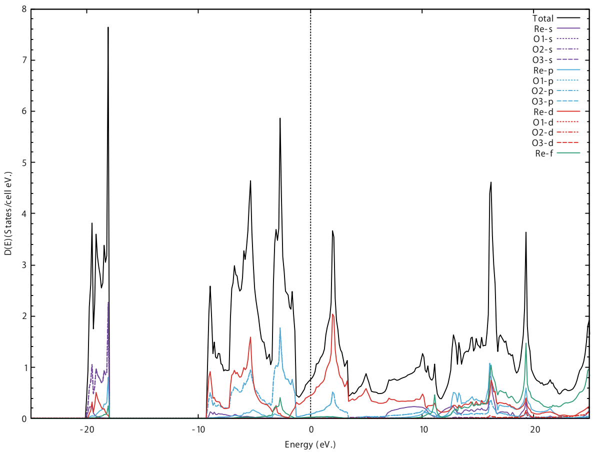

Figure 4: The density of states for ReO_3. E_F indicates the position of the Fermi level shown by the dashed line.

References

[1] L. E. Toth: *Transition Metal Carbides and Nitrides.*, Academic, New York(1971).

[2] E.K. Storms: *The Refractory Carbides.*, Academic, New York(1967).

[3] M. Kawamura: Phys. Rev. B 89, 094515 (2014).

First-principles Study of Defects of Magnesium Alloys

Daisuke Matsunaka
Department of Mechanical Systems Engineering,
Shinshu University, 4-17-1 Wakasato, Nagano 380-8553

Magnesium (Mg) has been of increasingly interest from the engineering viewpoint, because of its low density and relatively high specific strength.

For molecular dynamics simulation widely used to obtain atomic-level information on strength and deformation of materials, an interatomic potential is very important. In this study, a highly accurate interatomic potential of pure magnesium was developed based on artificial neural network (ANN)[1]. The reference data for training the ANN potential were systematically constructed using density functional theory (DFT) calculations. The developed ANN potential can accurately estimate lattice constants and elastic moduli. Additionally, generalized stacking fault energies of slip systems in magnesium calculated with the ANN potential are also in agreement with the DFT results. We also developed the ANN potentials for several kinds of magnesium alloys; Mg-Y, Mg-Ca, Mg-Al, Mg-Zn. The ANN potentials of magnesium alloys successfully described interactions between a basal dislocation and each solute atom, consistent with the previous DFT study.

Several magnesium alloys include long period stacking ordered (LPSO) structures which consist of periodic arrangement of basal stacking faults and enrichment of solute atoms in the vicinity of the stacking faults. The solute-enriched layers give rise to a significant mass change as well as local stiffness due to the L12-type solute clusters, which affect the lattice vibration properties of the LPSO structures. Our previous study showed that for a heavy enough mass change, a phonon-mediated interaction of the solute-enriched layers is attractive and stabilizes the periodic stacking of the solute-enriched layers. In this study, we analyze phonon states of LPSO magnesium alloys, using first-principles calculations. We calculate phonon density of states and phonon dispersion based on the density functional perturbation theory.

References

[1] T. Nagata: Master Thesis, Shinshu Univ. (2022).

[2] D. Matsunaka, K. Oboso, Y. Shiihara and H. Mori: Proceedings of CMD2021, 204.

3.3 Strongly Correlated Quantum Systems

Tensor-Network Renormalization-Group Study of Critical Phenomena

Naoki KAWASHIMA

Institute for Solid State Physics,

The University of Tokyo, Kashiwa-no-ha, Kashiwa, Chiba 277-8581

We developed efficient methods, algorithms, parallelized programs, and sometimes new concepts, based on novel numerical techniques including the tensor network (TN) method and applied them to relevant physical problems. To list subjects of our research in 2021, (1) development of new numerical methods based on the TN representation [1,2], (2) study of TN ground states such as Kitaev spin liquid [3], (3) study of spin liquid in frustrated spin systems [4], (4) development of open-source applications [5].

In [1], we re-considered the method for extracting the critical information from the RSRG calculation with TNs. The most common method for obtaining the scaling dimension is to form a transfer matrix from the scale-invariant tensor. Then, we can obtain the scaling dimensions from its eigenvalues using the relationship derived from the conformal field theory. However, this method has not been generalized to three or higher dimensions. In our scheme, we construct a super-operator that represents the RSRG tarnsformation. Without explicitly relying on the CFT, we derive the relashion between the eigenvalues of the super-operator and the scaling dimensions. Our benchmark calculation on the 2D Ising model established validity of this basic idea. The new scheme may provide a direct method for estimating the scaling dimensions in higher dimensions.

In [2], we proposed a method for obtaining the excitation spectrum based on TN calculations. In this method, we consider an imprurity tensor representing a locally excited state, and construct an eigenvalue equation in the space of such excited states, which can be block-diagonalized by Frourier transformation. By diagonalizing each block we can obtain excitation spectra of various excitations. We applied this scheme to one-dimensional quantum spin chain and successfully computed its excited states and the dynamical structure factor. We further investigated entanglement properties of excited states.

In [3], we considered in the Kitaev model on the honeycomb lattice and its extention to S=1. The models with arbitrary spin quantum numbers are not exactly solvable in contrast to the well-known Kitaev spin liquid solution of the spin-1/2 system. To unveil the important difference between these states, we use the tensor-network wave functions, which proved, in our previous work, to be essential in capturing the nature of the Kitaev spin liquid. We found that the distinct sign structures of the tensor-network wave function for the integer- and half-integer-spin quantum spin liquids are responsible for completely different ground states in the spatially anisotropic limit.

In [4], we investigated S=1/2 XXZ ladder system with four-spin interaction. The model can be viewed as a one-dimensional variant of the J-Q model on a square lattice. By means of variational uniform matrix product state (VUMPS) calculations and an effective field theory, we determine the phase diagram of the model and present evidence that the Néel-VBS transition is continuous and belongs to the Gaussian universality class with the central charge c=1. The full phase diagram consists of 8 distinct phases including magnetically ordered phases, Haldane-like phases, and VBS phases.

In [5], we developed DSQSS, an open-source software for quantum Monte Carlo simulation of lattice system. In [6], we applied it to the Bose-Hubbard model in the case of extereme dilution to clarify the validity of the analytical predictions for the universal behavior of the model in this region. We confirmed the universal behaviors. In addition, we estimated model-dependent parameters such as the s-wave scattering length in a good agreement with the prediction as well as the non-universal correction term of the third order in the particle density, which has never been estimated before.

References

[1] X. Lyu, R. G. Xu and N. Kawashima, Phys. Rev. Research 3, 023048 (2021).

[2] W.-L. Tu, H.-K. Wu, N. Schuch, N. Kawashima and J.-Y. Chen, Phys. Rev. B 103, 205155 (2021).

[3] H.-Y. Lee, T. Suzuki, Y. B. Kim and N. Kawashima, Phys. Rev. B 104, 024417 (2021).

[4] T. Ogino, S. Furukawa, R. Kaneko, S. Morita and N. Kawashima, Phys. Rev. B 104, 075135 (2021).

[5] Y. Motoyama, K. Yoshimi, A. Masaki-Kato, T. Kato and N. Kawashima, Comput. Phys. Commun. 264, 107944 (2021).

[6] A. Masaki-Kato, Y. Motoyama and N. Kawashima, J. Phys. Soc. Jpn. 90, 034711 (2022).

Quantum Spin Liquids

Masatoshi IMADA
Toyota Physical and Chemical Research Institute,
41-1 Yokomichi, Nagakute, Aichi, 480-1192
and
Research Institute for Sicence and Engineering, Waseda University,
3-4-1 Okubo, Shinjuku-ku, Tokyo, 169-8555

1 Introduction

In this project, we have studied mechanisms of fractionalization in strongly correlated electron systems. One is the electron fractionalization, where an electron near the Mott insulator is splintered into a conventional quasipaticle and a dark fermion, which triggers the high temperature superconductivity in the copper oxide superconductors [1]. The second is the fractionalization of an electronic spin into spinons leading to quantum spin liquids.

Two types of quantum spin liquids were established by a high-accuracy quantum many-body solver that applies machine learning algorithm. In the quantum spin liquids, spin orientations are not ordered even at zero temperature. The first example is the case of J_1-J_2 Heisenberg model on the square lattice, where the geometrical frustration effect is crucial [3].

The other case is found in the Mott insulating phase of a molecular solid, in which the existence of the quantum spin liquid has been proposed for decades without clear understanding of its nature [4]. For the latter case, experimental results are reproduced with one-to-one correspondence by employing the first-principles methods based on real materials without adjustable parameters. In both cases, “spinon” emerging from the fractionalization of the ordinary spin excitation is suggested to be an elementary excitation, with gapless Dirac-type dispersion in the excitation structure. They also share long-ranged quantum entanglement of spins and algebraic decay of spin correlation as common properties. However, there exists difference in that the isotropic 2D excitation in the J_1-J_2 Heisenberg model is contrasted with the strong 1D anisotropy in the molecular solid. These two typical examples offer a clue toward the understanding of the universality and diversity of the physics of quantum entanglement. In the present project, we also studied a possible spin liquid on a 3D pyrochlore lattice, which will be reported elsewhere. In this report, we focus on the *ab initio* study of quantum spin liquid in the molecular solid [4].

2 Quantum spin liquid in molecular solid

Molecular solids host various electronic phases. Especially, β'-X[Pd(dmit)$_2$]$_2$ with X=EtMe$_3$Sb shows quantum spin-liquid (QSL) properties. We have studied five molecular-solid compounds with different X using 2D *ab initio* single-band effective Hamiltonian derived in Ref. [5, 6] in the form

$$\mathcal{H} = -\sum_{\sigma}\sum_{i,j} t_{ij} c^{\dagger}_{i\sigma} c_{j\sigma} + \sum_{i} U n_{i\uparrow} n_{i\downarrow} + \sum_{i<j} V_{ij}(n_i - 1)(n_j - 1), \qquad (1)$$

where i, j represent the dimer indices, and $c^{\dagger}_{i\sigma}$ ($c_{i\sigma}$) is the creation (annihilation) opera-

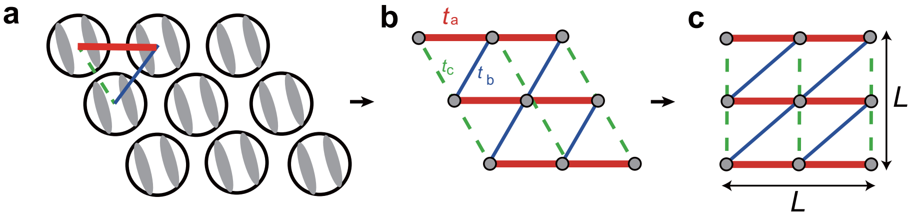

Figure 1: Lattice structure of β'-$X[\mathrm{Pd(dmit)_2}]_2$ [4]. **a**: Schematic triangular structure of β'-$X[\mathrm{Pd(dmit)_2}]_2$ consisting of dimerized $\mathrm{Pd(dmit)_2}$ molecules, where a $\mathrm{Pd(dmit)_2}$ molecule is depicted as a long gray oval. **b**: Modeled triangular lattice with three different electronic transfers. The strongest, middle and weakest transfers, t_a (on the red bond), t_b (on the blue bond), and t_c (on the green bond), respectively. **c**: Deformed structure on a $L \times L$ lattice with the system size $N_s = L^2$ used in the present calculation.

tor of electrons with spin σ ($=\uparrow$ or $\downarrow$) at the i-th Wannier orbital, and the number operator is $n_i = \sum_\sigma n_{i\sigma}$ with $n_{i\sigma} = c^\dagger_{i\sigma} c_{i\sigma}$. Here, t_{ij} is the hopping parameters depending on the relative coordinate vector $\boldsymbol{r}_i - \boldsymbol{r}_j$, where $\boldsymbol{r}_i$ is the position vector of the center of the i-th Wannier orbital. For t_{ij}, the nearest neighbor pair of $\boldsymbol{r}_i$ and $\boldsymbol{r}_j$ in each triangular direction is retained. U and V_{ij} are the screened on-site and off-site Coulomb interactions, respectively. V_{ij} is retained up to the third neighbor. The lattice structure we study is illustrated in Fig. 1. A variational Monte Carlo (VMC) method [7, 8, 9] is applied to the *ab initio* Hamiltonians to reach highly accurate ground states.

We have correctly reproduced experimental phase diagram with antiferromagnetic order for X=$\mathrm{Me_4P}$, $\mathrm{Me_4As}$, $\mathrm{Me_4Sb}$, $\mathrm{Et_2Me_2As}$ and a QSL for X=$\mathrm{EtMe_3Sb}$ without adjustable parameters [4]. as is shown in Fig. 2. It allows us to study the nature of the QSL at the microscopic level. The spin-spin correlations in real space $C(\boldsymbol{r})$ for the QSL state of X=$\mathrm{EtMe_3Sb}$ indicates a power law $C(\boldsymbol{r}) \propto |\boldsymbol{r}|^{-p}$ with $p = 1.88 \pm 0.01$ in the strongest transfer direction suggesting the algebraic QSL with the gapless excitation. On the other hand, in the ohter directions, $C(\boldsymbol{r}) \propto \exp[-|\boldsymbol{r}|/\xi_\perp]$ shows expnential decay with the correlation length $\xi_\perp \sim 1.33 \pm 0.04$. Therefore, the QSL for X=$\mathrm{EtMe_3Sb}$ exhibits 1D nature. It indicates a dimensional reduction from 2D to 1D. The 1D nature indeed accounts for the experimental specific heat, thermal conductivity and magnetic susceptibility. The identified QSL, however, preserves 2D nature as well consistently with spin fractionalization into spinon with Dirac-like gapless excitations and reveals duality bridging the 1D and 2D QSLs. The power $p \sim 1.9$ is similar to the value obtained for the QSL in the square-lattice J_1-J_2 Heisenberg model with the nearest (J_1) and the next-nearest-neighbor (J_2) exchange interactions, where $p \sim 1.4$-1.7 [2]. However, in sharp contrast to isotropic 2D spin correlation in the J_1-J_2 model, the correlation decays exponentially in the interchain direction.

On the other hand, the signature of the 2D properties is also found in a prominent peak of the spin structure factor at $(\pi, 0)$ and in the structure of the ground-state wave function itself [4]. In fact the excitation structure inferred from the wave-function form strongly supports the fractionalization of a spin into two spinons, similarly to the J_1-J_2 model [3]. The finding of the two types of QSL clarifies universal and system-dependent features of the QSL.

This is a combined report for E project 2020-Ea-0005 and 2020-Eb-0005 as well as shared project for Fugaku project. The present work was obtained by the collaboration with Kota

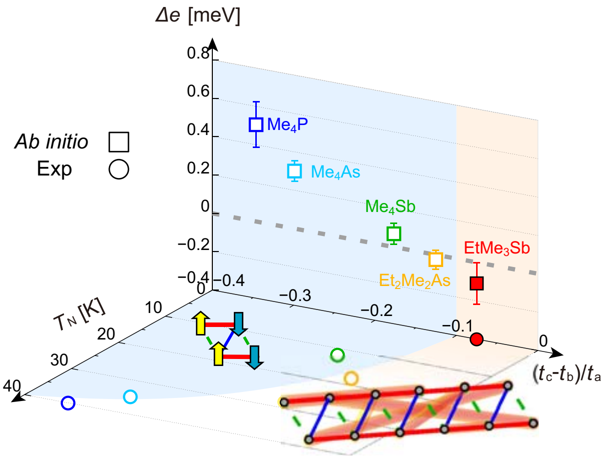

Figure 2: Ground-state phase diagram revealed by *ab initio* simulations (vertical plane), which shows agreement with the experimental phase diagram (bottom plane) [4].

Ido, Kazuyoshi Yoshimi and Takahiro Misawa. The work is also supported by JSPS Kakenhi 16H06345, the RIKEN Center for Computational Science under the HPCI project (hp200132,hp210163, hp220166). The computation in this work has been done partially using the facilities of the Supercomputer Center, the Institute for Solid State Physics, the University of Tokyo. This project has used the software mVMC.

References

[1] M. Imada: J. Phys. Soc. Jpn. **90** (2021) 111009.

[2] Y. Nomura and M. Imada: Phys. Rev. X **11** (2021) 031034.

[3] Y. Nomura and M. Imada: Phys. Rev. X **11** (2021) 031034.

[4] K. Ido, K. Yoshimi, T. Misawa and M. Imada: npj Quantum Materials: **7** (2022) 48.

[5] K. Yoshimi, T. Misawa and T. Tsumuraya: Phys. Rev. Research **2**, (2020) 032072(R).

[6] K. Yoshimi, T. Tsumuraya and T. Misawa: Phys. Rev. Research **3** (2021) 043224.

[7] D. Tahara, and M. Imada: J. Phys. Soc. Jpn. **77** (2008) 114701.

[8] T. Misawa *et al.* Comput. Phys. Commun. **235** (2019) 447.

[9] Y. Nomura, A. S. Darmawan, Y. Yamaji and M. Imada: Phys. Rev. B **96** (2017) 205152.

Numerical studies of Mott transitions in quantum spin liquid candidates

Youhei YAMAJI
Center for Green Research on Energy and Environmental Materials,
National Institute for Materials Science
Namiki, Tsukuba-shi, Ibaraki 305-0044

The Kitaev model is a unique solvable two-dimensional quantum system [1]. As shown by Kitaev, the ground state of the model hamiltonian is a quantum spin liquid. Later, Jackeli and Khaliullin proposed that the effective low-energy hamiltonian of Mott insulating phases of honeycomb iridium oxides such as $\mathrm{Na_2IrO_3}$ could be the Kitaev model [2]. Although the ground state of $\mathrm{Na_2IrO_3}$ was found to show a magnetic long-range order, the dominant terms in the *ab initio* effective spin hamiltonian of $\mathrm{Na_2IrO_3}$ are given by the Kitaev-type exchange couplings [3].

Even though there emerge new candidate materials represented by α-$\mathrm{RuCl_3}$ on the front of the search for the spin-liquid ground states, an important question has not been solved yet: It has not been clarified yet whether the small Mott gaps of these candidate materials affect the properties of them or not. To elucidate an impact of the itinerant nature of electrons on the properties of a spin-liquid candidate, we studied the original *ab initio* itinerant hamiltonian consisting of iridium t_{2g} orbitals [3], instead of the spin hamiltonian.

In the present research, we studied the *ab initio* t_{2g} hamiltonian of $\mathrm{Na_2IrO_3}$ [3]. The t_{2g} hamiltonian consists of the kinetic energy and the intra-atomic and inter-atomic Coulomb repulsions as,

$$\hat{H}_{t_{2g}} = \hat{H}_K + \hat{H}_U + \hat{H}_V, \tag{1}$$

where $\hat{H}_K$ represents the kinetic terms including trigonal distortion and spin-orbit couplings, $\hat{H}_U$ denotes the intra-atomic Coulomb interactions, and $\hat{H}_V$ is the inter-atomic Coulomb repulsion.

Naïvely, $\hat{H}_V$ is expected to be relevant to charge channels but irrelevant to spin degrees of freedom. However, it is not true. When inter-atomic exchange couplings are estimated by the second-order perturbation theory, the intra-atomic and intra-orbital Coulomb repulsion U in the energy denominator is replaced by $U-V$, where V is the inter-atomic Coulomb repulsion. Therefore, when the inter-atomic Coulomb repulsions are controlled as parameters, not only the charge but also the spin degrees of freedom are affected.

We controlled the nearest-neighbor, second nearest-neighbor, and $1/r$ long-range Coulomb interactions to examine the competition among the magnetic and charge orders and suppression of the magnetic orders, by using an open-source code mVMC [4].

References

[1] A. Kitaev: Ann. Phys. (Amsterdam) **321** (2006) 2.

[2] G. Jackeli and G. Khaliullin: Phys. Rev. Lett. **102** (2009) 017205.

[3] Y. Yamaji, *et al.*: Phys. Rev. Lett. **113** (2014) 107201.

[4] T. Misawa, *et al.*: Comput. Phys. Commun. **235** (2019) 447.

Theoretical study of symmetry breaking and quantum transport phenomena in charge-spin-orbital coupled systems

Yukitoshi MOTOME
Department of Applied Physics,
The University of Tokyo, Bunkyo, Tokyo 113-8656

We have theoretically studied a variety of intriguing phenomena in correlated electron systems with charge-spin-orbital coupling (project numbers: 2021-Ca-0050 and 2021-Cb-0014). During the last fiscal year, we have achieved substantial progress on the following topics. We summarize the main results below.

(i) *Topological spin crystals*: Regarding topological spin crystals, such as skyrmion and hedgehog lattices, as moiré interferences between spin helices, we clarified how their magnetic and topological properties can be modulated by changing twist angles between the directions of the constituent spin density waves [1] and shifting relative phases [2,3,4]. We also elucidated charge modulation on such topological spin crystals [5]. In addition, we clarified the ground state phase diagrams [6] and spin excitations [7] for effective spin models with long-range interactions. We also clarified linear and nonlinear optical responses in quasi-one-dimensional chiral magnets [8,9]. We have collaborated with experimental groups [10,11]. We wrote a review article on the itinerant frustration mechanism [12].

(ii) *Kitaev quantum spin liquids*: We clarified the effect of randomness on the spin dynamics in the Kitaev quantum spin liquid [13]. We also elucidated linear and nonlinear thermal transport in the presence of both uniform and staggered magnetic fields [14]. We have made collaborations with experimental groups on the topological nature in an external magnetic field [15,16]. In addition, we showed how to create and control fractional excitations by analyzing the effect of local lattice distortions [17]. We also proposed that iridium ilmenites can be good candidates for Kitaev magnets [18].

(iii) *Multipole physics*: We collaborated with experimental groups on a chiral magnet Pb(TiO)$Cu_4(PO_4)_4$ to clarify the control of magnetic domains [19] and nonreciprocal directional dichroism [20,21].

(iv) *Development of new theoretical methods*: We developed a many-body numerical method for quantum spin systems based on the Lefschetz thimbles technique [22]. We also developed new methods based on machine learning techniques: determinant-free fermionic wave function approach [23] and inverse design of Hamiltonians by using automatic differentiation [24].

References

[1] K. Shimizu, S. Okumura, Y. Kato, and Y. Motome, Phys. Rev. B **103**, 184421 (2021).

[2] S. Hayami, T. Okubo, and Y. Motome, Nat. Commun. **12**, 6927 (2021).

[3] K. Shimizu, S. Okumura, Y. Kato, and Y. Motome, preprint (arXiv:2201.03290).

[4] K. Shimizu, S. Okumura, Y. Kato, and Y. Motome, J. Phys.: Conf. Ser. **2164** 012069 (2022).

[5] S. Hayami and Y. Motome, Phys. Rev. B **104**, 144404 (2021).

[6] Y. Kato and Y. Motome, preprint (arXiv:2202.04407).

[7] Y. Kato, S. Hayami, and Y. Motome, Phys. Rev. B **104**, 224405 (2021).

[8] S. Okumura, T. Morimoto, Y. Kato, and Y. Motome, Phys. Rev. B **104**, L180407 (2021).

[9] S. Okumura, T. Morimoto, Y. Kato, and Y. Motome, J. Phys.: Conf. Ser. **2164** 012068 (2022).

[10] K. Fujiwara, Y. Kato, T. Seki, K. Nomura, K. Takanashi, Y. Motome, and A. Tsukazaki, Commun. Mater. **2**, 113 (2021).

[11] N. D. Khanh, T. Nakajima, S. Hayami, S. Gao, Y. Yamasaki, H. Sagayama, H. Nakao, R. Takagi, Y. Motome, Y. Tokura, T. Arima, and S. Seki, Adv. Sci. 2105452 (2022).

[12] S. Hayami and Y. Motome, J. Phys.: Condens. Matter **33**, 443001 (2021).

[13] J. Nasu and Y. Motome, Phys. Rev. B **104**, 045116 (2021).

[14] K. Nakazawa, Y. Kato, and Y. Motome, preprint (arXiv:2201.04274), accepted for Phys. Rev. B.

[15] T. Yokoi, S. Ma, Y. Kasahara, S. Kasahara, T. Shibauchi, N. Kurita, H. Tanaka, J. Nasu, Y. Motome, C. Hickey, S. Trebst, and Y. Matsuda, Science **373**, 568 (2021).

[16] S. Suetsugu, Y. Ukai, M. Shimomura, M. Kamimura, T. Asaba, Y. Kasahara, N. Kurita, H. Tanaka, T. Shibauchi, J. Nasu, Y. Motome, and Y. Matsuda, preprint (arXiv:2203.00275).

[17] S.-H. Jang, Y. Kato, and Y. Motome, Phys. Rev. B **104**, 085142 (2021)

[18] S.-H. Jang and Y. Motome, Phys. Rev. Materials **5**, 104409 (2021).

[19] K. Kimura, Y. Kato, S. Kimura, Y. Motome, and T. Kimura, npj Quantum Mater. **6**, 54 (2021).

[20] T. Katsuyoshi, K. Kimura, Z. Yang, Y. Kato, S. Kimura, Y. Motome, Y. Kohama, and T. Kimura, J. Phys. Soc. Jpn. **90**, 123701 (2021).

[21] M. Akaki, K. Kimura, Y. Kato, Y. Sawada, Y. Narumi, H. Ohta, T. Kimura, Y. Motome, and M. Hagiwara, Phys. Rev. Research **3**, L042043 (2021).

[22] P. A. Mishchenko, Y. Kato, and Y. Motome, Phys. Rev. D **104**, 074517 (2021).

[23] K. Inui, Y. Kato, and Y. Motome, Phys. Rev. Research **3**, 043126 (2021).

[24] K. Inui and Y. Motome, preprint (arXiv:2203.07157).

Low-energy excitations of skyrmion crystals in a centrosymmetric spin-charge coupled magnet

Masahito MOCHIZUKI
Department of Applied Physics, Waseda University
Okubo, Shinjuku-ku, Tokyo 169-8555

In this project, we have theoretically studied the low-energy dynamics of skyrmion crystals in a centrosymmetric Kondo-lattice magnet with conduction-electron-mediated magnetic interactions (project ID: 2021-D-0002).

We computed the dynamical spin- and charge-structure factors of skyrmion crystals in a centrosymmetric spin-charge coupled magnet by taking the Kondo-lattice model with a classical treatment of localized spins. Our large-scale adiabatic molecular dynamics simulations revealed four Goldstone modes in the absence of an external magnetic field [Figure 1]. Three of the four Goldstone modes are associated with the spontaneous breaking of the SO(3) symmetry in spin space, and thus linearly dispersing. The remaining one is the so-called phonon mode associated with the displacement of skyrmions, and thus quadratically dispersing. Surprisingly, we observed clear segregation of spin and charge excitations: the three linearly dispersive Goldstone modes have full contribution from the spin sector and the quadratically dispersive Goldstone mode has full contribution from the charge sector [1]. Note that the dynamical structure factors obtained with the adiabatic molecular dynamics simulations perfectly coincide with the dispersion relations obtained with the linear-spin-wave calculation.

In our adiabatic molecular dynamics simulations, instead of repeated full diagonalizations of the quadratic form Hamiltonian, we utilized the kernel polynomial method in combination with the automatic differentiation technique to evaluate the local physical quantities, for example, expectation values of itinerant electron spins and local charge occupations. The Chebyshev moments are evaluated using the combination of processing and threaded parallelization techniques on 18,432 cores (144 nodes) of System B Ohtaka.

(a) S(q,ω)

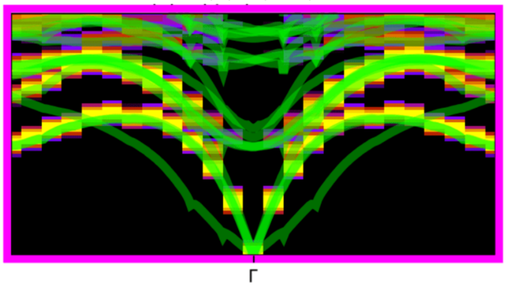

(b) N(q,ω)

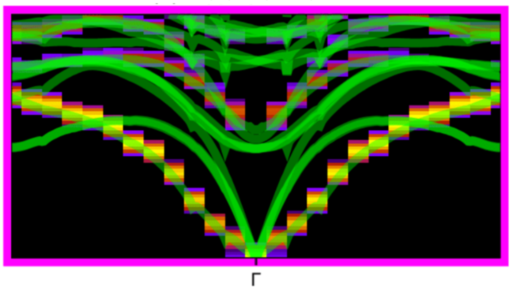

Figure 1: Dynamical (a) spin- and (b) charge-structure factors of the skyrmion crystal in the absence of an external magnetic field.

References

[1] R. Eto, R. Pohle, and M. Mochizuki, preprint [arXiv:2203.01496].

Theoretical study on the photodriven spin and charge dynamics of topological materials

Masahito MOCHIZUKI
Department of Applied Physics, Waseda University
Okubo, Shinjuku-ku, Tokyo 169-8555

We have theoretically studied the dynamics of topological magnetism and topological electron states under periodic driving (project ID: 2021-Ba-0015, 2021-Cb-0009). The main results of these projects are listed below.

(i) *Dynamical magnetic topology switching of skyrmion crystals*: We revealed novel dynamics of skyrmion crystals in a centrosymmetric spin-charge coupled system under the microwave magnetic field [1]. By taking the Kondo-lattice model with a classical treatment of localized spins, we clarified the dynamic topological phase transitions of the skyrmion crystals among their skyrmion number $N_{\rm sk} =$ 2, 1, and 0 through the large-scale spin dynamics simulations in combination with the kernel polynomial method and the automatic differentiation technique. The topological phase transitions are induced by the effective magnetic field perpendicular to the rotating plane of the circularly polarized microwave magnetic field. In our numerical simulations with the kernel polynomial method and the automatic differentiation technique, we utilized our own hybrid parallelization code using both the processing parallelization with the message passing interface and the threaded parallelization with OpenMP. Moreover, in the automatic differentiation process, we reduced the computational cost for the evaluation of Chebyshev moments by using the relation $2T_m(x)T_n(x) = T_{m+n}(x) + T_{|m-n|}(x)$ where $T_m(x)$ denotes the m-th order first-kind Chebyshev polynomial.

(ii) *Spin-wave eigenmodes of the quadruple-Q magnetic hedgehog lattices in chiral magnets*: We studied the spin-wave eigenmodes of the quadruple-Q hedgehog lattices which appear in the Kondo-lattice model on the cubic lattice by the spin-dynamics simulations in combination with the kernel polynomial method [2]. As a result, under the [001] magnetic field, we clarified two eigenmodes with counterclockwise fashion for the ac magnetic field perpendicular to [001] and four eigenmodes for the ac magnetic field parallel to [001]. Three of the four eigenmodes parallel to [001] are localized around point defects of magnetic textures, and the remaining one is closely related to the phase degrees of freedom.

(iii) *Photodriven dynamical phase transitions in the α-type organic salt*: We clarified the dynamical phase transitions in the charge ordered organic salt α-(BEDT-TTF)$_2$I$_3$ under the irradiation of laser by the time-dependent mean-field calculation and the Floquet theory [3]. The sufficient intensity of laser melts the charge order and induces the semimetal phase. A much stronger laser induces the Chern insulator phase with nonzero Hall conductivity.

References

[1] R. Eto and M. Mochizuki, Phys. Rev. B **104**, 104425 (2021).

[2] R. Eto and M. Mochizuki, in preparation.

[3] Y. Tanaka and M. Mochizuki, preprint [arXiv:2203.04542].

Topological phases, excitation modes, effects of exceptional points and transport phenomena in strongly correlated systems

Norio KAWAKAMI

Department of Physics,

Kyoto University, Kitashirakawa, Sakyo-ku, Kyoto 606-8502

Correlated materials have appeared as an arena to study non-Hermitian phenomena, such as exceptional points emerging in the single-particle Green’s function. Exceptional points are degeneracies of eigenvalues due to the non-Hermiticity of a matrix. Contrary to Hermitian degeneracies, the eigenvalues and the eigenvectors coalesce at an exceptional point, giving rise to novel phenomena.

In [1], we show that topological Kondo insulators are an ideal platform for studying these phenomena due to a combination of strong correlations and surface states. Using numerical simulations, we demonstrate the emergence of exceptional points in the single-particle Green’s function on the surface of the material while the bulk is still insulating. We believe that this situation is perfect for experimental observation of exceptional points. In particular, we reveal how quasiparticle states with long lifetimes are created on the surface by non-Hermitian effects while the Dirac cones are smeared. This effect is related to the surface Kondo breakdown at which heavy Dirac cones disappear from the single-particle spectrum and are replaced by light states.

Furthermore, we study nonlinear responses in strongly correlated systems, specifically analyzing the effect of renormalization and non-Hermiticity on the second-order nonlinear response.

Nonlinear responses in condensed matter are recently intensively studied because they provide rich information about the materials and hold the possibility of being applied in diodes or high-frequency optical devices. While nonlinear responses in noninteracting models have been explored widely, the effect of strong correlations on the nonlinear response is still poorly understood. In [2], we first derive a formula for calculating the nonlinear response at finite temperatures that is entirely based on single-particle Green’s functions. We furthermore analytically show that nonlinear responses are significantly enhanced by the renormalization of the band structure and non-Hermiticity in the Green’s function. Finally, we confirm our analytical prediction by performing numerical calculations for several strongly correlated models.

In [3], we use this Green’s function method to study the nonlinear Hall effect in $Ce_3Bi_4Pd_3$. Experiments measured a huge nonlinear Hall effect in this material. From symmetry analysis, we develop a model describing $Ce_3Bi_4Pd_3$ as a Weyl-Kondo semimetal. Performing dynamical mean-field calculations for this model, we find that below the Kondo temperature, Weyl points emerge close to the Fermi energy in the band structure; at high temperatures, this material is a metal. Due to strong correlations, the band structure is strongly renormalized. We then directly calculate the nonlinear longitudinal conductivity and the nonlinear Hall conductivity and find that the nonlinear Hall resistivity is strongly enhanced compared to a noninteracting system. We find good agreement between our numerical calculations and the experimental observations.

In [4], we analyze the effect of strong correlations on fragile topological insulators. Fragile topological insulators (FTIs) offer obstruction to the formation of exponentially localized Wannier functions, but they can be trivialized by adding certain trivial degrees of freedom. For the same reason, FTIs do not host symmetry-protected flow of edge states between bulk bands in cylindrical boundary conditions. Still, they are expected to have a spectral flow between the fragile bands and other bands under certain twisted boundary conditions. We analyze commonly observed effects of strong correlations, such as the Mott insulator transition and magnetism, on a known model hosting fragile topology. We show that fragile topology, along with the twisted boundary states, is stable with interactions below a critical interaction strength in the nonmagnetic case. Above this interaction strength, a transition to the Mott insulating phase occurs, and the twisted boundary states disappear. Furthermore, the fragile topology is destroyed by a homogeneous magnetic field. However, we show that a magnetic field can induce a topological phase transition which converts a fragile topological insulator to a Chern insulator. Finally, we study ferromagnetic solutions of the fragile topological model.

In [5], we investigate magnetic instabilities in charge-neutral twisted bilayer graphene close to so-called "magic angles" using a combination of real-space Hartree-Fock and dynamical mean-field theories. We find that localized magnetic states emerge for values of the Coulomb interaction U that are significantly smaller than what would be required to render an isolated layer antiferromagnetic. Our findings shed new light on perspectives for experimental realization of magnetic states in charge-neutral twisted bilayer graphene.

In [6], we analyze the impact of critical nematic fluctuations on the low energy properties of phonons. We propose how to identify the three-state Potts nematic fluctuations by ultrasound attenuation. The Landau damping term becomes isotropic due to fluctuations of the C_3-breaking bond-order, and the nemato-elastic coupling is also isotropic. The transverse sound attenuation coefficient diverges isotropically, in contrast to the case of the C_4-breaking bond-order that shows strong anisotropy. The shift of the first order transition line at low temperatures toward the second-order line renders the transition a weak first order in a wide range of parameters.

References

[1] R. Peters, K. Kimura, Y. Michishita, T. Yoshida, and N. Kawakami: "Surface exceptional points in a topological Kondo insulator" Phys. Rev. B **104** (2021) 235153.

[2] Y. Michishita and R. Peters: "Effects of renormalization and non-Hermiticity on nonlinear responses in strongly-correlated electron systems" Phys. Rev. B **103** (2021) 195133.

[3] A. Kofuji, Y. Michishita, and R. Peters: "Effects of strong correlations on the nonlinear response in Weyl-Kondo semimetals" Phys. Rev. B **104** (2021) 085151.

[4] A. Joshi and R. Peters: "Mott transition and magnetism in a fragile topological insulator" Phys. Rev. B **103** (2021) 165130.

[5] J. Vahedi, R. Peters, A. Missaoui, A. Honecker, and G. T. de Laissardière: "Magnetism of magic-angle twisted bilayer graphene" SciPost Phys. **11** (2021) 083.

[6] K. Kimura, M. Sigrist, and N. Kawakami: "Probing three-state Potts nematic fluctuations by ultrasound attenuation" Phys. Rev. B **105** (2022) 035130.

Finite-temperature methods for quantum many-body systems using Boltzmann machines

Yusuke NOMURA

RIKEN Center for Emergent Matter Science, 2-1 Hirosawa, Wako, 351-0198

The thermal behavior of many-body systems is a fundamental problem. Celebrated statistical mechanics provides a theoretical framework for describing finite-temperature properties. However, in quantum many-body systems, due to the "curse of dimensionality" of Hilbert space, it is very difficult to capture the complex competition between thermal and quantum fluctuations. Although various numerical methods have been developed, such as quantum Monte Carlo, diagrammatic, and tensor network methods, it is challenging to establish a reliable methodology that can be extended to the most exotic and interesting regions in quantum many-body physics.

Here, we take a novel approach using artificial neural networks. In particular, we employ deep Boltzmann machines that have flexible representability. We propose two different approaches, offering paths to encode many-body thermal physics into deep Boltzmann machines. In the first method, we find a completely deterministic way to construct deep Boltzmann machines that reproduce the exact purified expression of finite temperature states. In the second method, we numerically optimize deep Boltzmann machines to reproduce imaginary time Hamiltonian evolution as accurately as possible within the representability of deep Boltzmann machines. We apply the methods to the transverse-field Ising model and the two-dimensional J_1-J_2 Heisenberg model. The numerical benchmarks show that our scalable approach can successfully simulate the finite-temperature properties of the quantum spin problems.

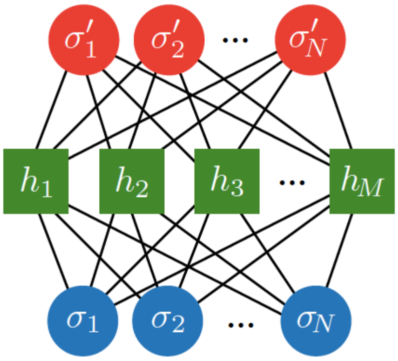

Fig. 1: Structure of deep Boltzmann machine employed in the present study.

References

[1] Y. Nomura, N. Yoshioka, and F. Nori, Phys. Rev. Lett. **127**, 060601 (2021)

Exotic phenomena induced by strong correlations and non-Hermitian topology

Tsuneya Yoshida
Department of Physics,
1-1-1 Tennodai, Tsukuba, Ibaraki, JAPAN 305-8571

In this year, we have mainly studied non-Hermitian topological phenomena by focusing on exceptional points [1-4]. In particular, we have analyzed exceptional points at surfaces of topological Kondo insulators[1]. Specifically, we have applied the dynamical mean-filed theory combined with the numerical renormalization group method to a variant of the periodic Anderson model which describes the topological Kondo insulator SmB6. Our numerical simulation has elucidated that finite lifetime of quasi-particles induces exceptional points at surfaces of the topological Kondo insulator. These exceptional points induce additional low energy excitations and change the spin structure of surface states (see Fig. 1).

We also have analyzed correlations effects on the non-Hermitian topology in zero dimension[4], where we have observed that the classification of the point-gap topology is reduced to Z_2 while the classification is Z at the non-interacting level.

Furthermore, we have explored the topological structure of the classical systems[5-7]. In particular, we have observed Hermitian and non-Hermitian topological physics in systems of the head conduction and the evolutionary game theory. The topological properties of superconductors are also discussed [8,9].

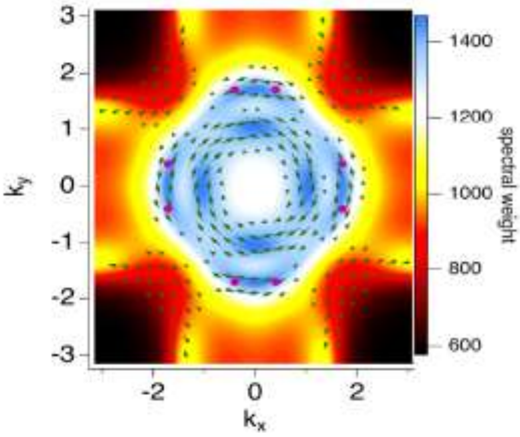

Fig.1 Spectral weight for a surface of a topological Kondo insulator. The emergence of exceptional points induces low energy excitations and affects the spin structure of the surface states (The figure is taken from Ref. [1])

References

[1] R. Peters, K. Kimura, Y. Michishita, T. Yoshida, and N. Kawakami, Phys. Rev. B **104** 235153 (2021).

[2] T. Yoshida, R. Okugawa, and Y. Hatsugai, Phys. Rev. B 105, 085109

[3] H. Wakao, T. Yoshida, and Y. Hatsugai arXiv:2203.05773

[4] T. Yoshida and Y. Hatsugai, Phys. Rev. B **104**, 075106 (2021).

[5] T. Yoshida, T. Mizoguchi, and Y. Hatsugai, Phys. Rev. E **104**, 025003

[6] S. Makino, T. Fukui, T. Yoshida, and Y. Hatsugai, Phys. Rev. E **105**, 024137 (2021)

[7] T. Yoshida, T. Mizoguchi, and Y. Hatsugai, Sci. Rep. **12**, 1-7 (2021)

[8] T. Yoshida, T. Mizoguchi, Y. Kuno, and Y. Hatsugai, Phys. Rev. B **103**, 235130 (2021)

[9] Y. Yanase, A. Daido, K. Takasan, and T. Yoshida, Physica E, **140**, 115143 (2022)

Extreme response of isotropic spin fluctuations emerging from anisotropic antiferromagnets under moderate spin dilution

Hidemaro SUWA
Department of Physics, University of Tokyo, Tokyo 113-0033

The stability and response of magnetic materials to external stimuli are determined by spin fluctuations dictated by magnetic anisotropy. The two-dimensional (2D) isotropic antiferromagnet is one of the ideal cases to pursue an extreme magnetic response. However, magnetic anisotropy is significant in most materials, reducing the magnetic response. As a perturbation, magnetic anisotropy introduces a characteristic length scale $\xi_{\rm ani}$. The significance of anisotropy follows from the fact that the correlation length increases rapidly with decreasing temperature and easily reaches $\xi_{\rm ani}$. In contrast, the Zeeman energy from a typical achievable magnetic field is weaker, and the length scale $\xi_{\rm ext}$ introduced by the external field is much larger, i.e., $\xi_{\rm ext} > \xi_{\rm ani}$. Moreover, the Zeeman field in antiferromagnets must be a staggered field that is linearly coupled to the staggered magnetization, which is difficult to realize.

Our primitive 2D antiferromagnet is realized on a pseudo spin-1/2 square lattice embedded in a $[(\mathrm{SrIrO}_3)_1/(\mathrm{SrTiO}_3)_2]$ superlattice, with the adjacent IrO_2 planes well separated by non-magnetic spacers. Strong spin-orbit coupling of iridium stabilizes the $J_{\rm eff} = 1/2$ moment antiferromagnetically coupled to each other via the Heisenberg super-exchange interaction. An essential feature of such a $J_{\rm eff} = 1/2$ square lattice is that the large Dzyaloshinskii–Moriya interaction arising from the staggered rotation of the IrO_6 octahedron around the c axis is canceled throughout the lattice, and the pseudospins tend to be almost completely isotropic, which is called a hidden SU(2) symmetry. This phenomenon allows the in-plane uniform magnetic field to act as an effective staggered field. Nevertheless, higher-order super-exchange paths due to Hund's coupling cause small easy-plane anisotropy, effectively reducing the spin symmetry from SU(2) to U(1).

We have theoretically and experimentally demonstrated that we can switch the order of $\xi_{\rm ext}$ and $\xi_{\rm ani}$ utilizing magnetic dilution. Using ISSP System B in class C projects (ID: 2021-Ca-0117) and the ALPS/looper (http://github.com/wistaria/alps-looper) code, we simulated large-scale 2D AFM systems of more than one million quantum spins. We calculated the Berezinskii–Kosterlitz–Thouless transition temperatures for several dilution fractions. Using the crossover argument with multiple perturbations, we have shown that the response to magnetic fields changes from the U(1) model to the SU(2) model above the threshold dilution fraction because of the length-scale switch ($\xi_{\rm ext} < \xi_{\rm ani}$). The theoretical calculation successfully accounts for the experimental observations, confirming the extreme response of isotropic fluctuations emerging from anisotropic antiferromagnets under moderate spin dilution.

Research of Multi-Channel Kondo Effect Emerging from Heavy Rare-Earth Ions

Takashi HOTTA
Department of Physics, Tokyo Metropolitan University
1-1 Minami-Osawa, Hachioji, Tokyo 192-0397

We have discovered the three-channel Kondo effect in the cubic Ho compound [1]. We have analyzed a seven-orbital impurity Anderson model hybridized with Γ_8 and Γ_7 conduction electrons for a case with ten local f electrons corresponding to a Ho^{3+} ion by using a numerical renormalization group (NRG) method. Then, we have found a residual entropy of $\log\phi$ with the golden ratio $\phi=(1+\sqrt{5})/2$ as a signal of the three-channel Kondo effect for the local Γ_5 triplet ground state.

For the construction of the local f-electron Hamiltonian $H_{\rm loc}$, we introduce one f-electron state, defined by the eigenstate of spin-orbit and crystalline electric field (CEF) potential terms. Under the cubic CEF potential, we obtain Γ_7 doublet and Γ_8 quartet from $j=5/2$ sextet, whereas we find Γ_6 doublet, Γ_7 doublet, and Γ_8 quartet from $j=7/2$ octet. By using those one-electron states as bases, we obtain $H_{\rm loc}$ as

$$\begin{aligned}H_{\rm loc} &= \sum_{j,\mu,\tau}(\lambda_j+B_{j,\mu})f^{\dagger}_{j\mu\tau}f_{j\mu\tau}+nE_f\\ &+ \sum_{j_1\sim j_4}\sum_{\mu_1\sim\mu_4}\sum_{\tau_1\sim\tau_4} I^{j_1j_2,j_3j_4}_{\mu_1\tau_1\mu_2\tau_2,\mu_3\tau_3\mu_4\tau_4}\\ &\times f^{\dagger}_{j_1\mu_1\tau_1}f^{\dagger}_{j_2\mu_2\tau_2}f_{j_3\mu_3\tau_3}f_{j_4\mu_4\tau_4},\end{aligned} \quad (1)$$

where $f_{j\mu\tau}$ is the annihilation operator of a localized f electron in the bases of (j,μ,τ), j is the total angular momentum, $j=5/2$ and $7/2$ are denoted by "a" and "b", respectively, μ distinguishes the cubic irreducible representation, Γ_8 states are distinguished by $\mu=\alpha$ and β, while the Γ_7 and Γ_6 states are labeled by $\mu=\gamma$ and δ, respectively, τ denotes the pseudo-spin, which distinguishes the degeneracy concerning the time-reversal symmetry, n is the local f-electron number at an impurity site, and E_f is the f-electron level to control n. Here we set $\hbar=k_{\rm B}=1$ and the energy unit as eV.

Concerning the spin-orbit term, we obtain $\lambda_a=-2\lambda$ and $\lambda_b=(3/2)\lambda$, where λ is the spin-orbit coupling of f electron. In this study, we set $\lambda=0.265$ for the Ho ions. Concerning the CEF potential term for $j=5/2$, we obtain $B_{a,\alpha}=B_{a,\beta}=1320B_4^0/7$ and $B_{a,\gamma}=-2640B_4^0/7$, where B_4^0 denotes the fourth-order CEF parameter for the angular momentum $\ell=3$. For $j=7/2$, we obtain $B_{b,\alpha}=B_{b,\beta}=360B_4^0/7+2880B_6^0$, $B_{b,\gamma}=-3240B_4^0/7-2160B_6^0$, and $B_{b,\delta}=360B_4^0-3600B_6^0/7$. In the present calculations, we treat B_4^0 and B_6^0 as parameters. For the Coulomb interaction terms, we do not show the explicit forms of I here, but they are expressed by the four Slater-Condon parameters, F^0, F^2, F^4, and F^6. These values should be determined from experimental results, but here we simply set the ratio as $F^0/10=F^2/5=F^4/3=F^6=U$, where U indicates the Hund's rule interaction among the f orbitals and the magnitude is set as unity in this study.

In Fig. 1, we show the local CEF ground-state phase diagram for $n=10$. The ground-state multiplet for $B_4^0=B_6^0=0$ is characterized by the total angular momentum $J=8$. Under the cubic CEF potentials, the sept-

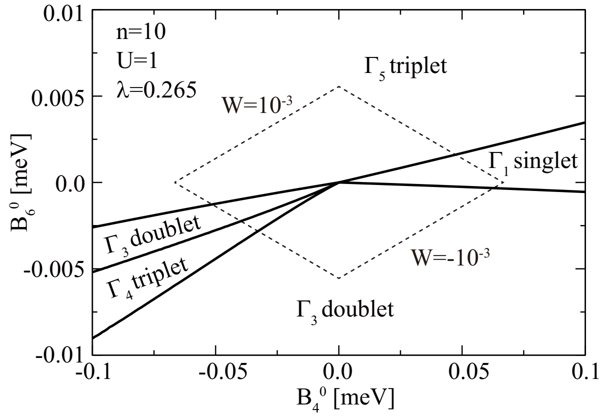

Figure 1: Local CEF ground-state phase diagram on the (B_4^0, B_6^0) plane for $n = 10$ with $U = 1$ and $\lambda = 0.265$.

dectet of $J = 8$ is split into four groups as one Γ_1 singlet, two Γ_3 doublets, two Γ_4 triplets, and two Γ_5 triplets. Then, we obtain four kinds of local ground states for $n = 10$, as shown in Fig. 1. The dashed rhombus denotes the trajectory of $B_4^0 = Wx/15$ and $B_6^0 = W(1 - |x|)/180$ for $-1 \leq x \leq 1$ with $W = \pm 10^{-3}$. Roughly speaking, the Γ_5 triplet appears widely for $B_6^0 > 0$, whereas the Γ_3 doublet is found for $B_6^0 < 0$. In the region of $B_6^0 \approx 0$ and $B_4^0 > 0$, the Γ_1 singlet was stabilized. For $B_4^0 < 0$, we find the Γ_3 doublet and Γ_4 triplet in a narrow region between the Γ_5 triplet and Γ_3 doublet.

Now we include the Γ_7 and Γ_8 conduction electron bands. Here we consider only the hybridization between the conduction and $j = 7/2$ electrons. The Hamiltonian is given by

$$\begin{aligned} H &= \sum_{\boldsymbol{k},\mu,\tau} \varepsilon_{\boldsymbol{k}} c^{\dagger}_{\boldsymbol{k}\mu\tau} c_{\boldsymbol{k}\mu\tau} + \sum_{\boldsymbol{k},\mu,\tau} V_{\mu} (c^{\dagger}_{\boldsymbol{k}\mu\tau} f_{b\gamma\tau} + \text{h.c.}) \\ &+ H_{\text{loc}}, \end{aligned} \tag{2}$$

where $\varepsilon_{\boldsymbol{k}}$ is the dispersion of conduction electron with wave vector $\boldsymbol{k}$, $c_{\boldsymbol{k}\gamma\tau}$ is an annihilation operator of conduction electrons, and V_μ denotes the hybridization between f electron in the μ orbital and conduction electron of the μ band. Here we set $V_\alpha = V_\beta = V_\gamma = V$.

In this research, we analyze the model by employing the NRG method [2]. We introduce a cut-off Λ for the logarithmic discretization of the conduction band. Due to the limitation of computer resources, we keep M low-energy states. Here we use $\Lambda = 8$ and $M = 5,000$. In the NRG calculation, the temperature T is defined as $T = D\Lambda^{-(N-1)/2}$, where D is half the conduction band width, which was set as 1 eV, and N is the number of renormalization steps.

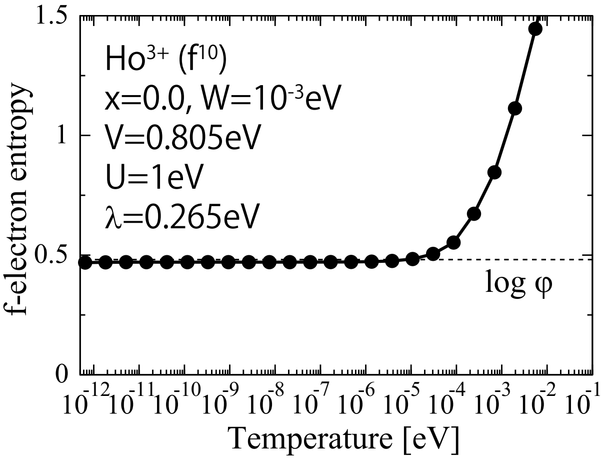

Figure 2: Entropy vs. temperature for $n = 10$ with $x = 0.0$ and $W = 10^{-3}$, corresponding to the Γ_5 triplet ground state.

Here we briefly discuss the typical result for $n = 10$ [1]. In Fig. 2, we show entropy vs. temperature for the Γ_5 triplet ground state. We observe a residual entropy of $\log \phi$ at low temperatures with the golden ratio $\phi = (1+\sqrt{5})/2$, which is characteristic of the three-channel Kondo effect. We confirm the residual entropy of $\log \phi$ in the wide region of the local Γ_5 triplet ground state. Thus, we conclude that the three-channel Kondo effect occurs in the Γ_5 triplet ground state of Ho^{3+} ions.

References

[1] T. Hotta, J. Phys. Soc. Jpn. **90**, 113701 (2021).

[2] H. R. Krishna-murthy, J. W. Wilkins, and K. G. Wilson, Phys. Rev. B **21**, 1003 (1980).

Numerical study of topological thermal transport in Kitaev-related systems

Joji NASU
Department of Physics, Tohoku University
Sendai 980-8578

The Kitaev quantum spin model has been intensively investigated since the proposal by A. Kitaev as a canonical model exhibiting quantum spin liquids. This model is considered to describe the magnetism of iridium oxides and α-RuCl$_3$ where the strong spin-orbit coupling and electron correlations are present. However, these materials show a magnetic order at low temperatures due to magnetic interactions additional to the Kitaev term. As additional terms, effects of the Heisenberg interaction and off-diagonal symmetric term (Γ term) have been examined intensively. Moreover, recent experiments in α-RuCl$_3$ clarified that an applied magnetic field induces nonzero thermal Hall conductivity, whose sign depends on the magnetic field direction. However, the field-angle dependence of the Kitaev-Heisenberg and Kitaev-Heisenberg-Γ models remains unclear in the presence of magnetic orders.

In this project, we systematically examine the field-angle dependence of magnetic orders and excitation spectra in these models. To address the case with arbitrary spin directions in a magnetic order, we have newly developed the calculation technique by extending the conventional spin-wave theory [1, 2]. In this method, we can implement large-sublattice calculations straightforwardly. Our spin-wave theory needs the Cholesky decomposition. We use the LAPACK library to perform it. First, we examine the ground-state spin configuration by changing the magnetic field direction and obtain the phase diagram. Based on the obtained ground-state magnetic orders, we calculate the energy and Berry curvature of the magnon bands. Furthermore, we calculate the temperature dependence of the thermal Hall conductivity. To compute the thermal Hall coefficient, we need to sum up the Berry curvature for the wave-number vector in the Brillouin zone. We parallelize the k-summation in the ISSP supercomputer to perform this procedure efficiently. The thermal Hall conductivity is enhanced in magnetically ordered states with noncoplanar spin configurations. Moreover, we also find that the thermal Hall effect originating from the topological nature of the magnon dispersion is absent when the field is applied along with one of the spin axes in the Kitaev-Heisenberg model. We also find that this feature disappears by introducing the off-diagonal symmetric Γ interaction. In addition, we clarify that the Γ interaction suppresses the thermal Hall conductivity because of enhancing the low-energy magnon gap.

References

[1] S. Koyama and J. Nasu: B **104** (2021) 075121.

[2] S. Koyama and J. Nasu: J. Phys.: Conf. Ser. **2164** (2022) 012071.

Searching for meron crystal in itinerant magnets

Satoru Hayami
Department of Applied Physics, The University of Tokyo, Tokyo 113-8656

Topological spin textures, such as a magnetic skyrmion, meron, and hedgehog, have attracted considerable attention, since they give rise to fascinating physical phenomena, such as the topological Hall effect. The fundamental understanding of the stabilization mechanisms for these nontrivial spin textures would be useful for potential applications to next-generation electronic and spintronic devices. In the project with number 2021-Ca-0042, we have theoretically investigated the possibility of such topological spin textures based on an itinerant electron model and its effective spin model. We have presented the main results this year below.

(i) Skyrmion crystals in trigonal systems: We have theoretically investigated a new stabilization mechanism of the skyrmion crystals in itinerant trigonal systems [1]. By focusing on the anisotropic exchange interaction that originates from the lack of horizontal mirror symmetry and twofold rotational symmetry along the threefold axis, we obtained two types of skyrmion crystals with the skyrmion number of one and two. We have shown that two SkXs are transformed with each other by changing the magnetic field. Our findings suggest itinerant trigonal systems as a new skyrmion-hosting system in addition to conventional hexagonal and tetragonal systems.

(ii) Mechanism of skyrmion crystals in EuPtSi: We have theoretically studied the stabilization mechanism of the skyrmion crystals in the f-electron compound EuPtSi based on an effective spin model [2]. We found two important ingredients to induce the skyrmion crystal: (1) the multiple-q superpositions of the spirals with low-symmetric ordering vectors and (2) the synergy between spin-charge and spin-orbit couplings in itinerant magnets. We have clarified that the model to satisfy two conditions well describes the skyrmion physics in EuPtSi by performing unbiased simulated annealing.

(iii) Meron-antimeron crystal on a triangular lattice: A meron-antimeron crystal consisting of the periodic array of merons and antimerons with a half skyrmion number has attracted growing attention since its observation in $Co_8Zn_9Mn_3$ and Gd_2PdSi_3. Nevertheless, its origin has not been fully identified owing to the lack of a stabilization mechanism and an appropriate model. To understand the origin of the meron-antimeron crystals on the basis of metallic magnets, we theoretically performed simulated annealing for an effective spin model derived from the Kondo lattice model on a noncentrosymmetric triangular lattice [3]. As a result, we showed that several types of meron-antimeron crystals are stabilized by the synergy among the biquadratic interaction, the single-ion anisotropy, and the Dzyaloshinskii-Moriya interaction. The emergent meron-antimeron crystals are owing to the nature of itinerant electrons, which have not been obtained in localized spin models. We also found other topological spin textures including the skyrmion crystal can be realized by the same effective model at zero fields.

(iv) Charge density waves in multiple-Q spin states: We elucidated the charge density wave formation in the presence of the spin density wave [4]. Based on the perturbation in terms of the spin-charge coupling, we theoretically

derived a useful formula for the relationship between charge density waves and spin density waves, which can be applied to any type of magnetic texture and lattice structure. We have tested the obtained formula for several single-Q and double-Q magnetic orderings including the skyrmion crystal on a square lattice. We have also shown the effects of large spin-charge coupling beyond the perturbative regime and the spin-orbit coupling to comprehensively understand the charge density wave formation in itinerant magnets.

(v) Phase shift in skyrmion crystals: We have theoretically studied the possibility of controlling the skyrmion crystals by using the phase degree of freedom among the spin density waves [5]. We have shown that a phase shift can occur in the skyrmion crystals to stabilize a new type of vortex crystals with a different pattern of an emergent magnetoelectric field through local scalar spin chirality, which gives rise to nonreciprocal transport phenomena without the spin-orbit coupling. Analyzing the Kondo lattice model and its effective spin model, we found three mechanisms to cause the phase shift: exchange interactions between the localized spins, thermal fluctuations, and long-range chirality interactions.

(vi) Skyrmion crystal in centrosymmetric bilayer magnets: We proposed a stabilization mechanism to realize the skyrmion crystal in centrosymmetric bilayer magnets [6]. By performing the simulated annealing on the bilayer triangular-lattice spin model, we have shown that the interplay between the layer-dependent Dzyaloshinskii-Moriya interaction and interlayer exchange interaction gives rise to the skyrmion crystal even without the frustrated exchange interaction and multiple-spin interactions. In addition, we have obtained two triple-Q states with a uniform scalar chirality while increasing and decreasing the magnetic field in the skyrmion crystal phase that has not been obtained in the single-layer system.

(vii) Multiple skyrmion crystals in tetragonal magnets: We theoretically investigated the possibility of realizing multiple skyrmion crystals against an external magnetic field in tetragonal itinerant magnets [7]. By focusing on multiple peaks at bare susceptibility of itinerant electrons, we found that three types of skyrmion crystals with the skyrmion numbers of one and two, which are characterized by different superpositions of helices, are stabilized in the ground state. Moreover, we found that they are transformed with each other by an external magnetic field.

References

[1] R. Yambe and S. Hayami, Sci. Rep. **11**, 11184 (2021)

[2] S. Hayami and R. Yambe, J. Phys. Soc. Jpn. **90**, 073705 (2021).

[3] S. Hayami and R. Yambe, Phys. Rev. B **104**, 094425 (2021).

[4] S. Hayami and Y. Motome, Phys. Rev. B **104**, 144404 (2021).

[5] S. Hayami, T. Okubo, and Y. Motome, Nat. Commun. **12**, 6927 (2021).

[6] S. Hayami, Phys. Rev. B **105**, 014408 (2022).

[7] S. Hayami, J. Phys. Soc. Jpn. **91**, 023705 (2022).

Analysis of string excitations in the optical conductivity of doped Mott insulators

Takami TOHYAMA
Department of Applied Physics, Tokyo University of Science, Tokyo 125-8585

The optical conductivity has provided important information on the nature of the hole-doped Mott insulators. The most striking feature is dynamical spectral-weight transfer upon chemical doping and photodoping appearing at mid-infrared (MIR) region. The weights at MIR are sensitive to dimensionality and are found in two dimensions but not in one dimension. MIR weights are expected to contain essential information on the dynamical properties of holes in the two-dimensional Mott insulators. A hole moving in antiferromagnetic (AFM) spin background creates misarranged spins with respect to their sublattice and consequently induces string-type excitation of spins. MIR weights may have a relation to string structures. However, it is unclear how MIR weights actually are related to string excitations that are the result of a complex process due to spin-charge coupling. If a hole moves in an AFM state, it leaves traces of spin mismatches with sublattice magnetization called S_z strings. The S_z strings are inadequate to describe a hole surrounded by AFM spins since the hole picks up a nontrivial $U(1)$ phase when it hops in an AFM spin background. This phase generates another type of strings, called phase strings, caused by transverse spin component.

In this project, we demonstrate how much S_z and phase strings contribute to MIR weights. We calculate the optical conductivity of the Hubbard model in the strong-coupling regime and the t-J model by using time-dependent Lanczos and time-dependent density-matrix renormalization group (tDMRG) methods. We focus on doped Mott insulators with a single hole and consider two-leg ladders up to a 20×2 sites [1] and square lattice up to 6×6 sites [2] under open boundary conditions. Turning on and off the effect of phase strings, we examine how they contribute to MIR weights. We find that phase strings play an essential role in MIR weights. MIR weights are crucially suppressed for both the Hubbard and t-J models if we remove phase strings. Although S_z strings also contribute to MIR weights, their contribution is smaller than phase strings. We consider that this is because S_z strings can be self-healed via quantum spin flips, while phase strings are not reparable. Our findings suggest that a mutual Chern-Simons gauge field, which is an elementary force between spin and charge in the phase-string theory, is significant for obtaining MIR weights. This indicates that a hole does not pick up a $U(1)$ phase when moving in AFM spin background if we remove this gauge field. As a result, we can characterize a doped hole surrounded by AFM spins via a spin-polaron quasiparticle, which has a cosinelike energy dispersion in the single-particle spectral function.

References

[1] K. Shinjo, S. Sota, and T. Tohyama: Phys. Rev. B **103** (2021) 035141.

[2] K. Shinjo, S. Sota, and T. Tohyama: in preparation.

Theoretical Calculation on Coulomb Repulsion of ED*X*T Oligomer Charge Transfer Salts

Tomoko FUJINO

Institute for Solid State Physics,

The University of Tokyo, Kashiwa-no-ha, Kashiwa, Chiba 277-8581

We have synthesized discrete oligomer models for doped poly(3,4-ethylenedioxythiophene) (PEDOT) [1,2]. Doped PEDOT is a commonly employed conductive polymer in organic electronic devices owing to their flexibility, lightness, transparency, and concise synthetic routes. However, their complicated packing structures based on a non-uniform molecular weight distribution severely limit structural data acquisition, especially electronic structural data, requisite for further improving the physical properties.

This study calculated the band structures based on the single-crystal structures of charge transfer salts of the dimer as the shortest models for doped PEDOT [1]. The band calculations functional theory (DFT)-based by OpenMX software revealed their one-dimensional (1D) metallic band structures with a strong intracolumnar orbital interaction (calculated band width $\boldsymbol{W} \approx 1$ eV). This interaction was significantly stronger than that observed for typical low molecular weight 1D conductors (TTF•TCNQ: $4t_{\mathrm{TTF}} \approx 0.2$–$0.4$ eV, $4t_{\mathrm{TCNQ}} \approx 0.5$ eV), revealing the origin of the high conductivity of doped PEDOT. Interestingly, the elongation of characteristic oligomer length from dimer to trimer exhibited decreased $\boldsymbol{W}$ (≈ 0.90 eV), while it improved the conductivity with 70% activation energy (0.20 eV) of that for dimer. These data indicated that extending the conjugation lengths of the oligomers markedly lowered effective Coulomb repulsion ($\boldsymbol{U}_{\mathbf{eff}}$), thereby decreasing the ratio of $\boldsymbol{U}_{\mathbf{eff}}/\boldsymbol{W}$ and improving the conductivity [2]. The details on $\boldsymbol{U}_{\mathbf{eff}}$ by theoretical calculations will be discussed in near future.

References

[1]. R. Kameyama, T. Fujino, S. Dekura, M. Kawamura, T. Ozaki, and H. Mori: Chem. Eur. J. **27** (2021) 6696.

[2] R. Kameyama, T. Fujino, S. Dekura, and H. Mori: Phys. Chem. Chem. Phys. **24** (2022), 9130.

Studies of the superconductivity and magnetic states in the strongly correlated electron systems based on Hubbard models.

Atsushi Yamada
Department of Physics, Chiba University
Chiba 263-8522, Japana, Chiba 277-8581

A spin liquid state, which is a purely nonmagnetic Mott insulator without spontaneously broken spatial or spin symmetry, has attracted a lot of interest. This state is realized in geometrically frustrated systems like the charge organic transfer salts κ-(BEDT-TTF)$_2$X[1] and Cs$_2$CuCl$_4$.[2]

A spin liquid could arise also in the intermediate coupling region of strongly correlated systems between a semi-metal and ordered state, because in this case a correlation-driven insulating gap might open before the system becomes ordered. This possibility might be realized in the half-filled Hubbard model on the honeycomb lattice, where a semi-metal is realized at $U = 0$, and in fact is studied, for example, using Quantum Monte Carlo (QMC) simulations. Meng *et al*[3] found that a spin liquid state is realized in the Honeycomb lattice Hubbard model. But suqsequent QMC studies[4] with larger lattice size ruled out this possibility.

We have studied the magnetic and metal-to-insulator transitions by variational cluster approximation using 10-site and 16-site clusters as a reference system. Parts of numerical calculations were done using the computer facilities of the ISSP. We found that $U_{\rm AF} = 2.7$ and $U_{\rm MI} = 3.0$ for 10-site cluster, and $U_{\rm AF} = 2.7$ and $U_{\rm MI} = 3.2$ for 16-site cluster.[5] This result also rules out the existence of the spin liquid in this model. Our results agree with recent large scale Quantum Monte Carlo simulations.[4] To study larger systems, we need to revise our program using MPI technique. We are now improving our programs, even though we encounter a lot of difficulties.

References

[1] Y. Shimizu, K. Miyagawa, K. Kanoda, M. Maesato, and G. Saito, Phys. Rev. Lett. **91**, 107001 (2003); Y. Kurosaki, Y. Shimizu, K. Miyagawa, K. Kanoda, and G. Saito, Phys. Rev. Lett. **95**, 177001 (2005).

[2] R. Coldea, D.A. Tennant, A.M. Tsvelik, and Z. Tylczynski, Phys. Rev. Lett. **86**, 1335 (2001); R. Coldea, D.A. Tennant, and Z. Tylczynski, Phys. Rev. Lett. **68**, 134424 (2003).

[3] Z. Y. Meng et al., Nature 464, 08942 (2010).

[4] S. Sorella, Y. Otsuka, and S. Yunoki, Sci. Rep. **2**, 992 (2012); F. F. Assaad and I. F. Herbut, Phys. Rev. X **3**, 031010 (2013); F. Parisen Toldin, M. Hohenadler, F. F. Assaad, and I. F. Herbut, Phys. Rev. B **91**, 165108 (2015).

[5] A. Yamada, Int. J. Mod. Phys. B **30**, 1650158 (2016).

Non-Abelian anyons trapped in vacancies of the Kitaev model and non-local spin correlations

Masahiro O. TAKAHASHI and Satoshi FUJIMOTO
Department of Materials Engineering Science, Osaka University
Machikaneyama 1-3, Toyonaka, Osaka 560-8531

We have clarified, using massive parallel computer simulations, that a non-local spin-spin correlation exists between specific spatially well-separated sites in the Kitaev spin liquid with some point vacancies, which reveals the realization of Majorana zero modes (MZMs) strongly trapped in vacanceis.

The Kitaev model [1] is a spin-1/2 model defined with bond-dependent Ising interactions on the honeycomb lattice and it is exactly solvable with the use of an itinerant Majorana fermion and a Z_2 flux defined on each plaquette. In a chiral spin liquid phase MZMs can appear exhibiting a non-local correlation and Z_2 fluxes binding them obey non-Abelian statistics, in principle. It is expected to exploit the composite particles for topological quantum computation. It is difficult, however, to introduce and control the composites in the ground state of the pure Kitaev model since they are thermal excitations. To avoid the difficulty, we focus on point vacancies in the system. It is well known that each vacancy binds Z_2 flux in the ground state, or the bound-flux sector [2], while MZMs strongly trapped in them are not yet reported.

In this study, we reveal the importance of localized Majorana fermions caused by vacancies, which have not been properly taken into account in previous studies. In the Kitaev's notation, a spin operator at j-site, S_j^γ ($\gamma = x, y, z$), is represented as $S_j^\gamma = ib_j^\gamma c_j/2$, using an itinerant Majorana fermion operator c_j and a localized Majorana fermion operator b_j^γ (Fig. 1). The former behaves as a free Majorana fermion described as a tight-binding model while the latter forms a Z_2 gage field with the other localized Majorana fermion from the nearest site on each bond. Then, if a vacancy exists, the localized Majorana fermion from the nearest site of the vacancy site loses the partner and it can couple with itinerant Majorana fermions, as shown in Fig. 1, when an external magnetic field is applied. This nontrivial Majorana hopping term, or b-c hopping term, contributes to realizing MZMs bound in Z_2 fluxes that should be naturally found in the bound-flux sector.

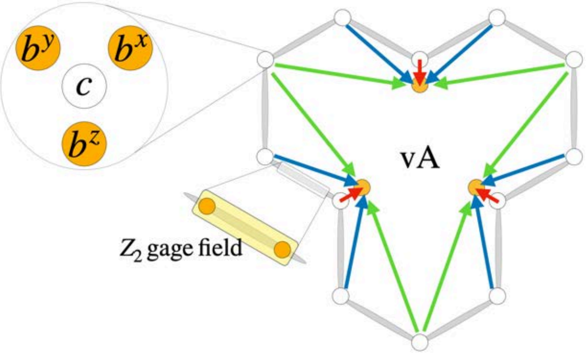

Figure 1: Majorana fermions for each spin and nontrivial Majorana hoppings between b_j^γ and c_k around a vacancy vA, represented as arrows.

The effective Majorana Hamiltonian H_{eff} for the Kitaev model with vacancies, which are spatially well-separated, works well to host MZMs. We assume two vacancies, vA and vB, for simplicity and the direction of a magnetic field parallel to the in-plane a-axis. At nonzero magnetic fields, a pair of MZMs appears in the bulk gap and is stable against an increase in a magnetic field strength unless the bound-flux ground state is valid. This property is not confirmed without b-c Majorana hopping terms: the Majorana gap grows as increasing the strength whereas pseudo-MZMs [3] disappear rapidly to form the bulk gap. Moreover, it is discovered that more than 99% of the real-space amplitudes of MZMs are on the localized Majorana fermions, which implies that they are strongly trapped in Z_2 fluxes in the ground state.

To approach a pair of MZMs by a physical observable using a non-local property, we consider a non-local spin correlation between the nearest sites of each vacancy, say j_{A} and j_{B} site. Our interest is written as below at inverse temperature β,

$$\langle S^z_{j_{\mathrm{A}}}(t)\, S^z_{j_{\mathrm{B}}}(0)\rangle \equiv \frac{\mathrm{Tr}\,\left[P_F\, S^z_{j_{\mathrm{A}}}(t)\, S^z_{j_{\mathrm{B}}}(0)\, e^{-\beta H_{\mathrm{eff}}}\right]}{\mathrm{Tr}\,\left[P_F\, e^{-\beta H_{\mathrm{eff}}}\right]}, \tag{1}$$

where P_F is a projection operator to the physical subspace. Especially the Fourier-transformed dynamical structure factor $\Psi^{zz}_{j_{\mathrm{A}}j_{\mathrm{B}}}(\omega) \equiv \int_0^\infty e^{i(\omega+i\delta)t}\langle S^z_{j_{\mathrm{A}}}(t)\, S^z_{j_{\mathrm{B}}}(0)\rangle$ clearly reveals the contribution from MZMs and b-Majorana excitations inside the bulk gap as shown in Fig. 2. Indeed, the structure factor in the zero-flux sector differs from the one in the bound-flux ground state in a point that the signal comes from b-Majorana excitations shift to a higher ω region, very close to the Majorana bulk gap, which implies the absence of MZMs.

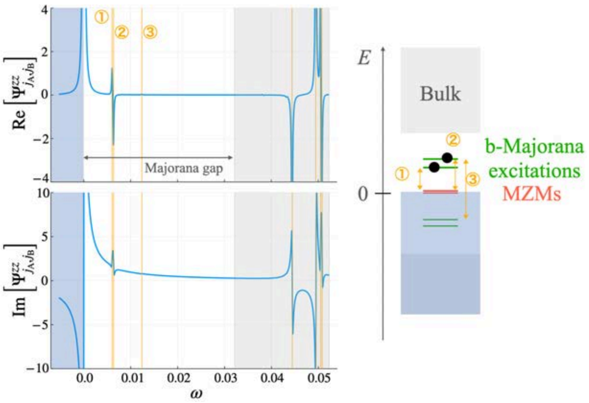

Figure 2: The structure factor of a non-local spin-spin correlation and the Majorana spectrum structure.

In summary, non-Abelian anyons composed of MZMs and Z_2 fluxes, both of which are trapped in vacancies, can stably exist in the ground state of the vacancy-induced Kitaev model with a magnetic field. They exhibit the non-local spin-spin correlation in a chiral *spin liquid* phase, and this system may become the new platform for topological quantum computation.

References

[1] A. Kitaev, Ann. Phys. **321** (2006) 2.

[2] A. J. Willans et al., Phys. Rev. Lett. **104** (2010) 237203.

[3] W.-H. Kao and N. B. Perkins, Ann. Phys. **435** (2021) 168506.

Discrete time crystals in solids

Tatsuhiko Ikeda
Institute for Solid State Physics, University of Tokyo
Kashiwa-no-ha, Kashiwa, Chiba 277-8581

We have studied a discrete time crystal (DTC) in solid-state materials using Supercomputer System B at the ISSP. This year, a paper on this project was published [1]. We will report this project below.

A DTC is an exotic nonequilibrium phase in periodically driven dissipative quantum systems that breaks the discrete time translation symmetry. The DTC had been well studied and experimentally demonstrated in artificial quantum systems without dissipation, such as trapped ions, NV centers in diamond, and quantum computers. However, it had not been explored in natural materials, like solids, with dissipation. Nonetheless, if we create the DTC in natural materials, it could offer a new possibility of time crystals in material science.

In this study, we have investigated the DTC in solid-state materials. To uncover the mechanism and properties of the DTC in solids, we have considered a periodically driven quantum Ising model with dissipation using the Floquet-Redfield equation that describes a periodically driven quantum system subject to dissipation. The Floquet-Redfield equation is much harder to solve than the usual Schrödinger equation because we need to treat a $D \times D$ density matrix rather than a D-dimensional wave function in the Floquet-Redfield equation (D is the Hilbert space dimension). Therefore, in this study, we have employed the mean-field theory and numerically solved the DTC order parameter self-consistently.

Performing a massive numerical calculation with the supercomputer, we have obtained the phase diagram of the DTC in solids (see Fig. 1). This phase diagram highlights a nontrivial behavior that the separate two DTC regions appear. Also, we have shown that this DTC is robust against any perturbation. We believe that these results pave the way for a new research field of time crystals in material science.

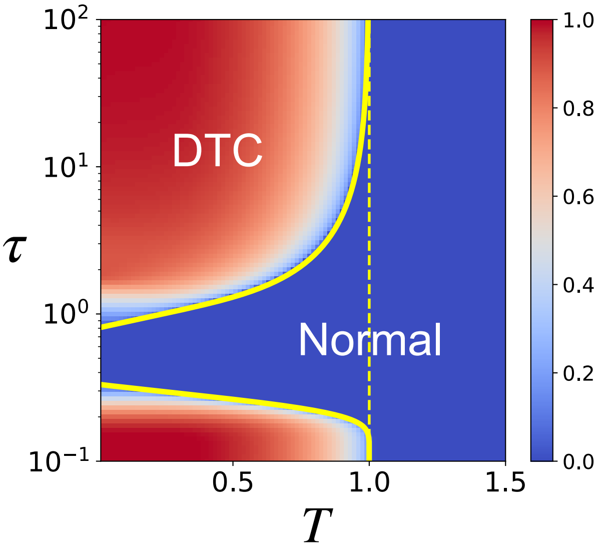

Figure 1: Phase diagram of the DTC in solids. The horizontal (vertical) axis denotes the temperature of the bath (the period of the Hamiltonian).

References

[1] K Chinzei and TN Ikeda: Phys. Rev. Research **4**, 023025 (2022).

Interaction-induced quantum spin Hall state in the Dirac electron system α-(BEDT-TSeF)$_2$I$_3$

Akito KOBAYASHI
Department of Physics, Nagoya University
Nagoya 464-8602

We have constracted extended-Hubbard model using first-principles calculations to deal with spin-orbit and non-local repulsive interactions and have shown that an interaction-induced quantum spin Hall (QSH) state is stabilized, focusing on the recently-discovered candidate topological insulator α-(BEDT-TSeF)$_2$I$_3$ having two-dimensional charge-neutral Dirac cones.[1, 2, 3, 4] In the absence of repulsive interactions, a topological insulator characterized by a nonzero spin Chern number appears by the spin-orbit coupling. By considering up to next-nearest neighbor repulsions at Hartree-Fock level, the intrinsic spin-orbit gap is found to grow and a QSH state appears that has both a nonzero spin Chern number and order parameter as shown in Fig. 1. The loops ϕ_i shown in Fig. 1 represents the spin current flowing between BEDT-TSeF molecules. The spin currents between next-nearest neighboring molecules also exist, but they are omitted in Fig. 1 for simplicity. These spin currents increase at low temperatures below 50 K and widen the gap. Transport coefficients and spin susceptibility have been calculated and found to be consistent with most of the experimental findings, including the metal-to-insulator crossover occurring at $\sim$ 50 K as well as the Berry phase change from 0 to *pi* under hydrostatic pressure. We argue that such a QSH state does not necessitate a sizeable spin-orbit interaction to generate a large insulating gap, which is highly advantageous for the search of novel topological phases in generic materials having small spin-orbit coupling.

References

[1] S. Kitou, et al., Phys. Rev. B 103, 035135 (2021).

[2] T. Tsumuraya et al., Eur. Phys. J. B, 94, 17 (2021).

[3] Y. Suzumura et al., JPSJ 90, 124707 (2021).

[4] D. Ohki, K. Yoshimi, and A. Kobayashi, arXiv:2110.05010

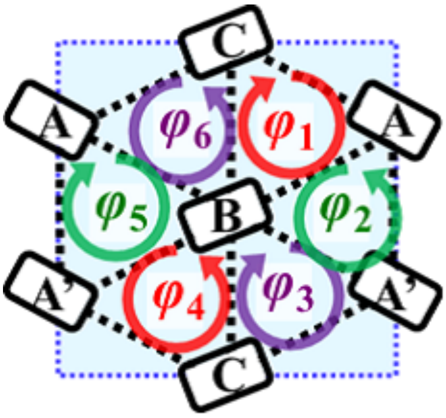

Figure 1: Interaction-induced quantum spin Hall state in α-(BEDT-TSeF)$_2$I$_3$.

Study of cuprate high-temperature superconductors using a four-band d-p model

Hiroshi WATANABE
Research Organization of Science and Technology, Ritsumeikan University
1-1-1 Noji-Higashi, Kusatsu-shi, Shiga 525-8577

The discovery of superconductivity in cuprates [1] has brought about the significant progress in strongly-correlated electron systems. However, we have not yet reached a unified understanding of their properties, including their material dependence of the superconducting transition temperature T_c. Recent development of theories and experiments sheds light on the importance of the orbital degree of freedom in cuprates [2, 3]. To obtain the unified description of cuprate high-temperature supercondctors, we study the four-band d-p model that properly includes the orbital degree of freedom [4]. We construct the tight-binding model for La_2CuO_4 and $HgBa_2CuO_4$ systems based on the first-principles calculation and examine the effect of Coulomb interactions with the variational Monte Carlo (VMC) method. The Gutzwiller-Jastrow type wave function is used for the VMC trial wave function. The system size for the calculation is N=24×24=576 unit cells (and thus 576×4=2304 orbitals in total), which is large enough to avoid finite size effects.

The superconducting correlation function P^{dd} vs hole doping rate x for the La_2CuO_4 system is shown in Fig. 1. At $x = 0$, the system is insulating and the superconductivity is completely suppressed: $P^{dd} = 0$. As x increases, mobile carriers are introduced into the system and the mobility of the Cooper pair increases. On the other hand, the strength of the d-d pairing itself is reduced by doping because the electron correlation is also reduced. The balance between these two factors results in the dome-shaped behavior of P^{dd}. The U_d/t_1 dependence of P^{dd} can be also understood with this picture. We consider that $U_d/t_1 \sim 8$ is a realistic value for the La_2CuO_4 system. For the $HgBa_2CuO_4$ system, while the dome-shaped behavior is observed for $U_d/t_1 = 7$ and 8, P^{dd} monotonically decreases with x for $U_d/t_1 = 6$. This is because the system is metallic for $U_d/t_1 = 6$ and the picture of "doped Mott insulator" is no longer valid. It results from the smaller Δ_{dp} in the $HgBa_2CuO_4$ system that leads to the weaker electron correlation compared with the La_2CuO_4 system. The difference between two systems are well described in our four-band d-p model.

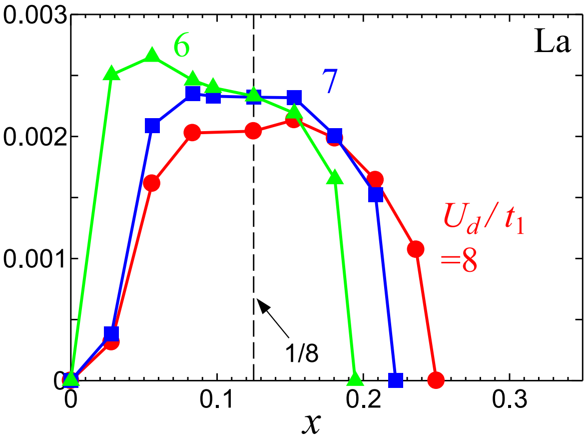

Figure 1: Superconducting correlation function P^{dd} vs hole doping rate x for the La_2CuO_4 system.

References

[1] J. G. Bednorz and K. A. Muller, Z. Phys. B **64**, 189 (1986).

[2] H. Sakakibara et al., Phys. Rev. Lett. **105**, 057003 (2010).

[3] C. E. Matt et al., Nat. Commun. **9**, 972 (2018).

[4] H. Watanabe et al., Phys. Rev. Research **3**, 033157 (2021).

Superconductivity in correlated electron systems

Takashi YANAGISAWA
National Institute of Advanced Industrial Science and Technology (AIST)
1-1-1 Umezono, Tsukuba 305-8568

1 Introduction

Our computations are mainly based on the optimized variational Monte Carlo method[1]. We also employ the Gutzwiller-Jastrow wave function where the doublon-holon correlation is taken into account. We have investigated the ground-state phase diagram of the two-dimensional Hubbard model and the two-dimensional d-p model. We performed parallel computation in Monte Carlo calculations. In order to reduce statistical errors, we carried out $\sim$ 500 parallel calculations. Parallel computing is very important to reduce Monte Carlo statistical errors.

The many-body wave function is written in the form $\psi^{(1)} = \exp(-\lambda K)P_G\psi_0$, where K denotes the kinetic energy part (non-interacting part) of the Hamiltonian and $P_G = P_G(g)$ is the Gutzwiller operator to control the double occupancy with the variational parameter g. ψ_0 indicates a trial wave function which is usually taken as the Fermi sea, the BCS wave function or the state with some magnetic (or charge) orders. We can improve the wave function systematically by multiplying by operators P_G and $e^{-\lambda K}$ repeatedly. We can consider $\psi^{(2)} = \exp(-\lambda' K)P_G(g')\psi^{(1)}$ for different variational parameters λ' and g'. This wave function is a very good many-body wave function because the ground-state energy is lowered greatly and the ground-state energy is lower than those that are evaluated by any other wave functions. We also employ the Jastrow-type wave function which is written as $\psi_J = P_G P_Q P_J \psi_0$ where P_J indicates a nearest-neighbor number correlation operator and P_Q controls the nearest-ngighbor doublon-holon correlation.

2 Why does the pairing state become stable?

We have shown that the superconducting phase exists in the strongly correlated region of electronic models[2]. We investigated kinetic-energy effect in superconductivity in the strongly correlated phase of the two-dimensional Hubbard model. Let us examine why the superconducting state becomes stable in the strongly correlated region. The Gutzwiller-BCS state is stabilized as a potential energy driven superconductivity because the Coulomb interaction energy is lowered while the kinetic energy increases in this state. In contrast, we showed that in the ψ_λ-BCS wave function $\psi_{\lambda-BCS} = e^{-\lambda K}P_G\psi_{BCS}$, the Coulomb energy increases and instead the kinetic energy is lowered in the strongly correlated phase where the Coulomb repulsive interaction U is large. The correlated superconducting state is realized as a kinetic energy driven pairing state and this indicates the enhancement of superconductivity due to kinetic-energy effect.

We estimate the kinetic energy in the superconducting state $\psi_{\lambda-BCS}$[3]. We define the SC condensation energy ΔE_{sc} as a sum of two contributions ΔE_{kin-sc} and ΔE_{U-sc}:

$$\begin{aligned}\Delta E_{sc} &= E(\Delta=0) - E(\Delta=\Delta_{\rm opt}),\\ \Delta E_{kin-sc} &= E_{kin}(\Delta=0) - E_{kin}(\Delta=\Delta_{\rm opt}),\\ \Delta E_{U-sc} &= E_U(\Delta=0) - E_U(\Delta=\Delta_{\rm opt}),\end{aligned}$$

where $\Delta = \Delta_{sc}$ is the SC order parameter and $\Delta_{\rm opt}$ is the optimized value which gives the energy minimum. We have

$$\Delta E_{sc} = \Delta E_{kin-sc} + \Delta E_{U-sc}. \qquad (1)$$

The kinetic energy in $\psi_{\lambda-BCS}$ is lower than the kinetic energy in the normal state ψ_λ. The

Coulomb energy expectation value increases as Δ_{sc} increases. The results show

$$\Delta E_{kin-sc} > 0, \qquad \Delta E_{U-sc} < 0, \tag{2}$$

for $\psi_{\lambda-BCS}$ with $U = 18t$ and the hole density $x = 0.12$.

3 Kinetic energy enhancement of superconductivity

We define the difference of the kinetic energy as

$$\Delta E_{kin} = E_{kin}(\psi_G) - E_{kin}(\psi_\lambda), \tag{3}$$

where $E_{kin}(\psi_G)$ and $E_{kin}(\psi_\lambda)$ indicate the kinetic energy for ψ_G and ψ_λ, respectively. We can write $\Delta E_{kin} = E_{kin}(\lambda = 0) - E_{kin}(\lambda)$ for the optimized value of λ. ΔE_{kin} has the close relation with the SC condensation energy ΔE_{sc} and its kinetic part ΔE_{kin-sc}.

We show $\Delta E_{kin}/N$ in Fig. 1 for $x = 0.12$ where x is the hole doping rate. The Coulomb energy E_U/N and the superconducting condensation energy $\Delta E_{sc}/N$ are also shown in Fig. 1. ΔE_{kin} begins to increase after the Coulomb energy E_U reaches the peak when $U \approx 8t$. The y axis on the right shows $\Delta E_{kin-sc}/N$ in Fig. 1. ΔE_{kin-sc} shows a similar behavior to ΔE_{kin}. ΔE_{kin-sc} may change sign as a function of U, which is consistent with the analysis for $Bi_2Sr_2CaCu_2O_{8+\delta}$[4]. This shows the kinetic energy enhancement of superconductivity.

4 Summary

We examined the kinetic energy effect in SC states. The Gutzwiller-BCS state is the potential energy driven SC state, because the SC condensation energy comes from the Coulomb interaction energy. This is the same as the original BCS state where the superconductivity appears due to the attractive interaction. We evaluated the kinetic energy in the improved SC state ($\psi_{\lambda-BCS}$) to find that the kinetic energy gain stabilizes SC state while the expectation value of Coulomb interaction energy increases. This indicates that superconductivity is enhanced due to the kinetic energy effect.

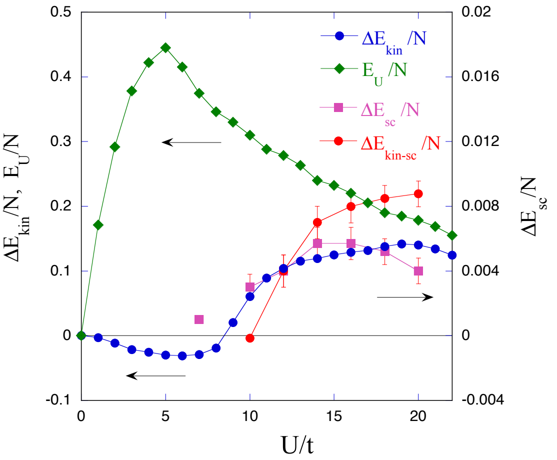

Figure 1: Kinetic-energy difference $\Delta E_{kin}/N$ and the kinetic-energy gain $\Delta E_{kin-sc}/N$ in the superconducting state $\psi_{\lambda-BCS}$ as a function of U on a 10×10 lattice where $N_e = 88$ and $t' = 0$. The Coulomb energy E_U/N for ψ_λ and the condensation energy ΔE_{SC} are also shown. We use the periodic boundary condition in one direction and antiperiodic one in the other direction. The y axis on the right shows the superconducting condensation energy ΔE_{sc} and the kinetic condensation energy $\Delta E_{kin-sc}/N$ for ψ_λ.

References

[1] T. Yanagisawa et al., J. Phys. Soc. Jpn. 67, 3867 (1998).
T. Yanagisawa, Phys. Rev. B75, 224503 (2007) (arXiv: 0707.1929).

[2] T. Yanagisawa, J. Phys. Soc. Jpn. 85, 114707 (2016).
T. Yanagisawa, J. Phys. Soc. Jpn. 88, 054702 (2019).
T. Yanagisawa, Condensed Matter 4, 57 (2019).

[3] T. Yanagisawa, Phys. Lett. A403, 127382 (2021).
T. Yanagisawa et al., EPL 134, 27004 (2021).

[4] G. Deutscher, A. F. Santander-Syro, N. Bontemps: Phys. Rev. B 72, 092504 (2005).

Photoinduced nonequilibrium dynamics in correlated electron systems

Atsushi ONO
Department of Physics, Tohoku University,
Sendai 980-8578

Antiferromagnets are promising for spintronics applications owing to their robustness against a perturbative field and to a higher energy scale compared with that of ferromagnets. Recently, a current-induced staggered torque, called Néel spin-orbit torque (NSOT), has been recognized as an efficient mechanism that rotates the Néel vector in antiferromagnets. However, since most of the previous studies considered the electrical switching of the antiferromagnets, it is not fully understood whether and how the NSOT is generated by optical pulses.

We have studied the real-time dynamics induced by a static electric field and a terahertz electric-field pulse [1]. We considered a minimal tight-binding model of antiferromagnetic Dirac semimetals, where a nonsymmorphic symmetry associated with the direction of the Néel vector protects the crossing of doubly degenerated energy bands, i.e., Dirac points. The time evolution is governed by the Landau–Lifshitz–Gilbert equation for the localized moments and the von Neumann equation for the itinerant electrons. We solved these coupled equations by using the ISSP supercomputer system.

Figure 1 shows the real-time dynamics induced by a mono-cycle electric-field pulse. We found that the Néel vector rotates in a picosecond timescale, depending on the amplitude and polarization of light, and the Néel-vector rotation accompanies the change in the energy gap at the Dirac points. Our analysis revealed that the Néel vector is canted by optical NSOT and then rotated by a magnetic-anisotropy torque. We also showed that in this system a magneto-optical effect can be used to observe the direction of the Néel vector in real time.

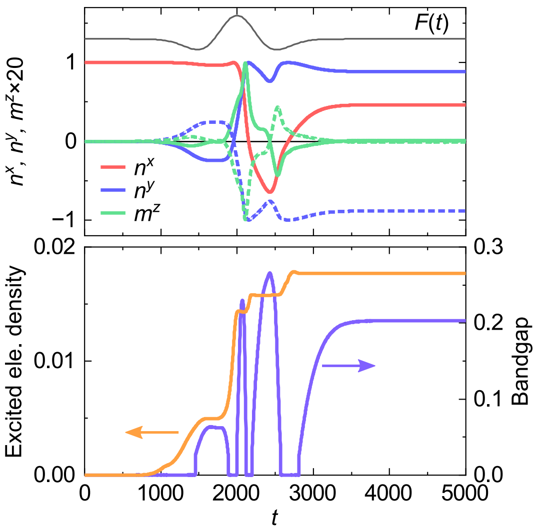

Figure 1: Time evolution of the Néel vector $\boldsymbol{n}$, uniform magnetization $\boldsymbol{m}$, excited electron density, and bandgap [1]. A mono-cycle electric-field pulse $F(t)$ is applied.

References

[1] A. Ono and S. Ishihara, npj Comput. Mater. **7**, 171 (2021).

3.4 Cooperative Phenomena in Complex Macroscopic Systems

Effects of cavitation on soundwaves

Yuta ASANO, Hiroshi WATANABE, and Hiroshi NOGUCHI
Institute for Materials Research, Tohoku University Katahira, Aoba-ku, Sendai, Miyagi 980-8577
Department of Applied Physics and Physico-Informatics,
Keio University, Hiyoshi, Kohoku-ku, Yokohama, Kanagawa 233-8522
Institute for Solid State Physics,
The University of Tokyo, Kashiwa-no-ha, Kashiwa, Chiba 277-8581

Cavitation is a flow phenomenon involving the formation of bubbles, caused by local pressure-drop in a liquid. Cavitation causes performance degradation, noise, vibration, and erosion in fluid machinery such as ship propellers and turbomachinery. On the other hand, the shock waves and localized high-temperature and -pressure fields generated by the bubble collapse are applied to a wide range of applications, including cleaning, processing, chemical reaction acceleration, and medicine. Therefore, it is vital to understand the cavitation mechanisms for many fields using liquid-gas multi-phase flows. In particular, understanding the effects of cavitation on sound waves is essential for the development of applied technology, such as the realization of highly efficient chemical reactors. However, cavitation is an extremely complex phenomenon in which a tremendous number of bubbles repeatedly generate, grow, split and coalesce, and disappear, making its analysis a challenging problem. Despite numerous experiments and numerical calculations, the mechanism remains thoroughly understood. In this project, we investigate the effect of phase transitions on sound waves by molecular dynamics (MD) simulations [1]. In particular, we clarify the differences in the effects of first- and second-order phase transitions on sound waves.

The fluids are modeled by a monoatomic molecule whose interaction is defined by the smoothed-cutoff Lennard-Jones potential. The system is a rectangular parallelepiped, and the periodic boundary conditions are applied to *y*- and *z*-directions. In *x*-direction, the oscillating and stationary walls are placed at both ends. The total number of particles is about 10 million. We investigate the differences in the waveform change by approaching the phase transition temperature for the liquid near the first-order transition region and supercritical fluid near the critical point. These waveforms are compared with the numerical solution of Burgers' equation.

In the first-order transition region, the waveform varies continuously until just above the phase transition point, in good agreement with the Burgers' equation. When the phase transition occurs, the waveform changes discontinuously due to the appearance of the gas phase, and the Burgers' equation is not applicable. On the other hand, in the continuous transition region, no discontinuous changes occur. Soundwave decay due to the density fluctuations are significant near the critical point. However, the Burgers' equation is applicable even for such large density fluctuations.

Finally, we investigated the bubble effects on the soundwaves by using 60 million particles. We observed a bubble generation and growth near the oscillating wall, movement in the soundwave propagation direction, and then disappearance. Bubbles repeat this long time (about 30-million-time steps) cycle. We found that the bubble motion affects the pressure wave.

The present computational scale could only treat the interaction between a single bubble and sound wave. The bubble generation causes a drastic change in soundwave, known as a change in sound speed, which is caused by the appearance of many bubbles. In order to reveal the peculiar phenomena, it is necessary to perform calculations for much larger systems.

References

[1] Y. Asano, H. Watanabe, and H. Noguchi, arXiv:2112.07139.

Coarse-Grained Molecular Dynamics Study of Biomolecular Assemblies and Nanocolloids

Wataru SHINODA
Research Institute for Interdisciplinary Science,
Okayama University, 3-1-1 Tsushima-naka, Kita-ku, Okayama 700-8530

We have extended the molecular library within the SPICA coarse-grained (CG) force field (FF), which was originally developed for lipids and surfactants. In this year, we have added a new class of lipids, proteins, and nucleic acids to the library. Especially, we improved the CG protein model to facilitate molecular dynamics (MD) simulation with a reproduction of multiple properties from both experiments and all-atom (AA) simulations.[1] The side chain analogs reproduced the transfer free energy profiles across the lipid membrane and showed reasonable association free energy (potential of mean force) in water compared to those from AA-MD. The CG-MD study of the adsorption or penetration of about 150 peptides/proteins into the membrane gave correct predictions of the penetration depth and inclination angle of peptides/proteins at the membrane periphery and transmembrane regions, consistent with the OPM (Orientation of protein in membrane) database. The dimerization free energies of some transmembrane helices in the lipid bilayer were found to be comparable to those obtained from experimental estimates. Application studies on a series of membrane protein assemblies, scramblases, and poliovirus capsids demonstrated the good performance of SPICA FF.

A series of MD simulations of Hepatitis B virus (HBV) capsid have also been carried out at AA and CG resolutions.[2] In this year, we have constructed a molecular model of the entire HBV virion particle including the envelope. The interaction between the membrane protein within the envelope and the capsid spike protein plays an important role in a strong anchoring of envelopes around the capsid. Due to a significant amount of membrane proteins in the envelope reduces the lipid diffusion within the envelope, which is supposed to help increasing the stability of virion particle.

We also analyzed the role of surfactants in the colloidal stability of nanoparticles in oil by CG-MD.[3] Again, SPICA FF was used to observe the molecular-level details of nanoparticle aggregation through simulation. A free energy pathway of aggregation is determined for different surfactant types and system configurations. The deformation of the surfactant layer surrounding the nanoparticle was shown to be the major source of colloid stabilization. This is evidenced by the surprising result that as the packing density of the surfactants is reduced, the role of the surfactant is reversed from stabilizer to nucleation agent.

References

[1] S. Kawamoto, H. Liu, Y. Miyazaki, S. Seo, M. Dixit, R. DeVane, C. MacDarmaid, G. Fiorin, M. L. Klein, W. Shinoda: *J. Chem. Theory Comput.* DOI:10.1021/acs.jctc.1c01207.

[2] K. Fujimoto, Y. Yamaguchi, R. Urano, W. Shinoda, T. Ishikawa, K. Omagari, Y. Tanaka, A. Nakagawa, S. Okazaki: *J. Chem. Phys.* **155** (2021) 145101.

[3] M. Griffiths and W. Shinoda: *J. Phys. Chem. B* **125** (2021) 6315. [cover title]

Finite temperature properties of generalized Kitaev models

Tsuyoshi OKUBO
Institute for Physics of Intelligence, The University of Tokyo
7-3-1 Hongo, Bunkyo-ku, Tokyo 133-0033

The Kitaev model on the honeycomb lattice has been widely investigated as a fundamental model to investigate the nature of the quantum spin liquid in two dimension[1, 2]. In the Kitaev model, the interactions are Ising type, $S_i^\gamma S_j^\gamma$, and the spin component $\gamma = x, y, z$ is determined from the direction to the neighboring site. The ground state is known to be a gapless spin liquid state, in which the nature is described by Majorana fermions[1]. When we apply a magnetic field to the Kitaev system, the excitation spectrum described by the mobile Majorana fermions opens a gap, and the ground state changes to a topological spin liquid, where a half-integer thermal Hall conductivity emerges in the low-temperature limit [1]. In the recent experiment on α-RuCl$_3$ under a moderate magnetic field, a similar half-integer thermal Hall conductivity was observed at a finite temperature [3], although its ground state seems to be a magnetically ordered state at zero magnetic field due to off-diagonal and (long-range) Heisenberg interactions.

In this year's project, we investigated a finite temperature properties of the Kitaev model with off-diagonal interactions, in paticular concerning the possible thermal Hall conductivity at a finite temperature. The model Hamiltonian is given as

$$\mathcal{H} = \sum_{\gamma \in x,y,z} \mathcal{H}_\gamma - \vec{h} \cdot \sum_i \vec{S}_i, \qquad (1)$$

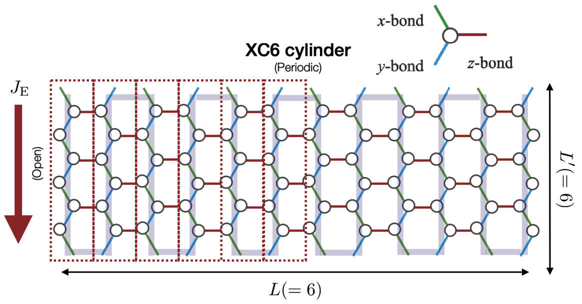

Figure 1: A typical lattice setup and a mappting to a one-dimensional matrix product operator.

where for $\gamma = z$,

$$\mathcal{H}_z = \sum_{\langle i,j \rangle_z} [K S_i^z S_j^z + \Gamma(S_i^x S_j^y + S_i^y S_j^x) + \Gamma'(S_i^z(S_j^x + S_j^y) + (S_i^x + S_i^y)S_j^z)]. \qquad (2)$$

In the cases of $\gamma = x, y$, we consider similar interactions with cyclic rotation of x, y, z components. To numerically calculate the thermal Hall conductivities at a finite temperature, we consider several finite-size clusters with open edges and represent their density matrix as a matrix product operator (MPO), as shown in Fig. 1.

The MPO representing a density matrix at a given temperature was obtained by the exponential tensor renormalization grope (XTRG) algorith [4], where we calculate the density matrix at an inverse temperature β, $\rho(\beta)$, through the relationship $\rho(\beta) = \rho(\beta/2)\rho(\beta/2)$ with the initial condition $\rho(\beta_0) = \exp(-\beta_0\mathcal{H}) \simeq 1-\beta_0\mathcal{H}$

for the sufficiently small β_0. Thus, when we have an MPO representation of the Hamiltonian, a stadard compression algorithm for the tensor network can be used. When the bond dimension of the MPO is D, both of the computation cost and the memory consumption of XTRG algorithm scale $O(D^4)$.

By such an MPO representation of the density matrix, we have successfully calculated the thermal Hall conductivity for various magnetic fields and temperatures up to $N = 72$ spins (see Fig. 1) with a typical bond-dimension $D = 500$. Our calculation showed that the thermal Hall conductivity typically has a peak as a function of the temperature, and it overshoots the half quantized value expected in the zero-temperature limit. Such an overshooting is consistent with the experimental observation [3].

We also investigated Γ and Γ' dependence of the thermal Hall conductivity. We found that depending on the sign of Γ and Γ', the thermal Hall conductivity is largely modified from that of the pure Kitaev model. Some of them could be explained by the increase of the gap, previously calculated through the perturbation theory [5], while overall finite temperature behaviors might not be explained only by Majorana fermion pictures.

A part of this work has been done in collaboration with J. Nasu, T. Misawa, and Y. Motome.

References

[1] A. Kitaev, Ann. Phys. **321** (2006) 2.

[2] Y. Motome and J. Nasu, J. Phys. Soc. Jpn. **89** (2020) 012002.

[3] Y. Kasahara, T. Ohnishi, Y. Mizukami, *et al.*, Nature **559** (2018) 227.

[4] H. Li, D.-W. Qu, H.-K. Zhang, *et al.* Phys. Rev. Research **2** (2020) 043015.

[5] D. Takikawa and S. Fujimoto, Phys. Rev. B **102** (2019) 174414.

Membrane shape deformation by binding of curvature-inducing proteins

Hiroshi NOGUCHI
Institute for Solid State Physics, University of Tokyo

In living cells, biomembrane shapes are controlled by curvature-inducing proteins. We have studied the binding of these proteins using mean-field theories and compared their results with simulation results. Clathrin and coat protein complexes bend membranes in a laterally isotropic manner and generate spherical buds. In contrast, Bin/Amphiphysin/Rvs (BAR) superfamily proteins bend the membrane anisotropically and generate cylindrical membrane tubes. The former and latter proteins can be modeled as laterally isotropic objects and anisotropic objects of a banana or crescent shape, respectively.

For isotropic proteins, we derived the free energy including the Gaussian curvature and area expansion by the protein insertion [1]. Then, we investigated the formation of spherical buds [1] and binding onto a tethered vesicle [2]. A narrow membrane tube (tether) is elongated from a spherical vesicle by an external force imposed by a micropipette and optical tweezers. A first-order transition occurs between a small number of large buds and a large number of small buds with increasing chemical potential of protein binding [1]. For the tethered vesicle, interestingly, a first-order transition occurs twice between low and high protein densities in the tube. The force-dependence curves of the protein density in the membrane tube and the tube curvature are reflection symmetric and point symmetric, respectively, from the force point, in which the tube curvature matches the protein (sensing) curvature [2]. This theory reproduces the meshless membrane simulation results of the homogeneous phases very well. In addition, beaded-necklace-like tubes with microphase separation are formed in the simulation.

For anisotropic proteins, an orientational-dependent excluded volume interaction is included in the free energy. We studied binding onto membrane tubes [3]. The proteins exhibit a second-order or first-order nematic transition with increasing protein density for intermediate and small radii of the membrane tube, respectively. The tube curvatures for the maximum protein binding (sensing) and orientational order are differently varied by the protein density and rigidity. As the external force along with the tube axis increases, a first-order transition from a large tube radius with low protein density to a small radius with high density occurs once, and subsequently, the protein orientation tilts to the tube-axis direction. The density-dependent sensing curvature and the number of transitions are characteristics due to the anisotropic bending energy. Each isotropic protein has a constant sensing curvature. This density-dependent sensing curvature has been measured in the experiment of BAR proteins. This theory quantitatively reproduces the results of meshless membrane simulation for short proteins. For long proteins, the formation of protein clusters generates a quantitative deviation from the theory, although qualitative agreements still hold.

References

[1] H. Noguchi, *Phys. Rev. E* **104**, 014410 (2021).

[2] H. Noguchi, *Soft Matter* **17**, 10469 (2021).

[3] H. Noguchi, C. Tozzi, and M. Arroyo, *Soft Matter* (2022) DOI:10.1039/D2SM00274D.

Development of Thermal Functional Materials Based on First-principles Simulations

Junichiro SHIOMI
Department of Mechanical Engineering,
The University of Tokyo, Hongo 7-3-1, Bunkyo-ku, Tokyo 113-8656, Japan

We have studied thermal functional materials using massive parallel computer system. This year, we focused on the thermoelectric performance of a ternary alloy system and a nanostructured multiphase material.

The main content of these two studies is briefly introduced as below. For the ternary alloys, lattice structures were predicted by Monte Carlo simulation, then thermoelectric properties and the compositional dependence of ternary alloys were studied by first-principle calculation. Fig. 1 shows the predicted energy by cluster expansion and ZT of alloy of a composition. For the multiphase material, the grain size dependence of thermoelectric properties was studied by first-principle calculation for two phases to enhance thermoelectric performance by nanostructure engineering. Fig. 2 shows the nanostructured

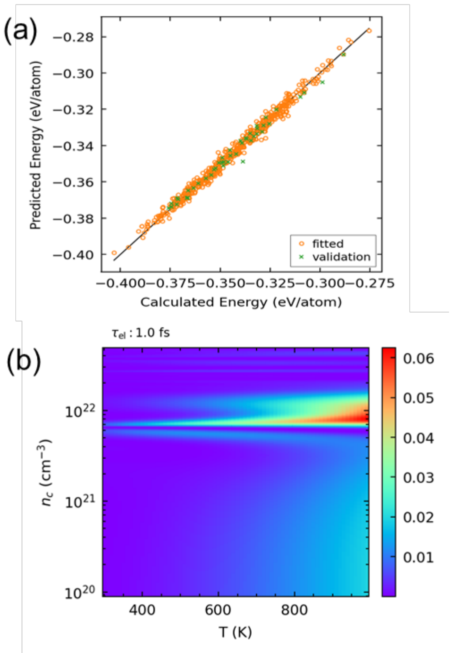

Fig. 1: (a) Formation energies from cluster expansion; (b) ZT of one of the alloys.

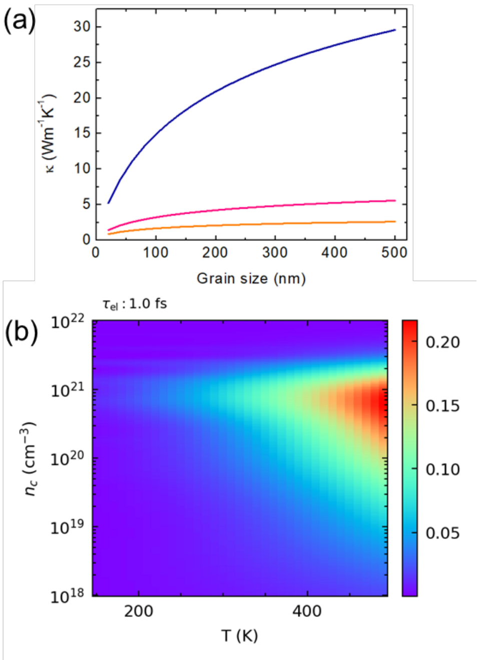

Fig. 2: (a) Thermal conductivity versus grain size; (b) ZT of a nanostructured material.

thermal conductivity at room temperature and ZT of a nanostructured phase.

To conduct these studies, the usage of supercomputer system was described as following. ICET package [1] was employed to predict lattice structures through performing Monte Carlo simulation and cluster expansion based on element substitution and formation energy prediction. BoltzTrap2 package [2] was carried out to calculate electrical transport properties by solving semiclassical linearized Boltzmann transport equation. ALAMODE package [3] was used to fit interatomic force constants by atomic displacements and forces from first-principle calculation, as well as calculate phonon thermal conductivity by relaxation time approximation method. VASP [4] was carried out to perform first-principle calculation for formation energy, band structure and atomic forces. By running our own python script, thermoelectric properties were calculated from phonon thermal conductivity and electrical properties.

References

[1] M. Ångqvist, W. A. Muñoz, J. M. Rahm, E. Fransson, C. Durniak, P. Rozyczko, T. H. Rod, and P. Erhart: Adv. Theor. Simul. 2 (2019) 1900015.

[2] G. K. H. Madsen, J. Carrete, and M. J. Verstraete: Comput. Phys. Commun. 231 (2018) 140.

[3] T. Tadano, Y. Gohda, and S. Tsuneyuki: J. Phys.-Condens. Mat. 26 (2014) 225402.

[4] G. Kresse and J. Furthmüller: Comp. Mater. Sci. 6 (1996) 15.

Feasibility study of Kitaev quantum spin liquid by functional renormalization approach

Kiyu FUKUI and Yusuke KATO
Department of Applied Physics, University of Tokyo, Bunkyo, Tokyo 113-8656
Department of Basic Science, University of Tokyo, Meguro, Tokyo 153-8902

The Kitaev model is an $S = 1/2$ quantum spin model defined on the honeycomb lattice [1]. In spite of its strong frustration due to the bond-dependent interaction, this model is exactly solvable, and its ground state is a quantum spin liquid state. Here we address the feasibility of the Kitaev quantum spin liquid (KQSL) for two extensions of the model, by using the pseudofermion functional renormalization group (PFFRG) method [2].

The first one is for ultracold polar molecules trapped in an optical lattice. While experimentally accessible implementation of the Kitaev-type interaction was proposed in 2013 [3], the stability of the KQSL has not been investigated so far. In this proposal, the bond-dependent anisotropic interactions are mimicked by angle-dependent dipole interactions between molecules. However, the interactions are long ranged with a spatial decay of r^{-3}, where r is the distance between the molecules, it is left as an open question whether the KQSL can survive against such long-range interactions. We studied the ground state of a quantum spin model with long-range angle-dependent Kitaev-type interactions, which was proposed as an implementation of the Kitaev model in ultracold polar molecules, by using the PFFRG method. We clarified that, regardless of the spatial anisotropy of the interactions, the ground state is magnetically ordered in both FM and AFM cases: we found magnetic instabilities toward the FM and zigzag ordered states in the FM and AFM models, respectively. By calculation of the anisotropy parameter dependence of the critical cutoff scale, we concluded that the system is most frustrated and closest to the realization of the KQSL when the interaction is isotropic in both cases. Our findings indicate that the QSL ground state arising from the nearest-neighbor bond-dependent anisotropic interactions in the Kitaev model is destroyed by the long-range interactions. By varying the range of the interactions, we unraveled that the KQSL is unstable even for the third-neighbor interactions. This is the first time that the stability of the KQSL within the above proposal has been revealed.

The other is the extension to higher-spin systems. Although the Kitaev model was originally introduced for the $S = 1/2$ moments, its higher-spin generalization has also attracted attention. While candidate materials with $S = 1$ [4] and $3/2$ [5] have begun to be proposed in recent years, the stability of the KQSL has not been systematically clarified for general spin S in the presence of non-Kitaev interactions, which are inevitably present in the candidate materials. In this study, we present our numerical results on the ground state of higher-spin generalization of the Kitaev model including the Heisenberg interaction, the spin-S Kitaev-Heisenberg model, which we consider to be one of the minimal models for the higher-spin candidate materials, by using an extension of the PFFRG method [6]. Performing the calculations for the models with $S = 1$, $3/2$, 2, $5/2$, and 50 in addition to $S = 1/2$, we elucidate the ground-state phase diagram by systematically changing the ratio between the Kitaev and Heisenberg interactions and S. We found four magnetically ordered phases: Néel AFM, zigzag AFM, FM, and stripy AFM for all S, and the phase boundaries between these ordered phases are consistent with the previous studies for $S = 1/2$, 1, and ∞. Our results indicated that the ground state is short-range QSL for arbitrary S at the ferromagnetic and antiferromagnetic Kitaev points. It is consistent with an analytical result in the previous study [7]. We clarified that the QSL regions near these Kitaev points are quickly shrunk by increasing S, namely, the KQSL is fragile against the Heisenberg interaction for $S \geq 2$. However, we find the KQSL remains stable for $S \leq 3/2$ around the both Kitaev points. Our findings will provide the search and design of the candidate materials with $S > 1/2$.

References

[1] A. Kitaev, Ann. Phys. **321**, 2 (2006).

[2] J. Reuther and P. Wölfle, Phys. Rev. B **81**, 144410 (2010).

[3] S. R. Manmana *et al.*, Phys. Rev. B **87**, 081106 (2013); A. V. Gorshkov, K. R. Hazzard, and A. M. Rey, Mol. Phys. **111**, 1908 (2013).

[4] P. P. Stavropoulos, D. Pereira, and H.-Y. Kee, Phys. Rev. Lett. **123**, 037203 (2019); A. M. Samarakoon *et al.*, Phys. Rev. B **104**, 184415 (2021).

[5] C. Xu *et al.*, npj Comput. Mater. **4**, 57 (2018); M. Kim *et al.*, Nat. Electron. **2**, 457 (2019); I. Lee *et al.*, Phys. Rev. Lett. **124**, 017201 (2020); C. Xu *et al.*, *ibidem*, 087205 (2020).

[6] M. L. Baez and J. Reuther, Phys. Rev. B **96**, 045144 (2017).

[7] G. Baskaran, D. Sen, and R. Shankar, Phys. Rev. B **78**, 115116 (2008).

Quantum effects on chiral magnets

SOHEI KODAMA and YUSUKE KATO

Department of Basic Science, the University of Tokyo, Tokyo 153-8902, Japan,

We consider the ground state of quantum spin chain of monoaxial chiral ferromagnet. The Hamiltonian is given by

$$H = \sum_i \left[-J \hat{\boldsymbol{S}}_i \cdot \hat{\boldsymbol{S}}_{i+1} - D\left(\hat{\boldsymbol{S}}_i \times \hat{\boldsymbol{S}}_{i+1}\right)_y - H\hat{S}_i^z + K\left(\hat{S}_i^y\right)^2 \right],$$

where, J, D, H, and K, respectively, denote exchange interaction, Dzyaloshinskii-Moriya (DM) interaction, the magnetic field perpendicular to the chiral axis (y -axis) and single ion anisotropy.

The magnetization curves for finite-sized systems obtained by *exact diagonalization* are distinctly different between half-odd-integer and integer spins; The level crossings occur for S=1/2,3/2, accompanied by π shift of the crystal momentum k while the magnetization process is continuous and k is always zero for S=1,2. These behaviors are commonly observed for arbitrary values of J/D. We argue that in the limit J=0 with D finite, single soliton has the minimum energy for k=π (k=0) for half-odd integer (integer) S, based on the Perron-Frobenius theorem within the subspace spanned by a single soliton basis. Our approach [1] is complementary to earlier studies on quantum effects on Ising domain wall [2] and skyrmions [3] based on semiclassical treatment of quantum spin taking account of the Berry phase term.

References

[1] S. Kodama, A. Tanaka, and Y. Kato, in preparation.

[2] H. B. Braun, Adv. Phys. **61**, 1 (2012).

[3] R. Takashima, H. Ishizuka, and L. Balents, Phys. Rev. B **94**, 134415 (2016).

New scaling analysis for graph percolations

Y. Ozeki and K. Hagiwara v

Graduate School of Informatics and Engineering, The University of Electro-Communications

We investigate the transition point and the critical exponent β for graph percolations. A new size-independent scaling analysis is proposed, which enables us to analyze numerical data without finite-size effects. This means that the results are equivalent to those in the infinite system. Such a scaling analysis has been applied as dynamical scaling analysis in the nonequilibrium relaxation method [1] for phase transitions and critical phenomena.

In graph percolations, a number of vertices are prepared instead of a lattice. Each edge between two of these vertices is considered to be connected or not. In the Erdős-Rényi (ER) model, a classical graph percolation, a new edge is connected to a graph at random. The probability of a vertex belonging to the infinite cluster, which is denoted by $P(r)$, is recognized as the order parameter, where r is the average number of edges per vertex. The function $P(r)$ can be written as [2]

$$P(r) \equiv 1 - \sum_{s} s n_s, \tag{1}$$

where n_s is the number of clusters with size s divided by N. $P(r)$ is expected to behave algebraically as

$$P(r) = a|r - r_{\rm c}|^{\beta}, \tag{2}$$

where β is referred to as a critical exponent. In the present study, we define a new function $P(x, r)$ by extending $P(r)$,and introduce a new parameter x representing the maximum cluster size:

$$P(x, r) \equiv 1 - \sum_{s<x} s n_s. \tag{3}$$

This function $P(x, r)$ represents the probability that a randomly selected vertex belongs to a cluster greater than or equal to x. We expect the following asymptotic ($x \to \infty$) behaviors for every r case:

$$P(x, r) \sim \begin{cases} A \exp(-x/\xi) & (r < r_{\rm c}) \\ x^{-\lambda_P} & (r = r_{\rm c}) \\ p_\infty + A' \exp(-x/\xi) & (r > r_{\rm c}) \end{cases} \tag{4}$$

where we introduce a function ξ depending on r as $\xi = \xi(r)$ and exponent λ_P. The asymptotic behavior of ξ is expected to be

$$\xi(t) = b|r - r_{\rm c}|^{-\nu}, \tag{5}$$

where we define a new exponent ν satisfying the relation

$$\lambda_P = \beta/\nu. \tag{6}$$

In the asymptotic regime in $r \sim r_{\rm c}$, $P(x, r)$ is expected to satisfy the following scaling form:

$$P(x, r) = \xi^{-\lambda_P} \Psi(x/\xi). \tag{7}$$

The transition point $r_{\rm c}$ and critical exponent β can be estimated from the behavior of $P(x, t)$. Appropriate values of $r_{\rm c}$ and β as well as a, b, ν in Eqs. (2) and (5) should be chosen such that $\xi^{\lambda_P} P(x, t)$ is fitted as a function of $x/\xi(r)$ on a scaling function Ψ. In order to carry out such a scaling plot efficiently, we apply the method introduced for the dynamical scaling, in which the Bayesian inference and the kernel method are used [3].

Here, we demonstrate the above scaling analysis to the ER model, for which the analytic solution is known; $r_{\rm c} = 1/2, \beta = 1$. For precise analysis, we need to check the size dependence. We have found that, for $x \leq 3000$, no size dependence appears in the data for the system with $N = 1 \times 10^8$ or larger. The simulation is performed using these parameters, and 2240 independent samples were used for averaging. The results for $P(x, r)$ are plotted in Fig. 3, and the resultant scaling plot is shown in Fig. 4. The transition points and the critical exponent are evaluated as $r_{\rm c} = 0.49978(7)$ and $\beta = 1.010(9)$, respectively, where the error bars are estimated by the bootstrap method [3]. The deviations from the analytic values $r_{\rm c} = 1/2, \beta = 1$ are approximately 0.044% and 1.0%, respectively, demonstrating that the present analysis is reliable.

We apply the above scaling method to the dCDGM model [4], in which a vertex is selected from randomly chosen m vertices so that the size of the connected cluster is smallest and the new edge connects two vertices selected twice with the aforementioned process; the integer value m is fixed and distinguishes the model as the dCDGM(m) model. We investigate the dCDGM($m = 2$) model. The same analysis was performed. It is confirmed that the simulation for the system with $N = 1 \times 10^8$ to $x \leq 3000$ is sufficiently large. The simulation is performed using these parameters, and 4480 inde-

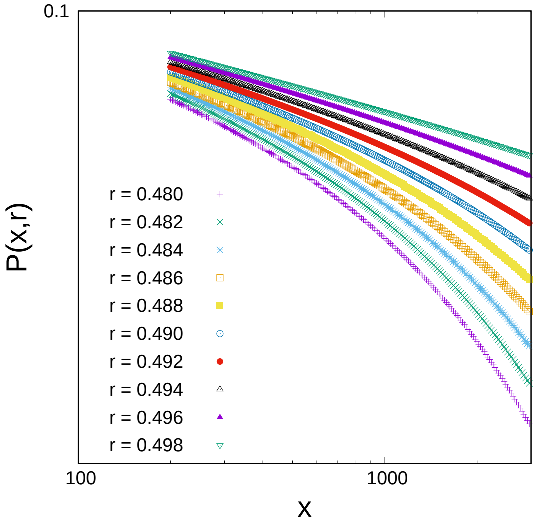

Figure 1: Results of $P(x,r)$ for the ER model.

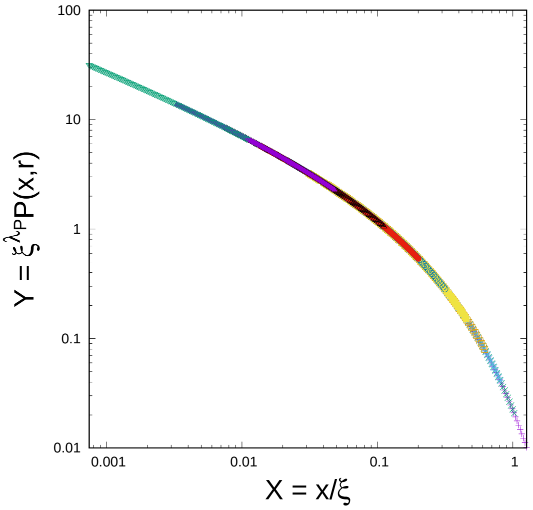

Figure 2: Scaling plot of $P(x,r)$ for the ER model.

pendent samples are used for averaging. The transition points and the critical exponent are evaluated as $r_c = 0.923211(5)$ and $\beta = 0.056(1)$, respectively, which are consistent with those of Da Costa ($r_c = 0.923207509297(2)$ and $\beta = 0.05557108(1)$) [4].

References

[1] Y. Ozeki and N. Ito, *J. Phys.: Math. Theor.* **40** R149 (2007).

[2] D. Stauffer and A. Aharony, "Introduction to percolation theory", (Taylor & Francis,1994)

[3] Y. Echinaka and Y. Ozeki, *Phys. Rev.* E**94** 043312 (2016).

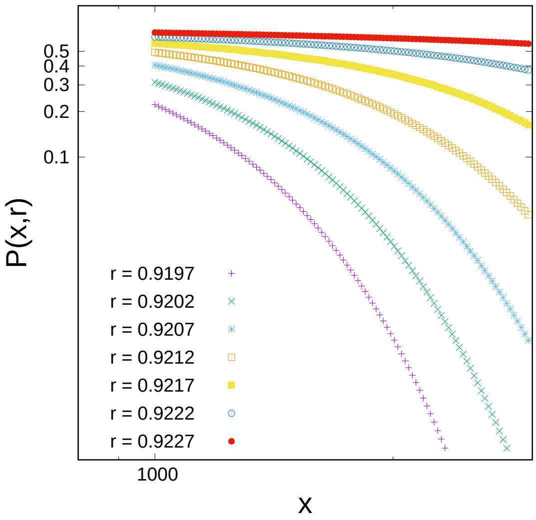

Figure 3: Results of $P(x,r)$ for the dCDGM(2) model.

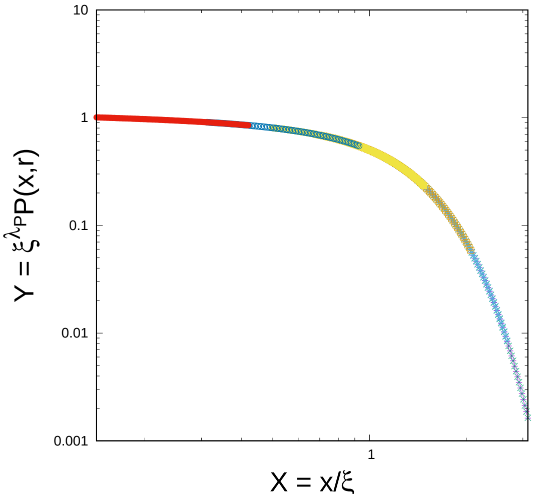

Figure 4: Scaling plot of $P(x,r)$ for the dCDGM(2) model.

[4] R. A. Da Costa, S. N.Dorogovtsev, A. V. Goltsev, and J. F. F. Mendes, *Phys. Rev.* E**89** 042148 (2014); *Phys. Rev.* E**90** 022145 (2014).

Computational design of proteins useful for medical and industrial applications

Masataka YOSHIMURA[1], Sairi MATSUMOTO[1], Mizuki TERANISHI[1],
Hirotaro SHIMAMURA[2], Rina AOYAMA[1], Koji OOKA[2], Shino MASUOKA[1],
Shunji SUETAKA[1], Nao SATO[1], Yuuki HAYASHI[1], and Munehito ARAI[1,2]
[1]*Department of Life Sciences, Graduate School of Arts and Sciences, and*
[2]*Department of Physics, Graduate School of Science,*
The University of Tokyo, Komaba, Meguro, Tokyo 153-8902

Proteins have been widely used as therapeutics for various diseases and as enzymes for industrial production of useful substances. Recently, theoretical design of proteins has attracted much attention; however, it is still difficult to theoretically design useful proteins. To solve this problem, we have designed various useful proteins using the Rosetta 3.13 suite [1] and have experimentally checked the validity of the computational design.

Magnets are optogenetic tools for manipulating protein-protein interactions (PPIs) [2]. They consist of pMag and nMag, which heterodimerize upon exposure to blue light. However, improvement of their binding affinity has been demanded. Here we computationally designed the Magnets mutants with higher pMag/nMag affinity than the original ones by theoretical mutagenesis using Rosetta. Experiments confirmed that the mutants enhanced the dimer affinity. Thus, these Magnets mutants may be useful for *in vivo* manipulation of PPIs.

Severe acute respiratory syndrome (SARS) coronavirus 2 (SARS-CoV-2) is an emerging virus that causes the pandemic of the coronavirus disease 2019 (COVID-19). Since the viral infection is caused by the binding of the receptor binding domain (RBD) of the spike protein of SARS-CoV-2 to the human angiotensin-converting enzyme 2 (ACE2) [3], we computationally designed a single-chain variable fragment (scFv) of an antibody against the SARS-CoV-2 RBD using the scFv against the SARS-CoV RBD as a template. Experiments showed that the designed antibody has a high affinity to SARS-CoV-2 RBD comparable to that of the antibody medicines for SARS-CoV-2.

Formation of a ternary complex by interleukin-33 (IL-33), interleukin-1 receptor accessary protein (IL-1RAcP), and the ST2 receptor of type 2 innate lymphoid cells is responsible for allergic asthma [4]. To develop a therapeutic agent for the disease, we are trying to computationally design a protein that tightly binds ST2 but does not bind IL-1RAcP using IL-

33 as a template. We have finished designing a protein that tightly binds to ST2. Further design of the IL-33 mutant that abolishes the binding with IL-1RAcP is under way.

The interaction between the programmed cell death protein 1 (PD-1) and the programmed death-ligand 1 (PD-L1) is important in suppressing T-cell inflammatory activity [5]. To develop an inhibitor of the T-cell activity, we computationally designed the mutants of a PD-L1 fragment that tightly bind PD-1. Experiments confirmed that some mutants have improved affinity with PD-1. We are trying to further improve the affinity by multiple mutations.

Alkane biosynthesis has attracted much attention as a promising way of producing carbon-neutral bioenergy. A key enzyme for cyanobacterial alkane biosynthesis is aldehyde deformylating oxygenase (ADO) [6]. We computationally designed ~10 mutants of ADO that are expected to have high activity. The experimental test of the ADO activity is ongoing.

Understanding protein dynamics is essential for improving catalytic activity of enzymes. We performed molecular dynamics simulations of ADO using the Gromacs 2021.4 program package [7]. An initial structure was constructed using the AmberTools21 package. The force fields for the substrate (aldehyde) and the product (alkane) were obtained using Antechamber module. The simulations were performed for ~800 ns each for the apo form, holo (iron-bound) form, substrate-bound form, and product-bound form of ADO. We found that the product has higher flexibility than the substrate inside the protein molecule, thereby facilitating the product release.

Finally, to predict the folding processes of proteins, we calculated free energy landscapes of multi-domain proteins using the Wako-Saitô-Muñoz-Eaton model, which is an Ising-like, structure-based statistical mechanical model [8]. By introducing modifications to the model, we succeeded in obtaining the folding pathways and intermediates that are fully consistent with experimental results. Thus, our method may pave the way for solving the folding mechanisms of multi-domain proteins that are abundant in proteomes.

References

[1] J. K. Leman, et al.: Nat Methods, **17** (2020) 665-680.

[2] F. Kawano, et al.: Nat Commun. **6** (2015) 6256.

[3] J. Shang, et al.: Nature, **581** (2020) 221-224.

[4] X. Liu, et al.: Proc Natl Acad Sci USA. **110** (2013) 14918-14923.

[5] C. N. Bryan, et al.: Proc Natl Acad Sci USA. **118** (2021) e2102164118.

[6] M. Arai, et al.: Adv Exp Med Biol. **1080** (2018) 119-154.

[7] M. J. Abraham, et al.: SoftwareX, **1-2** (2015) 19-25.

[8] M. Sasai, et al.: Biophys Physicobiol. **13** (2016) 281-293.

Topological order and quantum operation in quantum many-body systems

Synge TODO
Department of Physics, University of Tokyo, Tokyo, 113-0033
Institute for Solid State Physics, University of Tokyo, Kashiwa, 277-8581

We developed novel numerical methods by combining quantum Monte Carlo methods, tensor-network algorithms, and other optimization techniques and investigated topological quantum phase transitions in strongly correlated many-body systems and optimization of quantum operations in quantum computing.

Phase transition in quantum dimer model: Based on the idea of stochastic series expansion, we implemented a Monte Carlo algorithm for investigating the phase transition of the quantum dimer model in an efficient way to simulate with shorter CPU time and extended it to simulation on larger Hilbert space, including monomer-dimer and monomer-monomer interaction. We obtained the phase-transition temperature between the critical and columnar phases by different order parameters by simulations at finite temperatures. We found it vanishes at around Rohksar-Kivelson (RK) point, while the classical limit merges smoothly to the value obtained by the classical Monte Carlo.

Tensor-network Markov-chain Monte Carlo: We developed a novel *quantum-inspired* method that combines the tensor-network representation of weight function and the sampling scheme based on the Markov-chain Monte Carlo method. We can remove the systematic bias due to the finiteness of the bond dimension in tensor network representation from the Markov-chain sampling. Furthermore, the statistical error of the sampling reduces exponentially as increasing bond dimension, and we can avoid the negative-sign problem in quantum lattice models by adopting a high-precision tensor network renormalization scheme.

Many-body localization in random spin chain: We study the many-body localization of the random-field Heisenberg chain using the nested shift-invert Lanczos method with an iterative linear solver. We use the minimum residual method (MINRES) inside each Lanczos iteration. As a probe of many-body localization transition, we propose a unitary operator called the twist operator, which has a straightforward interpretation in the real space. We estimate the transition point of the random-field Heisenberg chain precisely [1].

Decomposition of multi-qubit gate: We obtain efficient decompositions of CCZ and CCCZ gates, typical multi-qubit gates, under several qubit connectivities, using the sequential quantum-circuit optimization algorithm. We can construct the CCZ gate with only four CZ-depth when the qubit is square-shaped, including one auxiliary qubit. In T-shaped qubit connectivity, which has no closed loop, we can decompose the CCCZ gate with 17 CZ gates [2].

References

[1] T. Kutsuzawa and S. Todo, preprint: arXiv:2203.09732.

[2] K. M. Nakanishi, T. Satoh and S. Todo, preprint: arXiv:2109.13223.

O(N) algorithm for the Monte Carlo simulation of the Kitaev model

Masahiko G. YAMADA[1]
Yutaka AKAGI[2]
Masafumi UDAGAWA[3]
[1]*Department of Materials Engineering Science, Osaka University*
Machikaneyama-cho, Toyonaka, Osaka 560-8531
[2]*Department of Physics, University of Tokyo*
Hongo, Bunkyo-ku, Tokyo 113-0033
[3]*Department of Physics, Gakushuin University*
Mejiro, Toshima-ku, Tokyo 171-8588

The thermodynamics of the Kitaev model is of great interest, especially after the characteristic specific heat behavior called a double peak has been discovered by the Monte Carlo simulation [1].

We extend their simulation using a new $O(N)$ calculation method for the Kitaev model Monte Carlo [2]. We newly employed the infinite product expansion (iPE) method instead of the previous Trotter decomposition method. By this iPE method, we succeeded in reducing the calculation cost of the Kitaev model drastically from $O(N^4)$ to $O(N)$. As a benchmark, we did a simulation for the Kitaev model on the honeycomb lattice and computed the heat capacity and its double-peak structure. Using the new algorithm and a supermassive parallelization in the ISSP supercomputer, we succeeded in reproducing the results in [1] within the errorbar (see Fig. 1). Though currently the calculation is limited up to the 54-site cluster with an open boundary, we will eventually extend this to the large-scale Monte Carlo simulation up to $O(1000)$-site simulations. If we also extend the calculation to three dimensions, we can potentially discuss the thermodynamic properties of the vaporization transition in the three-dimensional Kitaev model, which was suggested in Ref. [1].

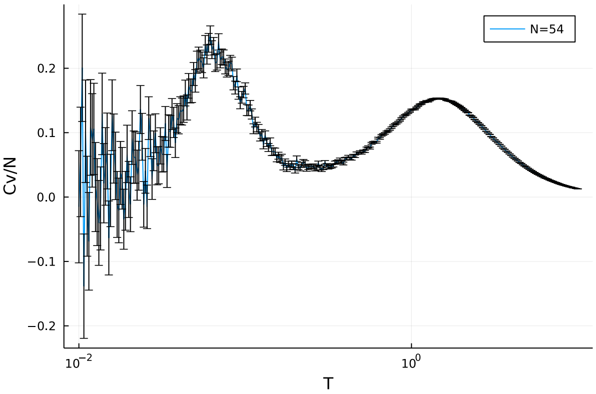

Figure 1: Specific heat data for the $N = 54$ cluster simulation.

References

[1] J. Nasu, M. Udagawa, and Y. Motome: Phys. Rev. Lett. **113** (2014) 197205.

[2] M. G. Yamada, Y. Akagi, and M. Udagawa: to appear.

DMRG algorithm with a full SU(N) implementation

Masahiko G. YAMADA
Department of Materials Engineering Science, Osaka University
Machikaneyama-cho, Toyonaka, Osaka 560-8531

The density matrix renormalization group (DMRG) is one of the most powerful numerical methods for strongly correlated condensed matter systems. Following the previous work, we extended DMRG to the case with the SU(N) symmetry with $N > 2$, even for two-dimensional systems. As a killer application, we simulated the ground state of the SU(4) Heisenberg model on the honeycomb lattice, which can potentially be realized in cold atomic systems and solid state systems like α-ZrCl$_3$ [2]. We keep up to 12800 SU(4) states equivalent to more than a million U(1) states. This supermassive DMRG simulation reveals the quantum spin-orbital liquid ground state, which has dubiously been expected for more than a decade. The methodology developed here can be extended to any classical Lie groups, paving the way to a next-generation DMRG with a full symmetry implementation [3].

References

[1] P. Nataf, and F. Mila: Phys. Rev. B **97** (2018) 134420.

[2] M. G. Yamada, M. Oshikawa, and G. Jackeli: Phys. Rev. Lett. **121** (2018) 097201.

[3] M. G. Yamada, K. Penc, and F. Pollmann: to appear.

Efficient Sampling Simulation of the Soft Modes Significantly Contribute to Protein Properties

K. TAKEMURA, D. TRAN, M.M. SOBEH, Y. MIYAZAWA, R. KIUCHI, T.N. WIJAYA, T. OGAWA, Y. TAIRA, R. MISU, R. Osawa, M. Yoshioka, H. NAKAYA and A. KITAO
School of Life Science and Technology, Tokyo Institute of Technology
Ookayama, Meguro, Tokyo 152-8550

Previously, we developed parallel cascade selection molecular dynamics (PaCS-MD) as an enhanced sampling strategy that uses cycles of multiple independent MD simulations done in parallel to improve the chance of biologically rare events occurring without external perturbation [1]. PaCS-MD consists of cycles of several independent parallel short all-atom MD simulations followed by selecting initial structures for the next cycle according to a specified quantity. We conducted the dissociation simulation of the p53 DNA binding domain (p53DNA) from DNA [2]. We used the inter-center of mass distance (inter-COM distance, d) between p53-DBD and DNA as a quantity for ranking the snapshots generated in each cycle. By repeating a series of cycles for the selected top-ranked snapshots (top 10 snapshots), dissociation PaCS-MD generates structures with larger inter-COM distances than those found in the previous cycle, which significantly enhances the probability of transitions from the bound to unbound states. Finally, we repeated the cycles until d = 70 Å to complete the dissociation, as we can see in the PaCS-MD flowchart in Fig. 1

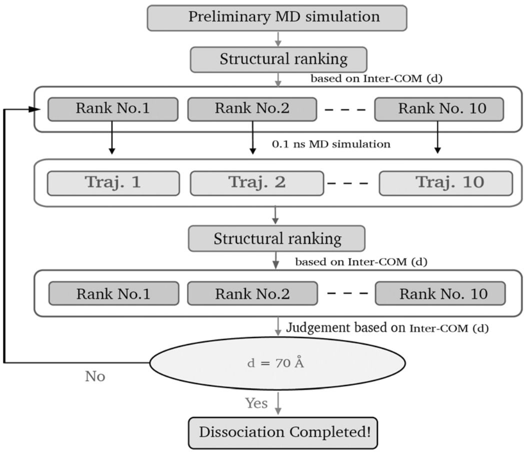

Fig. 1 The flowchart of PaCS-MD

We successfully generated 75 different dissociation pathways of p53-DBD from DNA. We used the COM positions of the p53-DBD interface residues relative to those of DNA to visualize the dissociation pathways, as shown in Fig. 2. Inspection of the dissociation pathways indicates that the sampled space formed a cone-like shape around the DNA. Around 93% of the sampling pathways (70 pathways) dissociated along the +X and −Y directions (namely, the −Y directions), while the other pathways moved along +X and +Y directions, which only occupy 7% (5 pathways), hereafter called the +Y directions.

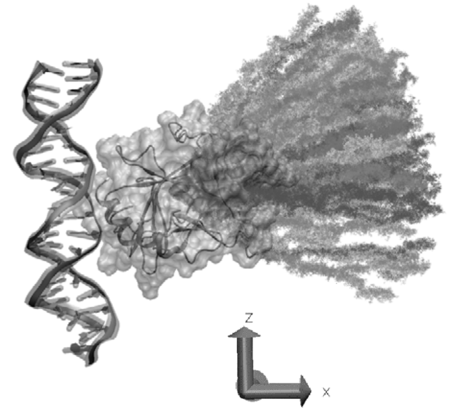

Fig. 2 Dissociation pathways of 75 PaCS-MD trials of p53-DBD from DNA.

Using the Markov state model (MSM), We obtained the free energy profile of p53-DBD dissociation from DNA and showed the projections onto the XY planes, as shown in Fig. 3. The global minimum of this profile represents the bound state. As discussed above, dissociation mainly (93%) occurred along the −Y directions on the XY-plane, and other dissociations (7%) occurred along the +Y directions. As we can see in Figure 4, during the dissociation process, the PMF increased at a higher rate in the bound state to achieve convergence (became flat) in the unbound region (d ≥ 45 Å). We calculated the binding free energy (ΔG°) for this system predicted at 11.8 kcal/ mol. This value is very close to the binding free energy of p53-DBD (residues 94−312) with the consensus DNA sequence of −11.1 kcal/ mol measured by isothermal titration calorimetry, suggesting that the calculated free energy profile is reasonable.

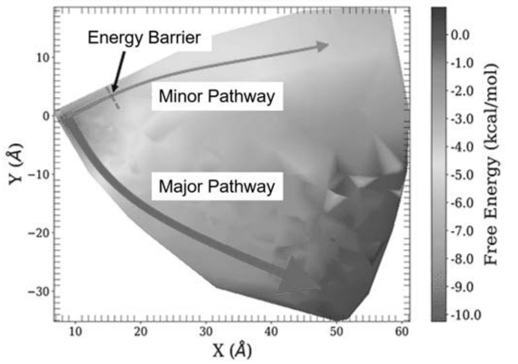

Fig. 3 Free energy profile mapped onto the XY-plane

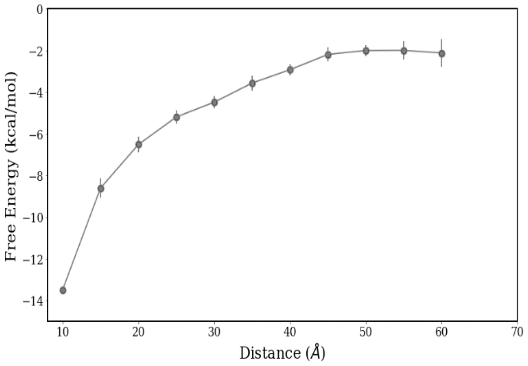

Fig.4 PMF as a function of X coordinate.

References

[1] R. Harada and A. Kitao. J Chem Phys 139, 035103 (2013).

[2] M.M. Sobeh and A. Kitao J. Chem. Inf. Model, 62, 1294–1307 (2022).

Molecular dynamics simulations for assembly and disassembly of protein aggregates

Hisashi Okumura
Exploratory Research Center on Life and Living Systems,
Institute for Molecular Science, Okazaki, Aichi 444-8585

Proteins are normally folded correctly and perform functions that are necessary to sustain life. However, when the concentration of proteins increases due to aging or other reasons, they can aggregate and cause a variety of diseases. For example, Alzheimer's disease, which is one type of dementia, is caused by amyloid-β (Aβ) peptides, which aggregate into spherical oligomers or amyloid fibrils. Molecular dynamics (MD) is nowadays a standard tool to investigate these systems. However, once a conformation gets trapped in a local-minimum free-energy state, it is hard to escape from there within the time scale of the simulation.

The replica-exchange method (REM), is widely used to overcome this difficulty because of its convenience. Recently, we proposed the replica-permutation method (RPM) and the replica sub-permutation method (RSPM) to improve the transition ratio of replicas in the temperature space. However, the RPM and RSPM are not available for general users because these methods are implemented only in our own molecular simulation programs and not in open-source packages. We implemented the RPM and RSPM into LAMMPS [1]. LAMMPS is an open-source classical MD simulation package that can be applied from material to biomolecular systems. We used the supercomputer at the Supercomputer Center, the Institute for Solid State Physics, the University of Tokyo to perform benchmark calculations for this program.

In addition, continuing from the last year, we performed non-equilibrium MD simulations of the destruction process of amyloid fibrils by an infrared laser. We first revealed the disruption process of Aβ amyloid fibrils [2]. We are now performing MD simulations of poly-alanine amyloid fibrils. We found that poly-alanine amyloid fibril is less easily destroyed by infrared laser than Aβ amyloid fibrils. We will try to clarify this difference.

References

[1] M. Yamauchi, G. La Penna, S. G. Itoh, and H. Okumura, Comput. Phys. Commun. **276**, 108362 (2022).

[2] H. Okumura, S. G. Itoh, K. Nakamura, and T. Kawasaki, J. Phys. Chem. B **125**, 4964–4976 (2021).

Critical phenomena in novel Anderson transitions

TOMI OHTSUKI[1]
TOHRU KAWARABAYASHI[2]
KEITH SLEVIN[3]
1) Dept. Phys., Sophia University, Chiyoda-ku, Tokyo 102-8554, Japan
2) Dept. Phys., Toho University, Miyama 2-2-1, Funabashi 274-8510, Japan
3) Dept. Phys., Osaka University, Toyonaka, Osaka 560-0043, Japan

Random quantum systems have no translational/rotational symmetries, but can have time reversal, spin rotation, chiral and particle-hole symmetries. According to these symmetries, the random quantum systems are classified to 10 symmetry classes. The three of them, the so-called Wigner-Dyson classes, were discovered in 1950's and 1960's and have been well studied. Recent experimental discoveries of topological insulators and Weyl semimetal (WSM) have inspired extensive research of random systems other than Wigner-Dyson classes. These 7 new classes contain discrete chiral or particle-hole symmetries.

Here we have introduced a set of Hamiltonians for these new classes, where the high accuracy numerical studies of the three dimensional Anderson transition is possible [1]. We have also studied the novel two dimensional systems, corresponding to a topological superconductor, both analytically [2] and numerically [3]. We especially focused on the critical behaviors near the tricritical point, where ordinary insulator, topological insulator and thermal metal phases meet.

When we introduce the non-Hermiticity to the Hamiltonian, the classification is extended and the systems are categorized to 38 classes. We have shown that adding the non-Hermiticity changes the universality class [4], and show that the transfer matrix method widely used in the Anderson transitions also works for non-Hermitian systems [5]. We have further shown that the critical behaviors of 38 classes are mapped to universality classes for the 10 Hermitian symmetry classes [6].

Machine learning is now widely used in condensed matter physics. We have studied the various quantum phase transitions by analyzing the wave functions via convolutional neural network (CNN). The method is adopted to classify wave functions obtained via density functional theory, which is applied to study the metal-insulator transitions in doped semiconductors [7]. In addition, using the long-short term memory network (LSTM), we have analyzed the time series of diffusion motion of quantum particles in kicked rotors. The model is equivalent to the Anderson model, where the dimensions of the Anderson transition is controlled by the modulation of the kick strength. We have drawn the phase diagram of higher dimensional Anderson transitions by LSTM [8].

References

1. T. Wang, T. Ohtsuki, and R. Shindou, Physical Review B **104**, 014206 (2021).
2. Z. Pan, T. Wang, T. Ohtsuki, and R. Shindou,, Physical Review B **104**, 174205 (2021).
3. T. Wang, Z. Pan, T. Ohtsuki, I.A. Gruzberg, and R Shindou, Physical Review B **104**, 184201 (2021).
4. X. Luo, T. Ohtsuki, R. Shindou, Physical Review Letters **126**, 090402 (2021).
5. X. Luo, T. Ohtsuki, and R. Shindou, Physical Review B **104**, 104203 (2021).
6. X. Luo, Z. Xiao, K. Kawabata, T. Ohtsuki, and R. Shindou, arXiv:2105.02514
7. Y. Harashima, T. Mano, K. Slevin, and T. Ohtsuki, Journal of the Physical Society of Japan **90**, 094001 (2021).
8. T. Mano, and T. Ohtsuki, Annals of Physics **435**, 168500 (2021).

Non-equilibrium relaxation analysis on the $J_1 - J_2$ frustrated Ising model

Keisuke Iikura and Hiroshi WATANABE
Department of Applied Physics and Physico-Informatics, Keio University
Yokohama, Kanagawa 223-8522, Japan

We consider frustrated J_1-J_2 Ising model on the square lattice which Hamiltonian is given by

$$H = J_1 \sum_{\langle i,j \rangle} \sigma_i \sigma_j + J_2 \sum_{\langle\langle i,j \rangle\rangle} \sigma_i \sigma_j,$$

where $\langle i,j \rangle$ and $\langle\langle i,j \rangle\rangle$ denote the summation over the nearest and the next-nearest neighbor pairs, respectively. Spins are Ising-like variable, $\sigma_i = \pm 1$ and $J_1 < 0$ and $J_2 > 0$ denote ferromagnetic and antiferromagnetic interactions, respectively. The parameter of the system is given by $g = J_2/|J_1|$. This model exhibits criticality with varying exponents as the parameter g changes. This behavior is believed to be Ashkin-Teller (AT) universality class. The AT-like behavior will end at some points g^*, and the phase transition becomes the first-order for $1/2 < g < g^*$. The end-point is predicted to be 4-state Potts universality class. However, the localtion of the end-point g^* varies from study to study. Furthermore, whether the phase transition in the range $1/2 < g < g^*$ is a first-order transition or a continuous transition is under debate [1]. Since the interactions of this model involves frustration, the cluster algorithm cannot be applied. Therefore, we apply non-equilibrium relaxation (NER) method to analize the criticality of this model.

We first observe the non-equilibrium relaxation of the order parameter. The stripe order of this system is defined as follows,

$$m_x \equiv \frac{1}{N} \sum_i (-1)^{x_i} \sigma_i, \quad m_y \equiv \frac{1}{N} \sum_i (-1)^{y_i} \sigma_i,$$

where (x_i, y_i) are the coordinates of the i-th spin on the lattice. Then the magnetizaiton is given by $m^2 = m_x^2 + m_y^2$. The order parameter decays exponentially in the disordered phase, converges to a constant in the ordered state, and exhibits power-law decay at the critical point. Then we can identify the critical point from the non-equilibrium behavior of the parameter. We determine the critical exponents from the non-equilibrium fluctuation of obervables [2]. The location of Potts point is determined to be $g^* \sim 0.58$. From the numerical analysis, the phase transition is continuous for $1/2 < g < g^*$ and we did not find any signs of the first order transition. We are currently analyzing the behavior of ordered structure under the fields, and we confirm the existence of a nematic phase. The identification of the nature of the phase transition is a subject for future work.

References

[1] S. Jin, A. Sen, and A. W. Sandvik, Phys. Rev. Lett. **108**, 045702 (2012).

[2] Y. Ozeki and N. Ito, J. Phys. A: Math. Theor. **40**, R149 (2007).

Structure and mechanical properties of crystalline polymers absorbing water molecules

Yuji HIGUCHI
Institute for Solid State Physics, University of Tokyo
Kashiwa-no-ha, Kashiwa, Chiba 277-8581
Research Institute for Information Technology, Kyushu University
Motooka Nishi-ku, Fukuoka 819-0395

We have studied soft matter by molecular simulations and revealed the fracture processes of semicrystalline polymers [1] for the improvement of the toughness and dynamics of lipid bilayers [2] as a model system for biological membranes.

This year, self-assembly processes of amphiphilic molecules were studied by dissipative particle dynamics (DPD) [3] simulations on systems B and C using the LAMMPS program [4]. We revealed that two different molecules were self-sorted or mixed and the processes depended on the hydrophobic length [5].

Furthermore, we studied the adsorption and absorption processes of water molecules to crystalline polymers by coarse-grained molecular dynamics simulation. Water molecules are represented as a sphere in the simulation. The attractive interaction between water and polymer spheres is sufficiently strong to treat polymers as hydrophilic. Figure 1 shows a snapshot at 10 ns and the number of adsorbed water molecules to polymers along the cell axis. Water molecules selectively attach to and absorb into amorphous layers. The tendency is the same as that in the different surfaces, where the water sphere selectively absorbs into amorphous parts. In the hydrophilic semicrystalline polymers, the absorption of water into amorphous parts leads to the gain of attractive interaction compared to that into crystal parts.

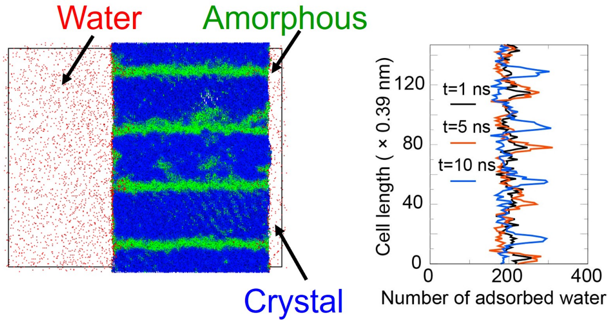

Figure 1: Adsorption and absorption processes of water molecules to polymers. Number of adsorbed water molecules to polymers along the cell axis.

References

[1] Y. Higuchi: Phys. Rev. E **103** (2021) 042502.

[2] Y. Higuchi, Y. Asano, T. Kuwahara, and M. Hishida: Langmuir **37** (2021) 5329.

[3] R. D. Groot and P. B. Warren, J. Chem. Phys. **107** (1997) 4423.

[4] S. Plimpton: J. Comput. Phys. **117** (1995) 1.

[5] R. Wakabayashi, R. Imatani, M. Katsuya, Y. Higuchi, H. Noguchi, N. Kamiya, and M. Goto: Chem. Commun. **58** (2022) 585.

Majorana-mediated spin transport in Kitaev model

Akihisa Koga
Department of Physics, Tokyo Institute of Technology, Meguro, Tokyo 152-8551

Spin transport has recently attracted much interest. One of the interesting examples is the spin transport in the Kitaev model [1]. In the model, quantum spins are fractionalized into itinerant Majorana fermions and local fluxes due to quantum many-body effects. Due to the existence of the local conserved quantities, spin moments never appear in the ground state. Nevertheless, the itinerant Majorana fermions carry the spin excitations and the spin transport is realized without spin oscillations. Since Majorana and flux excitations have distinct energy scales, it is highly desired to clarify how stable such a Majorana-mediated spin transport is against thermal fluctuations.

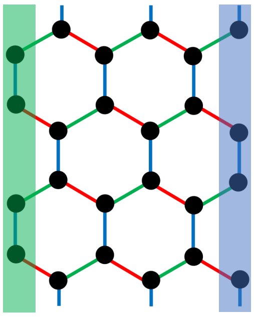

Figure 1: Kitaev model with armchair edges. Green, red, and blue lines indicate x-, y-, and z-bonds, respectively. The static magnetic field h_R is applied in the right region, and no magnetic field is applied in the middle region. Time-dependent pulsed magnetic field is introduced in the left region.

Motivated by this, we deal with the Kitaev model with armchair edges, which is shown in Fig. 1, and consider the spin transport at finite temperatures. Applying the thermal pure quantum state method to the 28-site cluster, we examine the dynamics of the system after the magnetic pulse is introduced at the left edges. When $T \sim T_L$, where T_L corresponds to an energy scale of local flux, larger oscillations in the spin moments are induced in the other edge, compared to the results at the ground state. At higher temperatures, excited Z_2 fluxes disturb the coherent motion of the itinerant Majorana fermions, which suppresses the spin propagation. Our results demonstrate a crucial role of thermal fluctuations in the Majorana-mediated spin transport [2].

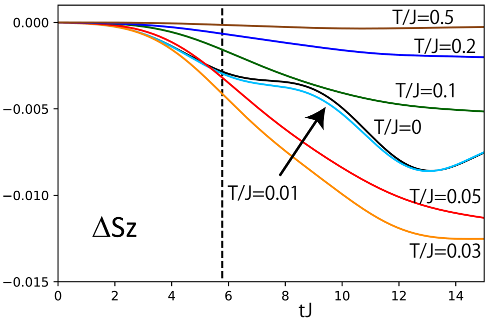

Figure 2: Real-time evolution of the change in the local magnetization in the right edge.

References

[1] T. Minakawa, Y. Murakami, A. Koga, and J. Nasu, Phys. Rev. Lett. **125**, 047204 (2020).

[2] H. Taguchi, Y. Murakami and A. Koga, Phys. Rev. B **105**, 125137 (2022).

Development of COMPutation ARchive of Exact Diagonalization (COMPARED)

Kota IDO

Institute for Solid State Physics,

The University of Tokyo, Kashiwa-no-ha, Kashiwa, Chiba 277-8581

Development of accurate numerical solvers for quantum many-body systems is one of the central issues in the field of computational materials sciences. To achieve this goal, the exact diagonalization method has been widely used for benchmarks on the systems smaller than 50 sites because this method enables us to obtain numerically exact results in the systems with arbitrary interactions. Although most numerical data obtained by the exact diagonalization method are available on articles, these representations such as definition of the Hamiltonians and the display digits of the results are dependent on the articles. Therefore, it is desirable for construction of database to easily check and obtain the exact diagonalization results without definition of notations.

In this project, we have constructed an open database for exact diagonalization results, which is called "COMPutation ARchive of Exact Diagonalization (COMPARED)" [1]. This database has been available on the ISSP data repository under the CC BY 4.0 license [2]. As a generator of the exact results, we use open-source software HPhi [3], which supports MPI/OpenMP hybrid parallelization to achieve highly efficient simulations on supercomputers. Although this parallelization is efficiently done for large system sizes such as 36 sites of quantum spin systems, it is not for single parameter set for small system sizes. To generate data for small system sizes, we develop a python tool which performs HPhi's simulations parallelly. This tool parallelizes input parameter sets and performs the simulations independently for each parameter set. Now we have released more than 20 million data focused on the energies of the ground state and the first excited state on quantum spin systems with small system sizes [2]. We will upload the results for large systems and electron systems.

This project has been done in collaboration with Kazuyoshi Yoshimi and Yuichi Motoyama.

References

[1] K. Yoshimi, K. Ido, Y. Motoyama, R. Tamura, T. Fukushima, Y. Nakanishi-Ohno: https://datarepo.mdcl.issp.u-tokyo.ac.jp/repo/3

[2] https://isspns-gitlab.issp.u-tokyo.ac.jp/compared/compared

[3] M. Kawamura, K. Yoshimi, T. Misawa, Y. Yamaji, S. Todo, and N. Kawashima: Comp. Phys. Commun. **217** (2017) 180.

Ground state and dynamical properties of the J_1-K-Heisenberg model on the square lattice

Matthias GOHLKE, Tokuro SHIMOKAWA
Theory of Quantum Matter Unit, Okinawa Institute of Science and Technology
1919-1 Tancha, Onna-son, Okinawa 904-0495

In the absence of conventional magnetic order of spin-dipolar moments, ordering with higher-order moments like spin-quadrupoles may occur. Such spin-quadrupolar—or spin-nematic (SN)—order was found theoretically in spin-1 model with biquadratic spin-exchange [1].

Magnets with spin-$\frac{1}{2}$ degrees of freedom, however, can only exhibit a SN states if two spin-$\frac{1}{2}$ are combined into an effective spin-1 [2]. In fact, such SN states on bonds has theoretically been observed in frustrated ferromagnets on the square lattice with dominant ferromagnetic Heisenberg exchange, J_1, antiferromagnetic next-nearest neighbor exchange, J_2, and cyclic permutation, K. It was found that the condensation of a two-magnon bound state, at strong magnetic fields along the z-axis, can stabilize a phase with bond-nematic order [3].

Experimentally, the nature of such a ground state is intrinsically difficult to verify, due to the lack of probes that couple directly to the spin-quadrupole moments. Instead, it is necessary to examine the dynamics of a SN: A continuous symmetry for the director of a spin-quadrupole remains, that give rise to a gapless Goldstone mode [4, 5].

We started by studying the square-lattice frustrated J_1-K model [2],

$$\begin{aligned} \mathcal{H} &= J_1 \sum_{\langle i,j \rangle} \boldsymbol{S} \cdot \boldsymbol{S} \qquad (1) \\ &+ K \sum_{(i,j,k,l)} \left(P_{ijkl} + P_{ijkl}^{-1} \right) + h_z \sum_i S_i^z \ , \end{aligned}$$

where J_1 represents dominant ferromagnetic Heisenberg exchange between nearest neighbor spins, K the cyclic ring exchange around squares, and h_z the Zeeman coupling to a magnetic field along the z-axis.

Using iDMRG and the matrix product states (MPS) framework as well as a recently developed exact diagonalization method near saturation [6], we confirm the existence of the bond-nematic phase in an extended range of $K/|J_1|$. In utilizing different methods combined with different geometries, we can assess possible finite-size effects, cf. Fig. 1. Overall we find a good agreement between high-field ED on symmetric clusters and iDMRG on cylindrical geometries with a circumference of $L_{\text{circ}} = 6$ sites.

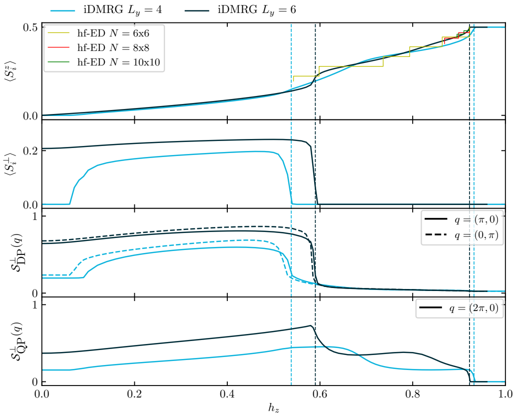

Figure 1: Ground-state of the square-lattice J_1-K-model in a magnetic field at fixed $K/|J_1|$. Different system sizes, geometries, and methods (iDMRG,high-field ED) are compared.

A significant amount of computational resources has been spent on mapping out the

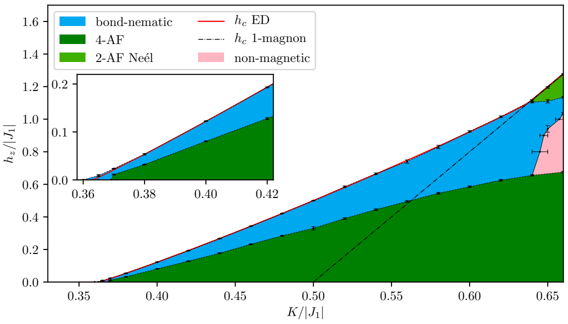

Figure 2: Phase diagram of the square-lattice J_1-K-model in a magnetic field obtained with iDMRG using $L_{circ} = 6$ sites circumference.

entire phase diagram using a cylinder with $L_{\text{circ}} = 6$, cf. Fig. 2. The bond-nematic phase is sandwiched between high-field polarized and 4-sublattice AF phase. Additional phases (Neél, non-dipolar) occur for large K.

Given the ground state wave function as an MPS, dynamical properties can then be studied by applying a time-evolution unitary $U(dt)$ represented as a matrix product operator. In doing so, we observe the condensation of two-magnon bound state at the corresponding wave vector of the SN state. Within the SN phase, we observe (1) the magnon-like excitation that remains fully gapped, and (2) a gapless mode with vanishing spectral weight in the dipolar structure factor and in the $\boldsymbol{q} \to 0$ & $\omega \to 0$ limit as predicted by prior mean-field studies, cf. Fig. 3. We do, however, observe relevant qualitative differences most prominent in the dynamical quadrupole-structure factor. Its origin is currently under investigation.

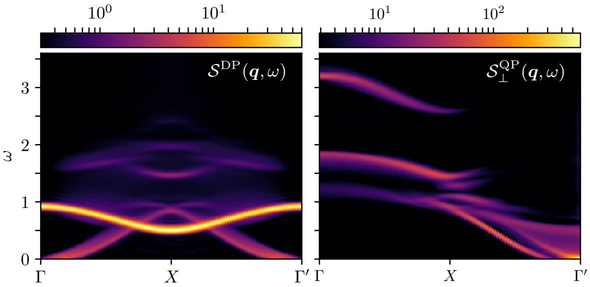

Figure 3: (a) Dynamical spin-structure factor and (b) dynamical quadrupole-structure factor.

References

[1] K. Harada and N. Kawashima, Phys. Rev. B **65** (2002) 052403.

[2] A. Andreev and I. Grishchuk, Sov. Phys. JETP **60** (1984) 267.

[3] N. Shannon, T. Momoi, and P. Sindzingre, Phys. Rev. Lett. **96** (2006) 027213.

[4] R. Shindou, S. Yunoki, and T. Momoi, Phys. Rev. B **87**, (2013) 054429.

[5] A. Smerald, H. T. Ueda, and N. Shannon, Phys. Rev. B **91** (2015) 174402.

[6] H. Ueda, S. Yunoki, and T. Shimokawa, Comp. Phys. Comm. **277** (2022) 108369.

Numerical Diagonalization Study on Quantum Phase Transitions of Frustrated Spin Systems

Tôru SAKAI[1,2], Hiroki NAKANO[1], Rito FURUCHI[1],
and Tokuro SHIMOKAWA[3]
[1] *Graduate School of Science, University of Hyogo,*
Kouto, Kamigori, Hyogo 678-1297, Japan
[2] *National Institute for Quantum Science and Technology,*
SPring-8, Kouto, Sayo, Hyogo 679-5148, Japan
[3] *Theory of Quantum Matter Unit,*
Okinawa Institute of Science and Technology Graduate University,
Onna-son, Okinawa 904-0495, Japan

1 Magnetization plateau of the distorted diamond spin chain with anisotropic ferromagnetic interaction

The $S = 1/2$ distorted diamond spin chain with the anisotropic ferromagnetic interaction is investigated using the numerical diagonalization and the level spectroscopy analysis. It is known that the system exhibits a plateau of the magnetization curve at the 1/3 of the saturation. The present study indicates that as the anisotropy is varied the quantum phase transition occurs between two different mechanisms of the 1/3 magnetization plateau. The phase diagram with respect to the anisotropy and the ferromagnetic coupling is also presented[1].

2 Magnetization process of the S=1/2 Heisenberg antiferromagnet on the floret pentagon lattice

We study the S = 1/2 Heisenberg antiferromagnet on the floret pentagonal lattice by numericaldiagonalization method. We found that magnetization plateaux appear at one-ninth height of the saturation magnetization, at one-third height, and at seven-ninth height. The magnetization plateaux at one-third and seven-ninth heights come from interactions linking the sixfold-coordinated spin sites. A magnetization jump appears from the plateau at one-ninth height to the plateau at one third height. Another magnetization jump is observed between the heights corresponding to the one third and seven-ninth plateaux; however the jump is away from the two plateaux, namely, the jump is not accompanied with any magnetization plateaux[2].

References

[1] T. Sakai, K. Okamoto, H. Nakano and R. Furuchi, AIP Advances 12 (2022) 035030.

[2] R. Furuchi, H. Nakano, N. Todoroki and T. Sakai, J. Phys. Commun. 5 (2021) 125008.

Numerical Diagonalization Study on Magnetization Process of Quantum Spin Chain with the Biquadratic Interaction

Tôru SAKAI[1,2], Hiroki NAKANO[1], Rito FURUCHI[1],
and Tokuro SHIMOKAWA[3]
[1] *Graduate School of Science, University of Hyogo,*
Kouto, Kamigori, Hyogo 678-1297, Japan
[2] *National Institute for Quantum Science and Technology,*
SPring-8, Kouto, Sayo, Hyogo 679-5148, Japan
[3] *Theory of Quantum Matter Unit,*
Okinawa Institute of Science and Technology Graduate University,
Onna-son, Okinawa 904-0495, Japan

1 Quantum spin nematic liquid in the S=1 antiferromagnetic chain with the biquadratic interaction

The magnetization process of the $S = 1$ antiferromagnetic chain with the biquadratic interaction is invesitgated using the numerical diagonalization. As a result, it is found that the quantum spin nematic liquid phase appears below the saturation magnetization for sufficiently large negative biquadratic interaction. The ground state phase diagram is also presented. [1].

2 Field-Induced Quantum Spin Nematic Liquid Phase in the S=1 Antiferromagnetic Heisenberg Chain with Additional Interactions

The $S = 1/2$ distorted diamond spin chain with the anisotropic ferromagnetic interaction is investigated using the numerical diagonalization and the level spectroscopy analysis. It is known that the system exhibits a plateau of the magnetization curve at the 1/3 of the saturation. The present study indicates that as the anisotropy is varied the quantum phase transition occurs between two different mechanisms of the 1/3 magnetization plateau. The phase diagram with respect to the anisotropy and the ferromagnetic coupling is also presented[2]

References

[1] T. Sakai, AIP Advances 11 (2021) 015306.

[2] T. Sakai, H. Nakano, R. Furuchi and K. Okamoto, J. Phys.: Conf. Ser. 2164 (2022) 012030.

A proximate Tomonaga-Luttinger state in the S=1/2 Kitaev-Γ model on a Honeycomb Lattice

Takafumi SUZUKI

Graduate School of Engineering,

University of Hyogo, Shosha, Himeji, Hyogo 670-2280

We have investigated the ground-state phase diagram and the dynamical properties of the S=1/2 Kitaev-Γ model [1] on a honeycomb lattice by the numerical exact diagonalization (ED) method and the density-matrix-renormalization-group (DMRG) method. The S=1/2 Kitaev- Γ model on a honeycomb lattice was proposed as the effective model of the honeycomb-lattice magnet, α-RuCl$_3$. The ground-state phase diagram of this model with the isotropic coupling strength has been much studied because of the simplicity of the model. However, the anisotropy of the coupling strength exists in α-RuCl$_3$, which originates from the reduction of the lattice symmetry, and the effect of the anisotropy has not been fully understood yet.

In the previous study, we reported the partial ground phase diagram of the S=1/2 Kitaev-Γ model on a honeycomb lattice shown in Fig. 1 and indicated that the dimerized phase, which appears in the isolated dimer limit (d =∞), can survives up to the isotropically interacting model (d=*1*), when the Kitaev interaction and the Γ interaction are negative and positive respectively [2]. In this study, we investigated the ground-state phase diagram in $0 \leq d \leq 1$ [3]. We find that a proximate Tomonaga-Luttinger liquid (pTTL) is expected in the ground state with the negative Kitaev interaction and the positive Γ interaction (Γ). This pTTL becomes the Tomonaga-Luttinger liquid (TLL) in the spin chain limit (d=0), which was pointed out in ref. [4]. When the condition, Γ/|K|=1 (K<0), is satisfied at d=0, the model is mapped on the antiferromagnetic Heisenberg chains and recovers the hidden SU(2) symmetry [4]. Thus, a gapless linear excitation derived from spinon excitations appears in the low-energy excitation. These characteristics is also observed in the low-energy excitation of the pTTL phase. From the ED calculations for the N=24 site cluster with the C$_3$ symmetry of the lattice, we find that the pTTL phase can survive up to d=*1*. Next, we calculated the temperature dependence of the specific heat to investigate the emergence of the Majorana fermions in the vicinity of d=*1* and Γ=0. At d=*1* in $0 \leq$ Γ/|K|, the presence of the double-peak structure was indicated in ref. [5]. We find that the higher-temperature peak at d=*1* corresponds to the prominent single peak in the spin chain limit and the lower-temperature peak rapidly develops in the vicinity of d=*1*. This means that the spinon-like excitation is continuously converted into the Majorana excitation.

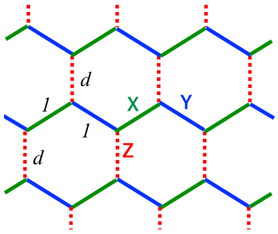

Fig. 1: Anisotropically interacting Kitaev-Γ model. The coupling strength on the X/Y bond is unity and d is the ratio of the coupling strength on the Z bond against that on the X/Y bond.

References

[1] J. G. Rau, E. Lee, and H. -Y. Kee, Phys. Rev. Lett. 112, 077204 (2014).

[2] T. Yamada, T. Suzuki, and S. Suga, Phys. Rev. B **102**, 024415 (2020).

[3] M. Gohlke, J. C. Pelayo, and T. Suzuki, in preparation.

[4] W. Yang, et al., Phys. Rev. Lett. 124, 147205 (2020) and W. Yang, A. Nocera, and I. Affleck, Phys. Rev. Research 2, 033268 (2020).

[5] A. Catuneanu, et al., npj Quant. Mater. 3, 23 (2018).

Hybrid Simulations on Fluid-Viscoelastic Membrane System Using Multi-Scale Simulation Platform for Complex Fluids

Yohei MORII and Toshihiro KAWAKATSU
Department of Physics, Tohoku University,
Aza-Aoba, Aramaki, Aoba-ku, Sendai 980-8578

We develop general multiscale simulation methods for inhomogeneous complex flows in viscoelastic fluids and elastoplastic solid. For such multiscale simulations, a general-purpose platform named Multis-Scale Simulation Platform for complex flows (MSSP) was developed by the present authors [1]. In our MSSP, the macroscopic flow is simulated by smoothed particle hydrodynamics (SPH) method, to which the microscopic information is introduced through a microscopic molecular dynamics (MD) simulator embedded in each of the SPH particles.

We simulate a viscoelastic flow of a dilute polymer solution passing through an obstacle and clarify the role of added polymers. To accurately simulate large scale dynamic flow patterns behind the obstacle, such as Karman vortex street, it is essential to use a large-scale system, where the flow velocity and velocity gradient are highly inhomogeneous. To avoid a large computational cost as well as a large unbalance in the computational load on the computer nodes, we proposed a hybrid method where we switch the MD simulators with simpler constitutive equations for the SPH particles with smaller velocity gradient. A preliminary result using linear viscoelastic constitutive equation was developed during the previous project in 2020 [1]. In the present project, we extended this hybrid method to nonlinear viscoelastic constitutive model. Figure 1 shows the flow pattern around the separation point on a cylindrical obstacle, where the red SPH particles contains particle MD simulators while blue SPH particles contain nonlinear constitutive equations. We can confirm that the switching is successfully implemented and 97% of 1,600,000 SPH particles are simulated with constitutive model.

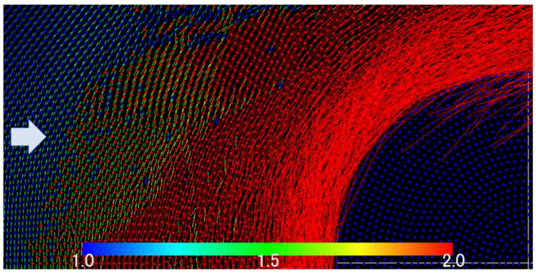

Fig.1 MSSP simulation of a polymer flow around a cylindrical obstacle. Bars attached to the particles show the average elongation and its direction of the polymer chains.

References

[1] Y. Morii and T. Kawakatsu: Phys. Fluids **33** (2021) 093106.

Thermal effects on quantum frustrated magnetisms

Tokuro Shimokawa

Theory of Quantum Matter Unit, Okinawa Institute of Science and Technology Graduate University, Onna-son Okinawa 904-0412

Quantum frustrated magnets are well-known sources of exotic states of matter, but investigating their true nature, particularly at finite temperatures, is still a demanding and challenging problem. This fiscal year, we have focused on the following topics with the ISSP supercomputer.

1) S=1/2 breathing bilayer kagome (BBK) magnet for $Ca_{10}Cr_7O_{28}$

$Ca_{10}Cr_7O_{28}$ is a newly quantum spin liquid (QSL) material, and the effective Hamiltonian was proposed as an S=1/2 BBK Heisenberg model. A recent semi-classical study [1] supported the scenario of a QSL ground state in this material and suggested possible realizations of exotic low-temperature multiple-*q* states in fields. But the true nature of the multiple-*q* states wasn't uncovered yet because of the difficulty of treating large systems.

We alternatively treated a classical J_1-J_2 Heisenberg model on the honeycomb lattice model, which could also be considered an effective model for $Ca_{10}Cr_7O_{28}$ to investigate the thermodynamic properties of the multiple-*q* states. Our large-scale Monte Carlo simulations succeeded in identifying them; we found that one of them is an intriguing six sub-lattice (anti) skyrmion-lattice state with topological nature.

2) High-field exact diagonalization code development and the low-*T* physics in the S=1/2 J_1-K square-lattice model

We developed an exact diagonalization code, quantum spin solver near saturation (QS^3), as an open-source software [2]. Using this high-field ED code, we investigated the low-T phase diagram of the S=1/2 square-lattice Heisenberg model with a ring exchange interaction (J_1-K model).

Our ED calculations revealed the existence of several ordered/disordered states in fields. Especially in the high-field regime around $K/J_1 \sim 0.5$, we clarified the realization of a bond-nematic state without any approximation to our Hamiltonian. We also computed the dynamical spin/quadrupole structure factors for future neutron scattering measurements on candidate materials.

References

[1] R. Pohle, et al, PRB **104**, 024426 (2021).

[2] H. Ueda, S. Yunoki, T. S., Comp. Phys. Commun. **277**, 108369 (2022).

Steady states realized by a global thermodynamic balance in nonequilibrium

Naoko NAKAGAWA
Department of Physics, Ibaraki University
2-1-1 Bunkyo, Mito, Ibaraki 310-8512

First-order phase transition and the separation of the phases have attracted scientific interests from various points of view, not only from physics but also from the biological mechanism. The phase coexistence induces sometimes complicated and singular properties to the system even though the bulks of respective phases may behave rather ordinary.

In this project, we work on particle systems interacting via a Lennard-Jones potential

$$V(r) = 4\epsilon\left[\left(\frac{\sigma}{r}\right)^{12} - \left(\frac{\sigma}{r}\right)^{6}\right] + \epsilon,$$

with a diameter σ of each particle and a coupling strength ϵ, which have been a standard model for numerical experiments. By choosing the total energy and the number density of the system appropriately, the system shows a liquid-gas transition. See Fig. 1 for the case of $N = 5 \times 10^4$. We also used Weeks-Chandler-Andersen (WCA) potential when we want to avoid the liquid-gas transition.

Our most interest is the liquid-gas coexistence in heat conduction. Due to the steady heat current, the coexistence pattern of the liquid and gas becomes much more stable compared with equilibrium systems. The local states around the liquid-gas interface become observable due to the induced stability. We here notice that the rich behaviors related to the first-order transition are often observed in complex systems such as mixtures and dense solutions. Their response to a nonequilibrium driving will be of great interest. To initiate them, we start with the construction of a method to know their thermodynamic properties in equilibrium. The details of the results follow.

We derived a formula for determining the mixing free energy for two-component fluids. The formula is numerically verified with a good accuracy by the molecular dynamics simulation using the LAMMPS package installed in the supercomputers at ISSP. We have compared two kinds of protocols creating a mixture of two pure substances. One is traditional protocol and the other is a protocol with "alchemical change" of molecules, which may be valid only in numerical experiments. We calculated the free energy changes of the two protocols by adopting the Jarzynski equality and information thermodynamics. The comparison of the two results in a formula for the mixing Gibbs free energy $\Delta_{\mathrm{mix}}G$ as

$$\Delta_{\mathrm{mix}}G = -k_{\mathrm{B}}T \ln\left[\frac{N!}{n!(N-n)!\rho_X(n)}\frac{\langle e^{-\beta\hat{W}_{(\#)}}\rangle}{\langle e^{-\beta\hat{W}_{(\mathrm{ii})}}\rangle}\right],$$

where n and $N-n$ are the numbers of particles for the two components and $\rho_X(n)$ is the number density of the first component in the region $x < X$. $\hat{W}_{(\#)}$ is the work in each trajectory according to the alchemical process to create a mixture from the first pure substance, whereas $\hat{W}_{(\mathrm{ii})}$ is the work according to the alchemical process to create the second from the first pure substance.

By applying the above formula, we examined $\Delta_{\mathrm{mix}}G$ for the mixture of argon and krypton. By changing the mole fraction of the krypton, the system shows liquid-gas transition for a fixed temperature and pressure. The properties of the transition are well characterized in the calculated $\Delta_{\mathrm{mix}}G$ as a double-well-shaped function. The violation of convexity is likely due to the finiteness of the system.

We have used the L4 CPU of System B with 4 nodes in 512 parallel computation using MPI for the calculation of 10^4 particles, the L16 CPU of System B with 16 nodes in 2048 parallel computation using MPI for the calculation of 5×10^5 particles, the L72 CPU of System B with 72 nodes in 9216 parallel computation using MPI for the calculation of 8×10^6 particles.

References

[1] A. Yoshida and N. Nakagawa: to appear in *Phys. Rev. Res.* (2022)

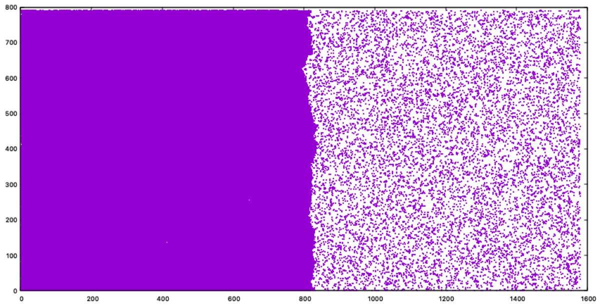

Figure 1: Snapshot of the particles interacting with Lennard-Jones potential in heat conduction. The system with $N = 5 \times 10^5$ exhibits a sharp liquid-gas interface.

Scrambling in quantum many-body systems

Masaki TEZUKA
Department of Physics,
Kyoto University, Kitashirakawa, Sakyo-ku, Kyoto 606-8502

Strongly correlated models realizable in condensed matter systems with possible holographic correspondence to gravitational systems including black holes have received much attention in the recent years. Of particular interest are scrambling and chaotic dynamics. The scrambling phenomena in quantum systems is delocalization of quantum information and has been discussed as the formation of quantum error correction (QEC) code. Thus, we have been trying to study scrambling and effect of dissipation in quantum many-body systems, toward experimental demonstration in condensed matter systems such as ultracold atoms.

The Sachdev-Ye-Kitaev (SYK) model is a model of Majorana fermions with all-to-all four-fermion interactions obeying the Gaussian distribution. It has an analytic solution in the limit of large number of fermions and is maximally chaotic at low temperatures. We have previously studied the effect of a random hopping term, two-fermion interactions, added to the model [1]. The maximally chaotic behavior is lost and the spectral statistics turns to an uncorrelated one. Furthermore, the localization transition is a Fock-space localization, a type of many-body localization, and quantities such as the location of the transition point, the moments of the eigenstate wavefunctions, and bipartite entanglement entropy have been obtained analytically with numerical confirmation [2].

A “sparse” version of the SYK model, in which the number of interaction terms is on the order of the number of fermions, instead of all the choices of four-fermion subsets, have been proposed a few years ago.

To quantify the scrambling properties of these models, we have studied the QEC capabilities of the unitary time evolution according to their Hamiltonians according to the Hayden-Preskill protocol [3]. In this protocol, the unknown quantum state thrown into a quantum many-body system is decoded by a person who, knowing the initial state of the remainder of the system and the time evolution, obtains the quantum state of some of the qubits comprising the system, and the error estimate for the time evolutions obeying the circular unitary ensemble (CUE) is known.

Using the ISSP Supercomputer, we analyzed the spectral statistics of a further simplification of the sparse SYK model [4]. Also, we numerically observed that while for the sparse SYK models, the QEC error estimate approaches the CUE value as soon as the spectral statistics becomes random-matrix like, for the case of two-fermion interactions, the departure from the CUE value is observed before the Fock space localization occurs [5].

References

[1] A. M. Garcia-Garcia, B. Loureiro, A. Romero-Bermudez, and M. Tezuka, Phys. Rev. Lett. **120** (2018), 241603.

[2] F. Monteiro, T. Micklitz, M. Tezuka, and A. Altland, Phys. Rev. Research **3** (2021), 013023; F. Monteiro, M. Tezuka, D. A. Huse, and T. Micklitz, Phys. Rev. Lett. **127** (2021), 030601.

[3] P. Hayden and J. Preskill, JHEP **0709** (2007), 120.

[4][5] M. Tezuka *et al.*, in preparation.

Investigation of the molecular origins of the mechanical and thermal properties of realistic biopolymers using all-atomistic molecular dynamics

Okazaki Susumu

Department of Advanced Materials Science,

The University of Tokyo, Kashiwa-no-ha, Kashiwa, Chiba 277-8581

Mechanical and thermal properties of biopolymers, PBI and its three copolymers PBO-*co*-PBI, PBI-*co*-PBO-*co*-*p*PA, and PBI-*co*-PBO-*co*-*m*PA, have been investigated based on all-atomistic molecular dynamics (MD) calculations to clarify molecular mechanism of fracture and glass transition of the polymers. We also investigated regular polymers, PC and PMMA [1], as a reference system. The calculations have been conducted on the supercomputers at ISSP using a MD software MODYLAS [2] developed by our group.

Modulus of elasticity, yielding stress, and fracture stress were studied in detail. The biopolymers showed the high modulus of elasticity at short strain followed by the high yielding stress and ductility showing strong strain hardening at large strains after the yielding point.

The biopolymers investigated here all exhibited very high glass transition temperatures at 800 K – 900 K. The temperatures are higher than their pyrolysis temperatures. These high glass transition temperatures are from hydrogen bonds among polymer chains forming network structures.

We also investigated the microscopic origins of the stress causing the elastic deformation, yield point, strain softening, and strain hardening observed in PC and OMMA, by decomposing the stress into contributions from various energetic energy terms. Our analysis showed that the stress of the fracture process is mainly determined by the bond, angle, and vdW terms, in addition to the system alignment in the pulling direction. In the elastic region, almost the entire system experiences affine deformation despite the existing local heterogeneous deformation in the later elastic region. As the deformation of the entanglement network begins, the stress on the bonds and angles rapidly increases.

References

[1] Z. Tang, K. Fujimoto, S. Okazaki, Polymer, **226**(2021)123809.

[2] Y. Andoh, S. Ichikawa, T. Sakashita, N. Yoshii, S. Okazaki, J. Comp, Chem., **42**(2021)1073.

Simulations of quantum-classical-hybrid algorithms for sensor materials with considering noise

Wataru Mizukami

Center for Quantum Information and Quantum Biology, Osaka University, Osaka 560-0043, Japan

The development of quantum computers has made significant progress in recent years: quantum computers with dozens or a hundred qubits have been built. We now expect to see quantum devices with hundreds or thousands of qubits near future. Such quantum computers are often called noisy-intermediate scale quantum devices (NISQs) since they do not have quantum error correction functionality. There have been intensive research efforts currently underway to exploit the computational potential of NISQs.

One promising algorithm for NISQs is the quantum-classical hybrid algorithm, which can operate even in the short coherence time of a NISQ. Among them, the variational quantum eigensolver (VQE) can be applied to first-principles calculations of materials or molecules. We are targeting applying the VQE to practical problems in material science. In particular, we aim to use the VQE for analyzing materials used in sensors. In this study, we use a quantum circuit simulator rather than real quantum computers to develop a new quantum-classical hybrid algorithm and validate it. The reasons we employ such an emulator are the following: the number of NISQs is limited at this moment; their use charges high fees; error rates of today's NISQs are still too high. Last year, we built a framework to efficiently emulate quantum circuits with (deplolarsing) noises using the supercomputer of the ISSP.

This year, we worked on improving the efficiency of the quantum circuit optimization part in the VQE. We parallelized the gradient evaluations of the VQE's cost function with respect to the quantum circuit parameters, using MPI. We tested our implementation by computing the H2O molecule with the 6-31G basis set. The benchmark calculation used a minimum of 128 cores and a maximum of 9216 cores. The observed parallelization efficiency was 75% with 4608 cores, relative to the execution time with 128 cores.

Moreover, we developed a method to consider solvation effects within the framework of the VQE. This was achieved by combining the VQE and 3D-RISM, an integral equation theory of molecular liquids. This method was used to investigate the impacts of solvents on the computational cost of quantum computing. Our calculations indicate that solvation effects virtually have no impact on it.

Molecular Dynamics Simulation of Stress Induced Crystallization in Robust-Toughening Hydrogel

Koichi Mayumi, Kosuke Aomura, Takeyoshi Masumoto, Haru Shinohara
Institute for Solid State Physics,
The University of Tokyo, Kashiwa-no-ha, Kashiwa, Chiba 277-8581

In this project, we studied crystallization of polymer chains in slide-ring gels under stretching by means of coarse-grained molecular dynamics simulation. In addition, we performed a full-atomistic molecular dynamics simulation of the melting process of stretched polymer crystals in water.

Coarse-Grained Molecular Dynamics Simulation of Strain-Induced Crystallization of Slide-Ring Gel

In this study, uniaxial elongation simulations of slide-ring gels were performed using coarse-grained molecular dynamics simulation [1]. In order to investigate the strain-induced crystallization of slide-ring gel which is observed in experiments [2], we introduced attractive interaction between polymer chains. Fig. 1 shows stress-extension ratio curve of a fixed crosslink (FC) gel and slide-ring (SR) gel with the same cross-linking density. SR shows smaller stress than FC gel because of the slidability of the cross-links.

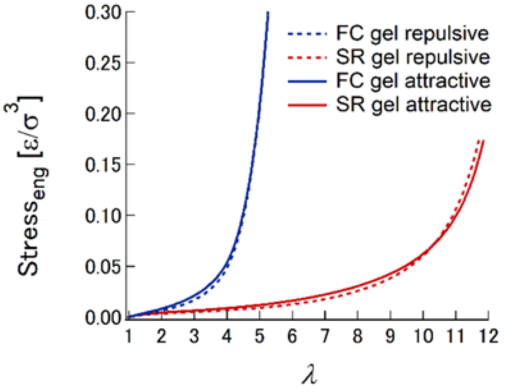

Fig. 1 Stress-extension ratio relation of fixed crosslink gel and slide-ring gel.

Further analysis was performed to clarify aggregated structure under stretching. We calculated scattering function of SR gel before and after stretching. At the extension ratio λ=12, scattering function shows a circular peak on $q_z = 0\,\sigma^{-1}$ plane at $\sqrt{q_x^2 + q_y^2} = 6\,\sigma^{-1}$. The peak suggests the formation of aggregate structures in which polymer chains are aligned in the direction perpendicular to the elongation.

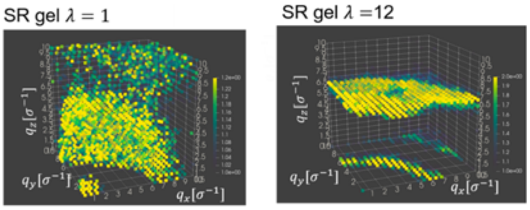

Fig. 2 Snapshots of a scattering function of SR gel at (a) λ=1 (b) λ=12

A region of neatly aligned polymer chains was extracted from the network, and the scattering function was calculated for the region. As a result, we observed spot peaks corresponding to a body-centered orthorhombic lattice crystal structure, as shown in Fig. 3. This indicates that the slidability of the cross-linking points equalizes the chain deformation and enhances the strain-induced crystallization.

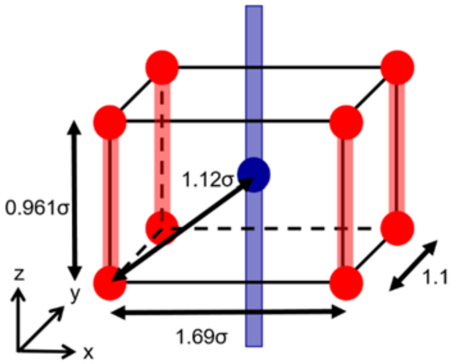

Fig. 3 Body-centered orthorhombic lattice crystal structure observed in SR gel at λ=12.

Analysis of Dissolution Process of Extended Polyethylene Glycol Crystal in Water

The reversibility of the strain-induced crystallization of PEG chains in water allows the tough hydrogel to rapidly recover from mechanical stress. To understand the dissolution process of extended PEG chain crystal in water, all-atom MD simulation was carried out. GROMACS 2016.5 [3] was used as simulation software. We investigated the dissolution process of helical PEG chain crystal and zigzag PEG chain crystal under stretching in water. For helical chain crystal, the crystal partly remain after 200 ns even at no elongation force. On the other hand, zigzag chain crystal dissolves faster than the helix chain crystal.

References

[1] Kremer, K.; Grest, G. S.: *J. Chem. Phys.* **92** (8), 5057–5086. (1990)

[2] C. Liu, N. Morimoto, L. Jiang, S. Kawahara, T. Noritomi, H. Yokoyama, K. Mayumi, K. Ito: *Science* **372** 1078-1081. (2021)

[3] Berendsen, H. J. C.; van der Spoel, D.; van Drunen, R. *Comp. Phys. Comm.* **91**, 43–56. (1995)

Molecular dynamics study of shear-induced long-range correlations in simple fluids

Hiroyoshi Nakano
Department of Applied Physics and Physico-Informatics, Keio University
Yokohama, Kanagawa 223-8522, Japan

We studied a nonequilibrium long-range correlation (LRC) in simple fluids using a molecular dynamics (MD) simulation. The nonequilibrium LRC means that same-time spatial correlations of locally conserved quantities exhibit power-law decays due to a lack of detailed balance condition [1]. It is known to be one of the general features of nonequilibrium systems with conserved quantities and anisotropy. Because in equilibrium the LRCs are specific to the critical phenomena, the nonequilibrium LRCs observed far from the critical points have been extensively studied as the novel phenomena induced by nonequilibrium conditions. However, the almost all of research have been performed using phenomenological models such as fluctuating hydrodynamics and stochastic lattice gases. Indeed, there are few attempts to directly observe the nonequilibrium LRCs and examine their nature from underlying molecular systems.

In the present study, with the aim of direct observation of the nonequilibrium LRCs, we focused on the simple fluids under uniform shear flow and performed the MD simulation [2]. All the MD simulations were performed by LAMMPS (Large-scale Atomic/Molecular Massively Parallel Simulator) [3, 4]. The schematic illustration of our system is given in Fig. 1. The particles interact via the Weeks–Chandler–Andersen (WCA) potential. The shear flow is imposed by using the Lees–Edwards boundary condition along the z-axis. Along the x and y-axes, the standard periodic boundary conditions are imposed. To maintain a constant temperature T under shear flow, the dissipative particle dynamics (DPD) thermostat is used. Thus, in the steady state, the following averaged velocity profile $\langle \boldsymbol{v}(\boldsymbol{r}) \rangle_{\rm ss} = (\dot{\gamma} z, 0, 0)$ is realized, where $\langle \cdot \rangle_{\rm ss}$ denotes time average in the steady state and the ensemble average over different noise realizations, and $\dot{\gamma}$ is shear rate.

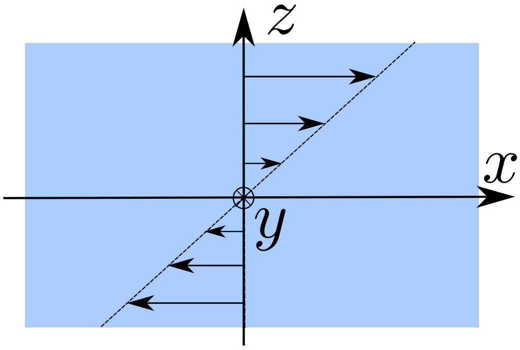

Figure 1: Schematic illustration of shear flow.

We observe the same-time correlations of momentum fluctuations in the steady state. The momentum fluctuations are given by

$$\delta \boldsymbol{g}(\boldsymbol{r}, t) = \sum_{i=1}^{N} \boldsymbol{p}_i(t) \delta(\boldsymbol{r} - \boldsymbol{r}_i(t)) - \langle \boldsymbol{v}(\boldsymbol{r}) \rangle_{\rm ss}, \quad (1)$$

where $\boldsymbol{r}_i(t)$ and $\boldsymbol{p}_i(t)$ are, respectively, the position and momentum of ith particle at time t. Then, the same-time correlations of momentum fluctuations are given by $C_{\alpha\beta}(\boldsymbol{r}, \boldsymbol{r}') = \langle \delta g^{\alpha}(\boldsymbol{r}, t) \delta g^{\beta}(\boldsymbol{r}', t) \rangle_{\rm ss}$, where $\alpha, \beta = x, y, z$.

We plot the Fourier transform of $C_{zz}(\boldsymbol{r}, \boldsymbol{r}')$ in Fig. 2. Because our system has the spe-

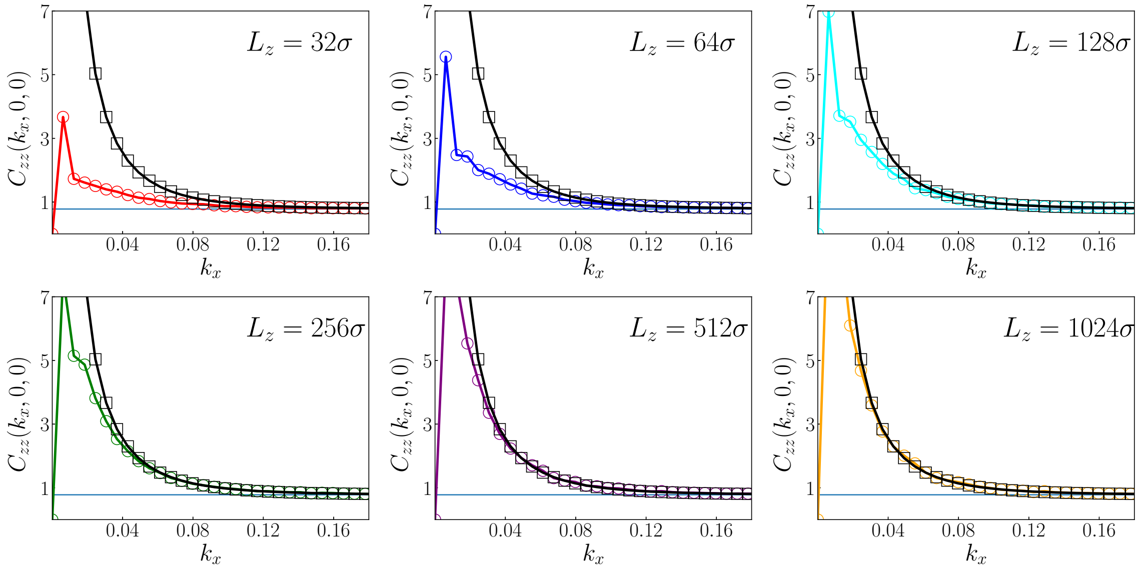

Figure 2: $C_{zz}(k_x, k_y = k_z = 0)$ for several system sizes $L_z = 32\sigma$, 64σ, 128σ, 256σ, 512σ, 1024σ. The color circle points represent the MD simulation results, and the black square points the results calculated from the fluctuating hydrodynamics.

cial Galelian invariance, the Fourier transform of $C_{zz}(\boldsymbol{r}, \boldsymbol{r}')$ is given as $C_{zz}(\boldsymbol{k}) = \int d^3\boldsymbol{r} C_{zz}(\boldsymbol{r}, \boldsymbol{0}) e^{-i\boldsymbol{k}\cdot\boldsymbol{r}}$. In Fig. 2, $C_{zz}(k_x, k_y = k_z = 0)$ for different L_z is presented. The other parameters are set to $L_x = 1024\sigma$, $L_y = 32\sigma$, and $\dot{\gamma} = 0.02\tau_{\mathrm{unit}}^{-1}$, where σ and τ_{unit} are, respectively, the unit of length and time. The black square points represent $C_{zz}(k_x, k_y = k_z = 0)$ calculated from the phenomenological theory called the fluctuating hydrodynamics [5]. The result obtained from the fluctuating hydrodynamics is independent of L_z.

From Fig. 2, we find that the strong finite-size effects exist for $C_{zz}(k_x, k_y = k_z = 0)$. For sufficiently large L_z, the result calculated from the fluctuating hydrodynamics is in quantitative agreement with the MD simulation results. In contrast, for smaller L_z (e.g. 32σ or 64σ), there is the clear deviation between their results. In other words, the quite large system size is required to observe the shear-induced long-range correlations.

In summary, we performed the MD simulations of the WCA fluids under uniform shear flow. We successfully observed the nonequilibrium long-range correlations for the sufficiently large system that contains over 10 million particles.

References

[1] J. Dorfman, T. Kirkpatrick, and J. Sengers, Annual Review of Physical Chemistry **45**, 213 (1994).

[2] H. Nakano, and Y. Minami, Physical Review Research (in press).

[3] S. Plimpton, Journal of Computational Physics **117**, 1 (1995).

[4] A. P. Thompson, H. M. Aktulga, R. Berger, D. S. Bolin-tineanu, W. M. Brown, P. S. Crozier, P. J. in ’ t Veld,A. Kohlmeyer, S. G. Moore, T. D. Nguyen, R. Shan, M. J.Stevens, J. Tranchida, C. Trott, and S. J. Plimpton, Computer Physics Communications **271**, 108171 (2022).

[5] J. Lutsko and J. W. Dufty, Phys. Rev. A **32**, 3040 (1985).

Theoretical analysis of absorption and fluorescence spectra for firefly bioluminescence related molecules

Miyabi HIYAMA
Graduate School of Science and Technology, Gunma University,
Tenjin-cho, Kiryu, Gunma 376-8515

Because firefly bioluminescence is widely used such as *in vivo* imaging and reporter assay, many analogs of firefly bioluminescence substrates (luciferin) are developed [1, 2]. AkaLumine is one of the analogs of luciferin and its bioluminescence with firefly luciferase produces the near-infrared emission, which can penetrate through biological tissues [3]. For studying the bioluminescence mechanism, basic knowledge about the chemical structures, electronic states, and absorption properties of AkaLumine solution at various pH values of solution has to be acquired.

In this study, the absorption spectra for Alakumine in aqueous solutions were studied theoretically [4]. The optimization structure of ground state for AkaLumine and its conjugate acids and bases, which are expected to be main component in the aqueous solutions, were obtained from the density functional theory (DFT). The time dependent DFT (TDDFT) calculations were carried out to estimate the theoretical absorption spectra for these structures. The Gibbs free energies for the chemical structures were obtained using the vibrational analysis. Form these free energies, pK_a values for protonation/deprotonation of AkaLumine in aqueous solutions were estimated and the relative concentrations of AkaLumine and its conjugate acids and bases were obtained. All calculations were performed using the GAUSSIAN09 program [5] on system B and C of Super Computer Center in ISSP.

It was found that the main absorption peaks for AkaLumine and its conjugate acids ad bases appear at 369, 465, 314, 353, 352, 440, 322, and 317 nm and that all of these peaks correspond to the excitation from S_0 to the first excited state (S_1) [4]. These S_1 states can be described dominantly by the one electron excitation configuration of which the coefficients are large (∼0.5). From the theoretical results, the peaks at pH 7–10, pH 4, and pH 2 of AkaLumine experimental absorption spectra are assigned to a carboxylate anion, a carboxylate anion with an N-protonated thiazoline ring, and a carboxylate anion with an N-protonated thiazoline ring and N-protonated dimethylamino group, respectively.

References

[1] Li et al. , Eur. J. Med. Chem., **211** (2020) 113111.

[2] Iwano et al. , Tetrahedron, **69** (2013) 3847.

[3] Kuchimaru et al. , Nat. Comm., **7** (2016) 1.

[4] Ogawa et al. Photochem. Photobiol. (2021) 97, 1016.

[5] Gaussian 09, Revision D.01, M. J. Frisch et al.

Skyrmion crystal phase in the RKKY Heisenberg model in two- and three- dimensions

Kota Mitsumoto and Hikaru Kawamura

Molecular Photoscience Research Center, Kobe University, Kobe 657-8501, Japan

Skyrmion, a swirling noncoplanar spin texture whose constituent spin directions wrap a sphere in spin space, has attracted much recent interest and been studied quite extensively. In magnets, skyrmion is usually stabilized in the form of the periodic array, i.e., the skyrmion crystal (SkX). While the SkX was first realized in chiral ferromagnets with the anti-symmetric Dzyaloshinskii-Moriya (DM) interaction, a recent study has revealed that the SkX state can also be realized in centrosymmetric magnets without the DM interaction [1]. Such a "symmetric" SkX state is induced by frustration among exchange interactions, and keeps the chiral degeneracy with respect to the right-left (R-L) symmetry, in sharp contrast to the DM-induced SkX.

Such a frustration-induced symmetric SkX is possible both in insulating and metallic magnets. In metallic magnets, the primary interaction is the long-range RKKY interaction which oscillates in sign with the distance leading to the frustration, in contrast to the insulating magnets possessing the short-range interactions. In this year's project, we study the ordering properties of the isotropic RKKY Heisenberg model on the two-dimensional triangular and the three-dimensional stacked-triangular lattices by extensive Monte Carlo simulations in order to get insights into the chiral-degenerate skyrmion crystal of metallic magnets in the weak-coupling regime [2].

We find that the symmetric SkX is stabilized under finite magnetic fields both in two and three dimensions, as shown in the temperature vs. magnetic-field phase diagram of the Figure below, both the 2D (upper) and 3D (lower) ones.

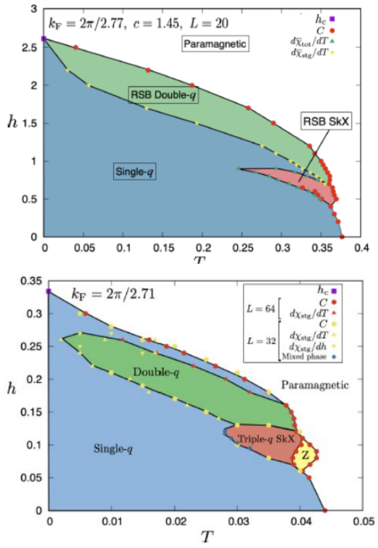

References

[1] T. Okubo, S. Chung and H. Kawamura, Phys. Rev. Letters, **108**, 017206-(1-5) (2012).

[2] K. Mitsumoto and H. Kawamura, Phys. Rev. B **104,** 184432-(1-17) (2021); Phys. Rev. B **105**, 094427(2022).

Topological phases and science of bulk-edge correspondence by numerical methods

Y. Hatsugai
Department of Physics, University of Tsukuba
1-1-1 Tennodai, Tsukuba 305-8571, Ibaraki, Japan

The bulk-edge correspondence[1] is widely used for the studies of topological phenomena in various systems that include not only microscopic quantum systems but also macroscopic classical ones such as photonic crystals and meta-materials. It is a scale-free concept. The abstract mathematical concept of topology is reflected by the physics of boundaries through generic edge states (zero to three-dimensional defects as well). We may further try to discuss various kinds of localized states as a consequence of non-trivial bulk. A typical example is an equatorial wave on earth where the equator is a boundary for the Coriolis force. Collecting such hidden reasons why the boundary states exist, we try to establish a universal view for the localized states in nature and more. This is the science of bulk-edge correspondence. In the current project, we try to apply the viewpoints for various systems using numerical techniques.

Topological pumps focusing on the role of edges are important systems where the bulk-edge correspondence governs the phenomena. We have numerically justified the bulk-edge correspondence of topological pumps for quantum spins and bosons with short-range interactions[2, 3] where a plateau transition analogous to the quantum Hall effects is realized in dimerized high-S quantum spins. Laughlin's argument of the quantum Hall effects can be assumed as a variant of the topological pump where bulk-edge correspondence plays a fundamental role. It is numerically considered for a series of anyons with various statistical parameters associated with the adiabatic heuristic argument[4]. Also, its spinful extension is discussed in details[5].

Fermion quantum Monte Carlo techniques are applied for three dimensional Hubbard model on a pyrochlore lattice where the bulk-corner correspondence has been justified[6]. We further develop bulk-edge correspondence to non-quantum systems. One is heat conduction in 1-dimension[7]. Surprising another example is a bulk-edge correspondence for the evolutional game theory[8] where non-zero Chern number characterizes a boundary flow in the two-dimensional game theory (Figure 1.).

References

[1] Y. Hatsugai, "Chern Number and Edge States in the Integer Quantum Hall effect", Phys. Rev. Lett. 71, 3697 (1993).

[2] Y. Kuno and Y. Hatsugai, "Plateau transitions of a spin pump and bulk-edge correspondence", Phys. Rev. B 104, 045113 (2021).

[3] Y. Kuno and Y. Hatsugai, "Topological pump and bulk-edge-correspondence in an extended Bose-Hubbard model", Phys. Rev. B 104, 125146 (2021).

[4] K. Kudo, Y. Kuno, and Y. Hatsugai, "Bulk-edge correspondence in the adiabatic heuristic principle", Phys. Rev. B **104**, L241113(2021)

[5] K. Kudo and Y. Hatsugai, "Adiabatic Continuity of the Spinful Quantum Hall States", arXiv:2201.07893

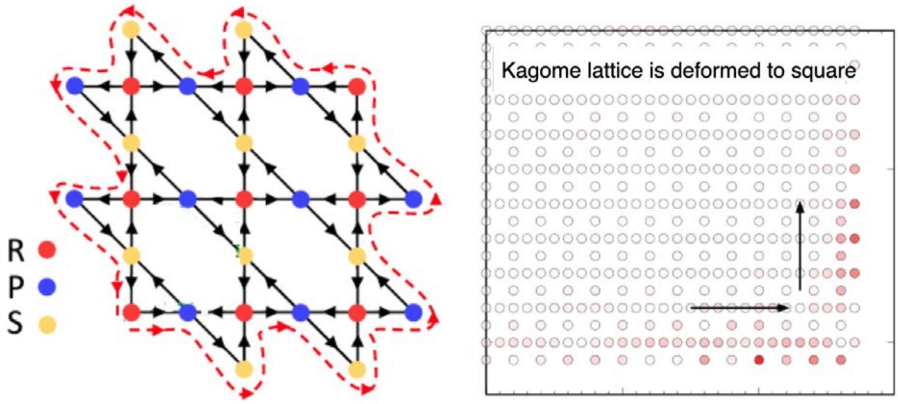

Figure 1: RPS-game on a Kagome lattice (left) and its bundary flow governed by non zero Chern number of the evolutionary game theory (right). (See ref.[8].)

[6] Y. Otsuka, T. Yoshida, K. Kudo, S. Yunoki and Y. Hatsugai , “Higher-order topological Mott insulator on the pyrochlore lattice”, Scientific Reports 11, 20270 (2021)

[7] S. Makino, T. Fukui, T. Yoshida and Y. Hatsugai, “Edge states of a diffusion equation in one dimension: Rapid heat conduction to the heat bath”, Phys. Rev. E 105, 024137 (2022).

[8] T. Yoshida, T. Mizoguchi, and Y. Hatsugai, “Chiral edge modes in evolutionary game theory: A kagome network of rock-paper-scissors cycles”, Phys. Rev. E 104, 025003 (2021).

Molecular dynamics simulation of $BaTiO_3$ nano structure

T. Hashimoto
National Institute of Advanced Industrial Science and Technology (AIST), Tsukuba Central 2, 1-1-1 Umezono, Tsukuba, Ibaraki 305-8568, Japan

Dielectrics clusters have fascinating new properties. It is shown that large off-center displacements of atoms exists even for very small clusters as small as 5 nm, and vortex structures of local polarization vectors could be used as memory devices[1, 2]. However, despite the efforts of preceding studies, the surface termination dependence of the vortex structures and the toroidal moments are not well understood. In this project, we studied these issues by molecular dynamics (MD) simulations using a shell model.

The calculations were performed with the code developed by us. We used a shell model potential developed by Tinte et al.[3, 4]. The calculations were performed under constant (N, V, T) conditions. To simulate isolated clusters, the open circuit boundary condition was used; i.e., we calculated interactions for all the atom pairs in the cluster. The temperature was fixed to 10 K to monitor the structures near the ground state while preventing the system from converging to false structures. We controlled the temperature by the massive Nose-Hoover chain method[5]. For each cluster model, the system was equilibrated for more than 20000 time steps, and data collection runs for more than 100000 time steps followed. One time step was 0.1 fs.

We studied BaO-terminated, TiO_2-terminated, and stoichiometric models. The former model was rounded apex cubic models with eight Ba atoms missing, while the latter two were cubic models. The number of the unit cells on one edge, n, were varied from 3 to 12. The TiO_2 terminated surfaces were unstable, and the TiO_2 terminated clusters were unstable for $n \leq 5$. In all terminations, the toroidal moments become non-zero for clusters larger than $n = 6$. We also studied the toroidal moment direction dependent energy for the BaO-terminated clusters, because they were stable for all n. In these clusters, the structures with the toroidal moments parallel to [111] which are naturally formed in other studies were stable, and structures in which the toroidal moments were parallel to [110] or [001] were metastable. We also analyzed the domain structures inside these clusters. They were found to have domain walls that are known to be stable in the rhombohedral phase.

[1] H. Fu and L. Bellaiche: Phys. Rev. Lett. **91** (2003) 257601.

[2] I. I. Naumov, L. Bellaiche, and H. Fu: Nature **432** (2004) 737.

[3] S. Tinte, M. Stachiotti, S. Phillpot, M. Sepliarsky, D. Wolf, and R. Migoni: J. Phys.: Condens. Matter **16** (2004) 3495.

[4] M. Sepliarsky, A. Asthagiri, S. R. Phillpot, M. G. Stachiotti, and R. L. Migoni: Curr. Opin. Solid. St. M. **9** (2005) 107.

[5] G. Martyna, M. Tuckerman, D. Tobias, and M. Klein: Mol. Phys. **87** (1996) 1117.

DPD simulations of cross-linked networks to study topological effect using MP-SRP method

Katsumi HAGITA,[1] Takahiro MURASHIMA,[2] and Hayato SHIBA[3]
[1]Department of Applied Physics, National Defense Academy, Yokosuka 239-8686
[2]Department of Physics, Tohoku University, Sendai 980-8578
[3]Information Technology Center, University of Tokyo, Kashiwa 277-0882

Ring-linear blends have garnered increasing interest among researchers in recent years for both basic science and industrial applications. In ring–linear blends, a deeper understanding of penetration behaviors among rings and linear chains is important for controlling the mechanical properties of the blends and their applications. Hagita and Murashima [1–4] investigated the dependence between ring size and the penetration of linear chains into the ring through coarse-grained molecular dynamics (CGMD) simulations of the Kremer–Grest (KG) model [5]. They estimated the distribution of the number of chains penetrating a ring by estimating the Gauss linking number (GLN) for all pairs of linear chains and rings. The number n_P of linear chains penetrating a ring was presented as a function of the size of the ring (the number of KG particles in a ring, N_{ring}). These penetration behaviors are governed by the spread and concentration of the ring polymers.

In this study, we investigated the topological effect caused by chain crossing prohibition in ring-linear blends through dissipative particle dynamics (DPD) simulations [6]. Multipoint segmental repulsive potential (MP-SRP) [7] was used to ensure thermodynamic consistency while comparing between the systems that permitted and prohibited chain crossing in DPD polymer simulations. To extract the topological effect of ring polymers, we observed the distribution of penetration in ring–linear blends and the radius of gyration of rings.

Based on a prototype code as an in-house user package of MP-SRP [7] for LAMMPS [8], we remade a public open version of the user package of MP-SRP [7,9]. To reduce computational cost, we improved several implementations as shown in Figure 1. We also confirmed the high scalability in the MPI-based parallel computing.

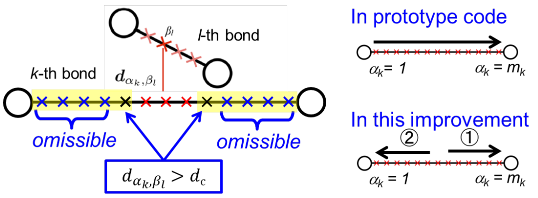

Fig. 1: Schematic of the applied improvement to reduce omissible computations by changing sweep of the SRP points along a bond.

In this study, DPD simulations (MP-SRP and sDPD) of ring–linear blends with a ring fraction of approximately 0.1. Here, sDPD means the standard DPD polymer simulation with the Groot–Warren model [6].

Figure 2 shows the results of (N_{ring}, N_{linear}) = (80, 80), where N_{ring} and N_{linear} denote the number of DPD particles in a ring and in a linear chain, respectively. Compared to the sDPD model, the number of penetrations in the MP-SRP model decreased owing to the prohibition of ring–ring crossing. It should be noted that the penetration state of the initial configuration generated by the push-off procedure was far from equilibrium in both models.

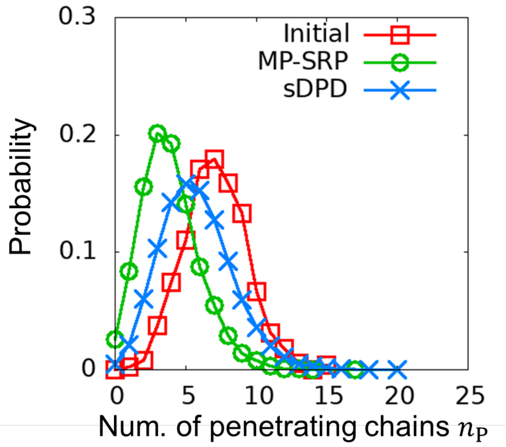

Fig. 2: Probability distributions of linear chains penetrating into a single ring with (N_{linear}, N_{ring}) = (80,80).

We also confirmed the decrease of the squared radius of gyration in comparison to the phantom chain of the sDPD model. The uncatenated rings repel each other because of the topological constraints.

We performed systematic investigations for other values of (N_{ring}, N_{linear}) as shown in the published paper [9]. We concluded that the topological effect prohibits ring–ring crossing, resulting in a small radius of gyration of the rings. In the DPD polymer system with MP-SRP, the minimum size of a ring with penetration was found to be 30, which is less than half of the value of 80 observed in previous work using the Kremer–Grest bead-spring model.

References

[1] K. Hagita and T. Murashima: Polymer **218** (2021) 123493.

[2] K. Hagita and T. Murashima: Polymer **223** (2021) 123705.

[3] K. Hagita and T. Murashima: Macromolecules **54** (2021) 8043-8051.

[4] T. Murashima, K. Hagita, and T. Kawakatsu: Macromolecules **54** (2021) 7210-7225.

[5] K. Kremer and G. S. Grest: J. Chem. Phys. **92** (1990) 5057.

[6] R. D. Groot and P. B. Warren: J. Chem. Phys. **107** (1997) 4423.

[7] N. Iwaoka, K. Hagita and H. Takano: J. Chem. Phys. **149** (2018)114901.

[8] S. Plimpton: J. Comp. Phys. **117** (1995) 117.

[9] K. Hagita, T. Murashima, H. Shiba, N. Iwaoka, and T. Kawakatsu: Comput. Mater. Sci., **203** (2022) 111104.

Kinetics of phase transition and polyamorphism

Kazuhiro Fuchizaki, Hiroki Naruta, and Katsumi Nakamura
Department of Physics, Ehime University, Matsuyama 790-8577

The problem of what drives a liquid-liquid transition motivated us to study entropy estimation for liquids. We first report the results attained in FY2021. The latter part of the report consists of the outcomes obtained from a study of memory hysteresis using machine learning (ML).

The two-phase model's justifiability for entropy estimation [1]

The two-phase model [2] extends the one-phase model for describing the thermodynamics of crystalline phases, regarding them as an aggregate of harmonic oscillators with $3N$ degrees of freedom (DF). Then, the logarithm of the partition function Z is given by $\ln Z = \sum_j \ln z_j$, where z_j is the partition function of the jth oscillator. If the microscopic states are densely distributed to allow a continuum description, we may rewrite this relation as $\ln Z = \int \mathrm{d}\epsilon D(\epsilon) \ln z(\epsilon)$, where $D(\epsilon)$ defines the density of states (DOS) in the energy range between ϵ and $\epsilon + \mathrm{d}\epsilon$. Berens *et al.* [3] prescribed obtaining the DOS from Fourier transforming the velocity autocorrelation function. Thus, the entropy for a solid state may be approximated as $S = k_\mathrm{B} \int_0^\infty \mathrm{d}\omega D(\omega) W_S^\mathrm{HO}(\omega)$, where k_B is Boltzmann's constant. The analytic expression for the entropy spectrum W_S^HO is easily obtainable.

The one-phase model is not applicable to estimating thermodynamic properties of liquid and amorphous states with non-negligible low-frequency modes of $D(\omega)$. Goddard *et al.* [2] have constructed the two-phase model based on their intuitive observation that the DOS of such non-crystalline systems looks like a superposition of DOSs of solid and gas states. They introduced the notion "fluidicity" f, in terms of which the DOS of non-crystalline systems could be divided into $3Nf$ DFs of gas component D^g and remaining crystalline component D^s. Thus, the two-phase model modifies the above expression for the entropy as

$$S/k_\mathrm{B} = \int_0^\infty \mathrm{d}\omega\, D^\mathrm{g}(\omega|f) W_S^\mathrm{g}(\omega) + \int_0^\infty \mathrm{d}\omega\, D^\mathrm{s}(\omega|1-f) W_S^\mathrm{HO}(\omega). \quad (1)$$

Goddard *et al.* [2] assumed a hard-sphere gas to evaluate D^g and W_S^g. For W_S^g, they employed the entropy per DF for a HS system W_S^HS obtainable from the Carnahan–Starling (CS) equation of state (EOS), whereas they invoked the Chapman–Enskog (CE) theory to settle the expression for D^g. The CE theory also allowed them to determine f. Thus, if the actual DOS $D(\omega)$ is available from experiments or simulations, Eq. (1) gives us an entropy estimate by putting $D^\mathrm{s} = D - D^\mathrm{g}$.

We employed a simple liquid whose thermodynamic properties are well studied to test the two-phase model's prediction. Thus, we chose the modified Lennard-Jones system [4] with 2048 particles, to which we conducted isothermal–isochore molecular dynamics simulation at slightly above the critical temperature. We adopted three densities; one was the critical density ρ_c, and the other two are below and above ρ_c. We used the λ- and thermodynamic integrations to estimate the entropies precisely. We calculated the entropy also from the modified Benedict–Webb–Rubin EOS [5].

The entropies resulting from the former three approaches coincided within the error margin. However, the two-phase model gave systematically lower entropies than those three. The deviation increases with density. However, the most significant deviation was limited to 6% at the highest density examined. Because both the CS EOS and the CE theory would not be appropriate to capture such a high-density liquid (even though simple), many factors employed in the two-phase model would cancel to attain such an accuracy. Unfortunately, because the two-phase model was constructed in an ad-hoc way, we cannot give any suggestions to improve it at this moment.

Judging the (dis)continuity of phase transition using ML [7]

Based on the valuable discovery that the sum of weights $W_{\rm sum}$ in a convolutional neural network (CNN) behaves like an order parameter when it learns spin configurations of a 2-dimensional Ising system as a function of (inverse) temperature, we have proposed a method to detect the phase-transition point at an early stage of learning processes. The latter work prompted us to consider whether a CNN can judge the order of phase transition from the viewpoint of memory hysteresis.

When we see a series of continuously changing pictures from, say, A to B, we notice a salient change at C on its way. However, when we view the same series in reverse order from B to A, the noticeable point of change does not necessarily coincide with C. This hysteresis may be related to the mechanism of our short-term memory equipped with our brain. A CNN could already implement such a mechanism. Thus, it will exhibit a hysteretic behavior depending on an impetus applied through a learning process.

Here we only outline what we examined. We used the same CNN as employed in [6]. However, the crucial difference was the way of learning. In [6], learning data has been input randomly, as usually employed in ML. This time, the data was input in order of increasing (decreasing) magnitude of external parameters such as magnetic field and temperature. Under various magnetic fields, we prepared equilibrium spin configurations of the 2-dimensional 64×64 Ising system below and above the critical temperature. We also made equilibrium patterns of 256 q-state Potts model for $q = 3$ through 7 at various temperatures below and above the critical temperature. System B took care of generating these data sets.

In all of the cases examined, for a discontinuous phase transition, a sharp peak showed up precisely at the transition point when $W_{\rm sum}$ was plotted as a function of the external parameter, regardless of the direction of its change. In contrast, $W_{\rm sum}$ offered a rounded peak for a continuous transition with the peak position shifted as if the CNN missed the exact transition point, leaving a clear-cut hysteresis against a cyclic change of the external parameter. We thus conclude that our approach will be applicable to judge the order of a general phase transition if the learning data are available.

References

[1] H. Naruta and K. Fuchizaki: to be presented at The 18th International Conference on Liquid and Amorphous Metals.

[2] S-T. Lin, M. Blanco, and W. A. Goddard: J. Chem. Phys. **119** (2003) 11792.

[3] P. H. Berens, D. H. J. Mackay, G. M. White, and K. R. Wilson: J. Chem. **79** (1983) 2375.

[4] Y. Asano and K. Fuchizaki: J. Chem. Phys. **137** (2012) 174502.

[5] Y. Asano and K. Fuchizaki: J. Phys. Soc. Jpn. **86** (2014) 034601.

[6] K. Fuchizaki, K. Nakamura, and D. Hiroi: J. Phys. Soc. Jpn. **90** (2021) 055001.

[7] K. Nakamura and K. Fuchizaki: in preparation.

Three-Dimensional Finite Element Analysis of Friction between solids

Michio OTSUKI

Graduate School of Engineering Science, Osaka University,

Osaka University, Kashiwa-no-ha, Kashiwa, Chiba 277-8581

According to Amontons' law, the maximum static friction force of a solid object is proportional to the applied loading force and independent of the apparent contact area, which indicates that the static friction coefficient does not depend on the applied pressure and the shape of the solid. Previous studies have clarified that Amontons' law systematically breaks down for macroscopic objects due to precursor slip before the onset of bulk sliding [1], which is consistent with experiments [2]. However, the analysis in the previous works is restricted to 2D systems. Therefore, it is not clear whether the result is applicable to more realistic 3D systems.

This year, we numerically investigate the sliding motion of a 3D viscoelastic object with length L, width W, height H, and Young's modulus E on a solid substrate using the finite element method (FEM) with 500,000 nodes by MPI of 1000 processors, as shown in Fig. 1. A rigid rod slowly pushes the object with a constant velocity. A uniform pressure P_{ext} is applied to the top of the object. The friction force at the bottom locally satisfies Amontons' law with the local static and kinetic friction coefficients μ_{S} and μ_{K}, respectively.

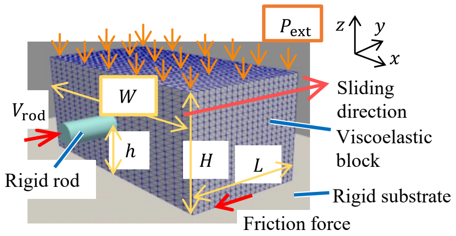

Fig. 1: Schematic of the 3D FEM calculation.

The object exhibits macroscopic stick-slip motions, which are characterized by the macroscopic static friction coefficient μ_{M}. μ_{M} decreases with the external pressure P_{ext} and the width W, as shown in Fig. 2, which contradicts Amontons' law. We also find that quasi-static precursor slip occurs in the 2D interface between the object and the substrate before bulk sliding, which is related to the decrease of μ_{M}.

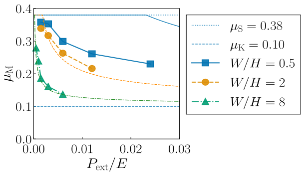

Fig. 2: Static friction coefficient μ_M against

References

[1] M. Otsuki and H. Matsukawa: Sci. Rep. **3** (2013) 1586.

[2] Y. Katano. et al.: Sci. Rep. **4** (2014) 6324

Constructing a Dataset of Dielectric and Thermal Properties of Polymeric Materials

Yuta YOSHIMOTO

Department of Mechanical Engineering,

The University of Tokyo, 7-3-1 Hongo, Bunkyo-ku, Tokyo 113-8656

We have constructed a dataset of dielectric and thermal properties of polymeric materials using quantum chemical (QC) calculations and molecular dynamics (MD) simulations. Seventy-seven polymer systems are constructed from the repeating units of previously synthesized polymers [1,2], where atomic charges are derived from QC calculations using the Gaussian 16 electronic structure package [3] and MD simulations are performed using the LAMMPS software package [4]. All calculations are automated using RadonPy [5] and performed on System B (ohtaka).

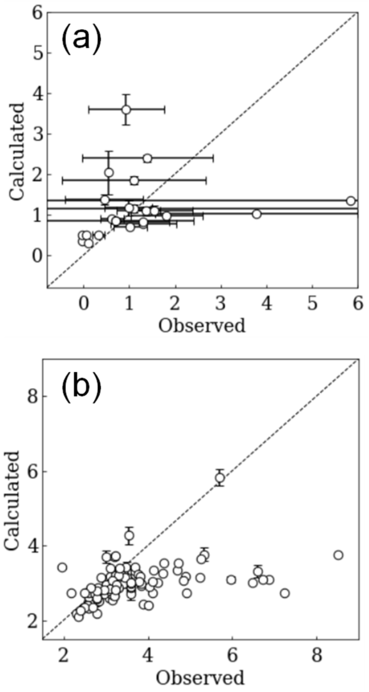

Fig. 1: Comparison of calculated and experimental values for coefficients of linear thermal expansion [10^{-4}/K] (a) and static dielectric constants (b).

Figure 1(a) compares calculated and experimental values of coefficients of linear thermal expansion, exhibiting a weakly linear relation between them, although the experimental values have large uncertainties. Calculated static dielectric constants also show reasonable agreements with the experimental values except for several polymers, as shown in Fig. 1(b). These results validate our simulation methodology, although more thorough investigation is required to further improve the predictive performance.

References

[1] L. Chen et al.: npj Comput. Mater. **6** (2020) 61.

[2] S. Otsuka et al.: Int. Conf. on Emerging Intelligent Data and Web Technologies (2011) 22.

[3] M. J. Frisch et al.: Gaussian 16, Revision C.01 (2019).

[4] A. P. Thompson et al.: Comput. Phys. Commun. **271** (2022) 108171.

[5] Y. Hayashi et al.: arXiv:2203.14090 (2022).

Nanoscale phonon transport across ceramics interfaces

Susumu FUJII
Division of Materials and Manufacturing Science, Osaka University
Yamadaoka, Suita, Osaka, 565-0871
Nanostructures Research Laboratory, Japan Fine Ceramics Center
Mutsuno, Atsuta, Nagoya 456-8587

Lattice thermal conductivity is a fundamental property of materials, which is important for a wide spectrum of applications, e.g., thermoelectrics, thermal barrier coatings, and electronic devices. Interfaces embedded in materials, such as grain boundaries and heterogeneous interfaces, are known to significantly suppress lattice thermal conduction because of their distinguished atomic/electronic structures from the corresponding crystal, which induce the scattering of group motion of atoms, i.e., phonons. Recently, miniaturization of electronic devices and development of nanostructuring techniques have led to an increase of number of cases in which the interfaces are the rate-limiting factor for the thermal conduction in materials. For more precise control of thermal conductivity, it is necessary to reveal the mechanisms of thermal transport across interfaces from the microscopic point of view. However, there are few studies that quantitatively reveal the correlations between interfacial atomic structures and thermal conduction, and that investigate the scattering mechanisms of phonons at interfaces. The main obstacles are follows: (1) the lack of method to quantitatively connect the structure and thermal conduction; and (2) the lack of method to evaluate thermal conductivity of local structure at atomic-scale.

In this project, we have attempted to elucidate the microscopic mechanisms of interfacial thermal transport by using two kinds of molecular dynamics simulations. One is the perturbed molecular dynamics simulations, in which atomic contributions to overall lattice thermal conduction (atomic thermal conductivity) can be estimated. The other is the phonon wave packet simulations, in which transmission coefficient of individual phonons can be estimated. Combinations of these two methods can provide the insights of interfacial phonon scattering from the phenomenological and theoretical perspectives. The necessary codes were developed by the author and implemented to the Large-scale Atomic/Molecular Massively Parallel Simulator (LAMMPS) [1]. We chose grain boundaries of crystalline silicons and interfaces between (1) crystalline silicon and amorphous silica (SiO_2) and (2) crystalline and amorphous silicons as model systems, because it has many technologically important applications.

For silicon grain boundaries, we used a machine learning potential for Si distributed in MACHINE LEARNING POTENTIAL REPOSITORY [2], which accurately reproduce the results of *ab initio* calculations but are less computationally demanding. Thermal conductivity calculations using perturbed molecular dynamics require a large computational cells with at least a few thousands of atoms, with the time steps of more than one million. Such large-scale calculations were performed with five different magnitudes of perturbations for each grain boundary, to obtain the thermal conductivity with high statistical accuracy. The results indicates that thermal conductivity of Si grain boundaries highly depends on their microscopic atomic structures as well as their crystal misorientations, as shown in Fig. 1 [3]. On the other hand, phonon wave packet simulations shows that acoustic phonons mainly conduct heat across interfaces and the transmission coefficients are not significantly different between the grain boundaries with different crystal orientation and/or atomic structures. This indicates that anharmonic nature of atomic vibrations at grain boundaries, which is naturally included in the perturbed molecular dynamics but is intentionally excluded in the phonon wave packet simulations, determines the interfacial thermal conduction. Additional calculations for 18 silicon grain boundaries suggest that bond strains induced by the open-core structures of silicon grain boundaries highly correlate with the reduction of atomic thermal conductivities, which should be related with the magnitude of anhamonicity.

For heterogenious interfaces between crystalline and amorphous silica, we have performed a large number of perturbed molecular dynamics and phonon wave packet simulations, by using an empirical Tersoff potential, which is less computationally demanding than the machine learning potential. The computational cells typically contains about a million of atoms for phonon wave packet simulations. It was found that the transmission coefficients of acoustic phonons dramatically decrease as a function of the thickness of amorphous SiO_2 layer, resulting in very low thermal conductivity. The significant amount of reflected phonons at the interface make the spatial depdendence of thermal conductivity even in the crystalline silicon. Comparisons with the interfaces between crystalline and amorphous silicons indicates that compositional differences between two materials enhance the scattering and reflection of phonons at the interfaces, because of the mismatch of phonon frequencies between the two adjoined materials.

All the molecular dynamics calculations were performed in a single node rather than multiple nodes. This is because it is necessary to perform many calculations with different structures and different conditions, and performing calculations on a single node is more efficient than parallel.

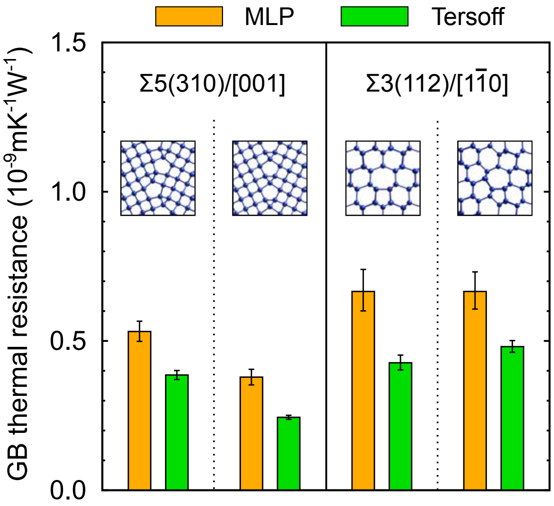

Figure 1: Interfacial thermal resistances of $\Sigma5(310)$ and $\Sigma3(112)$ grain boundaries estimated by perturbed molecular dynamics simulations, with the machine learning potential (MLP) and an empirical atomic potential (Tersoff) [3]. The results of two different atomic sturctures are shown for each grain orientation.

References

[1] S. Plimpton, J. Comput. Phys. **117** (1995) 1.

[2] A. Seko, arXiv:2007.14206.

[3] S. Fujii, A. Seko, Comput. Mater. Sci. **204** (2022) 111137.

Numerical Study of Spin Systems on the Honeycomb Lattice

Chitoshi YASUDA
Department of Physics and Earth Sciences, Faculty of Science,
University of the Ryukyus, Okinawa 903-0213, Japan

The quasi-two-dimensional (quasi-2D) antiferromagnetic Heisenberg (AFH) model on a cubic lattice consisting of the nearest-neighbor intra-layer ($J = 1$) and inter-layer (J') interactions has a finite-temperature phase transition at which the critical behavior belongs to the universality class same as the three-dimensional classical Heisenberg system. In the previous work [1] on the quasi-2D square-lattice AFH model using the quantum Monte Carlo method, it was numerically found that the Néel temperature $T_{\rm N}$ obeys an universal relation between J' and the staggered susceptibility $\chi_{\rm s}(T_{\rm N})$ of the 2D system on the square lattice, i.e., besides an effective coordination number defined by $\zeta(J') \equiv 1/(J'\chi_{\rm s}(T_{\rm N}(J')))$ does not depend on J' for $J' \leq 0.02$, the value becomes $\zeta(J') \approx 0.65z$ ($z = 2$) all for $S = 1/2$, 1 and ∞. The universal relation has also been predicted by an analysis of the quantum nonlinear sigma model [2].

In this project, we research the renormalized coordination number in the quasi-2D honeycomb lattice AFH model with spin $S = 1/2$ using the quantum Monte Carlo method with the continuous imaginary-time loop algorithm, and compare the results with those of the square lattice to investigate the universality. The Néel temperatures were evaluated by finite-size scaling analysis using data up to the system size $80 \times 40 \times 40$, and it was confirmed that there is a relation $T_N \propto 1/(b - \ln(J'))$. Here, b is a constant. We have also estimated the renormalized coordination numbers by evaluating the staggered susceptibility on the honeycomb lattice at the Néel temperature. Our results suggest that $\zeta/z \approx 0.65$ in the small J' region. The consistent value of ζ/z in the square and honeycomb lattices indicates that ζ is a universal quantity independent of the lattice. However, the accuracy of the result for the smallest J', $J' = 0.001$, is not yet sufficient, and further calculations for larger sizes might be needed in the future. Hastings *et al.* have proposed that there exists a universal function even in the region of J' larger than J' where ζ is constant [2]. Our results suggest that there is one lattice-independent function $\zeta(J')$ at $J' = 0.05$ and 0.1.

In this project, we also research zinc phthalocyanine ($ZnC_{32}N_8H_{16}$(ZnPc)) and the fluorinated ZnPc ($ZnC_{32}N_8F_{16}$ (F_{16}ZnPc)) consisting of hexagon as with the honeycomb lattice as testing calculations for the density functional method using the program package VASP. The compound ZnPc is an aromatic compound composed of four isoindoline units (C_8H_4N) consisting of a six-membered ring of benzene bonded to hydrogen and a five-membered ring containing nitrogen. We confirmed that the energy levels of F_{16}ZnPc are deeper than those of ZnPc. The numerical result corresponds to the electron-accepting property of F_{16}ZnPc and the electron-releasing property of ZnPc.

References

[1] C. Yasuda *et al*, Phys. Rev. Lett. **94** (2005) 217201.

[2] M. B. Hastings and C. Mudry, Phys. Rev. Lett. **96** (2006) 027215.

Data analysis method using a tensor network representation

KENJI HARADA
Graduate School of Informatics, Kyoto University, Kyoto 606-8501, Japan

We study data analysis methods based on tensor network representations in this study project.

The first topic is quantum machine learning. Using tensor network schemes, we numerically study the relationship between the performance of a quantum circuit and the entanglement properties. In particular, the quantum circuits on a tree tensor network structure can be efficiently estimated about the entanglement capability[1]. We found that a quantum circuit with a high entanglement capability shows good performance in a classification problem until some hundred qubit cases. Therefore, the entanglement capability is an important property for estimating performance[2]. In this study, we use the system B for calculation of a tensor contraction to estimate the entanglement capability through tensor network representations.

The second topic is tensorized neural networks[3]. A tensor network as MPO represents the weight matrix in a neural network. We numerically evaluate the profile of an entanglement property in MPO in the learning process. It much depends on the initial tensors in MPO[4]. We derive a stable initialization method for MPO in the tensorized neural network. The deeper tensorized neural network can also be stably converged by the initialization. In this study, we use the system B for the systematic calculation of the profile of entanglement in MPO in the learning process.

[1] S. Sim, Peter D. Johnson, and Alán Aspuru-Guzik, Expressibility and entangling capability of parameterized quantum circuits for hybrid quantum-classical algorithms. Advanced Quantum Technologies 2, 1900070 (2019).

[2] H. Manabe and K. Harada, Quantum circuit learning with tensor network structure, 23pA1-1, JPS Autumn meeting (2021).

[3] A. Novikov, D. Podoprikhin, A. Osokin, D. Vetrov, Tensorizing Neural Networks, NIPS 2015.

[4] Y. Asoshina and K. Harada, Entanglement Analysis of Neural Networks, 22pL4-9, JPS Autumn meeting (2021).

Numerical Analysis for Stability and Dynamics of Magnetic Structures such as Skyrmions

Kenji KONDO

Research Institute for Electronic Science, Hokkaido University,
Sapporo, Hokkaido, 001-0020.

Magnetic skyrmions are expected to be promising candidates for representing and transferring one bit of information. This is because they are topologically protected from external perturbations, which ensures the stability of information. Moreover, they are very small in size and they are able to be driven using the current. In this study, we utilize the spin dynamics code *"Spirit"* [1] which can incorporate the demagnetization fields or can calculate three-dimensional magnetic structures in order to perform the numerical calculations of the dynamics of topological magnetic structures such as skyrmions. In our previous work, we investigated the dynamics of skyrmions driven by the spin polarized current [2,3] using a handmade finite-element-method (FEM) program. At that time, we did not take the demagnetization fields into consideration since we considered the influence to be negligible. Also, there was an aspect that we avoided considering the demagnetization fields since it takes much time to calculate them. Thus, in this study, we investigate the influence on the velocities of the skyrmions with the demagnetization fields or without them using *Spirit*. Figure 1 shows the current density dependences of the average velocities of the skyrmions in the ferromagnets (FMs) driven by the spin-transfer torque (STT) with the demagnetization fields or without them. In this calculation, we assume Co thin film as the FM and use the material parameters of the FM from the references [4–6]. The blue and the red lines represent the average velocities of the skyrmions in the FMs with and without the demagnetization fields, respectively. It is found that the existence or the non-existence of the demagnetization fields have only 3.729% influences on the velocities of the skyrmions, which is almost negligible. Our previous estimation of the influences on the velocities of the skyrmions is found to be right. On the other hand, we investigate the dynamics of three-dimensional topological magnetic structures, so-called skyrmion strings, using *Spirit*. The skyrmions can form string structures by spreading in the out-of-plane direction. Especially, we investigate the differences of the skyrmion string structures under the positive and negative Dzyaloshinskii-Moriya interaction (DMI) constants. The signs of DMI constants are defined in Fig. 2. When the DMI vectors point outwards, we define the DMI constant as positive. When the DMI vectors point inwards, we define the DMI constant as negative. Figures $2(a)$ and $2(b)$ show the skyrmion string structures in the FMs in the cases of the positive and negative DMI constants, respectively. It is found that the directions of the magnetization vectors of the skyrmion strings are counterclockwise and clockwise when seeing from the top view in the cases of the positive and negative DMI constants, respectively. Figures $3(a)$-$3(c)$ show the contour plots of the x, y, and z components of the effective magnetic fields H_{eff} in the case of the positive DMI constant, respectively. Moreover, figures $3(d)$-$3(f)$ show the contour plots of the x, y, and z components of H_{eff} in the case of the negative DMI constant, respectively. Comparing these results, it is found that the effective magnetic fields H_{eff} point to the opposite directions in the xy-plane.

Therefore, the positive and negative DMI constants cause the magnetization vectors of the skyrmion strings to point to the opposite directions in the xy-plane. As a result, there manifest themselves the counterclockwise skyrmion strings and the clockwise skyrmion strings depending on the signs of DMI constants. It took approximately one month to perform all of these calculations as the computer run time using the ISSP supercomputer system B (Ohtaka). Also, we have calculated the dynamics of the logic gates consisting of the skyrmions in the antiferromagnets, which we will not state here in detail. We are preparing the paper concerning the logic gates consisting of the skyrmions in the antiferromagnets.

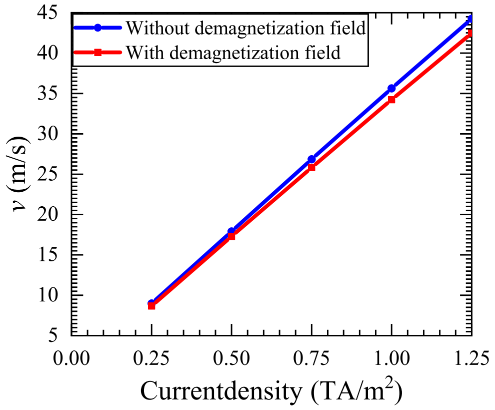

Fig. 1: The current density dependences of the average velocities of the skyrmions in the FMs with the demagnetization fields or without them.

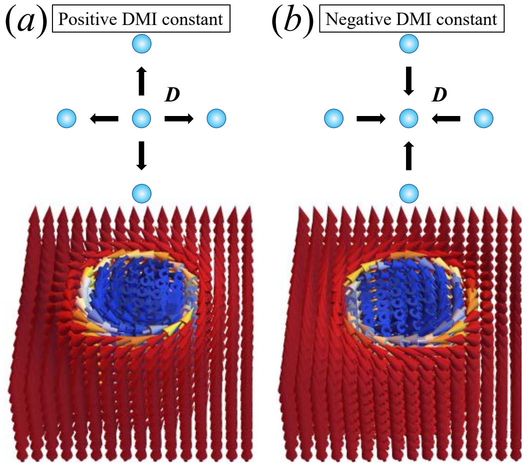

Fig. 2: The 3D vector plots of the skyrmion string structures in the FMs in the cases of (a) the positive and (b) the negative DMI constants.

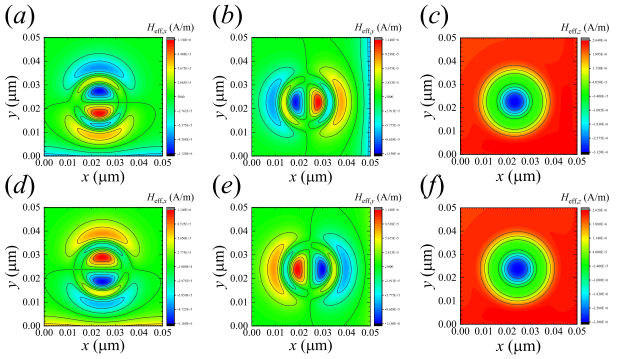

Fig. 3: The contour plots of the x, y, and z components of H_{eff} of skyrmion strings are shown in figures (a)-(c) in the case of the positive DMI constant, respectively. The contour plots of the x, y, and z components of H_{eff} of skyrmion strings are shown in figures (d)-(f) in the case of the negative DMI constant, respectively.

References

[1] G. P. Müller, M. Hoffmann, C. Dißelkamp, D. Schürhoff, S. Mavros, M. Sallermann, N. S. Kiselev. H. Jónsson, and S. Blügel, Phys. Rev. B. **99**, 224414 (2019).

[2] Y. Ishida and K. Kondo, J. Magn. Magn. Mater. **493**, 165687 (2020).

[3] Y. Ishida and K. Kondo, Jpn. J. Appl. Phys. **59**, SGGI04 (2020).

[4] J. Sampaio, V. Cros, S. Rohart, A. Thiaville, and A. Fert, Nat. Nanotechnology. **8**, 839-844 (2013).

[5] L. S. E. Alvarez, K.-Y. Wang, S. Lepadatu, S. Landi, S. J. Bending, and C. H. Marrows, Phys. Rev. Lett. **104**, 137205 (2010).

[6] D. J. Monsma and S. S. P. Parkin, Appl. Phys. Lett. **77**, 883 (2000).

Numerical study on low-energy states of quantum spin systems

Hiroki NAKANO
Graduate School of Science, University of Hyogo
Kouto, Kamigori, Hyogo 678-1297, Japan

Many-body problems have to been tackled in the field of the condensed matter physics; therefore, it is difficult to estimate physical quantities precisely in many cases. Quantum spin systems are such a typical one. To investigate these systems, numerical approaches have widely and effectively been used. A lot of computational studies have been carried out; useful information of the target systems has been provided.

Generally speaking, three methods are effectively used within the Field of quantum spin systems. The first and traditional one is the numerical diagonalization method; the second is the quantum Monte Carlo (QMC) method. The third method is the density matrix renormalization group (DMRG) method. Each of them has some advantages; on the other hand, it has disadvantages, too. The QMC simulations can treat significantly large systems irrespective of the spatial dimensions of the systems; however, the negative sign problem in this approach prevent us with a difficulty in precise evaluation of physical quantities in frustrated systems. The DMRG method is a very useful method for a one-dimensional system irrespective of whether the target system includes frustration or not. However, this method is still under development for the cases when the spatial dimension is larger than one. The numerical diagonalization method can be applicable irrespective of the presence of frustrations and the spatial dimension. This method, on the other hand, has a severe weak point that it can treat only very small system sizes. To overcome this disadvantage of the numerical diagonalization, we developed a hybrid-type parallelized code of Lanczos diagonalization[1]. This code enables us to treat various large systems that have not been previously treated yet within this method and to evaluate physical quantities precisely. Therefore, we examine various quantum spin systems by this method as a primary approach in this project.

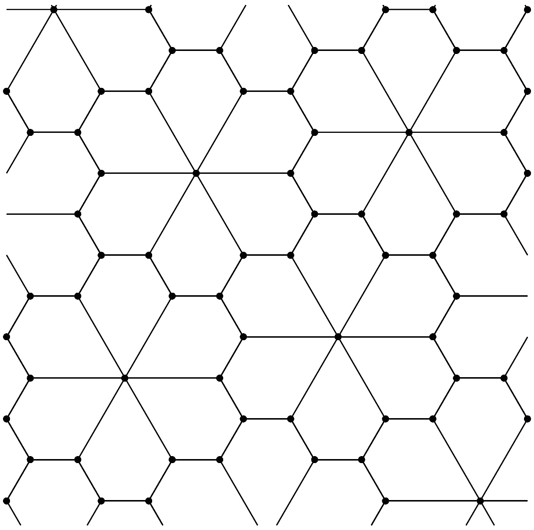

Figure 1: Floret-pentagonal lattice.

In the project in 2021, we tackled the $S = 1/2$ Heisenberg antiferromagnet on the floret-pentagonal lattice[5]. Among pentagonal lattices, studies concerning the Cairo-pentagonal-lattice antiferromagnet has been known[2, 3, 4]. However, the floret-pentagonal-lattice antiferromagnet has not been investigated to the best of our knowledge; this system is the second example as pentagonal lattices that include equivalent two directions in the system. (See Fig.1.) We have observed the magnetization process of this system and find magnetization plateaux at one-ninth height of the saturation magnetization, at one-third height, and at seven-ninth height. We have also discovered a magnetization jump between the one-third-height and seven-ninth-height plateaux. The jump is a peculiar phenomenon because this jump is away from the two plateaux. Our study contributes much to our deeper understandings of the frustrated quantum antiferromagnets. Further investigations would clarify nontrivial quantum effects due to frustration.

References

[1] H. Nakano and A. Terai: J. Phys. Soc. Jpn. **78**, 014003 (2009).

[2] I. Rousochatzakis, A. M. Läuchli and R. Moessner: Phys. Rev. B **85**, 104415 (2012).

[3] H. Nakano, M. Isoda, and T. Sakai: J. Phys. Soc. Jpn. **83**, 053702 (2014).

[4] M. Isoda, H. Nakano, and T. Sakai: J. Phys. Soc. Jpn. **83**, 084710 (2014).

[5] R. Furuchi, H. Nakano, N. Todoroki, and T. Sakai: J. Phys. Commun. **5**, 125008 (2021).

Development of the Low-Temperature Oxidation Model for Alternative Fuels Using Machine Learning

Minhyeok LEE, Tomotaka MIZUNO, and Yuji SUZUKI
Department of Mechanical Engineering, School of Engineering,
The University of Tokyo, 7-3-1 Hongo, Bunkyo-ku, Tokyo 113-8656

To improve thermal efficiencies and reduce pollutant emissions of Internal Combustion engines simultaneously, it is crucial to understand the detailed reaction mechanism of fuels. Recently, various reaction kinetic models have been proposed to precisely explain the reaction process of the target fuel. However, as shown in Fig. 1, as increasing the size of the fuel molecule, the number of reactions involved is increased exponentially. It makes hard to solve the entire model numerically without reducing the reaction size due to high computational costs. Note that such model reduction causes a decrease in accuracy of the numerical estimation, particularly in the low-temperature region [1]. Therefore, we conducted numerical simulations with full mechanisms by means of the supercomputer system at ISSP to evaluate the ignition process of cool flames.

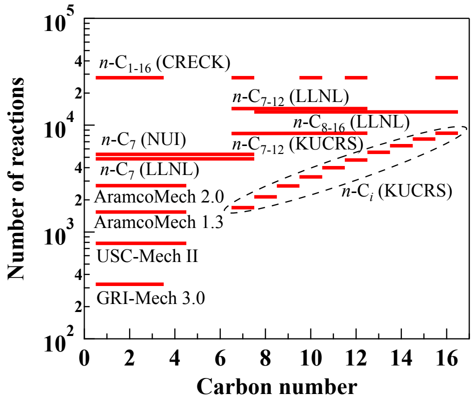

Fig. 1: Reaction size of various kinetic models for normal-alkane fuels.

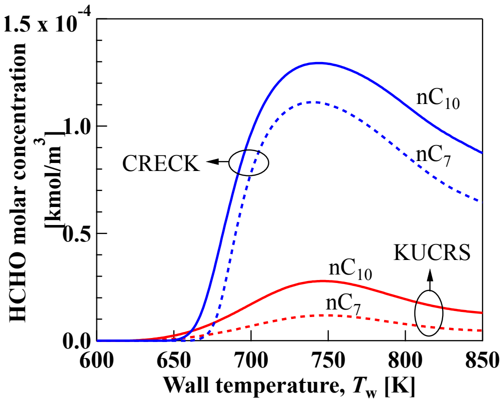

Fig. 2: Cool flame ignition of n-C_7 and n-C_{10}.

One-dimensional axisymmetric stagnation flows formed by impinging a mixture of fuel and air on a heated wall were assumed. The nozzle-to-wall distance was 15 mm. The outlet velocity, temperature, and equivalence ratio of the fuel/air mixture were 50 cm/s, 300 K, and 1, respectively. The wall temperature was ramped up from 600 K to 850 K under the quasi-steady state. Normal-heptane (n-C_7H_{16}) and -decane (n-$C_{10}H_{22}$) were used as the fuel. Two reaction models including both fuels were used, which respectively proposed by the CRECK modeling group [2] and generated by using the KUCRS (Knowledge-basing utilities for complex reaction systems) [3]. The Cantera code [4] was employed to conduct numerical simulation under the above condition.

As increasing the wall temperature, cool flames are ignited on the wall due to initiation of the low-temperature oxidation. Figure 2 shows increases of the calculated HCHO molar concentration on the wall as a function of the wall temperature. While the HCHO concentration estimated by the CRECK model is higher, the onset temperature calculated by the KUCRS model is slightly lower for both fuels. Furthermore, a difference in the onset temperature between two fuel is negligible for the KUCRS model, but *n*-decane's onset temperature is approximately 12 K lower than that of *n*-heptane in the CRECK model. It means that two models show the discrepancy in estimating not only the low- and intermediate-temperature reactivity of each fuel, but also hierarchical difference with respect to the molecule (chain) size.

Further improvements in the reaction model should be made through the experimental validation.

References

[1] C.B. Reuter, M. Lee, S.H. Won, Y. Ju: Combust. Flame **179** (2017) 23.

[2] A. Miyoshi: KUCRS software library, http://akrmys.com/KUCRS/

[3] The CRECK Modeling Group: http://creckmodeling.chem.polimi.it

[4] D.G. Goodwin, R.L. Speth, H.K. Moffat, B.W. Weber: Cantera: An object-oriented software toolkit for chemical kinetics, thermodynamics, and transport processes, https://www.cantera.org

Formation of Lipid Rafts Studied by Molecular Dynamics Simulation

Satoru G. ITOH
Institute for Molecular Science, Okazaki, Aichi 444-8787
Exploratory Research Center on Life and Living Systems, Okazaki, Aichi 444-8787
The Graduate University for Advanced Studies, Okazaki, Aichi 444-8787

In cell membranes, lipid rafts are formed by aggregation of sphingolipids and cholesterol molecules [1]. It has been clarified that lipid rafts play important roles in functions such as signal transduction and protein transport in vivo [2,3]. Lipid rafts are also related to virus infection and protein aggregation [4,5]. It is essential to elucidate their structures and formation processes to understand their functions. Therefore, we aim to elucidate these by using molecular dynamics (MD) simulation. In particular, we are interested in lipid rafts containing GM1 gangliosides, which are abundant in nerve cell membranes. To investigate the structure of GM1 ganglioside clusters, we employed the Coulomb replica-permutation molecular dynamics simulation [6]. The Coulomb replica-permutation method is one of the Hamiltonian replica-permutation methods, and it is possible to efficiently investigate the complex structure of biomolecules by using this method.

In the last year, we have made significant improvements to our own program to be able to perform MD simulations with various force fields for the all-atom model. We have also made it possible to perform MD simulations on molecules other than proteins. In addition, the program has been modified to allow the Coulomb replica-permutation method to scale only the intermolecular electrostatic interactions between GM1 ganglioside molecules.

References

[1] K. Simons and E. Ikonen: Nature **387** (1997) 569.

[2] K. Simons and D. Toomre: Nat. Rev. Mol. Cell Biol. **1**, (2000) 31.

[3] D. Lingwood and K. Simons: Sience **327** (2010) 46.

[4] N. Chazal and D. Gerlier: Microbiol. Mol. Biol. Rev. **67** (2003) 226.

[5] J. M. Cordy, N. M. Hooper and A. J. Turner: Mol. Membr. Biol. 23 (2006) 111.

[6] S. G. Itoh and H. Okumura: J. Comput. Chem. **34** (2013) 2493.

Numerical calculation of spin Hall magnetoresistance by the quantum Monte Carlo method

Takeo KATO
Institute for Solid State Physics, University of Tokyo
Kashiwa-no-ha, Kashiwa, Chiba 277-8581

Spin Hall magnetoresistance (SMR), that is a magnetoresistance caused by the absorption of spin current generated by the spin Hall effect in a bilayer system composed of a metal and a magnetic insulator [1], is being actively studied for potential applications in spintronics devices such as memory applications. Although SMR is well described quantitatively by a phenomenological theory [2], its temperature dependence for a metal/antiferromagnetic-insulator bilayer system [3] are difficult to be described by it.

In this numerical study, we evaluate the spin conductance at the interface by expanding the theory of Ref. [4]. The spin current is expressed in terms of the spin susceptibility of the antiferromagnetic insulator and is calculated by the quantum Monte Carlo method. In order to obtain dynamic properites, we need to perform the numerical analytic continuation. However, this is usually an ill-defined probpem and is difficult to be applied for obtaining the spin conductance. We improved the method to stably obtain the spin conductance using only the component of Matsubara frequency of Green's function and succeeded in its accurate calculation.

As a result of examining the temperature dependence and the thickness dependence of the SMR, the sign was reversed as the rising temperature rose in the negative sign from the low temperature region, and the result agreed with the experimental result with the peak of the positive sign. In addition, it was confirmed that the behavior of SMR differed depending on the size of the spin of the antiferromagnetic insulator, and that SMR at $S = 1$ was larger than $S = 1/2$. We also showed that SMR vanishes above the magnetic transition temperature unlike the experiment. We are now preparing for a paper on these results [5].

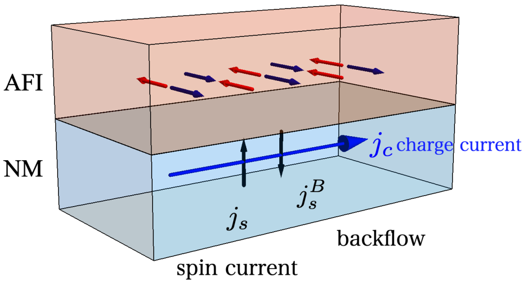

Figure 1: SMR Measurement Setup.

References

[1] H. Nakayama, et al., Phys. Rev. Lett. **110**, 206601 (2013).

[2] Y. T. Chen, et al., Phys. Rev. B **87**, 144411(2013).

[3] D. Hou, et al., Phys. Rev. Lett. **118**, 147202 (2017).

[4] T. Kato, Y. Ohnuma, and M. Matsuo, Phys. Rev. B **102**, 094437(2020).

[5] T. Ishikawa, M. Matsuo, and T. Kato in preparation.

Dynamical property of a resistively shunted Josephson junction

Tsuyoshi Yamamoto
Institute for Solid State Physics, University of Tokyo
Kashiwa-no-ha, Kashiwa, Chiba 277-8581

Physical properties of quantum systems are drastically changed by interaction with an environment, because thousand of modes in the environment are complexly entangled with quantum states of systems. A typical example is the Kondo problem, in which a spin of a magnetic impurity is screened by surrounding conduction electrons in a normal metal [1]. Such kind of a dissipative system has been a central topic of condensed matter physics for a long time.

One of the most notable problems in dissipative systems is a dissipation-driven quantum phase transition. In 1983, Schmid predicted that a single Josephson junction connected to a resistance, which is called the resistively shunted Josephson junction (RSJJ), undergoes a superconductor-insulator transition at zero temperature [2]. When the resistance is larger than a resistance quantum ($R > R_Q = h/4e^2$), the Josephson junction becomes insulating, while when $R < R_Q$, it becomes superconducting (see Fig. 1). However, there is no clear experimental evidence to have observed the transition, and it is still controversial [3]. The recent development of superconducting circuits allows us to access the dynamical property of the RSJJ using microwave spectroscopy while it has been discussed in the dc limit. This development motivates us to approach the RSJJ from the dynamical response, and it provides a new perspective to solve the controversial problem, the Schmid transition.

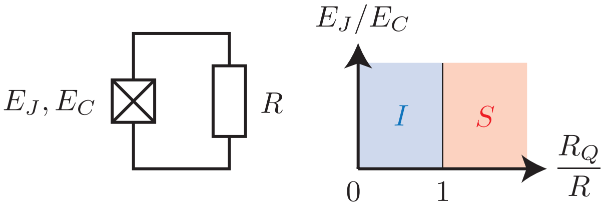

Figure 1: (left) A Josephson junction with the Josephson energy E_J and the charging energy E_C connected to a resistance R. (right) Schmid transition diagram. In the phase I (S), the Josephson junction becomes an insulator (a superconductor) at zero temperature.

To this end, we calculated frequency dependence of an impedance of the RSJJ circuit and examined dynamic properties in the microwave reflection via the RSJJ circuit. We first calculated the phase-phase correlation function defined on the imaginary-time axis using the path-integral Monte Carlo simulation [4] and then performed the analytical continuation to the phase-phase correlation function numerically to obtain the dynamic impedance of the RSJJ. We checked that our numerical results agree well with analytical results at some solvable points such as the Toulouse point and the free-fermion point. This work is expected to provide a deep understanding of the Josephson junction on environments, which pushes further development for the superconducting circuit using Josephson junctions.

References

[1] J. Kondo, Prog. Theor. Phys. **32**, 37 (1964).

[2] A. Schmid, Phys. Rev. Lett. **51**, 1506 (1983).

[3] A. Murani *et al.*, Phys. Rev. X **10**, 021003 (2020).

[4] P. Werner and M. Troyer, Phys. Rev. Lett. **95**, 060201 (2005).

Elucidation of Pathways for the Crystallization of Ionic Liquids by Large-Scale Metadynamics Simulation

Hiroki NADA

Environmental Management Research Institute,

National Institute of Advanced Industrial Science and Technology (AIST), Onogawa 16-1, Tsukuba 305-8569

A classical molecular dynamics (MD) simulation combined with the metadynamics (MTD) method (hereafter, MTD simulation) was performed for an ionic liquid, 1-alkyl-3-methylimidazolium hexafluorophosphates ($[C_n\text{min}]PF_6$, n=1 [1]), at 298 K in the NVT ensemble. A force field proposed by Canongia Lopes et al. was used for estimation of the interionic interaction [2]. The simulation system was a rectangular-parallelepiped consisting of 108 ion pairs. The MTD simulation was carried out using DL_POLY 2.20 [3], in which PLUMED 1.3 [4] was implemented to permit combination with the MTD method.

A free energy surface (FES) obtained using discrete C-C and P-F radial distribution functions quantified by Gaussian window functions as collective variables indicated a few shallow local minima. The structure of the system at each shallow local minimum represented an ordered arrangement of ions. The pathway for the formation of this ordered structure from the bulk ionic liquid, which was predicted with the FES, did not show any energetic barrier.

In addition, a crystal-like structure, which was different from the ordered structures for the shallow local minima, also appeared at a high free energy region on the FES. The arrangement of ions in this crystal-like structure was different from those for the crystalline forms, which were reported in literature [1]. This crystal-like structure might correspond to a high-pressure phase, which has not yet been found experimentally.

References

[1] T. Endo, H. Masu, K. Fujii, T. Morita, H. seki, S. Sen and K. Nishikawa: Cryst. Growth & Des. **13** (2013) 5383.

[2] J. N. Canongia Lopez, J. Deschamps and A. A. H. Pádua: J. Phys. Chem. B **108** (2004) 2038.

[3] W. Smith and T. R. Forester: J. Mol. Graph. **14** (1996) 136.

[4] M. Bonomi et al.: Comput. Phys. Commun. **180** (2009) 1961.

Creation of a Method for Design of Scale Formation Control Molecules by a Metadynamics Method

Hiroki NADA

Environmental Management Research Institute,

National Institute of Advanced Industrial Science and Technology (AIST), Onogawa 16-1,

Tsukuba 305-8569

Classical molecular dynamics (MD) simulations combined with the metadynamics (MTD) method [1] (hereafter, MTD simulation) were conducted to elucidate the stable binding conformations of a deprotonated polymaleic acid (PMA) additive and two deprotonated polyacrylic acid (PAA) additives with different polymerization degrees in the presence of various countercations at a hydrated $CaCO_3$ calcite (104) surface. The MTD simulations were performed using DL_POLY 2.20 [2] in which PLUMED 1.3 [3] was implemented.

The simulated free-energy surfaces (FES) suggested the existence of several slightly different stable binding conformations for each additive. The appearance of these distinct binding conformations is speculated to originate from different balances of the interactions between the additive, calcite surface, and countercations. The binding conformations and binding stabilities at the calcite surface were affected by the countercations, with Ca^{2+} ions displaying a more pronounced effect than Na^+ ions. Furthermore, the simulation results suggested that the binding stability at the calcite surface was higher for the PMA additive than for the PAA additives, and the PAA additive with a polymerization degree of 10 displayed a binding stability that was similar to or lower than that of the PAA additive with a polymerization degree of 5.

The present simulation method provides a new strategy for analyzing the binding conformations of complex additives at material surfaces, developing additives that stably bind to these surfaces, and designing additives to control crystal growth.

References

[1] A. Laio and M. Parrinello: Proc. Natl. Acad. Sci. USA **99** (2002) 12562.

[2] W. Smith and T. R. Forester: J. Mol. Graph. **14** (1996) 136.

[3] M. Bonomi et al.: Comput. Phys. Commun. **180** (2009) 1961.

Stability of the hedgehog-lattice topological spin texture in breathing-pyrochlore antiferromagnets

Kazushi AOYAMA
Department of Earth and Space Science, Graduate School of Science, Osaka University
Machikaneyama-cho, Toyonaka-shi, Osaka 560-0043

The quest for topological spin textures in solids is one of the central issues in condensed matter physics because of their possible applications to spin-electronic devices. A magnetic skyrmion in two dimensions and a magnetic hedgehog in three dimensions are typical examples of such topological objects. In magnetic materials, they often appear in the form of crystal orders, so-called skyrmion crystal (SkX) and hedgehog lattice (HL), where the Dzaloshinskii-Moriya (DM) interaction is known to be essential for their stabilities. Concerning the SkX, it has been shown that magnetic frustration serves as another stabilization mechanism [1], but as for the HL, a counter ordering mechanism has not been reported so far. In view of such a situation, we have searched for a new mechanism other than the DM interaction for the HL. Previously, we theoretically demonstrated that the HL is realized in breathing-pyrochlore antiferromagnets in the absence of the DM interaction, where the nearest-neighbor (NN) exchange interactions for small and large tetrahedra, J_1 and J_1', are assumed to be antiferromagnetic [2]. In this work, we extend our previous theoretical work, examining the stability of the HL in a wider parameter space.

We consider the J_1-J_3 classical Heisenberg model on the breathing pyrochlore lattice which is given by

$$\mathcal{H} = J_1 \sum_{\langle i,j\rangle_S} \mathbf{S}_i \cdot \mathbf{S}_j + J_1' \sum_{\langle i,j\rangle_L} \mathbf{S}_i \cdot \mathbf{S}_j + J_3 \sum_{\langle\langle i,j\rangle\rangle} \mathbf{S}_i \cdot \mathbf{S}_j \qquad (1)$$

where J_1 and J_1' take different positive or negative values due to the breathing bond-alternation and J_3 is the third NN antiferromagnetic interaction along the bond direction. In the model, the breathing bond-alternation of the lattice is characterized by J_1'/J_1, and J_3 is essential for the occurrence of the HL which in the present case, is a quadruple-$\mathbf{Q}$ state characterized by the ordering vectors of $(\pm\frac{1}{2}, \pm\frac{1}{2}, \pm\frac{1}{2})$. By performing Monte Carlo simulations, we investigate the ordering properties of the Hamiltonian (1). In our simulations, 2×10^5 MC sweeps are carried out under the periodic boundary condition and the first half is discarded for thermalization. Our 1 MC sweep consists of 1 heatbath sweep and successive 10 overrelaxation sweeps, and observations are done at every MC sweep. The statistical average is taken over 4 independent runs starting from different random initial configurations.

It is found that the quadruple-$\mathbf{Q}$ $(\frac{1}{2}, \frac{1}{2}, \frac{1}{2})$ HL is stable irrespective of the signs of J_1 and J_1' and that in an applied magnetic field, there appear six quadruple-$\mathbf{Q}$ states depending on the values of J_1 and J_1', among which three phases including the in-field hedgehog-lattice state exhibit nonzero total chirality [3]. We have also checked that the HL is robust against relatively weak single-ion magnetic anisotropies.

In addition to the three-dimensional system, we investigate an associated two-dimensional system. We have demonstrated that the J_1-J_3 Heisenberg model on the breathing kagome lattice exhibits a chiral transition and that the low-temperature chiral state can be viewed as a miniature SkX [4]. In contrast to conventional SkX appearing in an applied magnetic field, the miniature SkX is realized at zero field, suggesting that a zero-field topological Hall effect is possible in a metallic system.

References

[1] T. Okubo, S. Chung, and H. Kawamura, Phys. Rev. Lett. **108**, (2012) 017206.

[2] K. Aoyama and H. Kawamura, Phys. Rev. B **103** (2021) 014406.

[3] K. Aoyama and H. kawamura, in preparation.

[4] K. Aoyama and H. Kawamura, Phys. Rev. B **105**, (2022) L100407.

Dimensional reduction effect in the two-dimensional maple-leaf lattice Heisenberg antiferromagnet

Chisa HOTTA
Department of Basic Science, University of Tokyo
3-8-1 Komaba, Meguro, Tokyo 153-8902, Japan

We aim to clarify the features of uniform magnetic susceptibilities of a series of frustrated magnets in two dimensions. This year, we focused on the maple-leaf lattice spin-1/2 Heisenberg model, whose lattice structure is regarded as a 1/7-site-depleted triangular lattice. There is recently experimental evidence that the material called bluebellite $\mathrm{Cu_6I_6O_3(OH)_{10}Cl}$ shows a particular magnetic susceptibility that almost perfectly matches the Bonner-Fisher curve, namely the susceptibility curve of the one-dimensional (1D) spin-1/2 antiferromagnetic Heisenberg model[1]. Motivated by this experiment, we analyzed the ground state and the finite temperature properties of the maple leaf lattice Heisenberg model. By combining the analysis of the several energy eigen states of the model on a finite cluster using the exact diagonalization (ED), we found that the constituent of the low energy eigenstates have the UUD/DDU configurations, i.e. the spins on all the triangular units of the lattice are two-up-one-down or two-down-one-up. This situation is similar to the antiferromagnetic triangular lattice Ising model, where the UUD/DDU state contributes macroscopically to the residual entropy. However, in our model, not all the interactions are antiferromagnetic, but the interactions on bonds forming a hexagon around the depleted sites are staggard in their sign. Even in such a case, there is a substantial frustration effect, and UUD/DDU are favored. Due to the quantum fluctuation effect, these UUD/DDU manifold mixes, and a stripe-type ground state appears. The temperature dependence of the susceptibility turned out not to match the Bonner-Fisher curve even though we vary the sign and amplitudes of five different Heisenberg interaction parameters. Instead, we found that the susceptibility shows an almost perfect coincidence with that of the 1D XXZ model having a finite spin gap. The reason for this dimensional reduction behavior is that the magnetic excitation from the ordered ground state resembles the spinon excitation of the 1D XXZ model above the spin gap. Indeed, flipping one of the spins of the stripge ground state, the two plaquettes(two+two triangles) with UUUD spins are formed, each carrying spin-1/2. The Heisenberg exchange interactions separate these two plaquettes into opposite directions, while such spinon propagation takes place only in a particular spatial direction. A series of calculations on the susceptibility of both the maple leaf lattice and the 1D XXZ model was done using a TPQ method combined with SSD[2] The variation of parameters we needed to search for was large and the 2D susceptibility is maximally given for $N = 24, 30$ sites[3].

References

[1] Y. Haraguchi, *et.al.*: Phys. Rev. B **104**, 174439 (2021).

[2] C Hotta and K Asano: Phys. Rev. B **98**, 140405 (2018).

[3] R. Makuta and C. Hotta: Phys. Rev. B **104**, 224415 (2021).

The effect of a quantum phase transition on quantum approximate optimization algorithm

Tatsuhiko Shirai
Department of Computer Science and Communications Engineering, Waseda University
Ookubo, Shinjuku-ku, Tokyo 169-8555

We have studied the effect of a quantum phase transition on the performance of quantum approximate optimization algorithm (QAOA) in the transverse-field Ising model. QAOA is a hybrid quantum-classical algorithm designed to approximate the ground state of a Hamiltonian H with N spins [1]. It has a wide application in chemistry, physics, and computer science.

QAOA consists of calculations in a quantum computer and classical computer. The quantum computer calculates the expectation value of H over a variational state, which is given by

$$|\vec{\beta},\vec{\gamma}\rangle := e^{-i\beta_p H} e^{-i\gamma_p X} \cdots e^{-i\beta_1 H} e^{-i\gamma_1 X} |+\rangle , \tag{1}$$

where $\vec{\beta} = (\beta_1, \ldots, \beta_p)$ and $\vec{\gamma} = (\gamma_1, \ldots, \gamma_p)$. p denotes a circuit depth. X is called a mixer and adopted as $X = \sum_{i=1}^{N} \sigma_i^x$ where $\vec{\sigma}_i = (\sigma_i^x, \sigma_i^y, \sigma_i^z)$ is the Pauli operator acting on site i. $|+\rangle$ is defined as $\sigma_i^x |+\rangle = |+\rangle$ for all i. The classical computer optimizes $(\vec{\beta},\vec{\gamma})$ to minimize the value of $\langle\vec{\beta},\vec{\gamma}| H |\vec{\beta},\vec{\gamma}\rangle$. Here, we adopt the transverse field Ising model given by

$$H = -g \sum_{i=1}^{N} \sigma_i^z \sigma_{i+1}^z - \sum_{i=1}^{N} \sigma_i^x , \tag{2}$$

where the periodic boundary condition is imposed (i.e., $\vec{\sigma}_{i+N} = \vec{\sigma}_i$). This model shows a quantum phase transition at $g = g_{\mathrm{c}} = 1$. The ground state is ferromagnetic for $g > g_{\mathrm{c}}$, while it is paramagnetic for $0 \le g < g_{\mathrm{c}}$.

We numerically study p-dependences of the residual energies ΔE (i.e., the energy difference between the variational state at the optimum values of $(\vec{\beta},\vec{\gamma})$ and the ground state) in the ferromagnetic phase, critical point, and paramagnetic phase in the thermodynamic limit. The numerics is based on the Jordan–Wigner transformation and time-dependent Bogoliubov transformation. Figure 1 shows that the asymptotic behavior discontinuously changes at the critical point. It indicates the intimate relation between the quantum phase transition and the performance of QAOA.

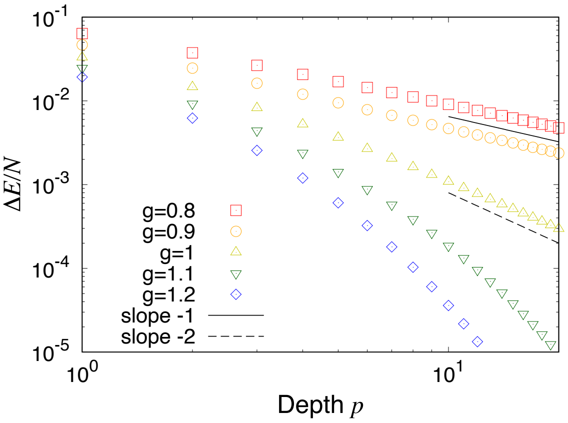

Figure 1: p-dependences of the residual energies ΔE

References

[1] E. Fahri, et al., arXiv:1411.4028 (2014).

Calculation of ordered structures, dynamics and optical properties of soft materials

Jun-ichi FUKUDA

Department of Physics, Kyushu University, Motooka 744, Nishi-ku, Fukuoka 819-0395

Motivated by a recent experimental study [1] demonstrating the structural transformation of a cholesteric blue phase liquid crystal (BPLC) by an electric field, we carried out a simulation study on the behavior of BPLC under an electric field. Ref. [1] showed that a structure with tetragonal ($I4_122$) symmetry, which had been known to be stable under an electric field, can be stable even after the cessation of the electric field when the temporal variation of the applied electric field is appropriately controlled. Possibility of stable (or metastable) tetragonal structures of BPLC under no electric field has never been discussed theoretically.

Previous numerical studies on BPLCs under an electric field focused on the bulk behavior (to be precise, in an infinite system with periodic boundaries). We are interested in how the planar boundaries confining the BPLC will affect its structural stability. Elucidation of the dynamical behavior under a temporally varying electric field turns out to be a daunting task even with the aid of the ISSP supercomputer, and therefore we restrict ourselves to static behavior.

Our numerical study is based on the Landau-de Gennes continuum theory describing the orientational order by a second-rank tensor. We use the program developed in Ref. [2] where we were particularly interested in the surface behavior, and dealt with relatively thin systems. In the present study, to simulate a system whose thickness is close to a realistic experimental value ($\simeq 12\mu$m in Ref. [1]), 1,351 grid points are taken in the thickness direction. Our numerical system is on a regular grid and allows a use of OpenMP for efficient calculations.

Our calculations demonstrate that the presence of confining boundaries discretize the number of periodic structures along the thickness direction, and that the tetragonal structure is indeed metastable under no electric field. We are carrying out systematic studies on the free energy versus the number of periodic structures, and on the optical properties of the BPLC structures we find numerically.

References

[1] D.-Y. Guo et al., Nature Mater. **19** (2020) 94.

[2] J. Fukuda and S. Žumer, Phys. Rev. Research 2 (2020) 033407.

Non-equilibrium response and phase transition in the dense hard sphere systems

Masaharu ISOBE
Nagoya Institute of Technology
Gokiso-cho, Showa-ku, Nagoya, 466-8555

As the simplest models, the hard disk/sphere systems have been investigated via molecular simulation in both equilibrium and non-equilibrium phenomena [1]. In this project, we focus on the equilibration and the non-equilibrium response interfered with the phase transition in the hard disk/sphere model system with modern algorithms, *i.e.*, Event-Chain Monte Carlo (ECMC) [2, 3], Newtonian ECMC (NEC) [4] and Event-Driven Molecular Dynamics(EDMD) [5].

Equilibration and relaxation times in dense molecular systems

The equilibration and relaxation times of the physical properties have historically been fundamental issues in molecular simulation. As practical tasks in the molecular simulation, 'equilibration' (relaxation toward equilibrium states) from initial non-equilibrium states is just preprocessing step before a production run. Such a step needs to obtain the physical properties in the equilibrium state in the specific system. However, the computational cost often becomes high, especially for high-density and larger scale particle systems, and may sometimes exceed the human lifetime. In general, the equilibration of particle positions in dense systems is much more difficult due to the excluded volume effect being dominant, which is why the crystallization and glass/jamming transition problems remain one of the critical issues and have been actively studied recently. The two standard molecular simulation methods for many-body systems are often used; one is molecular dynamics (MD) using Newton's equations of motion, and the other is Markov chain Monte Carlo (MC) using a pseudo-random number generator. Various novel algorithms focusing on equilibration based on MD and MC have been implemented in the history of molecular simulation, which enables to reduce the relaxing time. An efficient algorithm for the acceleration of equilibration, termed the 'event-chain Monte Carlo (ECMC)' [2] was the breakthrough on this topic. The ECMC has become one of the milestones, and its variants have been investigated actively over the past decade [3]. To obtain the 'true' equilibrium states, it is a reasonable choice to use ECMC for positional relaxation at first, which is the idea of a hybrid scheme [1]. Recently, an ECMC variant termed the Newtonian ECMC (NEC) was proposed [4]. In NEC, the velocity collision rule was added to dictate the direction of particle movement. This is often used in EDMD of hard-sphere systems. The NEC clearly improves the efficiencies of the diffusion coefficient, nucleation rate, and melting process. Recently, this efficient algorithm has been extended to anisotropic hard polygons without any approximations [6].

In these ECMC and its variants (including NEC), the systems are driven by the sequential collisions composed of a dozen of particles that seem to behave like a chain. The efficiency depends on chain length, physical properties, and system size. However, the microscopic mechanism of equilibration for each parameter remains elusive. To identify key factors affecting equilibration in the hard disk system, we focus on the event-based algorithms [2, 4, 5] described above and investigate the comparison between them in cases of (i) the diffusional characteristics per event (collision) and (ii) the relaxing process toward the liquid states as a non-equilibrium response after disturbance of the homogeneous expansion.

(i) Diffusional characteristics of the event-based algorithms in hard disk systems

To survey the key factors explaining why the efficiency of equilibration differed between the event-based algorithms, we focus on the diffusional characteristics per event (collision) between event-based algorithms in the liquid states of the hard disk systems. We defined the self- and pair-diffusion coefficient based on the displacement number of disks and compared the dependence in terms of the chain length and the system size systematically. In ECMC and NEC, as the chain length increases, the diffusion coefficient grows and reaches the highest values at a specific chain length. We visualized the spatial distribution of the accumulated number of displacements per particle and calculated its probability density distribution. We found that NEC has an advantage over ECMC in the diffusion coefficient in this system since NEC samples homogeneously in the system due to the Maxwell Boltzmann distribution of disk velocities for each displacement during the event chain, which can sample disks uniformly in the liquid state [7].

(ii) *Non-equilibrium response and equilibration in hard disk melting*

We then focus on the non-equilibrium response during the equilibration process induced by a disturbance of the homogeneous expansion. In the case of EDMD, we observed the anomalous slow equilibration in the hard disk systems around the co-existence phases toward the liquid states in large-scale simulation via a couple of physical properties. As the physical mechanism of this anomalous slow equilibration, we assumed that the spatial inhomogeneity of the initial equilibrated phases would contribute to the relaxation time significantly. The assumption was confirmed by the probability distribution of local density and orientational order parameter [8]. We also observed anomalous slow equilibration both in ECMC and NEC; however, the distinct differences between methods in the efficiency and functional forms of relaxation of physical properties are detected. We found that NEC and NEC are more efficient than EDMD.

As a typical non-equilibrium response, we also investigated the thermodynamic cycles by modeling the Stirling engine (SE) at the nanoscale molecular level [9]. We established a numerical model of a β-type SE with a displacer piston and figured out the minimal necessary conditions for stable rotation, as well as the lower limits of both the difference in temperature and the particle number.

References

[1] M. Isobe: Mol. Sim. **42** (2016) 1317.

[2] E. P. Bernard, W. Krauth, and D. B. Wilson: Phys. Rev. E **80** (2009) 056704.

[3] W. Krauth: Front. Phys. **9** (2021) 229.

[4] M. Klement and M. Engel, J. Chem. Phys. **150** (2019) 174108.

[5] M. Isobe: Int. J. Mod. Phys. C **10** (1999) 1281.

[6] M. Klement, S. Lee, J. A. Anderson and M. Engel, J. Chem. Theor. and Comp. **17** (2021) 4686.

[7] H. Banno, D. Mugita, and M. Isobe: J. of Phys.: Conf. Ser. **2207** 012011 (2022).

[8] D. Mugita and M. Isobe: EPJ Web Conferences, **249** 14004 (2021).

[9] K. Kitaya and M. Isobe: J. of Phys.: Conf. Ser. **2207** 012006 (2022).

Structural Formation of Patchy Particles

Takamichi TERAO
Department of Electrical, Electronic and Computer Engineering,
Gifu University, Yanagido 1-1, Gifu, 501-1132

Patchy particles are spheres in which the effective interaction between particles is anisotropic. Among the patched particles, there is interest in those that have anisotropy in interparticle interactions due to inhomogeneous surface charges [1]. Charged patchy particles are expected to have a new structure, different from previous patchy particle systems, because the interaction between particles can be both attractive and repulsive.

In this study, we focused on the structural formation of charged patchy particles, in which the particle surface is charged and the sign of the surface charge is reversed between the bipolar part and the other parts. Cluster formation in these systems was studied by molecular dynamics simulations. Modeling of charged Patchy particles is shown in Figure 1. Figure 2 shows an example of the structure formation of the system when the motion of the charged patchy particles was constrained between a pair of two-dimensional planes. In thermal equilibrium, the charged patchy particles exhibit a variety of configurations, including triangular, square, pentagonal, and hexagonal lattices.

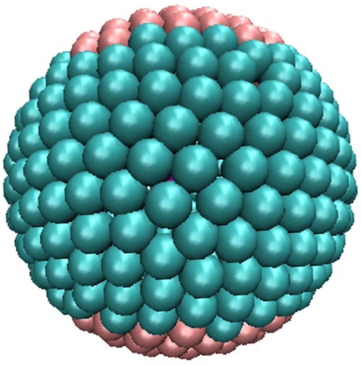

Fig. 1: Modeling of a charged patchy particle

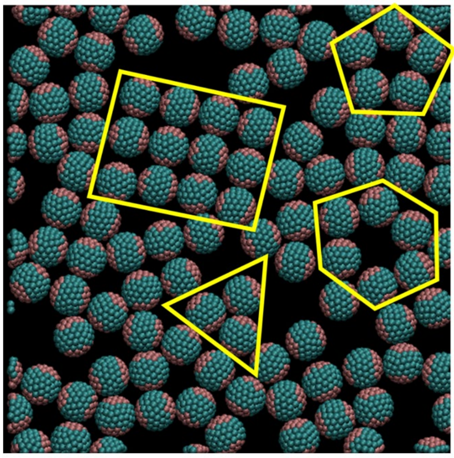

Fig. 2: Snapshot of charged patchy particles

References

[1] P. D. J. van Oostrum, M. Hejazifar, C. Niedermayer, and E. Reimhult: J. Phys.: Condens. Matter **27** (2015) 234105.

Tensor-network study of real-time dynamics in two-dimensional quantum many-body systems

Ryui KANEKO
Department of Physics, Kindai University
Higashi-Osaka, Osaka 577-8502, Japan

The nonequilibrium physics of quantum many-body systems have attracted much interest in recent years. Among others, real-time dynamics of isolated quantum systems has been investigated intensively in experiments very recently. Such examples include analog quantum simulators using ultracold atoms in optical lattices [1–3] and those using Rydberg atom arrays [4, 5]. The former is suitable for studying the Bose-Hubbard models in 1D, 2D, and 3D, and the latter is often used for studying the quantum Ising systems. The number of controllable Rydberg atoms has now exceeded 200 [6–8], which would be more qubits than classical computers can handle. These recent developments of analog quantum simulators demand cross-validating the accuracy of experiments and numerical simulations. Although numerical methods based on matrix product states are powerful in 1D [1, 3, 9], no decisive methods exist for simulating dynamics in 2D systems.

In the present study, we examine the applicability of the 2D tensor-network method based on the infinite projected entangled pair state (iPEPS) [10, 11] for simulating the real-time dynamics. We first focus on the 2D Bose-Hubbard model, whose time-dependent single-particle correlation functions have been measured in the recent experiment [3], and investigate sudden and short-time quench dynamics starting from the Mott insulator [12]. We calculate the real-time evolved states by the simple update algorithm. The tensor-network library TeNeS [13] is adopted.

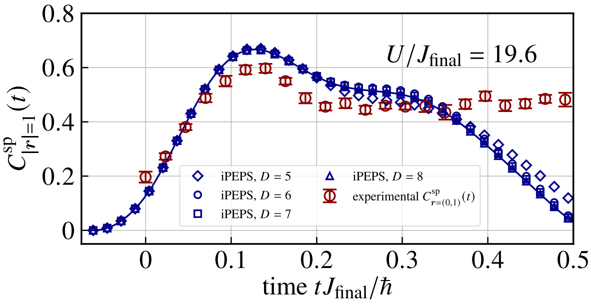

Figure 1: Comparison of the time-dependent single-particle correlation functions between the experiment (red squares) and the iPEPS simulations (blue line with symbols). We consider a finite-time quench and optimize the wave functions up to the bond dimensions $D = 8$.

We show the calculated single-particle correlation functions for the short-time quench to the Mott insulating region in Fig. 1. They are in good agreement with the recent experiment. We also predict how group and phase velocities behave for the sudden quench to the weaker interaction region, which has not been explored in experiments. Our findings would serve as a quantitative benchmark for future experiments.

After checking the applicability of the iPEPS method to the 2D Bose-Hubbard model, we apply the method to the 2D transverse-field Ising model. We focus on a sudden quench starting from the fully disordered state ($\Gamma/J \to \infty$) to the disordered region ($\Gamma > \Gamma_{\mathrm{c}}$). Calculated longitudinal spin-

spin correlation functions agree very well with the results obtained by the small-size exact diagonalization method and by the spin-wave approximation. We extract the group velocity from the correlation functions in the stronger field region. The group velocity is known to be bounded above by the Lieb-Robinson bound [14, 15]. The estimated group velocity in the present iPEPS study is much slower than the recently updated bound [16], suggesting that there is room for improving the analytical bound.

References

[1] M. Cheneau *et al.*, Nature **481**, 484 (2012).

[2] P. Jurcevic *et al.*, Nature **511**, 202 (2014).

[3] Y. Takasu *et al.*, Sci. Adv. **6**, eaba9255 (2020).

[4] E. Guardado-Sanche *et al.*, Phys. Rev. X **8**, 021069 (2018).

[5] V. Lienhard *et al.*, Phys. Rev. X **8**, 021070 (2018).

[6] S. Ebadi *et al.*, Nature **595**, 227 (2021).

[7] P. Scholl *et al.*, Nature **595**, 233 (2021).

[8] D. Bluvstein *et al.*, Science **371**, 1355 (2021).

[9] P. Barmettler *et al.*, Phys. Rev. A **85**, 053625 (2012).

[10] T. Nishino *et al.*, Prog. Theor. Phys. **105**, 409 (2001).

[11] F. Verstraete and J. I. Cirac, arXiv:cond-mat/0407066.

[12] R. Kaneko and I. Danshita, Commun. Phys. **5**, 65 (2022).

[13] Y. Motoyama *et al.*, arXiv:2112.13184.

[14] E. H. Lieb and D. W. Robinson, Commun. Math. Phys. **28**, 251 (1972)

[15] M. B. Hastings, arXiv:1008.5137.

[16] Z. Wang and K. R. Hazzard, PRX Quantum **1**, 010303 (2020).

Tensor-network study of the SU(4) Heisenberg model on a tetramerized square lattice

Ryui KANEKO
Department of Physics, Kindai University
Higashi-Osaka, Osaka 577-8502, Japan

The SU(N) Hubbard and Heisenberg models have attracted much attention recently [1–4]. They can be realized in the ultracold atoms in optical lattices and in specific antiferromagnets. Since these models possess many internal degrees of freedom and would realize novel quantum states that are absent in the well-known SU(2) model, it is desirable to explore ground states of the models on various lattices.

In the present study, we focus on how multimerization affects the ground states of the SU(N) Heisenberg model. To this end, we consider the SU(4) antiferromagnetic Heisenberg model [5]

$$H_0 = J \sum_{\langle ij \rangle_{\mathrm{intra}}} P_{ij} + J' \sum_{\langle ij \rangle_{\mathrm{inter}}} P_{ij} \qquad (1)$$

on a tetramerized square lattice [6] (see Fig. 1), where P_{ij} is a transposition operator which exchanges flavors at site i and j, namely, $P_{ij}|\alpha_i \beta_j\rangle = |\beta_i \alpha_j\rangle$ ($\alpha_i, \beta_i \in \{0,1,2,3\}$). It can be written by using the flavor-changing operator $S_\alpha^\beta(i) = |\alpha_i\rangle\langle\beta_j|$ as

$$\begin{aligned} H_0 = J &\sum_{\langle ij \rangle_{\mathrm{intra}}} \sum_{\alpha\beta} S_\alpha^\beta(i) S_\beta^\alpha(j) \\ + J' &\sum_{\langle ij \rangle_{\mathrm{inter}}} \sum_{\alpha\beta} S_\alpha^\beta(i) S_\beta^\alpha(j). \end{aligned} \qquad (2)$$

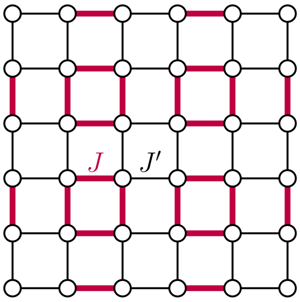

Figure 1: Tetramerized square lattice. When $J \gg J'$ or $J \ll J'$, the system decouples into isolated four-site chains. When $J = J'$, the system becomes the conventional square lattice, whose ground state is believed to exhibit simultaneous dimerization and SU(4) symmetry breaking [5].

We specifically investigate the ground state of the model in the presence of the population imbalance (effective field), which favors the flavors 0 and 1:

$$H = H_0 + H_{\mathrm{imb}} \qquad (3)$$

$$H_{\mathrm{imb}} = D_z \sum_i [-S_0^0(i) - S_1^1(i) + S_2^2(i) + S_3^3(i)]. \qquad (4)$$

In the limit of $J'/J = 0$ or $J/J' = 0$, the system decouples into four-site chains. The ground state is an SU(4) singlet for lower fields, while it is a resonating-valence-bond (RVB) state consisting of the 0 and 1 flavors for higher fields. In the presence of weak couplings among four-site chains ($0 < J'/J \ll 1$), a previous cluster-mean-field study with a small 2×1 sublattice structure [6] suggests the emergence of the crystal, which is a mixture of the singlet and RVB states, in the intermediate field region.

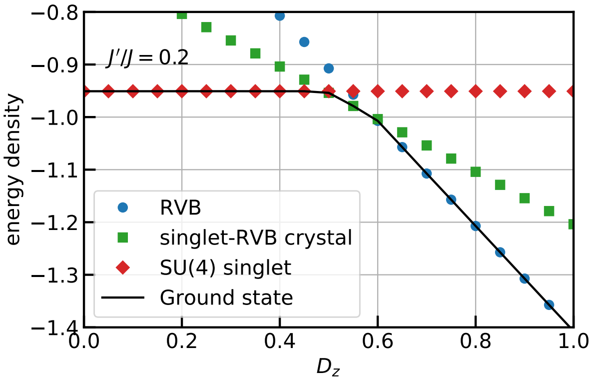

Figure 2: Energy comparison of selected ground-state candidate states at $J'/J = 0.2$. The states are obtained for the bond dimensions $D = 7$. In the intermediate field region ($0.5 \lesssim D_z/J \lesssim 0.6$), we have confirmed that the ground state is the singlet-RVB crystal.

To investigate the stability of such a crystal state beyond the mean-field study, we apply the 2D tensor-network method based on the infinite projected entangled pair state (iPEPS) [7,8]. The ground-state candidate singlet and RVB states can be represented by the iPEPS with the bond dimensions $D = 7$ and $D = 3$, respectively. The singlet-RVB crystal can also be represented by the iPEPS with $D = 7$. We consider a variety of crystal states that can be realized within a 2×2 sublattice. We take these states as initial states and optimize these wave functions. We adopt the TeNeS library [9] and calculate the ground-state candidates at $D = 7$ using the simple update algorithm [10].

Figure 2 shows the energy comparison of selected ground-state candidate states in the presence of weak couplings $J'/J = 0.2$. The iPEPS energy is slightly lower than the result obtained by the previous cluster-mean-field study [6]. On the other hand, the phase boundaries are found to be nearly consistent with the previous study; the singlet-RVB crystal ($0.5 \lesssim D_z/J \lesssim 0.6$) emerges between the lower-field SU(4) singlet and the higher-field RVB states. The ground-state singlet-RVB crystal is found to be a mixture of the SU(4) singlet and RVB states in equal proportions, and mixing in different ratios result in higher energy. As for the ground-state candidate states we have studied, the intermediate singlet-RVB crystal is stable in the presence of weak couplings among four-site chains.

References

[1] C. Wu *et al.*, Phys. Rev. Lett. **91**, 186402 (2003).

[2] C. Honerkamp and W. Hofstetter, Phys. Rev. Lett. **92**, 170403 (2004).

[3] M. A. Cazalilla *et al.*, New J. Phys. **11**, 103033 (2009).

[4] A. V. Gorshkov, Nat. Phys. **6**, 289 (2010).

[5] P. Corboz *et al.*, Phys. Rev. Lett. **107**, 215301 (2011).

[6] Y. Miyazaki *et al.*, AIP Advances **11**, 025202 (2021).

[7] T. Nishino *et al.*, Prog. Theor. Phys. **105**, 409 (2001).

[8] F. Verstraete and J. I. Cirac, arXiv:cond-mat/0407066.

[9] Y. Motoyama *et al.*, arXiv:2112.13184.

[10] H. C. Jiang *et al.*, Phys. Rev. Lett. **101**, 090603 (2008).

Simulated scanning tunneling microscopy images of graphene nanoribbons with armchair edges

Junhuan LI, Kenta ARIMA

Graduate School of Engineering, Osaka University, Yamada-oka, Suita, Osaka 565-0871

We are aiming at elucidating local electronic structures of finite-size graphene sheets and their impacts on scanning tunneling microscopy (STM) images [1]. For this purpose, we simulated STM images of armchair-edged graphene nanoribbons (AGNRs), using a simulation package named STATE (Simulation Tool for Atom TEchnology).

We simulated STM images at a V_s of -0.05 V for AGNRs with the width ranging from $W=22$ to $W=30$ (in terms of ribbon width, W is defined as the number of dimer lines across the ribbon width). STM images change periodically as the ribbon width increases. Figures 1(a)−1(c) summarize the results for AGNRs with $W=3a-2$, $3a-1$, $3a$, respectively. For Figure 1(a) and 1(b), the electron density is slightly high at the armchair edges. The dot patterns form a $(\sqrt{3}\times\sqrt{3})R30°$ superstructure in the interior of the ribbons. In contrast, for the case of $W=3a$ in Figure 1(c), electrons are not localized at edges and bright dots in the images appear to form a rectangular lattice, which resembles superstructures observed experimentally. This periodic change of simulated images was also confirmed to continue until reaching a width of at least 8 nm, in which the value of W was 65.

Simulated STM images at higher sample biases, or larger absolute values than that in Figure 1, were also calculated in the same ribbons. Besides, the bandgaps of ribbons were investigated based on their band structures. It helps to check the validity of our simulations and discuss more details in simulated images.

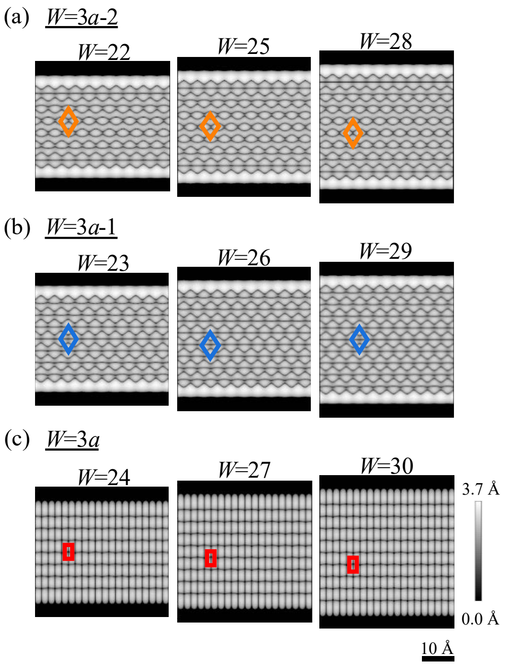

Fig. 1: Simulated STM images. A unit structure is superimposed in each image.

References

[1] J. Li, S. Li, T. Higashi, K. Kawai, K. Inagaki, K. Yamamura, and K. Arima: Phys. Rev. B **103** (2021) 245433.

Towards a unified understanding of thermodynamic properties in S=1/2 spherical kagome systems $\{W_{72}V_{30}\}$ and $\{Mo_{72}V_{30}\}$

Yoshiyuki Fukumoto
Department of Physics, Faculty of Science and Technology, Tokyo University of Science
2641 Yamazaki, Noda, Chiba 278-8510

The spherical kagome systems, or quantum-spin icosidodecahedrons, are frustrated magnetic clusters with 30 spins. It has been argued that $\{W_{72}V_{30}\}$ can be described as a regular, non-distorted, icosidodecahedron, and $\{Mo_{72}V_{30}\}$ contains structural distortion [1]. The experimental magnetization curves for those increase linearly with magnetic field [2], although a cluster Heisenberg antiferromagnet should show stepwise behavior. In a theoretical study on $\{W_{72}V_{30}\}$, Schnack *et al.* has reported that the discrepancies are attributed to the distribution of nearest-neighbor exchange couplings, which is called bond-randomness, where the width of the variance in exchange interactions was estimated to be 30% of the average value $J = 115$K [2]. On the other hand, our group has reported that the incorporation of about 10% of Dzyaloshinskii-Moriya (DM) interactions also leads to the collapse of the staircase structure [3].

Subsequently, Kihara *et al.* experimentally measured specific heats of both materials at temperatures $T < 11$K under magnetic fields up to 15T [4], and revealed that magnitudes of the specific heats are comparable to calculated results of the non-distorted and distorted Heisenberg models [1]. For $\{Mo_{72}V_{30}\}$, temperature dependence of the specific heats has a shoulder around $2 \sim 3$K and depends on magnetic field, which is consistent with calculated results with the distorted Heisenberg model [1]. However, for $\{W_{72}V_{30}\}$, the calculated specific heats with the non-distorted Heisenberg model shows a peak around 2K and significant magnetic field dependence, but the experimental result has no peak and does not show magnetic field dependence. As for the disappearance of the 2K peak, a possible origin is blurring of the density of states due to the bond randomness. Because the 2K peak comes from low-energy singlet excitations, we expect that the 2K peak is readily dispersed by about 10% bond randomness, which is much smaller than Schnack's value [2]. We actually calculate the density of state and specific heat to confirm this expectation [5]. However, quantitative reproduction of experiment is not achieved.

It is interesting to study whether larger bond randomness leads to quantitative reproduction of experimental specific heat or not. We also calculate the case of 30% bond randomness and find that the magnetic field dependence becomes smaller and the shape of the curve approaches to the experiment, which suggests an adequate choice of bond randomness, which would be 40-50%, gives quantitative reproduction. On the other hand, because the specific heat of $\{Mo_{72}V_{30}\}$ has magnetic field dependence and a shoulder in it's temperature dependence, we naively expect $\{Mo_{72}V_{30}\}$ has no bond randomness. The investigation of the origin of presence or absence of the bond randomness will be an issue in the future.

[1] N. Kunisada *et al.*, PTEP 2014, 41I01 (2014).
[2] J. Schnack *et al.*, arXiv:1304.2603v1.
[3] Y. Fukumoto *et al.*, JPSJ 87, 124710, 2018.
[4] T. Kihara *et al.*, PRB 99, 064430 (2019).
[5] M. Motohashi *et al.*, arXiv:2112.07923v1.

Numerical studies on excitation spectra of Heisenberg antiferromagnets on the triangular and kagome lattices

Yoshiyuki Fukumoto
Department of Physics, Faculty of Science and Technology, Tokyo University of Science
2641 Yamazaki, Noda, Chiba 278-8510

This project consists of two research topics, (i) virational study of the triangular-lattice system with the fermionic representation and (ii) series expansion study of the kagome-lattice system in $\mathrm{Cs_2Cu_3SnF_{12}}$.

As for (i), a neutron scattering experiment on $\mathrm{Ba_3CoSb_2O_9}$ revealed the existence of spinon continuum in the dynamical structure factor, in addition to magnon excitations [1]. Zhang *et al.* used the fermionic spinon operators to study the spinon continuum within random-phase approximation (RPA) [2]. This RPA treatment, however, does not exclude unphysical states exactly. This year, we have developed a program code using Monte-Carlo method to obtain the energy of the variational wave function proposed by Zhang *et al.* [1], completely considering the constraints. We also developed a program code to calculate the variational energy for a 36-site system exactly, without using Monte-Carlo sampling. The variational parameter is the strength of the staggered magnetic field conjugate to the 120 degree structure. We use wavenumbers that satisfy periodic or anti-periodic conditions in two directions of the triangular lattice. There are four combinations of wave numbers, and we make four states from each. The optimal combination of the four states is found by solving the generalized eigenvalue problem. In the next fiscal year, we will start developing a program code for the particle-hole excitations to obtain the dynamic structure factor.

As for (ii), $\mathrm{Cs_2Cu_3SnF_{12}}$ has the q=0 order, and a theoretical analysis, based on the linear spin wave theory, of the observed magnon dispersion resulted in the exchange parameter which is 40% less than the result by an analysis of susceptibility. This fact indicates difficulty in the linear spin wave theory for frustrated systems.

In this study, we calculate the dispersion relation by series expansion from the Ising limit. We include Dzyaloshinskii-Moriya (DM) interactions into our model, where we set the DM vector to be perpendicular to the plane on which ordered moment lies. The direction of the DM vector is chosen to stabilize the q=0 state. The linked cluster expansion algorithm is used to make expansion coefficients. We developed a calculation program using the previous research that applied the cluster expansion method to the triangular-lattice system as a benchmark test [3], and extended it to the kagome-lattice system. As a result, it is clarified that the bandwidth of the magnon spectrum in the series expansion is about 1/4 of the linear spin wave theory, and its shape is also changed significantly. We also find that the correction for the linear spin wave theory is larger in the kagome lattice than in the case of the triangular lattice. Also, the shape of the magnon spectrum obtained by series expansion is comparable to the experimental results of $\mathrm{Cs_2Cu_3SnF_{12}}$. It is speculated that the agreement can be improved by making the DM interaction more realistic in the future.

[1] S. Ito *et al.*, Nat. commn. 8, 235, 2017.
[2] C. Zhang *et al.*, PRB 102, 075108, 2020.
[3] W. Zheng *et al.*, PRB 74, 224420, 2006.

Gapless symmetry-protected topological phase of quantum spin system

Yuichiro HIDAKA[1], Shunsuke C. FURUYA[2,3], Atsushi UEDA[1], and Yasuhiro TADA[4]
[1]*Institute for Solid State Physics, University of Tokyo*
Kashiwa-no-ha, Kashiwa, Chiba 277-8581
[2]*Department of Physics, Ibaraki University*
Mito, Ibaraki 310-8512
[3]*Department of Basic Science, University of Tokyo*
Meguro, Tokyo 153-8902
[4]*Quantum Matter Program, Graduate School of Advanced Science and Engineering,*
Hiroshima University, Higashihiroshima, Hiroshima 739-8530

Classifying phases of matter is one of the paramount issues in condensed matter physics. One of the important classes of the quantum phase of matter is symmetry-protected topological (SPT) phases. A SPT phase is a gapped phase which preserves some given symmetries but not adiabatically connected to a trivial phase without breaking the symmetries [1]. Recently many researchers attempt to extend the concept of SPT phase into gapless system [2, 3].

In the present study, we proposed a quantum spin model that has the properties of gaplessness and nontrivial SPT phase simultaneously. The model we proposed is the anisotropic triangular strip (ATS) XXZ model, shown in Fig.1, which consists of three-leg antiferromagnetic ladder with frustrated interchain couplings. We used the density matrix renormalization group (DMRG) method to calculate the ground state of the ATS XXZ model at the specific parameters, $J = 1.0$, $\Delta = 0.8$, and $J_\times = 0.5$. We used the ITensor and TeNPy libraries [4, 5].

We found that the entanglement entropy of the ATS XXZ model fits with Calabrese-Cardy formula of open boundary condition. According to the conformal field theory, it is expected that the central charge of the ATS XXZ model is one. The calculation result of central charge is shown in Fig.2, and the central charge become close to one, which is derived from the extrapolation of the entanglement entropy about the system size. In addition, Fig.3 shows the calculation result of entanglement spectrum and we can see double degeneracy, which is an important feature of Haldane state in quantum spin system. From these two results, the ground state of ATS XXZ model is Tomonaga-Luttinger liquid which has the property of nontrivial SPT phase. Therefore we can conclude that the ground state of ATS XXZ model with $J = 1.0$, $\Delta = 0.8$, and $J_\times = 0.5$, is in gapless SPT phase. We presented these results at the 2022 Annual (77th) Meeting of the Physical Society of Japan [6].

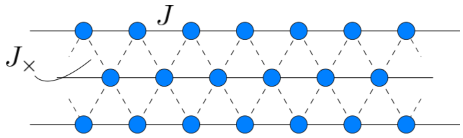

Figure 1: ATS XXZ model

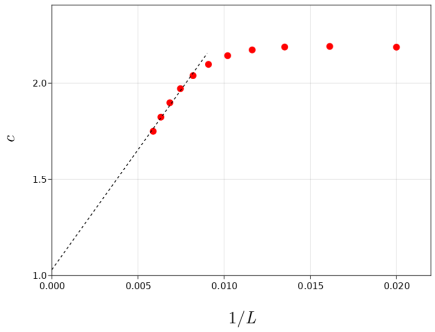

Figure 2: Entanglement entropy of the ATS XXZ model. The purple line is the fitting line of entanglement entropy by the Calabrese-Cardy formula.

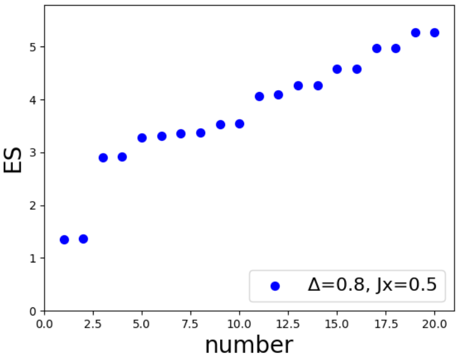

Figure 3: Entanglement spectrum of ATS XXZ model.

References

[1] X. Chen, Z.-C. Gu, and X.-G. Wen, Phys. Rev. B 83, 035107 (2011).

[2] T. Scaffidi, D. E. Parker, and R. Vasseur, Phys. Rev. X 7, 041048 (2017).

[3] S. C. Furuya and M. Oshikawa, Phys. Rev. Lett. 118, 021601(2017).

[4] M. Fishman, S. R. White, and E. M. Stoudenmire, arXiv:2007.14 (2020).

[5] J. Hauschild and F. Pollmann, SciPost Phys. Lect. Notes , 5 (2018).

[6] Y. Hidaka, S. C. Furuya, A. Ueda, and Y. Tada: in preparation.

Development of multiscale simulation technique for liquids and solids

Takahiro MURASHIMA

Department of Physics, Tohoku University,

6-3, Aramaki-Aza-Aoba, Aoba-Ward, Sendai, Miyagi 980-8578

Predicting the flow and deformation of soft matter and composite materials is still a very difficult problem. Aside from the problem of solving macroscale continuum equations, there are difficulties in determining constitutive laws that characterize materials. An approach to determine the constitutive law (rheology) of a material using molecular simulations has been popular in recent years. Multiscale simulations that connect these molecular simulations to continuum simulations as constitutive laws do not explicitly require constitutive laws, thus avoiding the difficulty of deriving constitutive laws [1]. However, there is a problem of boundary conditions for treating general flow fields in molecular dynamics simulations. Therefore, in this research project, we attempted to extend the boundary conditions to solve this problem.

Recently, we have developed the UEFEX method [2], which enables large-elongation flow simulations. Here, the elongation axis and the unit cell are not parallel to each other to avoid collapsing the unit cell under elongational deformation. (Figure 1 shows the steady state of polymer chains under uniaxial elongational flow.)

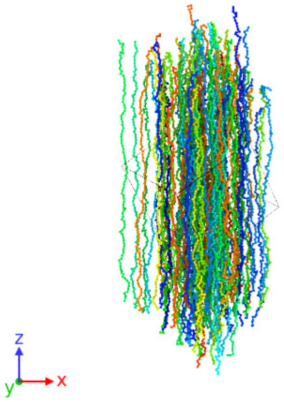

Fig.1: Polymers under uniaxial elongation $\kappa = \begin{pmatrix} \dot{\epsilon} & 0 & 0 \\ 0 & \dot{\epsilon}/2 & 0 \\ 0 & 0 & \dot{\epsilon}/2 \end{pmatrix}$.

For general deformations in the molecular dynamics simulation, we proposed a method that uses QR decomposition to exclude the rotational component of the deformation tensor and impose only pure deformations on the molecular simulation system [3]. Here, we considered problems in which large deformations and rotations do not occur. This time, we extended this method to include vortex flow in fluids. (Figure 2 shows a polymer chain in a rotating flow.) Before conducting multiscale simulations using this method, we are currently conducting an analysis assuming a corner vortex phenomenon that appears in polymer melts. We intend to summarize the results in a future paper.

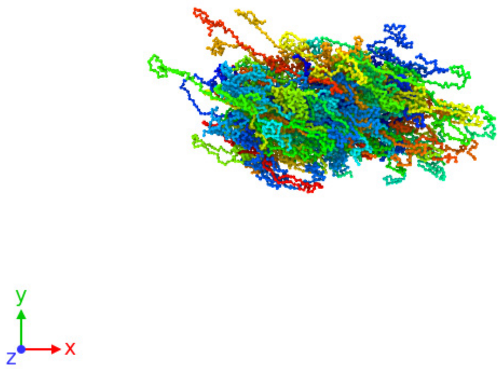

Fig. 2: Polymers under rotational flow $\kappa = \begin{pmatrix} 0 & \dot{a} & 0 \\ -\dot{b} & 0 & 0 \\ 0 & 0 & 0 \end{pmatrix}$, where $\dot{a} > \dot{b}$.

References

[1] T. Murashima, T. Taniguchi, EPL **96** (2011) 18002.

[2] T. Murashima, K. Hagita, T. Kawakatsu, Nihon Reoroji Gakkaishi **46** (2018) 207.

[3] T. Murashima, S. Urata, S. Li, Euro. Phys. J. B **92** (2019) 211.

Ashkin-Teller-like phase transition in the two-dimensional classical dimer-monomer model

Satoshi MORITA
Institute for Solid State Physics, University of Tokyo
Kashiwa-no-ha, Kashiwa, Chiba 277-8581

An attractive interaction between dimers aligning on a square induces finite-temperature phase transitions [1, 2]. The phase transition between the liquid and columnar phases is known as the Kosterlitz-Thouless transition. When monomers are introduced, the critical exponents smoothly change and its universality class is the same as the Ashkin-Teller (AT) model. On the other hand, another ordered phase appears between the two phases when the nearest-neighbor attractive interaction along the dimer direction is sufficiently large [3]. This phase called the nematic phase breaks only the lattice rotational symmetry. Although preceding studies reported these interesting features, an intermediate parameter region, where two attractive interactions are comparable, were not investigated. It is not known yet how the phase transition between the columnar and disordered phases splits into two transitions involving the nematic phase.

To address this problem, we investigate a classical dimer-monomer model on the square lattice by using the Monte Carlo (MC) method and the tensor network (TN) method. For the MC method, we generalize the worm algorithm to the grand-canonical ensemble of this dimer model. The TN method for infinite systems is complementary to the MC method. From the TN representation of the partition function, the row-to-row transfer matrix is constructed as the matrix product operator (MPO). Its eigenvector with the maximum eigenvalue is approximated by the uniform matrix product state (uMPS). We determine the phase structure and find the existence of the multi-critical point. The universality classes of the phase transitions are discussed by estimating the scaling dimension and the central charge. We find that the columnar and nematic orders correspond to the magnetization and polarization in the Ashkin-Teller model, respectively. The estimated scaling dimensions clearly indicate the Ashkin-Teller universality class. We also confirm the 4-state Potts universality at the multi-critical point.

Figure 1: A typical configuration of the nematic and disordered phases generated by the MC simulations.

References

[1] F. Alet, et al., Phys. Rev. Lett. **94**, 235702 (2005).

[2] F. Alet, et al., Phys. Rev. E **74**, 041124 (2006).

[3] S. Papanikolaou, D. Charrier, and E. Fradkin, Phys. Rev. B **89**, 035128 (2014).

[4] S. Morita, H. Lee, K. Damle, N. Kawashima, in preparation

Nematic Tomonaga-Luttinger Liquid Phase in an $S=1/2$ Ferromagnetic-Antiferromagnetic Bond-Alternating Chain

Takashi Tonegawa

Kobe University, University of Hyogo, and Osaka Metropolitan University

Recently, using mainly numerical methods, we [1] have investigated the ground-state phase diagram of an anisotropic $S=1/2$ two-leg ladder with different leg interactions. The xy and z components of the leg interactions between nearest-neighbor spins in the a (b) leg are denoted, respectively, by $J_{\mathrm{l},a}$ and $\Delta_{\mathrm{l}} J_{\mathrm{l},a}$ ($J_{\mathrm{l},b}$ and $\Delta_{\mathrm{l}} J_{\mathrm{l},b}$). On the other hand, the xy and z components of the uniform rung interactions are, respectively, denoted by $\Gamma_{\mathrm{r}} J_{\mathrm{r}}$ and J_{r}. In the above, Δ_{l} and Γ_{r} are the XXZ-type anisotropy parameters for the leg and rung interactions, respectively. This system has a frustration when $J_{\mathrm{l},a} J_{\mathrm{l},b} < 0$ irrespective of the sign of J_{r}.

We [1] have numerically determined the phase diagram on the Δ_{l} $(0.0 \le |\Delta_{\mathrm{l}}| \le 1.0)$ versus $J_{\mathrm{l},b}$ $(-2.0 \le J_{\mathrm{l},b} \le 3.0)$ plane in the case where $J_{\mathrm{l},a} = 0.2$, $J_{\mathrm{r}} = -1.0$, and $\Gamma_{\mathrm{r}} = 0.5$. It is noted that the rung interaction is ferromagnetic and its anosotropy is of the Ising-type. Furthermore, the a leg interaction is antiferromagnetic, while the b leg interaction are either ferromagntic or antiferromagnetic, the anisotropies of both leg interations being of the XY-type. We have employed the physical consideration, and the level spectroscopy and phenomenological renormalization-group analyses of the numerical date obtained by the exact diagonalization method. Interestingly enough, we have found that two kinds of nematic Tomonaga-Luttinger Liquid (nTLL) phases appear; one of which appears in the unfrustrated and the other in the frustrated one. The nTLL state is characterized not only by the formation of two-magnon bound pairs but also by the dominant nematic four-spin correlation function. It shuold be emphasized that the asymptotic form of this correlation function in the unfrustrated region and that in the frustrated region show the power-law decay with the uniform chracter and the power-law decay with the staggered character, respectively. Thus, both nTLL phases are different phases, and the latter nTLL phase may be called the staggered nTLL phase.

According to the above result, it is reasonably expected that the nTLL state appears as the zero-field ground state in general $S=1/2$ unfrustrated one-dimensional systems in which pairs of $S=1/2$ spins coupled strongly with the Ising-type ferromagnetic interaction are connected by the weak XY-type antiferromagnetic interactions. Some examples of such systems are (A) the $S=1/2$ ferromagnetic-antiferromagnetic bond-alternating chain, (B) the $S=1/2$ two-leg ladder with ferromagnetic rung and antiferromagnetic leg interactions, (C) the $S=1/2$ Kondo necklace chain with ferromagnetic rung and antiferromagnetic leg interactions, and so on.

The purpose of this report is to discuss the system (A), which is governed by the Hamiltonian

$$\mathcal{H} = -J_{\mathrm{F}} \sum_{j=1}^{N/2} [\vec{S}_{2j-1}, \vec{S}_{2j}] + J_{\mathrm{AF}} \sum_{j=1}^{N/2} [\vec{S}_{2j}, \vec{S}_{2j+1}]\,,$$

with

$$[\vec{S}_{2j-1}, \vec{S}_{2j}] = \Gamma_{\mathrm{F}} \bigl(S^x_{2j-1} S^x_{2j} + S^y_{2j-1} S^y_{2j}\bigr) + S^z_{2j-1} S^z_{2j}\,,$$

$$[\vec{S}_{2j}, \vec{S}_{2j+1}] = S^x_{2j} S^x_{2j+1} + S^y_{2j} S^y_{2j+1} + \Delta_{\mathrm{AF}} S^z_{2j} S^z_{2j+1}\,,$$

where $J_{\mathrm{F}} > J_{\mathrm{AF}} > 0.0$ and $1.0 \ge \Gamma_{\mathrm{F}}, |\Delta_{\mathrm{AF}}| \ge 0.0$, and also N, being assumed to be a multiple of four, is the number of spins in the ststem. It is noted that the ferromagnetic interactions are stronger than the antiferromagnetic ones, and the anisotropies of the former and latter interactions are of the Ising-type and the XY-type, respectively.

We have determined three ground-state phase diagrams; these are for $J_{\mathrm{F}} = 1.0$, $J_{\mathrm{AF}} = 0.1$, for $J_{\mathrm{F}} = 1.0$, $\Gamma_{\mathrm{F}} = 0.8$, and for $J_{\mathrm{F}} = 1.0$, $\Delta_{\mathrm{AF}} = -0.12$. The results are shown in Fig. 1, Fig. 2, and Fig. 3, respectively. These diagrams contain the ferromagnetic (F), $XY1$, singlet-dimer (SD), and up-up-down-down (uudd) phases as well as the nematic Tomonaga-Luttinger liquid (nTLL) phase which appears in wide regions, where $J_{\mathrm{F}} \gg J_{\mathrm{AF}} > 0.0$, of the interaction parameters.

Finally, we discuss how to obtain the phase boundary lines in these phase diagrams. We denote, respectively, by $E_0^{\mathrm{P}}(N, M)$ and $E_1^{\mathrm{P}}(N, M)$, the lowest and second-lowest energy eigenvalues of the Hamiltonian $\mathcal{H}$ under the periodic boundary condition within the subspace of N and M, where $M(=0, \pm 1, \cdots, \pm N/2)$ is the total magnetization. Furthermore, we denote by $E_0^{\mathrm{T}}(N, M, P)$ the lowest eigenvalue of $\mathcal{H}$ under the twisted boundary

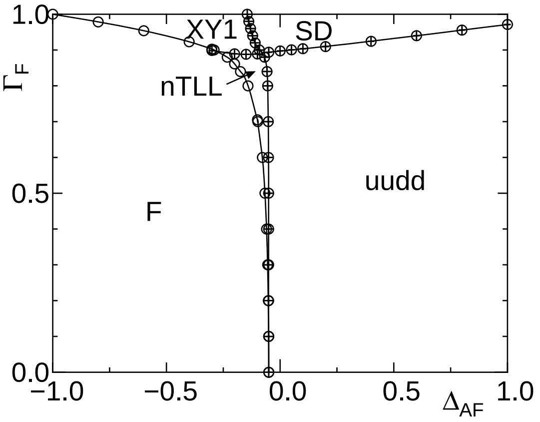

Figure 1: Ground-state phase diagram for $J_{\mathrm{F}}=1.0$ and $J_{\mathrm{AF}}=0.1$.

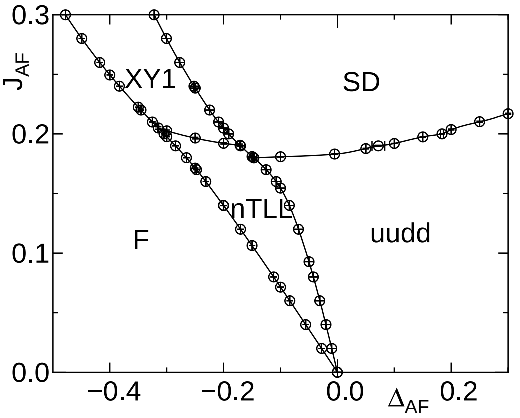

Figure 2: Ground-state phase diagram for $J_{\mathrm{F}}=1.0$ and $\Gamma_{\mathrm{F}}=0.8$.

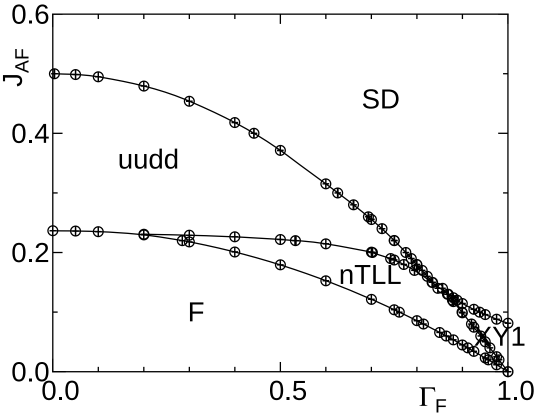

Figure 3: Ground-state phase diagram for $J_{\mathrm{F}}=1.0$ and $\Delta_{\mathrm{AF}}=-0.12$.

condition within the subspace of N, M, and P, where $P(=\pm 1)$ is the eigenvalue of the space inversion operator with respect to the twisted bond. We have numerically calculated these energies for finite-size systems with up to $N=28$ spins by means of the exact-diagonalization method. The ground-state energy of the finite-N system is given by $E_0^{\mathrm{P}}(N,N/2)$ in the F region and by $E_0^{\mathrm{P}}(N,0)$ in the other regions. In the following way, we have estimated the finite-size critical values of the interaction parameters for each phase transition. Then, the phase boundary line for the transition has been obtained by connecting the results for the $N\to\infty$ extrapolation of the finite-size critical values.

First, the phase transitions between the $XY1$ and SD phases and between the nTLL and uudd phases are the Berezinskii-Kosterlitz-Thouless transition [2]. In these transitoions, the level spectroscopy method develped by Nomura and Kitazawa [3] is very powerful for calculating the finite-size critical values, which are esimated from $E_0^{\mathrm{P}}(N,0)=E_0^{\mathrm{T}}(N,M,-1)$. Secondly, the phase transition between the SD and uudd phases is the 2D Ising-type transition. It is well known that the phase transition line is determined by the phenomenological renormalization-group (PRG) method [4]. Then, to estimate the finite-size critical values, we solve the PRG equation, $N\,\Delta_{00}(N)=(N+4)\,\Delta_{00}(N+4)$, where $\Delta_{00}(N)=E_1^{\mathrm{P}}(N,0)-E_0^{\mathrm{P}}(N,0)$. Thirdly, the nTLL state accompanies two-magnon bound-states, while the $XY1$ state does not. Then, in the ground-state magnetization curve for the finite-size system, the magnetization increases from $M=0$ to $M=2$ in the former state and from $M=0$ to $M=1$ in the latter state. Thus, the finite-size critical values are estimated from $\Delta_{10}(N)=\Delta_{20}(N)/2$, where $\Delta_{M0}(N)=E_0^{\mathrm{P}}(N,M)-E_0^{\mathrm{P}}(N,0)$. Lastly, it is apparent that the finite-size critical values for the phase transitions between the F phase and one of the nTLL, $XY1$, and uudd phases are estimated from $E_0^{\mathrm{P}}(N,N/2)=E_0^{\mathrm{P}}(N,0)$.

In conclusion, we have found the appearance of the nTLL phase in the ground-state phase diagram of an unfrustrated $S=1/2$ chain under no external magnetic field.

The present work has been done in collaboration with Kiyomi Okamoto, Kiyohide Nomura, and Tôru Sakai.

[1] T. Tonegawa, T. Hikihara, K. Okamoto, S. C. Furuya, and T. Sakai, J. Phys. Soc. Jpn. **87**, 104002 (2018).

[2] Z. L. Berezinskii, Sov. Phys. JETP **34**, 610 (1971); J. M. Kosterlitz and D. J. Thouless, J. Phys. C **6**, 1181 (1973).

[3] K. Nomura and A. Kitazawa, J. Phys. A **31**, 7341 (1998).

[4] M. P. Nightingale, Physica A **83**, 561 (1976).

First Principle Calculation and Charge Order Structure in Organic Charge Order Materials

Masatoshi SAKAI, Ryoma ISHII

Department of Electrical and Electronic Engineering,

Chiba University, 1-33 Yayoi-cho Inage, Chiba 263-8522

We tried to calculate the electronic structure of β-$(BEDT\text{-}TTF)_2PF_6$ from the first principle calculation using Quantum Espresso, RESPACK, and mVMC. Starting from the loading cif file into Quantum Espresso, we obtained the results of the scf calculation. After that, Wannier calculation was carried out by RESPACK to calculate Wannier orbitals so that the band dispersion curve around HOMO orbitals in scf calculation is reproduced by using the Wannier function. Fig. 1 (a) shows one of the selected Wannier functions used in this calculation, and Fig. 1(b) shows the band dispersion curves of the Wannier function superimposed into the result of the scf calculation. Wannier function represents the molecular orbital of the BEDT-TTF, and band dispersion curves are also well reproduced. Therefore, we obtained reasonable results in RESPACK calculation in the 3x3x3 K-mesh condition. Then we carried out the cRPA calculation to obtain dielectric function, Coulomb integrals, and exchange integrals. We spent a long time converging these calculations; however, we obtained the interaction parameters in β-$(BEDT\text{-}TTF)_2PF_6$. Now we are trying to execute mVMC calculation both in β-$(BEDT\text{-}TTF)_2PF_6$ and α-$(BEDT\text{-}TTF)_2I_3$ organic charge order system to elucidate our experiment.

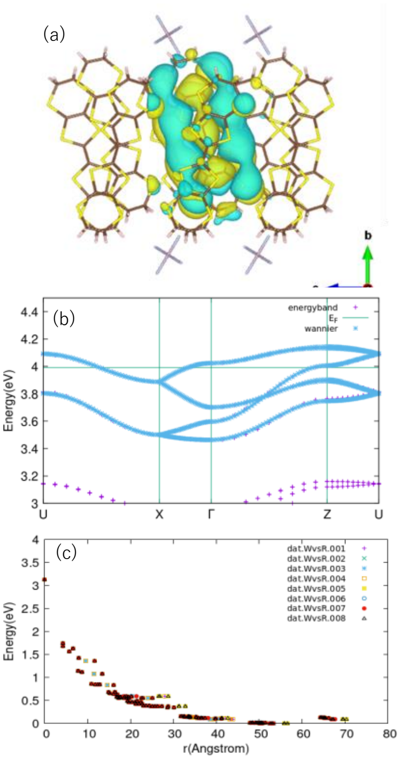

Fig. 1 (a) One of the calculated Wannier orbital around the Fermi level of β-$(BEDT\text{-}TTF)_2PF_6$. (b) Band dispersion curves of Wannier function superimposed in the scf calculation. (c) Coulomb interaction as a function of inter center distance.

Structural analysis of surface superstructures and atomic layer materials using by 2DMAT on supercomputer system at ISSP

Akari TAKAYAMA

Department of Physics,

Waseda University, Ohkubo, Shinjuku-ku, Tokyo 169-8555

In our research, we use supercomputers for structural analysis in terms of determining the structure of materials. Since structure and physical properties are closely related, it is essential to know the exact structure in order to correctly understand the physical properties. Generally, surface and interface structures are complicated than bulk crystal due to structural relaxation and structural reconstruction at surface and interface. For instance, structure of epitaxial graphene growth on SiC is still controversial due to the underlying-buffer layer with a long-period (6√3×6√3-R30°). Also the √3×√3-Pb/Si(111) surface superstructure, which is known to undergo a structural phase transition at $T = 86$ K, forms a “mosaic” structure, thus its detailed structure is fully understood. In this study, we investigated the structure of graphene on SiC including a buffer layer and Pb/Si(111) surface superstructure by using total reflection high-energy positron diffraction (TRHEPD) method. For structure analysis, we used “2DMAT” [1], an open source framework for 2D material structure analysis, which is included as standard software in ISSP’s supercomputer. Using massive parallel computer simulations on supercomputer is very useful for structure analysis of large periodic structure and surface superstructure with lattice reconstruction because they require many variables for analysis.

Figure 1 shows the rocking curve under the one-beam condition obtained from the experiment (circles) and from calculation (solid line) for 0-BL graphene (buffer layer) of SiC(0001). From the fitting calculation for this rocking curve, we determined the buckling structure of buffer layer and found that our determined structure corresponds well with the structural model proposed by Lima *et al.* [2]. Moreover, the ratio of bounding and free-standing regions with/from substrate were determined to be 22 % and 78 %, respectively, in this sample. The ratio is consistent with previous studies [3, 4].

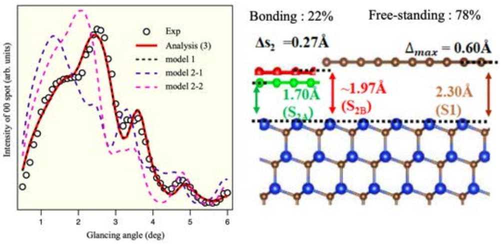

Fig. 1: Structure analysis results of buffer layer on SiC.

Figure 2 shows the rocking curve under the one-beam condition obtained from the experiment (circles) and from calculation (solid line) for mosaic phase of √3×√3-Pb/Si(111). We have succeeded in determining the structure of the mosaic phase by analyzing the Pb occupancy as a variable. In addition, no noticeable changes in the rocking curves were observed at low (T = 13 K) and room temperatures. This suggests that the phase transition in this structure is caused by soft phonons [5].

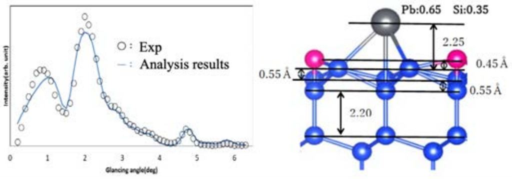

Fig. 2: Structure analysis results of mosaic phase of Pb/Si(111).

References

[1] Y. Motoyama, *et al*., arXiv:2204.04484

[2] L. H. de Lima, *et al*, Chem. Commun., **50** (2014) 13571.

[3] M. Conrad, *et al*., Phys. Rev. B **96** (2017) 195304.

[4] J. D. Emery, *et al*., Phys. Rev. Lett. **111** (2013) 215501.

[5] I. Brihuega *et al*., Phys. Rev. Lett. **94** (2005) 046101.

Minority Driving Transition in Collective Movement

Katsuyoshi Matsushita
Department of Biological Science, Osaka University
Machikaneyama, Toyonaka 560-0043

In biological organisms, cells aggregate and form tissues to function. Cell aggregation exhibits various dynamics, including rotation and translational movements. The transition from the rotation to the translational movements is well known in the developmental process in *Dictyostelium Discoideum* (dicty) [1]. The physical mechanism of this transition has been theoretically investigated on the basis of the behavior of cells [2, 3]. In particular, the works consider the response of cells to chemical gradients, which is observed in a earlier stage of development. These works successfully explained the transition and apperently unified the cell movements throughout the developmental process of dicty combined with the works for later stages [4].

These works assume homogeneous cell systems. However, as well known, the transition is tightly associated with cell differentiation. Cell differentiation means the change in the material properties of the cells. Therefore, the response property to the chemical gradient may not be conserved in the transition. Recent advances in the investigations of this transition showed the lack of the response of dicty cells [5]. Furthermore, both the rotational and translational movements do not depend on the response [6, 7]. These results imply the existence of another physical mechanism associated with cell differentiation.

A possible mechanism is the material parameter change in the cells. In particular, the rate of differentiation in population gradually changes during the transition process with several hours [1]. Therefore, we can expect the following situation: The collective movement is rotational when the differentiated cells are a minority in the cell population. Otherwise, the collective movement is a transnational movement. Namely, the minority change in cell population in the differentiation process drives the transition in collective movements.

To examine this scenario of the transition, we theoretically considered the process of cell population change [8]. We use the cellular Potts model [9, 10]. The cell population is assumed to consist of leader and follower cells [11]. The leader cells correspond to the differentiated cells and can lead the following cells using the cell-cell adhesion [12]. We also consider cell polarities by memorizing the cell trajectories [13, 14]. These polarities correlate with the adhesion [15] and stabilize the ordering of the cell movements [16, 17].

From the simulation results based on the above model, we examine the population dependence of the collective cell movements. We showed that the minority change in cell population in the differentiation process drives the transition of collective movements. A motility-inducing phase separation (MIPS) inner the cell aggregation appears for intermediate populations. The MIPS divides the cell aggregation into two aggregations: a homogeneous un-differentiated population and a highly differentiated population. Therefore, this minority change cannot explain the transition from rotation to translational movements for stable cell aggregations. The improvement of the scenario based on the minority change remains in the future.

The clarification of the origin of this aggregation division is expected to give us hints to improve the scenario. In our recent work, we investigate a homogeneous cell system to identify the parameters of collective movements [18]. We find that the occurrence of the collective movement, including the rotation and transnational movements, depends on the interface tension of the cell aggregations. This result implies the transition due to minority change originates from a change in the interface tension of the aggregation. The minority change is speculated to reduce the interface tension, and aggregation division is associated with the transition. This speculation implies the fine-tuning of the interface tension in the differentiation. However, it is not realizable in a realistic system and the necessity for another idea.

References

[1] J. T. Bonner, The Social Amoebae: The Biology of Cellular Slime Molds (Princeton University Press, Princeton, 2009).

[2] T. Umeda and K. Inouye, J. theor. Biol. **219**, 301 (2002).

[3] B. Vasiev C. J. Weijer. J. Theor. Biol. **223**, 347 (2003)

[4] A. Maree et al. J Their. Biol. **199**, 297 (1997); Proc. Natl. Acad. Sci. USA **98**, 3879 (2001) (2000).

[5] H. Hashimura, Y. V. Morimoto, M. Yasui, and M. Ueda, Communications Biology **2**, 34 (2019).

[6] W.-J. Rappel, A. Nicol, A. Sarkissian, H. Levine, and W. F. Loomis, Phys. Rev. Lett. **83**, 1247 (1999)

[7] Y. Kida, K. Pan, and H. Kuwayama, Differentiation **105**, 71 (2019).

[8] K. Matsushita, S. Yabunaka, H. Hashimura, H. Kuwayama, and K. Fujimoto, Proc. Sympo. Traffic Flow Self-Driven Particles **26** 39-42 (2020).

[9] F. Graner and J. A. Glazier, Phys. Rev. Lett. **69**, 2013 (1992).

[10] F. Graner, J. Theor. Biol. **164**, 455 (1993).

[11] A. J. Kabla, J. R. Soc. Interface **9**, 3268 (2012).

[12] K. Matsushita, Phys. Rev. E **97**, 042413 (2018).

[13] P. Szabó, M. Nagy, and T. Vicsek, Phys. Rev. E **79**,021908 (2007).

[14] K. Matsushita, Phys. Rev. E **97**, 042413 (2018).

[15] J. C. Coates and A. J. Wood. J. Cell Sci. **114**, 4349 (2001)

[16] K. Matsushita, K. Horibe, N. Kamamoto, and K. Fujimoto, J. Phys. Soc. Jpn. **88**, 103801 (2019).

[17] K. Matsushita, S. Yabunaka, and K. Fujimoto, J. Phys. Soc. Jpn. **90**, 054801 (2021).

[18] K. Matsushita, N. Kamamoto, M. Sudo, and K. Fujimoto, Proc. Sympo. Traffic Flow and Self-Driven Part. **27**, 23 (2021).

Non-uniform thermal transport properties in proteins

Takahisa YAMATO
Graduate School of Science,
Nagoya University, Furo-cho, Chikusa-ku, Nagoya 464-8602

Protein molecules are thermally fluctuating and tightly packed amino acid residues strongly interact with each other. Such interactions are characterized in terms of heat current at the atomic level. We calculated the thermal conductivity of a small globular protein, villin headpiece subdomain, based on the linear response theory using equilibrium molecular dynamics simulation. The value of its thermal conductivity was 0.3 ± 0.01 [W m^{-1} K^{-1}], which is in good agreement with experimental and computational studies on the other proteins in the literature (Figure 1). Heat current along the main chain was dominated by local vibrations in the polypeptide bonds, with amide I, II, III, and A bands on the Fourier transform of the heat current autocorrelation function [1] (Figure 2).

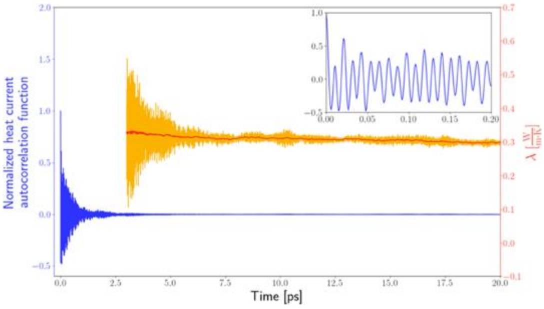

Figure 1: Thermal conductivity. The time evolution of the average heat current autocorrelation function is shown in blue. Its short time behavior is shown in the inset. The value of λ is shown in orange as a function of integration time, τ, for τ > 3.0 ps. The red line indicates the running mean of λ with a window size of 100 fs.

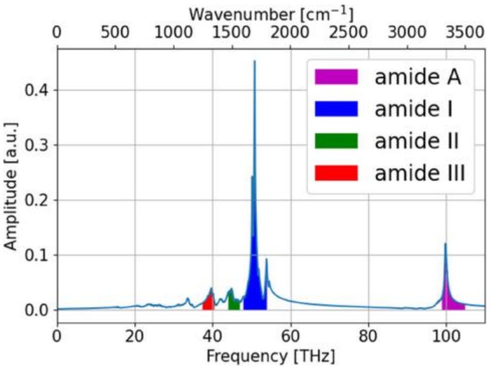

Figure 2: Fourier transform of the backbone heat current autocorrelation function. The Fourier transform of the average heat current autocorrelation function is shown for the backbone heat current.

References

[1] T. Yamato, T. Wang, W. Sugiura, O. Laprévote, T. Katagiri: J. Phys. Chem. B (2022) https://doi.org/10.1021/acs.jpcb.2c00958

Majorana Kramers Qubits and Yang-Lee Anyons in Topological Superconductors

Takeshi MIZUSHIMA
Department of Materials Engineering Science, Osaka University
Toyonaka, Osaka 560-8531

We have investigated non-Abelian statistics of Majorana Kramers pairs (MKPs) in time-reversal invariant topological superconductors (TRITSCs) [1]. We have also demonstrated that a Yang-Lee anyon system is constructed from Majorana bound states in topological superconductors [2].

In Ref. [1], we numerically simulated braiding dynamics of MKPs in a network of one-dimensional TRITSCs, and examined the tolerance against various perturbations which may cause decoherence of MKPs. We first considered effects of a magnetic field which breaks time-reversal symmetry. In contrast to a naive expectation, we find the non-Abelian braiding of MKPs is robust against applied magnetic fields provided that the initial and final states of a braiding process are invariant under the combination of a time reversal and a mirror reflection, even when intermediate states break the combined symmetry. In addition, we investigated the tolerance of non-Abelian braidings against gate-induced inhomogeneous potentials at junctions between superconducting nanowires. The potential generally generates a non-Majorana nearly zero-energy Andreeev bound state at the junctions. We demonstrated that the non-Majorana states interfere with MKPs, resulting in the failure of non-Abelian braidings.

Yang-Lee anyons, described by the non-unitary conformal field theory with the central charge $c = -22/5$, are non-unitary counterparts of Fibonacci anyons, obeying the same fusion rule. Therefore, the Yang-Lee anyon system is expected to be a platform for realizing universal topological quantum computation. In Ref. [2], we considered a topological superconductor junction system coupled with dissipative electron baths (see Fig. 1), which realizes a non-Hermitian interacting Majorana system. Numerically estimating the central charge, we examined the condition that the non-Hermitian Majorana system can simulate the Ising spin model of the Yang-Lee edge singularity, and confirmed that, by controlling model parameters in a feasible way, the Yang-Lee edge criticality is realized. We also discuss the scheme for the measurement and the braiding of Yang-Lee anyons, aiming at the application to the universal quantum computation.

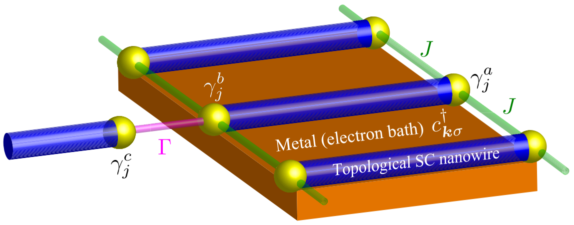

Figure 1: Schematics of Yang-Lee anyon system with Majorana quasiparticles.

References

[1] Y. Tanaka, T. Sanno, T. Mizushima, and S. Fujimoto: submitted.

[2] T. Sanno, M. G. Yamada, T. Mizushima, and S. Fujimoto: submitted.

Extension of susceptibilities, screened exchange and spin-fluctuation integrals into ultrasoft pseudopotentials

Mitsuaki KAWAMURA
Institute for Solid State Physics, University of Tokyo
Kashiwa-no-ha, Kashiwa, Chiba 277-8581

In the Eliashberg theory or density functional theory for superconductors (SCDFT) [1], where the electron-phonon, screened Coulomb, spin-fluctuation mediated interactions are included non-empilically, we need to compute the folowing product of two Kohn-Sham orbitals

$$\rho_{n\mathbf{k}n'\mathbf{k}'}(\mathbf{r}) = \varphi^*_{n\mathbf{k}}(\mathbf{r})\varphi_{n'\mathbf{k}'}(\mathbf{r}), \qquad (1)$$

where n (n') and $\mathbf{k}$ ($\mathbf{k}'$) are the band index and Bloch wavenumber, respectively. To perform this product together with the ultrasoft pseudopotentials (USPP) or projector augumented waves (PAW) that are widely used because of the good accuracy and reasonable numerical costs [2], we need a correction term for the norm-conservation. Such a correction is originally proposed for the calculation of the susceptibility [3] as

$$\Delta\rho_{n\mathbf{k}n'\mathbf{k}'}(\mathbf{r}) = \sum_{\tau i i'} \langle\varphi_{n\mathbf{k}}|\beta_{\tau i'}\rangle\langle\beta_{\tau i}|\varphi_{n'\mathbf{k}'}\rangle Q_{\tau i i'}(\mathbf{r}), \qquad (2)$$

where $\beta_{\tau i}$ is the projector dual to the atomic pseudo orbital $\psi^{PS}_{\tau i}$ at atom τ and orbital i, and the augumentation charge $Q_{\tau i i'}(\mathbf{r})$ is computed from the pseudo (PS) and all-electron (AE) atomic orbitals as follows:

$$Q_{\tau i i'}(\mathbf{r}) \equiv \psi^{AE*}_{\tau i}(\mathbf{r})\psi^{AE}_{\tau i'}(\mathbf{r}) - \psi^{PS*}_{\tau i}(\mathbf{r})\psi^{PS}_{\tau i'}(\mathbf{r}). \qquad (3)$$

To utilise this correction to the calculation of the spin-fluctuation mediated interaction,

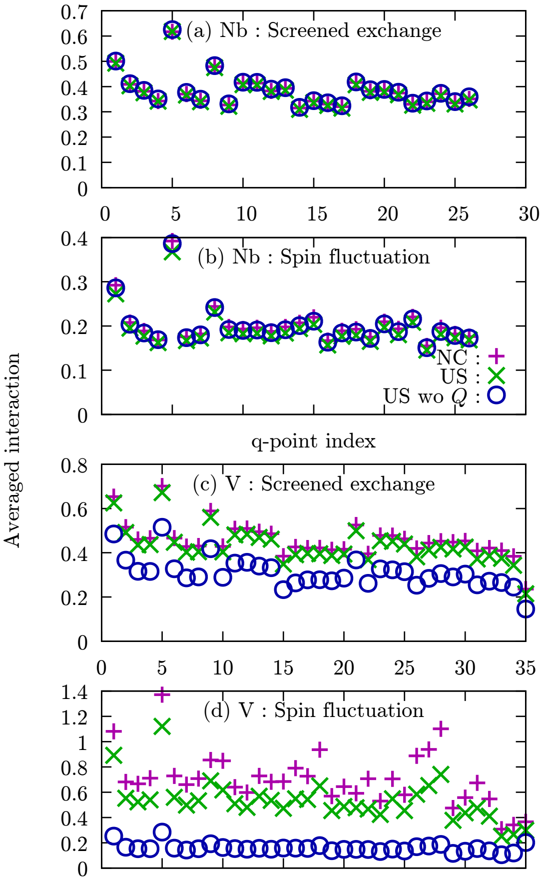

Figure 1: Spin-fluctuation mediated- (a, c) and screened exchange- (b, d) interactions averaged over the Fermi surface of Nb (a, b) and V (c, d). "+", "×", and "○" idicate results with norm-conserving (NC) ultrasoft (US) with and without augumentation charge $Q(\mathbf{r})$, respectivelly.

we implemented this formalism into our first-principles program package Superconducting-Toolkit [4] which is based on SCDFT.

Figure 1 shows the screened exchange and spin-fluctuation interactions averaged over the Fermi surface of Nb and V. In Nb, the effect of the augmentation charges Q is small because the USPP for this atom is almost norm-conserving. At the same time, V has a significant contribution from Q due to the nodeless 3d orbitals. In Fig. 1(d), we can see a deviation between the result by NC and US pseudopotential even if we include the correction. This deviation may be because the exchange-correlation kernel included in the spin-fluctuation is sensitive to the charge density in the vicinity of atoms.

We also performed the benchmark of the calculation of T_c for 15 materials, namely Al, V, Ta, In, Zn, Cd, Sn, ZrN, TaC, MgB_2, H_3S (at a pressure of 200 GPa), CaC_6, YNi_2B_2C, and V_3Si. Figure 2 shows the experimental, and calculated T_c; we performed four kind of calculations by changing superconducting density functional, namely the conventional plasmon-assisted [5], Sanna's Eliashberg-mimic (Sanna) [6], Sanna+Coulomb renormalization ($Z_\mathbf{C}$) [7], and Sanna + $Z_\mathbf{C}$ + Spin-fluctuation [9, 8] functional.

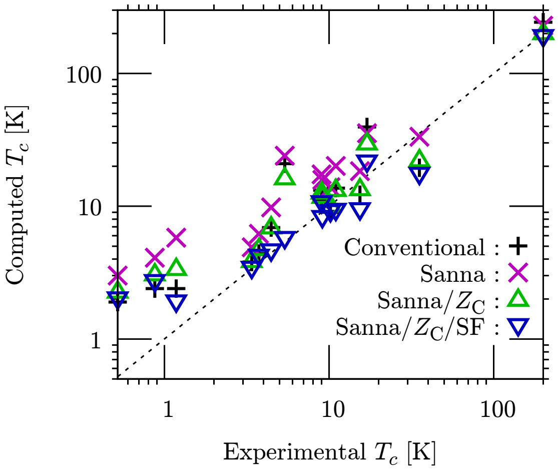

Figure 2: Computed- and experimental T_c. "+", "×", "△", and "▽" indicate result with conventional plasmon-assisted [5], Sanna's Eliashberg-mimic (Sanna) [6], Sanna+Coulomb renormalization ($Z_\mathbf{C}$) [7], and Sanna + $Z_\mathbf{C}$ + Spin-fluctuation [9, 8] functional, respectively.

References

[1] M. Lüders, M. A. L. Marques, N. N. Lathiotakis, A. Floris, G. Profeta, L. Fast, A. Continenza, S. Massidda, and E. K. U. Gross Phys. Rev. B **72**, 024545 (2005).

[2] G. Prandini, A. Marrazzo, I. E. Castelli, N. Mounet and N. Marzari: npj Computational Materials **4**, 72 (2018). https://materialscloud.org/sssp

[3] M. Gajdoš, K. Hummer, G. Kresse, J. Furthmüller and F. Bechstedt: Phys. Rev. B **73**, 045112 (2006).

[4] M. Kawamura, Y. Hizume, and T. Ozaki: Phys. Rev. B **101**, 134511 (2020). https://sctk.osdn.jp/index.html

[5] R. Akashi and R. Arita Phys. Rev. Lett. **111**, 057006 (2013).

[6] A. Sanna, C. Pellegrini, and E. K. U. Gross Phys. Rev. Lett. **125**, 057001 (2020).

[7] A. Davydov, A. Sanna, C. Pellegrini, J. K. Dewhurst, S. Sharma, and E. K. U. Gross Phys. Rev. B **102**, 214508 (2020).

[8] K. Tsutsumi, Y. Hizume, M. Kawamura, R. Akashi, and S. Tsuneyuki Phys. Rev. B **102**, 214515 (2020).

[9] F. Essenberger, A. Sanna, A. Linscheid, F. Tandetzky, G. Profeta, P. Cudazzo, and E. K. U. Gross Phys. Rev. B **90**, 214504 (2014).

Development of Algorithms for Ising Machines Based on Statistical Mechanics

Shu TANAKA
Department of Applied Physics and Physico-Informatics, Keio University
Hiyoshi, Yokohama, Kanagawa, 223-8522

Ising machines are a promising computational technique for highly efficient combinatorial optimization problems. Simulated annealing and quantum annealing are known as the internal algorithms of Ising machines, and a thorough investigation of the statistical dynamic properties of the Ising model is expected to improve the performance of Ising machines. In addition, investigating new ways of utilizing Ising machines is also an essential topic in the field of Ising machines. In this research project, we concentrated on the following two points.

(I) Dynamical properties of one-dimensional random Ising model with random transverse field [1]

Quantum annealing is a method of introducing an Ising Hamiltonian and Hamiltonian expressing noncommutative quantum fluctuations. We wish to search the ground state, and by varying the coefficients of each Hamiltonian with time, we eventually find the ground state of the Ising Hamiltonian. One of the factors that deteriorate the computational performance of quantum annealing is the reduction of the energy gap. The study of quantum phase transitions, where the energy gap systematically decreases with system size, is a common strategy for understanding the performance of quantum annealing from the perspective of statistical mechanics.

We considered an Ising model with random interactions defined as a one-dimensional chain. We investigate the system size dependence of the energy gap and the behavior of the dynamical critical exponent when a transverse magnetic field with randomness uncorrelated with the randomness of the interaction is applied and when a transverse magnetic field with randomness correlated with the randomness of the interaction is applied. As a result, it was found that there is a difference between the two cases.

(II) Black-box continuous optimization using Ising machines [2]

An Ising machine is a hardware that takes an Ising model or equivalent QUBO representation as input format and operates to search its ground state. Ising machines have been applied in various situations to combinatorial optimization problems that Ising models or QUBOs can represent. On the other hand, a method for utilizing Ising machines for black-box discrete optimization, i.e., discrete optimization problems for which the objective function is not explicitly given, was proposed by us in 2020 [3]. We extended it and proposed a method to perform black-box continuous optimization with Ising machines.

References

[1] T. Shirai and S. Tanaka: Ann. Phys. **435** (2021) 168483

[2] S. Izawa, K. Kitai, S. Tanaka, R. Tamura, and K. Tsuda: Phys. Rev. Res. **4** (2022) 023062.

[3] K. Kitai, J. Guo, S. Ju, S. Tanaka, K. Tsuda, J. Shiomi, and R. Tamura: Phys. Rev. Res. **2** (2020) 013319.

Numerical Study of One Dimensional Frustrated Quantum Spin Systems

Kazuo HIDA
Professor Emeritus, Division of Material Science,
Graduate School of Science and Engineering,
Saitama University, Saitama, Saitama 338-8570

We investigate the ground-state phases of mixed diamond chains with bond alternation described by the following Hamiltonian : [1]

$$\mathcal{H} = \sum_{l=1}^{L}\Big[(1+\delta)\boldsymbol{S}_l(\boldsymbol{\tau}_l^{(1)}+\boldsymbol{\tau}_l^{(2)}) + (1-\delta)(\boldsymbol{\tau}_l^{(1)}+\boldsymbol{\tau}_l^{(2)})\boldsymbol{S}_{l+1} + \lambda\boldsymbol{\tau}_l^{(1)}\boldsymbol{\tau}_l^{(2)}\Big], \quad (1)$$

where $\boldsymbol{S}_l, \boldsymbol{\tau}_l^{(1)}$ and $\boldsymbol{\tau}_l^{(2)}$ are spin operators with magnitudes $S_l = \tau_l^{(1)} = 1/2$ and $\tau_l^{(2)} = 1$. The number of unit cells is denoted by L, and the total number of sites is $3L$. Here, the parameters λ and δ control the frustration and bond alternation, respectively, as depicted in Fig. 1.

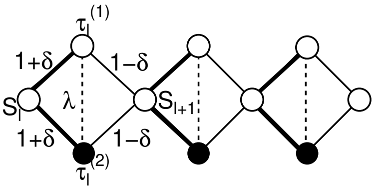

Figure 1: Structure of the diamond chain investigated in this work.

Defining the composite spin operators $\boldsymbol{T}_l$ as $\boldsymbol{T}_l \equiv \boldsymbol{\tau}_l^{(1)} + \boldsymbol{\tau}_l^{(2)}$, it is evident that $\forall l\ [\boldsymbol{T}_l^2, \mathcal{H}] = 0$. Thus, we have L good quantum numbers $\boldsymbol{T}_l^2 \equiv (T_l+1)T_l$ where $T_l = 1/2$ and $3/2$. The total Hilbert space of the Hamiltonian (1) consists of separated subspaces, each of which is specified by a definite set $\{T_l\}$.

For large λ, $\forall l\ T_l = 1/2$. Hence, for $\delta \neq 0$, the ground state is equivalent to that of the spin 1/2 chain with bond alternation δ. Therefore, the ground state is a gapped spin liquid.

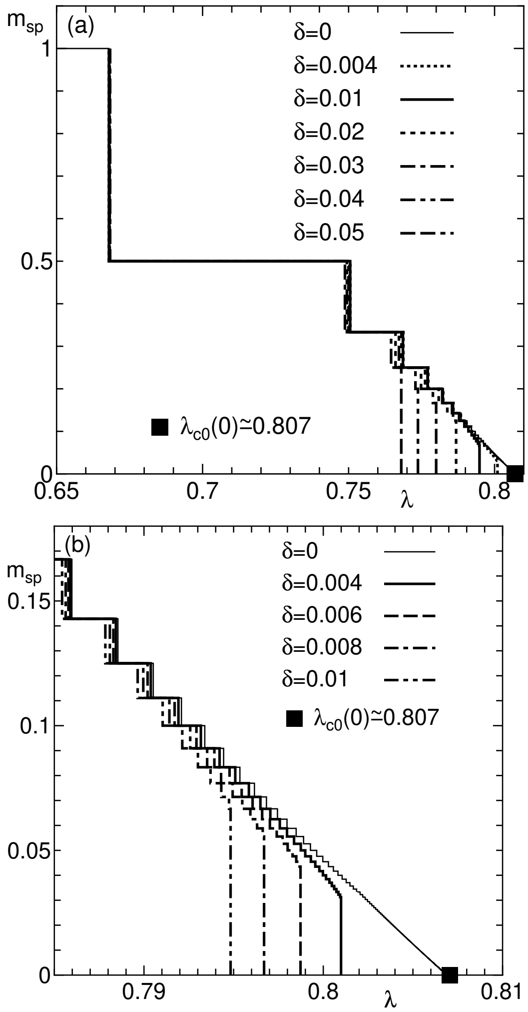

Figure 2: (a) λ-dependence of $m_{\rm sp}$ calculated by the infinite-size DMRG method. (b) Magnified figure around $\lambda \sim \lambda_{\rm c0}(0)$.

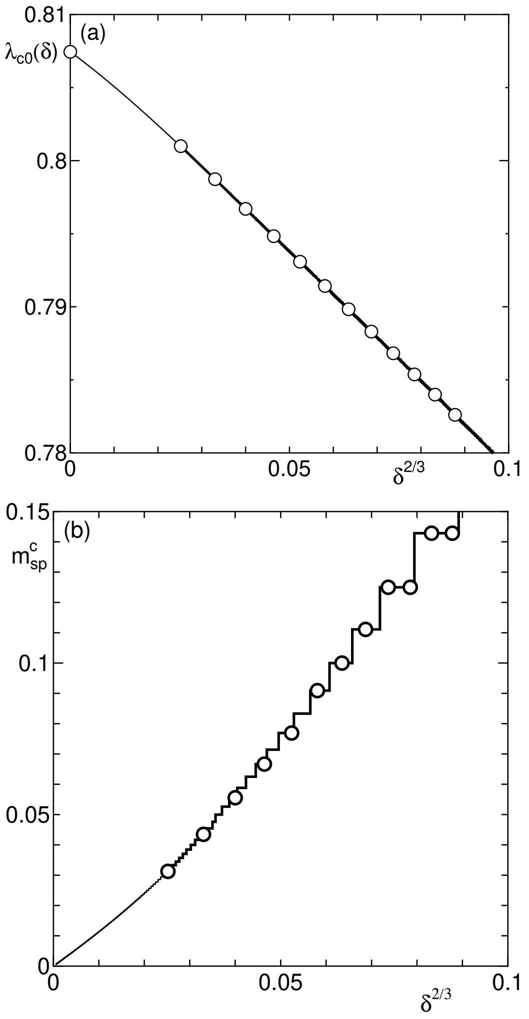

Figure 3: δ-dependence of (a) $\lambda_{c0}(\delta)$ and (b) $m_{\rm sp}^{\rm c}$.plotted against $\delta^{2/3}$.

This energy gap vanishes for $\delta = 0$. For small λ, $\forall l$ $T_l = 3/2$. Hence, the ground state is equivalent to that of the spin 1/2-3/2 alternating chain. Therefore, the ground state is a ferrimagnetic phase with a spontaneous magnetization $m_{\rm sp} = 1$ per unit cell. Between these two phases, we carry out the infinite-size DMRG calculations for various configurations of $\{T_l\}$ to obtain the ground-state energy per unit cell. As a result, we find that the ground state undergoes a transition at $\lambda = \lambda_{\rm c0}(\delta)$ to a series of ferrimagnetic phases with $m_{\rm sp} = 1/p$ where p takes positive integer values. This transition is a first-order transition for $\delta \neq 0$ with a discontinuous change $m_{\rm sp}^{\rm c}$ in $m_{\rm sp}$, while no discontinuity is found for $\delta = 0$.[2]

The critical behaviors of $m_{\rm sp}^{\rm c}$ and $\lambda_{\rm c0}(\delta)$ around the critical point $(\delta, \lambda) = (0, \lambda_{\rm c0}(0))$ turned out to be

$$m_{\rm sp}^{\rm c} \propto \delta^{2/3}, \qquad (2)$$

$$\lambda_{\rm c0}(\delta) - \lambda_{\rm c0}(0) \propto \delta^{2/3}. \qquad (3)$$

These relations are also explained analytically.[1]

References

[1] K. Hida, J. Phys. Soc. Jpn. **91**, 024706 (2022).

[2] K. Hida, J. Phys. Soc. Jpn. **90**, 054701 (2021).

Quantum simulation using Ising models

Yuya SEKI

Graduate School of Science and Technology, Keio University, Kanagawa 223-8522

We have studied properties of factorization machine with annealing (FMA) [1] for quantum simulations. The FMA method approximates the Hamiltonian of the target system with Ising model through a machine learning model called factorization machine (FM) [2]. Instead of finding the low-energy states of the target system that is hard to analysis, we investigate low-energy states of the approximated Ising spin system. In FMA procedure, we use Monte Carlo methods to generate low-energy samples from the trained FM. In addition, the training process of FM includes the backpropagation method for updating the model parameters in FM, which requires a linear algebra library for calculation. These calculations were performed using multithreading to reduce the execution time. FMA includes various hyperparameters that should be optimized to achieve high accuracy solutions. To search for optimal hyperparameters efficiently, we performed the calculation in parallel by changing the parameters.

This year we developed a new method that combines FMA with integer-encoding methods. The developed method enables us to calculate the ground state of quantum systems approximately. As a benchmark problem, we consider the problem of finding the ground state of the hydrogen molecule, whose Hamiltonian consists of fermions. In this project, we used three encoding methods: binary encoding, one-hot encoding, and domain-wall encoding. To investigate performance for each encoding method, we calculate the distribution of the accuracy of solution of the developed method by running the developed method repeatedly. As a result, we obtained the optimal region of parameters where the developed method provides a solution that is close to the true ground state with a high probability for each encoding method. Adjusting the parameters, we obtain the ground-state of the hydrogen molecule where relative energy error is less than 10^{-5}. Also, we determined the proper encoding method from the obtained data. Among the encoding methods, one-hot encoding shows better performance than the others. This result indicates that the sparsity of data expression determines the performance of FMA.

References

[1] K. Kitai *et al.*: Phys. Rev. Research **2** (2020) 013319.

[2] S. Rendle: 2010 IEEE Int. Conf. Data Min. (2010) 995.

Large-scale molecular-dynamics simulation of silica melt and glass under high pressure with ANN potentials by active learning

Daisuke WAKABAYASHI

Photon Factory, Institute of Materials Structure Science,
High Energy Accelerator Research Organization (KEK), Tsukuba 305-0801

Silica is well known as an archetypal oxide and the compression behavior of silica glass and melt has attracted considerable attention in various research fields of physical sciences. Due to the strong covalent bonding, the melting point is extremely high. It is difficult to perform experiments on silica melt under high pressure, and theoretical calculations are a powerful research tool.

In contrast to crystalline materials, non-crystalline materials do not have long-range order, and therefore, in order to obtain reliable information, it is necessary to perform theoretical calculations on a system as large as possible. There is a limit to the size of the system which can be calculated by ab-initio methods. In this study, we have fitted the potential with a machine-learning technique (ANN potential) on the basis of the results of ab-initio calculations, and have applied it for the calculations with an extended system. However, in our previous projects, it has been observed that the large-scale calculations of melt were difficult to stabilize and quickly diverged, making them impossible to continue. In this project, we tested a new method of efficiently obtaining required training data through active learning.

An active-learning method can be roughly divided into three stages. First, multiple ANN potentials are decided for the same set of training data and MD simulations are made with each potential. Second, ab-initio calculations are made for the atomic arrangement corresponding to the steps for which the calculation results in the first stage differ significantly among the potentials. Finally, the ab-initio results are added as new training data for the next potential fitting.

The test calculations were performed for the solidification process of silica melt under high pressure. The ANN potential was determined by the machine-learning method with the potential, force, and stress data obtained by ab-initio calculations for a temperature range of 300-5,000 K at 60 GPa with 144 atoms. Active learning was performed three times to search for the conditions under which calculations on silica melt do not diverge at 60 GPa and 4,000 K for a system expanded to about 30,000 atoms.

The number of data was originally 15,000 and about 2,000 were added for each active learning. Although there was improvement in the differences in calculation results between ANN potentials and in the number of steps at which divergence occurred in the expanded system up to the second active learning, there was almost no improvement after the third learning. This may be due to the fact that the active learning process increases the likelihood of mixing training data of unrealistic atomic arrangements. It was found that active learning enables us to delay, if not completely prevent, divergence.

Theoretical study of thermoelectric properties in doped Fe_2VAl: A weak-coupling approach

Kazutaka NISHIGUCHI
Graduate School of System Informatics, Kobe University
Rokkodai-cho, Nada-ku, Kobe 657-8501

1 Heusler compound Fe_2VAl

Heusler compound Fe_2VAl is one of the promising thermoelectric materials, which exhibits large power factor $P = \sigma S^2$ with σ and S being the electrical conductivity and Seebeck coefficient, respectively, although the thermal the dimensionless figure of merit $ZT = \sigma S^2 T/\kappa$ is not so large yet reflecting its large thermal conductivity κ.

Recently, it is experimentally observed in doped Fe_2VAl (i.e., $Fe_2V_{0.9}Cr_{0.1}Al_{0.9}Si_{0.1}$ and $Fe_{2.2}V_{0.8}Al_{1-y}Si_y$) as a weekly ferromagnetic material that ferromagnetic fluctuations enhance the thermoelectric properties such as S and P around the Curie temperature (T_c = 285 K). [1] It is not only a desirable property for practical use in realistic (room) temperatures, but also a fundamental and intriguing quantum phenomena where quantum fluctuations and thermoelectric effects are entangled by electron correlations.

Motivated above, we have studied electronic properties of Fe_2VAl using first-principles calculations based on the density functional theory (DFT) within the generalized gradient approximation (GGA). We performed DFT calculations with the Perdew–Burke–Ernzerhof (PBE) exchange-correlation functional and the projector augmented wave (PAW) method using The Vienna Ab Initio Simulation Package (VASP) [2] and QUANTUM ESPRESSO package. [3] One could observe from the band structure and density of states (DOS) are shown in Figure 1 that the Fe and V d-orbitals around the Fermi level mainly contribute to the low-energy electronic structures.

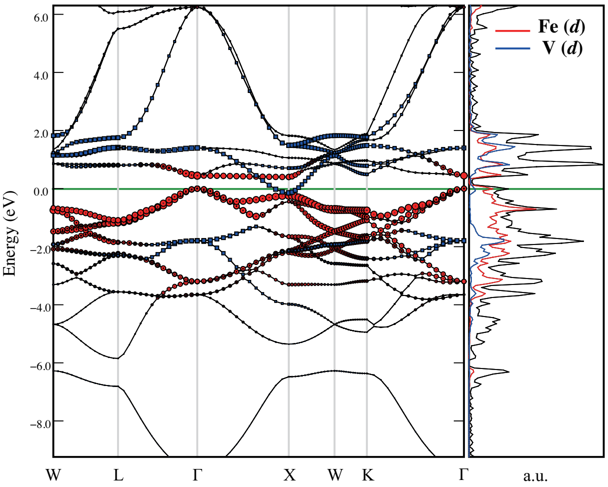

Figure 1: (Left) Band structure and (Right) DOS of Fe_2VAl. The energy is measured from the Fermi level. The components of Fe and V d-orbitals are projected (by red and blue), respectively.

We have also considered the dopant effects on the doped Fe_2VAl to investigate its magnetic properties: the Cr and Fe substitution for V and the Si substitution for Si were taken into account by the (2 × 2 × 2) supercell calculations. We could observe that the Cr and Fe substitution for V induce the spin-polarized states and the magnetic moment arises at the Cr and Fe, respectively, while the electronic structure for the Si substitution for Si is still paramagnetic state.

Furthermore, we have constructed the first-principles effective model for Fe_2VAl using the maximally localized Wannier functions with Wannier90. [4] We here found that the effective model has to involve not only Fe and V d-orbitals mentioned above but also Al s- and p-orbitals in order to reproduce the original band structure around the Fermi level since these orbitals highly entangle with each other and have large hybridization. Therefore, we adopted a 19-orbital effective model for Fe_2VAl: $5(\mathrm{Fe}-d)\times 2+5(\mathrm{V}-d)+4(\mathrm{Al}-sp)$.

2 122 Zintl Phase Compound $CaZn_2X_2$ (X = As, P)

In order to search for high-performance thermoelectric materials, the possibility of n-type doping of $CaAl_2Si_2$-type Zintl phase compound $CaZn_2X_2$ (X = As, P) is explored using first-principles calculations based on DFT. [5] We consider n-type (electron carrier) doping of $CaZn_2X_2$ with the following two situations: interstitial-site doping of alkaline earth metals AE (= Mg, Ca, Sr, Ba) and group 3 elements G3 (= Sc, Y, La), and G3 substitutional doping for the Ca site.

To see this, the defect formation energy of these charged states is evaluated within GGA using the supercell approach. Among the considered possibilities, the interstitial-site doping of AE = Ca, Mg or G3 = Sc, Y, and the G3 = La, Y substitutional doping for the Ca have been found to have relatively small formation energies. In particular, the formation energy of the La substitutional doping is found to be negative for both $CaZn_2As_2$ and $CaZn_2P_2$ (Figure 2). This suggests that La can substitute the Ca site spontaneously and hence provide electron carriers, as far as these calculation results are concerned. We have also found that the formation energies of the defects are smaller for $CaZn_2As_2$ than for $CaZn_2P_2$, which suggests that n-type doping is relatively easier for the former than for the latter.

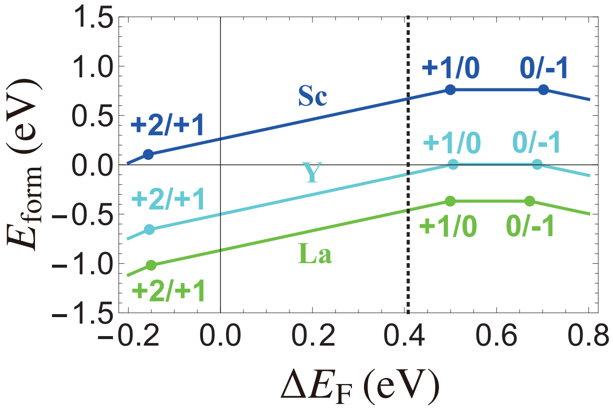

Figure 2: The formation energy of the G3 substitutional doping for the Ca site E_{form} against the Fermi energy $\Delta E_{\mathrm{F}} = E_{\mathrm{F}} - E_{\mathrm{V}}$ for $CaZn_2As_2$. The group 3 elements G3 (= Sc, Y, La) are chosen as dopant D. The dotted line denotes the position of the conduction band minimum ($E_{\mathrm{F}} = 0.408$ eV).

References

[1] N. Tsujii, A. Nishide, J. Hayakawa, and T. Mori: Sci. Adv. **5** (2019) eaat5935.

[2] G. Kresse *et. al.*: Phys. Rev. B **47** (1993) 558; Phys. Rev. B **49** (1994) 14251; Computational Materials Science **6** (1996) 15; Phys. Rev. B **54** (1996) 11169.

[3] P. Giannozzi *et. al.*: J. Phys.: Condens. Matter **21** (2009) 395502; J. Phys.: Condens. Matter **29** (2017) 465901; J. Chem. Phys. **152** (2020) 154105.

[4] I. Souza, N. Marzari, and D. Vanderbilt: Phys. Rev. B **65** (2001) 035109; A. A. Mostofi *et. al.*: Comput. Phys. Commun. **178** (2008) 685; A. A. Mostofi *et. al.*: Comput. Phys. Commun. **185** (2014) 2309; G. Pizzi *et. al.*: J. Phys.: Condens. Matter **32** (2020) 165902.

[5] K. Nishiguchi, M. Ochi, C. H. Lee, and K. Kuroki: J. Phys. Soc. Jpn. (to be published).

Spontaneous formation of multiple-Q orders in inversion-symmetric Hubbard Models

Takashi UCHIDA
Hokkaido University of Science
4-1, 7-15, Maeda, Teine-ku, Sapporo 006-8585

In the last decade, multiple-Q orders in magnetic systems have attracted attention because they sometimes reveal topologically protected magnetic structures such as magnetic skyrmions. Typically, these structures are realized in the Dzyaloshinskii-Moriya (DM) interaction driven systems under magnetic field. The multiple-Q orders can also be realized in inversion-symmetric systems where the DM interaction is absent [1, 2]. In the present work, we have attempted to explore theoretically the possibility of multiple-Q orders in the inversion-symmetric systems in the absence of external magnetic field. For this purpose, we have applied the molecular spin dynamics (MSD) method [3] to the triangular-lattice single-band Hubbard model.

The MSD method is based on the functional integral method for the spin fluctuation theories and the isothermal molecular dynamics method. The method allows us to find automatically the magnetic structure of a large system with thousands of atoms in a unit cell at finite temperatures. Starting from the Hamiltonian expressed in terms of the locally rotated coordinates and by adopting the static approximation to the functional integral technique, the MSD method reduces to the generalized Hartree-Fock approximation at the ground state.

In the numerical calculations the most time-consuming process is the magnetic force calculation at each time step, where the local electronic structures are calculated in real space by means of the recursion method. We have adopted the automatic parallel calculation scheme and found it effective in saving both computing time and CPU resources.

We have performed magnetic structure calculations on a hexagonal supercell with 972 lattice points, which is embedded in a large cluster consisting of 6 such supercells, each of which are connected by the periodic boundary condition. Under zero magnetic field and the fixed value of the temperature $T/t = 0.0005$, we have explored the magnetic structures changing the Coulomb interaction strength U/t ($U/t = 3.0 \sim 8.0$) and the electron number n ($n = 1.10 \sim 1.60$) along the antiferromagnetic-ferromagnetic boundary. We have found that for $U/t \sim 3.5$ and $n = 1.48 \sim 1.53$ the dominant state is 3Q-structure with $\boldsymbol{Q}_1 = (0.3889, -0.2245)2\pi/a$, $\boldsymbol{Q}_2 = (0.3889, 0.2245)2\pi/a$, and $\boldsymbol{Q}_3 = (0.0, 0.4491)2\pi/a$ (with a being the lattice constant), which is superimposed with satellite 3Q structures with the Q vectors pointing in the same direction (in the direction of three axes of the triangular lattice).

References

[1] T. Okubo, S. Chung, and H. Kawamura: Phys. Rev. Lett. **108** (2012) 017206

[2] Y. Kakehashi: J. Phys. Soc. Jpn. **89** (2020) 094710.

[3] Y. Kakehashi, S. Akbar, and N. Kimura: Phys. Rev. B**57** (1998) 8354.

Molecular Dynamics Simulations of Reversibly Cross-linked Rubbers

Yusuke Yasuda
Research Center for Computational Design of Advanced Functional Materials.
National Institute for Advanced Industrial Science and Technology, Ibaraki 305-8568.

Reversibly cross-linked rubbers, whose cross-links are made of reversible bonds, such as hydrogen bonds, ionic bonds, and dynamic covalent bonds, have self-healing property and toughness. Though many researchers have studied those materials, the molecular mechanisms of these properties are still unclear due to the difficulty of the observations of molecular dynamics. To understand those materials, it is needed to study the relationship between structure, dynamics, and properties of these rubbers from several research methods.

In this work, we constructed coarse-grained model for reversibly cross-linked rubbers based on Kremer-Grest model [1], by introducing associating and dissociating condition (Fig.(a)) changing bond dissociation energy and bond potential shape. Calculation was conducted using molecular dynamics simulation software packages OCTA and LAMMPS on ISSP Supercomputer System. From equilibrium simulation, we found that association constants and bond lifetime are controlled by bond dissociation energy and bond potential shape. Mechanical simulation was conducted via loading-unloading test conducted in the range of elongation ratio λ= 1 – 4. From loading-unloading simulation, stress-extension rate curve shows stress retardation and specific hysteresis (Mullins effect, Fig.(b)) which is observed experimentally in reversibly cross-linked elastomer. We also found that the dynamic bonds dissociate by elongation, and that dissociation synchronizes to stress retardation. Self-healing test was conducted via equilibrium calculation at high temperature after loading and unloading. In the elongation after equilibrium, stress recovered completely, and our model can reproduce the feature of self-healing. (Fig.(b)) From these results, we have succeeded in constructing coarse-grained model of reversibly cross-linked rubbers.

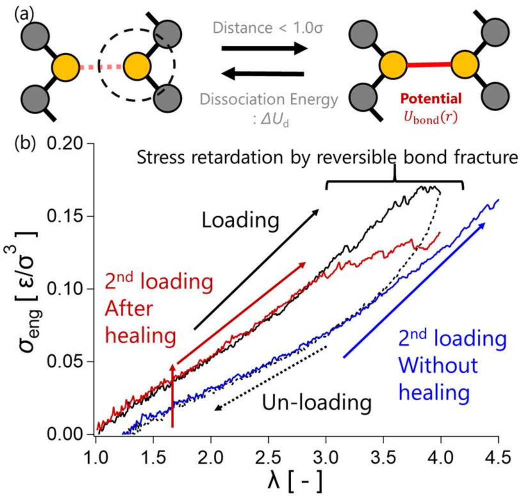

Fig. (a) The schematic illustration of coarse-grained dynamic bonds, (b) loading-unloading curves of the model.

References [1] K, Kremer, G. S. Grest; J. Chem. Phys., **92**, (1990) 5057.

Acknowledgement This work is partially supported by a project JPNP18016, commissioned by the New Energy and Industrial Technology Development Organization(NEDO).

Development of integrated interface of eigensolvers Rokko and application to quantum spin systems

Tatsuya Sakashita
Center for Quantum Information and Quantum Biology, Osaka University
1-2 Machikaneyamachō, Toyonaka, Osaka 560-0043

To establish universal exact diagonalization package for quantum lattice models including the Heisenberg-Kitaev model, we focused on developing integrated interfaces for eigensolvers, "Rokko"[1].

In Rokko, we implemented the integrated interfaces for the following types:

- Serial solvers for dense matrices (Eigen3, LAPACK)
- MPI parallelized solvers for dense matrices (EigenExa[2], ELPA[3], Elemental[4], ScaLAPACK)
- MPI parallelized solvers for sparse matrices (Anasazi in Trilinos[5], SLEPc[6]) to cover matrix representations below:
  - CRS (Compressed Row Storage)
  - Matrix-free method (the method to give matrix-vector product routines to solvers)

Rokko has the following features:

- Integrated interfaces for eigensolvers and matrices, independent of individual eigensolver libraries
- Rokko's interfaces are implemented by utilizing factory. It enables the user to dynamically select a solver.
- C, Fortran, and Python bindings of Rokko
- Automatically detecting libraries by using CMake in building Rokko
- Unit and integrated test programs by GoogleTest
- Install scripts of eigensolvers for various architectures

We prepare a paper to report design policy, software structure, and usage examples of Rokko.

References

[1] T. Sakashita, R. Igarashi, Y. Motoyama, T. Okubo, and S. Todo. Repository of Rokko. `https://github.com/t-sakashita/rokko.git`, 2012.

[2] T. Imamura, T. Hirota, and T. Fukaya. EigenExa web page. `https://www.r-ccs.riken.jp/labs/lpnctrt/projects/eigenexa/`, 2021.

[3] ELPA Consortium. ELPA (Eigenvalue soLvers for Petaflop Applications web page). `http://elpa.rzg.mpg.de`, 2013.

[4] J. Poulson. Distributed-memory dense linear algebra Elemental web page. `https://github.com/elemental/Elemental`, 2013.

[5] M. A. Heroux, R. A. Bartlett, and V. E. Howle. Trilinos Project web page. `https://trilinos.github.io`, 2003.

[6] V. Hernandez, J. E. Roman, and V. Vidal. SLEPc web page. `http://slepc.upv.es`, 2002.

Molecular dynamics analyses of ion migration at grain boundaries in solid state electrolyte

Ryo KOBAYASHI

Department of Applied Physics, Nagoya Institute of Technology,

Gokiso-cho, Showa-ku, Nagoya, Aichi 466-8555

All-solid-state battery (ASSB) is considered as a candidate of next generation Li-ion batteries because it uses a solid-state electrolyte instead of liquid-state electrolytes that are used in conventional Li-ion batteries. The key to achieve high-performance in ASSB is to reduce/control the resistivities at interfaces such as electrode/electrolyte interface and grain boundary (GB) inside electrolyte. For this purpose, we need deeper understandings about the atomic structure and precise mechanisms of ion migration of the GBs, and the goal of this project is to obtain new insights about them by using large-scale molecular dynamics (MD) simulation.

In order to obtain atomistic insights on Li-ion migration mechanism at GBs, we performed non-equilibrium MD simulation of large-scale poly-crystalline Li2Zr(PO4)3 (LZP) system containing half a million atoms and extracted local ion flux information around

.

GBs. From the simulation and local ion-flux analyses[1], we showed that, in poly-crystalline materials, the ions migrate towards the lower reaches of grain and go through spots at GBs, and the high-flux spots contain migration paths as low energy as the bulk ones.

In this study, we have developed a new technique to obtain local ion-flux information from non-equilibrium MD implemented in our own code, nap[2]. And several MD simulation runs and the local-ion flux analyses were performed on the ISSP supercomputers.

References

[1] R. Kobayashi, K. Nakano, M. Nakayama, Acta Materialia, 226 (2022) 117596.

[2] Nagoya Atomistic-simulation Package (nap) http://github.com/ryokbys/nap

Electronic structure in mismatched multilayer systems: evaluation and application of the modeling scheme

Toshikaze KARIYADO

International Center for Materials Nanoarchitectonics,
National Institute for Materials Science, Tsukuba, Ibaraki 305-0044

After the report of superconductivity in twisted bilayer graphene, artificially stacked two-dimensional (2D) materials with moiré pattern induced by some mismatches between the layers attracts much attention. Generically, the moiré pattern affects the electronic band structure, and can be used to realize unique band structures. Then, designing interesting band structures in artificially stacked systems is a current urgent topic to explore.

In this project, we have analyzed electronic structures of twisted bilayer GeSe, where the anisotropic band flattening is expected. Here, the anisotropic band flattening means that originally 2D band dispersion is squeezed into quasi 1D one in twisted bilayers. To analyze the band structure, we derived an effective model for twisted bilayer GeSe. There are multiple important quantities in the effective model such as the effective mass for each layer or the effective interlayer tunneling. We obtain these quantities making use of the first-principles calculations. Our analysis clarifies the relation between the crystal structure of GeSe and the anisotropy in the effective interlayer tunneling, which gives us an intuitive understanding of the physics behind the anisotropic band flattening.

The first-principles calculations have been done using Quantum Espresso package, which is adapted to the parallel computation and suitable to use the supercomputing resources efficiently.

Not only calculating electronic band structures itself, we also tried to extract some characteristic response tied to the unique band structure, focusing on the orbital magnetic susceptibility. For that, we first derived a new formula to calculate the orbital magnetic susceptibility, and numerically tested its validity using several types of toy models by our homemade program [2]. In order to access the low temperature regime, we need fine mesh in k-point sampling, where the parallelization by MPI is applied in our homemade program.

References

[1] M. Fujimoto and T. Kariyado: Phys. Rev. B **104** (2021) 125427.

[2] T. Kariyado, H. Matsuura, and M. Ogata: J. Phys. Soc. Jpn. **90** (2021) 124708.

Compact spin qubits using the common gate structure of fin field-effect transistors

Tetsufumi Tanamoto
Department of Information and Electronic Engineering, Teikyo University
Utsunomiya 320-8511, Japan.

By using the ISSP supercomputer, we numerically investigate a transport properies of the compact spin-qubit system embedded into the common multi-gate FinFET transistors [1], where all gates are electrically tied togther as the common gate. The quantum dots (QDs) as qubits are coupled with their nearest Fin conducting channels. The Hamiltonian of the QDs and the channel is given by the tunneling Hamiltonian:

$$\begin{aligned}H_0 &= E_2 d_{2s}^\dagger d_{2s} + E_4 d_{4s}^\dagger d_{4s} + \sum_{i=1,3,5} \sum_{k_i,s} E_{k_i} c_{k_i s}^\dagger c_{k_i s} \\ &+ \sum_{k_1} [V_{k_1} c_{k_1 s}^\dagger d_{2s} + V_{k_1}^* d_{2s}^\dagger c_{k_1 s}] \\ &+ \sum_{k_3} [V_{k_3} c_{k_3 s}^\dagger (d_{2s} + d_{4s}) + V_{k_3}^* (d_{2s}^\dagger + d_{4s}^\dagger) c_{k_3 s}] \\ &+ \sum_{k_5} [V_{k_5} c_{k_5 s}^\dagger d_{4s} + V_{k_5}^* d_{4s}^\dagger c_{k_5 s}], \qquad (1)\end{aligned}$$

where the channels are numbered as 1, 3, and 5, and the two QDs are numbered as 2 and 4. d_{is} and $c_{k,s}$ are the annihilation operators of the QD i and the conducting electrons in the channel, respectively. The qubit states are detected by the channel currents. The conductance $g_{yy}(\omega)$ is calculated from the Kubo formula given by $g_{yy}(\omega) = -\frac{1}{i\omega}[\Phi_{yy}^{\rm R}(\omega) - \Phi_{yy}^{\rm R}(0)]$, $\Phi_{yy}^{\rm R}[t] = -\frac{i}{\hbar V}\theta(t)\langle J_y(t)J_y(0) - J_y(0)J_y(t)\rangle$. The current operator J_y^i of the ith channel is given by $J_y^i = (e\hbar/(m^* L))\sum_{k_i} k_i c_{k_i s}^\dagger c_{k_i s}$, where L is the channel length and the summation of k_i is carried out over the channel. The expression for $g_{yy}^{(3)}$ is

$$g_{yy}^{(3)} = \frac{2e^2}{h} k_d \frac{4[\Delta^2 + \delta^2]^2}{[(\Delta^2 - 2s_{33}\Delta - \delta^2)^2 + 4\Delta^2\Gamma_3^2]^2}, \qquad (2)$$

where $k_1 = 1$, $k_2 = \pi n_{e2} W^2$, $\Delta = (2E_{k_F} - E_{SL} - E_{SR} - s_{11} - s_{55})/2$, and $\delta = E_{SL} - E_{SR}$. n_{e2} is the number of the carriers per nm^2, and $s_{ij} \equiv \int |V_{\rm tun}(k_i)|^2/(E_{k_i} - E_{k_j})$ is the self-energy. $\Gamma_i \approx 2\pi|V_{\rm tun}(k_i)|^2\rho_F$ (ρ_F is the density of state at Fermi energy E_F, and $V_{\rm tun}$ is the overlap of wave functions between the channel and the QDs in the tunneling Hamiltonian).

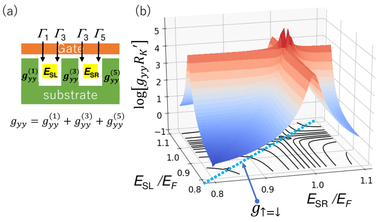

Figure 1: (a) Three current lines. (b)g_{yy} as functions of energy levels of two quantum dots.

Figure 1(b) shows the conductance g_{yy} of the summation of the three current lines $g_{yy}^{(i)}$ ($i \in 1,3,5$) as a function of the energy levels of the two QDs, where E_{SL} and E_{SR} are either $E_{S\downarrow}$ or $E_{S\uparrow}$. We can observe a double-peak structure around the Fermi energy where E_{SL} is close to E_{SR} but $E_{SL} \neq E_{SR}$. The symmetric case $\delta = 0$ gives the conventional resonant tunneling form $g = 4/[(\Delta - 2s_{33})^2 + 4\Gamma_3^2]^2$.

References

[1] T. Tanamoto and K. Ono, AIP Advances 11 (4), 045004 (2021).

Change in period of ordinary earthquakes due to the interaction with slow earthquakes

Takehito SUZUKI
Dept. Phys. Sci., Aoyama Gakuin University
5-10-1, Fuchinobe, Chuo-ku, Sagamihara, Kanagawa 252-5258

Two qualitatively different behaviors of earhtquakes have been known. One is the ordinary earthquake, which we feel naturally. The other one is slow earthquakes, which generate negligible seismic waves. Although the slow earthquakes are not disastrous, they are considered to sometimes change to the ordinary earthquakes after several repetitions. Whether this transition occurs or not is a fatal problem to the human society, and we should clarify the condition for the transition to occur.

The fault rocks can be considered as poroelastic media, including pores inside it. The pores are usually considered to be filled with water. If the dynamic earthquake slip (frictional slip) occurs, we can consider the interaction among heat, fluid pressure, and porosity [1, 2]. The slip is interpreted as the deformation around the contact area, called slip zone, which has a finite width. During the dynamic slip, the generation of pores [frictional heating] reduces [raises] the fluid pressure in the slip zone, inducing the increase [reduction] in the friction stress and the reduction [increase] in the slip velocity [1, 2]. Therefore, the slow and ordinary earthquakes are dominated by the generation of pores and the frictional heating, respectively.

The spring-block model and the interaction between three quantities are employed to analyze the slow-ordinary transition. The single block is assumed here. The upper substrate is drived with the constant speed V_p, and it also loads the block via a spring whose spring constant is k_p. As widely known, this system repeats the dynamic slip and cessation. The healing of pores in the cessation time is also taken into account. However, the choice of the healing law does not induce qualitative changes in the result below.

We neglect the heat and fluid diffusions during the dynamic slips. The governing equations for the fluid pressure, porosity, and temperature in the slip zone during the dynamic slip are given by

$$\dot{p} = C_1\dot{T} - M_0\dot{\phi}, \tag{1}$$

$$\dot{\phi} = \alpha_0\dot{u}\left(1 - \frac{\phi}{\phi_\infty}\right), \tag{2}$$

$$\dot{T} = -C_2(\sigma_n^0 + p)\dot{u}, \tag{3}$$

respectively, where C_1 and C_2 are positive constants. From here and below, quantities not explained are summarized in Ref. [2]. From Eq. (2), we obtain

$$\phi = \phi_\infty - (\phi_\infty - \phi_0)e^{-\alpha_0 u/\phi_\infty}, \tag{4}$$

where ϕ_0 is the porosity at the intant of the slip onset. Note that this value need not equal to the value at time $t = 0$. Additionally, from Eqs. (1)–(4), we obtain

$$\dot{p} = \left(-C_1C_2(\sigma_n^0 + p) - M_0\left(1 - \frac{\phi_0}{\phi_\infty}\right)\alpha_0 e^{-\alpha_0 u/\phi_\infty}\right)\dot{u}, \tag{5}$$

where $\gamma = C_1C_2 > 0$. From this representation, we can write p in terms of u to obtain

$$p = \left(\sigma_n^0 + p_0 - \frac{M_0'\alpha_0}{\frac{\alpha_0}{\phi_\infty} - \gamma}\right)e^{-\gamma u} + \frac{M_0'\alpha_0}{\frac{\alpha_0}{\phi_\infty} - \gamma}e^{-\alpha_0 u/\phi_\infty} - \sigma_n^0, \tag{6}$$

where $M_0' \equiv M_0(1-\phi_0/\phi_\infty)$ and p_0 is the fluid pressure at the instant of slip onset.

We now consider the energy conservation law. First, note that the loading stress from the upper substrate must be equal to the macroscopic static friction stress at the instant of the slip onset, which leads to

$$k_p V_p t_i = -\mu_{\mathrm{stat}}(\sigma_n^0 + p_0), \tag{7}$$

where t_i is the time when the slip initiated. Using Eq. (7), the energy stored in the upper spring just before the dynamic slip is given by

$$E_1 = \frac{1}{2}k_p(V_p t_i)^2 = \frac{1}{2}\frac{\mu_{\mathrm{stat}}^2}{k_p}(\sigma_n^0 + p_0)^2. \tag{8}$$

Moreover, the energy stored in the upper spring after the cessation is written as (we assume that the upper spring does not move during the dynamic slip)

$$\begin{aligned} E_2 &= \frac{1}{2}k_p(V_p t_i - u_f)^2 \\ &= \frac{1}{2}k_p\left(-\frac{\mu_{\mathrm{stat}}}{k_p}(\sigma_n^0 + p_0) - u_f\right)^2, \end{aligned} \tag{9}$$

where u_f is the final slip distance for the single slip. Furthermore, the work done to the block by the friction stress during the dynamic slip is obtained using Eq. (6):

$$\begin{aligned} E_{\mathrm{fric}} &= \int_0^{u_f}\Big(-\mu_{\mathrm{slid}}(\sigma_n^0 + p)\Big)\,du \\ &= -\mu_{\mathrm{slid}}\int_0^{u_f}\left[\left(\sigma_n^0 + p_0 - \frac{M_0\alpha_0}{\frac{\alpha_0}{\phi_\infty}-\gamma}\right)e^{-\gamma u} \right.\\ &\qquad \left. + \frac{M_0\alpha_0}{\frac{\alpha_0}{\phi_\infty}-\gamma}e^{-\alpha_0 u/\phi_\infty}\right]du \\ &= -\mu_{\mathrm{slid}}\left[\frac{1}{\gamma}\left(\sigma_n^0 + p_0 - \frac{M_0\alpha_0}{\frac{\alpha_0}{\phi_\infty}-\gamma}\right)(1-e^{-\gamma u_f}) \right.\\ &\qquad \left. + \frac{M_0\phi_\infty}{\frac{\alpha_0}{\phi_\infty}-\gamma}(1-e^{-\alpha_0 u_f/\phi_\infty})\right]. \end{aligned} \tag{10}$$

Therefore, from the energy conservation law, we found an equation which u_f must satisfy:

$$\begin{aligned} &\frac{1}{2}k_p u_f^2 + \mu_{\mathrm{stat}}(\sigma_n^0 + p_0)u_f \\ &-\mu_{\mathrm{slid}}\left[\frac{1}{\gamma}\left(\sigma_n^0 + p_0 - \frac{M_0'\alpha_0}{\frac{\alpha_0}{\phi_\infty}-\gamma}\right)(1-e^{-\gamma u_f}) \right.\\ &\qquad \left. + \frac{M_0'\phi_\infty}{\frac{\alpha_0}{\phi_\infty}-\gamma}(1-e^{-\alpha_0 u_f/\phi_\infty})\right] = 0. \end{aligned} \tag{11}$$

We define $F(u_f)$ as the left hand side of Eq. (11). The condition $F(u_f) = 0$ corresponds to the condition where the elastic energy change is equal to the energy loss due to the friction during the single slip. It is also important that $F(u_f)$ includes p_0 and ϕ_0. As mentioned, these initial values are not values at $t = 0$, but the values at the slip onset of each slip.

Notably, $F(u_f)$ is the double-well form, and the first well is much shallower than the second one. If $F(u_f) = 0$ has a solution between the wells, the slow earthquakes occur because we can consider that the slip is inhibited. On the other hand, if $F(u_f) = 0$ does not have a solution there, the solution jumps to almost two orders larger one. This behavior is interpreted as the first-order phase change. The slow-ordinary earthquake transition can be understood as the first-order phase change. Additionally, we can conclude that this phase change is governed by p_0 and ϕ_0.

The analytical result described here was confirmed by ISSP supercomputer. The numerical study can treat the BK model with several blocks, and we confirmed that the results here can give useful implications to such a several-block case. Detailed and comprehensive numerical treatments will be a potential future work.

References

[1] T. Suzuki, and T. Yamashita: J. Geophys. Res. **119** (2014)

[2] T. Suzuki: Phys. Rev. E **96** (2017)

3.5 SCCMS Projects

Development of machine learning-aided simulations methods for molecular liquids

Hayato SHIBA
Information Technology Center, University of Tokyo
6-2-3 Kashiwa-no-ha, Kashiwa, Chiba 277-0882

Thanks to the present status of the art where basic simulation methodology for parallel MD simulations is approaching its maturity, many open source packages are commonly available for usage on supercomputers. However, how to simulate long-time phenomena remains a long-standing unresolved issue in molecular dynamics simulations. It is difficult to perform numerical time integration over 10^{10} steps which corresponds to 10 μs in all-atom modeling. I am pursuing a methodology for realizing simulation that can allow computations on both large-scale and long-time. The key to realizing this is the efficient usage machine learning for capturing the dynamical paths in the phase space. For a class of glassy materials, it is recently found that static structure have the power to predict in which regions particles have a high tendency to move over a long time by means of deep learning in terms of the graph neural networks (GNNs) [1]. In FY 2021, after October, we have started to further extend the predictive power of GNN.

Firstly I confirmed that results of a previous study [1] can be fully reproduced, both quantitatively and qualitatively, by using the dataset provided by its authors. The system I consider is Kob-Andersen-type Lennard-Jones (KALJ) liquid, wherein two types of particles are enclosed in a box with different interaction parameters and particle radii to bypass crystallization.

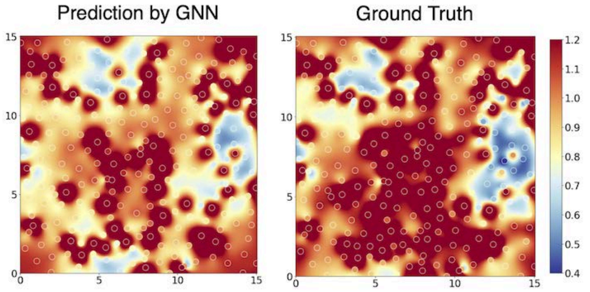

Figure 1: Color map indicating the predictive ability of particle propensity in KALJ liquid at a low temperature. where the 2D cross sections are shown here in the 3D system.

In Fig. 1, predicted propensity map is compared with the ground data in which the particle propensity is evaluated from direct molecular dynamics simulation. Further, I have extended the GNN learning model so that changeover in each neighbor pair distances can be learned as an edge feature on the GNN. As a result, the predictive ability has been extended into a wider temporal range, exceeding the propensity ability of the node feature (particle propensity) in Ref. [1] in the range-from 10^3 to 10^8 MD steps. I have also clarified that predictive ability of the original model is decreased because of its inability to treat the collective motion induced by strain displacement.

Most of the resources allocated for my ISSP project in FY2021 are spent on extending the dataset to longer-time. I have extended the dataset to cover the time region up to $100\tau_\alpha$, where τ_α represents glassy relaxation time called α-relaxation time. As a large number of simulation snapshot is required for learning, the dataset is, in fact, very large. By providing 32 different random initial velocities 500 independent initial particle configurations which are fully relaxed at a target temperature of consideration, I have conducted 16,000 simulation in total of 3D KALJ liquids with 4,096 particles by my in-house simulation code. As a result, I have successfully revealed that the GNN begins to lose its predictive ability at the time scale close to τ_α. All the above results mentioned will be soon submitted as an original paper [2]. In association with this work, we have conducted machine learning performance evaluation by using the same model on NVIDIA A100 GPUs, wherein the evaluation itself is performed on Wisteria/BDEC-01 supercomputer at ITC, Univ. of Tokyo [3].

Further, I have analyzed the internal structure of the code and rewritten it in full for PyTorch Geometric (PyG) code which is a library for training on GNNs on PyTorch, while all the original code written for TensorFlow and JAX is distributed by the authors of Ref. [1]. This PyTorch extension will enable the community to further combine these prediction methods with existing tools used in molecular simulations, because PyTorch has now become the most popular frameworks used in ML-aided molecular simulations. The PyG code will soon be made publicly available via our GitHub repository [4].

References

[1] V. Bapst *et al.*: Nat. Phys. **16**, 448-454 (2020).

[2] H. Shiba *et al.*: in preparation.

[3] H. Shiba and T. Shimokawabe: IPSJ SIG Technical Report, Vol. 2020-HPC-183(22), 1-11 (2022) (in Japanese).

[4] `https://github.com/h3-Open-BDEC/`

Finite temperature dependence of ab-initio Hamiltonians and its analysis for two-dimensional organic conductors Pd(dmit)$_2$ Salts

Kazuyoshi YOSHIMI[1], Takao TSUMURAYA[2], and Takahiro MISAWA[3]
[1]*Institute for Solid State Physics, University of Tokyo, Kashiwa 277-8581, Japan*
[2]*Priority Organization for Innovation and Excellence, Kumamoto University,*
Kumamoto 860-8555, Japan
[3]*Beijing Academy of Quantum Information Sciences, Haidian District, Beijing 100193, China*

The molecular solids β'-X[Pd(dmit)$_2$]$_2$ (where X represents a cation) exhibit various phases such as an antiferromagnetic phase, a quantum spin liquid, and a charge-ordered phase depending on the choice of X [1]. Comprehensive analyses of band calculations and transfer integrals based on the extended Hückel method and first-principles calculations have been carried out, and quantitative evaluation of the electronic states has been successfully performed [2]. However, electron correlation effects are expected to play a major role in order to elucidate the origin of these phenomena. Therefore, a quantitative derivation of the effective interactions using the constrained Random Phase Approximation (cRPA) is necessary for clarifying the microscopic origin of the stability of the quantum spin liquid. Moreover, it has been reported that the temperature dependence of the transfer integral is large for these materials [3]. The effective interactions are expected to have a similar temperature dependence.

In this study [4,5], we used the program RESPACK [6], which can derive the effective Hamiltonian describing low-energy degrees of freedom based on band structures obtained by first-principles calculations, to derive an effective Hamiltonian for the crystal structures reported in Ref. [3]. As a result, the transfer integrals tend to increase with decreasing temperature, while the effective interactions tend to decrease. The ratio of the transfer integral to the effective interaction was found to be about 20% smaller than that at room temperature. We also analyzed the obtained effective Hamiltonians using the exact diagonalization method with the boundary condition average by HΦ [7]. We find that the spin correlation function varies with the temperature dependence of the effective model, and in particular, the antiferromagnetic order moment decreases at β'-EtMe$_3$Sb[Pd(dmit)$_2$]$_2$, where the emergence of the quantum spin liquid is reported experimentally.

The overall tendency of the compound

dependence of the antiferromagnet ordered moment is consistent with the available experimental results. Our results demonstrate that the comprehensive derivation of the effective Hamiltonian and its analysis is a powerful method for elucidating the microscopic origin of exotic quantum states found in organic materials. In future research, we plan to apply this method to other organic materials that exhibit exotic quantum phases.

References

[1] R. Kato, Chem. Rev., 104, 5319–5346 (2004).

[2] K. Kanoda and R. Kato, Annu. Rev. Condens. Matter, Phys. 2, 167 (2011).

[3] K. Ueda, T. Tsumuraya and R. Kato, Crystals 8, 138(2018).

[4] T. Misawa, K. Yoshimi, T. Tsumuraya, Phys. Rev. Research 2, 032072(R) (2020).

[5] K. Yoshimi, T. Tsumuraya, T. Misawa, Phys. Rev. Research 3, 043224 (2021).

[6] K. Nakamura, Y. Yoshimoto, Y. Nomura *et al.*, Comp. Phys. Comm. 261, 100781(2021).

[7] M Kawamura, K Yoshimi, T Misawa *et al.*, Comp. Phys. Comm. 217, 180(2017).

Large-Scale GW/BSE electronic structure calculations for metal-organic hybrid materials

Takatoshi Fujita
National Institutes for Quantum Science and Technology
Tokai-mura, Naka-gun, Ibaraki 319-1106

Accurate calculations of electronic states are essential for computational studies of organic materials which are directed toward understanding of fundamental processes in organic electronic devices. We have recently developed the large-scale GW method based on the fragment molecular orbital method. The fragmentation approximation for the total polarization function and the ΔCOHSEX approximation have been employed for efficient evaluations of GW quasiparticle energies from localized molecular orbitals. More recently, we have proposed the novel large-scale excited-state methods based on the FMO, exciton model, and GW/BSE with Tamm-Dancoff approximation (TDA). In this method, the excited-state Hamiltonian matrix elements at the GW/TDA-BSE level is calculated in the basis of fragment configuration state functions which describe intrafragment excitations or interfragment charge-transfer excitations. The excited-state Hamiltonian is then diagonalized to approximate the adiabatic excited states of an entire system. We have confirmed that for molecular clusters, the novel fragment-based GW/TDA-BSE can reasonably reproduce the excited states obtained from conventional GW/TDA-BSE method. Our developments enables the applications of GW/TDA-BSE method to large molecular assemblies, which will be useful for investigating charge separation in condensed phase.

Recently, we have demonstrated that the accuracy of the total polarization function can be systematically improved by including the two-body correction terms. At the static COHSEX level, errors of less than 10 meV relative can be achieved for realistic molecular aggregates. However, residual errors of up to 100 meV are still present, originating from the Δ COHSEX approximation. In addition, we assessed the dependence of the total polarization function on the threshold distance and found that the convergence with respect to the threshold is slow. However, the threshold distance range of 1.5–2.0 nm was determined to be a reasonable compromise between the accuracy and computational effort, and the HOMO–LUMO gap and excitation energies reasonably reproduced in comparison with the results obtained without the cutoff. The present implementation offers a practical scheme for investigating large molecular systems. Applications to realistic molecular systems, such as organic light-emitting device materials and organic solar cells, are currently underway.

References

[1] T. Fujita, Y. Noguchi, J. Phys. Chem. A **13** (2020) 2728.

Doping effects on P2 $Na_xMn_{1-y}M_yO_2$ (M=Li, Mg, Al, Ti, V, Cr, Fe, Co, Ni) for sodium-ion rechargeable batteries: *Ab initio* investigations

Huu Duc LUONG[1,2], Hiroyoshi MOMIDA[2,3], Tamio OGUCHI[2,3]
[1]*Graduate School of Engineering, Osaka University, Suita, Osaka 565-0871, Japan*
[2]*SANKEN, Osaka University, Ibaraki, Osaka 567-0047, Japan*
[3]*ESICB, Kyoto University, Kyoto 615-8245, Japan*

P2 layered oxide Na_xMnO_2 exhibits a voltage window from 2.0 to 3.5V and high specific capacity up to 220mAh/g. However, the material suffers from the serious phase transformation during its charging/discharging.

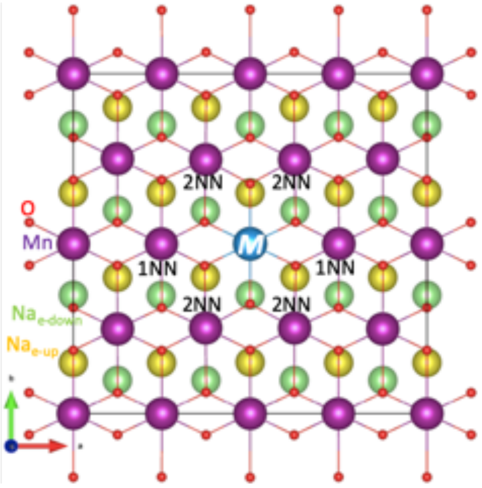

Fig. 1: Crystal structure of doped structure $NaMn_{1-y}M_yO_2$(y=0.0625, M = Li, Mg, Al, Ti, V, Cr, Fe, Co, and Ni) along c-axis. Purple, red, blue, yellow and green balls illustrate Mn, O, M, upper-layered and lower-layered Na atoms. Surrounding each dopant, there are two nearest Mn^{1NN} and four second nearest Mn^{2NN} atoms.

Through the highly accurate hybrid functional method (HSE06), we computationally evaluate the doping influences on the lattice distortions, stabilities, electronic structures, redox potentials, and diffusion mechanisms [1]. The model for calculation is shown in Fig. 1. Our calculations indicate that dopants not only reduce the lattice distortion degree, especially for Li, Mg, Ti, and V cases, but also increase the stability of the structure, implying the dopants would alleviate the Jahn-Teller lattice distortion, as shown in Figs. 2(a) and 2(b). Figure 2(c) illustrates that at full Na concentrations, all the considered dopants, except for Ti and V, have a small effect on the redox potential. At low Na concentrations, the Li dopant preferably diffuses out of the MnO_2 layer, but hardly moves to the Na layer, suggesting that P2-layered oxides can prevent the dopant's migrations during the Na extractions due to the high relative energies.

The effect on the diffusion mechanism is described through the diffusion of a Na ion–

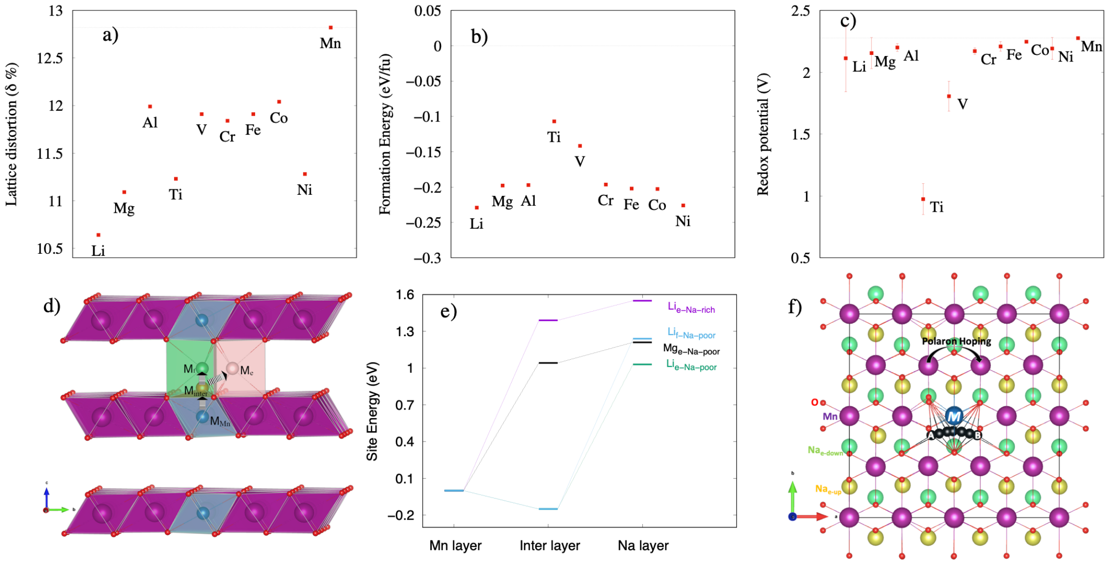

Fig. 2: a) Lattice distortion. b) Formation energy. c) Redox potential of $NaMn_{1-y}M_yO_2$. d) Dopant's migration path from Mn-layer site (blue balls) to intermediate site (brown balls) and to Na-layer face-shared sites (green balls) or edge-shared site (pink balls). e) Relative site energies of structures containing dopants at the Mn-layer site, intermediate site, edge-shared site and face-shared site in the Na-layer calculated along the dopant's migration paths (M=Li, Mg) at rich and poor Na contents. f) Diffusion path of a Na ion near the dopants. Green, yellow, red, purple, blue and black balls represent Na atoms at lower and upper layers, O, Mn, dopant M, and Na-vacancy trace. A and B stand for the initial and final position of Na ion for diffusion. An arrow indicates the polaron hopping between two adjacent Mn sites.

polaron complex near the dopant's environments, as shown in Fig. 2(f). Fe, Mg, Ti, and Cr dopants can hinder the Na ion-polaron complex diffusion with significantly higher activation energies, respectively, while the Al dopant almost remains the activation energy as well as the perfect structure. However, Li, V, Co, and Ni dopants benefit from such complex diffusion with much lower activation energy so the ion diffusivities increase significantly. It is found that the doping influence on the activation energy for Na ion diffusion is associated with the M–O bond change and charges of the neighboring dopants.

References

[1] H. D. Luong, H. Momida, V. A. Dinh, T. Oguchi, Phys. Rev. Materials **6**, 015802 (2022).

Ab initio study toward abundant element nanocatalysts with less precious metals

Tetsuya TAKETSUGU
Faculty of Science, Hokkaido University
N10W8, Sapporo, Hokkaido 060-0810

DFT computations with QuantumEspresso (QE) are used to gain chemical insights and to design novel catalysts with abundant elements such as hexagonal boron-nitride (h-BN) for reducing costs and dependences on precious metals used in various heterogeneous catalysts.

We have elucidated the catalytic activity of oxygen functionalized hexagonal boron nitride (h-BN) with *B-O-O-B* and *B-O-B* active sites at the zigzag edges for oxidative dehydrogenation (ODH) of light alkanes, specifically ethane (C_2H_6), propane (C_3H_8), butane (C_4H_{10}), and isobutane ($HC(CH_3)_3$) [1]. It has been found that the reaction pathway involves two H atom transfer steps with small activation energies. We have demonstrated that the synergy of two active sites, *B-O-O-B* and *B-O-B*, is crucial for the first and second H-transfer, respectively. We have demonstrated that these active sites play an important role in producing alkenes counterpart of the mentioned alkanes. The charge redistribution during H-transfers and localized oxygen atomic states in the conduction band are explored to suggest possible descriptors for the rational design of new catalysts. The universal action of the *B-O-O-B* and *B-O-B* active sites for ODH of the light alkanes paves the way for metal-free BN-based materials for future catalytic applications.

Alumina-supported nickel-based catalysts, $Ni@Al_2O_3$, constitute an important class of catalytic materials with a wide range of industrial applications, such as natural gas reforming for syngas production and oxidative dehydrogenation (ODH) of alkanes. When used in ODH catalysis, it has been assumed that the active species in these materials are NiO crystallites dispersed on alumina and nickel aluminate species ($NiAl_2O_4$), both with Ni in its common +2 oxidation state. These morphologies are believed to be responsible for the high selectivity of this class of catalysts as compared to unsupported pure NiO crystallites. However, more recently, the formation of a Ni^{3+} species, which promotes the isolation of electrophilic oxygen (O^-), has been invoked to explain the high selectivity for ethylene formation from ethane. The complexity and inhomogeneity of the condensed phase reaction environment often preclude a complete molecular-level understanding of the active species and underlying reaction mechanisms. Therefore, it proves helpful to study small metal oxide clusters in the gas phase. Such clusters provide atom-specific insights into the interactions governing structure-reactivity correlations at the molecular level and ultimately can serve as isolated model systems for active sites in real catalysts. Therefore, we have studied the geometric and electronic structures of $Ni_xAl_yO_z^+$ clusters to identify such model systems for $Ni@Al_2O_3$ ODH catalysts [2]. As charged clusters are required for mass selection, we have chosen mixed metal oxide cations with the composition $(NiO_m)(Al_2O_3)_n(AlO)^+$ with m = 1-2 and n = 1-3. For m = 1, the addition of the NiO moiety ensures formally fully oxidized clusters with all metal atoms in their most common oxidation state (Al^{3+} and Ni^{2+}). Addition of one more O atom in the m = 2 series allows for the study of oxygen-rich species, which may contain less common Ni^{3+} centers in combination with O^{-} species such as those invoked to explain enhanced ODH selectivity.

Borophene is a collective name for two-dimensional (2D) boron sheets or crystalline atomic monolayers of boron. Typically, such sheets have to contain periodic B vacancies to maintain structural stability, and these vacancies may appear in a great variety of different motifs. This makes borophene a highly polymorphic material. A great variety of borophene structures were extensively studied in the past decade in the quest for graphene-like materials with potential for advanced applications in catalysis and technology. Among them, the 2D honeycomb boron is of specific interest as a structural analog of graphene. Recently it has been synthesized on the Al(111) substrate; however, it remains unknown to what extent does honeycomb boron behaves like graphene. Therefore, we have elucidated the structural and electronic properties of this unusual 2D material using extensive DFT calculations in order to explain recent experimental findings [3]. We have demonstrated that in contrast to graphene on lattice-mismatched metal surfaces, honeycomb boron cannot wiggle like a blanket on Al(111), but rather induces reconstruction of the top metal layer, forming a stoichiometric AlB_2 sheet on top of Al. Our conclusions from theoretical modeling are fully supported by X-ray absorption spectra showing strong similarity in the electronic structure of honeycomb boron on Al(111) and thick AlB_2 films. On the other hand, a clear separation of the electronic states of the honeycomb boron into $\pi-$ and $\sigma-$subsystems indicates an essentially 2D nature of the electronic system in both one-layer AlB_2 and bulk AlB_2. In other words, honeycomb boron essentially matched the metallic substrate aluminum' s structure so closely that it could not be considered an independent, freestanding layered material.

References

[1] S. Kumar, A. Lyalin, Z. Huang, and T. Taketsugu, *Catalytic Oxidative Dehydrogenation of Light Alkanes over Oxygen Functionalized Hexagonal Boron Nitride*, ChemistrySelect **7**, e202103795 (2022).

[2] Y. Li, M. C. Babin, S. Debnath, T. Iwasa, S. Kumar, T. Taketsugu, K. R. Asmis, A. Lyalin, D. M. Neumark, *Structural Characterization of Nickel-Doped Aluminum Oxide Cations by Cryogenic Ion Trap Vibrational Spectroscopy*, J. Phys. Chem. A **125**, 9527-9535 (2021).

[3] A. Preobrajenski, A. Lyalin, T. Taketsugu, N. A. Vinogradov, and A. S. Vinogradov, *Honeycomb Boron on Al(111): from the Concept of Borophene to the Two-Dimensional Boride*, ACS Nano **15**, 15153 – 15165 (2021).

Development of fundamental simulation code for magnetic materials

Tetsuya FUKUSHIMA
Institute for Solid State Physics, University of Tokyo
Kashiwa-no-ha, Kashiwa, Chiba 277-8581

This year, we have developed a fundamental simulation code for calculating the magnetic properties of permanent magnets and spintronics materials. The automatic exhaustive calculations in this study are based on the all-electron full-potential (Korringa-Kohn-Rostoker) KKR Green's function method (FP-KKR). Since the potential is anisotropic rather than spherically symmetric, we can calculate not only the magnetization and Curie temperature but also the magnetocrystalline anisotropy energy constant (K_u) with high accuracy. The KKR Green's function method can also be conveniently combined with the coherent potential approximation (CPA). It is free from using supercells, resulting in reduced computational costs drastically. Therefore, it is possible to perform efficient calculations for a huge number of compositions of disordered alloys. We have applied this calculation method to $\mathrm{YCo_5}$ $\mathrm{SmCo_5}$, and $\mathrm{Sm_2Fe_{17}N_3}$ based alloys.

Fig. 1 shows the calculated K_u and magnetization (J_s) of $\mathrm{Y(Co,Fe,Ni,Cu)_5}$. The addition of low concentrations of iron, nickel, and copper alone increases K_u as compared to the value of $\mathrm{YCo_5}$. On the other hand, J_s decreases at low concentrations regardless of the type of added elements. For high concentration ranges, the addition of cobalt and nickel constantly decreases the J_s. In contrast, an increase in J_s can be confirmed for the iron additions in the high concentration region; from the upper right of Fig. 1, $\mathrm{YFe_3Co_2}$ can be recognized as the material with the largest K_u and J_s among calculated compositions.

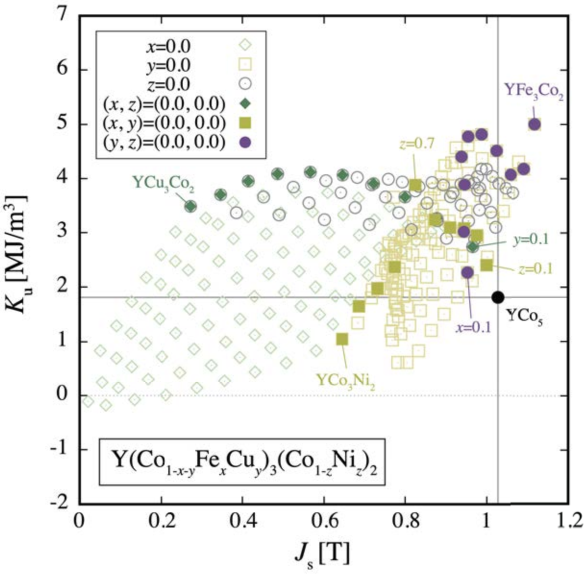

Figure 1: Calculated K_u and J_s for disordered $\mathrm{Y(Co,Fe,Ni,Cu)_5}$.

In practice, the 1-5 phases cannot exist stably at high iron concentrations. In samarium systems, nickel has been added as a stabilizing element to the 1-5 phases [1]. A similar composition, $\mathrm{YFe_3(Co_{1-z}Ni_z)_2}$, is also considered for the yttrium system. However, the performance deteriorates as a trade-off for phase stability; thus it is necessary to search for the optimum composition. In the present study, it was confirmed that up to $z \sim 0.5$, the anisotropy field is comparable to that of $\mathrm{YCo_5}$.

References

[1] A. Landa, P. Söderlind, E. E. Moore, and A. Perron, Appl. Sci. **10**, 1 (2020).

Novel chloride solid electrolytes for all solid-state sodium metal battery (2)

Masanobu NAKAYAMA, Naoto TANIBATA, Ryo KOBAYASHI

Department of Advanced Ceramics,

Nagoya Institute of Technology, Gokiso-chi, Showa-ku, Nagoya, Aichi 466-8555

Since discovery of fast Li^+ conductive chloride, Li_3YCl_6, by Asano *et al.* in 2018[1], much attention has been developed for searching high ionic conductive chlorides. In this study, we focused on search for novel Na^+ conductive chlorides in terms of “element strategy” (Japanese government policy in science and technology since 2007). Using high-throughput force field (FF) calculations, Na ion conductivities are evaluated exhaustively for chloride materials registered in the Materials Project database.[2] Total 135 compounds which contains Na and Cl (excluding H, Li, B, C, N, O, F, S, and so on) are selected from the database, and their FF potential parameters are optimized by using cuckoo search algorithm. So far, ~ 80 compounds are optimized by referring first-principles molecular dynamics (FPMD) datasets and their Na ionic conductivities are evaluated by using FF molecular dynamics (FFMD) approach. Note that FF parameter optimization and FFMD calculations were performed using NAP software.[3,4]

Figure 1 shows a typical example of radial distribution function (RDF) for a Na and Cl-containing compound calculated by FPMD and FFMD, showing good accordance between two approaches. Hence, the optimized FF parameters are reliable. Figure 2 displays histogram of Na ion conductivity at room temperature for 86 Na-Cl containing materials. The results indicate a few samples show fast Na+ conductivities, > 10^{-3} S/cm. Currently, we are synthesizing and evaluating ionic conductivity experimentally.

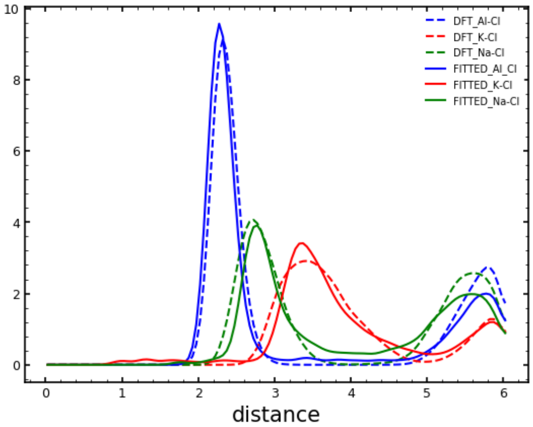

Fig. 1: Comparison between FPMD and FFMD derived RDF. FF parameters are optimized by cuckoo search algorithm.

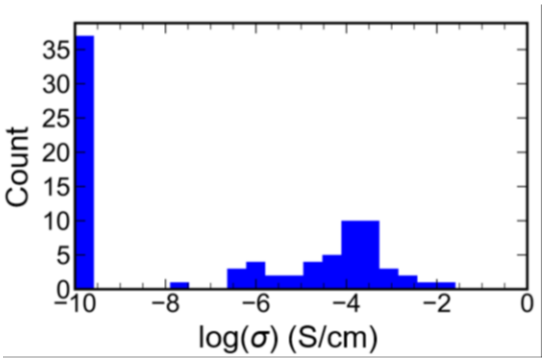

Fig. 2: Histogram of Na+ conductivities for Na-Cl containing materials.

References

[1] T. Asano, A. Sakai, S. Ouchi, M. Sakaida, A. Miyazaki, S. Hasegawa, Solid Halide Electrolytes with High Lithium-Ion Conductivity for Application in 4 V Class Bulk-Type All-Solid-State Batteries, Adv. Mater. 30 (2018) 1803075. https://doi.org/https://doi.org/10.1002/adma.201803075.

[2] A. Jain, S.P. Ong, G. Hautier, W. Chen, W.D. Richards, S. Dacek, S. Cholia, D. Gunter, D. Skinner, G. Ceder, K.A. Persson, Commentary: The Materials Project: A materials genome approach to accelerating materials innovation, APL Mater. 1 (2013) 11002. https://doi.org/10.1063/1.4812323.

[3] R. Kobayashi, nap: A molecular dynamics package with parameter-optimization programs for classical and machine-learning potentials, J. Open Source Softw. 6 (2021) 2768. https://doi.org/10.21105/joss.02768.

[4] R. Kobayashi, Y. Miyaji, K. Nakano, M. Nakayama, High-throughput production of force-fields for solid-state electrolyte materials, APL Mater. 8 (2020). https://doi.org/10.1063/5.0015373.

Development of high-performance permanent magnets by large-scale simulation and data-driven approach

Takashi MIYAKE
CD-FMat, AIST
Umezono, Tsukuba, Ibaraki 305-8568

Rare-earth transition-metal compounds are potential main-phase for strong permanent magnets. High content of 3d transition metals (Fe or Co) leads to high saturation magnetization, whereas rare-earth elements are essential for strong magnetocrystalline anisotropy. Because of this, structure search for Fe/Co-rich rare-earth compounds have attracted great interest. There are several known structures, such as the $CaCu_5$-type structure, the Th_2Zn_{17}-type structure and the $ThMn_{12}$-type structure. The $CaCu_5$-type structure is the simplest among them, and the others are obtained by substituting transition-metal pairs (dumbbells) for rare-earth sites. There are variety of other structures obtained by different arrangement of dumbbells. In this study, we have investigated stability of these structures [1].

As a first step, we prepare a 2×2×2-supercell of $SmFe_5$ and $SmCo_5$ in the $CaCu_5$-type structure, and generate hypothetical structures by replacing a part of Sm atoms with dumbbells. We compute the formation energy of all possible arrangements by density functional theory in the generalized gradient approximation. We then construct a cluster expansion model. We evaluate the formation energy of complex structures using the cluster expansion model. The result is shown in Fig.1, where the formation energies for various structures are plotted against dumbbell concentration (x). We see many structures between x=1/3 and x=1/2 whose formation energy is comparable with those of the Th_2Zn_{17}- and $ThMn_{12}$-type structures. In contrast, the formation energy increases for $x > 1/2$.

The black solid line in the figure is the formation energy of disordered phase (so-called $TbCu_7$-type structure). We compute the configuration entropy in the Bragg-Williams approximation, and evaluate the formation free energy. We found that as the temperature increases, the disordered phase is stabilized, and the solubility limits of dumbbells in $SmFe_z$ and $SmCo_z$ are estimated to be $z \sim 9$ at high temperature (T=0.15 eV).

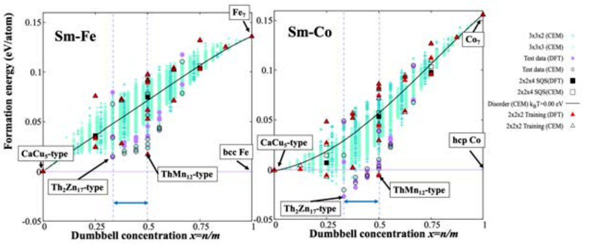

Figure 1: Formation energy of Sm-Fe and Sm-Co systems as a function of dumbbell concentrations [1].

References

[1] Fumiaki Kuroda, Taro Fukazawa and Takashi Miyake, Phys. Rev. Materials **5**, 124405 (2021).

Search for the optimum interface structure with sodium ion and ion liquid on graphene using topological descriptor and machine learning

Yohei Shimizu & Hitoshi Washizu
Graduate school of simulation studies, University of Hyogo
7-1-28 Minatojima-minamimachi, Chuo-ku, Kobe, Hyogo 650-0047

1 Background and Objective

1.1 Importance of controlling the Interface of sodium ion battery

Inexpensive and large-capacity sodium-ion batteries are attracting attention as a stationary secondary power source. Ionic liquids as electrolyte is known to have the effect of increasing the diffusion of sodium ions, and optimal compounding is required.

1.2 Needs and challenges of Materials Informatics (MI)

MI predicts the properties of unknown materials from information on known materials [1] and are expected to shorten the development period. Interface MI is difficult and few previous research because of Unknown descriptor representing interface state and Infinite combinations.

1.3 Objective of our research

We establish prediction method of optimizing Interface condition of cathode sodium ion battery with physical backing using by new topolgical descriptor as persistent homology.

2 Simulation and Estimation method

In this research, the objective variable is the self-diffusion coefficient of sodium ion. we etsimate optimizing self-diffusion coefficient condition by using results of MD simulation as teaching data. Table 1 is the method of MD simulation using LAMMPS. Considering machine learning model, we use topological descriptor as persistent homology. In general method of MI estimation model, experimentail conditions such as temprature and quantity etc. is used as descriptor. The problem of these method applied to the interface simulation MI is that the search range of interface cannot be simulated infinitely and these descriptor cannot represent the physical phenomenon directly. In our previous research [2], persistent homology can express amorphas structure of polymer as persistent diagram in two dimensions based on atomic coordinates (Fig. 1). We consider persistent homology as descriptor of interface MI.

3 Results

3.1 Ability to express Interface condition using persistent homology

We compare the bulk and the interface, the diffusion coefficient in the direction parallel to the interface increased. The effect on the interface is clarified by the inverse analysis of the persistent diagram. In this results, persistent diagrams can describe the state of the interface directly (Fig. 2). It can be found of the conditions for controlling the diffusion coefficient.

3.2 Prediction of self-diffusion coefficient

Regardless of the type of ionic liquid, the structure with a high diffusion coefficient shows the uniformity of the cluster. Predictions while preserving the physical meaning by directly machine learning the persistent diagram. The predictability of the interface condition using the persistent diagram as a descriptor is shown although improving accuracy is an issue (Fig. 3).

4 Conclutions

Persistent homology can express differences sodium ion and ion liquid state near graphene. Optimal interface condition can be predicted from the search range by using a persistent diagram as a descriptor.

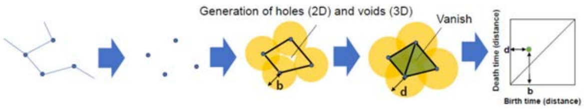

Figure 1: Principle of Persistent homology [3, 4]

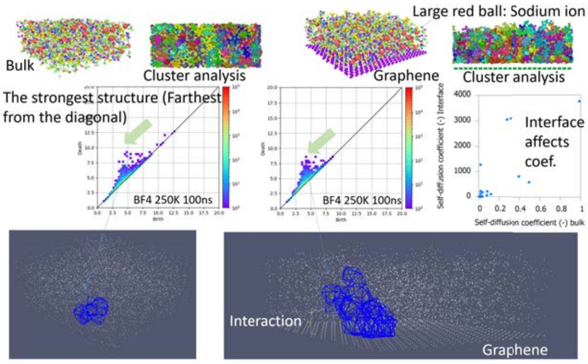

Figure 2: Difference between ion liquid bulk and interface by using persistent homology

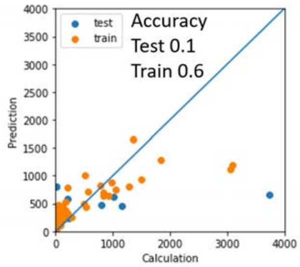

Figure 3: Prediction of the self-diffusion coefficient of sodium ion by random forest model

References

[1] Fujimura, K., Seko, A. Tanaka, I, et al.: Adv. Energy Mater. **3** (2013) 980-985.

[2] Shimizu, Y., Kurokawa, T., Arai, H. Washizu, H.: Sci. Rep. **11** (2021) 2274.

[3] I.Obayashi: Siam J. Appl. Algebra Geometry **vol.2 No.4** (2018) 508-534.

[4] http://www.wpi-aimr.tohoku.ac.jp /hiraoka_labo/homcloudenglish.html

Table 1: LAMMPS calculation conditions

conditions	value
Cell size	$9.12 \times 51.048 \times 20$Å
Boundary condition	Periodic
Force field & Charge	Lopes' OPLS & AM1-BCC
Graphene LJ parameter	$\sigma = 0.319/nm$, $\epsilon = 0.392/KJ/mol$
Ion liquid quantity	Na^+ 79 $\sim$ 159, $TFSI^-$ 134 or BF^{4-} 214, EMI^+ (Total charge = 0)
Calculation method	NVT ensemble
Temperature	250K, 300K, 350K, 400K, 450K
Time	100ns (Used to create the initial structure)

3.6 Software Advancement Projects and Workshop Support

Improvement of Quantum ESPRESSO implementing the ESM-RISM method

Minoru OTANI
Center for Computational Sciences, University of Tsukuba
1-1-1 Tennodai, Tsukuba, Ibaraki, 305-8577

In this project, we modified the source code of the Quantum ESPRESSO (QE) package, a popular open-source code for studying the electronic structure of materials with the density functional theory (DFT).

Before starting the project, we implemented several simulation techniques to elucidate a microscopic detail of an electrochemical reaction and atomic geometry under an electrochemical environment at the electrode and electrolyte interface, called the electrochemical interface. To reduce the calculation time for obtaining the equilibrium electrolyte distribution, we utilized the classical liquid theory, called the reference interaction site model (RISM), in a particular part of the electrolyte region [1]. The RISM region can describe the electric double layer near the interface, which includes the accumulation and depletion of the counter-ions in the electrolyte when introducing an excess charge on the electrode surface by applying a bias voltage. These techniques are made possible by introducing a grand canonical ensemble for both electrons on the electrode [2] and ions in the electrolyte [1] and solving the Poisson equation of the system under the open boundary condition along the perpendicular direction of the interface [3]. We call this hybrid simulation technique applicable to interfacial electrochemistry the ESM-RISM method.

In the ESM-RISM method, we need to solve the Laue represented Poisson and RISM equations.

$$\{\partial_z^2 - g_\parallel^2\} V(\boldsymbol{g}_\parallel, z) = -4\pi\rho(\boldsymbol{g}_\parallel, z), \tag{1}$$

$$h_\gamma(\boldsymbol{g}_\parallel, z) = \sum_\alpha \int \mathrm{d}z' c_\alpha(\boldsymbol{g}_\parallel, z') \times \chi_{\alpha\gamma}(\boldsymbol{g}_\parallel, |z - z'|), \tag{2}$$

where $\boldsymbol{g}_\parallel$, $g_\parallel$, ρ, h, c, χ, α, and γ represent, respectively, a wave vector parallel to the interface, the absolute value of $\boldsymbol{g}_\parallel$, the total charge density, the total correlation function, the direct correlation function, the solution susceptibility, the atomic sites of implicit and explicit solutions. These two equations are related through the electrostatic potential $V(\boldsymbol{g}_\parallel, z)$ [1]. In the first implementation of ESM-RISM, we used a common z mesh points for both Eqs. (1) and (2). Figure 1(a) shows the schematic illustration of the z mesh in the calculation cell. Since the mesh points along the z direction are common, the electrostatic potential can be easily shared in the equations, and this model is relevant for the thin electric double layer (EDL) system. However, we need to solve the RISM equation in a wide range of solution regions at low electrolyte concentrations because the EDL becomes thicker according to the Debye-Hückel theory. In this situation, it is more versatile to be able to solve the Eqs. (1) and (2) with different mesh spacing and different unit cell along z direction, L_z^{DFT} and L_z^{RISM} (see Fig. 1(c)). Thus we modify our ESM-RISM code from the original common mesh to an individual one.

To accomplish the goal, we need to map an arbitrary function f on the common mesh onto $\tilde{f}$ on the individual mesh. As seen in the figure. 1(d), we employ the Fourier interpolation

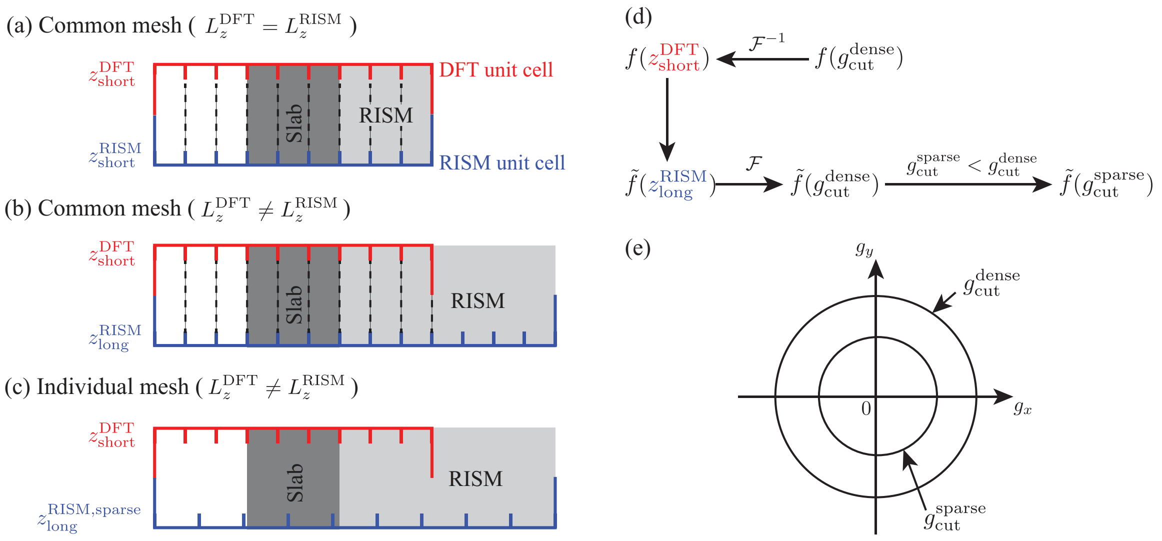

Figure 1: Schematic illustrations of a calculation cell. The z-mesh points used in DFT and RISM calculations for (a) a common mesh with same cell sizes along z-direction ($L_z^{\rm DFT} = L_z^{\rm RISM}$), (b) a common mesh with different cell sizes, and (c) an individual mesh with different cell size. The horizontal red and blue lines with grids represent the unit cell size along the z-direction for the DFT and RISM calculations. Conceptually, the $z_{\rm x}^{\rm y}$ indicates a grid point of x (= long or short) unit cell for y (= DFT or RISM) calculation. (d) The mapping sequence of an arbitrary function $f(g_{\rm cut}^{\rm dense})$ to $\tilde{f}(g_{\rm cut}^{\rm sparce})$, where $\mathcal{F}$ and $\mathcal{F}^{-1}$ are the forward and backward Fourier transform, respectively. (e) Schematic illustration of cutoff radii in the reciprocal space ($g_{\rm cut}^{\rm dense}$ and $g_{\rm cut}^{\rm sparse}$). The "sparse" in (c) means a sparse mesh with a small cutoff radius, $g_{\rm cut}^{\rm sparce}$.

scheme. First, we did the backward Fourier transform from $f(g_{\rm cut}^{\rm dense})$ to $f(z_{\rm short}^{\rm DFT})$, and then we map the f in the DFT cell onto the $\tilde{f}$ in the RISM cell by the following condition:

$$\tilde{f}(z) = \begin{cases} f(z) & z = z_{\rm short}^{\rm DFT}, \\ 0 & z \neq z_{\rm short}^{\rm DFT}. \end{cases} \tag{3}$$

After the forward Fourier transformation, the dense FFT grids $g_{\rm cut}^{\rm dense}$ is reduced to the sparse FFT grids $g_{\rm cut}^{\rm sparse}$ (see Fig. 1(e)). In the program, we first apply the mapping sequence from ρ to $\tilde{\rho}$. Secondly, by solving the Eq. (1) with $\tilde{\rho}$, the electrostatic potential in the RISM cell can include the contribution from the DFT charge. Finally, we solve the RISM equation Eq. (2) on the sparse grids $z_{\rm long}^{\rm RISM,sparse}$.

After finishing the code development, we checked the validity of our implementation by comparing the total energy and the force acting on atoms between the two calculations with Figs. 1 (a) and (c) configurations.

I would like to acknowledge Dr. Y. Motoyama, Dr. K. Yoshimi, and Dr. S. Hagiwara for their enthusiastic contribution to code development. This function is implemented under the support of " Project for advancement of software usability in materials science " in fiscal year 2021 by The Institute for Solid State Physics, The University of Tokyo.

References

[1] S. Nishihara and M. Otani: Phys. Rev. B **96** (2017) 115429.

[2] N. Bonnet, T. Morishita, O. Sugino, and M. Otani: Phys. Rev. Lett. **109** (2012) 266101.

[3] M. Otani and O. Sugino: Phys. Rev. B **73** (2006) 115407.

Unified platform of experiment-data analysis for 2D material structure

Takeo HOSHI[1,2]

[1] *Department of Mechanical and Physical Engineering, Tottori University,*
4-101 Koyama-Minami, Tottori 680-8550, Japan.

[2]Slow Positron Facility, Institute of Materials Structure Science, High Energy Accelerator Research Organization (KEK), Oho 1-1, Tsukuba, Ibaraki, 305-0801, Japan

In a PASUMS project at FY2021, an open-source data-analysis framework 2DMAT [1-4] has been developed for experimental measurements of two-dimensional material structures. The present project is the successor of one at FY2020. The current version of 2DMAT is an unified platform for the analysis of different experimental measurement techniques, total-reflection high-energy positron diffraction (TRHEPD) [5], surface X-ray diffraction (SXRD), and low-energy electron diffraction (LEED) experiments by installing corresponding forward problem solvers that generate diffraction intensity data from a given dataset of the atomic positions. Among them, SXRD and LEED were supported as a result of the present project. The current version of 2DMAT offers five analysis methods: (i) Nelder-Mead optimization, (ii) grid search, (iii) Bayesian optimization, (iv) replica exchange Monte Carlo (REMC) method, and (v) population-annealing Monte Carlo (PAMC) method. Methods (ii) through (v) are implemented by parallel computation, which is efficient not only for personal computers but also for supercomputers. Among the above five methods, the PAMC method was implemented in the present project. In addition, the forward problem solver of TRHEPD was also published as an open-source software package by the present project [6,7].

2DMAT was applied to the structure analysis of $Si_4O_5N_3$ / 6H-SiC(0001)-($\sqrt{3} \times \sqrt{3}$)R30° surface, a novel two-dimensional semiconductor, by TRHEPD experiment [2]. A data-driven sensitivity analysis was proposed for the quantitative analysis of experimental uncertainties. The variation over individual fitting parameters was analyzed by solving the eigenvalue problem of the variance-covariance matrix. 2DMAT was used also in other application studies by TRHEPD experiment and the study by T. Takeda (Waseda U.) *et al*. won a poster-session prize [8]. The analysis methods in 2DMAT are general and can be applied also to other problems and was applied to a performance prediction of massively parallel computation by Bayesian inference [4].

As activities to promote 2DMAT, hands-on workshops were held in April 2021 and April

2022, and a study group was held in September 2021. Test calculations in massively parallel computations by the Fugaku supercomputer are underway (hp210228, hp210267).

References

[1] https://www.pasums.issp.utokyo.ac.jp/2DMAT

[2] T. Hoshi, *et al.*, Comp. Phys. Commun. 271 108186 (2022).

[3] Y. Motoyama *et al.*, Preprint: arXiv:2204.04484

[4] H. Kohashi, *et al.*, JSIAM Letters 14, 13 (2022).

[5] (Review) Y. Fukaya, *et al*, J. Phys. D: Appl. Phys. 52, 013002 (2019).

[6] https://github.com/sim-trhepd-rheed/

[7] T. Hanada, *et al.*, Comp. Phys. Commun., in press; Preprint: arXiv: 2110.09477

[8] T. Takeda *et al*., the Best Poster Presentation Award at the 2022 Kanto Chapter Conference of the Surface and Vacuum Society of Japan.

Report of CCMS hands-on sessions in the 2021 fiscal year

Kota IDO
Institute for Solid State Physics,
The University of Tokyo, Kashiwa-no-ha, Kashiwa, Chiba 277-8581

In the 2021 fiscal year, Center for Computational Materials Science (CCMS) in the Institute for Solid State Physics (ISSP) held three hands-on sessions where the ISSP supercomputer was used [1-3]. In this report, we briefly summarize the hands-on sessions.

Table 1 shows the list of the hands-on sessions in the 2021 fiscal year. Software used in the hands-on sessions are 2DMAT, PHYSBO, and HΦ: 2DMAT is a Python package to search an optimal result by applying a search algorithm to a direct-problem solver [4], PHYSBO is a Python library to perform a fast and scalable Bayesian optimization [5], and HΦ is a package of solvers for quantum many body systems [6]. Development of these software was supported by “Project for advancement of software usability in materials science” (PASUMS) [7]. In all of the hands-on sessions, lecturers explained the basics of each software and gave its tutorial. Materials of these hands-on sessions are available on each official page (in Japanese) [8-10].

Table 1: List of CCMS hands-on sessions where the ISSP supercomputer was used in the 2021 fiscal year.

Date	Lecturer	Software
Apr. 20	T. Hoshi et al.	2DMAT[4]
May 24	K. Tsuda et al.	PHYSBO[5]
Oct. 1	Y. Yamaji et al.	HΦ[6]

References

[1] https://ccms.issp.u-tokyo.ac.jp/event/4570

[2] https://ccms.issp.u-tokyo.ac.jp/event/4881

[3] https://ccms.issp.u-tokyo.ac.jp/event/5078

[4] https://www.pasums.issp.u-tokyo.ac.jp/2dmat/

[5] https://www.pasums.issp.u-tokyo.ac.jp/physbo/

[6] https://www.pasums.issp.u-tokyo.ac.jp/hphi/

[7] https://www.pasums.issp.u-tokyo.ac.jp/

[8] https://www.pasums.issp.u-tokyo.ac.jp/2dmat/doc/paper/

[9] https://www.pasums.issp.u-tokyo.ac.jp/physbo/doc/paper/

[10] https://www.pasums.issp.u-tokyo.ac.jp/hphi/doc/presentation/

Supercomputer course of Computational Materials Design (CMD®) workshop

Masaaki GESHI[1], Yoshitada MORIKAWA[2], Tomoya ONO[3]
[1]*Institute for NanoScience Design,*
Osaka University, Machikaneyama, Toyonaka, Osaka 560-0043
[2] *Department of Precision Engineering,*
Osaka University, Yamada-oka, Suita, Osaka 565-0871
[3]*Center for Computational Science,*
University of Tsukuba, Tenno-dai, Tsukuba, Ibaraki 305-8577

The 39th Computational Materials Design (CMD®) workshop (CMD39) has been held from September 6th to September 10th and the 40th CMD® workshop (CMD40) has been done from February 21st to February 25th. Both were held online. In this workshop we have the supercomputer course to train up human resources to advance research by using system B supercomputer of ISSP, the University of Tokyo.

In CMD39 eight participants took the supercomputer course and got a tutorial on STATE-Senri developed by Y. Morikawa. After giving the introductory lecture of large-scale computing by M. Geshi and explaining how to use the supercomputer of ISSP, participants started constructing calculation models of their own research subjects with the help of the lecturers. Then they carried out calculations using supercomputers. Concrete themes were molecular adsorption on solid surfaces, chemical reactions at electrode interfaces, oxygen reduction reaction on carbon electrodes, and so on. The participants performed the calculations and examined the results.

In CMD38 two participants took the supercomputer course and used the supercomputer of ISSP. They got a tutorial on RSPACE developed by T. Ono. After giving the introductory lecture of large-scale computing by M. Geshi and introducing the calculation method of electronic states and electron conduction property using RSPACE, exercises instructed in the manual were carried out. Then, electronic structure calculations were carried out for various molecules, and the electronic density distribution was visualized. The attendees also performed massively parallel calculations to confirm the efficiency for parallel computing. Finally, the electron conduction property of molecules connected to atomic wires was analyzed.

4 PUBLICATION LIST

Example:

LASTNAME, Firstname [project class; # points (B), # points (C)] (Page #)
— *Project title*

1. First paper
   Names of Authors, etc.
2. Second paper
   ...

☐ ISSP Joint Research Projects

○ B–E classes

AKAI, Hisazumi [B class; 1300 (B), 90 (C)] (24)
— *Finite temperature magnetic properties of permanent magnet materials*
— *First-principles calculation of magnetocrystalline anisotropy of permanent magnet materials*

1. First-principles investigation of Nd(Fe,M)$_{12}$ (M = K–Br) and Nd(Fe,Cr,Co,Ni,Ge,As)$_{12}$: Possible enhancers of Curie temperature for NdFe$_{12}$ magnetic compounds
   T. Fukazawa, H. Akai, Y. Harashima, and T. Miyake, Acta.Mater. **226**, 117597 (2022).
   DOI:10.1016/j.actamat.2021.117597

2. Direct observation of magnetic Friedel oscillation at Fe(001) surface
   T. Mitsui, S. Sakai, S. Li, T. Ueno, T. Watanuki, Y. Kobayashi, R. Masuda, M. Seto, and H. Akai Hyperfine Interactions **242**,37 (2021).
   DOI:10.1007/s10751-021-01772-0

3. Atomistic theory of thermally activated magnetization processes in Nd$_2$Fe$_{14}$B permanent magnet
   Seiji Miyashita, Masamichi Nishino, Yuta Toga, Taichi Hinokihara, Ismail Uysal, Takashi Miyake, Hisazumi Akai, Satoshi Hirosawa, and Akimasa Sakumaa Sci. Tech. Adv. Mater. **22**,658 (2021).
   DOI:10.1080/14686996.2021.1942197

4. Data assimilation method for experimental and first-principles data: Finite-temperature magnetization of (Nd, Pr, La, Ce)$_2$(Fe, Co, Ni)$_{14}$B
   Y. Harashima, K. Tamai, S. Doi, M. Matsumoto, H. Akai, N. Kawashima, M. Itho, N. Sakuma, K. Kato, T. Shoji, and T. Miyake, Phys. Rev. Mater. **5**, 013806 (2021).
   DOI:10.1103/PhysRevMaterials.5.013806

5. Spin-wave dispersion and exchange stiffness in Nd$_2$Fe$_{14}$B and RFe$_{11}$Ti (R=Y, Nd, Sm) from first-principles calculations
   Fukazawa, H. Akai, Y. Harashima, and T. Miyake, Phys. Rev. B **103**, 024418 (2021).
   DOI:10.1103/PhysRevB.103.024418

AKASHI, Ryosuke [B class; 600 (B), 100 (C)] (141)
— *Development of the first-principles method for calculating Tc based on density functional theory for superconductors*

AOYAMA, Kazushi [B class; 1000 (B), 120 (C)] (276)
— *Effect of magnetic anisotropy on spin textures in pyrochlore antiferromagnets*
— *Stability of the hedgehog-lattice topological spin texture in breathing-pyrochlore antiferromagnets*

1. Emergent skyrmion-based chiral order in zero-field Heisenberg antiferromagnets on the breathing kagome lattice
   K. Aoyama and H. Kawamura, Phys. Rev. B **105**, (2022) L100407.
   DOI:10.1103/PhysRevB.105.L100407

2. Effects of spin-lattice coupling and a magnetic field in classical Heisenberg antiferromagnets on the breathing pyrochlore lattice
   K. Aoyama, M. Gen, and H. Kawamura, Phys. Rev. B **104**, (2021) 184411.
   DOI:10.1103/PhysRevB.104.184411

3. Spin Dynamics Simulation of the Z_2-vortex Fluctuations
   Yo. P. Mizuta, K. Aoyama, K. Tomiyasu, M. Matuura, and H. Kawamura, J. Phys. Soc. Jpn. **91**, (2022) 035001 SHORT NOTES.
   DOI:10.7566/JPSJ.91.035001

ARAI, Munehito [C class; 7600 (B), 0 (C)] (220)
— *Rational design of novel proteins for medical and industrial applications*
— *Theoretical Design of Novel Artificial Proteins to Inhibit Viral Infection*

ARAI, Toyoko [C class; 1400 (B), 500 (C)] (117)
— *RSDFT calculation of atomic displacement captured by energy dissipation channel of noncontact atomic force microscope*

ARIMA, Kenta [B class; 600 (B), 110 (C)] (288)
— *First-principles simulation of graphene nanoribbon and investigation of reactivity as machining catalyst*
— *Investigations of electronic structures and reactivity of graphene nanoribbons with different widths*

1. Atomic-scale insights into the origin of rectangular lattice in nanographene probed by scanning tunneling microscopy
   J. Li, S. Li, T. Higashi, K. Kawai, K. Inagaki, K. Yamamura, and K. Arima, Phys. Rev. B **103**, 245433 (2021).
   DOI:10.1103/PhysRevB.103.245433

ARUGA, Tetsuya [B class; 300 (B), 80 (C)] (166)
— *Interaction between magnetic metal phthalocyanine molecules and bi-layer metal films*

ASANO, Yuta [E class; 23500 (B), 2550 (C)] (206)
— *Effects of cavitation on soundwaves*
— *Molecular Dynamics Simulation of Complex Fluids*

1. Effects of polymers on the cavitating flow around a cylinder: A Large-scale molecular dynamics analysis
   Y. Asano, H. Watanabe, and H. Noguchi, J. Chem. Phys. **155**, 014905 (2021).
   DOI:10.1063/5.0056988

2. Effects of gas-liquid phase transitions on soundwave propagation: A molecular dynamics study
   Y. Asano, H. Watanabe, and H. Noguchi, Phys. Rev. Fluids, (2022) in press.

BUI, VANPHO [C class; 2200 (B), 350 (C)] (110)
— *Study on removal mechanism of single crystalline Si planarized by catalyst referred etching in pure*

water

EGAMI, Yoshiyuki [C class; 8600 (B), 1000 (C)] (64)
— *Development and application of first-principles method for electron-transport calculations of large-scale interface structures*
— *First-principles study on electron-transport through semiconductor interface structures*

FUCHIZAKI, Kazuhiro [C class; 3000 (B), 0 (C)] (256)
— *Kinetics of phase transition and polyamorphism*

1. Thermodynamics of polyamorphism
   K. Fuchizaki Mem. Fac. Sci. Ehime Univ. **24**, 43 (2022).

FUJII, Susumu [C class; 2600 (B), 0 (C)] (260)
— *Nanoscale phonon transport across ceramics interfaces*

1. Structure and lattice thermal conductivity of grain boundaries in silicon by using machine learning potential and molecular dynamics
   S. Fujii and A. Seko, Comput. Mater. Sci. **204**, 111137 (2022).
   DOI:10.1016/j.commatsci.2021.111137

FUJIMOTO, Satoshi [B class; 600 (B), 90 (C)] (196)
— *Topological nematic phase transition in Kitaev spin liquid*

FUJIMOTO, Yoshitaka [C class; 600 (B), 0 (C)] (145)
— *Physical properties of layered graphene*

1. Electronic states and modulation doping of hexagonal boron-nitride trilayer
   T. Haga, Y. Matsuura, Y. Fujimoto and S. Saito, Physical Review Materials **5**, 094003 (2021).

2. Stability of Hydrogen Boride Sheets in Water
   K. I. Rojas, N. T. Cuong, H. Nishino, R. Ishibiki, S. Ito, M. Miyauchi, Y. Fujimoto, S. Tominaka, S. Okada, H. Hosono, N. Arboleda, T. Kondo, Y. Morikawa, and I. Hamada, Communications Materials **2**, 1 (2021).

3. Chemistry and Physics of Carbon Nanotube Structures
   Y. Fujimoto, Handbook of Carbon Nanotubes, pp.1-19, edited by J. Abraham, S. Thomas, and N. Kalarikkal (Springer Nature 2021).

4. Detection of environmentally toxic molecules using carbon nanotubes: A first principles theoretical study
   Y. Fujimoto and S. Saito, Journal of The Electrochemical Society, **169**, 037512 (2022).

5. Theoretical study on quantum transport of carbon nanotubes for detecting toxic molecules: The role of dopants
   Y. Fujimoto, Journal of Electrochemical Science and Engineering, Accepted.

FUJINO, Tomoko [D class; 2500 (B), 0 (C)] (194)
— *Estimation of Coulomb repulsion in charge transfer salts of EDXT oligomers*

1. Conjugation length effect on the conducting behavior of single-crystalline oligo(3,4-ethylenedioxythiophene) (nEDOT) radical cation salts
   R. Kameyama, T. Fujino, S. Dekura, and H. Mori, Chem. Phys. Phys. Chem, 2022, 24, 91309134.
   DOI:10.1039/D2CP00250G

2. Band-filling Effects in Single-crystalline Oligomer Models for Doped PEDOT: 3,4-Ethylenedioxythiophene (EDOT) Dimer Salt with Hydrogen-bonded Infinite Sulfate Anion Chains
   R. Kameyama, T. Fujino, S. Dekura, S. Imajo, T. Miyamoto, H. Okamoto, and H. Mori, submitted to J. Mat. Chem. C, accepted.

FUJISHIRO, Hiroki [C class; 2600 (B), 0 (C)] ()
— *Strained Band-Structure Engineering for Antimonide-Based Terahertz Transistors*

FUKUDA, Jun-ichi [B class; 900 (B), 0 (C)] (280)
— *Calculation of ordered structures, dynamics and optical properties of soft materials*

1. Liquid Crystalline Half-Skyrmions and Their Optical Properties
   Jun-ichi Fukuda, Andriy Nych, Uliana Ognysta, Slobodan Žumer, and Igor Muševič, Annalen der Physik **534**, 2100336 (2022).
   DOI:10.1002/andp.202100336

FUKUDA, Masahiro [B class; 400 (B), 70 (C)] (156)
— *AB type 2D materials search by high-throughput DFT calculations*

1. A structure map for AB_2 type 2D materials using high-throughput DFT calculations
   Masahiro Fukuda, Jingning Zhang, Yung-Ting Lee, and Taisuke Ozaki, Mater. Adv., **2**, 4392 (2021).
   DOI:10.1039/d0ma00999g

FUKUDA, Tuneo [C class; 800 (B), 0 (C)] (139)
— *Molecular dynamics simulation of substitution reaction on metal surface*

FUKUMOTO, Yoshiyuki [B class; 700 (B), 0 (C)] (289, 290)
— *Numerical studies on excitation spectra of Heisenberg antiferromagnets on the triangular and kagome lattices*
— *Towards a unified understanding of thermodynamic properties in S=1/2 spherical kagome systems* $W_{72}V_{30}$ *and* $Mo_{72}V_{30}$

GOHDA, Yoshihiro [C class; 5200 (B), 800 (C)] (79)
— *Maximization of interface magnetoelectric coupling with Bayesian optimization*

1. Role of ferroelectricity, delocalization, and occupancy of d states in the electrical control of interface-induced magnetization
   R. Costa-Amaral and Y. Gohda, Phys. Rev. Appl. **15**, 064014 (2021).
   DOI:10.1103/PhysRevApplied.15.064014

2. Giant converse magnetoelectric effect in a multiferroic heterostructure with polycrystalline Co_2FeSi
   S. Fujii, T. Usami, Y. Shiratsuchi, A.M. Kerrigan, A.M. Yatmeidhy, S. Yamada, T. Kanashima, R. Nakatani, V.K. Lazarov, T. Oguchi, Y. Gohda, and K. Hamaya, NPG Asia Mater., in press.

3. Intrinsic superconductivity of two-monolayer-thick indium film
   T. Ogino, I. Seo, H. Tajiri, M. Nakatake, S. Takakura, Y. Sato, Y. Hasegawa, Y. Gohda, K. Nakatsuji, and H. Hirayama, submitted to Phys. Rev. Lett.

4. Origin of anisotropic magnetoresistance tunable with electric field in Co2FeSi/BaTiO3 multiferroic inetrfaces
   S. Tsuna, R. Costa-Amaral, and Y. Gohda, submitted to Phys. Rev. Mater.

GOHLKE, Matthias [C class; 4400 (B), 600 (C)] (233)

— *Ground state and dynamical properties of the J_1J_2K-Heisenberg model on the square lattice*

HAGITA, Katsumi [C class; 3600 (B), 0 (C)] (254)
— *DPD simulations of cross-linked networks to study topological effect using MP-SRP method*

1. Viscosity Overshoot in Biaxial Elongational Flow: Coarse-Grained Molecular Dynamics Simulation of RingLinear Polymer Mixtures
   T. Murashima, K. Hagita and T. Kawakatsu, Macromolecules **54**, 7210–7225 (2021).
   DOI:10.1021/acs.macromol.1c00267

2. Molecular Dynamics Simulations of Ring Shapes on a Ring Fraction in Ring-Linear Polymer Blends
   K. Hagita and T. Murashima, Macromolecules **54**, 8043–8051 (2021).
   DOI:10.1021/acs.macromol.1c00656

3. Role of chain crossing prohibition on chain penetration in ring-linear blends through dissipative particle dynamics simulations
   K. Hagita, T. Murashima, H. Shiba, N. Iwaoka, and T. Kawakatsu, Comput. Mater. Sci. **203**, 111104 (2022).
   DOI:10.1016/j.commatsci.2021.111104

HAMAGUCHI, Satoshi [C class; 8800 (B), 1050 (C)] (62)
— *Analysis of Surface Reactions in Atomic Layer Etching Processes*

HAMAMOTO, Yuji [C class; 1600 (B), 0 (C)] (123)
— *Global search for the structures of two-dimensional materials by Gaussian process regression*

HARADA, KENJI [C class; 2200 (B), 0 (C)] (263)
— *Data analysis method using a tensor network representation*

HARASHIMA, Yosuke [C class; 1000 (B), 0 (C)] (134)
— *Critical concentration of metal-insulator transition in doped semiconductors and Coulomb gap*
— *Critical exponent of metal-insulator transition in doped semiconductors and spin ordering*

1. Analysis of Kohn-Sham Eigenfunctions Using a Convolutional Neural Network in Simulations of the Metal-Insulator Transition in Doped Semiconductors
   Y. Harashima, T. Mano, K. Slevin, and T. Ohtsuki, J. Phys. Soc. Jpn. **90**, 094001 (2021).
   DOI:10.7566/JPSJ.90.094001

HARUYAMA, Jun [C class; 2800 (B), 750 (C)] (100)
— *Electrochemical reaction analysis using density functional calculation + implicit solvation model 3*

1. Thermodynamic Analysis of Li-Intercalated Graphite by First- Principles Calculations with Vibrational and Configurational Contributions
   J. Haruyama, S. Takagi, K. Shimoda, I. Watanabe, K. Sodeyama, T. Ikeshoji, and M. Otani, J. Chem. Phys. C **125**, 27891 (2021).
   DOI:10.1021/acs.jpcc.1c08992

HASHIMOTO, Tamotsu [C class; 3000 (B), 600 (C)] (253)
— *Molecular dynamics simulation of $BaTiO_3$ nano structure*

HATANO, Naomichi [B class; 400 (B), 70 (C)] ()
— *Novel Spectral Clustering Method of Directed Networks*

HATSUGAI, Yasuhiro [C class; 3200 (B), 600 (C)] (251)

— *Topological phases and science of bulk-edge correspondence by numerical methods*

1. Chiral edge modes in evolutionary game theory: A kagome network of rock-paper-scissors cycles
   T. Yoshida, T. Mizoguchi, and Y. Hatsugai, Phys. Rev. E 104, 025003 (2021).
   DOI:10.1103/PhysRevE.104.025003

2. Bulk-edge correspondence in the adiabatic heuristic principle
   K. Kudo, Y. Kuno, and Y. Hatsugai, Phys. Rev. B **104**, L241113 (2021).
   DOI:10.1103/PhysRevB.104.L241113

3. Adiabatic Continuity of the Spinful Quantum Hall States
   K. Kudo and Y. Hatsugai, arXiv:2201.07893
   DOI:10.48550/arXiv.2201.07893

HATTORI, Ken [B class; 300 (B), 60 (C)] ()
— *Atomic structure and electronic states for silicide films*

HAYAMI, Satoru [C class; 3400 (B), 650 (C)] (191)
— *Searching for meron crystal in itinerant magnets*

1. Essential role of anisotropic magnetic dipole in anomalous Hall effect
   S. Hayami and H. Kusunose, Phys. Rev. B **103**, L180407 (2021).
   DOI:10.1103/PhysRevB.103.L180407

2. Skyrmion crystals in centrosymmetric itinerant magnets without horizontal mirror plane
   R. Yambe and S. Hayami, Sci. Rep. **11**, 11184 (2021).
   DOI:10.1038/s41598-021-90308-1

3. Field-Direction Sensitive Skyrmion Crystals in Cubic Chiral Systems: Implication to 4f-Electron Compound EuPtSi
   S. Hayami and R. Yambe, J. Phys. Soc. Jpn. **90**, 073705 (2021).
   DOI:10.7566/JPSJ.90.073705

4. In-plane magnetic field-induced skyrmion crystal in frustrated magnets with easy-plane anisotropy
   S. Hayami, Phys. Rev. B **103**, 224418 (2021).
   DOI:10.1103/PhysRevB.103.224418

5. Spin-orbital-momentum locking under odd-parity magnetic quadrupole ordering
   S. Hayami and H. Kusunose, Phys. Rev. B **104**, 045117 (2021).
   DOI:10.1103/PhysRevB.104.045117

6. Multipole classification in 122 magnetic point groups for unified understanding of multiferroic responses and transport phenomena
   M. Yatsushiro, H. Kusunose, and S. Hayami Phys. Rev. B **104**, 054412 (2021).
   DOI:10.1103/PhysRevB.104.054412

7. Meron-antimeron crystals in noncentrosymmetric itinerant magnets on a triangular lattice
   S. Hayami and R. Yambe, Phys. Rev. B **104**, 094425 (2021).
   DOI:10.1103/PhysRevB.104.094425

8. Charge density waves in multiple-Q spin states
   S. Hayami and Y. Motome, Phys. Rev. B **104**, 144404 (2021).
   DOI:10.1103/PhysRevB.104.144404

9. Nonreciprocal magnon excitations by the Dzyaloshinskii-Moriya interaction on the basis of bond magnetic toroidal multipoles

T. Matsumoto and S. Hayami, Phys. Rev. B **104**, 134420 (2021).
DOI:10.1103/PhysRevB.104.134420

10. Temperature-driven transition from skyrmion to bubble crystals in centrosymmetric itinerant magnets
    S. Hayami, New J. Phys. **23**, 113032 (2021).
    DOI:10.1088/1367-2630/ac3683
11. Phase Shift in Skyrmion Crystals
    S. Hayami, T. Okubo, and Y. Motome, Nat. Commun. **12**, 6927 (2021).
    DOI:10.1038/s41467-021-27083-0
12. Locking of skyrmion cores on a centrosymmetric discrete lattice: Onsite versus offsite
    S. Hayami and R. Yambe, Phys. Rev. Research **3**, 043158 (2021).
    DOI:10.1103/PhysRevResearch.3.043158
13. Spin excitation spectra in helimagnetic states: Proper-screw, cycloid, vortex-crystal, and hedgehog lattices
    Y. Kato, S. Hayami, and Y. Motome Phys. Rev. B **104**, 224405 (2021).
    DOI:10.1103/PhysRevB.104.224405
14. Essential model parameters for nonreciprocal magnons in multisublattice systems
    S. Hayami and T. Matsumoto, Phys. Rev. B **105**, 014404 (2022).
    DOI:10.1103/PhysRevB.105.014404
15. Skyrmion crystal and spiral phases in centrosymmetric bilayer magnets with staggered Dzyaloshinskii-Moriya interaction
    S. Hayami, Phys. Rev. B **105**, 014408 (2022).
    DOI:10.1103/PhysRevB.105.014408
16. Mechanism of antisymmetric spin polarization in centrosymmetric multiple-Q magnets based on effective chiral bilinear and biquadratic spin cross products
    S. Hayami, Phys. Rev. B **105**, 024413 (2022).
    DOI:10.1103/PhysRevB.105.024413
17. Multiple Skyrmion Crystal Phases by Itinerant Frustration in Centrosymmetric Tetragonal Magnets
    S. Hayami, J. Phys. Soc. Jpn. **91**, 023705 (2022).
    DOI:10.7566/JPSJ.91.023705
18. Skyrmion crystals in centrosymmetric triangular magnets under hexagonal and trigonal single-ion anisotropy
    S. Hayami, J. Magn. Magn. Mater. **553**, 169220 (2022).
    DOI:10.1016/j.jmmm.2022.169220
19. Helicity locking of a square skyrmion crystal in a centrosymmetric lattice system without vertical mirror symmetry
    S. Hayami and R. Yambe, Phys. Rev. B **105**, 104428 (2022).
    DOI:10.1103/PhysRevB.105.104428

HIDA, Kazuo [B class; 400 (B), 70 (C)] (309)
— *Numerical Study of One Dimensional Frustrated Quantum Spin Systems*

1. Infinite Series of Ferrimagnetic Phases Emergent from the Gapless Spin Liquid Phase of Mixed Diamond Chains

Kazuo Hida, J. Phys. Soc. Jpn. **90**, 054701 (2021).
DOI:10.7566/JPSJ.90.054701

2. First Order Transitions Between the Gapped Spin-Liquid and Ferrimagnetic Phases in (1/2,1/2,1) Mixed Diamond Chains with Bond Alternation
   Kazuo Hida, J. Phys. Soc. Jpn. **91**, 024706 (2022).
   DOI:10.7566/JPSJ.91.024706

HIGUCHI, Yuji [C class; 4600 (B), 750 (C)] (230)
— *Structure and mechanical properties of crystalline polymers absorbing water molecules*
1. Hydrophobic immiscibility controls self-sorting or co-assembly of peptide amphiphiles
   R. Wakabayashi, R. Imatani, M. Katsuya, Y. Higuchi, H. Noguchi, N. Kamiya, and M. Goto, Chem. Commun. **58**, 585 (2021).
   DOI:10.1039/D1CC05560G

HINUMA, Yoyo [B class; 800 (B), 80 (C)] (135)
— *Exploration of exotic surface sites for catalyst informatics*
1. Surface activation by electron scavenger metal nanorod adsorption on TiH2, TiC, TiN, and Ti2O3
   Yoyo Hinuma, Shinya Mine, Takashi Toyao, Zen Maeno and Ken-ichi Shimizu, Phys. Chem. Chem. Phys. 23, 16577 (2021).

2. Factors determining surface oxygen vacancy formation energy in ternary spinel structure oxides with zinc
   Yoyo Hinuma, Shinya Mine, Takashi Toyao, Takashi Kamachi and Ken-ichi Shimizu, Phys. Chem. Chem. Phys. 23, 23768 (2021).

HIRATSUKA, Masaki [B class; 900 (B), 120 (C)] ()
— *Calculation of Infrared and Raman spectra by molecular dynamics simulation using machine learning*
— *Validation of a Machine Learning Method for Predicting Vibration Spectra*

HIRAYAMA, Naomi [C class; 1800 (B), 0 (C)] ()
— *Development of inter-atomic potentials of Fe-based amorphous alloys and MD simulation of crystallization process*

HIYAMA, Miyabi [C class; 3200 (B), 800 (C)] (249)
— *Theoretical analysis of absorption and fluorescence spectra for firefly bioluminescence related molecules*
1. Absorption Spectra for Firefly Bioluminescence Substrate Analog: TokeOni in Various pH Solutions
   H. Ogawa, R. Ono, Y. Noguchi, N. Kitada, R. Saito-Moriya, S. A. Maki, H. Akiyama, H. Itabashi, and M. Hiyama, Photochem. Photobiol. **97**, 1016 (2021).
   DOI:10.1111/php.13458

HOSHI, Takeo [C class; 5200 (B), 0 (C)] (344)
— *HPC-based fusion of experiment analysis, simulation and data-driven science*
1. Data-driven sensitivity analysis in a total-reflection high-energy positron diffraction (TRHEPD)
   Takeo Hoshi, Daishiro Sakata, Shotaro Oie, Izumi Mochizuki, Satoru Tanaka, Toshio Hyodo, and Koji Hukushima, Comput. Phys. Commun. 271, 108186 (2022).
   DOI:10.1016/j.cpc.2021.108186

2. Performance prediction of massively parallel computation by Bayesian inference
   Hisashi Kohashi, Harumichi Iwamoto, Takeshi Fukaya, Yusaku Yamamoto, and Takeo Hoshi

JSIAM Letters 14 13-16 (2022).

3. sim-trhepd-rheed – Open-source simulator of total-reflection high-energy positron diffraction (TRHEPD) and reflection high-energy electron diffraction (RHEED)
   Takashi Hanada, Yuichi Motoyama, Kazuyoshi Yoshimi, and Takeo Hoshi, Comput. Phys. Commun. in press (arXiv:2110.09477).

4. Data-analysis software framework 2DMAT and its application to experimental measurements for two-dimensional material structures
   Yuichi Motoyama, Kazuyoshi Yoshimi, Harumichi Iwamoto, Hayato Ichinose, and Takeo Hoshi, arXiv:2204.04484
   DOI:10.48550/arXiv.2204.04484

HOTTA, Chisa [B class; 1000 (B), 80 (C)] (278)
— *Development and application of methods to calculate thermodynamic properties in low dimensional magnets*

1. Dimensional reduction in quantum spin-1/2 system on a 1/7-depleted triangular lattice
   R. Makuta and C. Hotta, Phys. Rev. B **104**, 224415 (2021).
   DOI:10.1103/PhysRevB.104.224415

HOTTA, Takashi [C class; 5000 (B), 0 (C)] (188)
— *Research of multi-channel Kondo effect emerging from heavy rare-earth ions*

1. Three-Channel Kondo Effect Emerging from Ho Ions
   Takashi Hotta, J. Phys. Soc. Jpn. **90**, 113701 (2021).
   DOI:10.7566/JPSJ.90.113701

IDO, Kota [B,C class; 4700 (B), 390 (C)] (232)
— *Development of COMPutation ARchive of Exact Diagonalization(COMPARED)*
— *Neural network quantum states for excited states in strongly correlated electron systems*

1. Unconventional dual 1D2D quantum spin liquid revealed by ab initio studies on organic solids family
   Kota Ido, Kazuyoshi Yoshimi, Takahiro Misawa, Masatoshi Imada, npj Quantum Materials 7, 48 (2022).
   DOI:10.1038/s41535-022-00452-8

Data Repository
COMPARED
https://isspns-gitlab.issp.u-tokyo.ac.jp/compared/compared

IITAKA, Toshiaki [C class; 2000 (B), 0 (C)] (115)
— *Structure and Property of Basalt Melt and Glass*

1. A comparative study on pressure-induced structural transformations in a basaltic glass and melt from Ab initio molecular dynamics calculations
   S. Q. Feng, A. Majumdar, H. Y. Kuang, Y. M. Pan, T. Iitaka, and J. S. Tse Phys. Chem. Miner. 48, 41 (2021).
   DOI:10.1007/s00269-021-01165-3

IKEDA, Hiroaki [B class; 400 (B), 70 (C)] ()
— *Electronic structure calculations in quantum liquid crystals*

IKEDA, Tatsuhiko [B class; 600 (B), 40 (C)] (198)

— *Numerical study of nonequilibrium phases in periodically driven systems with dissipation*

1. Criticality and rigidity of dissipative discrete time crystals in solids
K. Chinzei and T.N. Ikeda, Phys. Rev. Research **4**, 023025 (2022).
DOI:10.1103/PhysRevResearch.4.023025

IKUHARA, Yuichi [C class; 2000 (B), 0 (C)] (113)

— *Determining grain-boundary stable atomic structure by first-principle calculations*

— *First principles calculations for proving stable grain-boundary structures in perovskite oxides*

1. Oxygen Atom Ordering on SiO2/4H-SiC 0001 Polar Interfaces formed by Wet Oxidation
M. Saito, H. Li, K. Inoue, H. Matsuhata, Y. Ikuhara, Acta Mater. **221**, 117360 (2021).
DOI:10.1016/j.actamat.2021.117360

2. Arrangement of polyhedral units for [0001]-symmetrical tilt grain boundaries in zinc oxide
K. Inoue, J.Y. Roh, K. Kawahara, M. Saito, M. Kotani, Y. Ikuhara, Acta Mater. **212** 116864 (2021).
DOI:10.1016/j.actamat.2021.116864

IMADA, Masatoshi [E class; 28500 (B), 3000 (C)] (174)

— *Quantum Spin Liquids on Pyrochlore Lattice*

— *Studies on Effects of Non-Local Coulomb Interaction for High Termperature Superconductivity*

1. Unconventional dual 1D-2D quantum spin liquid revealed by ab initio studies on organic solids family
Kota Ido, Kazuyoshi Yoshimi, Takahiro Misawa, and Masatoshi Imada, npj Quantum Mater. **7**, 48 (2022).
DOI:0.1038/s41535-022-00452-8

2. Hidden self-energies as origin of cuprate superconductivity revealed by machine learning
Youhei Yamaji, Teppei Yoshida, Atsushi Fujimori, and Masatoshi Imada Phys. Rev. Research **3**, 043099 (2021).
DOI:10.1103/PhysRevResearch.3.043099

3. Order-N orbital-free density-functional calculations with machine learning of functional derivatives for semiconductors and metals
Fumihiro Imoto, Masatoshi Imada, and Atsushi Oshiyama, Phys. Rev. Research **3**, 033198 (2021).
DOI:10.1103/PhysRevResearch.3.033198

4. *Ab initio*derivation of low-energy Hamiltonians for systems with strong spin-orbit interaction: Application to $Ca_5Ir_3O_{12}$
Maxime Charlebois, Jean-Baptiste Morée, Kazuma Nakamura, Yusuke Nomura, Terumasa Tadano, Yoshihide Yoshimoto, Youhei Yamaji, Takumi Hasegawa, Kazuyuki Matsuhira, and Masatoshi Imada, Phys. Rev. B **104**, 075153 (2021).
DOI:10.1103/PhysRevB.104.075153

5. Dirac-type nodal spin liquid revealed by refined quantum many-body solver using neural-network wave function, correlation ratio, and level spectroscopy
Yusuke Nomura and Masatoshi Imada, Phys. Rev. X **11**, 031034 (2021).
DOI:10.1103/PhysRevX.11.031034

6. Charge Order and Superconductivity as Competing Brothers in Cuprate High-Tc Superconductors
Masatoshi Imada J. Phys. Soc. Jpn. **90**, 111009 (2021).
DOI:10.7566/JPSJ.90.111009

7. Resonant Inelastic X-Ray Scattering Spectra of Cuprate Superconductors Predicted by Model of Fractionalized Fermions
   Masatoshi Imada J. Phys. Soc. Jpn. **90**, 074702 (2021).
   DOI:10.7566/JPSJ.90.074702

8. High-temperature superconductivity
   Xingjiang Zhou, Wei Sheng Lee, Masatoshi Imada, Nandini Trivedi, Philip Phillips, Hae Young Kee, Päivi Törmä, Mikhail Eremets Nat. Rev. Phys. **3**, 125137 (2021).
   DOI:10.1038/s42254-021-00324-3

9. Local moments versus itinerant antiferromagnetism: Magnetic phase diagram and spectral properties of the anisotropic square lattice Hubbard model
   Marcin Raczkowski, Fakher F. Assaad, Masatoshi Imada Phys. Rev. B **103**, 462 (2021).
   DOI:10.1103/PhysRevB.103.125137

INAGAKI, Kouji [B class; 400 (B), 70 (C)] (155)
— *First-principles calculation of graphitization of diamond surface and its exfoliation process*

ISHIBASHI, Shoji [C class; 1800 (B), 0 (C)] (121)
— *Prediction of properties of organic ferroelectrics and piezoelectrics by first-principles calculation*

1. Hydrogen-bonded single-component organic ferroelectrics revisited by van der Waals density-functional theory calculations
   S. Ishibashi, S. Horiuchi, and R. Kumai, Phys. Rev. Mater. **5**, 094409 (2021).
   DOI:10.1103/PhysRevMaterials.5.094409

2. Large Polarization and Record-High Performance of Energy-Storage Induced by a Phase Change in Organic Molecular Crystals
   S. Horiuchi and S. Ishibashi, Chem. Sci. **12**, 14198 (2021).
   DOI:10.1039/d1sc02729h

ISHII, Fumiyuki [C class; 5200 (B), 850 (C)] (74)
— *First-Principles Calculation of Spin Splitting and Anomalous Hall Conductivity in Energy Conversion Materials*
— *First-principles study of interface structure prediction and electronic structures*

1. First-principles calculation of anomalous Hall and Nernst conductivity by local Berry phase
   H. Sawahata, N. Yamaguchi, S. Minami, and F. Ishii, arXiv:2204.05949, submitted to Phys. Rev. B.

2. First-principles LCPAO Approach to Insulators Under Finite Electric Fields
   N. Yamaguchi and F. Ishii, arXiv:2203.10441

3. Statistical analysis of properties of non-fullerene acceptors for organic photovoltaics
   N. Yamaguchi, H. Sano, H. Sawahata, M. Nakano, T. Taima, F. Ishii, M. Karakawa Jpn. J. Appl. Phys. **61**, 030905 (2022).

ISOBE, Masaharu [B class; 800 (B), 0 (C)] (281)
— *Equilibration and phase transition in the dense hard sphere systems*
— *Nonequilibrium response and phase transition in the dense hard sphere systems*

1. Non-equilibrium response and equilibration in hard disk systems
   D. Mugita and M. Isobe, EPJ Web Conferences **249**, 14004 (2021).
   DOI:10.1051/epjconf/202124914004

2. Diffusional characteristics of a Newtonian event-chain Monte Carlo in hard disk systems
   H. Banno, D. Mugita, and M. Isobe, J. of Phys.: Conf. Ser. **2207** 012011 (2022).
   DOI:10.1088/1742-6596/2207/1/012011

3. Molecular dynamics study of a nano-scale beta-type Stirling engine
   K. Kitaya and M. Isobe, J. of Phys.: Conf. Ser. **2207** 012006 (2022).
   DOI:10.1088/1742-6596/2207/1/012006

ITOH, Satoru [C class; 1800 (B), 0 (C)] (270)
— *Formation of lipid rafts studied by molecular dynamics simulation*

JESCHKE, Harald [C class; 3800 (B), 0 (C)] ()
— *Magnetism and superconductivity in ternary chromium chalcogenides*

JOUTSUKA, Tatsuya [B,C class; 1800 (B), 0 (C)] (119, 120)
— *Elucidation of Photocatalytic Reaction Mechanism by Ab Initio Calculations*
— *Theoretical Analysis of Metal Film Growth Mechanism in Chemical Vapor Deposition*

1. Efficient Free-Energy Calculation of Proton Transfer by Constrained Density Functional Theory and Geometrically Restrained Molecular Dynamics Simulation
   Tatsuya Joutsuka and Koji Ando, Chem. Lett. 50, 1325 (2021).
   DOI:10.1246/cl.210132

2. Understanding the structure of Cu-doped MgAl2O4 for CO2 hydrogenation catalyst precursor using experimental and computational approaches
   Tatsuya Joutsuka, Ryu Hamamura, Kakeru Fujiwara, Tetsuo Honma, Masahiko Nishijima, and Shohei Tada, submitted.

3. Active sites on ZnxZr1 − xO2 − x solid solution catalysts for CO2-to-methanol hydrogenation
   Shohei Tada, Nagomu Ochiai, Hiroka Kinoshita, Mitsuhiro Yoshida, Natsumi Shimada, Tatsuya Joutsuka, Masahiko Nishijima, Tetsuo Honma, Noriko Yamauchi, Yoshio Kobayashi, Kenta Iyoki, submitted.

4. Molecular Mechanism of Autodissociation in Liquid Water: Density Functional Theory Molecular Dynamics Simulations
   Tatsuya Joutsuka, submitted.
   DOI:10.26434/chemrxiv-2022-9t6vf

KAGESHIMA, Hiroyuki [C class; 1200 (B), 0 (C)] (129)
— *Study on structural elementary excitations at semiconductor surfaces and interfaces*

KANEKO, Ryui [B class; 700 (B), 90 (C)] (284, 286)
— *tensor-network calculation of real time dynamics in two-dimensional cold atom systems*
— *tensor-network study of the magnetization process of the SU(N) Heisenberg model*

1. Reentrance of the Disordered Phase in the Antiferromagnetic Ising Model on a Square Lattice with Longitudinal and Transverse Magnetic Fields
   R. Kaneko, Y. Douda, S. Goto, and I. Danshita, J. Phys. Soc. Jpn. **90**, 073001 (2021).
   DOI:10.7566/JPSJ.90.073001

2. Symmetry-protected topological phases and competing orders in a spin-1/2 XXZ ladder with a four-spin interaction
   T. Ogino, S. Furukawa, R. Kaneko, S. Morita, and N. Kawashima, Phys. Rev. B **104**, 075135 (2021).

DOI:10.1103/PhysRevB.104.075135

3. Multiple magnetization plateaus induced by farther neighbor interactions in an $S = 1$ two-leg Heisenberg spin ladder
   H. Kohshiro, R. Kaneko, S. Morita, H. Katsura, and N. Kawashima, Phys. Rev. B **104**, 214409 (2021).
   DOI:10.1103/PhysRevB.104.214409

4. Tensor-network study of correlation-spreading dynamics in the two-dimensional Bose-Hubbard model
   R. Kaneko and I. Danshita, Commun. Phys. **5**, 65 (2022).
   DOI:10.1038/s42005-022-00848-9

KARIYADO, Toshikaze [B class; 300 (B), 0 (C)] (320)
— *Electronic structure in mismatched multilayer systems: evaluation and application of the modeling scheme*

1. Effective continuum model of twisted bilayer GeSe and origin of the emerging one-dimensional mode
   M. Fujimoto and T. Kariyado, Phys. Rev. B **104**, 125427 (2021).
   DOI:10.1103/PhysRevB.104.125427

2. Disentangling Orbital Magnetic Susceptibility with Wannier Functions
   T. Kariyado, H. Matsuura, and M. Ogata, J. Phys. Soc. Jpn. **90**, 124708 (2021).
   DOI:10.7566/JPSJ.90.124708

KASAMATSU, Shusuke [C class; 10000 (B), 1150 (C)] (51)
— *Understanding superionic conduction in disordered materials systems*
— *Understanding superionic conductivity in disordered systems using machine learning potential molecular dynamics*

1. Enabling ab initio configurational sampling of multicomponent solids with long-range interactions using neural network potentials and active learning
   Shusuke Kasamatsu, Yuichi Motoyama, Kazuyoshi Yoshimi, Ushio Matsumoto, Akihide Kuwabara, and Takafumi Ogawa, submitted.

KATO, Takeo [B class; 1100 (B), 180 (C)] (271, 272)
— *Numerical study of heat transport through a mesoscopic device*
— *Theoretical study of spin Hall magnetoresistance by the quantum Monte Carlo method*

KATO, Yusuke [C class; 8800 (B), 800 (C)] (215, 217)
— *Effects of non-diagonal spin interactions and dipole interaction on quantum spin liquids*
— *Quantum effects on chiral magnets*

1. Feasibility of Kitaev quantum spin liquid in ultracold polar molecules
   Kiyu Fukui, Yasuyuki Kato, Joji Nasu, and Yukitoshi Motome, submitted to Phys. Rev. B

KAWAKAMI, Norio [C class; 8200 (B), 1100 (C)] (182)
— *Excitation modes and transport phenomena in strongly correlated systems*
— *Topological phases, transport phenomena and effects of exceptional points in strongly correlated systems*

1. Mott transition and magnetism in a fragile topological insulator
   Ashish Joshi and Robert Peters, Phys. Rev. B **103**, 165130 (2021).
   DOI:10.1103/PhysRevB.103.165130

2. Effects of renormalization and non-Hermiticity on nonlinear responses in strongly correlated electron systems
   Yoshihiro Michishita and Robert Peters, Phys. Rev. B **103**, 195133 (2021).
   DOI:10.1103/PhysRevB.103.195133

3. Effects of strong correlations on the nonlinear response in Weyl-Kondo semimetals
   Akira Kofuji, Yoshihiro Michishita, and Robert Peters, Phys. Rev. B **104**, 085151 (2021).
   DOI:10.1103/PhysRevB.104.085151

4. Surface exceptional points in a topological Kondo insulator
   Robert Peters, Kazuhiro Kimura, Yoshihiro Michishita, Tsuneya Yoshida, and Norio Kawakamia
   Phys. Rev. B **104**, 235153 (2021).
   DOI:10.1103/PhysRevB.104.235153

5. Magnetism of magic-angle twisted bilayer graphene
   Javad Vahedi, Robert Peters, Ahmed Missaoui, Andreas Honecker, Guy Trambly de Laissardire
   SciPost Phys. **11**, 083 (2021).
   DOI:10.21468/SciPostPhys.11.4.083

6. Probing three-state Potts nematic fluctuations by ultrasound attenuation
   Kazuhiro Kimura, Manfred Sigrist, and Norio Kawakami, Phys. Rev. B **105**, 035130 (2022).
   DOI:10.1103/PhysRevB.105.035130

KAWAKATSU, Toshihiro [C class; 4600 (B), 0 (C)] (238)
— *Hybrid simulations on fluid-viscoelastic membrane system using multiscale simulation platform on complex fluids (MSSP)*

1. Lagrangian multiscale simulation of complex flows
   Y. Morii and T. Kawakatsu, Phys. Fluids **33**, 093106 (2021).
   DOI:10.1063/5.0063059

KAWAMURA, Hikaru [C class; 3800 (B), 0 (C)] (250)
— *Novel order in frustrated magnets*

1. Hedgehog-lattice spin texture in classical Heisenberg antiferromagnets on the breathing pyrochlore lattice
   K. Aoyama and H. Kawamura, Phys. Rev. B **103**, 014406 (2021).
   DOI:10.1103/PhysRevB.103.014406

2. Frustration-induced quantum spin liquid behavior in the s = 1/2 random-bond Heisenberg antiferromagnet on the zigzag chain
   K. Uematsu, T. Hikihara, and H. Kawamura, J. Phys. Soc. Jpn. **90**, 124703 (2021).
   DOI:10.7566/JPSJ.90.124703

3. Effects of spin-lattice coupling and a magnetic field in classical Heisenberg antiferromagnets on the breathing pyrochlore lattice
   K. Aoyama, M. Gen, and H. Kawamura, Phys. Rev. B **104**, 184411 (2021).
   DOI:10.1103/PhysRevB.104.184411

4. Replica symmetry breaking in the RKKY skyrmion crystal system
   K. Mitsumoto and H. Kawamura, Phys. Rev. B **104**, 184432 (2021).
   DOI:10.1103/PhysRevB.104.184432

5. Skyrmion crystal in the RKKY system on the two-dimensional triangular lattice

K. Mitsumoto and H. Kawamura, Phys. Rev. B **105**, 094427(2022).
DOI:10.1103 /PhysRevB.105.094427

6. Emergent skyrmion-based chiral order in zero-field Heisenberg antiferromagnets on the breathing kagome lattice
   K. Aoyama and H. Kawamura, Phys. Rev. B **105**, L100407 (2022).
   DOI:10.1103/PhysRevB.105.L100407

7. Spin Dynamics Simulation of the Z_2-vortex Fluctuations
   Y.P. Mizuta, K. Aoyama, K. Tomiyasu, M. Matsuura, and H. Kawamura, J. Phys. Soc. Jpn. **91**, 035001 (2022).
   DOI:10.7566/JPSJ.91.035001

KAWAMURA, Mitsuaki [B class; 400 (B), 80 (C)] (305)
— *Crystal structure search guided by multicomponent sphere packing*

KAWANO, Shoya [D class; 1000 (B), 0 (C)] (132)
— *Optical conductivity of* $Ca_5Ir_3O_{12}$ *by first-principles calculations*

KAWASHIMA, Naoki [E class; 38000 (B), 3600 (C)] (172)
— *Tensor-Network Renormalization-Group Study of Critical Phenomena*

1. Anisotropy as a diagnostic test for distinct tensor-network wave functions of integer- and half-integer-spin Kitaev quantum spin liquids
   H.-Y. Lee, T. Suzuki, Y. B. Kim and N. Kawashima, Phys. Rev. B 104, 024417(1-13) (2021).
   DOI:10.1103/PhysRevB.104.024417

2. Generating function for tensor network diagrammatic summation
   W.-L. Tu, H.-K. Wu, N. Schuch, N. Kawashima and J.-Y. Chen, Phys. Rev. B 103, 205155 (2021).
   DOI:10.1103/PhysRevB.103.205155

3. Multiple magnetization plateaus induced by farther neighbor interactions in an S=1 two-leg Heisenberg spin ladder
   H. Kohshiro, R. Kaneko, S. Morita, H. Katsura and N. Kawashima, Phys. Rev. B 104, 214409 (2021).
   DOI:10.1103/PhysRevB.104.214409

4. Open spin chain realization of a topological defect in a one-dimensional Ising model:
   Boundary and bulk symmetry: Y. Fukusumi and S. Iino, Phys. Rev. B 104, 125418 (2021).
   DOI:10.1103/PhysRevB.104.125418

5. Symmetry-protected topological phases and competing orders in a spin-1/2 XXZ ladder with a four-spin interaction
   T. Ogino, S. Furukawa, R. Kaneko, S. Morita and N. Kawashima, Phys. Rev. B 104, 075135 (2021).
   DOI:10.1103/PhysRevB.104.075135

6. Mott-insulator-like Bose-Einstein condensation in a tight-binding system of interacting bosons with a flat band
   H. Katsura, N. Kawashima, S. Morita, A. Tanaka and H. Tasaki, Phys. Rev. Research 3, 033190 (2021).
   DOI:10.1103/PhysRevResearch.3.033190

7. Scaling dimensions from linearized tensor renormalization group transformations

X. Lyu, R. G. Xu and N. Kawashima, Phys. Rev. Research 3, 023048 (2021).
DOI:10.1103/PhysRevResearch.3.023048

8. Universal and non-universal correction terms of Bose gases in dilute region: a quantum Monte Carlo study
A. Masaki-Kato, Y. Motoyama and N. Kawashima, J. Phys. Soc. Jpn. 90, 034711(1-8) (2022).
DOI:10.7566/JPSJ.91.024001

KITAO, Akio [C class; 6600 (B), 0 (C)] (225)
— *Efficient sampling simulation of the soft modes significantly contribute to protein properties*

1. Binding free energy of protein/ligand complexes calculated using dissociation Parallel Cascade Selection Molecular Dynamics and Markov state model
H. Hata, D. Phuoc Tran, M. Marzouk Sobeh and A. Kitao, Biophys. Physicobiol. **18**, 305 (2021).

2. The role of the half-turn in determining structures of Alzheimer's Abeta wild-type and mutants
S. Hayward and A. Kitao, J. Struct. Biol. **213**, 107792 (2021).

3. Regulatory Switching by Concerted Motions on the Microsecond Time Scale of the Oxygen Sensor Protein FixL
T. Yamawaki, M. Mizuno, H. Ishikawa, K. Takemura, A. Kitao, Y. Shiro and Y. Mizutani, J. Phys. Chem. B. **16**, 2835 (2021).

4. Dissociation Pathways of the p53 DNA Binding Domain from DNA and Critical Roles of Key Residues Elucidated by dPaCS-MD/MSM
M. M. Sobeh and A. Kitao, J. Chem. Inf. Model **62**, 1294 (2021).

KOBAYASHI, Akito [B class; 400 (B), 80 (C)] (199)
— *Ordered states in strongly correlated Dirac electron systems of organic conductors*

KOBAYASHI, Katsuyoshi [B class; 400 (B), 70 (C)] (154)
— *Theoretical study on electronic properties of new nanoscale surfaces and interfaces*

1. Short-range magnetic interaction in a monolayer 1T-VSe$_2$ film revealed by element-specific x-ray magnetic circular dichroism
K. Sumida, Y. Takeda, S. Kusaka, K. Kobayashi, and T. Hirahara, Phys. Rev. Materials **6**, 014006 (2022).
DOI:10.1103/PhysRevMaterials.6.014006

KOBAYASHI, Nobuhiko [C class; 3400 (B), 600 (C)] (92)
— *First-principles study of quantum transport in nanostructures*

KOBAYASHI, Ryo [B class; 300 (B), 0 (C)] (319)
— *Molecular dynamics analyses of ion migration at grain boundaries in solid state electrolyte*

1. Non-equilibrium molecular dynamics study on atomistic origin of grain boundary resistivity in NASICON-type Li-ion conductor
R. Kobayashi, K. Nakano, and M. Nakayama, Acta Materialia **226**, 117596 (2022).
DOI:10.1016/j.actamat.2021.117596

KOGA, Akihisa [C class; 4400 (B), 750 (C)] (231)
— *Spin transport through Kitaev spin liquids*

1. Role of Majorana fermions in spin transport of anisotropic Kitaev model
H. Taguchi, Y. Murakami, A. Koga and J. Nasu, Phys. Rev. B **104**, 125139 (2021).

2. Ferrimagnetically ordered states in the Hubbard model on the hexagonal golden-mean tiling
   A. Koga and S. Coates, Phys. Rev. B **105**, 104410 (2022).

3. Photoinduced dynamics of a quasicrystalline excitonic insulator
   K. Inayoshi, Y. Murakami, and A. Koga, Phys. Rev. B **105**, 104307 (2022).

4. Thermally enhanced Majorana-mediated spin transport in the Kitaev model
   H. Taguchi, Y. Murakami and A. Koga, Phys. Rev. B **105**, 125137 (2022).

KOMATSU, Yu [C class; 4000 (B), 700 (C)] (89)
— *A unified understanding of thermodynamic properties in icy planets and icy moons*

KONDO, Kenji [C class; 2000 (B), 100 (C)] (264)
— *Numerical Analysis for Stability and Dynamics of Magnetic Structures such as Skyrmions*

KOURA, Akihide [C class; 1400 (B), 0 (C)] (127)
— *Ab initio molecular dynamics study on static structure of glass materials*

1. Reproduction of Melting and Crystallization of Sodium by Machine-Learning Interatomic Potential Based on Artificial Neural Networks
   A. Irie, S. Fukushima, A. Koura, K. Shimamura and F. Shimojo, J. Phys. Soc. Jpn. **90** (2021) 094603.
   DOI:10.7566/JPSJ.90.094603

2. Importance of Adjusting Coefficients in Cost Function for Construction of High-Accuracy Machine-Learning Interatomic Potential
   A. Irie, K. Shimamura, A. Koura, and F. Shimojo, J. Phys. Soc. Jpn. **91** (2022) 045002.

3. Thermal conductivity calculation based on GreenKubo formula using ANN potential for β-Ag_2Se
   Y. Takeshita, K. Shimamura, S. Fukushima, A. Koura, and F. Shimojo, J. Phys. Chem. Solids **163**, 110580 (2022).

KUNISADA, Yuji [C class; 6200 (B), 0 (C)] (73)
— *Reduction of Rare Metals in Formic Acid Decomposition Catalysts and Oxygen Storage Materials*

1. Anisotropic Growth of Copper Nanorods Mediated by Cl Ions
   M. J. Saw, M. T. Nguyen, Y. Kunisada, T. Tokunaga, T. Yonezawa, ACS Omega **7** (2022) 74147420.
   DOI:10.1021/acsomega.2c00359

KUROKI, Kazuhiko [C class; 10000 (B), 900 (C)] (53, 55)
— *First principles study on defect formations in new thermoelectric materials*
— *Study on new-type of nickelate superconductors based on multiorbital models*

1. Development of an efficient impurity solver in dynamical mean field theory for multiband systems: Iterative perturbation theory combined with parquet equations
   R. Mizuno, M. Ochi, and K. Kuroki, Phys. Rev. B **104**, 035160 (2021).
   DOI:10.1103/PhysRevB.104.035160

2. Simplification of the Local Full Vertex in the Impurity Problem in DMFT and Its Applications for the Nonlocal Correlation
   R. Mizuno, M. Ochi, and K. Kuroki, J.Phys. Soc. Jpn. **91**, 034002 (2022).
   DOI:10.7566/JPSJ.91.034002

3. First-principles study of defect formation energies in LaOXS_2(X =Sb,Bi)
   M. Ochi and K. Kuroki, Phys.Rev.B **105**, 094110 (2022).
   DOI:10.1103/PhysRevB.105.094110

KUSAKABE, Koichi [C class; 2600 (B), 300 (C)] (104)
— *Evolutionary algorithm for simulation of fast chemical reaction process*

1. Effect of on-site Coulomb repulsion on ferromagnetic fluctuations in heavily overdoped cuprates
   S. Teranishi, K. Nishiguchi, S. Yunoki, and K. Kusakabe, J. Phys. Soc. Jpn. **90**, 094707 (2021).
   DOI:10.7566/JPSJ.90.094707

2. Material Optimization of Potenetial High-Tc Superconducting Single-layer Cuprates
   S. Teranishi, K. Nishiguchi, and K. Kusakabe, J. Phys. Soc. Jpn. **90**, 054705 (2021).
   DOI:10.7566/JPSJ.90.054705

3. High magnetoresistance of a hexagonal boron nitride-graphene heterostructure-based MTJ through excited-electron transmission
   H. Harfah, Y. Wicaksono, G. K. Sunnardianto, M. A. Majidi, and K. Kusakabe, Nanoscale Adv. **4**, 117 (2022).
   DOI:10.1039/D1NA00272D

4. S=1 antiferromagnetic electron-spin systems on hydrogenated phenalenyl-tessellation molecules for material-based quantum-computation resources
   N. Morishita, Y. Oishi, T. Yamaguchi, and K. Kusakabe, Appl. Phys. Express **14**, 121005 (2021).
   DOI:10.35848/1882-0786/ac3b9d

5. Zero-energy modes in a super-chiral nanographene network of phenalenyl-tessellation molecules
   N. Morishita, and K. Kusakabe, Phys. Lett. A **408**, 127462 (2021).
   DOI:10.1016/j.physleta.2021.127462

6. Terahertz-induced martensitic transformation in partially stabilized zirconia
   M. Nagai, Y. Higashitani, M. Ashida, K. Kusakabe, H. Niioka, A. Hattori, H. Tanaka, G. Isoyama, and N. Ozaki Research square, DOI:10.21203/rs.3.rs-130295/v1 (Preprint)
   DOI:10.21203/rs.3.rs-130295/v1

LEE, Minhyeok [C class; 1800 (B), 0 (C)] (268)
— *Development of the Low-Temperature Oxidation Model for Alternative Fuels Using Machine Learning*

LIAO, YUXUAN [C class; 4200 (B), 800 (C)] ()
— *Machine-learning-assisted Development of Giant Thermal-Property Database for Polymer Materials*
— *Ultimate Suppression of Nanoheat Transport with Quasi-phononic Crystal*

1. Akhiezer mechanism dominates relaxation of propagons in amorphous material at room temperature
   Yuxian Liao, Junichiro Shiomi, J. Appl. Phys. 130, 035101 (2021).
   DOI:10.1063/5.0050159

MAEHIRA, Takahiro [B class; 300 (B), 30 (C)] (168)
— *Electronic Structure and Fermiology of d-electron compounds*

MAKINO, Takayuki [B class; 400 (B), 0 (C)] (164)
— *Electron-phonon interaction under electric fields in oxides*
— *Parallel nonlinear regression analysis for spectroscopic data with existing Julia packages*

1. Contactless Determination of Optimal Chloride Concentration for Power Conversion Efficiency in

PVKMAI Using Photoluminescence Spectroscopy
T. Asai et al., Photonics 8, 412 (2021).
DOI:10.3390/photonics8100412

2. Optical properties of LiNbO2 thin films
T. Kurachi et al., Physica B 621, 413259 (2021).
DOI:10.1016/j.physb.2021.413259

MAO, WEI [C class; 1600 (B), 500 (C)] ()
— *First-principles calculation of microscopic behaviors of hydrogen in metal oxides*

MASAKI, Yusuke [B class; 400 (B), 0 (C)] ()
— *Fractional Vortices in Topological Nematic Superfluids*

MATSUKAWA, Hiroshi [C class; 1600 (B), 500 (C)] ()
— *Physics of Friction*

MATSUMOTO, Munehisa [C class; 2000 (B), 650 (C)] ()
— *Data assimilation of measurement and simulation for rare-earth permanent magnets*

MATSUNAKA, Daisuke [B class; 300 (B), 0 (C)] (170)
— *First-principles Study of Defects of Magnesium Alloys*

MATSUSHITA, Katsuyoshi [C class; 200 (B), 300 (C)] (301)
— *Numerical Study of Rotation-Translation Motion Transition of Cell Clusters*
— *Simulation of Cell Collective Rotatopm*

MATSUSHITA, Yu-ichiro [C class; 9600 (B), 1100 (C)] (58)
— *Identification of interface-state defects in power semiconductors: Approach from ab-initio calculations*

1. Effect of magnetocrystalline anisotropy on magnetocaloric properties of an $AlFe_2B_2$ compound
Hung Ba Tran, Hiroyoshi Momida, Yu-ichiro Matsushita, Kazunori Sato, Yukihiro Makino, Koun Shirai, and Tamio Oguchi, Phys. Rev. B 105, 134402 (2022).
DOI:10.1103/PhysRevB.105.134402

2. Insight into anisotropic magnetocaloric effect of CrI3
Hung Ba Tran and Hiroyoshi Momida and Yu-ichiro Matsushita and Koun Shirai and Tamio Oguchi, Acta Materialia 231, 117851 (2022).
DOI:10.1016/j.actamat.2022.117851

MAYUMI, Koichi [C class; 3400 (B), 800 (C)] (245)
— *Molecular Dynamics Simulations of Strain-Induced Crystallization in Robust and Tough Polymer Gels*

MISAWA, Masaaki [B class; 500 (B), 0 (C)] (149)
— *Large-Scale Molecular Dynamics Simulations on Non-Equilibrium Phenomena Using First-Principles Calculation and Machine Leaning*

1. 第一原理計算と機械学習による固体材料における衝撃圧縮特性の分子動力学解析
三澤賢明, 島村孝平, 下條冬樹, セラミックス **56**, 674 (2021).

2. 第一原理計算と機械学習に基づく衝撃圧縮挙動の分子動力学計算
三澤賢明, 島村孝平, 下條冬樹, 高圧力の科学と技術 **31**, 132 (2021).
DOI:10.4131/jshpreview.31.132

MIZUKAMI, Wataru [C class; 4200 (B), 0 (C)] (244)

— *Simulations of quantum-classical-hybrid algorithms for sensor materials with considering noise*

1. Variational quantum simulation for periodic materials
   Nobuyuki Yoshioka, Takeshi Sato, Yuya O. Nakagawa, Yu-ya Ohnishi, and Wataru Mizukami, Phys. Rev. Research 4, 013052 (2022).
   DOI:10.1103/PhysRevResearch.4.013052

2. Solving quasiparticle band spectra of real solids using neural-network quantum states
   Nobuyuki Yoshioka, Wataru Mizukami, and Franco Nori, Commun. Phys. 4, 106 (2021).
   DOI:10.1038/s42005-021-00609-0

MIZUSHIMA, Takeshi [B class; 400 (B), 80 (C)] (304)

— *Numerical study on the tolerance of Majorana-based qubits in topological superconductors*

1. Manipulation of Majorana Kramers Qubit and its Tolerance in Time-Reversal-Invariant Topological Superconductor
   T. Sanno, M. G. Yamada, T. Mizushima, and S. Fujimoto, submitted

2. Engineering Yang-Lee anyons via Majorana bound states
   Y. Tanaka, T. Sanno, T. Mizushima, and S. Fujimoto, submitted

MOCHIZUKI, Masahito [B,C,D class; 12100 (B), 0 (C)] (180, 181)

— *Novel dynamics of magnetic skyrmion crystal phases due to extra degrees of freedom*

— *Numerical studies on the photoinduced phenomena of magnetic skyrmion lattices in metallic magnets*

— *Theoretical study on the spin-wave excitations of multiple-Q magnetic hedgehogs*

1. Dynamical switching of magnetic topology in microwave-driven itinerant magnet
   R. Eto and M. Mochizuki, Phys. Rev. B **104**, 104425 (2021).
   DOI:10.1103/PhysRevB.104.104425

2. Low-energy excitations of skyrmion crystals in a centrosymmetric Kondo-lattice magnet: Decoupled spin-charge excitations and nonreciprocity
   R. Eto, R. Pohle, and M. Mochizuki, arXiv:2203.01496
   DOI:10.48550/arXiv.2203.01496

3. Dynamical phase transitions in the photodriven charge-ordered Dirac-electron system
   Y. Tanaka and M. Mochizuki, arXiv:2203.04542
   DOI:10.48550/arXiv.2203.04542

MOMIDA, Hiroyoshi [C class; 2600 (B), 400 (C)] (102)

— *Structure stability and electronic structures of point defects in wide-gap oxide materials*

1. Tavorite-like orthorhombic $A_x\mathrm{VPO_4F}$ ($A = \mathrm{Li, Na}$) for novel high-voltage cathodes in rechargeable batteries
   H. D. Luong, V. A. Dinh, H. Momida, and T. Oguchi, J. Alloys Compd. **875**, 159963 (2021).
   DOI:10.1016/j.jallcom.2021.159963

2. First-principles study on cathode properties of $\mathrm{Li_2}M\mathrm{TiO_4}$ and $\mathrm{Na_2}M\mathrm{TiO_4}$ ($M = \mathrm{V, Cr, Mn, Fe, Co, Ni}$)
   K. Yamauchi, H. Momida, and T. Oguchi, J. Phys. Soc. Jpn. **91**, 034704 (2022).
   DOI:10.7566/JPSJ.91.034704

3. Performance and reaction mechanisms of tin compounds as high-capacity negative electrodes of lithium and sodium ion batteries

H. Kotaka, H. Momida, and T. Oguchi, Mater. Adv. **3**, 2793 (2022).
DOI:10.1039/d1ma00967b

4. Understanding doping effects on P2 $Na_xMn_{1-x}M_yO_2$ (M = Li, Mg, Al, Ti, V, Cr, Fe, Co, Ni) cathode materials for Na-ion batteries
H. D. Luong, H. Momida, V. A. Dinh, and T. Oguchi, Phys. Rev. Materials **6**, 015802 (2022).
DOI:10.1103/PhysRevMaterials.6.015802

5. Insight into anisotropic magnetocaloric effect of CrI_3
H. B. Tran, H. Momida, Y. Matsushita, K. Shirai, and T. Oguchi, Acta Materialia, Accepted.
DOI:10.1016/j.actamat.2022.117851

6. Effect of magnetocrystalline anisotropy on magnetocaloric properties of $AlFe_2B_2$ compound
H. B. Tran, H. Momida, Y. Matsushita, K. Sato, Y. Makino, K. Shirai, and T. Oguchi, Phys. Rev. B, Accepted.

MORIKAWA, Yoshitada [C,E class; 10100 (B), 1500 (C)] (49)
— *Quantum Simulations on Dynamical Heterogeneous Catalysts*

1. Theoretical study on adsorption and reaction of polymeric formic acid on the Cu(111) surface
S. E. M. Putra, F. Muttaqien, Y. Hamamoto, K. Inagaki, A. Shiotari, J. Yoshinobu, Y. Morikawa, and I. Hamada, Phys. Rev. Materials 5, 075801 (2021).
DOI:10.1103/PhysRevMaterials.5.075801

2. A flat-lying dimer as a key intermediate in NO reduction on Cu(100)
K. Kuroishi*, M. R. Al Fauzan*, T. N. Pham, Y. Wang, Y. Hamamoto, K. Inagaki, A. Shiotari, H. Okuyama, S. Hatta, T. Aruga, I. Hamada, and Y. Morikawa, Phys. Chem. Chem. Phys. 23, 16880 (2021).
DOI:10.1039/D1CP02746H

3. Chemical stability of hydrogen boride nanosheets in water
K. I. M. Rojas, N. T. Cuong, H. Nishino, R. Ishibiki, S. Ito, M. Miyauchi, Y. Fujimoto, S. Tominaka, S. Okada, H. Hosono, N. B. Arboleda Jr., T. Kondo, Y. Morikawa and I. Hamada, Commun. Mater. 2, 81 (2021).
DOI:10.1038/s43246-021-00184-5

4. Isotope effect of methane adsorbed on fcc metal (111) surfaces
S. E. M. Putra, Y. Morikawa, and I. Hamada, Chem. Phys. Lett. 780, 138943 (2021).
DOI:10.1016/j.cplett.2021.138943

5. Mechanistic insight into oxygen vacancy migration in SrFeO3 δ from DFT+U simulations
M. Alaydrus, I. Hamada, and Y. Morikawa, Phys. Chem. Chem. Phys. 23, 18628-18639 (2021).
DOI:10.1039/D1CP02452C

6. Dry reforming of methane on Co catalysts: DFT-based insight into carbon deposition vs removal
Y.-J. Wong, H. H. Halim; N. F. Khairudin, T. N. Pham, S. E. M. Putra, Y. Hamamoto, K. Inagaki, I. Hamada, A. R. Mohamed, and Y. Morikawa, J. Phys. Chem. C 125, 21902-21913 (2021).
DOI:10.1021/acs.jpcc.1c04819

7. Adsorption of CO2 on Terrace, Step, and Defect Sites on Pt Surfaces: A Combined TPD, XPS, and DFT Study
Y.-J. Wong, Y.-H. Choi, S. Tanaka, H. Yoshioka, K. Mukai, H. H. Halim, A. R. Mohamed, K. Inagaki, Y. Hamamoto, I. Hamada, J. Yoshinobu, Y. Morikawa, J. Phys. Chem. C 125, 23657-23668 (2021).

DOI:10.1021/acs.jpcc.1c05228

8. Analysis of atomic structure, magnetic ordering, and oxygen diffusion in oxygen deficient $Sr_3Fe_2O_{7}-\delta$ perovskite: Toward rational catalysts design
   T. Ota, M. Alaydrus, H. Kizaki and Y. Morikawa, Phys. Rev. Materials 6, 015801 (2022).
   DOI:10.1103/PhysRevMaterials.6.015801

MORITA, Satoshi [B class; 600 (B), 90 (C)] (295)
— *Improvement of tensor network renormalization for high-dimensional systems*

1. Symmetry-protected topological phases and competing orders in a spin-1/2 XXZ ladder with a four-spin interaction
   Takuhiro Ogino, Shunsuke Furukawa, Ryui Kaneko, Satoshi Morita, and Naoki Kawashima, Phys. Rev. B **104**, 075135 (2021).
   DOI:10.1103/PhysRevB.104.075135

2. Mott Insulator-like Bose-Einstein Condensation in a Tight-Binding System of Interacting Bosons with a Flat Band
   Hosho Katsura, Naoki Kawashima, Satoshi Morita, Akinori Tanaka, and Hal Tasaki, Phys. Rev. Research **3**, 033190 (2021).
   DOI:10.1103/PhysRevResearch.3.033190

MOTOME, Yukitoshi [C class; 11600 (B), 1250 (C)] (178)
— *Theoretical study of symmetry breaking and quantum transport phenomena in charge-spin-orbital coupled systems*

1. Fractional corner magnetization of collinear antiferromagnets
   H. Watanabe, Y. Kato, H. C. Po, and Y. Motome, Phys. Rev. B **103**, 134430 (2021).
   DOI:10.1103/PhysRevB.103.134430

2. Spin moiré engineering of topological magnetism and emergent electromagnetic fields
   K. Shimizu, S. Okumura, Y. Kato, and Y. Motome, Phys. Rev. B **103**, 184421 (2021).
   DOI:10.1103/PhysRevB.103.184421

3. Crystal-chirality-dependent control of magnetic domains in a time-reversal-broken antiferromagnet
   K. Kimura, Y. Kato, S. Kimura, Y. Motome, and T. Kimura, npj Quantum Mater. **6**, 54 (2021).
   DOI:10.1038/s41535-021-00355-0

4. Spin dynamics in the Kitaev model with disorder: Quantum Monte Carlo study of dynamical spin structure factor, magnetic susceptibility, and NMR relaxation rate
   J. Nasu and Y. Motome, Phys. Rev. B **104**, 035116 (2021).
   DOI:10.1103/PhysRevB.104.035116

5. Topological spin crystals by itinerant frustration
   S. Hayami and Y. Motome, J. Phys.: Condens. Matter **33**, 443001 (2021).
   DOI:10.1088/1361-648X/ac1a30

6. Vortex creation and control in the Kitaev spin liquid by local bond modulations
   S.-H. Jang, Y. Kato, and Y. Motome, Phys. Rev. B **104**, 085142 (2021).
   DOI:10.1103/PhysRevB.104.085142

7. Charge density waves in multiple-Q spin states
   S. Hayami and Y. Motome, Phys. Rev. B **104**, 144404 (2021).
   DOI:10.1103/PhysRevB.104.144404

8. Quantum Monte Carlo method on asymptotic Lefschetz thimbles for quantum spin systems: An application to the Kitaev model in a magnetic field
   P. A. Mishchenko, Y. Kato, and Y. Motome, Phys. Rev. D **104**, 074517 (2021).
   DOI:10.1103/PhysRevD.104.074517

9. Electronic and magnetic properties of iridium ilmenites $A\mathrm{IrO}_3$ (A=Mg, Zn, and Mn)
   S.-H. Jang and Y. Motome, Phys. Rev. Materials **5**, 104409 (2021).
   DOI:10.1103/PhysRevMaterials.5.104409

10. Quadratic optical responses in a chiral magnet
    S. Okumura, T. Morimoto, Y. Kato, and Y. Motome, Phys. Rev. B **104**, L180407 (2021).
    DOI:10.1103/PhysRevB.104.L180407

11. Determinant-free fermionic wave function using feed-forward neural networks
    K. Inui, Y. Kato, and Y. Motome, Phys. Rev. Research **3**, 043126 (2021).
    DOI:10.1103/PhysRevResearch.3.043126

12. Phase shift in skyrmion crystals
    S. Hayami, T. Okubo, and Y. Motome, Nat. Commun. **12**, 6927 (2021).
    DOI:10.1038/s41467-021-27083-0

13. Phase degree of freedom and topology in multiple-Q spin textures
    K. Shimizu, S. Okumura, Y. Kato, and Y. Motome, arXiv:2201.03290.
    DOI:10.48550/arXiv.2201.03290

14. Feasibility of Kitaev quantum spin liquids in ultracold polar molecules
    K. Fukui, Y. Kato, J. Nasu, and Y. Motome, arXiv:2204.06144
    DOI:10.48550/arXiv.2204.06144

MURASHIMA, Takahiro [B class; 600 (B), 90 (C)] (293)

— *Development of multiscale simulation technique for liquids and solids*

1. Viscosity Overshoot in Biaxial Elongational Flow: Coarse-Grained Molecular Dynamics Simulation of Ring-Linear Polymer Mixtures
   T. Murashima, K. Hagita and T. Kawakatsu, Macromolecules **54**, 7210 (2021).
   DOI:10.1021/acs.macromol.1c00267

NADA, Hiroki [B,C class; 500 (B), 750 (C)] (274, 275)

— *Creation of a Method for Design of Scale Formation Control Molecules by a Metadynamics Method*

— *Elucidation of pathways for the crystallization of ionic liquids by large-scale metadynamics simulation*

1. Stable Binding Conformations of Polymaleic and Polyacrylic Acids at a Calcite Surface in the Presence of Countercations: A Metadynamics Study
   H. Nada, submitted to Langmuir

NAKAGAWA, Naoko [C class; 3800 (B), 700 (C)] (240)

— *Steady states realized by a global thermodynamic balance in nonequilibrium*

1. Work relation for determining the mixing free energy of small-scale mixtures
   A. Yoshida and N. Nakagawa, Phys. Rev. Research, to appear (2022).

NAKAMURA, Kazuma [C class; 2600 (B), 0 (C)] (108)

— *Ab initio calcualtion for reflectivity for SrVO3/SrTiO3 CaCuO2/SrTiO3, and Ca5Ir3O12*

— *Ab initio derivation of effective low-energy models for SrVO3/SrTiO3 and CaCuO2/SrTiO3 multi-*

layer system

1. Ab initio derivation of low-energy Hamiltonians for systems with strong spin-orbit interaction: Application to $Ca_5Ir_3O_{12}$
   M. Charlebois, J. B. Moree, K. Nakamura, Y. Nomura, T. Tadano, Y. Yoshimoto, Y. Yamaji, T. Hasegawa, K. Matsuhira, and M. Imada, Phys. Rev. B **104**, 075153 (2021).
   DOI:10.1103/PhysRevB.104.075153

2. RESPACK: An ab initio tool for derivation of effective low-energy model of material
   Kazuma Nakamura, Yoshihide Yoshimoto, Yusuke Nomura, Terumasa Tadano, Mitsuaki Kawamura, Taichi Kosugi, Kazuyoshi Yoshimi, Takahiro Misawa, and Yuichi Motoyama, Comput. Phys. Commun. **261**, 107781 (2021).
   DOI:10.1016/j.cpc.2020.107781

NAKANO, Hiroki [C class; 1400 (B), 450 (C)] (266)
— *Numerical study on low-energy states of quantum spin systems*

1. Magnetization process of the S=1/2 Heisenberg antiferromagnet on the floret pentagonal lattice
   R. Furuchi, H. Nakano, N. Todoroki, and T. Sakai, J. Phys. Commun. 5 125008 (2021).
   DOI:10.1088/2399-6528/ac3f7a

NAKANO, Hiroyoshi [C class; 4000 (B), 0 (C)] (247)
— *Molecular dynamics study of surface nanobubbles under non-equilibrium conditions*

1. Molecular dynamics study of shear-induced long-range correlations in simple fluids
   Hiroyoshi Nakano and Yuki Minami, Phys. Rev. Research in press.

NAKAYAMA, Takashi [C class; 3000 (B), 700 (C)] (93)
— *First-principles study on charging-induced structure phase transitions of thin film oxides*

1. Clustering feature of metal atoms in pentacene molecular solids: the first-principles study
   S. Watanabe, Y. Tomita, K. Kawabata, T. Nakayama, Jpn. J. Appl. Phys. **61**, 021003 (2022).
   DOI:10.35848/1347-4065/ac41e2

2. Impacts of terminal molecules on metal-atom diffusion into alkane self-assembled-monolayer films: first-principles study
   S. Watanabe, T. Nakayama, Jpn. J. Appl. Phys. **60**, 125505 (2021).
   DOI:10.35848/1347-4065/ac3181

3. New types of resonant tunneling currents at Si-p/n junctions: One-dimensional model calculation
   S. Cho, T. Nakayama, Jpn. J. Appl. Phys. **60**, 054002 (2021).
   DOI:10.35848/1347-4065/abf782

NASU, Joji [C class; 3800 (B), 800 (C)] (190)
— *Numerical study of topological thermal transport in Kitaev-related systems*

1. Role of Majorana fermions in spin transport of anisotropic Kitaev model
   H. Taguchi, Y. Murakami, A. Koga, and J. Nasu, Phys. Rev. B **104**, 125139 (2021).

2. Field-angle dependence of thermal Hall conductivity in a magnetically ordered Kitaev-Heisenberg system
   S. Koyama and J. Nasu, Phys. Rev. B **104**, 075121 (2021).

3. Spin dynamics in the Kitaev model with disorder: Quantum Monte Carlo study of dynamical spin structure factor, magnetic susceptibility, and NMR relaxation rate
   J. Nasu and Y. Motome, Phys. Rev. B **104**, 035116-1-17 (2021).

4. Majorana correlations in the Kitaev model with ordered-flux structures
   A. Koga, Y. Murakami, and J. Nasu, Phys. Rev. B **103**, 214421 (2021).

5. Field-angle dependence of thermal transport in Kitaev-Γ model
   S. Koyama and J. Nasu, J. Phys.: Conf. Ser. **2164**, 012071 (2022).

NIKI, Kaori [B,C class; 400 (B), 250 (C)] (143)
— *Calculation of photoelectron angle distribution in the photoexcitation process on the organic molecules adsorbed surface*
— *Development of time-resolved analysis method for molecular crystal surface*

1. A Faster Method of Photoelectron Intensity Calculation Based on Multiple Scattering Theory
   M. Haniuda, M. Nozaki, and K. Niki, J. Surf. Sci. and Nanotech.

2. The electronic and structural dynamics of CuPc
   Kiana Baumgartner, Misa Nozaki, Christian Metzger, Masato Haniuda, Kaori Niki, Daria Popova-Gorelova, Kai Rossnage, Markus Scholz, Science

NISHIDATE, Kazume [C class; 400 (B), 0 (C)] (163)
— *First-principles electronic structure calculation of double-perovskite photocatalyst*

NISHIGUCHI, Kazutaka [B class; 400 (B), 0 (C)] (314)
— *Theoretical study of thermoelectric properties in doped Fe_2VAl: A weak-coupling approach*

1. Possibility of N-type Doping in $CaAl_2Si_2$-type Zintl Phase Compound $CaZn_2X_2$ (X = As, P)
   K. Nishiguchi, M. Ochi, C. H. Lee, and K. Kuroki, J. Phys. Soc. Jpn., in press.

NOGUCHI, Hiroshi [C class; 11600 (B), 1250 (C)] (212)
— *structure formation of biomembrane*

1. Binding of anisotropic curvature-inducing proteins onto membrane tubes
   H. Noguchi, C. Tozzi, and M. Arroyo Soft Matter **18**, 3384 (2022).
   DOI:10.1039/D2SM00274D

2. Hydrophobic immiscibility controls self-sorting or co-assembly of peptide amphiphiles
   Rie Wakabayashi, Rino Imatani, Mutsuhiro Katsuya, Yuji Higuchi, Hiroshi Noguchi, Noriho Kamiya, and Masahiro Goto Chem. Commun. **58**, 585 (2022).
   DOI:10.1039/D1CC05560G

3. Effects of gas-liquid phase transitions on soundwave propagation: A molecular dynamics study
   Y. Asano, H. Watanabe, and H. Noguchi Phys. Rev. Fluids, (2022) in press.

NOGUCHI, Yoshifumi [C class; 5200 (B), 800 (C)] (78)
— *XAS simulations by first-principles GW+Bethe-Salpeter method*

1. Absorption Spectra for Firefly Bioluminescence Substrate Analog: TokeOni in Various pH Solutions
   Haruhisa Ogawa, Ryohei Ono, Yoshifumi Noguchi, Nobuo Kitada, Ryohei Saito-Moriya, Shojiro A. Maki, Hidefumi Akiyama, Hideyuki Itabashi, and Miyabi Hiyama, Photochem. Photobiol. **97**, 1016 (2021).
   DOI:10.1111/php.13458

2. Exciton maps for thermally activated delayed fluorescence active/inactive carbazole benzonitrile derivatives

Yoshifumi Noguchi, J. Chem. Phys. **155**, 204302 (2021).
DOI:10.1063/5.0068402

3. Fragment-Based Excited-State Calculations Using the GW Approximation and the Bethe − Salpeter Equation
   Takatoshi Fujita and Yoshifumi Noguchi, J. Phys. Chem. A **125**, 10580 (2021).
   DOI:10.1021/acs.jpca.1c07337

NOMURA, Yusuke [C class; 5200 (B), 800 (C)] (184)
— *Finite-temperature calculations for quantum many-body systems using Boltzmann machine*

1. RESPACK: An ab initio tool for derivation of effective low-energy model of material
   Kazuma Nakamura, Yoshihide Yoshimoto, Yusuke Nomura, Terumasa Tadano, Mitsuaki Kawamura, Taichi Kosugi, Kazuyoshi Yoshimi, Takahiro Misawa, and Yuichi Motoyama, Comput. Phys. Commun. **261**, 107781 (2021).
   DOI:10.1016/j.cpc.2020.107781

2. Helping restricted Boltzmann machines with quantum-state representation by restoring symmetry
   Yusuke Nomura, J. Phys.: Condens. Matter **33**, 174003 (2021).

3. qeirreps: An open-source program for Quantum ESPRESSO to compute irreducible representations of Bloch wavefunctions
   Akishi Matsugatani, Seishiro Ono, Yusuke Nomura, and Haruki Watanabe, Comput. Phys. Commun. **264**, 107948 (2021).
   DOI:10.1016/j.cpc.2021.107948

4. Purifying Deep Boltzmann Machines for Thermal Quantum States
   Yusuke Nomura, Nobuyuki Yoshioka, and Franco Nori, Phys. Rev. Lett. **127**, 060601 (2021).

5. Dirac-Type Nodal Spin Liquid Revealed by Refined Quantum Many-Body Solver Using Neural-Network Wave Function, Correlation Ratio, and Level Spectroscopy
   Yusuke Nomura and Masatoshi Imada, Phys. Rev. X **11**, 031034 (2021).

6. Ab initio derivation of low-energy Hamiltonians for systems with strong spin-orbit interaction: Application to Ca5Ir3O12
   Maxime Charlebois, Jean-Baptiste More, Kazuma Nakamura, Yusuke Nomura, Terumasa Tadano, Yoshihide Yoshimoto, Youhei Yamaji, Takumi Hasegawa, Kazuyuki Matsuhira, and Masatoshi Imada, Phys. Rev. B **104**, 075153 (2021).
   DOI:10.1103/PhysRevB.104.075153

NOZAWA, Kazuki [C class; 400 (B), 400 (C)] (137)
— *First-principles calculations of complex metallic alloy surfaces*

OBATA, Masao [B class; 700 (B), 120 (C)] (136)
— *Analysis of ferroelectric-ferromagnetic interface and magnetic material with an anisotropic crystal structure*
— *Analysis of insulator-ferromagnetic interface and magnetic material with an anisotropic crystal structure*

1. Effect of electron localization in theoretical design of Ni-Mn-Ga based magnetic shape memory alloys
   Zelený, Martin and Sedlák, Petr and Heczko, Oleg and Seiner, Hanuš and Vertát, Petr and Obata, Masao and Kotani, Takao and Oda, Tatsuki and Straka, Ladislav, Mater. Des. **209**, 109917 (2021).
   DOI:10.1016/j.matdes.2021.109917

ODA, Tatsuki [C class; 4800 (B), 950 (C)] (83)
— *Analyses on electronic structure and magnetoelectric effect in high-performance spintronics and magnetic materials*

1. Effect of electron localization in theoretical design of Ni-Mn-Ga based magnetic shape memory alloys
   Martin Zelen, Petr Sedlk, Oleg Heczko, Hanu Seiner, Petr Vett, Masao Obata, Takeo Kotani, Tatsuki Oda, and Ladislav Straka, Materials & Design **209**, 109917 (2021).

OGUCHI, Tamio [C class; 3200 (B), 350 (C)] (99)
— *Magnetocaloric Effect of Transition-Metal Alloys*

1. Tavorite-type orthorhombic A_xVPO$_4$F (A = Li, Na) for novel high-voltage cathodes in rechargeable batteries
   Huu Duc Luong, Van An Dinh, Hiroyoshi Momida, Tamio Oguchi, J. Alloys Compd. **875**, 159963 (2021).

2. CrySPY: a crystal structure prediction tool accelerated by machine learning
   Tomoki Yamashita, Shinichi Kanehira, Nobuya Sato, Hiori Kino, Kei Terayama, Hikaru Sawahata, Takumi Sato, Futoshi Utsuno, Koji Tsuda, Takashi Miyake, Tamio Oguchi, Sci. Technol. Adv. Mater.: Methods **1**, 87 (2021).

3. Atomic-layer stacking dependence of the magnetocrystalline anisotropy in Fe-Co multilayer thin films at MgO(001) interface
   K. Nakamura, K. Nozaki, K. Hayashi, A.-M. Pradipto, M. Weinert, T. Oguchi, J. Magn. Magn. Mater. **537**, 168175 (2021).

4. Electric-field tuning of magnetic properties of bilayer VI$_3$: A first-principles study
   Thi Phuong Thao Nguyen, Kunihiko Yamauchi, Tamio Oguchi, Danila Amoroso, Silvia Picozzi, Phys. Rev. B **104**, 014414 (2021).

5. First-Principles Study on Cathode Properties of Li$_2M$TiO$_4$ and Na$_2M$TiO$_4$ (M = V, Cr, Mn, Fe, Co, Ni)
   Kunihiko Yamauchi, Hiroyoshi Momida, Tamio Oguchi:, J. Phys. Soc. Jpn. **91**, 034704 (2022).

6. Understanding doping effects on P2 Na$_x$Mn$_{1-y}M_y$O$_2$ (M=Li, Mg, Al, Ti, V, Cr, Fe, Co, Ni) cathode materials for Na-ion batteries
   Huu Duc Luong, Hiroyoshi Momida, Van An Dinh, Tamio Oguchi, Phys. Rev. Mater. **6**, 015802 (2022).

7. Performance and reaction mechanisms of tin compounds as high-capacity negative electrodes of lithium and sodium ion batteries
   Hiroki Kotaka, Hiroyoshi Momida, Tamio Oguchi, Mater. Adv. **3**, 2793-2799 (2022).

8. Spin-Polarized Band Structure in MoTe$_2$/Bi$_2$Se$_3$ Heterostructure Designed from First Principles
   Kunihiko Yamauchi, Ryoma Shimazu, Tamio Oguchi, J. Phys. Soc. Jpn. **91**, 044705 (2022).

9. Insight into anisotropic magnetocaloric effect of CrI$_3$
   Hung Ba Tran, Hiroyoshi Momida, Yu-ichiro Matsushita, Koun Shirai, Tamio Oguchi, Acta Mater. **231**, 117851 (2022).

10. Effect of magnetocrystalline anisotropy on magnetocaloric properties of an AlFe$_2$B$_2$ compound
    Hung Ba Tran, Hiroyoshi Momida, Yu-ichiro Matsushita, Kazunori Sato, Yukihiro Makino, Koun Shirai, Tamio Oguchi, Phys. Rev. B **105**, 134402 (2022).

OHKUBO, Yuji [B class; 400 (B), 0 (C)] (161)
— *Clarification of atomistic mechanism application of process design for adhesion interface between metal and plasma-treated fluoropolymers using first principles calculation*

OHMURA, Satoshi [C class; 2200 (B), 0 (C)] (112)
— *Ab initio molecular dynamics study on ion-conduction mechanisms of perovskite-type oxide*

1. Liquid Structure of Tantalum under Internal Negative Pressure
   Katagiri, K. and Ozaki, N. and Ohmura, S. and Albertazzi, B. and Hironaka, Y. and Inubushi, Y. and Ishida, K. and Koenig, M. and Miyanishi, K. and Nakamura, H. and Nishikino, M. and Okuchi, T. and Sato, T. and Seto, Y. and Shigemori, K. and Sueda, K. and Tange, Y. and Togashi, T. and Umeda, Y. and Yabashi, M. and Yabuuchi, T. and Kodama, R., Phys. Rev. Lett. 126, 175503 (2021).
   DOI:10.1103/PhysRevLett.126.175503

2. Tracking the light-driven layer stacking of graphene oxide
   Yajima and Ryo Shikata and Tomohiro Iguchi and Keishi Akada and Shoji Yoshida and Jun-ichi Fujita and Shin-ya Koshihara and Yuta Nishina, Carbon 183, 612 (2021).
   DOI:10.1016/j.carbon.2021.07.058

OHNISHI, Masato [C class; 4600 (B), 750 (C)] (87)
— *Low Thermal Conductance Generated by van der Waals Interaction*

1. Strain-induced band modulation of thermal phonons in carbon nanotubes
   Masato Ohnishi, Junichiro Shiomi, Phys. Rev. B 104, 014306 (2021).

OHNO, Akira [B class; 400 (B), 70 (C)] ()
— *Correlation between Order Parameter and Electron Transport Mechanism in Liquid Crystal*

OHNO, Kaoru [C class; 6600 (B), 950 (C)] (68)
— *Improvement and application of all-electron mixed basis program*

1. Study on Ni-Ti alloys around equiatomic composition by the first-principles phase field method
   K. Ohno, M. Tsuchiya, R. Kuwahara, R. Sahara, S. Bhattacharyya, and T. N. Pham, Comp. Mat. Sci. **191**, 110284 (2021).
   DOI:10.1016/j.commatsci.2021.110284

2. Effect of the Pt concentration on microstructures of Ti-Pt alloys using the first-principles phase field method
   Thi Nu Pham, Kaoru Ohno, Ryoji Sahara, Riichi Kuwahara, and Swastibrata Bhattacharyya, Acta Materialia **215**, 117050 (2021).
   DOI:10.1016/j.actamat.2021.117050

OHSAWA, Kazuhito [C class; 400 (B), 0 (C)] (159)
— *Study of interaction between radiation damage and interstitial atom*

OHTO, Tatsuhiko [C class; 4000 (B), 0 (C)] (91)
— *First-principles transport calculations for single-molecular junctions*

OHTSUKI, Tomi [C class; 5600 (B), 850 (C)] (228)
— *Critical phenomena in novel Anderson transitions*

1. Analysis of KohnSham Eigenfunctions Using a Convolutional Neural Network in Simulations of the MetalInsulator Transition in Doped Semiconductors

Y. Harashima, T. Mano, K. Slevin, T. Ohtsuki, J. Phys. Soc. Jpn. **90**, 094001 (2021).
DOI:10.7566/JPSJ.90.094001

OKADA, Ken [C class; 3600 (B), 650 (C)] ()
— *Variational Monte Carlo study of twisted bilayer graphene*

OKAZAKI, Susumu [C class; 3600 (B), 700 (C)] (243)
— *Investigation of the molecular origins of the mechanical and thermal properties of realistic biopolymers using all-atomistic molecular dynamics*

1. Algorithm to minimize MPI communications in the parallelized fast multipole method combined with molecular dynamics calculations
   Yoshimichi Andoh,Shin-ichi Ichikawa,Tatsuya Sakashita,Noriyuki Yoshii,Susumu Okazaki, J. comput. chem. **42**, 1073 (2021),
   DOI:10.1002/jcc.26524

2. A comparison of the brittle PMMA with the ductile PC on the elasticity and yielding from a molecular dynamics perspective
   Zhiye Tang, Kazushi Fujimoto, Susumu Okazaki, Polymer **226**,123809 (2021),
   DOI:10.1016/j.polymer.2021.123809

3. Three-dimensional free-energy landscape of hydrogen and oxygen molecules in polymer electrolyte membranes: Insight into diffusion paths
   Tetsuro Nagai, Kazushi Fujimoto, Susumu Okazaki, J. Chem. Phys. **156**, 044507 (2022),
   DOI:10.1063/5.0075969

4. Dynamic Monte Carlo calculation generating particle trajectories which satisfy diffusion equation for heterogeneous systems with position-dependent diffusion coefficient and free energy
   Tetsuro Nagai, Akira Yoshimori, Susumu Okazaki, J. Chem. Phys. **156**, 154506 (2022),
   DOI:10.1063/5.0086949

OKUBO, Masashi [B class; 400 (B), 30 (C)] (157)
— *Development of all-solid-state capacitors using sulfide-based solid electrolytes*

OKUBO, Tsuyoshi [C class; 11600 (B), 1300 (C)] (210)
— *Finite temperature property of the Kitaev models*
— *Finite temperature property of the Kitaev spin liquid*

1. Bond-weighted Tensor Renormalization Group
   D. Adachi, T. Okubo and S. Todo, Phys. Rev. B, **105**, L060402 (2022).
   DOI:10.1103/PhysRevB.105.L060402

2. Phase Shift in Skyrmion Crystals
   S. Hayami, T. Okubo, and Y. Motome, Nature Commun., **12**, 6927 (2021).
   DOI:10.1038/s41467-021-27083-0

3. TeNeS: Tensor Network Solver for Quantum Lattice Systems
   Y. Motoyama, T. Okubo, K. Yoshimi, S. Morita, T. Kato, and N. Kawashima, arXiv:2112.13184
   DOI:10.48550/arXiv.2112.13184

4. Possibility of a topological phase transition in two-dimensional frustrated Heisenberg spin systems
   T. Okubo and N. Kawashima, arXiv:2112.15053
   DOI:10.48550/arXiv.2112.15053

OKUMURA, Hisashi [C class; 5600 (B), 850 (C)] (227)
— *Molecular dynamics simulations for assembly and disassembly of protein aggregates*

1. Role of water molecules in the laser-induced disruption of amyloid fibrils observed by nonequilibrium molecular dynamics simulations
   H. Okumura, S. G. Itoh, K. Nakamura, and T. Kawasaki, J. Phys. Chem. B **125**, 4964 (2021).
   DOI:10.1021/acs.jpcb.0c11491

2. Implementations of replica-permutation and replica sub-permutation methods into LAMMPS
   M. Yamauchi, G. La Penna, S. G. Itoh, and H. Okumura, Comput. Phys. Commun. **276**, 108362 (2022).
   DOI:10.1016/j.cpc.2022.108362

ONO, Atsushi [B class; 300 (B), 0 (C)] (204)
— *Photoinduced nonequilibrium dynamics in correlated electron systems*

1. Ultrafast reorientation of the Néel vector in antiferromagnetic Dirac semimetals
   A. Ono and S. Ishihara, npj Comput. Mater. **7**, 171 (2021).
   DOI:10.1038/s41524-021-00641-2

ONO, Shota [B,C class; 1100 (B), 300 (C)] (126)
— *Stability of atomically thin alloys*
— *Stability of atomically thin alloys: II*

1. Theoretical prediction on the immiscible Pb-Sn alloy stabilized on metal surfaces
   S. Ono, J. Yuhara, and J. Onoe, Chem. Phys. Lett. **776**, 138696 (2021).
   DOI:10.1016/j.cplett.2021.138696

2. Metastability relationship between two- and three-dimensional crystal structures: a case study of the Cu-based compounds
   S. Ono, Sci. Rep. **11**, 14588 (2021).
   DOI:10.1038/s41598-021-94034-6

3. Comprehensive search for buckled honeycomb binary compounds based on noble metals (Cu, Ag, and Au)
   S. Ono, Phys. Rev. Materials **5**, 104004 (2021).
   DOI:10.1103/PhysRevMaterials.5.104004

ONO, Tomoya [C class; 9400 (B), 800 (C)] (60)
— *Development of first-principles electronic-structure and transport calculation code RSPACE and simulations for device*

1. Theoretical investigation of vacancy related defects at 4H-SiC($000\bar{1}$)/SiO_2 interface after wet oxidation
   M. Tsunasaki, T. Ono and M. Uemoto, Jpn. J. Appl. Phys. **61** (2022) SH1001.

2. First-Principles Study on Structure and Anisotropy of High N-atom Density Layer in 4H-SiC
   M. Uemoto, N. Komatsu, Y. Egami and T. Ono, J. Phys. Soc. Jpn. **90** (2021) 124713.

ORIMOTO, Yuuichi [C class; 1600 (B), 350 (C)] (116)
— *First principles calculations of two-dimensional ordering process at organic/inorganic materials interface*

OSHIKAWA, Masaki [B class; 600 (B), 90 (C)] (291)
— *Study on gapless SPT phases in quantum spin systems*

1. $\mathbf{Z}_2$-enriched symmetry indicators for topological superconductors in the 1651 magnetic space groups
   Seishiro Ono, Hoi Chun Po, and Ken Shiozaki, Phys. Rev. Research 3, 023086 (2021).
   DOI:10.1103/PhysRevResearch.3.023086

2. qeirreps: An open-source program for Quantum ESPRESSO to compute irreducible representations of Bloch wavefunctions
   Akishi Matsugatani, Seishiro Ono, Yusuke Nomura, and Haruki Watanabe, Comput. Phys. Commun. **264**, 107948 (2021).
   DOI:10.1016/j.cpc.2021.107948

3. Resolving the Berezinskii-Kosterlitz-Thouless transition in the two-dimensional XY model with tensor-network-based level spectroscopy
   Atsushi Ueda and Masaki Oshikawa, Phys. Rev. B 104, 165132 (2021).
   DOI:10.1103/PhysRevB.104.165132

4. Tensor Network Renormalization Study on the Crossover in Classical Heisenberg and RP2 Models in Two Dimensions
   Atsushi Ueda and Masaki Oshikawa, arXiv.2202.07042
   DOI:10.48550/arXiv.2202.07042

OSHIYAMA, Atsushi [E class; 32500 (B), 3300 (C)] (42)
— *Clarification of Microscopic Mechanisms of Semiconductor Epitaxial Growth and Device-Interface Formation by Large-Scale Quantum-Theory-Based Computations*

1. Gallium-gallium weak bond that incorporates nitrogen at atomic steps during GaN epitaxial growth
   K. M. Bui, K. Shiraishi and A. Oshiyama, Appl. Surf. Sci. **557**, 149542 (2021).

2. Microscopic mechanism of adatom diffusion on stepped SiC surfaces revealed by first-principles calculations
   K. Seino and A. Oshiyama, Appl. Surf. Sci. **561**, 149927 (2021).

3. Defect-free interface between amorphous $(\mathrm{Al_2O_3})_{1-x}(\mathrm{SiO_2})_x$ revealed by first-principle molecular dynamics simulations
   K. Chokawa, K. Shiraishi and A. Oshiyama, Appl. Phys. Lett. **119**, 011602 (2021).

4. Order-N orbital-free density-functional calculations with machine learning of functional derivatives for semiconductors and metals
   F. Imoto, M. Imada adn A. Oshiyama, Phys. Rev. Research **3**, 033198 (2021).

OTANI, Minoru [E class; 14500 (B), 2200 (C)] (342)
— *Development and Application of electrochemical-reaction simulation methods at the solid/solution interfaces*

OTSUKI, Michio [C class; 2200 (B), 550 (C)] (258)
— *Three-Dimensional Finite Element Analysis of Friction between solids*

OZAKI, Taisuke [C class; 5000 (B), 350 (C)] (85)
— *Prediction of new crystal structures based on the densest ternary sphere packings*

1. Densest ternary sphere packings
   Ryotaro Koshoji and Taisuke Ozaki, Phys. Rev. E 104, 024101 (2021).
   DOI:10.1103/PhysRevE.104.024101

OZEKI, Yukiyasu [C class; 7600 (B), 0 (C)] (218)
— *Development and improvement of dynamical scaling analysis for critical phenomena*
— *Development and improvement of dynamical scaling analysis for critical phenomena II*

RAEBIGER, Hannes [C class; 5000 (B), 800 (C)] (81)
— *First principles theory of carrier localization in transition metal compounds*

1. Parallel alignment of methylammonium cations in orthorhombic $CH_3NH_3PbCl_3$ single crystal observed by polarized micro-Raman scattering spectroscopy
   Y. Kim, S. Bae,J. Park, T. T. .T. Nguyen, H. R. Jung, W. Jo, Y.-H. Kim, H. Raebiger, S. Yoon, Chem. Mater. **34**, 2972 (2022).
   DOI:10.1021/acs.chemmater.1c03744

2. Strain engineering to release trapped hole carriers in p-type haeckelite GaN
   S. Bae, Y.-G. Kang, K. Ichihashi, M. Khazaei, V. Swamy, M. J. Han, K. J. Chan, K.-i. Shudo, H. Raebiger, ACS Appl. Electron. Mater. **3**, 5257 (2021).
   DOI:10.1021/acsaelm.1c00765

3. MXene Phase with C3 Structure Unit: A Family of 2D Electrides
   S. Bae, W. Espinoza-García, J-G. Kang, N. Egawa, J. Lee, K. Kuwahata, M. Khazaei, K. Ohno, Y-H. Kim, M. J. Han, H. Hosono, G. M. Dalpian, and H. Raebiger, Adv. Funct. Mater. **31**, 2100009 (2021).
   DOI:10.1002/adfm.202100009

SAITO, Mineo [C class; 8200 (B), 0 (C)] (67)
— *First-principles calculations on muon in solids*

1. Electronic Band Structures of Group-IV Two-Dimensional Materials: Spin-Orbit Coupling and Group Theoretical Analysis
   S. A. Puturi, Y. Yamaguchi, T. A. Ariasoca, M. Y. H. Widianto, K. Tagami and M. Saito, Surf. Sci. **714**, 121917 (2021) .
   DOI:10.1016/j.susc.2021.121917

2. Electronic Structures of Puckered Bilayer Group-V Two-Dimensional Materials: Group Theoretical analysis
   M. Y. H. Widianto, A. Zaharo, N. A. P. Namari1, and M. Saito, Jpn. J. Appl. Phys. **60**, 061001 (2021) .
   DOI:10.35848/1347-4065/ac0004

3. Analysis of Band Structures of Phosphorene and Bithemauthene Based on the Double Group Theory
   M. Y. H. Widianto and M. Saito, Jpn. J. Appl. Phys. **61**, 035503 (2022) .
   DOI: 10.35848/1347-4065/ac4c4e

SAKAGUCHI, Norihito [C class; 6200 (B), 0 (C)] (72)
— *Reduction of Rare Metals in Fuel Cell Catalysts and Hydrogen Permeable Membrane*

1. Anisotropic Growth of Copper Nanorods Mediated by Cl^- Ions
   M. J. Saw, M. T. Nguyen, Y. Kunisada, T. Tokunaga, T. Yonezawa, ACS Omega **7**, 7414 (2022).
   DOI:10.1021/acsomega.2c00359

SAKAI, Masatoshi [B class; 500 (B), 100 (C)] (298)
— *Charge order structure in organic charge order materials*
— *Origin of the electronic conductivity on organic charge order materials*

SAKAI, Toru [C class; 4800 (B), 150 (C)] (235, 236)
— *Numerical Diagonalization Study on Magnetization Process of Quantum Spin Chain with the Biquadratic Interaction*
— *Numerical Diagonalization Study on Quantum Phase Transitions of Frustrated Spin Systems*

1. Quantum spin nematic liquid in the S=1 antiferromagnetic chain with the biquadratic interaction
   T. Sakai, AIP Advances 11, 015306 (2021).

2. EPR Theories for Selection Rules to Observe the Spin Gap
   T. Sakai, Applied Magnetic Resonance 52, 507 (2021).

3. Magnetization process of the S=1/2 Heisenberg antiferromagnet on the floret pentagon lattice
   R. Furuchi, H. Nakano, N. Todoroki and T. Sakai, J. Phys. Commun. 5, 125008 (2021).

4. Field-Induced Quantum Spin Nematic Liquid Phase in the S=1 Antiferromagnetic Heisenberg Chain with Additional Interactions
   T. Sakai, H. Nakano, R. Furuchi and K. Okamoto, J. Phys.: Conf. Ser. 2164, 012030 (2022).

5. Magnetization plateau of the distorted diamond spin chain with anisotropic ferromagnetic interaction
   T. Sakai, K. Okamoto, H. Nakano and R. Furuchi, AIP Advances 12, 035030 (2022).

SAKAKIBARA, Hirofumi [B class; 400 (B), 70 (C)] (152)
— *Automatic generation of first-principle effective models based on MLO*

SAKASHITA, Tatsuya [B class; 200 (B), 120 (C)] (318)
— *Development of integrated interface of eigensolvers Rokko and application to quantum spin systems*

SASAKI, Takehiko [C class; 2200 (B), 400 (C)] (106)
— *Study on Hydration Process of Cellobiose by First Principles Calculations*

1. The mechanism of sorbitol dehydration in hot acidic solutions
   T. Kondo, T. Sasaki, M. Shiga, J. Comput. Chem. **42**, 1783 (2021).
   DOI:10.1002/jcc.26710

2. X-ray absorption spectra of aqueous cellobiose: Experiment and theory
   D. Akazawa, T. Sasaki, M. Nagasaka, M. Shiga, J. Chem. Phys. **156**, 044202 (2022).
   DOI:10.1063/5.0078963

SATO, Kazunori [B class; 500 (B), 40 (C)] (147)
— *Computational materials design of Ag, Cu chalcogenide based thermoelectric materials*

SATO, Taku [B class; 400 (B), 70 (C)] ()
— *Magnetic excitations in the quantum pyrochlore magnet*

SEKI, Yuya [B class; 400 (B), 30 (C)] (311)
— *Quantum simulation using Ising models*

SHAO, Cheng [C class; 5200 (B), 850 (C)] ()
— *First principles based investigation of phonon-magnon coupling in ferromagnetic insulator*
— *Machine-learning optimization of metal-insulator superlattice thermoelectric materials*

SHIMADA, Toshihiro [B class; 400 (B), 70 (C)] (151)
— *Electronic structure calculation of organic crystals with high molecular weight*

1. Interaction between alkali metals and diamond: etching and charge states of NV centers
   Hiroki Takehana, Ichiro Yamane, Takashi Yanase, Taro Nagahama, Toshihiro Shimada, Carbon, **182**, 585 (2021).
   DOI:10.1016/j.carbon.2021.06.059

2. DFT Calculation of Square MoS2 Nanotubes
   Meiqi Zhang, Mengting Weng, Takahiro Tamura, Manami Goto, Ichiro Yamane, Takashi Yanase, Taro Nagahama, Toshihiro Shimada, Physica E, **130**, 114693 (2021).
   DOI:10.1016/j.physe.2021.114693

SHIMAMURA, Kohei [C class; 2600 (B), 900 (C)] (101)
— *Study of Efficient Training Data Generation Method for Constructing Artificial Neural Network Force Field III*

1. Estimating Thermal Conductivity of α-Ag_2Se Using ANN Potential with Chebyshev Descriptor
   K. Shimamura, Y. Takeshita, S. Fukushima, A. Koura, and F. Shimojo, Chem. Phys. Lett. **778**, 138748 (2021).
   DOI:10.1016/j.cplett.2021.138748

SHIMOJO, Fuyuki [C class; 9400 (B), 1150 (C)] (59)
— *First-Principles Molecular-Dynamics Study of Structural and Electronic Properties of Covalent Liquids and Glasses under Pressure*

1. Estimating Thermal Conductivity of α-Ag_2Se Using ANN Potential with Chebyshev Descriptor
   K. Shimamura, Y. Takeshita, S. Fukushima, A. Koura, and F. Shimojo, Chem. Phys. Lett. **778**, 138748 (2021).
   DOI:10.1016/j.cplett.2021.138748

2. Reproduction of Melting and Crystallization of Sodium by Machine-Learning Interatomic Potential based on Artificial Neural Networks
   A. Irie, S. Fukushima, A. Koura, K. Shimamura, and F. Shimojo, J. Phys. Soc. Jpn. **90**, 094603 (2021).
   DOI:10.7566/JPSJ.90.094603

SHIMOKAWA, Tokuro [C class; 4000 (B), 500 (C)] (239)
— *Thermal effects on quantum frustrated magnetisms*

1. Quantum spin solver near saturation: QS^3
   H. Ueda, S. Yunoki, and T. Shimokawa, Comput. Phys. Commun. **277**, 108369 (2022).
   DOI:10.1016/j.cpc.2022.108369

SHINODA, Wataru [E class; 13500 (B), 2150 (C)] (208)
— *Molecular Simulation of Soft Materials using All-Atom and Coarse-Grained Force Field*

1. Hemimicelle formation of semi-fluorocarbon chains at airwater interface: coarse-grained molecular dynamics study with an extension of the SPICA force field
   Hari OS Yadav, Shogo Harada, An-Tsung Kuo, Shingo Urata, Wataru Shinoda, Mol. Phys. **119**, e21910355 (2021).
   DOI:10.1080/00268976.2021.1910355

2. Analyzing the Role of Surfactants in the Colloidal Stability of Nanoparticles in Oil through Coarse-Grained Molecular Dynamics Simulations
   Mark Z Griffiths, Wataru Shinoda, J. Phys. Chem. B **125**, 6315 (2021).
   DOI:10.1021/acs.jpcb.1c01148

3. All-atom molecular dynamics study of hepatitis B virus containing pregenome RNA in solution
   Kazushi Fujimoto, Youhei Yamaguchi, Ryo Urano, Wataru Shinoda, Tetsuya Ishikawa, Katsumi Omagari, Yasuhito Tanaka, Atsushi Nakagawa, Susumu Okazaki, J. Chem. Phys. **155**, 145101 (2021).
   DOI:10.1063/5.0065765

4. SPICA Force Field for Proteins and Peptides
   Shuhei Kawamoto, Huihui Liu, Yusuke Miyazaki, Sangjae Seo, Mayank Dixit, Russell DeVane, Christopher MacDermaid, Giacomo Fiorin, Michael L Klein, Wataru Shinoda, J. Chem. Theory Comput. 18, 3204 (2022).
   DOI:10.1021/acs.jctc.1c01207

SHINOHARA, Yasushi [C class; 1200 (B), 0 (C)] (128)
— *Atomistic simulations for optical absorption of solids*

1. Semiclassical description of electron dynamics in extended systems under intense laser fields
   Mizuki Tani, Tomohito Otobe, Yasushi Shinohara, and Kenichi L. Ishikawa, Phys. Rev. B **104**, 075157 (2021).
   DOI:10.1103/PhysRevB.104.075157

SHIOMI, Junichiro [C class; 10000 (B), 1100 (C)] (213)
— *Analysis for Thermal Functional Materials using Multi-scale Simulation*

1. Akhiezer mechanism dominates relaxation of propagons in amorphous material at room temperature
   Yuxian Liao, Junichiro Shiomi, J. Appl. Phys. 130, 035101 (2021).
   DOI:10.1063/5.0050159

2. Strain-induced band modulation of thermal phonons in carbon nanotubes
   Masato Ohnishi, Junichiro Shiomi, Phys. Rev. B 104, 014306 (2021).

3. Heat conduction below diffusive limit in amorphous superlattice structures
   Yuxian Liao, Sotaro Iwamoto, Michiko Sasaki, Masahiro Goto, Junichiro Shiomi, Nano Energy 84, 105903 (2021).

4. Exploring diamondlike lattice thermal conductivity crystals via feature-based transfer learning
   Shenghong Ju, Ryo Yoshida, Chang Liu, Stephen Wu, Kenta Hongo, Terumasa Tadano, Junichiro Shiomi, Phys. Rev. Materials 5 , 053801 (2021).

5. Nanoconfinement between Graphene Walls Suppresses the Near-Wall Diffusion of the Ionic Liquid
   Cheng Shao, Wee-Liat Ong, Junichiro Shiomi, Alan JH McGaughey, J. Phys. Chem. B 125, 4527 (2021).

6. Phonon transport in multiphase nanostructured silicon fabricated by high-pressure torsion
   Cheng Shao, Kensuke Matsuda, Shenghong Ju, Yoshifumi Ikoma, Masamichi Kohno, Junichiro Shiomi, J. Appl. Phys. 129, 085101 (2021).

SHIRAI, Tatsuhiko [B class; 900 (B), 0 (C)] (279)
— *Circuit-depth dependence of quantum approximate optimization algorithm*
— *The effect of quantum phase transition on the performance of QAOA*

1. Exact bounds for dynamical critical exponents of transverse-field Ising chains with a correlated disorder
   T. Shirai and S. Tanaka, Ann. Phys. (N. Y.) **435**, 168483 (2021).
   DOI:10.1016/j.aop.2021.168483

SHIRAISHI, Kenji [C class; 10800 (B), 0 (C)] (56, 57)
— *First Pricnciples Study of N Vacancies in Si3N4 for Flash Memory Application*
— *First principles studies of impurity-dislocation complexes in GaN*

SHUDO, Ken-ichi [B class; 300 (B), 30 (C)] ()
— *Virtical Magnetic distribution of nano-scale Co film*

SUGINO, Osamu [E class; 24500 (B), 3200 (C)] (45)
— *First-principles calculation of functionality of hydrogen*
— *First-principles prediction of stability and functionality of complex materials*

1. Machine-learning-based exchange correlation functional with physical asymptotic constraints
   R Nagai, R Akashi, O Sugino, Phys. Rev. Research 4, 013106 (2022).
   DOI:10.1103/PhysRevResearch.4.013106

2. Optical representation of thermal nuclear fluctuation effect on band-gap renormalization
   Kohei Ishii, Jun Haruyama, Osamu Sugino, Phys. Rev. B 104, 245144 (2021).
   DOI:10.1103/PhysRevB.104.245144

3. Functional-renormalization-group approach to classical liquids with short-range repulsion: A scheme without repulsive reference system
   Takeru Yokota, Jun Haruyama, Osamu Sugino, Phys. Rev. E 104, 014124 (2021).
   DOI:10.1103/PhysRevE.104.014124

SUWA, Hidemaro [C class; 5200 (B), 0 (C)] (187)
— *Charge-spin-orbital entanglement of iridates*

1. Extraordinary magnetic response due to emergent isotropic fluctuations in an anisotropic 2D antiferromagnet
   Junyi Yang, Hidemaro Suwa, D. Meyers, Han Zhang, Lukas Horak, Zhan Zhang, Jenia Karapetrova, Jong-Woo Kim, Philip J. Ryan, M. P. M. Dean, Lin Hao, and Jian Liu, submitted to Phys. Rev. Lett.

2. Nematicity and fractional magnetization plateaus induced by spin-lattice coupling in the classical kagome-lattice Heisenberg antiferromagnet
   Masaki Gen and Hidemaro Suwa, submitted to Phys. Rev. B

SUZUKI, Takafumi [C class; 3800 (B), 800 (C)] (237)
— *Supersolid phases in the hard-core bosonic hubbard model on a triangular lattice*
— *Supersolid state in a square-lattice Bose-Hubbard model with dipole interactions*

1. Anisotropy as a diagnostic test for distinct tensor-network wave functions of integer- and half-integer-spin Kitaev quantum spin liquids
   Hyun-Yong Lee, Takafumi Suzuki, Yong Baek Kim, Naoki Kawashima, Phys. Rev B **104**, 024417 (2021).
   DOI:10.1103/physrevb.104.024417

2. Ground-state phase diagram of anisotropically interacting Heisenberg-Γ models on a honeycomb lattice
   Takafumi Suzuki, Takuto Yamada, and S.-I. Suga, Phys. Rev B **103**, 224425 (2021).
   DOI:10.1103/physrevb.103.224425

SUZUKI, Takehito [B class; 100 (B), 10 (C)] (322)

— *Change in period of ordinary earthquakes due to the interaction with slow earthquakes*

SUZUKI, Yuji [C class; 8400 (B), 0 (C)] (65)
— *Development of Polymer Electret Materials for Energy Harvesting Using Machine Learning*

1. Discovery of Polymer Electret Material via de Novo Molecule Generation and Functional Group Enrichment Analysis
   Zhang, Y., Zhang, J., Suzuki, K., Sumita, M., Terayama, K., Li, J., Mao, Z., Tsuda, K., and Suzuki, Y., Appl. Phys. Lett. 118, 223904 (2021).
   DOI:10.1063/5.0051902

TAKAYAMA, Akari [B class; 500 (B), 0 (C)] (299)
— *Structure analysis of 2D materials by using 2DMAT*

TAMURA, Ryo [B class; 200 (B), 80 (C)] (32)
— *Evaluation method of error in effective model estimation*

1. Structural analysis based on unsupervised learning: Search for a characteristic low-dimensional space by local structures in atomistic simulations
   R. Tamura, M. Matsuda, J. Lin, Y. Futamura, T. Sakurai, and T. Miyazaki, Phys. Rev. B **105**, 075107 (2022).
   DOI:10.1103/PhysRevB.105.075107

2. Bayesian optimization package: PHYSBO
   Y. Motoyama, R. Tamura, K. Yoshimi, K. Terayama, T. Ueno, and K. Tsuda, submitted.

TANAKA, Shu [B class; 400 (B), 70 (C)] (307)
— *Development of Algorithms for Ising Machines Based on Statistical Mechanics*

1. Exact bounds for dynamical critical exponents of transverse-field Ising chains with a correlated disorder
   T. Shirai and S. Tanaka, Ann. Phys. (N. Y.) **435**, 168483 (2021).
   DOI:10.1016/j.aop.2021.168483

2. Continuous black-box optimization with an Ising machine and random subspace coding
   S. Izawa, K. Kitai, S. Tanaka, R. Tamura, and K. Tsuda, Physical Review Research, **4** (2022) 023062.
   DOI:10.1103/PhysRevResearch.4.023062

3. Structural analysis based on unsupervised learning: Search for a characteristic low-dimensional space by local structures in atomistic simulations
   R. Tamura, M. Matsuda, J. Lin, Y. Futamura, T. Sakurai, and T. Miyazaki, Phys. Rev. B **105**, 075107 (2022).
   DOI:10.1103/PhysRevB.105.075107

4. Bayesian optimization package: PHYSBO
   Y. Motoyama, R. Tamura, K. Yoshimi, K. Terayama, T. Ueno, and K. Tsuda, submitted.

TANAMOTO, Tetsufumi [B class; 200 (B), 60 (C)] (321)
— *Analysis of transport properties of spin-qubit based on FinFET*

TATETSU, Yasutomi [C class; 2600 (B), 350 (C)] (103)
— *Theoretical analyses for surfaces and grain boundaries with magnetic elements from first-principles calculations*

1. Inter-element miscibility driven stabilization of ordered pseudo-binary alloy

K. Matsumoto, R. Sato, Y. Tatetsu, R. Takahata, S. Yamazoe, M. Yamauchi, Y. Inagaki, Y. Horibe, M. Kudo, T. Toriyama, M. Auchi, M. Haruta, H. Kurata, and T. Teranishi, Nat. Commun., **13**, 1047 (2022).
DOI:10.1038/s41467-022-28710-0

TERAO, Takamichi [B class; 700 (B), 90 (C)] (283)
— *Structural formation of patchy particles*

1. Eigenvalue analysis of the three-dimensional tight-binding model with non-Hermitian disorder
   T. Terao, Phys. Rev. B **103**, 224201 (2021).

TERASAWA, Asako [B class; 400 (B), 80 (C)] ()
— *First-principles analysis of structure and exchange coupling constants of subphases and interface in Nd-based permanent magnets*

TEZUKA, Masaki [C class; 4400 (B), 0 (C)] (242)
— *Scrambling and effect of dissipation in quantum many-body systems*

TODO, Synge [C class; 6000 (B), 900 (C)] (222)
— *Topological order and quantum operation in quantum many-body systems*

1. Bond-weighted tensor renormalization group
   D. Adachi, T. Okubo, and S. Todo, Phys. Rev. B **105**, L060402 (2022).
   DOI:10.1103/PhysRevB.105.L060402

TOHYAMA, Takami [C class; 3000 (B), 700 (C)] (193)
— *Analysis of string excitations in the optical conductivity of doped Mott insulators*

1. Resonating dimer-monomer liquid state in a magnetization plateau of a spin-12 kagome-strip Heisenberg chain
   K. Morita, S. Sota, and T. Tohyama, Commun. Phys. **2**, 161 (2021).
   DOI:10.1038/s42005-021-00665-6

2. Coexistence of strong and weak Majorana zero modes in an anisotropic XY spin chain with second-neighbor interactions
   K. Wada, T. Sugimoto, and T. Tohyama, Phys. Rev. B **104**, 035119 (2021).
   DOI:10.1103/PhysRevB.104.075119

3. Density-matrix renormalization group study of optical conductivity of the Mott insulator for two-dimensional clusters
   K. Shinjo, Y. Tamaki, S. Sota, and T. Tohyama, Phys. Rev. B **104**, 205123 (2021).
   DOI:10.1103/PhysRevB.104.205123

4. Magnetic phase diagrams of the spin-12 Heisenberg model on a kagome-strip chain: Emergence of a Haldane phase
   K. Morita, S. Sota, and T. Tohyama, Phys. Rev. B **104**, 224417 (2021).
   DOI:10.1103/PhysRevB.104.224417

5. Discord effects of inter-cluster interactions on a cluster-based Haldane state in a triangular spin tube
   T. Sugimoto and T. Tohyama, J. Phys.: Conf. Ser. **2164**, 012029 (2022).
   DOI:10.1088/1742-6596/2164/1/012029

6. Antiphase oscillations in the time-resolved spin structure factor of a photoexcited Mott insulator on a square lattice

T. Tohyama, K. Shinjo, and K. Tsutsui, J. Phys.: Conf. Ser. **2164**, 012049 (2022).
DOI:10.1088/1742-6596/2164/1/012049

7. Numerical simulations of spectroscopic properties in two-dimensional Mott insulator
   T. Tohyama, K. Shinjo, S. Sota, and K. Tsutsui, J. Phys.: Conf. Ser. **2207**, 012028 (2022).
   DOI:10.1088/1742-6596/2207/1/012028

TOKUMOTO, Yuki [B class; 400 (B), 70 (C)] (150)
— *Defect formation energy and band structure of Pb-based topological insulators*

TONEGAWA, Takashi [B class; 600 (B), 0 (C)] (296)
— *Numerical Study of the One-Dimensional Quantum Spin Systems with Spatial Structures*

TOYODA, Masayuki [B class; 500 (B), 0 (C)] (148)
— *Thickness-dependent electronic structure of exfoliated boron monosulfide*

TSUMURAYA, Takao [C class; 1000 (B), 550 (C)] (124)
— *Origins of phase stabilities and physical properties in Mg based alloys: A first-principles study*

1. Origin of phase stability in Fe with long-period stacking order as an intermediate phase in cyclic γ-ϵ martensitic transformation
   Takao Tsumuraya and Ikumu Watanabe and Takahiro Sawaguchi Phys. Rev. Research 3, 033215 (2021).
   DOI:10.1103/PhysRevResearch.3.033215

TSUNEYUKI, Shinji [C class; 6000 (B), 900 (C)] (70)
— *Elucidation of mechanism and theoretical prediction of super-functional materials using high-density hydrogen*

1. Superionic Conductivity Combined CB9H10 − Rotation and Li-ion Concerted Motion in LiCB9H10: An Ab Initio and Neural-Net Potential Molecular Dynamics Study
   Ryuhei Sato, Shigeyuki Takagi, Tamio Ikeshoji, Toyota Sato, Takashi Honda, Toshiya Otomo, Shin-ichi Orimo, Shinji Tsuneyuki, submitted to J. Phys. Chem. Lett.

TSURUTA, Kenji [C class; 600 (B), 550 (C)] (130)
— *Ab-initio and artificial neural-network molecular-dynamics calculations for molecule-modified nanointerfaces*

UCHIDA, Takashi [B class; 300 (B), 90 (C)] (316)
— *Multiple spin density waves in inversion-symmetric two-dimensional Hubbard models*
— *Spontaneous formation of multiple-Q orders in inversion-symmetric Hubbard models*

UMEMOTO, Koichiro [C class; 2200 (B), 650 (C)] ()
— *Order-disorder transitions in post-post-perovskite phases in Mg-Si-O system*

WAKABAYASHI, Daisuke [B class; 400 (B), 0 (C)] (312)
— *Large-scale molecular-dynamics simulation of silica melt and glass under high pressure with ANN potentials by active learning*

WATANABE, Haruki [B class; 500 (B), 100 (C)] ()
— *Comprehensive material search based on symmetry indicators*

WATANABE, Hiroshi [B,C class; 5300 (B), 430 (C)] (229)
— *Analysis of the phase boundary under the steady-state heat conduction*

— *Development of an Efficient Phase Diagram Exploration Method Using Gaussian Process Regression*

WATANABE, Hiroshi [B class; 400 (B), 70 (C)] (200)
— *Study of cuprate high-temperature superconductors using 4-band d-p model*

1. Unified description of cuprate superconductors using a four-band *d-p* model
   H. Watanabe, T. Shirakawa, K. Seki, H. Sakakibara, T. Kotani, H. Ikeda, S. Yunoki, Phys. Rev. Research **3**, 033157 (2021).
   DOI:10.1103/PhysRevResearch.3.033157

WATANABE, Satoshi [C class; 10800 (B), 1150 (C)] (47)
— *Analyses related to atomic structures and atom dynamics at complex structures such as surfaces, interfaces and defects*

1. ニューラルネットワークポテンシャルによる金–リチウム合金化過程の解析
   清水康司, E. F. Arguelles, 李文文, 安藤康伸, 南谷英美, 渡邉聡表面と真空 **64**, 369 (2021).
   DOI:10.1380/vss.64.369

2. 窒化物半導体におけるフォノン関連物性の解析のための 機械学習ポテンシャルの開発
   渡邉聡, 清水康司, 南谷英美日本結晶成長学会誌 **48**, 48-4-05 (2021).

3. Ionic Rectification across Ionic and Mixed Conductor Interfaces
   K. Nishio, S. Ichinokura, A. Nakanishi, K. Shimizu, Y. Kobayashi, N. Nakamura, D. Imazeki, R. Shimizu, T. Hirahara, S. Watanabe, and T. Hitosugi, Nano Lett. **21**, 10086 (2021).
   DOI:10.1021/acs.nanolett.1c03872

4. Neural network potential study of point defect properties in multiple charge states: GaN with nitrogen vacancy
   K. Shimizu, Y. Dou, E. F. Arguelles, T. Moriya, E. Minamitani, and S. Watanabe, arXiv.2203.16789
   DOI:10.48550/arXiv.2203.16789

YAMADA, Atsuo [C class; 6200 (B), 900 (C)] (69)
— *First principles analysis on novel energy storage device materials*

1. Soft X-ray Emission Studies on Hydrate-Melt Electrolytes
   T. Shimada, N. Takaneka, E. Watanabe, Y. Yamada, Y. T. Cui, Y. Harada, M. Okubo, A. Yamada, J. Phys. Chem. B **125**, 11534 (2021).
   DOI:10.1021/acs.jpcb.1c07246

2. Relationship between Electric Double-Layer Structure of MXene Electrode and Its Surface Functional Groups
   T. Shimada. N. Takenaka, Y. Ando, M. Otani, M. Okubo, A. Yamada, Chem. Mater. **34**, 2069 (2022).
   DOI:10.1021/acs.chemmater.1c03328

YAMADA, Atsushi [C class; 600 (B), 400 (C)] (195)
— *Studies of the superconductivity and magnetic states in the strongly correlated electron systems based on Hubbard models.*

YAMADA, Masahiko [C class; 6000 (B), 650 (C)] (223, 224)
— *Glass transition in the disordered Kitaev model*
— *Heat capacity and magnetic susceptibility of the SU(N) Heisenberg models*

YAMAGUCHI, Naoya [B class; 900 (B), 110 (C)] (131)
— *First-principles Calculations of Magnetic Insulators Under Uniform Electric Fields*

— *First-principles Calculations of Spin-to-charge Conversion Materials Utilizing Organic Molecules*

1. First-principles LCPAO Approach to Insulators Under Finite Electric Fields
   N. Yamaguchi and F. Ishii, submitted to Comp. Phys. Commun.

2. First-principles calculation of anomalous Hall and Nernst conductivity by local Berry phase
   H. Sawahata, N. Yamaguchi, S. Minami and F. Ishii, submitted to Phys. Rev. B

YAMAJI, Youhei [E class; 14500 (B), 2150 (C)] (177)
— *Numerical studies of Mott transitions in quantum spin liquid candidates*

1. Ab initio derivation of low-energy Hamiltonians for systems with strong spin-orbit interaction: Application to $Ca_5Ir_3O_{12}$
   Maxime Charlebois, Jean-Baptiste More, Kazuma Nakamura, Yusuke Nomura, Terumasa Tadano, Yoshihide Yoshimoto, Youhei Yamaji, Takumi Hasegawa, Kazuyuki Matsuhira, Masatoshi Imada, Phys. Rev. B **104**, 075153 (2021).
   DOI:10.1103/PhysRevB.104.075153

YAMASHITA, Tomoki [C class; 5200 (B), 800 (C)] (76)
— *Development of crystal structure prediction methods using machine learning*

1. CrySPY: a crystal structure prediction tool accelerated by machine learning
   T. Yamashita, S. Kanehira, N. Sato, H. Kino, H. Sawahata, T. Sato, F. Utsuno, K. Tsuda, T. Miyake, and T. Oguchi, Sci. Technol. Adv. Mater. Meth. **1**, 87 (2021).
   DOI:10.1080/27660400.2021.1943171

2. Hybrid algorithm of Bayesian optimization and evolutionary algorithm in crystal structure prediction
   T. Yamashita, H. Kino, K. Tsuda, T. Miyake, and T. Oguchi, Sci. Technol. Adv. Mater. Meth. **2**, 67 (2022).
   DOI:10.1080/27660400.2022.2055987

3. Improvement of look ahead based on quadratic approximation for crystal structure prediction
   T. Yamashita and H. Sekine, Sci. Technol. Adv. Mater. Meth. **2**, 84 (2022).
   DOI:10.1080/27660400.2022.2059335

YAMATO, Takahisa [B class; 400 (B), 80 (C)] (303)
— *Non-uniform thermal transport properties in proteins*

1. Computational study on the thermal conductivity of a protein
   T. Yamato, T. Wang, W. Sugiura, O. Laprvote, T. Katagiri, J. Phys. Chem. B 126, **16**, 3029 (2022).
   DOI:10.1021/acs.jpcb.2c00958

YAMAUCHI, Kunihiko [C class; 5000 (B), 800 (C)] (80)
— *First-principles design of topological interfaces toward next-generation spintronics application*

1. Electric-field tuning of the magnetic properties of bilayer VI3: A first-principles study
   Thi Phuong Thao Nguyen, Kunihiko Yamauchi, Tamio Oguchi, Danila Amoroso, and Silvia Picozzi, Phys. Rev. B **104**, 014414 (2021).
   DOI:10.1103/PhysRevB.104.014414

2. First-principles Study on Piezoelectricity and Spontaneous Polarization in Bi(Fe,Co)O3
   Hiroshi Katsumoto, Kunihiko Yamauchi, and Tamio Oguchi, J. Phys. Soc. Jpn. **90**, 124712 (2021).
   DOI:10.7566/JPSJ.90.124712

3. First-Principles Study on Cathode Properties of Li2MTiO4 and Na2MTiO4 (M = V, Cr, Mn, Fe, Co, Ni)
   Kunihiko Yamauchi, Hiroyoshi Momida, and Tamio Oguchi, J. Phys. Soc. Jpn. **91**, 034704 (2022).
   DOI:10.7566/JPSJ.91.034704

4. Spin-Polarized Band Structure at MoTe2=Bi2Se3 Interface Designed from First Principles
   Kunihiko Yamauchi, Ryoma Shimazu1, and Tamio Oguchi, J. Phys. Soc. Jpn. **91**, 044705 (2022).
   DOI:10.7566/JPSJ.91.044705

YANAGISAWA, Susumu [C class; 5800 (B), 650 (C)] ()
— *First-principles band structure calculation of organic crystals at finite-temperature*
— *First-principles investigation on the electronic properties of polymer organic semiconductors*

YANAGISAWA, Takashi [B class; 300 (B), 30 (C)] (202)
— *New quantum phenomena in strongly correlated many-body electron systems*

1. Ground-state phase diagram of the three-band d-p model
   T. Yanagisawa, M. Miyazaki, K. Yamaji, EPL 134, 27004 (2021).

2. Enhancement of superconductivity due to kinetic energy effect in the strongly correlated phase in the two-dimensional Hubbard model
   T. Yanagisawa: Phys. Lett. A 403, 127382 (2021).

YASUDA, Chitoshi [C class; 2400 (B), 0 (C)] (262)
— *Numerical study of spin systems on the honeycomb lattice*

YASUDA, Yusuke [B class; 300 (B), 30 (C)] (317)
— *Molecular Dynamics Simulations of Reversiblly Cross-linked Rubbers*

YOKO, Akira [B,C class; 3000 (B), 580 (C)] (95)
— *Hydrogen formation by reaction of water on reduced CeO_2 (100) surface*
— *Interaction between metallic atom and instable CeO2 (100) facet*

1. Atomistic Origin of High-Concentration Ce3+ in 100-Faceted Cr-Doped CeO2 Nanocrystals
   X. Hao, A. Yoko, K. Inoue, Y. Xu, M. Saito, C. Chen, G. Seong, T. Tomai, S. Takami, A.L. Shluger, B. Xu, T. Adschiri, Y. Ikuhara, Acta Materialia. **203**, 116473 (2021).
   DOI:10.1016/j.actamat.2020.11.015

YOSHIDA, Tsuneya [C class; 5200 (B), 0 (C)] (185)
— *Exotic phenomena induced by strong correlations and non-Hermitian topology*

1. Surface exceptional points in a topological Kondo insulator
   R. Peters, K. Kimura, Y. Michishita, T. Yoshida, and N. Kawakami, Phys. Rev. B 104, 235153 (2021).
   DOI:10.1103/PhysRevB.104.235153

2. Chiral edge modes in evolutionary game theory: A kagome network of rock-paper-scissors cycles
   T. Yoshida, T. Mizoguchi, and Y. Hatsugai, Phys. Rev. E 104, 025003 (2021).
   DOI:10.1103/PhysRevE.104.025003

3. Topological d-wave superconductivity in two dimensions
   Y. Yanase, A. Daido, K. Takasan, and T. Yoshida, Physica E: Low-dimensional Systems and

Nanostructures, 140, 115143 (2022).
DOI:10.1016/j.physe.2022.115143

YOSHIMOTO, Yuta [C class; 2600 (B), 0 (C)] (259)
— *Next-generation integrated engineering for developing polymer materials*

○ A class

Since this class is for trial use, research reports are not required.
When other classes are also used, their publications are shown in the list of B–E classes.
Then, the pages of their reports and publications are given in ( ).

AKIYAMA, Ryota [A class; 100 (B), 40 (C)] ()
— *Band calculation of topological insulator systems*

FUJINO, Tomoko [A class; 100 (B), 40 (C)] (194, 351)
— *Electronic states of electron-rich oligomer-based conductors*

GONOME, Hiroki [A class; 100 (B), 40 (C)] ()
— *Study of the principle of photothermal conversion by ab initio calculations*

ISHITANI, Yoshihiro [A class; 100 (B), 40 (C)] ()
— *Phonon-property analysis for phonon control in electronic/photonic devices by wide-bandgap semiconductors*

IWASE, Fumitatsu [A class; 100 (B), 40 (C)] ()
— *The ground state of cairo-fractal lattice*

KITAGAWA, Kentaro [A class; 100 (B), 40 (C)] ()
— *Screening test for crystal nucleation of flux method*

KOTA, Yohei [A class; 100 (B), 40 (C)] ()
— *First-principles calculation of physical properties in various magnetic materials*

MASAKI, Yusuke [A class; 100 (B), 50 (C)] (367)
— *Microscopic calculations of fractional vortices in topological superfluids*

MITARAI, Yoko [A class; 100 (B), 40 (C)] ()
— *Phase stability of high-entropy alloys*

NISHIGUCHI, Kazutaka [A class; 100 (B), 50 (C)] (314, 373)
— *First-principles study of thermoelectric and magnetic properties in doped* Fe_2VAl

OKUBO, Masashi [A class; 100 (B), 50 (C)] (157, 377)
— *Development of all-solid-state capacitors using sulfide-based solid electrolytes*

OYA, Yutaka [A class; 100 (B), 40 (C)] ()
— *Molecular dynamics simulation of matrix resin for composite materials*

SATO, Shunsuke [A class; 100 (B), 40 (C)] ()
— *Theoretical investigation on THz-field induced electron dynamics in graphene*

SUZUKI, Yoshikazu [A class; 100 (B), 40 (C)] ()
— *Electronic state calculation of inorganic solid materials using Quantum Espresso*

1. Reassessment of vibration spectra in alkali phosphate crystals
   J. Endo, Y. Suzuki, J. Ceram. Soc. Jpn. **130**, 324 (2022).
   DOI:10.2109/jcersj2.21180

2. Reassessment of vibration spectra in alkaline earth metaphosphate crystals
   J. Endo, Y. Suzuki, J. Ceram. Soc. Jpn. **130**, in press (2022).

DOI:10.2109/jcersj2.22034

TSUKAHARA, Noriyuki [A class; 100 (B), 40 (C)] ()
— *Adsorption states of an organic halogen molecule on semiconductor and metal surfaces*

UCHIDA, Ken [A class; 100 (B), 40 (C)] ()
— *Calculation of thermal conductivity of Hexagonal Tungsten Bronze*

WAKABAYASHI, Daisuke [A class; 100 (B), 50 (C)] (312, 387)
— *Large-scale molecular-dynamics simulation of silica melt under high pressure with ANN potentials*

□ SCCMS Projects

FUJITA, Takatoshi [4000 (B), 0 (C)] (329)

— *Large-Scale GW/BSE electronic structure calculations for metal-organic hybrid materials*

— *Developments of non-linear optical response theory based on electronic structure calculations and their applications to nano and biological systems*

1. Fragment-Based Excited-State Calculations Using the GW Approximation and the Bethe–Salpeter Equation
   T. Fujita and Y. Noguchi J. Phys. Chem. A **125**, 10580 (2021).

FUKUSHIMA, Tetsuya [4000 (B), 700 (C)] (334)

— *Development of high-throughput calculation tools and evaluation of magnetic properties in hard magnetic materials*

— *High-throughput calculation of magnetic anisotropy energy in permanent magnet materials*

1. A novel method for generating p-type wide- and ultrawide-bandgap III-nitride by doping with magnetic elements
   A. Masago, H. Shinya, T. Fukushima, K. Sato, and H. Katayama-Yoshida, Appl. Phys. Exp. **14**, 091007 (2021).
   DOI:10.35848/1882-0786/ac197f

Data Repository

Automatic exhaustive calculations of large material space by Korringa-Kohn-Rostoker coherent approximation method — Applied to equiatomic quaternary high entropy alloys
https://zenodo.org/record/5606502#.Ym8-3y_3Jqs
DOI:10.5281/zenodo.5606502

GOHDA, Yoshihiro [2000 (B), 200 (C)] (79)

— *First-principles study of magnetic interfaces*

1. Role of ferroelectricity, delocalization, and occupancy of d states in the electrical control of interface-induced magnetization
   R. Costa-Amaral and Y. Gohda, Phys. Rev. Appl. **15**, 064014 (2021).
   DOI:10.1103/PhysRevApplied.15.064014

2. Giant converse magnetoelectric effect in a multiferroic heterostructure with polycrystalline Co_2FeSi
   S. Fujii, T. Usami, Y. Shiratsuchi, A.M. Kerrigan, A.M. Yatmeidhy, S. Yamada, T. Kanashima, R. Nakatani, V.K. Lazarov, T. Oguchi, Y. Gohda, and K. Hamaya, NPG Asia Mater., in press.

3. Intrinsic superconductivity of two-monolayer-thick indium film
   T. Ogino, I. Seo, H. Tajiri, M. Nakatake, S. Takakura, Y. Sato, Y. Hasegawa, Y. Gohda, K. Nakatsuji, and H. Hirayama, submitted to Phys. Rev. Lett.

4. Origin of anisotropic magnetoresistance tunable with electric field in Co2FeSi/BaTiO3 multiferroic inetrfaces
   S. Tsuna, R. Costa-Amaral, and Y. Gohda, submitted to Phys. Rev. Mater.

IMADA, Masatoshi [10000 (B), 1400 (C)] (174)

— *Integrated analyses on spectroscopic experiments and ab initio electronic structure calculations for mechanisms of unconventional superconductors*

— *Analysis on Superconducting Mechanism of Cuprate Superconductors*

1. Unconventional dual 1D-2D quantum spin liquid revealed by ab initio studies on organic solids

family
Kota Ido, Kazuyoshi Yoshimi, Takahiro Misawa, and Masatoshi Imada, npj Quantum Mater. **7**, 48 (2022).
DOI:0.1038/s41535-022-00452-8

2. Hidden self-energies as origin of cuprate superconductivity revealed by machine learning
Youhei Yamaji, Teppei Yoshida, Atsushi Fujimori, and Masatoshi Imada Phys. Rev. Research **3**, 043099 (2021).
DOI:10.1103/PhysRevResearch.3.043099

3. Order-N orbital-free density-functional calculations with machine learning of functional derivatives for semiconductors and metals
Fumihiro Imoto, Masatoshi Imada, and Atsushi Oshiyama, Phys. Rev. Research **3**, 033198 (2021).
DOI:10.1103/PhysRevResearch.3.033198

4. *Ab initio* derivation of low-energy Hamiltonians for systems with strong spin-orbit interaction: Application to $\mathrm{Ca_5Ir_3O_{12}}$
Maxime Charlebois, Jean-Baptiste Morée, Kazuma Nakamura, Yusuke Nomura, Terumasa Tadano, Yoshihide Yoshimoto, Youhei Yamaji, Takumi Hasegawa, Kazuyuki Matsuhira, and Masatoshi Imada, Phys. Rev. B **104**, 075153 (2021).
DOI:10.1103/PhysRevB.104.075153

5. Dirac-type nodal spin liquid revealed by refined quantum many-body solver using neural-network wave function, correlation ratio, and level spectroscopy
Yusuke Nomura and Masatoshi Imada, Phys. Rev. X **11**, 031034 (2021).
DOI:10.1103/PhysRevX.11.031034

6. Charge Order and Superconductivity as Competing Brothers in Cuprate High-Tc Superconductors
Masatoshi Imada J. Phys. Soc. Jpn. **90**, 111009 (2021).
DOI:10.7566/JPSJ.90.111009

7. Resonant Inelastic X-Ray Scattering Spectra of Cuprate Superconductors Predicted by Model of Fractionalized Fermions
Masatoshi Imada J. Phys. Soc. Jpn. **90**, 074702 (2021).
DOI:10.7566/JPSJ.90.074702

8. High-temperature superconductivity
Xingjiang Zhou, Wei Sheng Lee, Masatoshi Imada, Nandini Trivedi, Philip Phillips, Hae Young Kee, Päivi Törmä, Mikhail Eremets Nat. Rev. Phys. **3**, 125137 (2021).
DOI:10.1038/s42254-021-00324-3

9. Local moments versus itinerant antiferromagnetism: Magnetic phase diagram and spectral properties of the anisotropic square lattice Hubbard model
Marcin Raczkowski, Fakher F. Assaad, Masatoshi Imada Phys. Rev. B **103**, 462 (2021).
DOI:10.1103/PhysRevB.103.125137

MIYAKE, Takashi [600 (B), 0 (C)] (338)
— *Development of high-performance permanent magnets by large-scale simulation and data-driven approach*

1. Evolutionary search for cobalt-rich compounds in yttrium-cobalt-boron system
Takahiro Ishikawa, Taro Fukazawa, Guangzong Xing, Terumasa Tadano and Takashi Miyake, Phys. Rev. Mater. **5**, 054408 (2021).
DOI:10.1103/PhysRevMaterials.5.054408

2. Ordered and disordered phases in $CaCu_5$-type derived structures: Dumbbell cluster modeling with first-principles calculations
   Fumiaki Kuroda, Taro Fukazawa and Takashi Miyake, Phys. Rev. Mater. **5**, 124405 (2021).
   DOI:10.1103/PhysRevMaterials.5.124405

3. First-principles investigation of $Nd(Fe,M)_{12}$ (M=K-Br) and $Nd(Fe,Cr,Co,Ge,As)_{12}$: possible enhancers of Curie temperature for $NdFe_{12}$
   Taro Fukazawa, Yosuke Harashima, Hisazumi Akai and Takashi Miyake, Acta Materialia, **226**, 117597 (2022).
   DOI:10.1016/j.actamat.2021.117597

4. Hybrid algorithm of Bayesian optimization and evolutionary algorithm in crystal structure prediction
   Tomoki Yamashita, Hiori Kino, Koji Tsuda, Takashi Miyake and Tamio Oguchi, Science and Technology of Advanced Materials: Methods (STAM-M) **2**, 67 (2022).
   DOI:10.1080/27660400.2022.2055987

NAKAYAMA, Masanobu [1500 (B), 0 (C)] (336)

— *Novel chloride solid electrolytes for all solid-state sodium metal battery (2)*

1. First-principles study of the morphology and surface structure of LaCoO3 and La0.5Sr0.5Fe0.5Co0.5O3 perovskites as air electrodes for solid oxide fuel cells
   Masanobu Nakayama, Katsuya Nishii, Kentaro Watanabe, Naoto Tanibata, Hayami Takeda, Takanori Itoh, and Toru Asaka, Science and Technology of Advanced Materials: Methods 1, 24 (2021).
   DOI:10.1080/27660400.2021.1909871

2. Exploring the diffusion mechanism of Li ions in different modulated arrangements of La(1-X)/3LixNbO3 with fitted force fields obtained via a metaheuristic algorithm
   Zijian Yang, Robyn E. Word, Naoto Tanibnata, Hayami Takeda, Masanobu Nakayama, and Ryo Kobayashi, Solid State Ionics 366–367, 115662 (2021).
   DOI:10.1016/j.ssi.2021.115662

3. Molecular Dynamics Simulation of Li-Ion Conduction at Grain Boundaries in NASICON-Type LiZr2(PO4)3 Solid Electrolytes
   Koki Nakano, Naoto Tanibnata, Hayami Takeda, Ryo Kobayashi, Masanobu Nakayama, and Naoki Watanabe, J. Phys. Chem. C 125, 23604 (2021).
   DOI:10.1021/acs.jpcc.1c07314

4. Density Functional Theory and Machine Learning-Based Analyses for Improved Surface Stability of a BaTiO3-Coated LiCoO2 Positive Electrode Material
   Kunihiro Ishida, Naoto Tanibnata, Hayami Takeda, Masanobu Nakayama, Takashi Teranishi and Naoki Watanabe, Phys. Status Solidi B 2021, 2100526 (2021).
   DOI:10.1002/pssb.202100526

5. Chemical Composition Data-Driven Machine-Learning Prediction for Phase Stability and Materials Properties of Inorganic Crystalline Solids
   Taruto Atsumi, Kosei Sato, Yudai Yamaguchi, Masato Hamaie, Risa Yasuda, Naoto Tanibnata, Hayami Takeda, Masanobu Nakayama, Masayuki Karasuyama and Ichiro Takeuchi, Phys. Status Solidi B 2022, 2100525 (2022).
   DOI:10.1002/pssb.202100525

OGUCHI, Tamio [2000 (B), 500 (C)] (330)
— *Electron Theory on Secondary-Battery Materials*

1. Tavorite-type orthorhombic A_xVPO$_4$F (A = Li, Na) for novel high-voltage cathodes in rechargeable batteries
   Huu Duc Luong, Van An Dinh, Hiroyoshi Momida, Tamio Oguchi, J. Alloys Compd. **875**, 159963 (2021).

2. CrySPY: a crystal structure prediction tool accelerated by machine learning
   Tomoki Yamashita, Shinichi Kanehira, Nobuya Sato, Hiori Kino, Kei Terayama, Hikaru Sawahata, Takumi Sato, Futoshi Utsuno, Koji Tsuda, Takashi Miyake, Tamio Oguchi, Sci. Technol. Adv. Mater.: Methods **1**, 87 (2021).

3. Atomic-layer stacking dependence of the magnetocrystalline anisotropy in Fe-Co multilayer thin films at MgO(001) interface
   K. Nakamura, K. Nozaki, K. Hayashi, A.-M. Pradipto, M. Weinert, T. Oguchi, J. Magn. Magn. Mater. **537**, 168175 (2021).

4. Electric-field tuning of magnetic properties of bilayer VI$_3$: A first-principles study
   Thi Phuong Thao Nguyen, Kunihiko Yamauchi, Tamio Oguchi, Danila Amoroso, Silvia Picozzi, Phys. Rev. B **104**, 014414 (2021).

5. First-Principles Study on Cathode Properties of Li$_2M$TiO$_4$ and Na$_2M$TiO$_4$ (M = V, Cr, Mn, Fe, Co, Ni)
   Kunihiko Yamauchi, Hiroyoshi Momida, Tamio Oguchi:, J. Phys. Soc. Jpn. **91**, 034704 (2022).

6. Understanding doping effects on P2 Na$_x$Mn$_{1-y}M_y$O$_2$ (M=Li, Mg, Al, Ti, V, Cr, Fe, Co, Ni) cathode materials for Na-ion batteries
   Huu Duc Luong, Hiroyoshi Momida, Van An Dinh, Tamio Oguchi, Phys. Rev. Mater. **6**, 015802 (2022).

7. Performance and reaction mechanisms of tin compounds as high-capacity negative electrodes of lithium and sodium ion batteries
   Hiroki Kotaka, Hiroyoshi Momida, Tamio Oguchi, Mater. Adv. **3**, 2793 (2022).

8. Spin-Polarized Band Structure in MoTe$_2$/Bi$_2$Se$_3$ Heterostructure Designed from First Principles
   Kunihiko Yamauchi, Ryoma Shimazu, Tamio Oguchi, J. Phys. Soc. Jpn. **91**, 044705 (2022).

9. Insight into anisotropic magnetocaloric effect of CrI$_3$
   Hung Ba Tran, Hiroyoshi Momida, Yu-ichiro Matsushita, Koun Shirai, Tamio Oguchi, Acta Mater. **231**, 117851 (2022).

10. Effect of magnetocrystalline anisotropy on magnetocaloric properties of an AlFe$_2$B$_2$ compound
    Hung Ba Tran, Hiroyoshi Momida, Yu-ichiro Matsushita, Kazunori Sato, Yukihiro Makino, Koun Shirai, Tamio Oguchi, Phys. Rev. B **105**, 134402 (2022).

OSHIYAMA, Atsushi [10000 (B), 1400 (C)] (42)
— *Quantum-theory-based multiscale simulation for next-generation power devices*

1. Gallium-gallium weak bond that incorporates nitrogen at atomic steps during GaN epitaxial growth
   K. M. Bui, K. Shiraishi and A. Oshiyama, Appl. Surf. Sci. **557**, 149542 (2021).

2. Microscopic mechanism of adatom diffusion on stepped SiC surfaces revealed by first-principles calculations
   K. Seino and A. Oshiyama, Appl. Surf. Sci. **561**, 149927 (2021).

3. Defect-free interface between amorphous $(Al_2O_3)_{1-x}(SiO_2)_x$ revealed by first-principle molecular dynamics simulations
   K. Chokawa, K. Shiraishi and A. Oshiyama, Appl. Phys. Lett. **119**, 011602 (2021).

4. Order-N orbital-free density-functional calculations with machine learning of functional derivatives for semiconductors and metals
   F. Imoto, M. Imada adn A. Oshiyama, Phys. Rev. Research **3**, 033198 (2021).

SAITO, Susumu [2000 (B), 200 (C)] ()
— *Electronic properties and materials design of stacked B-C-N atomic layers for next-generation devices*

SHIBA, Hayato [4000 (B), 700 (C)] (325)
— *Interfacial tension of dilute electrolyte liquid: large-scale molecular simulation study*
— *Ion dissociation and association in dilute electrolyte liquid: long-time molecular dynamics study*

1. Enhancing efficient computation of long-wavelength relaxation dynamics in a 2D liquid involving millions of particles
   H. Shiba J. Phys: Conf. Ser. **2207**, 012026 (2022).
   DOI:10.1088/1742-6596/2207/1/012026

2. グラフニューラルネットワークによる長時間分子動力学予測と性能評価
   芝隼人, 下川辺隆史研究報告ハイパフォーマンスコンピューティング **2022-HPC-183**, No.22 (2022).

Data Repository
PyTorch Geometric (PyG) implementation of BOnd TArgetting Network (BOTAN, 牡丹)
https://github.com/h3-Open-BDEC/pyg_botan

SUGINO, Osamu [2000 (B), 200 (C)] (45)
— *Design of oxide electrocatalyst for next-generation fuel cells*

1. Machine-learning-based exchange correlation functional with physical asymptotic constraints
   R Nagai, R Akashi, O Sugino, Phys. Rev. Research 4, 013106 (2022).
   DOI:10.1103/PhysRevResearch.4.013106

2. Optical representation of thermal nuclear fluctuation effect on band-gap renormalization
   Kohei Ishii, Jun Haruyama, Osamu Sugino, Phys. Rev. B 104, 245144 (2021).
   DOI:10.1103/PhysRevB.104.245144

3. Functional-renormalization-group approach to classical liquids with short-range repulsion: A scheme without repulsive reference system
   Takeru Yokota, Jun Haruyama, Osamu Sugino, Phys. Rev. E 104, 014124 (2021).
   DOI:10.1103/PhysRevE.104.014124

TAKETSUGU, Tetsuya [4000 (B), 700 (C)] (332)
— *Ab initio study toward abundant element nanocatalysts with less precious metals*

1. Catalytic Oxidative Dehydrogenation of Light Alkanes over Oxygen Functionalized Hexagonal Boron Nitride
   S. Kumar, A. Lyalin, Z. Huang, and T. Taketsugu ChemistrySelect, **7**, e202103795 (2022).
   DOI:10.1002/slct.202103795

WASHIZU, Hitoshi [2000 (B), 500 (C)] (339)
— *Search for the optimum state of the ionic liquid at the solid electrolyte interface*

YAMADA, Atsuo [2000 (B), 200 (C)] (69)
— *Theoretical Analysis of Anion Insertion Mechanism into Conductive Carbon*

1. Soft X-ray Emission Studies on Hydrate-Melt Electrolytes
   T. Shimada, N. Takaneka, E. Watanabe, Y. Yamada, Y. T. Cui, Y. Harada, M. Okubo, A. Yamada, J. Phys. Chem. B **125**, 11534 (2021).
   DOI:10.1021/acs.jpcb.1c07246

2. Relationship between Electric Double-Layer Structure of MXene Electrode and Its Surface Functional Groups
   T. Shimada. N. Takenaka, Y. Ando, M. Otani, M. Okubo, A. Yamada, Chem. Mater. **34**, 2069 (2022).
   DOI:10.1021/acs.chemmater.1c03328

YOSHIMI, Kazuyoshi [4000 (B), 700 (C)] (327)
— *A systematic ab initio study of quasi-two-dimensional molecular conductors κ-type BEDT-TTF salts*
— *Finite temperature dependence of ab-initio Hamiltonians and its analysis for Pd(dmit) 2 Salts*

1. *Ab initio* derivation and exact-diagonalization analysis of low-energy effective Hamiltonians for β'-X[Pd(dmit)$_2$]$_2$
   Kazuyoshi Yoshimi, Takao Tsumuraya, Takahiro Misawa, Phys. Rev. Research 3, 043224 (2021).
   DOI:10.1103/PhysRevResearch.3.043224

Data Repository
physrevresearch_vol3_page043224_year2021
https://isspns-gitlab.issp.u-tokyo.ac.jp/k-yoshimi/physrevresearch_vol3_page043224_year2021

□ Doctor Theses

1. **BAE, Soungmin**
   Ab initio study of electronic structure and carrier localization in two-dimensional materials
   Yokohama National University, 2022-03

2. **CHINZEI, Koki**
   Theoretical Study on Discrete Time Crystals in Dissipative Quantum Systems
   The University of Tokyo, 2022-03

3. **IINO, Shumpei**
   Tensor network renormalization study on surface critical behavior from boundary-CFT viewpoint
   The University of Tokyo, 2022-03

4. **KAMEYAMA, Ryohei**
   Development of Crystalline Doped Oligomers as Single-molecular-weight Models for Conductive Polymers
   The University of Tokyo, 2021-09

5. **KIMURA, Kazuhiro**
   Correlation induced topological states and magnetic/electron-nematic phase transitions
   Kyoto University, 2022-03

6. **MICHISHITA, Yoshihiro**
   Non-Hermitian Aspect of Strongly Correlated Electron Systems
   Kyoto University, 2022-03

7. **NAITO, Tomoya**
   On isospin symmetry breaking in nuclear density functional theory
   The University of Tokyo, 2022-03

8. **NAKANO, Hayate**
   Study of Semiclassical Periodic Orbits in Kinetically Constrained Quantum Many-Body Systems
   The University of Tokyo, 2022-03

9. **NAKANO, Koki**
   Analysis and Exploration of NASICON-type Ion-Conductive Oxides Using Materials Simulation
   Nagoya Institute of Technology, 2022-03

10. **NAKASHIMA, Takeru**
    The fundamental studies for the exact excitation calculation; spin-orbit coupling in the all-electron mixed basis approach and normalization in quasiparticle theory by the Ward identity
    Yokohama National University, 2022-03

11. **OTA, Tadashi**
    First-principles study on ionic and electronic transport in advanced materials
    Osaka University, 2022-03

12. **PUTRA, Septia Eka Marsha**
    Importance of van Der Waals Interaction and Hydrogen Bonding in the Adsorptions of Formic Acid and Methane on Metal Surfaces:Density Functional Theory Study
    Osaka University, 2021-09

13. **SHIMADA, Tatau**
    Computational study on structure/electronic state of next-generation energy storage materials
    The University of Tokyo, 2022-03

14. **TAMEMOTO, Naoki**
    Reaction-diffusion systems coupled with biomembrane deformation
    The University of Tokyo, 2022-03

15. **WATANABE, Syunta**
    Formation and electronic structures of nanoscale defects in organic molecular solids
    Chiba University, 2022-03

16. **WONG, Yee Jie**
    Theoretical and Experimental Study on Dry Reforming of Methane Over Cobalt-Based Catalysts: Insights Into Carbon Dioxide Activation and Carbon Deposition
    Osaka University, 2022-03

17. **YAMADA, Takuto**
    Ground-state phase diagram and dynamical properties of Kitaev magnets
    University of Hyogo, 2022-03

18. **YAMAMOTO, Tsuyoshi**
    Many-body effect on quantum transport in superconducting circuits
    The University of Tokyo, 2022-03

19. **ZAHARO, Aflah**
    Atomic and electronic structures of group IV-VI two dimensional materials
    Kanazawa University, 2022-03

20. **SAWAHATA, Hikaru**
    First-principles study of topological phase transition in two dimensional materials
    Kanazawa University, 2021-03

21. **YAMAUCHI, Masataka**
    Development and Application Studies on the Generalized-Ensemble Algorithms: Stability and Aggregation of Proteins
    The Graduate University for Advanced Studies, 2021-03

□ Master Theses

1. **AKAZAWA, Daisuke**
   XAS measurements for liquid phase sugar molecules and analysis by First Principles Calculations
   The University of Tokyo, 2022-03

2. **AKIYAMA, Shuhei**
   Catalytic effect of graphene with nitrogen- and phosphorus-doped defect structures on propane dehydrogenation
   Osaka University, 2022-03

3. **AMI, Satoki**
   Density of states evaluated by machine learning for design of Ir-base alloys
   Tokyo Institute of Technology, 2022-3

4. **ARAI, Kazuaki**
   First-principles study on structure change of metal oxides induced by oxygen-vacancy charging
   Chiba University, 2022-03

5. **BANBA, Ryota**
   Theoretical study of light-element impurities at grain boundaries of α-Al2O3
   Hokkaido University, 2022-03

6. **BANNO, Hirotaka**
   An efficient method to detect collision in hard polygon systems and its applications -Diffusional characteristics and local structure analyses
   Nagoya Institute of Technology, 2022-03

7. **EGAWA, Noriyuki**
   Failure of SCAN functional for systems containing copper at different valences
   Yokohama National University, 2022-03

8. **HAMADA, Masashi**
   Structural analysis and tracking of phase transitions in Pb/Si(111)-$\sqrt{3} \times \sqrt{3}$ using total-reflection high-energy positron diffraction (TRHEPD) and data-driven science
   Waseda University, 2022-03

9. **HYODO, Ko**
   Parallelization in the code of quasi-particle self-consistent GW and electronic structure in the magnetic shape memory alloy Ni_2MnGa
   Kanazawa University, 2022-03

10. **INOUE, Naoki**
    Electronic structures of the complexes of screw dislocation and Mg and H impurities in GaN
    Nagoya University, 2022-03

11. **ISHIKAWA, Takuto**
    Theoretical study of spin Hall magnetoresistance by the quantum Monte Carlo method
    The University of Tokyo, 2022-03

12. **IWASHITA, Wataru**
    Breakdown of Amontons' Law due to precursor slip in the frictional interface of a 3d viscoelastic object
    Osaka University, 2022-03

13. **JOSHI, Ashish**
    Mott transition and Magnetism in a fragile topological insulator
    Kyoto University, 2021-09

14. **KAKIHARA, Yuito**
    Microscopic origin of slow relaxation in binary hard disk glassy systems - Correlation between hopping-chain motions and quasi-voids distribution
    Nagoya Institute of Technology, 2022-03

15. **KASHIMOTO, Takayuki**
    Mixing enthalpy for phase diagram of Ti-Al-based alloys
    Tokyo Institute of Technology, 2022-3

16. **KATO, Jyurai**
    Theoretical study on impurity/defect-induced fluctuation of tunneling currents at semiconductor pn junctions
    Chiba University, 2022-03

17. **KITAYA, Kaito**
    Molecular dynamics study of a nano-scale β-type Stirling engine - Stable conditions and thermal efficiency
    Nagoya Institute of Technology, 2022-03

18. **KOGURE, Shingo**
    A series expansion study for magnon spectrum of the q=0 state in the kagome-lattice Heisenberg antiferromagnet
    Tokyo University of Science, 2022-03

19. **KUTSUZAWA, Taito**
    Large-scale sparse-matrix diagonalization study of many-body localization in disordered systems
    The University of Tokyo, 2022-03

20. **LORTARAPRASERT, Chayaphol**
    Quantitative prediction of thermoelectrics properties by machine learning
    The University of Tokyo, 2022-03

21. **MACHIDA, Narumi**
    First-principles analysis of stearic acid adsorption on calcite (104) surface
    Okayama University, 20022-03

22. **MASUOKA, Shino**
    Structural dynamics analysis of a cyanobacterial alkane-producing enzyme by molecular dynamics simulations
    The University of Tokyo, 2022-03

23. **MATSUMOTO, Sairi**
    Rational design of neutralizing antibodies against the receptor-binding domain of the SARS-CoV-2 Spike protein
    The University of Tokyo, 2022-03

24. **MASUMOTO, Takeyoshi**
    Coarse-grained Molecular Dynamics Simulations for Strain Induced Crystallization in Slide-Ring Gels
    The University of Tokyo, 2022-03

25. **MATSUMOTO, Yuma**
    Research of Kondo Effect in Two-Orbital Anderson Model Dynamically Coupled with Local Jahn-Teller Phonons
    Tokyo Metropolitan University, 2022-03

26. **MATSUTANI, Kenta**
    Pressure-induced structural transition in GeO2 glassAnalysis by experimental data and machine learning potential molecular dynamics
    Yamagata University, 2022-03

27. **MOTOHASHI, Mikio**
    Theoretical study for effects of Dzyaloshinskii-Moriya interaction and bond randomness in the spherical kagome system W72V30
    Tokyo University of Science, 2022-03

28. **MUGITA, Daigo**
    Study on microscopic mechanism of equilibration and its efficiency with event-driven algorithms
    Nagoya Institute of Technology, 2022-03

29. **MURAKAMI, Chika**
    Phase separation and stress field induced by the motility of self-propelled particles
    Ibaraki University, 2022-03

30. **NAKAMURA, Katsumi**
    Judging the phase-transition order using the non-stochastic steepest descent method
    Ehime University, 2022-03

31. **NGUEYN, Bao Anh Trinh**
    Density Functional Theory-based research on Spin filtering in Electron transport through Chiral Molecules
    Osaka University, 2022-03

32. **NISHIMOTO, Akira**
    First-principles study of Fermi-level depinning at simple metal/Ge interfaces
    Chiba University, 2022-03

33. **NISHIMURA, Takehiro**
    First-Principles Study of Charging Effect on Defects in Strained SiO2
    Shimane University, 2022-03

34. **OKAMOTO, Junichi**
    Study on Cu diffusion in amorphous Ta_2O_5 containing H_2O using machine-learning potentials
    The University of Tokyo, 2022-03

35. **SATO, Masanori**
    First-principles study of atomic and molecular adsorption on the Ag-In-Yb quasicrystal surface
    Kagoshima University, 2022-03

36. **SERRAON, Ace Christian Feraren**
    Prospecting the Electrochemical Nitrogen Reduction Reaction(e-NRR) Catalysis on Alkaline Earth Atom Doped Graphenes via Density Functional Theory Calculation
    Osaka University, 2022-03

37. **SHIMADA, Takanori**
    First-principles study on adsorption geometries and electronic states of phthalocyanine on the Cu(100) surface
    Osaka University, 2022-03

38. **SHIMIZU, Kotaro**
    Theoretical study on control of topological spin textures based on spin moiré picture
    The University of Tokyo, 2021-03

39. **SHINADA, Koki**
    Research on nonlinear responses in strongly correlated systems
    Kyoto University, 2022-03

40. **SHIOTA, Tomoya**
    First principles calculations of dynamical phenomena on Si and Ge(001) surfaces
    Kyushu University, 2022-03

41. **SOFI, Nurul Ainu**
    Active Sites of Pt single-atom catalyst supported on N-doped Graphene
    Osaka University, 2021-09

42. **SUGITA, Koichiro**
    First principles calculation of nitride MXenes
    Yokohama National University, 2022-03

43. **SUZUKI, Ken**
    Electronic structures and modulation spectroscopic properties of LiNbO2 thin films
    University of Fukui, 2022-03

44. **TAKAGI, Daichi**
    First-principles evaluation on magnetic anisotropy in antiferromagnetic Mn alloys
    Kanazawa University, 2022-03

45. **TAKAHASHI, Kazuki**
    Structure and superionic conductivity in AgI-As2Se3 glasses-Molecular dynamics analysis based on first-principles calculations and machine learning force fields
    Yamagata University, 2022-03

46. **TAKAHASHI, Masahiro**
    Topological nematic phase transition in Kitaev magnets and Majorana zero mode trapped in vacancies
    Osaka University, 2022-03

47. **TAKEHANA, Hiroki**
    Interaction between alkali metals and diamond and its application to diamond machining
    Hokkaido University, 2022-03

48. **TAMAGAKI, Yuya**
    First Principles effective Hamiltonian of 3d / 4f Localized Electron Orbits in Nd_2CuO_4
    Osaka University, 2022-03

49. **TAN, Beatriz Andrea Choi**
    Magnetism and Semiconducting Behavior in NiS, and NiO:a Density Functional Theory-Based Investigation
    Osaka University, 2021-09

50. **UEHARA, Taiga**
    Quantum Monte Carlo study on Neel temperature in quasi-two-dimensional honeycomb lattice antiferromagnets
    University of the Ryukyus, 2022-03

51. **YAMAGUCHI, Shota**
    Theoretical study on zinc phthalocyanines by van der Waals density functional theory
    University of the Ryukyus, 2022-03

52. **YAMAGUCHI, Takuma**
    Electronic structures and vibrational properties of YO monoxide thin films
    University of Fukui, 2022-03

53. **YOKOO, Syota**
    First-principles exploration of permanent-magnet materials
    Tokyo Institute of Technology, 2022-3

54. **YOSHIKAWA, Yuki**
    Accuracy verification and improvement of machine-learning potentials based on deep learning models
    The University of Tokyo, 2022-03

55. **YOSHIMURA, Masataka**
    Improving Magnets photodimerizers for subcellular optogenetics by computational design
    The University of Tokyo, 2022-03

56. **YOSHINARI, Hiroto**
    Facet Dependence of Photocatalytic Activity in Anatase TiO_2 by Electronic Structure Calculation
    Ibaraki University, 2022-03

57. **YUNITASARI, Sefty**
    Studies on electronic structures of nanographene using band unfolding method
    Kanazawa University, 2021-09

58. **ZHANG, Yaotang**
    First-principles study of energy-saving materials
    Kanazawa University, 2022-03